Functionalized and Conformationally Stable Monkey Saddles as Building Blocks for Organic Cages

Simone Felicia Ebel

2026

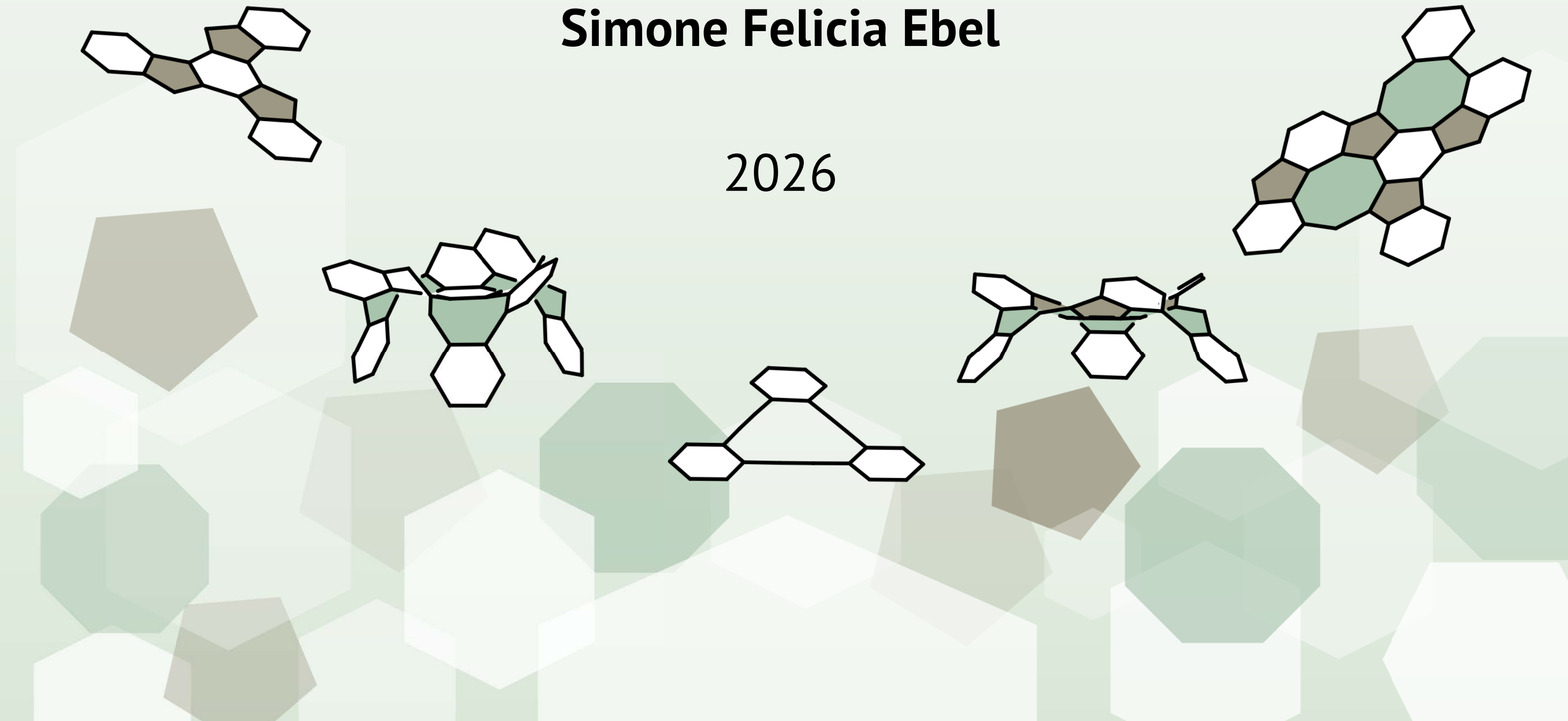

INAUGURAL DISSERTATION

to obtain the academic degree
Doctor rerum naturalium (Dr. rer. nat.)
of the combined faculties of mathematics, engineering sciences,
and natural sciences of Heidelberg University

by

Simone Felicia Ebel

born in Sulzbach-Rosenberg

2026

Date of the defence: February 6, 2026

Functionalized and Conformationally Stable Monkey Saddles as Building Blocks for Organic Cages

First referee	Prof. Dr. Michael Mastalerz
Second referee	Prof. Dr. Milan Kivala

The experimental and computational work presented within this dissertation was carried out from April 2021 to April 2025 under the supervision of Prof. Dr. Michael Mastalerz at the *Institute of Organic Chemistry* at *Ruprecht-Karls-Universität Heidelberg* and the *Max-Planck-Institut für Kohlenforschung* in *Mülheim an der Ruhr* hosted by Prof. Dr. Alois Fürstner. Some of the described results were obtained by the students Julius Alexander Guenther, Franziska Martina Fies (née Dürr), and Sarah Schott as part of their bachelor's theses under my supervision.

Parts of this dissertation have already been published:

S. F. Ebel, F. Rominger, M. Mastalerz, *Org. Lett.* **2025**, *27*, 7944-7949: "Embedding a Planar Antiaromatic Cyclooctatetraene into a Truxene-Derived Polycyclic Aromatic Hydrocarbon".

S. F. Ebel^{+}, T. Kirschbaum^{+}, F. Rominger, M. Mastalerz, *Helv. Chim. Acta* **2024**, *107*, e202400158: "Suppressing Inversion of a Chiral Polycyclic Aromatic Aza Monkey Saddle by Molecular Editing". $^{+}$: equal contributions.

Talks:

S. F. Ebel, M. Mastalerz, 27. Tag der Organischen Chemie an der Universität Stuttgart (TOCUS), 2024, Stuttgart: "Chiral Polycyclic Hydrocarbons with Monkey Saddle Structure".

S. F. Ebel, M. Mastalerz, Conjugated Oligomers and Polymers (KOPO), 2022, Bad Honnef: "Monkey Saddles as Precursor for Tetrameric Organic Cages".

Abstract

Organic cages are well-defined molecular entities with internal cavities that facilitate a variety of applications, including the separation and storage of chemicals, in particular of gases. In this dissertation, triptycene and so-called monkey saddles – truxene-based, negatively curved polycyclic aromatic hydrocarbons in which three pentagons are fused with three octagons – were explored as building blocks for the construction of shape-persistent organic cages by alkyne metathesis. For triptycene, the previously prepared alkyne metathesis catalyst was initially tested on the generation of the respective hexadehydro[12]annulene cage subunit, and the reversibility of this reaction was scrutinized through scrambling experiments. For the monkey saddle, an alkyne metathesis catalyst screening was performed in collaboration with the Fürstner group at the Max-Planck-Institut für Kohlenforschung. Nevertheless, the racemic nature of the substrate likely impeded successful cage formation, while its configurational instability under alkyne metathesis reaction conditions simultaneously precluded the use of enantiopure material.

This challenge motivated the second major goal of this thesis: the development of conformationally stable, functionalized monkey saddles. Building on the inversion stability observed for the so-called chromene monkey saddle, both post- and pre-functionalization strategies were pursued. Moreover, the results of different computational methods were benchmarked against experimental data to reliably predict the barrier heights of monkey saddles. This computational study further revealed that substitution at either the cyclooctatetraene or benzene units could significantly increase the inversion barrier. Consequently, diverse synthetic approaches were explored, whereby functionalization of the benzene rings was ultimately achieved, and the target compound's racemization behavior was experimentally analyzed.

The introduction of this specific substitution pattern also led to the isolation of a compound, in which the intramolecular construction of a dibenzofuran moiety forced the adjacent cyclooctatetraene ring into planarity. The structure was unambiguously confirmed by single-crystal X-ray diffraction. To gain deeper insight into the formation mechanism, deuterium labeling experiments and quantum-chemical calculations were carried out. Finally, the antiaromatic character of the planar cyclooctatetraene was investigated through a combination of ^{1}H NMR spectroscopy and DFT studies.

Overall, this dissertation explores avenues for the formation of alkyne-based cages and establishes essential synthetic and conceptual fundamentals for the design of conformationally stable, functionalized monkey saddles. These systems represent promising building blocks for the preparation of chiral three-dimensional architectures reminiscent of carbon schwarzites.

German Abstract

Organische Käfige sind klar definierte molekulare Einheiten mit inneren Hohlräumen, die eine Vielzahl von Anwendungen ermöglichen, darunter die Trennung und Speicherung chemischer Substanzen, insbesondere von Gasen. In dieser Dissertation wurden Triptycen und sogenannte Affensättel – ein auf Truxen basierender, negativ gekrümmter polyzyklischer aromatischer Kohlenwasserstoff, in dem drei Fünfringe von drei Achtringen umgeben sind – als Bausteine für die Bildung von formstabilen organischen Käfigen mittels Alkinmetathese untersucht. Für Triptycen wurde der hergestellte Alkinmetathese-Katalysator zunächst zur Darstellung der Hexadehydro[12]annulen-Käfiguntereinheit erprobt; die Reversibilität dieser Reaktion wurde anschließend durch Austausch-Experimente überprüft. Für den Affensattel erfolgte ein Alkinmetathese-Katalysatoren-Screening in Zusammenarbeit mit der Fürstner Gruppe am Max-Planck-Institut für Kohlenforschung. Nichtsdestoweniger verhinderte die razemische Natur des Substrates vermutlich eine erfolgreiche Käfigbildung, während seine Konfigurationsinstabilität unter den Bedingungen der Alkinmetathese zugleich den Einsatz von enantiomerenreinem Material ausschloss.

Aus dieser Hürde ergab sich das zweite Hauptziel dieser Arbeit: die Synthese konformationsstabiler, funktionalisierter Affensättel. Da sich der sogenannte Chromen-Affensattel bereits als inversionsstabil erwiesen hatte, wurden sowohl post- als auch präsynthetische Funktionalisierungen verfolgt. Zudem wurden die Ergebnisse verschiedener quantenchemischer Methoden mit experimentellen Daten verglichen, um eine zuverlässige Vorhersage der Inversionsbarrieren von Affensätteln zu gewährleisten. Dabei zeigte sich, dass Substitutionen an den Cyclooctatetraen- oder Benzoleinheiten die Konformationsstabilität signifikant erhöhen könnten. Infolgedessen wurden mehrere Syntheserouten getestet, wobei eine gezielte Funktionalisierung der Benzolringe gelang und das Razemisierungsverhalten der Zielverbindung experimentell analysiert wurde.

Die Einführung des gewünschten Substitutionsmusters führte außerdem zur Isolierung einer Verbindung, in der eine intramolekulare Dibenzofuran-Bildung den benachbarten Cyclooctatetraen-Ring in eine planare Konformation zwang. Die Struktur konnte eindeutig durch Einkristall-Röntgenbeugung bestätigt werden. Um den Bildungsmechanismus besser zu verstehen, wurden Deuterium-Markierungsexperimente sowie quantenchemische Berechnungen durchgeführt. Zuletzt wurde der antiaromatische Charakter des planaren Cyclooctatetraens mittels ^{1}H-NMR-Spektroskopie in Kombination mit DFT-Studien bestätigt.

Insgesamt untersucht diese Dissertation Möglichkeiten zur Bildung von Alkin-basierten Käfigen und legt wesentliche synthetische und konzeptionelle Grundlagen für das Design von konformationsstabilen, funktionalisierten Affensätteln. Solche Systeme stellen vielversprechende Bausteine für die Erzeugung chiraler drei-dimensionaler Architekturen dar, die strukturell an Kohlenstoff-Schwarzite erinnern.

Table of Contents

1 Introduction

1.1 Preface

Porosity refers to the presence of void spaces within a material and is defined as the ratio of pore volume to the total volume.[1] Materials with accessible pores are particularly attractive owing to their diverse applications, ranging from gas storage and separation to catalysis and optoelectronics.[2-6] Classic inorganic examples of porous materials are zeolites, whose frameworks consist of AlO_4^- or SiO_4 tetrahedra.[6-7] A hybrid class that bridges inorganic and organic chemistry is represented by metal-organic frameworks (MOFs), where small organic linkers connect transition-metal nodes into extended networks.[8-12] When analogous architectures are constructed exclusively from organic components, dynamic covalent chemistry (DCC) is typically required.[13-17] This strategy exploits the reversible formation of covalent bonds, allowing the self-correction of misalignments and enabling the system to evolve toward the thermodynamically most stable structure.[17-20] In 2005, Yaghi and coworkers employed DCC to pioneer the synthesis of covalent organic frameworks (COFs), forming extended lattices of benzene or triphenylene units linked by boroxine rings and boronate esters, respectively.[21]

Building on these seminal contributions, research soon expanded toward the development of discrete porous organic molecules, commonly referred to as organic cages.[22-27] Unlike MOFs and COFs, cages are often soluble in organic solvents, which facilitates their characterization by standard solution-phase techniques such as NMR spectroscopy and mass spectrometry.[28-31] Their solubility also broadens the scope of potential applications, including thin-film deposition or co-crystallization of multiple components.[32-37] To date, most organic cages have been prepared through reversible condensation reactions, especially imine or boronic ester condensations.[38-50] More recently, however, alkyne metathesis has emerged as an alternative, with the inherent rigidity of alkynes offering a key advantage: it imparts shape persistence to the resulting cages, which in turn protects them from structural collapse and preserves their porosity.[51-52]

In the following chapters, the fundamentals of alkyne metathesis will be discussed, with emphasis on the development of alkyne metathesis catalysts, given that they are critical for the reaction's success (*Chapter 1.2: Alkyne Metathesis*). Selected literature examples will then highlight the potential of alkyne metathesis in the synthesis of shape-persistent organic cages (*Chapter 1.3: Organic Cages by Alkyne Metathesis*). Regarding possible cage-building blocks, curved polycyclic aromatic hydrocarbons (PAHs) are of special interest, as they can be considered cutouts of carbon schwarzites – hypothetical conjugated carbon networks predicted to exhibit remarkable properties (*Chapter 1.4: Negatively Curved Polycyclic Aromatic Hydrocarbons*). The group of Mastalerz has contributed to this field by establishing a new family of curved PAHs, termed *monkey saddles*, which are promising candidates for the assembly of conjugated organic cages, and their current state of research is summarized (*Chapter 1.5: Monkey Saddles*). Lastly, the introduction concludes with an overview of planar cyclooctatetraene (COT) derivatives, owing to their relevance to the final project presented in this dissertation (*Chapter 1.6: Planar Cyclooctatetraenes*).

1.2 Alkyne Metathesis

In 1968, Pennella, Banks, and Bailey discovered the interchange of alkynes – specifically the conversion of 2-pentyne to 2-butyne and 3-hexyne – employing a tungsten trioxide/silica mixture.[53] This reaction was the first example of a heterogenous alkyne metathesis, though it required high temperatures (250-400 °C) and was hampered by competing polymerization of the substrate.[53] The first homogeneous variant followed in 1974 by Mortreux and Blanchard, who observed equilibration between *p*-toylphenylacetylene (**1**) and the products 1,2-diphenylacetylene (**2**) and 1,2-di-*p*-tolylethyne (**3**) using Mo(CO)$_6$ with resorcinol as catalyst system at 160 °C (**Scheme 1.1A**).[54]

Building on these findings, Katz and McGinnis proposed a mechanism for alkyne metathesis analogous to the Chauvin mechanism for olefin metathesis (**Scheme 1.1B**).[55-56] The steps in the cycle involve a [2+2] cycloaddition of the alkyne substrate with the metal-carbon triple bond forming a metallacyclobutadiene. A subsequent cycloreversion releases the product. Iteration of this process with the cycloreversion along the other metallocycle bond delivers a second product while restoring the initial metal alkylidyne.[55, 57] Schrock and coworkers later provided experimental support for this mechanism.[58-60]

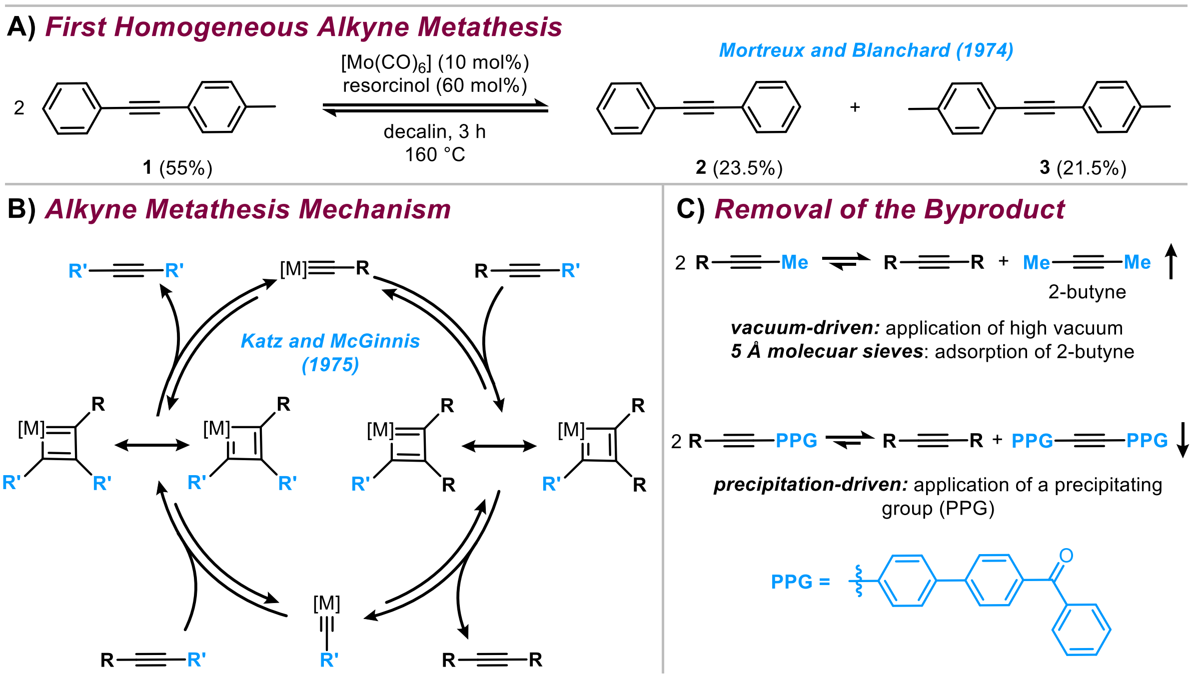

Scheme 1.1: A) First homogeneous alkyne metathesis discovered by Mortreux and Blanchard in 1974. They observed an equilibrium between the starting material *p*-tolylphenylacetylene (**1**) and the products 1,2-diphenylacetylene (**2**) and 1,2-di-*p*-tolylethyne (**3**).[54] **B)** Mechanism of alkyne metathesis proposed by Katz and McGinnis in 1975.[55] **C)** Different strategies to remove the byproduct of an alkyne metathesis reaction from the reaction mixture, shifting the equilibrium toward the product side.[61-62]

Since alkyne metathesis is a reversible reaction and generates two products per cycle, continuous removal of one product is essential to drive the conversion forward.[63-64] The first strategy to achieve this exploits methyl-capped alkynes, whereby the arising 2-butyne is removed as a volatile byproduct under high vacuum. However, this method suffers from scale-up limitations and solvent restrictions, as only high-boiling solvents can be used.[61, 64-65] In 2004, Moore and Zhang introduced the precipitation-driven approach in which a large aromatic precipitating group (PPG) was incorporated into the precursor.[61] The resulting bis(benzoyl-biphenyl)acetylene (PPG–C≡C–PPG) byproduct precipitated during alkyne metathesis, effectively shifting the equilibrium (**Scheme 1.1C**). Although this approach was scalable to gram quantities with excellent yields, drawbacks included poor atom economy, additional synthetic effort to prepare the precursor, and potential solubility issues caused by the PPG.[61, 64] The breakthrough came in 2010, when Fürstner and coworkers found that powdered 5 Å molecular sieves efficiently adsorb 2-butyne into their pores.[62] As the combination of methyl-capped alkynes with molecular sieves provided a simple and broadly applicable solution, it is now widely used as standard method for performing alkyne metathesis.[51, 66-75]

Alongside byproduct management, the catalyst is central to the success of the reaction. Mortreux-type systems remain attractive for their simplicity and commercial availability, yet they often require high temperatures and catalyst loadings in addition to a narrow functional group tolerance.[63, 76-89] In the 1980s, the group of Schrock presented several tungsten-based alkylidyne catalysts such as $(^tBuO)_3W\equiv C^tBu$, which enabled catalysis under relatively mild conditions (room temperature to 90 °C).[90-93] This complex is commercially available today, though its functional group compatibility is limited, particularly with thioethers, amines, and crown ether segments.[94-98]

Around the 2000s, the Fürstner group turned to the molybdenum-based complex **4**, which has been originally designed for the cleavage of molecular nitrogen and, as is, lacks catalytic activity for alkyne metathesis (**Scheme 1.2A**).[99-101] Treatment of **4** with dichloromethane in toluene afforded a mixture of monochloride **5** and methylidyne complex **6**, whereby the former complex accomplished the reaction with numerous internal triple bonds. In contrast, **6** was rendered inactive after one turnover of the substrate.[99-100, 102-103] Replacing dichloromethane with higher *gem*-dichloro compounds ($RCHCl_2$) furnished the catalytically active alkylidyne complexes **7** (R = Me) and **8** (R = Et).[65] In 2003, Moore and coworkers presented the so-called reductive cycle strategy, in which the monochloride species **5** was reduced with magnesium turnings to the starting material **4** while the alkylidyne complexes **6**, **7**, and **8** remained unaffected, facilitating their high-yielding syntheses (**Scheme 1.2A**).[104]

Since then, numerous ligand systems have been developed for **8**, typically forming the active alkyne metathesis catalyst *in situ* upon mixing in solution.[65, 70-71, 105-108] In 2004, the group of Moore began with *p*-nitrophenol (**9**), which opened the door to the efficient synthesis of conjugated polymers and shape-persistent macrocycles (**Scheme 1.2B**).[61, 65, 109-111] In 2011, Zhang's multidentate amine-based ligand **10** was able to improve the catalyst's lifetime, overall catalytic activity, and functional group tolerance on account of the chelate effect.[105] Concurrently, the nitrogen of the ligand strongly coordinated to the molybdenum(VI) center, reducing its Lewis acidity and thus the catalyst's activity.[105] Replacing the nitrogen with a C–H unit in ligand **11** led to the two-component catalyst **8**/**11** with unprecedented stability, retaining its catalytic activity over months in tetrachloromethane (CCl_4) solution (**Scheme 1.2B**).[71] Unfortunately, the yields obtained for the tested substrates showed a strong solvent dependence, with CCl_4 outperforming less toxic alternatives such as chloroform, toluene, or methyl *tert*-butyl ether (MTBE). Besides, **8**/**11** exhibited an excellent functional group tolerance, including substrates like benzaldehyde, pyridine, or nitrobenzene derivatives containing aldehydes, but reached its limits with propargyl alcohols and terminal alkynes.[71]

Fürstner's trisilanol ligand **12** further expanded the substrate scope and managed the conversion of alkynes bearing primary, secondary or phenolic OH groups as well as (bis)propargylic alcohol derivatives.[107] In 2021, the group of Zhang prepared the triphenylmethane-based ligand **13**, whose enhanced rigidity was envisioned to minimize the configurational entropic cost during the assembly of the catalyst system **8**/**13** (**Scheme 1.2B**).[108] Similar to its precursor **11**, the best yields were again observed with CCl_4 as solvent. On the plus side, **8**/**13** facilitated the conversion of various difficult substrates, e.g., containing formyl, nitrile or nitro groups, and it could even operate under open air.[108] Despite all these advances, the synthesis of **8** remains challenging, requiring strict exclusion of oxygen and moisture,[112] and its combination with all ligands presented, **13** excluded, also demand inert conditions for alkyne metatheses.[61, 71, 105, 107]

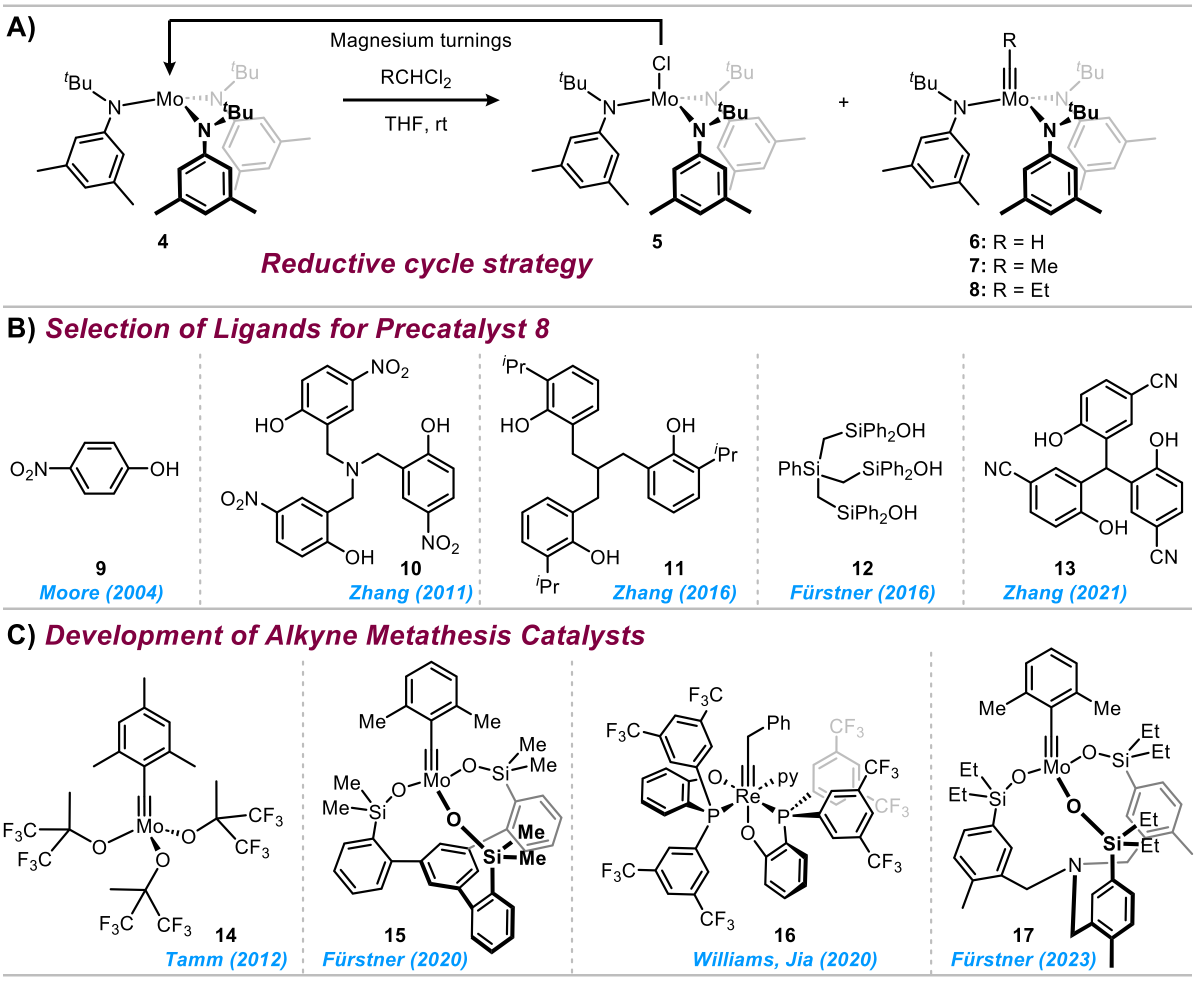
A) Reductive cycle strategy

B) Selection of Ligands for Precatalyst 8

C) Development of Alkyne Metathesis Catalysts

Scheme 1.2: Development of selected alkyne metathesis catalysts. **A)** Optimized synthesis of precatalyst **8** by the reductive cycle strategy. The complexes **6**, **7**, and **8** are resistant to reduction with magnesium. **B)** Selection of ligands, which form an active alkyne metathesis catalyst *in situ* upon mixing them with precatalyst **8**. **C)** Selection of four different alkyne metathesis catalysts designed to further increase their catalytic activity and user-friendliness.

Beyond the **8**/ligand systems, many other alkyne metathesis catalysts have emerged to date.[62, 113-117] To name a few, the group of Tamm introduced the 2,4,6-trimethylbenzylidyne complex **14**, the first catalyst to efficiently promote alkyne metathesis of selected terminal alkynes, including terminal ring-closing transformations (TRAM) of α,ω-diacetylenes (**Scheme 1.2C**).[118] In 2020, Fürstner and coworkers designed the well-defined 'canopy catalyst' **15**, notable for its scalable synthesis, tolerance toward various free OH groups or other protic sites in the substrate, and partial water stability because of the chelation.[119] That same year, Williams and Jia reported on the Re(V) alkylidyne catalyst **16**.[72] Complex **16** exhibited a remarkable stability toward air and moisture as well as a broad functional group tolerance (e.g., alcohols, amines, carboxylic acids), marking a major step toward user-friendly catalysts for alkyne metathesis.[72] Recently, the group of Fürstner revised the ligand framework of **15**, resulting in the catalyst **17**, which revealed a significantly optimized stability (storage in air over months) while preserving highest standards in terms of reactivity and selectivity (**Scheme 1.2C**).[120] These developments illustrate the steady progress in alkyne metathesis catalyst design, with emphasis on their user-friendliness, catalytic activity and functional group tolerance.

1.3 Organic Cages by Alkyne Metathesis

Dynamic covalent chemistry (DCC) has emerged as a powerful strategy for constructing elaborate three-dimensional architectures in a single step and often in high yields as the reaction reversibility allows the system to equilibrate to thermodynamic sinks.[17-20] Since alkyne metathesis (see *Chapter 1.2*) falls within the scope of DCC, it has proven to be a suitable method for synthesizing organic cages, as substantiated by several successful examples reported in the literature.[66-67, 69, 121-124] For instance, in 2011, Zhang and coworkers prepared the porphin-based precursor **18** – equipped with four precipitating groups – which was dimerized in a precipitation-driven alkyne metathesis using 16 mol% of the two-component catalyst system **8**/**10** (**Scheme 1.3**).[121] The resulting cage **19** was thermally robust and chemically resistant to water and acids. Considering that **19**'s design was originally inspired by the strong binding affinity of porphin-containing macrocycles and supramolecular cages toward fullerenes,[125-127] the cage was exposed to a mixture of C_{60} and C_{70} fullerenes, displaying a remarkable binding selectivity (>1000:1) for C_{70}.[121] Moreover, the association and dissociation of C_{70} could be reversibly modulated by acid/base treatment, enabling a selective separation of C_{70} from a fullerene mixture. Computational studies attributed this selectivity to slight host-guest distance variations, which translated into significant differences in the stabilization energies of the respective supramolecular assemblies.[121]

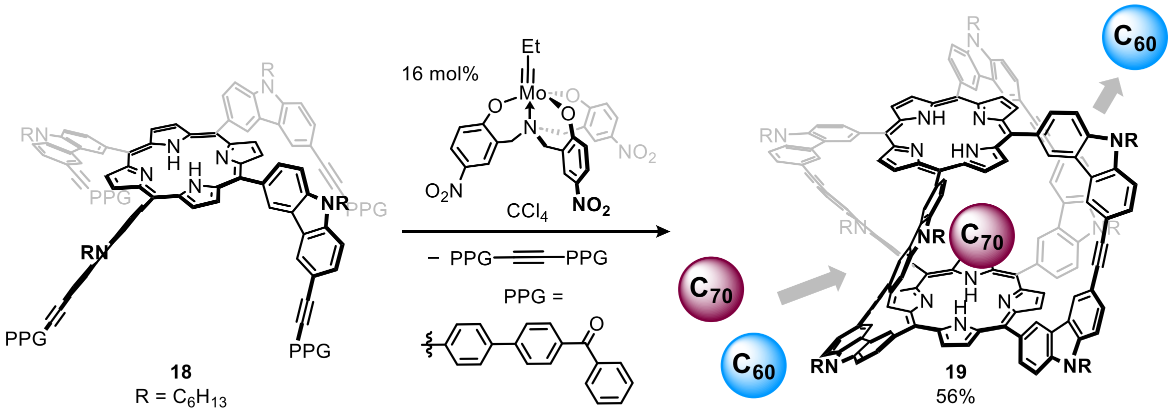

Scheme 1.3: Synthesis of the porphin-based cage **19** from precursor **18** by precipitation-driven alkyne metathesis, reported by the group of Zhang in 2011. The cage's C_{70} fullerene selectivity (>1000:1) compared to C_{60} fullerene is illustrated schematically with blue and purple spheres.

In 2015, the group of Zhang further expanded the scope of organic cages accessible *via* precipitation-driven alkyne metathesis by synthesizing the C_3-symmetrical precursor **20**, bearing either hexadecyl chains (**20a**) or *tert*-butyloxycarbonyl (BOC) groups (**20b**) (**Scheme 1.4**).[122] After the respective building blocks were subjected to alkyne metathesis at 40-50 °C, mixtures of the single cage (**21a**/**21b**) and the interlocked arylene-ethynylene cage (**22a**/**22b**) were obtained. Regarding the hexadecyl derivatives **21a** and **22a**, their similar polarities hindered their effective separation, and the products were isolated in a combined yield of 90%. In contrast, the BOC-functionalized compounds could be separated by flash column chromatography, giving **21b** in 6% and **22b** in 59% yield.[122] The interlocked cages **22a**/**22b** exhibited an excellent stability against air, moisture, and silica, and could even be stored on the benchtop without noticeable degradation. Kinetic studies of **20b**'s conversion revealed that the catenane **22b** formed predominantly within the first 30 min, while the monomeric cage **21b** did not undergo further transformation into **22b** as the reaction progressed, reflecting the relative thermodynamic stability of the two species at equilibrium. Moreover, the generation of **22b** was favored at higher monomer concentrations, whereas the use of toluene mostly resulted in the assembly of **21b**. Notably, resubjecting **22b** to alkyne metathesis in toluene partially converted it into the monomeric cage **21b**, underlining the dynamic nature of this reaction.[122] To date, **22b** remains the only interlocked cage synthesized by alkyne metathesis.

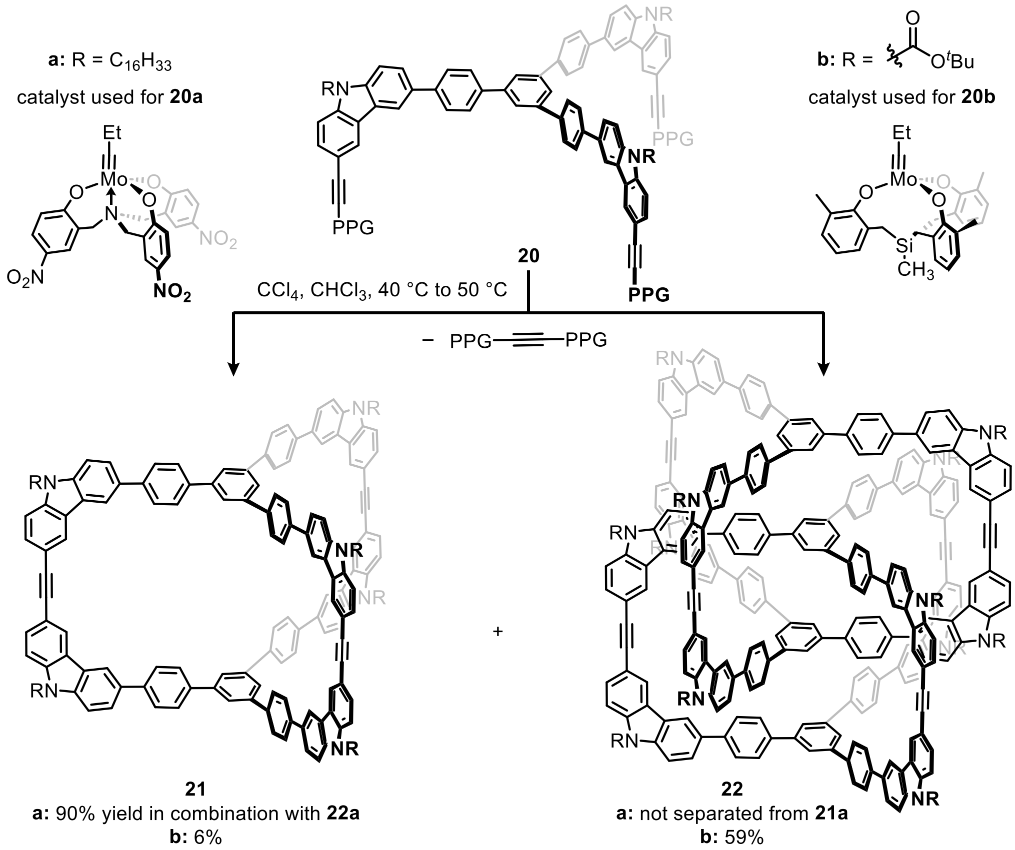

Scheme 1.4: Synthesis of the interlocked arylene-ethynylene molecular cage **22** from precursor **20** by a precipitation-driven alkyne metathesis published by the group of Zhang in 2015.

One year later, Moore and coworkers presented the tribenzylbenzene building block **23**, whose bowl-shaped geometry – with the ethyl and benzyl groups oriented in opposite directions – predisposed it toward tetrahedral cage construction (**Scheme 1.5**).[67] Alkyne metathesis of **23** was carried with the catalyst system **8**/Ph_3SiOH and 5 Å molecular sieves to scavenge the formed 2-butyne, delivering the cage **24** in quantitative yield. The unexpectedly high yield was thereby attributed to a combination of thermodynamic stability and kinetic trapping. To test this hypothesis, the authors resynthesized **24** with isopentoxy instead of ethyl substituents and examined potential scrambling of the two cages under alkyne metathesis conditions. Yet, no building blocks were interchanged during this experiment, while self-sorting of the precursors was ruled out by deliberately synthesizing the corresponding scrambled cages. These observations suggest that **24** is either exceptionally stable, creating kinetic barriers preventing its opening, or that it is a kinetically trapped intermediate rather than a product generated under thermodynamic control.[67]

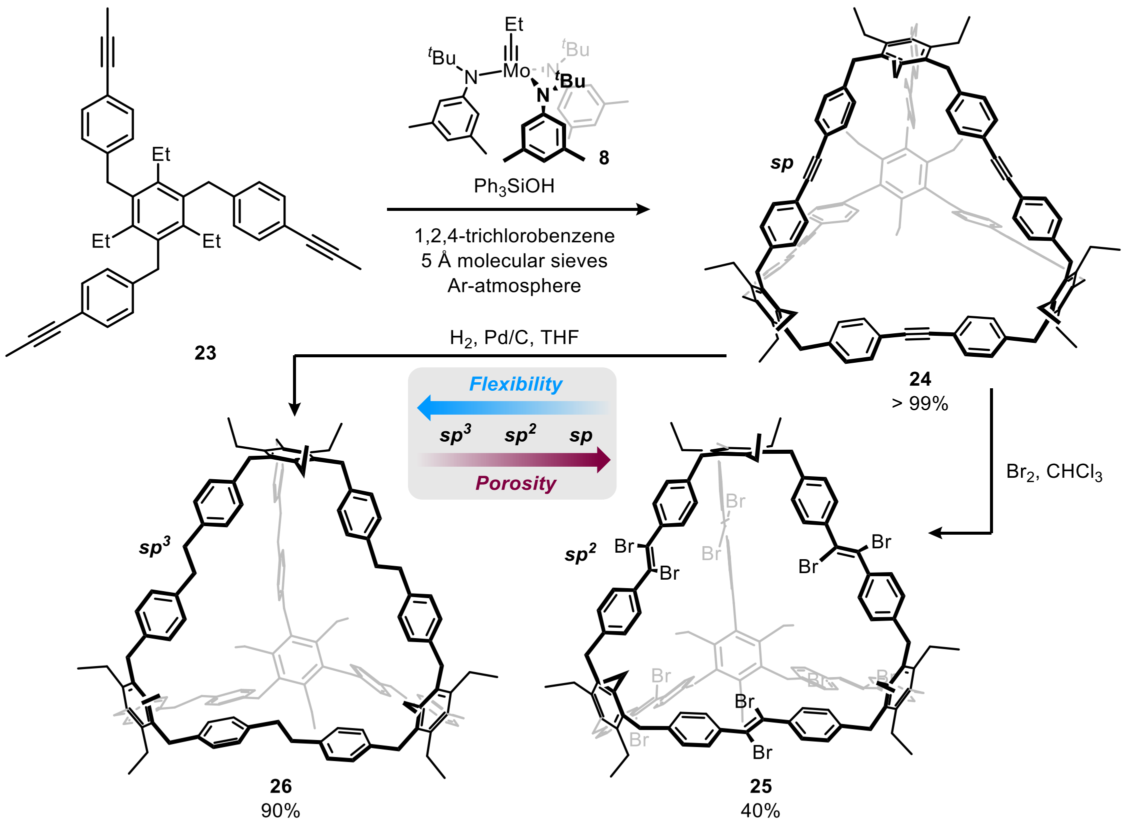

Scheme 1.5: Synthesis of the kinetically trapped tetrahedral cage **24** by alkyne metathesis and its transformation into the alkene cage **25** and alkane cage **26** developed by Moore and coworkers.

In follow-up studies, the alkyne cage **24** was transformed into the *trans*-alkene analogue **25** by bromination and the alkane cage **26** by hydrogenation of the triple bonds, respectively (**Scheme 1.5**).[52] Nitrogen adsorption experiments on **24**-**26** revealed that the porosity increased with cage rigidity (alkynyl > alkenyl > alkyl). Complementary computational investigations of the molecular motion of the individual cages further confirmed a direct correlation between porosity and shape persistency.[52]

Overall, alkyne metathesis has provided promising advances in the design of organic cages. Additionally, unlike imine or boronic ester condensations, its principal advantage lies in the inherent stability of triple bonds, which leads to highly robust cage architectures and contributes to their porosity.[42, 52, 128-129]

1.4 Negatively Curved Polycyclic Aromatic Hydrocarbons

Polycyclic aromatic hydrocarbons (PAHs) are compounds composed of multiple fused aromatic rings in which all carbon atoms are *sp*^{2} hybridized.[130] Depending on the ring sizes incorporated into the PAH framework, the overall structure can either be planar or adopt a contorted geometry, which can be classified according to their Gaussian curvature (K) (**Figure 1.1**).[131] In differential geometry, the Gaussian curvature at a point on a surface is defined as the product of two principal curvatures ($K = \kappa_1 \cdot \kappa_2$), with κ_1 and κ_2 being the minimum and maximum principal curvatures along the intersections between the surface and the normal planes. The latter are any plane containing a vector perpendicular to the surface.[131]

Three general cases can be distinguished. First, if one of the principal curvatures equals zero, the Gaussian curvature is also zero, which in molecular terms applies to planar systems such as [6]circulene (**Figure 1.1B**, **E**).[131-132] Second, when both κ_1 and κ_2 are greater than zero, a positive Gaussian curvature is obtained, giving rise to a bowl-shaped surface. In PAHs, this typically occurs through the inclusion of rings smaller than hexagons, as in [5]circulene, where the central pentagon bends the surrounding benzene units uniformly in one direction (**Figure 1.1A**, **D**).[131, 133-134] Finally, if one principal curvature is below zero, the surface exhibits a negative Gaussian curvature. Such geometries can be accessed synthetically by embedding rings larger than hexagons into the PAH core. A representative example is [8]circulene, whose central octagon adopts a tub conformation that distorts the adjacent benzene moieties out of planarity, yielding an overall saddle-shaped architecture (**Figure 1.1C**, **F**).[131, 135-139]

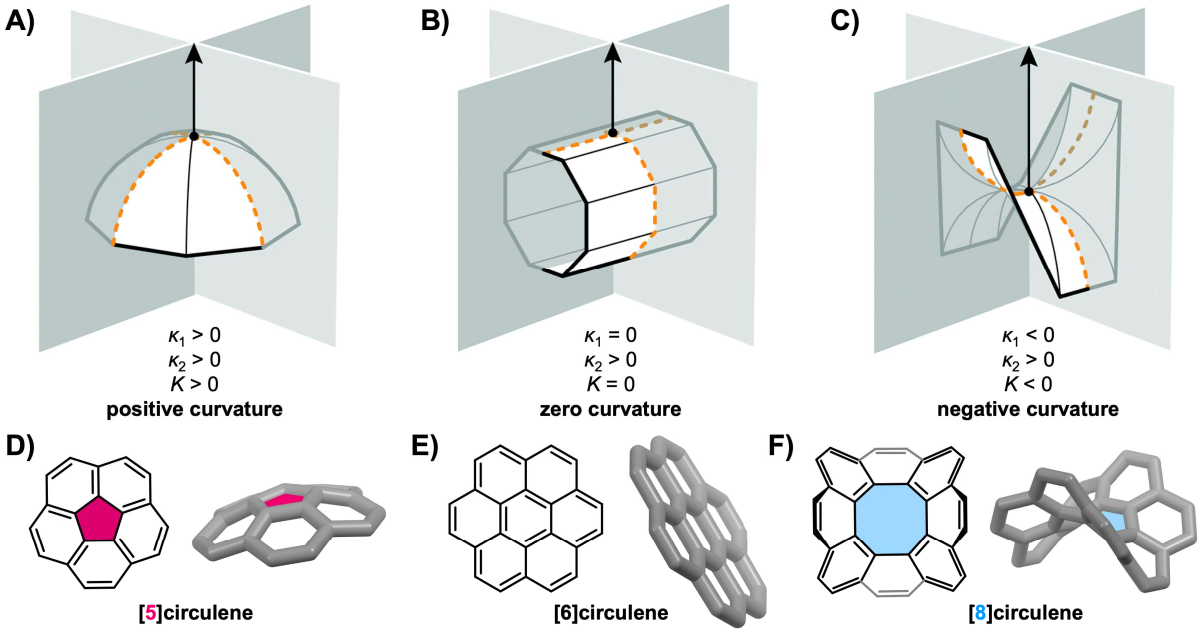

Figure 1.1: Schematic illustration of the three different types of Gaussian curvature ($K = \kappa_1 \cdot \kappa_2$) at a point (black dot) on a surface: **A)** Positive curvature illustrated by a bowl-shaped surface, **B)** zero curvature (planar structure) and **C)** negative curvature of a saddle shaped surface. The orange dashed line represents the intersection between the surface and the normal planes (grey planes). The different curvatures were exemplified with the molecules **D)** [5]circulene (CCDC 1129824),[133] **E)** [6]circulene (CCDC 1129883),[132] and **F)** [8]circulene (CCDC 938414).[135] The [8]circulene has only been synthesized with substituents on the framework, which are not shown in this figure for clarity. **A**-**C)** were adapted from reference 131 with kind permission from Copyright Clearance Center, Inc.

In 1991, Mackay and Terrones used the negative curvature induced by cyclooctatetraenes (COTs) to decorate the periodic minimal surface of H. A. Schwarz[140] with an sp^2-conjugated carbon lattice, now known as Mackay crystal.[141] Shortly thereafter, Lenosky *et al.*, as well as Vanderbilt and Tersoff, expanded this concept by employing heptagons instead of octagons, referring to these carbon networks as *schwarzites*.[142-143] Since then, numerous theoretical studies were conducted, predicting remarkable functional properties and diverse applications for schwarzites.[144] For instance, their anticipated high mechanical robustness and large specific surface area suggest utility in gas storage and separation, while extended π-conjugation across the carbon lattice adverts to energy storage applications, e.g., in batteries.[145-149] Moreover, calculations on the electronic structure indicated conducting properties ranging from insulating to metallic behavior.[150-151]

Given this intriguing set of predicted features, the experimental realization of these carbon networks has attracted considerable attention over the past decade.[136-139] Although there have been reports on the production of three-dimensional carbon materials using zeolite-templating to mimic the topology of schwarzite pores, their amorphous character prevented an unambiguous determination of the structure and atomic composition.[152-154] Consequently, research efforts have focused on bottom-up strategies, particularly the synthesis of discrete negatively curved PAHs – molecules that can be regarded as cut-outs of schwarzites – whose size is progressively expanded.[137] Nevertheless, constructing carbon frameworks containing rings of different sizes remains challenging. The following section highlights selected negatively curved PAHs, illustrating recent advances in this rapidly evolving field.

A remarkable example was published in 2013 by Itami and coworkers, who modified commercially available corannulene (**27**) by borylation and a subsequent Suzuki-Miyaura cross-coupling (**Scheme 1.6**).[155] After the resulting intermediate **28** was further exposed to a cyclodehydrogenation, also known as Scholl reaction,[156-157] the warped nanographene **29** was provided in 40% yield through the formation of five new six-membered rings and five heptagons. Single crystal analysis of **29** revealed that its structure contained five helical hexa[7]circulene moieties, which imparted chirality and led to the isolation of a racemate consisting of *MPMPM* and *PMPMP* enantiomers. However, rapid racemization precluded enantiomeric separation. Owing to its pronounced distortion, **29** exhibited several unique properties, including an improved solubility and widened band gap compared to its planar analogue, as well as fluorescence. Additionally, electrochemical studies displayed three reversible reductions and two reversible oxidations, even though compounds containing five-membered rings – such as corannulene or C_{60} fullerene – can be difficult to oxidize.[155, 158-160] This redox behavior might stem from having both five- and seven-membered rings in compound **29**.[155]

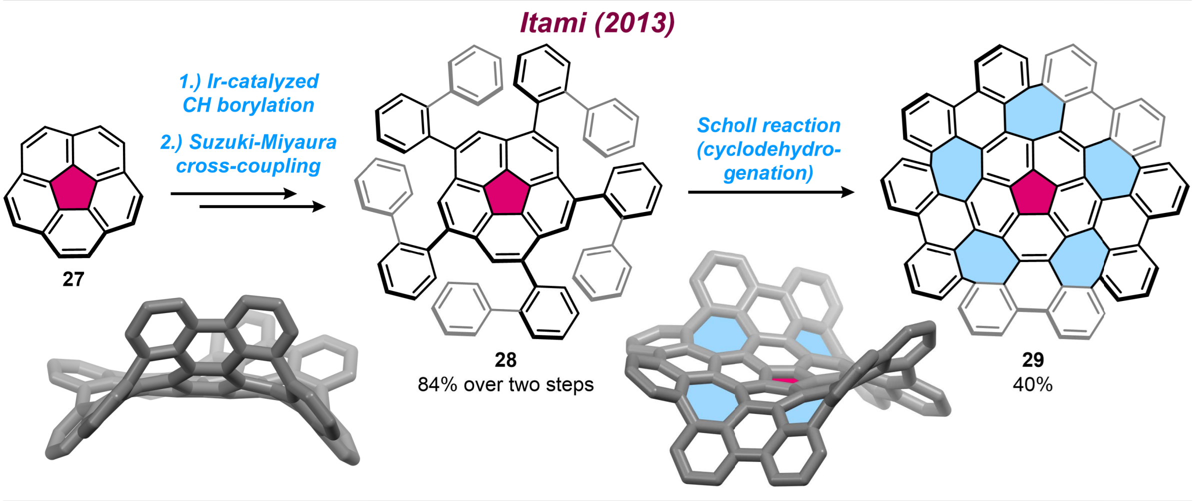

Scheme 1.6: Synthesis of the grossly-warped nanographene **29** from commercially available corannulene **27** published by Itami and coworkers in 2013. The negative curvature of **29** is illustrated by its single crystal structure (CCDC 919707).[155] For a clearer visualization, the pentagon is highlighted in pink and the heptagons in blue.

In 2019, Würthner and coworkers used a four-fold Pd-catalyzed C–C coupling between borinic acid **30** and 2,3-dibromonaphthalene (**31**) to furnish the negatively curved PAH **32** (**Scheme 1.7**).[161] X-ray diffraction analysis confirmed the generation of two heptagons, giving rise to a highly warped, saddle-shaped structure that represents an eleven-ring fragment of a carbon schwarzite. Similar to **29**, compound **32** was excellently soluble in common organic solvents, fluorescent, and could be reversibly oxidized at mild potentials.[161]

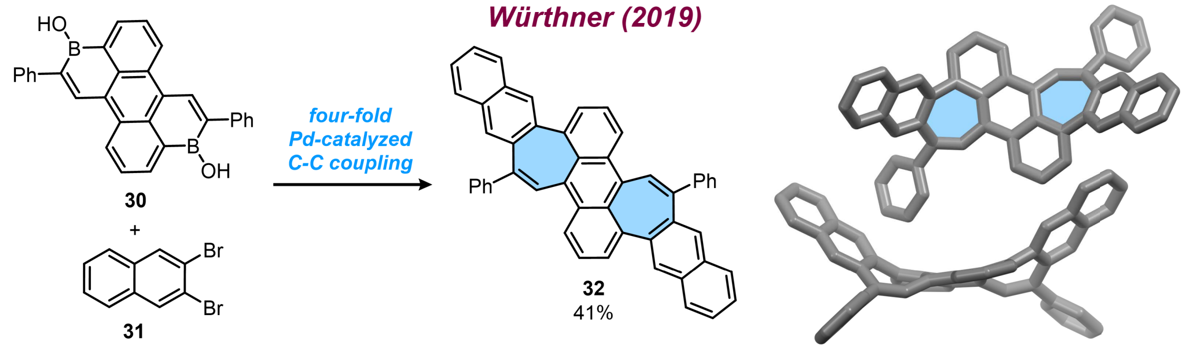

Scheme 1.7: Synthesis of the highly warped PAH **32** published by the group of Würthner in 2019. The curvature of **32** is illustrated by its single crystal structure (CCDC 1945356).[161] For a clearer visualization, the heptagons are highlighted in blue.

In 2021, the group of Campaña designed a series of hexa-*peri*-hexabenzocoronene (HBC) analogues, whose synthesis began with a Diels-Alder reaction between dibenzocyclooctyne **33** and cyclopentadienone **34**, accompanied by the elimination of carbon monoxide (**Scheme 1.8**).[162] The *tert*-butyldimethylsilyl (TBDMS) protecting group was then removed, the free hydroxy functionality oxidized, and the resulting intermediate subjected to a Scholl reaction, producing **35** in 50% yield over four steps. From compound **35**, two distinct synthetic pathways were pursued: reduction of the ketone followed by elimination provided the cyclooctatetraene-containing substance **36**, whereas an aldol condensation and subsequent Pd-catalyzed intramolecular arylation yielded **37**. All three compounds (**35**-**37**) possessed a distorted π-extended carbo[5]helicene with an embedded octagon, which imparts chirality to the molecules. After the *P*- and *M*-enantiomers were successfully separated, their enantiomeric excess decay was monitored over time using chiral high performance liquid chromatography (HPLC) and circular dichroism (CD), delivering a racemization barrier of $\Delta G^{\ddagger}$(25 °C) = 104 kJ mol^{-1} (24.8 kcal mol^{-1}) for **37**. In contrast, **35** and **36** showed neither racemization nor decomposition while heating solutions of the single enantiomers at 200 °C for 5 hours.[162] Such conformationally stable chiral nanostructures are promising candidates for applications in organic electronics.[163-165]

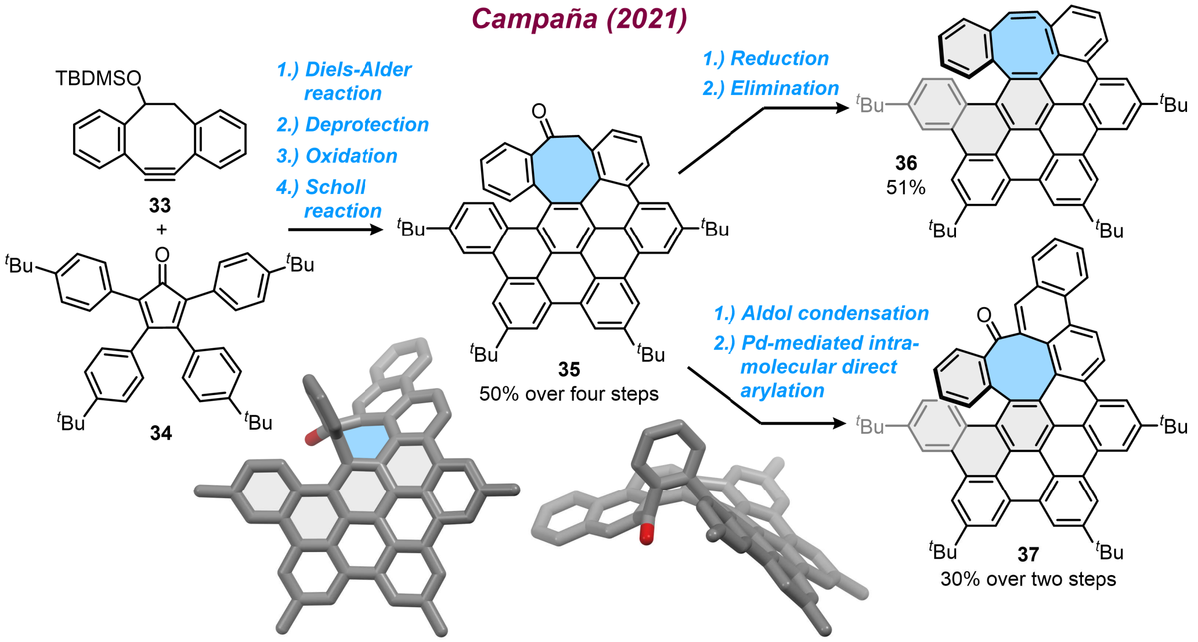

Scheme 1.8: Synthesis of the octagon-embedded carbohelicenes **35**, **36**, and **37** reported by the group of Campaña in 2021. The contortion of the helicene is pictured by the single crystal structure of **37** (CCDC 2032602).[162] The *tert*-butyl groups were shortened to methyl groups. For clearer visualization, the octagon is highlighted in blue and the benzene rings, which are part of the helicene, in light grey.

In 2023, Miao and coworkers achieved to merge the negatively curved octabenzo[8]circulene (OB8C) with two [9]cycloparaphenylene ([9]CPP) units (**Scheme 1.9**).[166] In the first step of the route, the bromides of OB8C derivative **38** were exchanged by pinacol boronic ester groups, which then underwent a Suzuki-Miyaura cross-coupling with a C-shaped paraphenylene precursor to generate intermediate **39**. As the flexibility of the OB8C moiety provided both C_{2v}- and D_2-symmetrical isomers of **39**, their subsequent exposure to an intramolecular Yamamoto coupling and reductive aromatization led to the formation of three different products: the C_{2v}-symmetrical compounds **40a** and **40b**, and the D_2-symmetrical product **40c**. Notably, **40a** combines a negatively curved scaffold with two loops, which resemble the channels in carbon schwarzites, thus marking a further step toward their bottom-up synthesis (**Scheme 1.9**).[166] It is worth mentioning that the group of Campaña published a related system in the same year, in which a heptagon-containing HBC (*hept*-HBC) was fused with a [10]CPP unit.[167] The resulting *hept*-HBC-CPP nanoring showed strong host-guest interactions with C_{60} and C_{70} fullerenes.[167]

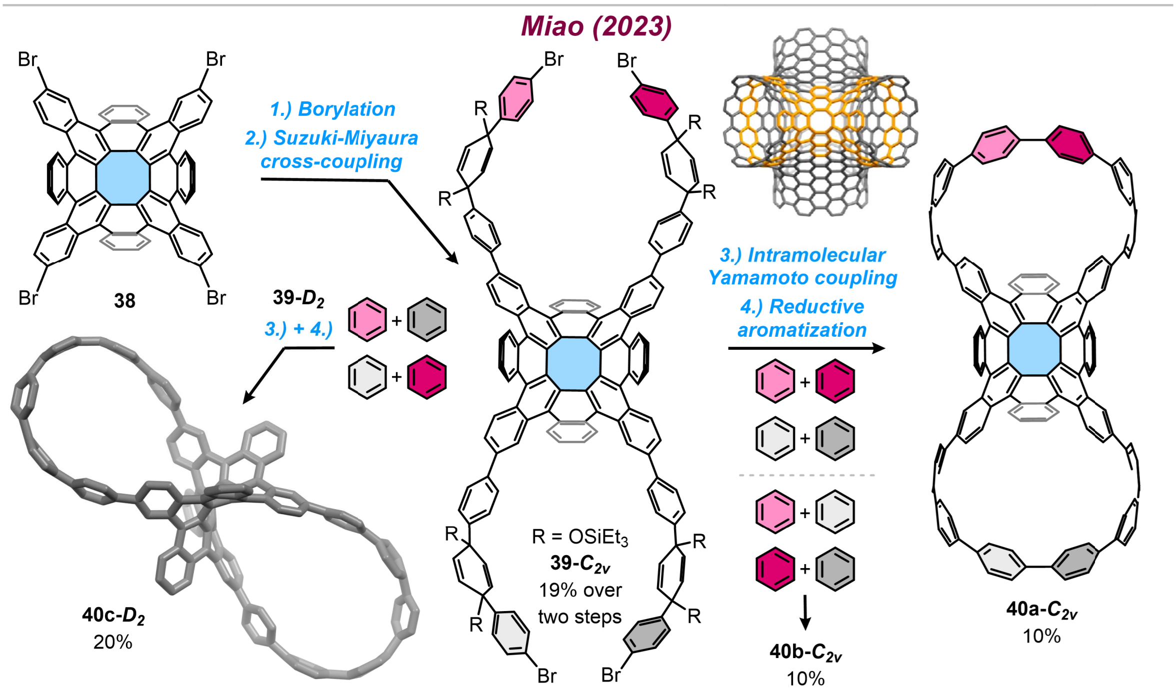

Scheme 1.9: Fusion of the octabenzo[8]circulene **38** with two [9]cycloparaphenylenes, published by the group of Miao in 2023. Intermediate **39** was obtained either as C_{2v}-symmetrical isomer, which yielded the two C_{2v}-symmetrical products **40a** and **40b** upon intramolecular Yamamoto coupling, or as a D_2-symmterical isomer, resulting in the formation of **40c**. The structure of **40c** was visualized by its single crystal structure (CCDC 2237020).[166] In compound **39-C_{2v}**, the benzene rings involved in the intramolecular Yamamoto coupling are highlighted in grey and pink, while the small colored benzene rings illustrate where the C–C bonds were ultimately formed during the Yamamoto reaction. **40a-C_{2v}** can be considered as a cut-out of a carbon schwarzite (highlighted in orange within the schwarzite unit cell). The unit cell of the carbon schwarzite was reproduced from reference 166.

In 2024, Mastalerz and coworkers prepared one of the largest schwarzite fragment reported to date: a molecular saddle corresponding to a C_{76} cut-out of the carbon lattice proposed by Lenosky *et al.* (**Scheme 1.10**).[142, 168] Its synthesis was accomplished in four steps from the tetraaryl-substituted pyrene **41**.[168] An initial iridium-catalyzed borylation selectively modified the 2,7-positions, which were then coupled with 1,2-dibromo-2-iodobenzene. Afterwards, another Suzuki-Miyaura cross-coupling between the introduced bromides and *tert*-butyl phenyl boronic acid produced compound **42** in 24% yield, without requiring a flash column chromatographic purification over these three steps. Finally, a ten-fold Scholl reaction led to the closure of four heptagons and provided the target saddle **43** in 9% yield.[168] Based on its substantial size, a single molecule of **43** already covers approximately 35% of the respective carbon schwarzite unit cell.[144] Further host-guest studies revealed that **43** forms 1:1 or 1:2 complexes with C_{60} fullerene and a 1:1 complex with C_{70}, as confirmed by single-crystal X-ray diffraction analysis.[168] Simultaneously, Feng and coworkers independently reported the same saddle core, albeit with 14 additional incorporated six-membered rings.[169] Despite this extended size, the saddle still corresponds to a C_{76} cut-out fragment of carbon schwarzite.[144] Like **43**, their saddle displayed host-guest interactions with both C_{60} and C_{70}.[169]

In conclusion, carbon schwarzites have attracted considerable interest because of the variety of theoretically predicted properties and potential applications. While the constructing of an entire schwarzite unit cell remains challenging, recent advances in the synthesis of distinct negatively curved PAHs demonstrate steady progress toward their bottom-up assembly.[131, 136-139, 170-176]

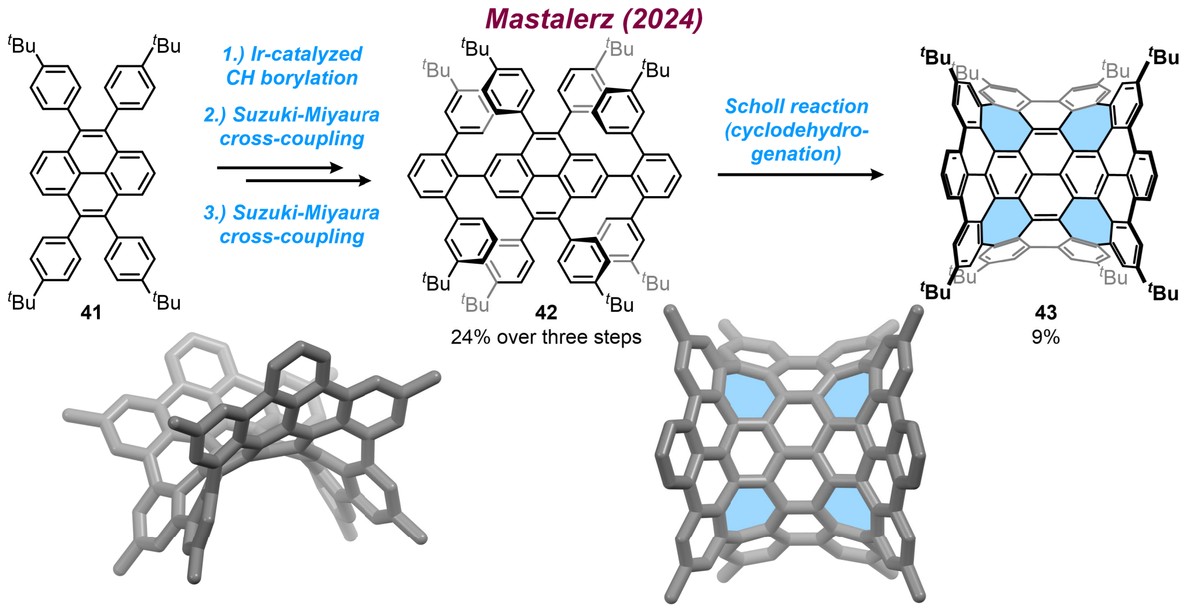

Scheme 1.10: Synthesis of nanographene **43** with four embedded heptagons published by Mastalerz and coworkers in 2024. The saddle-shape of **43** was displayed by its single crystal structure (CCDC 2364982).[168] For a better visualization, the *tert*-butyl groups were shortened to methyl substituents, and the seven-membered rings are highlighted in blue.

1.5 Monkey Saddles

In 2020, the Mastalerz group found a special case of negative molecular curvature by expanding the framework of tribromotruxene precursor **44** in only two steps.[177] At first, a three-fold Suzuki-Miyaura cross-coupling with 2-formylphenylboronic acid (**45**) delivered the aldehyde species **46** as a mixture of C_1- and C_3-symmetrical atropisomers (**Scheme 1.11**). Since their separation was not possible by flash column chromatography, the isomeric mixture was treated with potassium hydroxide, inducing intramolecular condensation of the aldehydes to the fluorenyl positions. This reaction sequence formed three eight-membered rings and afforded the product **47** in 68% yield.[177-178]

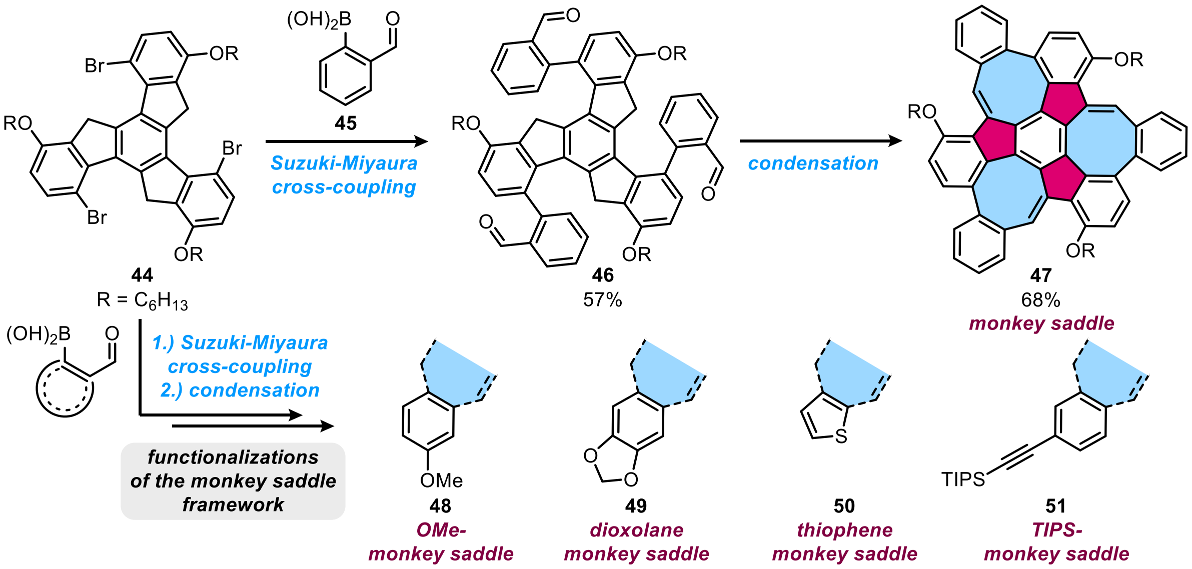

Scheme 1.11: Synthesis of the monkey saddle **47** starting from tribromotruxene **44**. The five-membered rings in **47** were highlighted in pink and the eight-membered ones in blue. The monkey saddle series **48**-**51** was produced by applying differently substituted aryl boronic acids.

Most negatively curved PAHs adopt a horse saddle-like geometry, whose surface can be described mathematically by the function $f(x,y) = x^2 - y^2$ (**Figure 1.2A**).[179] Yet X-ray diffraction analysis of **47** revealed a more complex distortion as its three alkoxy-substituted benzene rings bend in one direction, while the other three peripheral benzene rings are oriented in the opposite direction.[177] This arrangement generates a surface topology corresponding to the equation $f(x,y) = x^3 - 3xy^2$, which is known as a monkey saddle surface (**Figure 1.2B**, **C**).[179] Based on **47**'s distinctive structural feature, Kirschbaum *et al.* referred to this new family of curved PAHs as 'monkey saddles'.[177]

The single crystal structure further showed that the monkey saddle crystallized as a racemate with three axially chiral biaryl units in the molecule.[177] Stereochemical assignment followed IUPAC conventions for axial chirality.[180] Consequently, viewing along the axis of chirality, the adjacent atoms are ranked according to the Cahn-Ingold-Prelog (CIP) priority rules,[181-182] and the descriptor is determined by the path from number 2 → 3 (**Figure 1.2C**). A clockwise sequence is specified by the (R_a) descriptor and a counterclockwise rotation by (S_a).[183] Hence, the obtained enantiomeric mixture comprised (R_a,R_a,R_a)-**47** and (S_a,S_a,S_a)-**47**.[177]

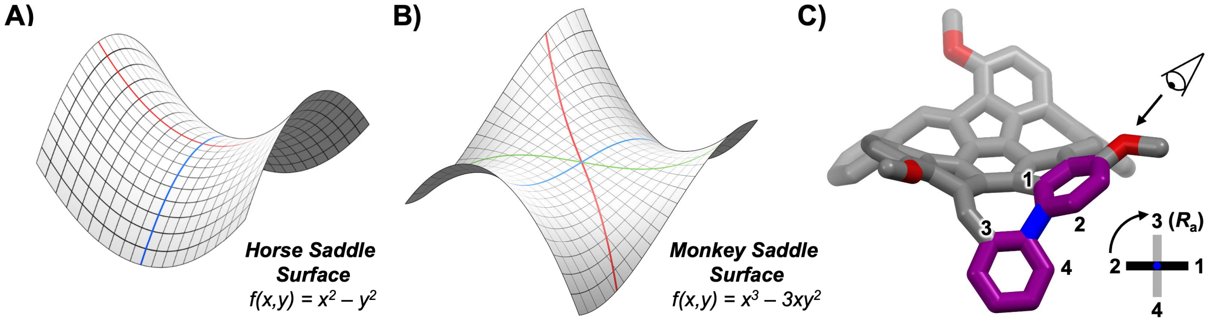

Figure 1.2: Comparison of negatively curved saddle surfaces according to the mathematical functions **A)** $f(x,y) = x^2 - y^2$ (horse saddle), and **B)** $f(x,y) = x^3 - 3xy^2$ (monkey saddle). The respective curvatures are highlighted by two parabolas (red and blue) or three sigmoidals (blue, red, and green). **C)** Single crystal structure of **47** (CCDC 1954750).[177] One of the three axes of chirality is highlighted in blue in the molecule, and the adjacent atoms are ranked according to CIP priority to illustrate the determination of the corresponding stereodescriptor. The hexyl chains were shortened to methyl groups and hydrogen atoms were omitted for clarity. Grey = carbon, red = oxygen. **A)** and **B)** were adapted from reference 184.

After successfully separating the enantiomers by chiral HPLC, their chiroptical properties were examined, and their conformational stability was assessed by kinetic CD measurements, revealing an inversion barrier of $\Delta G^{\ddagger}$(25 °C) = 104 ± 2 kJ mol^{-1} and a half-life of $t_{1/2}$(25 °C) = 23 ± 1 h.[177, 184] DFT calculations at the B3LYP/6-311G(d,p) level of theory corroborated this experimental finding with a computed barrier height of ΔG^{DFT}(25 °C) = 104 kJ mol^{-1} provided that enantiomerization proceeds by successive tub-to-tub inversions of the eight-membered rings. In contrast, a concerted flipping of all three COT moieties, meaning the formation of a fully planar transition structure, gave a calculated barrier of ΔG^{DFT}(25 °C) = 1813 kJ mol^{-1}, thus rendering this pathway energetically inaccessible.[177]

Building on this discovery, several derivatives of **47**, namely the OMe- (**48**), dioxolane- (**49**), thiophene- (**50**) and TIPS-functionalized (**51**) monkey saddles, were synthesized by applying substituted boronic acids or the respective pinacol ester in the cross-coupling step (**Scheme 1.11**).[178, 184] With the exception of thiophene, the substituents had little influence on the inversion barrier, which remained in the range of $\Delta G^{\ddagger}$(25 °C) = 103 to 108 kJ mol^{-1}.[184] In **50**, however, replacement of the benzene units with smaller thiophene rings led to a significantly reduced conformational stability and prevented enantiomeric resolution. Therefore, variable-temperature NMR spectroscopy combined with line-shape analysis was employed to establish an experimental inversion barrier of $\Delta G^{\ddagger}$(25 °C) = 42 ± 6 kJ mol^{-1}.[178]

Moreover, the group of Mastalerz explored late-stage functionalization of **50**, for instance through a three-fold iridium-catalyzed C−H borylation, generating compound **52** in 94% yield (**Scheme 1.12**).[178] A subsequent Suzuki-Miyaura reaction with mono-iodinated **50** produced dimeric, trimeric, and tetrameric monkey saddle assemblies, while coupling between **52** and 4-bromobenzaldehyde delivered the aldehyde species **53** in 64% yield. Since this π-extended monkey saddle represents a promising building block for the synthesis of organic cage compounds, it was tested in an acid catalyzed condensation with enantiopure (−)-(*P*)-tribenzo triquinacene (TBTQ)-triamine **54** (**Scheme 1.12**). After five days, MALDI mass spectrometry confirmed the formation of the cube-shaped [4+4]-cage, whose isolation and purification was accomplished in 53% yield by recycling gel permeation chromatography (rec-GPC).[178]

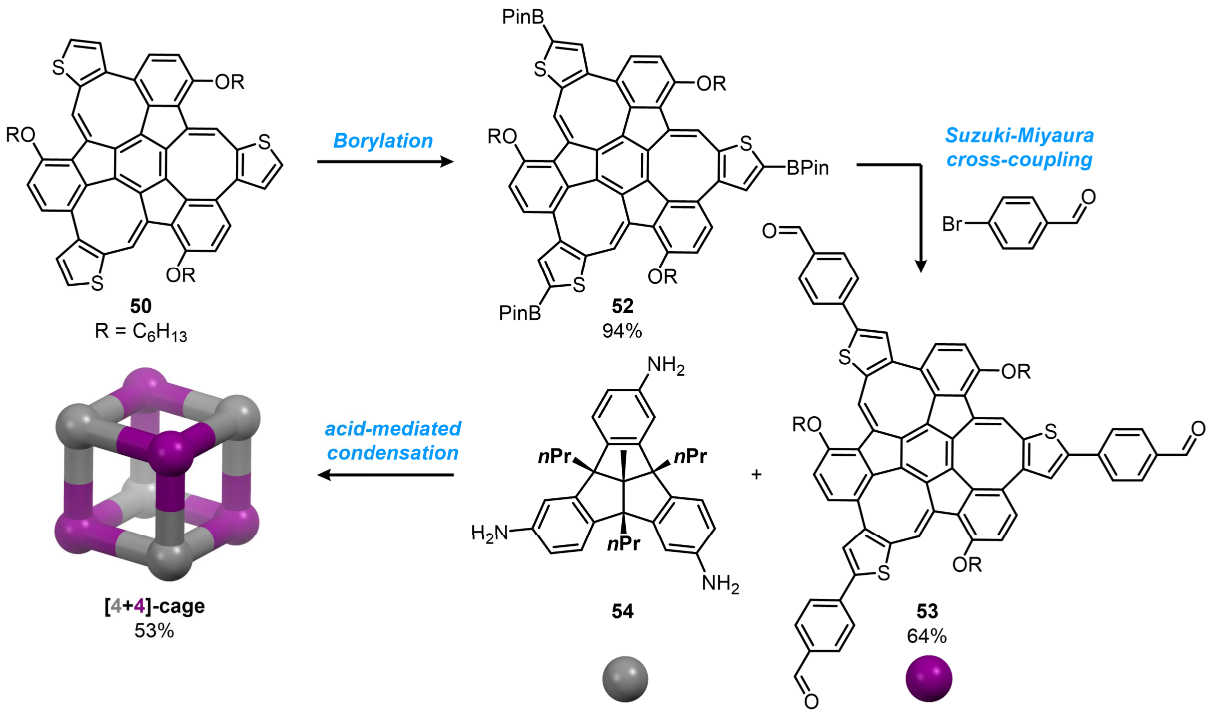

Scheme 1.12: Post-functionalization of the thiophene monkey saddle **50** to generate the [4+4]-cage using the enantiopure TBTQ triamine building block **54**.

When investigating the scope of potential monkey saddle cores, Kirschbaum *et al.* also achieved nitrogen doping of the COT methine units in three steps.[185] The route started with an oxidation of tribromotruxene **44** to the ketone derivative **55**, followed by a Suzuki-Miyaura cross-coupling with 2-aminophenyl boronic acid. Intramolecular condensation of the amino groups with the ketones then furnished the respective azocine moieties and, by extension, the aza monkey saddle **56** in 47% yield over two steps (**Scheme 1.13**).[185]

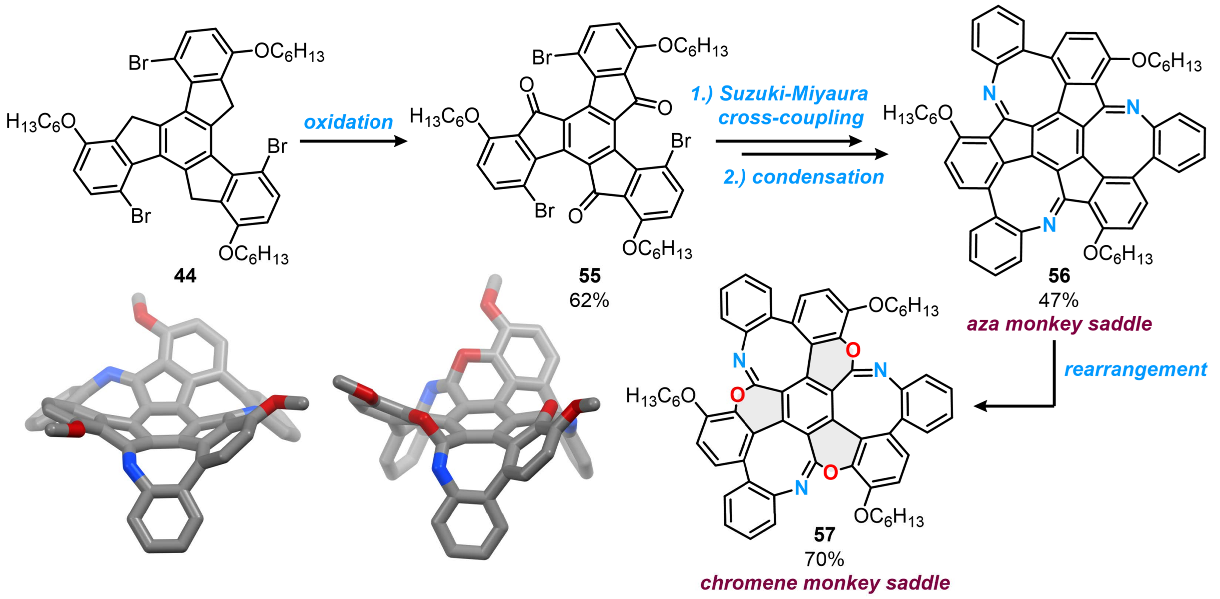

Scheme 1.13: Synthesis of aza monkey saddle **56** and chromene monkey saddle **57** starting from tribromotruxene **44**. Single crystal structures of **56** (CCDC 1994480)[185] and **57** (CCDC 2389442)[186] are pictured to emphasize the curved nature of the molecules. Hexyl groups were shortened to methyl and hydrogen atoms were omitted for clarity. Grey = carbon, red = oxygen, and blue = nitrogen.

Although nitrogen incorporation had only a minor effect on the optoelectronic properties compared to monkey saddle **47**, such as a slight bathochromic shift (11 nm) in the UV/vis absorption spectrum, it increased the inversion barrier by 9 kJ mol^{-1} and accordingly, extended the half-life from $t_{1/2}$(70 °C) = 6.6 ± 0.1 minutes for **47** to $t_{1/2}$(70 °C) = 7.7 ± 0.1 hours for **56**.[185] The authors attributed this improved conformational stability to stronger repulsion between the nitrogen and oxygen lone pairs in relation to the σ-electrons of the isosteric CH-bond in **47**.[185] To suppress racemization even further, aza monkey saddle **56** was treated with *m*CPBA in an attempt to generate the corresponding *N*-oxide.[186] However, X-ray diffraction analysis of the product **57** revealed that oxygen atoms had been inserted into the five-membered rings of the truxene subunit, resulting in the formation of chromene moieties (**Scheme 1.13**). This rearrangement reaction not only enhanced the curvature of the molecular framework but also rendered **57** conformationally stable for at least 47 days at temperatures up to 220 °C.[186] Owing to the inherent chirality of the monkey saddle motif, along with its conformational stability and potential for functionalization, this new family of curved PAHs represent highly attractive building blocks for the construction of elaborate chiral architectures. Moreover, an appropriately closed carbon network composed of monkey saddles can be regarded as a cutout of carbon schwarzites.

1.6 Planar Cyclooctatetraenes

[*n*]Circulenes are PAHs composed of a central *n*-membered ring that is surrounded by a band of *ortho*-fused benzene rings.[187] When one or more of these benzene rings are replaced by heterocycles such as furan, pyrrole, thiophene, or selenophene, hetero[*n*]circulenes are obtained (**Figure 1.3**).[188-189] To estimate whether a (hetero)[*n*]circulene adopts a planar or curved structure without computational modeling, Pittelkow and coworkers proposed a simple model in which the wedge angles of the peripheral aromatic units are summed ($\Sigma_{\angle}$).[189] Rings with $\Sigma_{\angle}$ close to 360°, or more specifically within the range of 336-380°, are expected to be planar, while lower $\Sigma_{\angle}$ indicate bowl-shaped structures and higher values saddles (**Figure 1.3**). Though, it should be emphasized that this model serves solely as a rough guideline rather than strict classification tool. For instance, $\Sigma_{\angle} = 420°$ for both [7]circulene and tetrathia[8]circulene, yet the former exhibits a saddle-shaped structure, whereas the latter remains planar.[189-191]

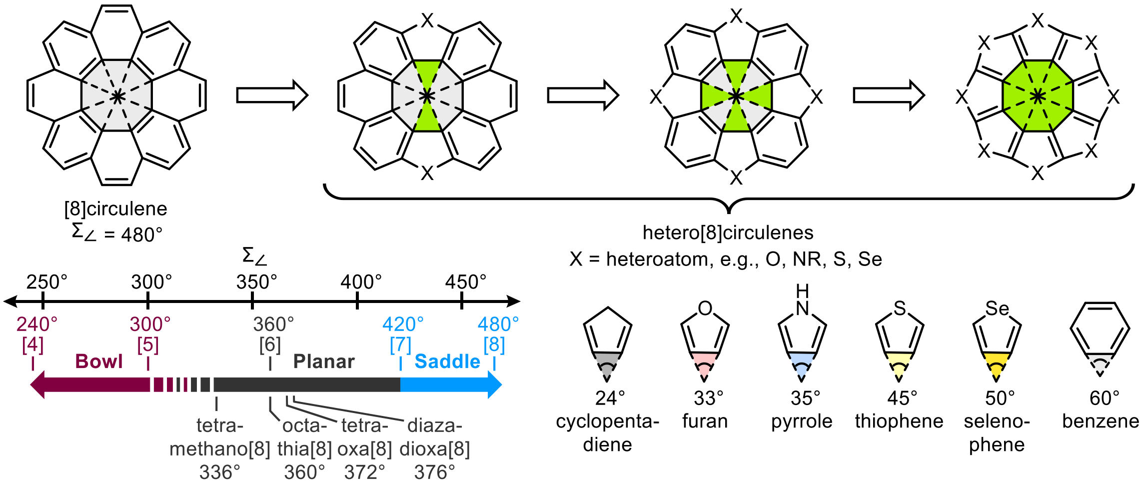

Figure 1.3: Structure of [8]circulene and selected heterocyclic derivatives, which are obtained by replacing two, four, or eight benzene rings with heterocycles.[188] The structure of the resulting hetero[8]circulenes can be estimated from the sum of wedge angles ($\Sigma_{\angle}$) of the rings annulated to the central eight-membered core.[189] Wedge angles for common aromatic rings are shown at the lower right, while the range of $\Sigma_{\angle}$ values and the corresponding geometries are illustrated at the lower left.[189] The circulene suffix for the selected examples was omitted for clarity.

For [8]circulene ($\Sigma_{\angle} = 8 \cdot 60° = 480°$), the sum of wedge angles clearly exceeds 380°, which, consistent with the Pittelkow model, manifests itself in the molecule's negative curvature (compare also *Chapter 1.4*).[135, 189] Substituting two of the benzene rings with pyrrole units lowers $\Sigma_{\angle}$ to 430°, suggesting a partial flattening of COT's characteristic tub-like conformation. The first solution-based synthesis of a diaza[8]circulene derivative was prepared in 2021 by Ema and coworkers, who transformed the carbazole precursor **58** into azahepta[8]circulene **59** by a three-fold ring-closing reaction (**Scheme 1.14A**).[192] Subsequent deprotection and triflation of the hydroxy groups, followed by a palladium-catalyzed double amination with benzylamine, generated the product **60**. Its structure was unambiguously confirmed by X-ray diffraction analysis, which also allowed quantification of the central octagon's curvature by determining the bent angle α (defined as the angle between COT's tub bottom and its sidewalls; *cf.* **Scheme 1.14A**).[192-193] A comparison of **60** with a substituted [8]circulene derivative published by Feng *et al.* revealed a reduction from α = 46° to α = 24°, highlighting the pronounced flattening effect caused by the two embedded heterocycles.[135, 192]

Pursuing this trend, *i.e.*, the incorporation of at least three five-membered rings into [8]circulene, the COT unit can even be forced into complete planarity.[188] The first report of a planar hetero[8]circulene dates back to the 1970s, when Erdtman and Högberg discovered that quinones such as 1,4-naphthoquinone (**61**) undergo cyclooligomerization under acidic conditions or in the presence of Lewis acids (**Scheme 1.14B**).[194-197] In the process, dihydroxydibenzofurane **62** arises as a key intermediate before the corresponding tetraoxa[8]circulene **63** is formed.[196] Building on these findings, the insertion of multiple heteroatoms into a single hetero[8]circulene became feasible and was later exploited by the group of Pittelkow, amongst others, to synthesize the azatrioxa[8]circulene **64** from 1,4-anthraquinone (**65**) and dihydroxycarbazol **66** (**Scheme 1.14C**).[198-201] With $\Sigma_{\angle}$ = 374°, compound **64** is expected to adopt a planar geometry, as was indeed confirmed by X-ray diffraction analysis.[201] Moreover, the single-crystal structure exhibited a close packing consisting of π-stacked columns in which the anthracene moieties of one molecule attractively interacted with the central octagon of another. In combination with its tuned optical properties due to a reduced HOMO-LUMO gap, **64** emerged as a promising ambipolar semiconductor and was tested in organic light-emitting diode (OLED) prototypes as an emissive and hole-transporting material.[201]

Nishinaga and coworkers were further interested in investigating the antiaromatic character of planar cyclooctatetraenes using ^{1}H NMR spectroscopy.[202] In the case of an antiaromatic COT ring, the induced paratropic ring current would shield the protons attached to it and cause their chemical upfield shift.[203] Hence, the group designed a planar COT derivative bearing four olefinic protons, while three annulated thiophene rings enforced the required planarity.[202] The synthetic route began with the functionalization of dithieno[3,4-*b*:3',4'-*d*]thiophene precursor **67** with two alkenyl chains, furnishing compound **68** over four steps (**Scheme 1.14D**). Next, the eight-membered ring was constructed by alkene metathesis, followed by a dehydration of intermediate **69** to yield the target compound **70**. Beyond verifying its planar geometry, **70**'s single-crystal structure also revealed distinct bond alternation within the COT ring, with double bond portions measuring 1.34-1.35 Å and single bonds 1.46-1.47 Å.[202] These values closely match those of 1,3-butadiene derivatives.[204-205] Finally, the ^{1}H NMR spectra of **70** and its precursor **69** were compared, especially the chemical shifts of proton H^b, as this position is less affected by the annelated thiophene units than H^a (**Scheme 1.14D**).[202] This way, an upfield shift of $\Delta\delta$ = 1.53 ppm was obtained, which is comparable to the downfield shift ($\Delta\delta$ = 1.55 ppm) of benzene (δ = 7.36 ppm) relative to 1,3-cyclohexadiene (δ = 5.81 ppm).[202, 206-207] Thus, a considerable paratropic ring current must be present in **70**, corroborating the antiaromatic character of its planar COT unit.[202]

In addition to experimental approaches, quantum-chemical methods like nucleus-independent chemical shifts (NICS) and anisotropy of the current-induced density (ACID) plots are frequently used to assess the (anti)aromaticity of molecules.[193, 208-212] For NICS values, ghost atoms are placed at the respective ring centers, and their absolute magnetic shieldings are computed. By convention, the sign of the calculated values is reversed so that negative NICSs denote aromaticity and positive ones antiaromaticity.[208] Since σ-electrons influence the magnetic shielding as well, NICS(1) values were later introduced, meaning the ghost atoms are positioned 1 Å above and below the ring center along the ring's normal vector, to better reflect the π-electron contribution.[209] ACID plots, developed by Herges and Geuenich, provide a graphical representation of the current density derived from occupied (π)-orbitals and are illustrated as isosurfaces with vector arrows indicating the current direction.[210] This visualization not only allows analysis of the overall (anti)aromaticity of a system but also whether double bonds are conjugated with each other. Anticlockwise ring currents are thereby paratropic and signify antiaromaticity, whereas clockwise ring currents are diatropic, corresponding to aromaticity.[210]

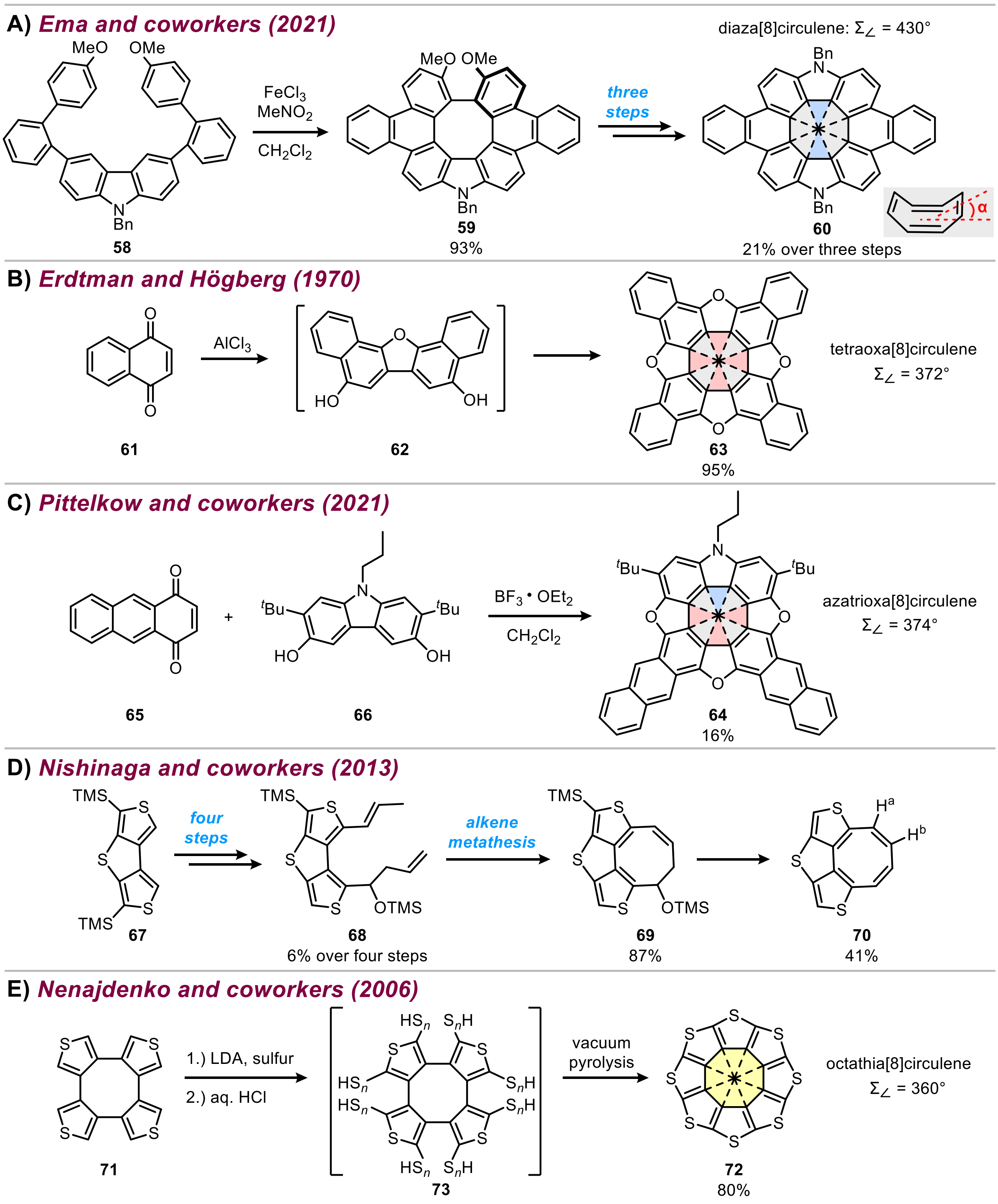

Scheme 1.14: Synthesis of various planar cyclooctatetraene derivatives. **A)** Diaza[8]circulene **60**, with illustration of the bent angle α in the COT unit. **B)** Tetraoxa[8]circulene **63**. **C)** Azatrioxa[8]circulene **64**. **D)** Thiophene-annelated planar COT derivative **70**. **E)** Octathia[8]circulene **72**, also referred to as 'sulflower'.

To date, numerous synthetic procedures have been developed for hetero[8]circulenes.[188-189] To name a few additional strategies, Tanaka, Osuka, and coworkers used a fold-in oxidative fusion approach to generate tetraaza[8]circulenes,[213-214] while Pittelkow's group compressed a hetero[7]helicene into a diazaoxathia[8]circulene.[215] Tetrathienylene **71** has served as a precursor to both tetrathia[8]circulene and octathia[8]circulene **72** (**Scheme 1.14E**).[216-219] The latter was prepared by sulfurization and acidification of **71**'s thiophene sites giving intermediate **73**, followed by vacuum pyrolysis. The resulting 'sulflower' **72** is insoluble in common organic solvents owing to strong intermolecular interactions, precluding optical studies, and structural characterization was achieved by X-ray powder diffraction.[219] These literature examples demonstrate that cyclooctatetraenes can be forced into (near) planarity when fused with at least two five-membered rings, whereby the resulting conformational change influences their optoelectronic properties, aromatic character, and potentially aggregation behavior.[198-199, 201-202, 220-221]

2 Motivation and Objectives

The primary objective of this dissertation is the synthesis of shape-persistent organic cages by alkyne metathesis. Building on the results of my master's thesis,[222] the first project focuses on the cuboctahedron-shaped cage **74**, which is to be assembled from triptycene precursor **75** through a 24-fold alkyne metathesis (**Scheme 2.1A**). Since this step entails the formation of hexadehydro[12]annulene subunits, the selected alkyne metathesis catalyst must exhibit high activity toward this motif.

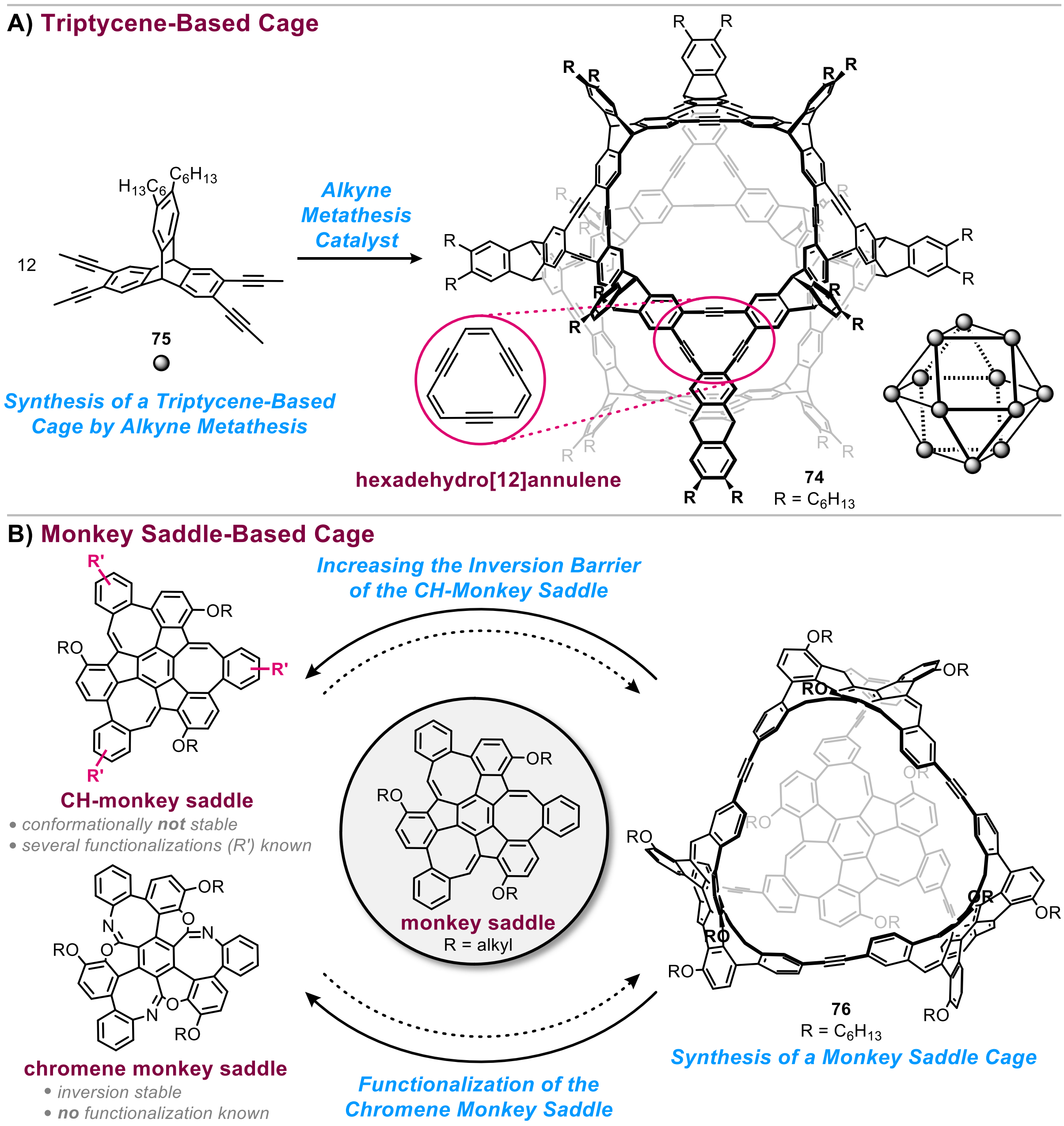

Scheme 2.1: Objectives of this dissertation (highlighted in blue writing). **A)** Synthesis of the cuboctahedron-shaped cage **74** by alkyne metathesis using the triptycene precursor **75**. **B)** Synthesis of the monkey saddle cage **76** by alkyne metathesis. Challenges encountered during **76**'s assembly led to an additional objective: the design of functionalized and conformationally stable monkey saddles suitable for enantiopure cage synthesis.

Moreover, the CH-monkey saddle first reported by Kirschbaum *et al.* in 2020[177] has been proposed as a building block for the tetrahedral cage compound **76** (**Scheme 2.1B**). For this undertaking, the monkey saddle core must first be equipped with alkyne groups before exposing the resulting precursor to alkyne metathesis. However, challenges encountered during the cage's construction led to a second research objective: the development of functionalized and conformationally stable monkey saddle derivatives suitable for the synthesis of enantiopure cages. Several strategies are thereby envisaged. For instance, the chromene monkey saddle, which already demonstrated inversion stability,[186] requires the introduction of functional groups to facilitate follow-up chemistry. In contrast, the CH-monkey saddle presents the opposite problem: its core has been decorated with a range of substituents, though none of them significantly enhanced the monkey saddle's conformational stability.[184] Thus, alternative substitution patterns should be developed to substantially increase its inversion barrier (**Scheme 2.1B**). Ultimately, successful progress in this direction could enable the generation of enantiopure monkey saddle-based cages, which are particularly appealing as they represent molecular models of carbon schwarzites and may display remarkable electronic and magnetic properties.[139, 144] In addition, their expected porosity makes them promising candidates for gas adsorption studies.

3 Results and Discussion

3.1 Synthesis of an Alkyne Metathesis Catalyst

To synthesize organic cages by alkyne metathesis, a suitable catalyst has to be applied. In 2016, Zhang and coworkers presented the tris(2-hydroxylbenzyl)methane-based ligand **11**, which formed an active alkyne metathesis catalyst upon mixing it with trisamido molybdenum(VI) alkylidyne complex **8** (**Scheme 3.1A**).[71] In addition to a broad functional group tolerance, the active catalyst species **77** was able to connect three of the 1,2-di(propynyl)benzene derivatives **78** to the corresponding hexadehydrotribenzo[12]annulene **79** in 95% yield under very mild conditions (40 °C, 4 h; *cf.* **Scheme 3.1B**).[71] As the first target cage relied on the formation of triptycene-based hexadehydro[12]annulene units, the preparation of precatalyst **8** and ligand **11** was addressed and is presented within this chapter.

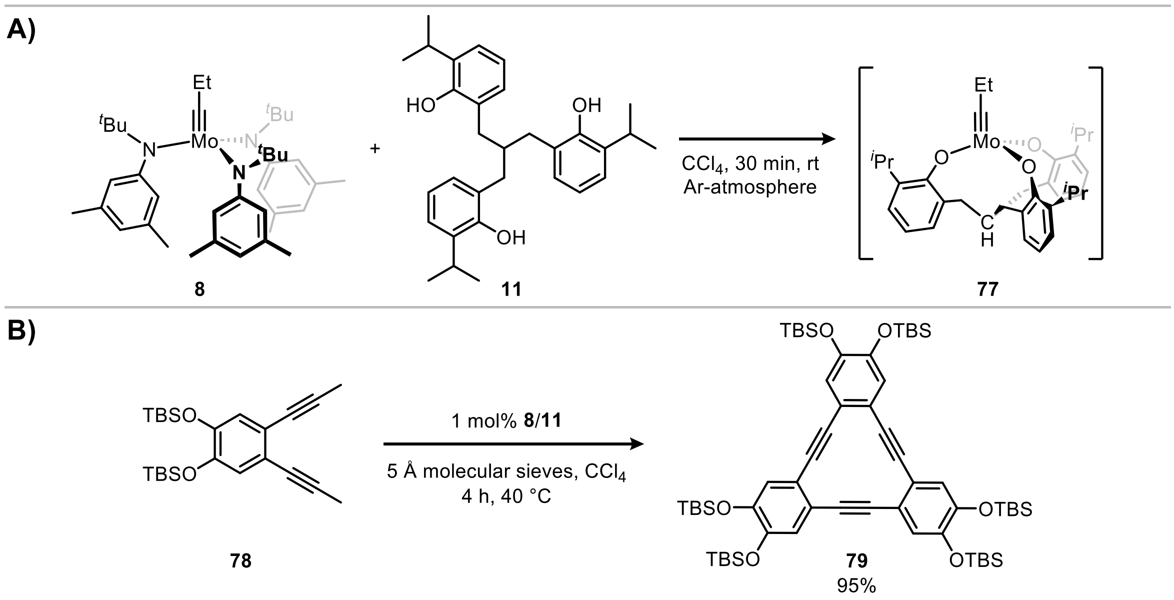

Scheme 3.1: A) *In situ* generation of the alkyne metathesis catalyst **77** developed by Zhang and coworkers in 2016.[71] **B)** Synthesis of hexadehydro[12]annulene **79** by alkyne metathesis under mild conditions performed by Zhang and coworkers.[71]

Synthesis of Trisamido Molybdenum(VI) Alkylidyne Precatalyst 8

Since complex **8** has been an important precursor for alkyne metathesis catalysts,[61, 70-71, 100, 105, 108] its synthesis was rendered high-yielding by Moore and coworkers' reductive cycle strategy in 2003 (compare also *Introduction Chapter 1.2*).[104] Despite this improved procedure, the generation of **8** remains challenging owing to its high sensitivity toward air and moisture.[104, 112] Hence, each step had to be handled with great care in dried glassware and under a constant argon flow or atmosphere.

To begin, the amine ligand **80** was produced by coupling 5-bromo-*m*-xylene (**81**) and *tert*-butylamine (**82**) in a Buchwald-Hartwig amination (**Scheme 3.2A**).[112] Due to incomplete conversion, the bromide **81** was recovered by flash column chromatography and simultaneously separated from **80**. Further purification of the latter by vacuum distillation gave **80** in 64% yield as a colorless liquid.

Subsequently, precatalyst **8** was produced within five steps starting from commercially available molybdenum(V) chloride (**83**) (**Scheme 3.2B**).[112] To accomplish this, complex **83** was stirred in acetonitrile overnight, delivering **84** in 85% yield, followed by replacing the two acetonitrile ligands by two THF molecules in 84% yield. Next, **85** was treated with tin shots in THF to reduce the molybdenum. After 30 minutes of reaction time, the orange suspension was decanted, leaving the tin shots in the reaction vessel, and compound **86** was isolated by filtration under argon in 80% yield. Elemental analysis of **84**, **85**, and **86** confirmed their correct elemental composition.

According to the literature, the next step consisted of deprotonating the amine **80** with *n*-butyllithium, removing the solvent *in vacuo,* and recrystallizing the lithiated amine.[112] Then, complex **86** is mixed with the lithiated amine, which leads to a ligand exchange under the precipitation of lithium chloride and the formation of **4**.[112] When I tried this procedure during my master's thesis, a colorless solid remained after removal of the solvents under reduced pressure. However, the solid turned green as soon as the flask was refilled with argon, and ^{1}H NMR investigations of the residue solely showed signals belonging to the starting material **80**.[222] Since the used argon was not predried, it was assumed that the remaining moisture sufficed to protonate the lithiated amine. Thus, the deprotonation of **80** was only performed *in situ* before it reacted with **86** to the trisamido molybdenum(III) complex **4** (**Scheme 3.2B**). Lastly, precatalyst **8** was obtained by exposing **4** to 1,1-dichloropropane and magnesium turnings. The latter reductively recycles the arising monochloride complex $ClMo[N(^tBu)Ar]_3$ to the starting material **4** while the product **8** remains unaffected.[104] Although the ^{1}H NMR spectrum of **8** is in accordance with the literature,[112] it also revealed the presence of free amine **80** in a ~1:1 ratio to the product. Considering that **80** will be released during the *in situ* generation of the active catalyst species **77**, its presence should not influence the alkyne metathesis, and therefore, **8** was not subjected to another purification step.

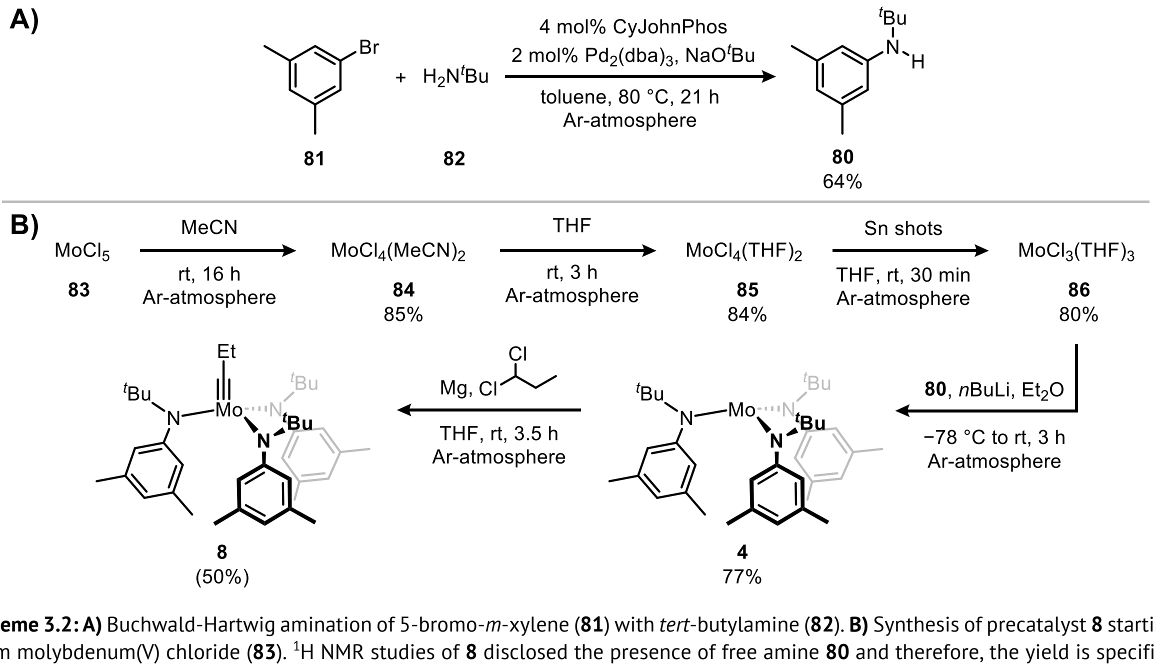

Scheme 3.2: A) Buchwald-Hartwig amination of 5-bromo-*m*-xylene (**81**) with *tert*-butylamine (**82**). **B)** Synthesis of precatalyst **8** starting from molybdenum(V) chloride (**83**). ^{1}H NMR studies of **8** disclosed the presence of free amine **80** and therefore, the yield is specified in brackets.

Synthesis of the Tris(2-hydroxylbenzyl)methane Ligand 11

The route toward **11** started with the *ortho*-formylation of 2-isopropylphenol (**87**) using paraformaldehyde and anhydrous magnesium chloride (**Scheme 3.3**).[223] After the corresponding salicylic aldehyde **88** was isolated in 88% yield, the hydroxy functionality needed to be protected. During my master's thesis, I followed Zhang and coworkers' procedure and introduced benzyl protecting groups.[71] However, major yield losses had to be accepted this way because of an incomplete conversion toward the tribenzylmethanol backbone.[222] It was assumed that the steric demand of the benzyl groups impeded this reaction. Hence, when repeating the synthesis of **11** within the scope of my PhD thesis, this issue was circumvented by applying methyl instead of benzyl protecting groups.

Consequently, salicylic aldehyde **87** was treated with methyl iodide and potassium carbonate to furnish methoxybenzaldehyde **89** in 98% yield.[224] Next, the aldehyde was reduced to the benzyl alcohol **90** with sodium borohydride, followed by a nucleophilic substitution using phosphorus tribromide to provide benzyl bromide **91** in 96% and 79% yields, respectively (**Scheme 3.3**).[225-226] Magnesium turnings then converted **91** into a Grignard reagent, which reacted three-fold with the C1-building block methyl chloroformate to the tribenzylmethanol **92** in 82% yield. Exposing **92** to phosphoryl chloride formally eliminated water and produced the alkene **93** in 74% yield. After the formed double bond was hydrogenated with hydrogen gas and palladium on carbon in 95% yield, the hydroxy groups of **94** were deprotected with boron tribromide, giving ligand **11** in 87% yield (**Scheme 3.3**).

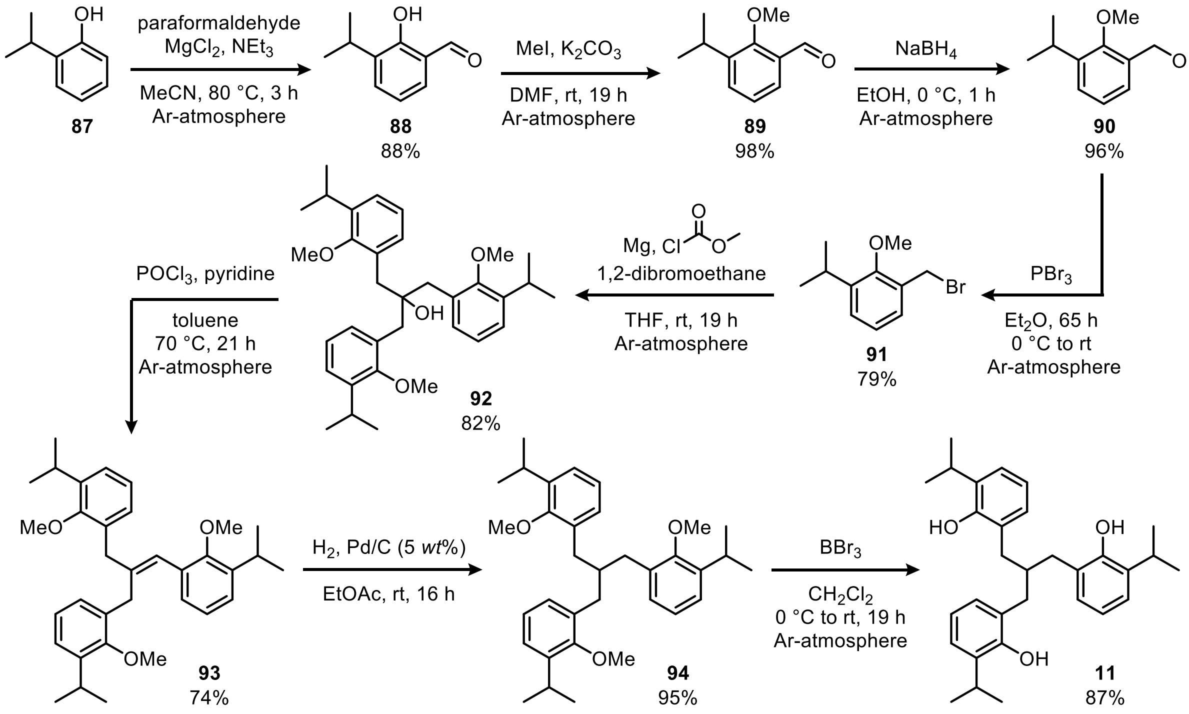

Scheme 3.3: Synthesis of ligand **11** over eight steps starting from commercially available 2-isopropylphenol **87**.

In conclusion, precatalyst **8** was successfully obtained by slightly modifying the literature procedure, generating the highly moisture-sensitive lithium *N*-(3,5-dimethylphenyl)-*tert*-butylamide only *in situ* rather than isolating it.[112] Final ^{1}H NMR studies of **8** revealed an approximately 1:1 mixture of product and the free amine ligand **80**, whereas the literature reported less than 5 *wt*% contamination of **8** with **80**.[112] Consequently, the deviation in procedure might have had a negative impact on the conversion toward **8**; nevertheless, given the lack of certain inert gas equipment such as predried argon or an argon-filled glovebox, this outcome represents a reasonable compromise, especially since residual **80** will not affect subsequent alkyne metatheses. Furthermore, ligand **11** was produced from 2-isopropylphenol (**87**) in eight steps, whereby the route was improved by replacing the benzyl with methyl protecting groups. As a result, each step could be conducted on a gram scale (5 to 20 grams) without any significant loss of material.

3.2 Triptycene-Based Hexadehydro[12]annulene Units

Some of the results presented within this chapter, namely the synthesis and characterization of ***75, 100-102, 103a****, and* ***103b****, as well as first synthetic approaches toward cage* ***74****, were initially carried out during my master's thesis*[222] *and repeated as part of this PhD thesis.*

Triptycene has been a sought-after building block for two- and three-dimensional constructs owing to its rigid and paddle-wheel-like framework.[227-229] Additionally, the variety of possible substitution patterns combined with a broad selection of potential reaction partners has enabled the production of functional, triptycene-based materials ranging from macrocycles,[230-231] organic cages,[31, 46, 48, 232] COFs,[233-235] and MOFs[236-237] to polymers.[238-240] So far, however, there has been only one example of a cage compound composed of triptycenes and phenyldiacetylenes units. Furthermore, the authors used a copper-mediated Eglinton-Glaser coupling to dimerize the precursor instead of a reversible reaction that would allow misalignments to correct themselves.[232]

In this chapter, two of the three triptycene wings will be modified with triple bonds in *ortho*-position to each other, and the resulting building block will be subjected to alkyne metathesis conditions in order to investigate its potential for cage synthesis. The chosen substitution pattern is expected to cause the formation of hexadehydro[12]annulene subunits, with the target cage structure adopting a cuboctahedron shape. Lastly, the reversibility of the subunit assembly will be examined by scrambling experiments.

Synthesis of Triptycene Precursor 75

When performing alkyne metathesis, each reaction cycle generates two new alkynes, one of which has to be continuously removed to shift the equilibrium toward the desired product.[63] The use of methyl-capped triple bonds quickly emerged as the superior approach, since the resulting 2-butyne can be efficiently adsorbed by powdered 5 Å molecular sieves (see also *Introduction Chapter 1.2*).[62] Based on this strategy, the triptycene scaffold has to be functionalized with propyne groups.

The route toward the corresponding precursor **75** began with hexabromotriptycene **95**, which underwent a six-fold nucleophilic aromatic substitution upon treatment with sodium methoxide and copper(I) bromide (**Scheme 3.4**).[241] After an aqueous work-up and purification by flash column chromatography, hexamethoxytriptycene **96** was obtained in 90% yield. According to Chen and coworkers' procedure, applying different concentrations of nitric acid to **96** can either oxidize one or two benzene rings to the respective *ortho*-quinone.[242] Indeed, when **96** was mixed with a nitric acid concentration of 0.44 M for 5 minutes at 0 °C, one wing was selectively oxidized, giving the quinone **97** in 99% yield as a dark red solid.[243] Next, to prevent any upcoming solubility issues, hexyl chains were introduced following the procedure developed by Dorothee Schindler in her master's thesis.[244] Hence, 1-hexyne was deprotonated with *n*-butyllithium, added to the quinone **97**, and the benzene ring was rearomatized with tin(II) chloride to provide **98** in 84% yield. A subsequent hydrogenation with hydrogen gas and palladium on carbon produced **99** in 93% yield (**Scheme 3.4**).[244] The analytical data of **96-99** were consistent with the literature.[241, 243-245]

In the second half of this route, the methyl-capped triple bonds were installed. During my master's thesis, the simultaneous oxidation of the two remaining 1,2-dimethoxybenzyl units was attempted, followed by the insertion of four propyne groups. However, due to poor yields, these steps had to be carried out sequentially. Thus, triptycene derivative **99** was stirred in a 0.36 M nitric acid concentration for 5 minutes, delivering **100** in 99% yield (**Scheme 3.4**). Analog to quinone species **97**, compound **100** exhibited a characteristic red color. Additionally, IR spectroscopy disclosed a band at $\tilde{\nu}$ = 1656 cm^{-1} typical for the C=O stretching in quinones.[246] To attach the required triple bonds, a solution of propyne in THF was deprotonated with *n*-butyllithium, subjected to **100**, and the intermediate was reduced using tin(II) chloride to gain **101** in 78% yield. In the ^{1}H NMR spectrum of **101**, a new singlet emerged at δ = 2.07 ppm, corresponding to the two methyl groups of the triple bonds, while the protons of the former quinone ring experienced a downfield shift from δ = 6.28 ppm to δ = 7.33 ppm as a consequence of the rearomatization (**Figure 3.1A**). High-resolution (HR) MALDI-TOF mass spectrometry (MS) analysis also confirmed the successful propyne addition with a peak at *m/z* 558.3493 (calcd. for $(C_{40}H_{46}O_2)^+$: 558.3492).

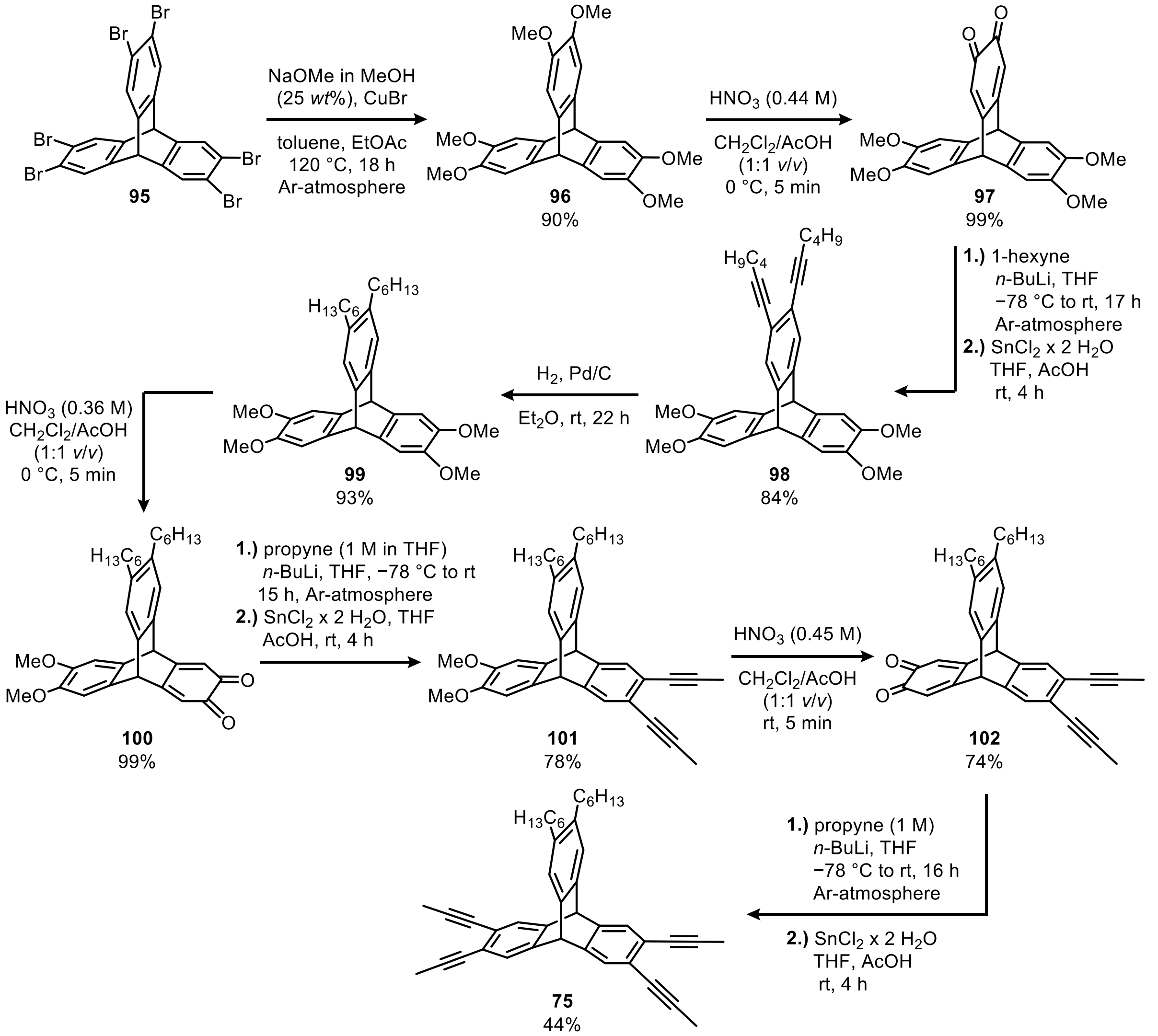

Scheme 3.4: Synthesis of precursor **75** starting from hexabromotriptycene **95**. The hexyl chains were introduced to prevent solubility issues.

Finally, the last two steps were repeated on triptycene derivative **101**, *i.e.*, the oxidation of two methoxy groups with 0.45 M nitric acid and the subsequent incorporation of two more propyne substituents, giving precursor **75** in 74% and 44% yields, respectively (**Scheme 3.4**). ^{1}H NMR studies of **75** disclosed two signals in the aromatic region at δ = 7.32 and 7.10 ppm with an integral ratio of 4:2, demonstrating that two of the three triptycene wings have the same substitution pattern. Moreover, the singlet at δ = 2.07 ppm with an integral value of 12 revealed the presence of four methyl groups, which is consistent with the four propyne groups in **75**.

Synthesis and Characterization of the Hexadehydro[12]annulene Subunit

Before precursor **75** was submitted to alkyne metathesis, compound **101** was used to verify whether the chosen catalyst system is able to construct the hexadehydro[12]annulene subunit underlying target cage **74** (**Scheme 3.5**). At first, the active catalyst species was generated *in situ* by stirring precatalyst **8** and ligand **11** in tetrachloromethane for 30 minutes at room temperature, then it was added to a mixture of the starting material **101** and activated, powdered 5 Å molecular sieves. The latter was required to capture arising 2-butyne and thus, to drive the conversion toward the product. After the reaction was stirred at 80 °C overnight, its progress was monitored by MALDI-TOF mass spectrometry, which showed only one signal at *m/z* 1512.9079 belonging to the trimeric subunit **103** (calcd. for $(C_{108}H_{120}O_6)^+$: 1512.9085).

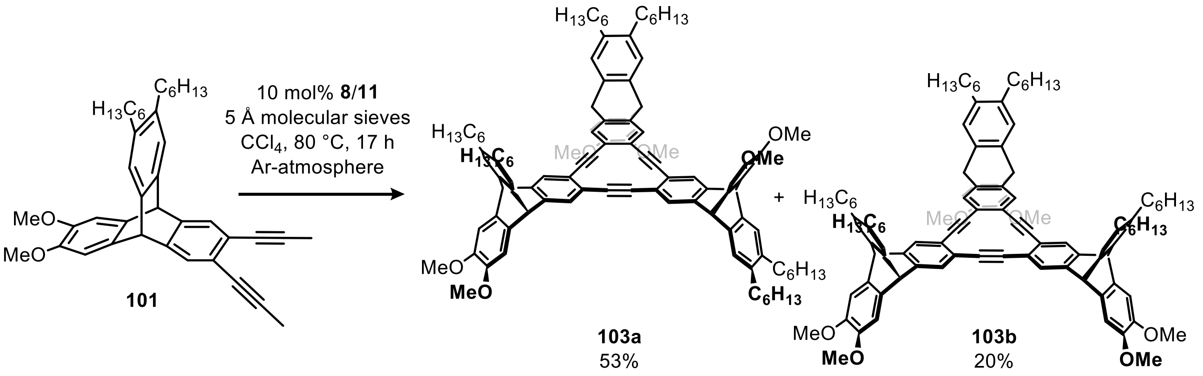

Scheme 3.5: Synthesis of hexadehydro[12]annulene subunits **103a** and **103b** by alkyne metathesis.

For work-up, a filtration over Celite removed the molecular sieves, followed by a flash column chromatographic purification. Due to the differing substituents on **101**'s triptycene wings, the constitutional isomers **103a** and **103b** were obtained in 53% and 20% yields, respectively. ^{1}H NMR analysis of both products featured identical chemical shifts (*cf.* **Figure 7.28** and **Figure 7.30** in the appendix), and even a comparison to the starting material **101** revealed only one primary difference, namely the absence of the singlet at δ = 2.07 ppm (**Figure 3.1B**). Given that this signal originates from the methyl groups capping the triple bonds, its disappearance clearly indicates successful alkyne metathesis with the release of 2-butyne. Meanwhile, ^{13}C NMR spectroscopy of **103a** and **103b** allowed the distinction of the isomers as the decreased symmetry of **103a** led to overlapping signals at δ = 141.89, 141.88 ppm, and δ = 137.4, 137.3 ppm, whereas **103b** exhibited solely one peak each at δ = 141.9 ppm and δ = 137.3 ppm (compare **Figure 7.29** and **Figure 7.31** in the appendix).

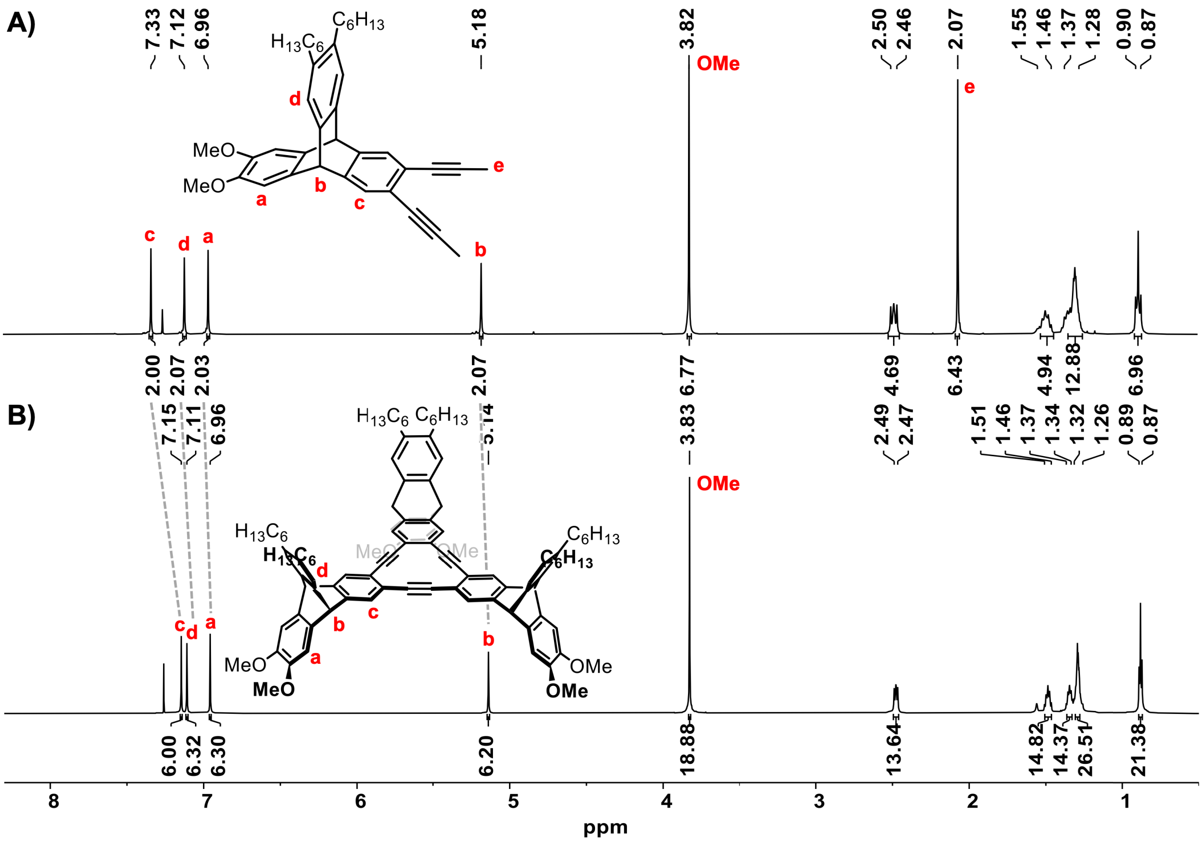

Figure 3.1: ^1H NMR spectra of **A)** triptycene precursor **101** (400 MHz, $CDCl_3$) and **B)** hexadehydro[12]annulene species **103b** (700 MHz, $CDCl_3$) with assignment of designated protons. Upon trimerization, the signals experienced a slight upfield shift, which is indicated by grey dotted lines.

Investigations of the optical properties displayed a minor bathochromic shift of the most intense absorption maximum from λ = 293 nm for **101** to λ = 311 nm for **103a** and **103b**. More noteworthy, however, is the increase of the extinction coefficient from $\varepsilon = 13.9 \times 10^3$ M^{-1} cm^{-1} for **101** to up to $\varepsilon = 182 \times 10^3$ M^{-1} cm^{-1} for **103a** (**Figure 3.2A**). Furthermore, both isomers are fluorescent with the most intense emission maximum located at λ_{em} = 530 nm. For **103b**, another emission maximum was detected at λ_{em} = 421 nm, resulting in Stokes shifts of $\tilde{\nu}$ = 13286 cm^{-1} for **103a** and $\tilde{\nu}$ = 8401 cm^{-1} for **103b** (**Figure 3.2B**).

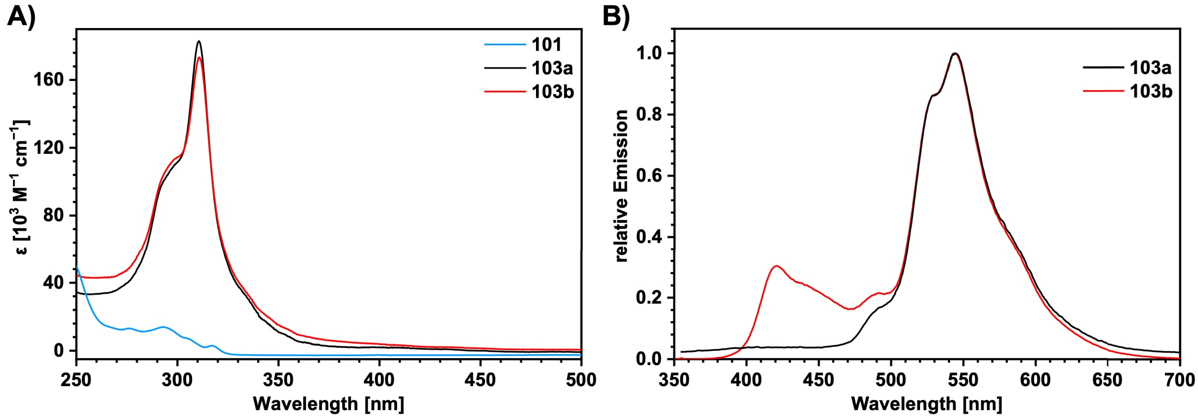

Figure 3.2: A) UV/vis and **B)** emission spectra of **101** (blue), **103a** (black), and **103b** (red) measured in CH_2Cl_2 at room temperature. The excitation wavelengths are λ_{ex} = 315 nm for **103a** and λ_{ex} = 311 nm for **103b**.

Alkyne Metathesis Approaches toward Cage Compound 74

Applying precatalyst **8** and ligand **11** on the model compound **101** successfully proved the catalyst's efficiency in producing the required hexadehydro[12]annulene subunits. Hence, precursor **75** was finally submitted to alkyne metathesis to synthesize the cuboctahedron-shaped cage **74** (**Scheme 3.6**). The conversion of the different approaches was monitored by MALDI-TOF mass spectrometry measurements in regular time intervals. For assigning the observed fragments, the **number** of **75** molecules minus the **number** of released **2-butynes** is specified in brackets in the following discussion. According to this designation, the cage **74** is referred to as [**12**-**24**].

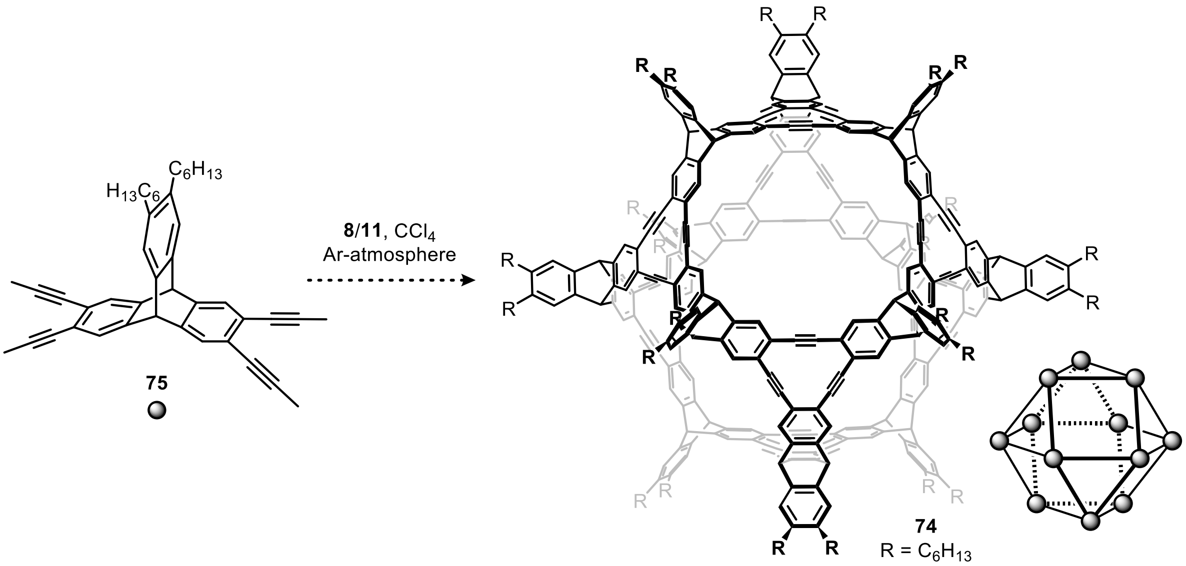

Scheme 3.6: Synthesis attempt toward cuboctahedron-shaped cage compound **74** exploiting building block **75**.

Initial attempts employed the same reaction conditions as subunit **103**, meaning a concentration of 33.3 mM, 80 °C, and the addition of powdered 5 Å molecular sieves. After one day, the mass spectrum displayed a simple polymerization of **75** up to the hexameric species [**6**-**5**] (**Figure 3.3A**). Since the detected mass-to-charge ratios showed that the fragments did not contain any hexadehydro[12]annulene subunits, the next entry was performed with a ten-fold dilution (3.33 mM) to favor intramolecular reactions.

The mixture was again stirred at 80 °C, and after three days, MALDI-TOF MS analysis revealed the accumulation of oligomeric compounds consisting of up to 13 monomers (**Figure 3.3B**). Though this time, a maximum of three subunits was generated within the structures. The first hexadehydro[12]annulene formed in the tetrameric species [**4**-**4**] at *m/z* 2082.578, while the second subunit assembled in the hexamer [**6**-**7**] at *m/z* 3069.969 and the third one in the decamer [**10**-**12**] at *m/z* 5098.785. It is also possible that the square subunit of target cage **74** was constructed instead of a hexadehydro[12]annulene moiety, yet the precise structural composition of the observed oligomers remained ambiguous. Due to the limited catalyst activity in solution, new loadings of **8**/**11** were added every two days. After eight days, the reaction control still exhibited an oligomeric distribution of **75** with little difference from the one after three days (**Figure 3.3C**). Moreover, despite the intramolecular closure of one additional triple bond in the dodecameric species (*cf.* [**12**-**15**] at *m/z* 6085.153), the cage compound **74** ([**12**-**24**]) stayed out of reach as its generation would necessitate the release of nine more 2-butyne molecules from this system.

Testing other concentrations (1.5 mM, 5 mM) or higher temperatures (140 °C) did not improve the conversion toward **74** and resulted again in polymerized starting material. The lack of positive findings posed the question whether the triptycene-based hexadehydro[12]annulenes are formed reversibly, thus allowing the system to self-heal toward the thermodynamically most stable product.[18] To further examine the reversibility of the subunit closure, compound **103** needed to be resynthesized with partially deuterated hexyl chains. This way, the molar mass is increased while preserving electronic effects, and mass spectrometry can be employed to monitor the outcome of dynamic scrambling experiments.

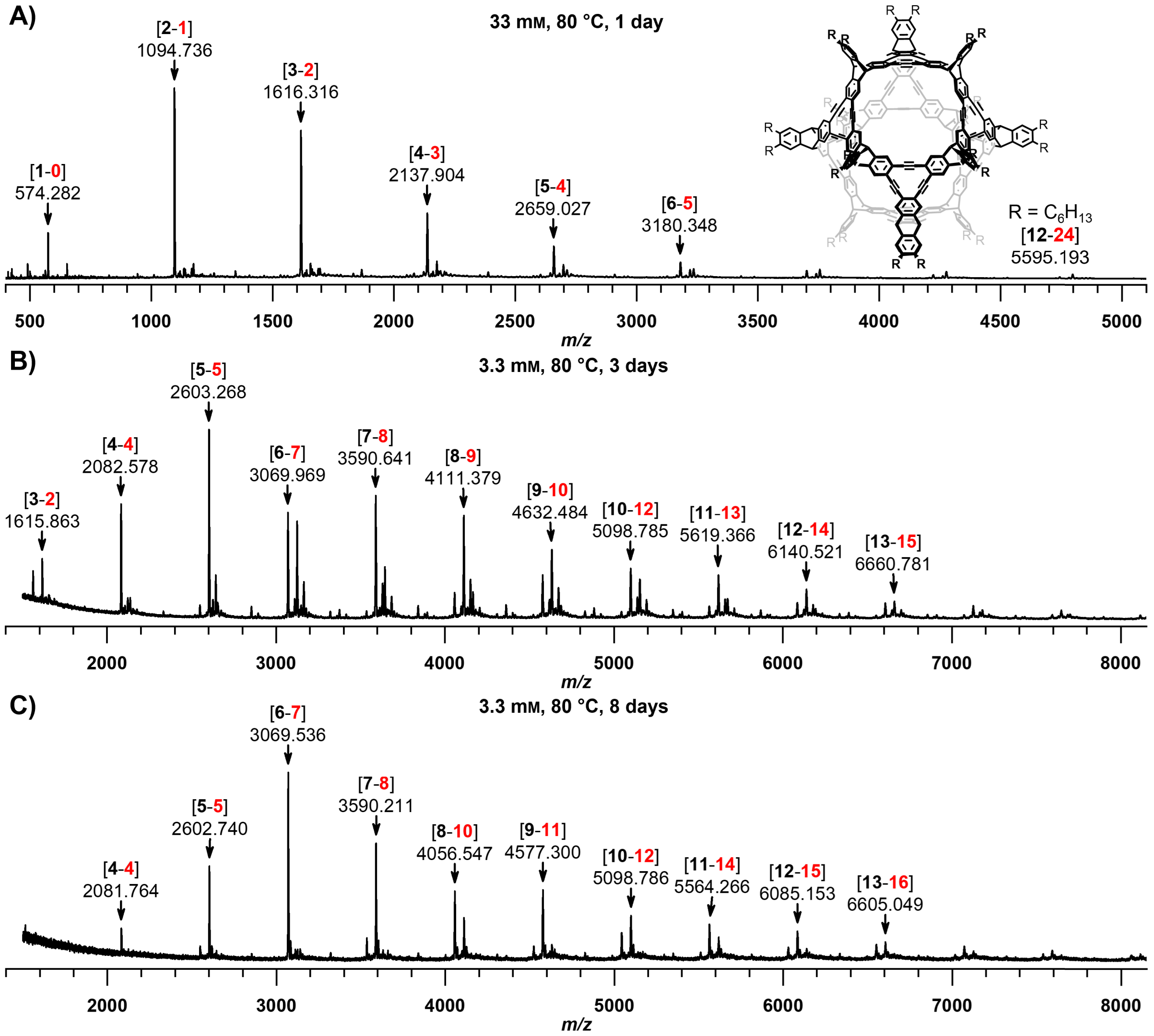

Figure 3.3: MALDI-TOF mass spectra of representative synthesis attempts toward cage **74**. The observed fragments were assigned by specifying the **number** of precursor molecules **75** minus the **number** of released **2-butynes** in brackets. According to this designation, the desired cage **74** is referred to as [**12**-**24**]. **A)** A concentration of 33.3 mM, temperature of 80 °C, and reaction time of one day were employed. **B**, **C)** The alkyne metathesis was performed at 80 °C with a concentration of 3.3 mM. The reaction controls after **B)** 3 days and **C)** 8 days are illustrated.

Synthesis of a Hexadehydro[12]annulene with Partially Deuterated Hexyl Chains

The incorporation of deuterium was achieved by hydrogenating the two hexyne groups of triptycene derivative **98** with deuterium gas (**Scheme 3.7**). However, palladium on carbon does not qualify as a suitable catalyst, since it promotes a distribution of isotopologues according to the Horiuti-Polanyi mechanism.[247-248] In contrast, the Wilkinson catalyst $RhCl(PPh_3)_3$ operates through an irreversible C–H insertion and subsequent reductive elimination, which should allow a selective deuteration of the triple bonds.[249-252] After applying $RhCl(PPh_3)_3$, stirring the reaction at room temperature overnight and purifying the crude material by flash column chromatography, **99-*d*$_8$** was furnished in 87% yield.

^{2}H NMR spectroscopy confirmed the partial deuteration of the hexyl chains with two singlets at $\delta = 2.45$ ppm and $\delta = 1.46$ ppm in a 1:1 ratio (**Figure 3.4A**). Besides, high-resolution MALDI-TOF mass spectrometry featured a peak at *m/z* 550.3866 belonging to the molecular ion $[M]^+$ (calcd for $(C_{36}H_{38}D_8O_4)^+$: 550.3893) (**Figure 3.4B**). Although the detected isotope pattern deviates slightly from the simulated one – attributed to an overlap of species containing zero to two hydrogen atoms instead of deuterium – the mass difference between **103** and **103-*d*$_{24}$** remains sufficient to collect unambiguous results in the scrambling experiments.

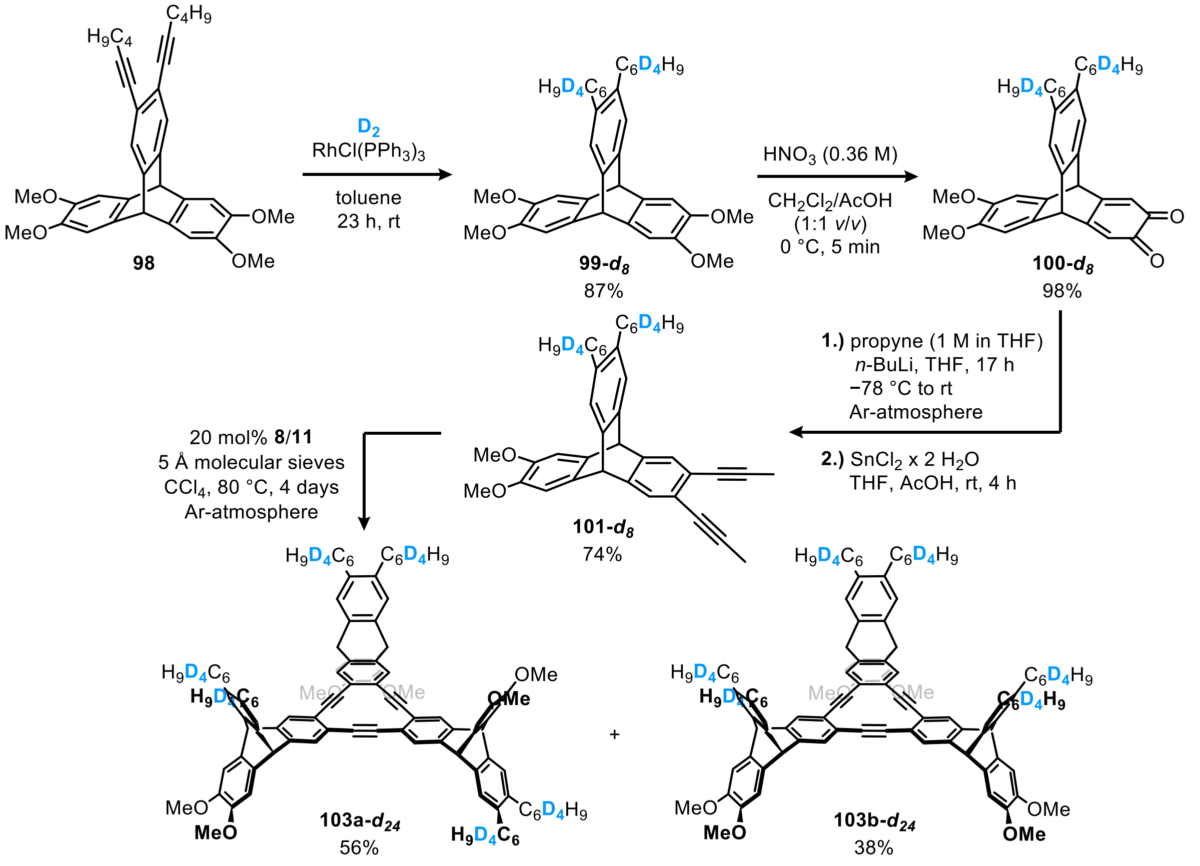

Scheme 3.7: Synthesis of the partially deuterated subunits **103a-*d*$_{24}$** and **103b-*d*$_{24}$** starting from **98**. The Wilkinson catalyst $RhCl(PPh_3)_3$ was employed for a selective deuteration of **98**'s triple bonds.

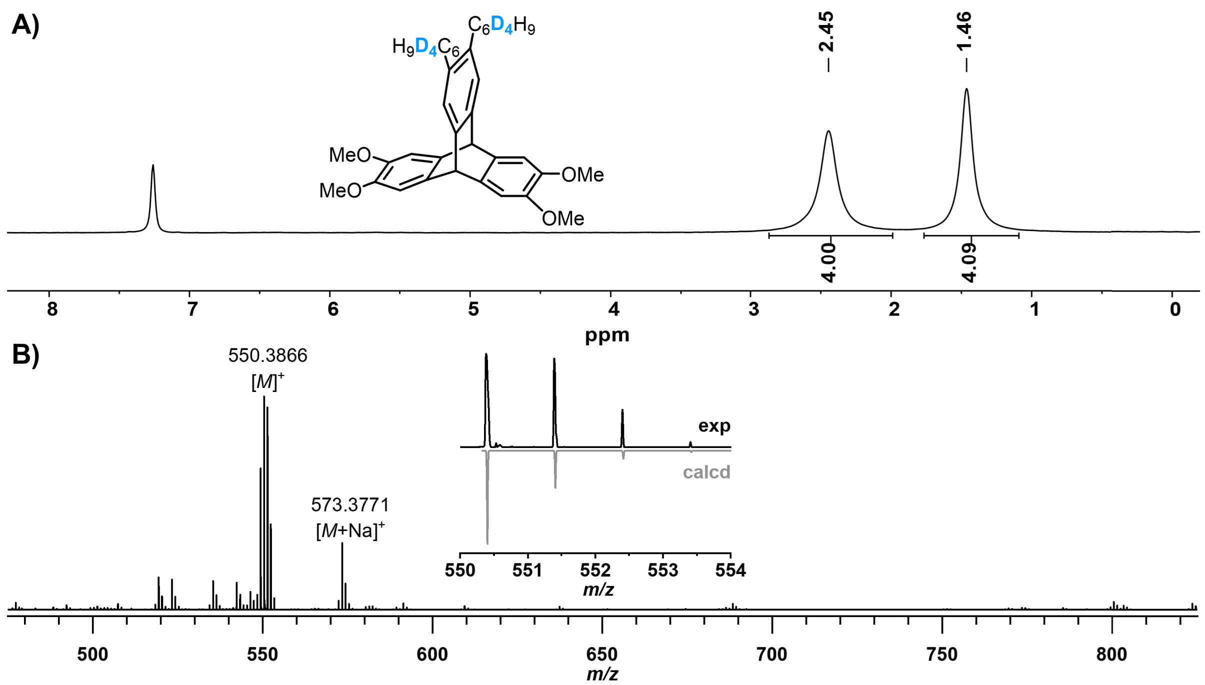

Figure 3.4: A) ^{2}H NMR (92 MHz, $CHCl_3/CDCl_3$) of **99-d_8**. **B)** MALDI-TOF mass spectrum of **99-d_8** with the experimental and calculated isotope pattern.

The residual steps toward **103-d_{24}** were carried out analog to **103** (**Scheme 3.7**). Correspondingly, compound **99-d_8** was oxidized with 0.36 M nitric acid, affording **100-d_8** in 98% yield, and the propyne groups were added in 74% yield. Finally, precursor **101-d_8** was subjected to alkyne metathesis, giving the hexadehydro[12]annulene isomers **103a-d_{24}** in 56% and **103b-d_{24}** in 38% yields. In addition to MS and NMR spectroscopic data, the presence of deuterated alkyl chains was also observed in the IR spectra through C–D stretching bands,[253] e.g., at $\tilde{\nu}$ = 2203 and 2111 cm^{-1} for **103a-d_{24}**, whereas the undeuterated substance **103a** does not exhibit any peaks in this region (*cf.* **Figure 7.174** and **Figure 7.179** in the appendix).

Scrambling experiments

Before exploring the reversibility of the subunit formation, equimolar amounts of **101** and **101-d_8** were treated with the catalyst system **8/11** to selectively synthesize a mixture of **103**, **103-d_8**, **103-d_{16}**, and **103-d_{24}** (**Scheme 3.8A**). MALDI-TOF MS analysis of the crude product delivered a reference spectrum, which illustrates the different degrees of deuteration at *m/z* 1512.528 for d_0 (calcd for $(C_{108}H_{120}O_6)^+$: 1512.909), *m/z* 1520.577 for d_8 (calcd for $(C_{108}H_{112}D_8O_6)^+$: 1520.959), *m/z* 1529.645 for d_{16} (calcd for $(C_{108}H_{104}D_{16}O_6)^+$: 1529.009), and *m/z* 1537.699 for d_{24} (calcd for $(C_{108}H_{96}D_{24}O_6)^+$: 1537.059) (**Figure 3.5A**). As previously noted for **99-d_8** (*cf.* **Figure 3.4B**), the obtained isotope pattern differed slightly from the calculated one due to the incorporation a few hydrogen atoms instead of deuterium. Though, since the scrambled species are clearly distinguishable from one another, the dynamic scrambling experiments can proceed unaffected.

In the first entry, 1.0 equiv. of annulene derivative **103a**, 3.0 equiv. of precursor **101-d_8**, and 20 mol% of catalyst **8/11** were stirred at 80 °C overnight without 5 Å molecular sieves (**Scheme 3.8B**). If the subunit forms reversibly under these conditions, the catalyst would be expected to open the trimer **103a** and replace one or two monomers with **101-d_8**, which should lead to the generation of **103-d_8** and **103-d_{16}** alongside **103** and **103a-d_{24}**. However, MALDI-TOF MS analysis showed only the fully undeuterated subunit **103a** at *m/z* 1512.658 as well as the partially deuterated compound **103-d_{24}** at *m/z* 1537.816 (**Figure 3.5B**). This outcome indicates that compound **103a** stayed intact and was not disassembled during the scrambling experiment.

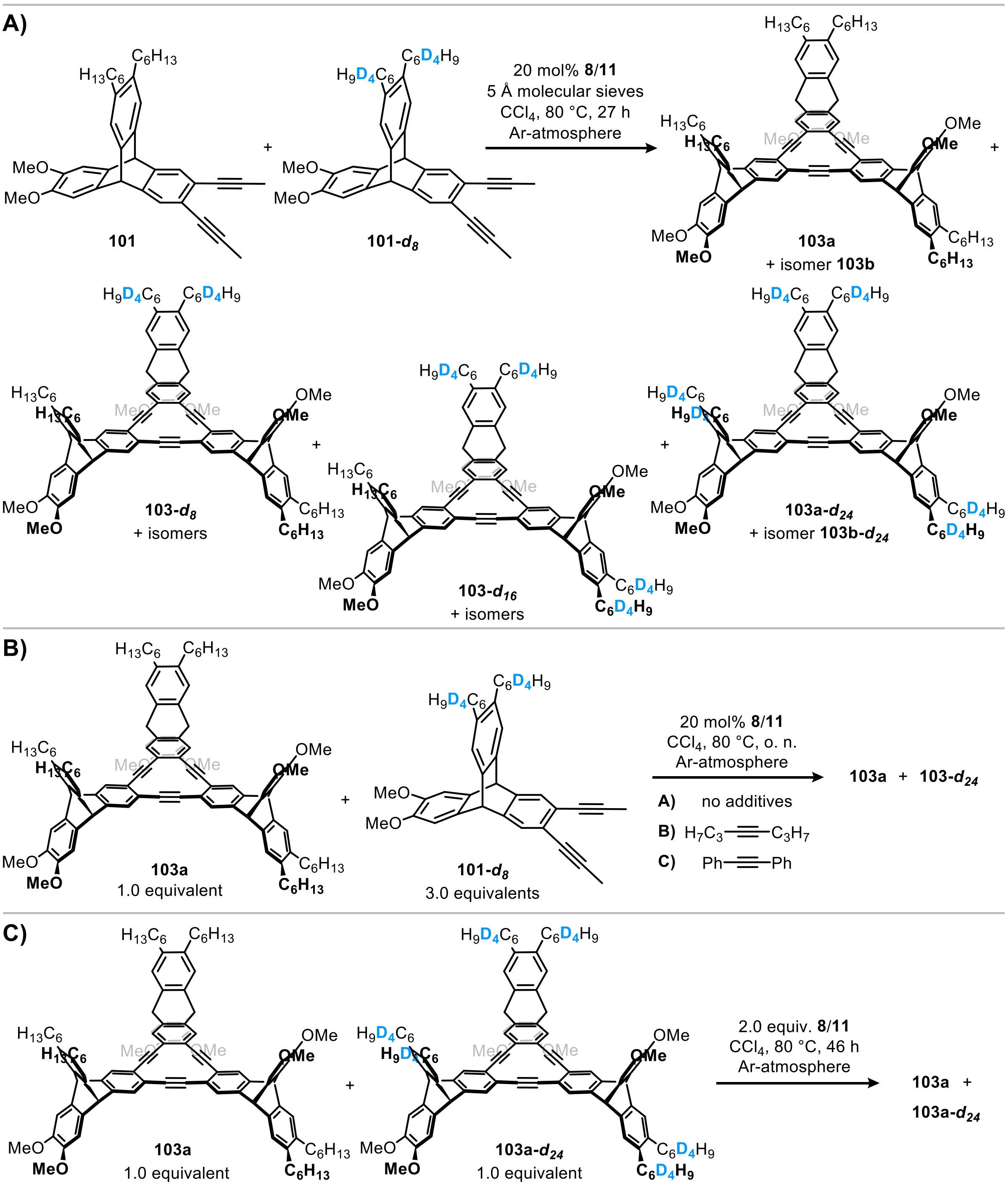

Scheme 3.8: Performed scrambling experiments to investigate the reversibility of the subunit formation. **A)** Selective synthesis of the scrambled species **103**, **103-d_8**, **103-d_{16}**, and **103-d_{24}** to obtain a reference mass spectrum. **B)** Scrambling experiments conducted by mixing **103a** and **101-d_8** under alkyne metathesis conditions either with (4-octyne, diphenylacetylene) or without additives. In all three cases, no scrambled species were observed by mass spectrometry. **C)** Scrambling experiment carried out by treating a 1:1 mixture of **103a** and **103a-d_{24}** with equimolar amounts of catalyst **8/11** under alkyne metathesis conditions. Again, mass spectrometry did not show any scrambling.

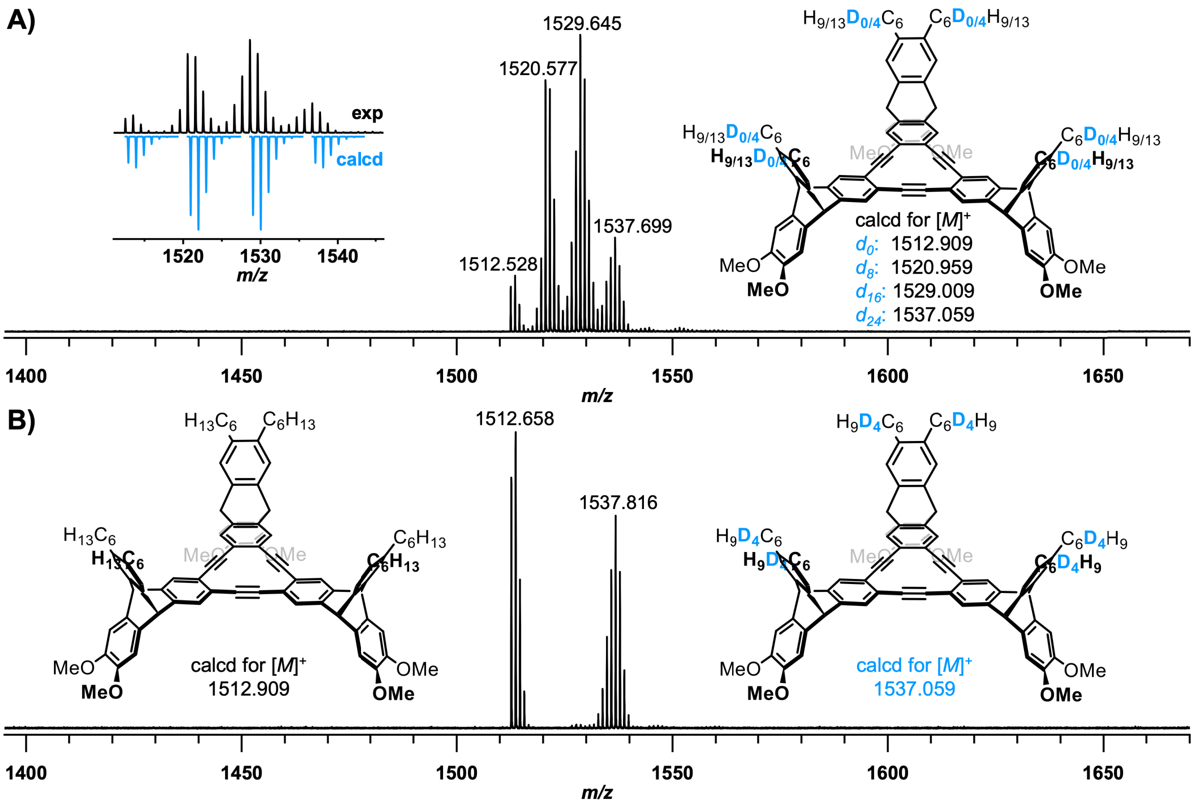

Figure 3.5: MALDI-TOF mass spectra of the scrambling experiments. **A)** Mixture of scrambled species **103**, **103**-d_8, **103**-d_{16}, and **103**-d_{24} with experimental and calculated isotope pattern. **B)** Representative mass spectrum of the scrambling experiments showing only **103** and **103**-d_{24}, but no scrambled species.

According to the general mechanism of alkyne metathesis,[55] each reaction cycle exchanges the substituents between two triple bonds, releasing 2-butyne as the second product if methyl-capped alkynes are used. Given its low boiling point of 27 °C[254] and the reaction temperature of 80 °C, most of the 2-butyne was probably located in the gas phase and therefore not available for the reaction. This issue was addressed by submitting 4-octyne and diphenylacetylene as additives in subsequent experiments (**Scheme 3.8B**). Still, MALDI-TOF MS studies of both entries exclusively detected compounds **103a** and **103-d_{24}**.

The last experiment was set up following the work of Moore and coworkers,[67] *i.e.*, the trimers **103a** and **103a-d_{24}** were mixed with equimolar amounts of catalyst **8**/**11** (**Scheme 3.8C**). As the active catalyst contains ethynyl groups, it has the necessary tools to open the subunits and scramble the monomers. Yet again, MALDI-TOF MS investigations provided no evidence of the compounds **103-d_8** or **103-d_{16}** over the 46-hour reaction period.

These findings demonstrate that the selected catalyst **8**/**11** cannot influence the triptycene-based hexadehydro[12]annulenes **103** once they have been closed. Conversely, the targeted cage **74** cannot be synthesized with **8**/**11** as this catalyst system lacks the ability to correct misaligned annulenes.

Summary and Outlook

This chapter focused on the synthesis of a triptycene-based building block suitable for alkyne metathesis and its potential application in generating the cuboctahedron-shaped cage **74**. To accomplish this undertaking, hexabromotriptycene **95** was substituted with four propyne units and two hexyl chains, yielding precursor **75** in eight steps. In the meantime, intermediate **101** – bearing two propyne, methoxy and hexyl groups each – was exploited as a model compound to explore the formation of the subunit underlying the target cage **74**. Hence, **101** and the previously prepared catalyst system **8**/**11** were mixed under alkyne metathesis conditions, whereby the desired hexadehydro[12]annulene subunits **103a** and **103b** were obtained in a combined yield of 73%, highlighting the efficiency of the selected alkyne metathesis catalyst.

Unfortunately, subsequent attempts to convert precursor **75** into the cage **74** remained unfruitful. All conditions screened consistently led to **75**'s polymerization, regardless of variations in concentration and temperature. In light of this outcome, the reversibility of the subunit construction was scrutinized next. Therefore, triptycene derivative **101** was resynthesized with partially deuterated hexyl chains, and compound **101-*d₈*** was received in three steps from **98**. Submitting **101-*d₈*** to alkyne metathesis then provided the partially deuterated subunits **103a-*d₂₄*** and **103b-*d₂₄*** in an excellent combined yield of 94%.

Following, scrambling experiments were carried out, exposing mixtures of **103** and **101-*d₈*** or **103** and **103-*d₂₄*** to alkyne metathesis conditions, with and without additives to enhance the reversibility of the reaction. However, each entry exclusively resulted in the isolation of **103** and **103-*d₂₄***, with no indication of the scrambled species **103-*d₈*** and **103-*d₁₆***. These findings suggested that the subunit formation is irreversible under the applied catalytic conditions (**8**/**11**), precluding any self-correction mechanism and thus rendering the cage **74** inaccessible.

Nevertheless, hexadehydro[12]annulene derivative **103b** still represents a promising candidate for the synthesis of organic cages, which may be prepared by alternative means such as a boronic acid condensation. To gain initial insights into the viability of this approach, the conversion of **103b** into the hydroxy-functionalized compound **104** was investigated (**Scheme 3.9**). First, the methoxy-substituted benzene rings of **103b** were oxidized to the corresponding quinone **105** using nitric acid in a CH_2Cl_2/acetic acid solvent mixture. The successful production of **105** was confirmed by ^1H NMR spectroscopy. Afterwards, the reduction of the 1,2-quinones to catechol moieties was attempted by treating **105**, dissolved in CH_2Cl_2, with sodium dithionite ($Na_2S_2O_4$) and disodium phosphate (Na_2HPO_4) (**Scheme 3.9**). The characteristic red color of the quinones disappeared during this process, and **104** was obtained according to ^1H NMR analysis. Though, this compound proved to be unstable under standard ambient conditions because its dihydroxybenzene rings started to re-oxidize to the quinone overnight. On account of this sensitivity toward oxidation and a similar case reported in the literature,[255] it was deemed more practical to generate **104** only *in situ* for the synthesis of respective boronic ester cages.

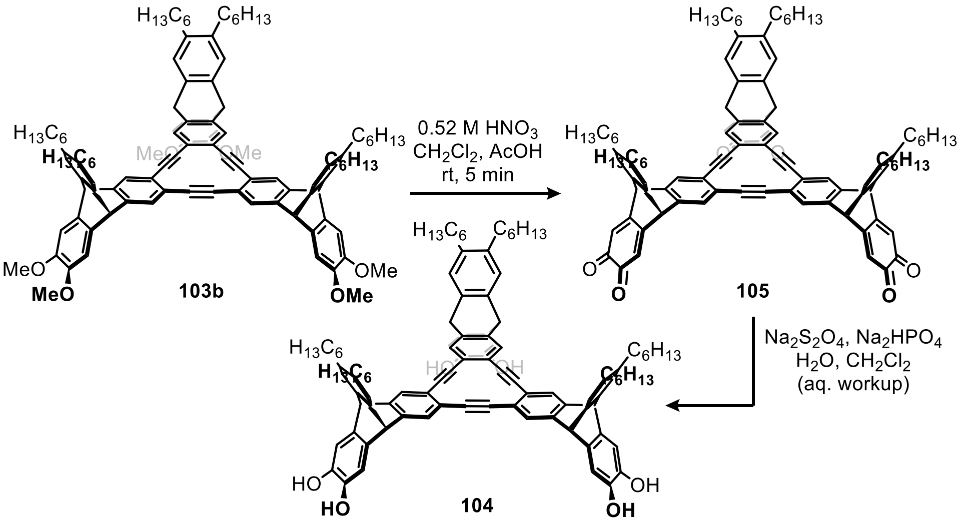

Scheme 3.9: Synthesis of hexadehydro[12]annulene species **104**. No yields are specified because **105** and **104** were not obtained in pure forms.

Models of potential boronic ester cages showed that a mixture of **104** and 1,4-phenylenediboronic acid (**106**) could result in the tetrahedral cage **107**, comprising four **104** units and six phenylene linkers (**Scheme 3.10**). Alternatively, the use of benzene-1,3,5-triyltriboronic acid (**108**) might enable the construction of cage **109**, which consists of four **104** molecules and four phenylene linkers.

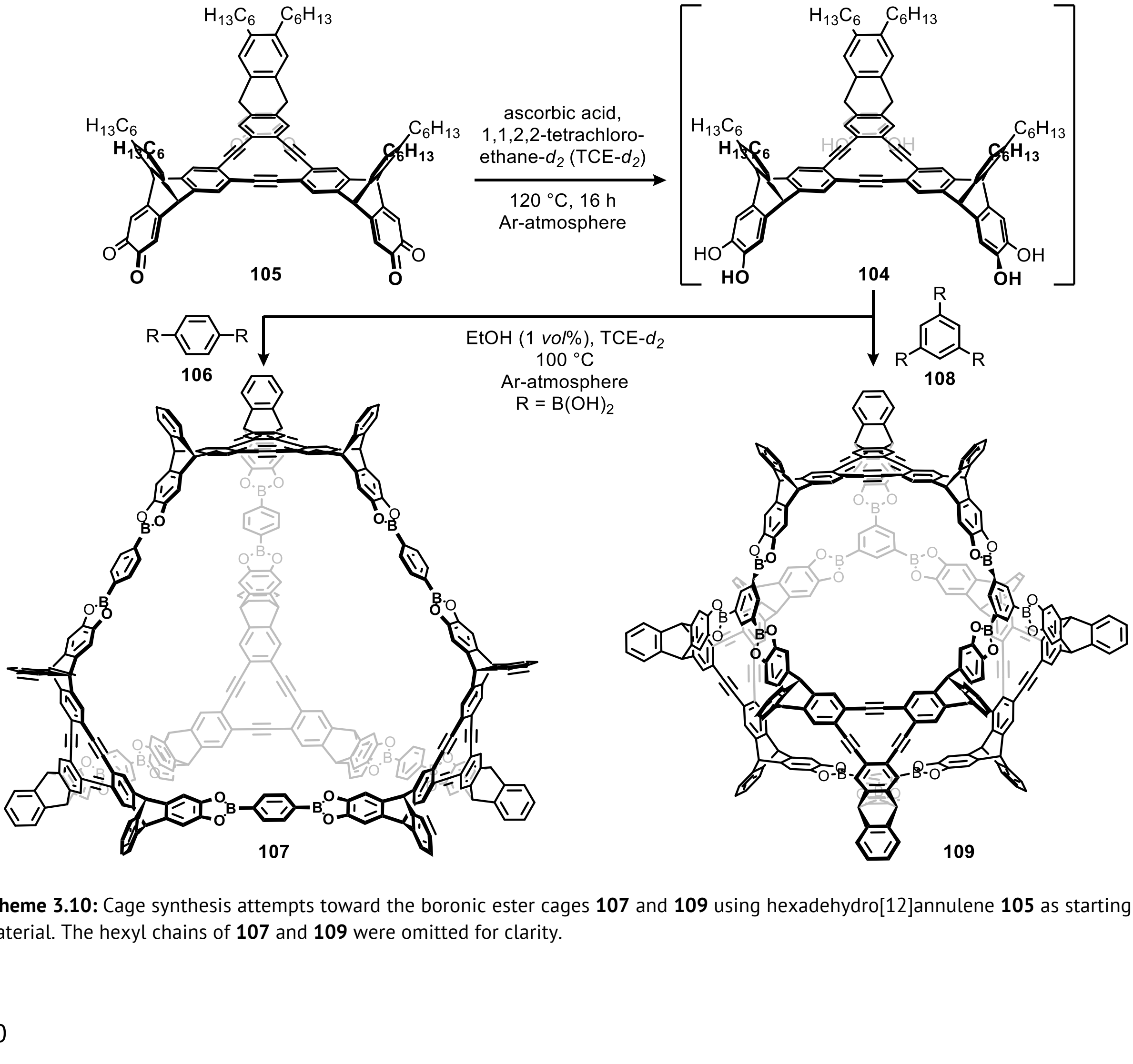

Scheme 3.10: Cage synthesis attempts toward the boronic ester cages **107** and **109** using hexadehydro[12]annulene **105** as starting material. The hexyl chains of **107** and **109** were omitted for clarity.

Both reactions toward **107** and **109** were tested once on an NMR scale. Hence, starting material **105** was weighed in a J. Young NMR tube, set under argon atmosphere and dissolved in dry and degassed 1,1,2,2-tetrachloroethane (TCE-d_2). Subsequently, ascorbic acid was added as a reducing agent for the quinone units. After ultrasonicating the mixture, which was crucial owing to the limited solubility of the ascorbic acid in TCE-d_2, the reaction was heated at 120 °C overnight (**Scheme 3.10**). The exhaustive conversion of **105** into **104** was thereby affirmed by ^{1}H NMR spectroscopy before continuing. Next, the boronic acids (**106** or **108**) and a catalytic amount (1 *vol*%) of ethanol were added while maintaining the inert gas atmosphere throughout. The entries were further heated at 100 °C, and the reaction progress was monitored at regular time intervals by MALDI-TOF mass spectrometry measurements.

In the case of boronic acid **108**, the MALDI-TOF mass spectrum disclosed two peaks after one week at *m/z* 1429.916 and 6127.305 (**Figure 3.6A**). The former signal belonged to the starting material **104** (calcd. for $(C_{102}H_{108}O_6)^+$: 1428.815), whose presence may be attributed to the small batch scale (2.2 µmol of **105**), rendering the accurate addition of stoichiometric amounts of **108** challenging. Yet, the latter peak provides strong evidence for a successful construction of the desired cage **109** (calcd. for $(C_{432}H_{420}B_{12}O_{24})^+$: 6125.808).

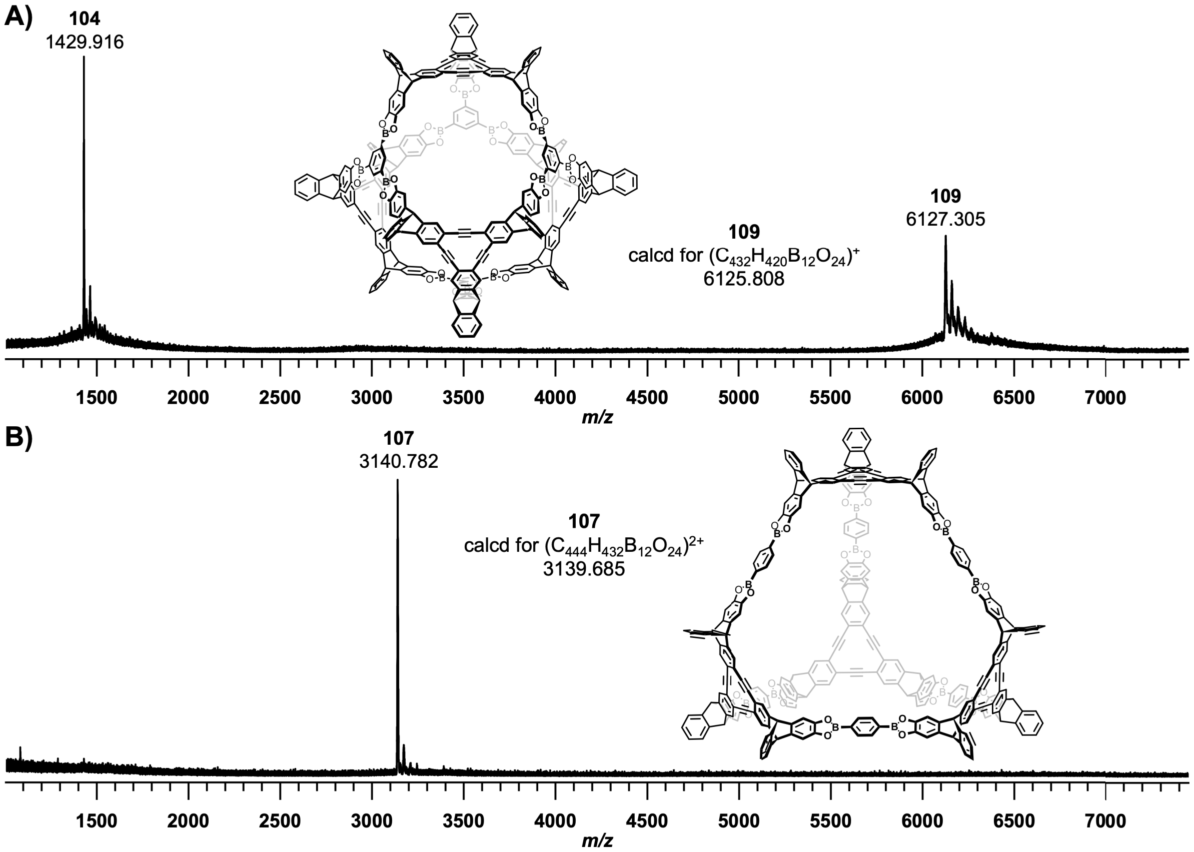

Figure 3.6: MALDI-TOF mass spectra of the synthesis attempts of cages **A) 109** after one week and **B) 107** after one day (also see **Scheme 3.10**). Both spectra revealed a peak that could belong to the respective cage compounds. The hexyl chains in both **109** and **107** were omitted for clarity.

The other boronic acid **106** delivered a mass-to-charge ratio of *m/z* 3140.782 after only one day, which did not change over the course of three weeks (**Figure 3.6B**). Notably, this peak appeared at approximately half the *m/z* value expected for the intended cage compound **107** (calcd. for $(C_{444}H_{432}B_{12}O_{24})^{+}$: 6279.370). Attempts to assign the signal to possible cage fragments – for instance to 2×**104**+2×**106**−6×H_2O (calcd. for $(C_{216}H_{220}B_4O_{14})^{+}$: 3081.687) or 2×**104**+3×**106**−8×H_2O (calcd. for $(C_{222}H_{224}B_6O_{16})^{+}$: 3211.727) – did not align with the experimental data. In contrast, it closely matched the doubly positively charged species of cage **107** (calcd. for $(C_{444}H_{432}B_{12}O_{24})^{2+}$: 3139.685). To conclude, although **103b** is not a suitable candidate for the synthesis of a shape-persistent cage by alkyne metathesis, it is still a valuable building block and offered promising initial results in the formation of boronic ester cages.

3.3 Propyne Monkey Saddle

*Some of the results presented within this chapter, namely the synthesis of propyne monkey saddle **116**, were first carried out by JULIUS ALEXANDER GUENTHER as part of his bachelor's thesis under my supervision.[256] Calculations on the enantiopure and -mixed cages were performed by DR. TOBIAS KIRSCHBAUM.*

Negatively curved polycyclic aromatic hydrocarbons (PAHs) have attracted considerable interest in recent years, as these molecules can be regarded as cutouts of Mackay crystals (see *Introduction Chapter 1.4*).[137-139, 141] In 2020, our group reported on monkey saddles, whose negative curvature arises from three eight-membered rings adjacent to three five-membered ones.[177] Although Dr. Tobias Kirschbaum presented a series of monkey saddles with different substituents (e.g., OMe, dioxolane, TIPS-acetylene, among others) in his dissertation, their assembly into fully conjugated cages remains elusive to this day.[184]

In this chapter, a new monkey saddle derivative suitable for alkyne metathesis is prepared. After its synthesis and characterization, its potential to generate a tetrameric monkey saddle-based cage is explored through an alkyne metathesis catalyst screening.

Synthesis of the Propyne Monkey Saddle

The addition of new groups to the monkey saddle scaffold is typically performed during the synthesis of the corresponding phenyl boronic acid pinacol esters, as this ensures their selective incorporation.[184] Accordingly, the required alkyne moieties were inserted in the first step by a Sonogashira cross-coupling between 5-bromosalicylaldehyde (**110**) and propyne, providing compound **111** in 97% yield (**Scheme 3.11A**). Subsequently, the hydroxy group of **111** was deprotonated and treated with triflic anhydride to give the triflate **112** in 77% yield, which in turn was converted to the boronic ester **113** by a Miyaura borylation using Pd(dppf)Cl_2 as catalyst, bis(pinacolato)diboron, and potassium acetate as base. Two-dimensional thin-layer chromatography (TLC) of **113** revealed its instability on silica gel, rendering flash column chromatography unsuitable for purification. Hence, impurities were first reduced by precipitating them with *n*-hexane, then excess bis(pinacolato)diboron was removed by sublimation, and the product **113** was finally isolated in 40% yield after distillation *in vacuo* (**Scheme 3.11A**).

In addition, trishexyloxytruxene **114** was brominated three-fold in the *para* positions following a literature procedure (**Scheme 3.11B**).[177] As a side reaction, one electrophilic aromatic substitution also occurs in the *ortho* instead of the *para* position, leading to a tedious separation of the two constitutional isomers by flash column chromatography.[177] To specify, the isolation of 2 grams of product **44** requires approximately 20 L of eluent (petroleum ether/toluene), which significantly limits its availability.

With tribromotruxene **44** and boronic ester **113** in hand, a three-fold Suzuki-Miyaura cross-coupling was carried out next to synthesize the aldehyde **115** (**Scheme 3.11B**). Based on the previously reported series of monkey saddles, reaction conditions exploiting the catalyst system $Pd_2(dba)_3$/XPhos and the solvent mixture THF/2 M $K_2CO_{3(aq)}$ proved to be broadly applicable.[184] Besides, it was found that the resulting aldehydes emerged as a mixture of C_1- and C_3-symmetrical atropisomers, which were not separable by flash column chromatography.[177, 184] Owing to their differing symmetries, the ^{1}H NMR spectra of the atropisomers displayed distinct signals, including four singlets belonging to the aldehydes and eight partially overlapping doublets for the fluorenyl protons, facilitating their rapid identification.[184]

Consequently, **44** and **113** were exposed to the catalyst system $Pd_2(dba)_3$/XPhos in the solvent mixture THF/2 M $K_2CO_{3(aq)}$. After vigorously stirring the reaction for 41 hours at 80 °C and an aqueous work-up, the ^{1}H NMR spectrum of the crude material lacked the distinctive chemical shifts expected for aldehyde **115**. Further investigations using MALDI-TOF mass spectrometry did not detect the product **115** either. Instead, three other compounds were observed, exhibiting mass-to-charge ratios of *m/z* 1014.375, 1032.416, and 1050.414 (**Figure 3.7A**). The difference of $\Delta m/z = 18$ between the signals strongly hinted at the loss of water from the system, and indeed the calculated masses of the one- (calcd for $(C_{75}H_{70}O_5)^+$: 1050.522), two- (calcd for $(C_{75}H_{68}O_4)^+$: 1032.512), and three-fold (calcd for $(C_{75}H_{66}O_3)^+$: 1014.501) intramolecularly condensed species aligned with this experimental data. Thus, the desired propyne monkey saddle **116** appears to have already formed during the cross-coupling reaction. Another closer examination of the ^{1}H NMR spectrum ultimately confirmed its generation with a characteristic singlet at $\delta = 8.29$ ppm attributed to the protons of the octagons.

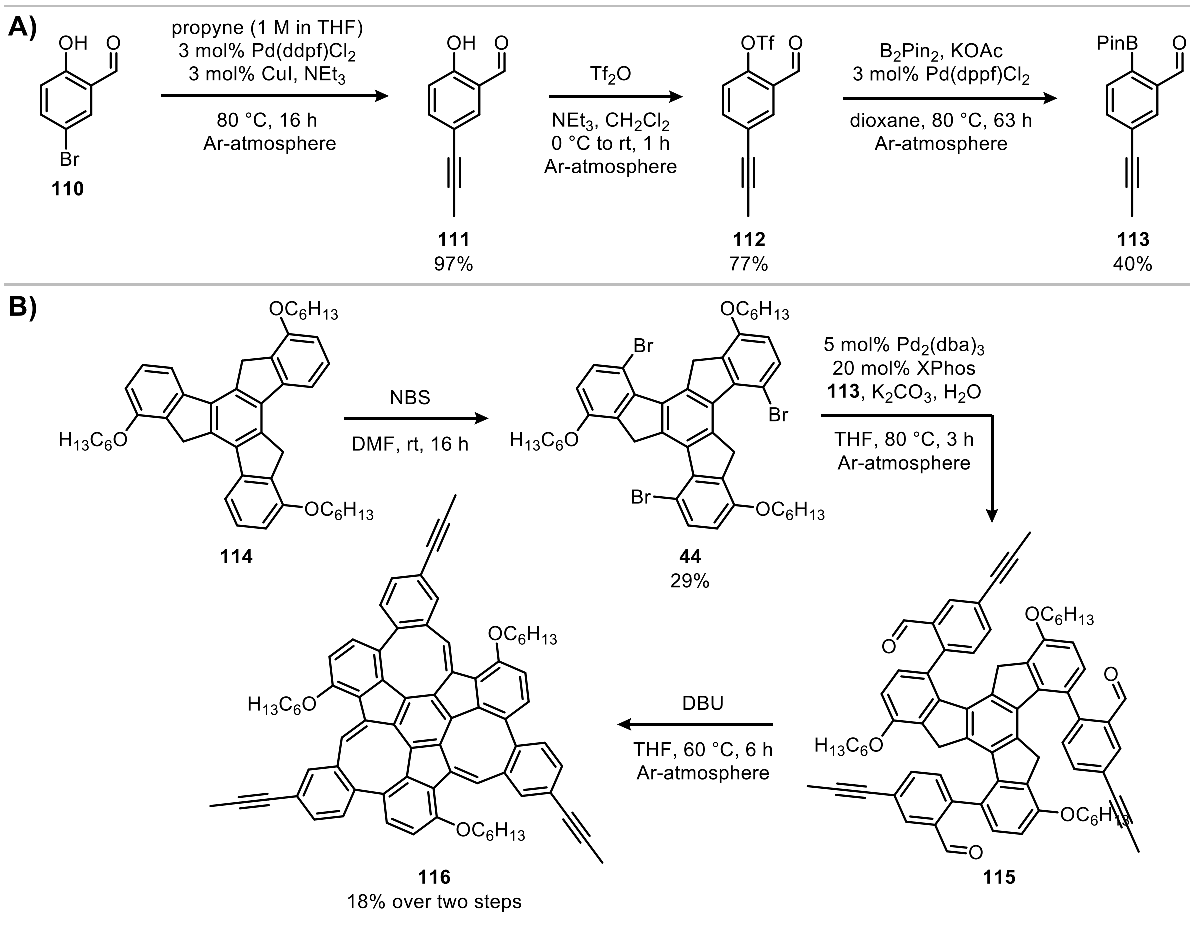

Scheme 3.11: A) Synthesis of boronic ester **113** containing a propyne group. **B)** Synthesis of propyne monkey saddle **116**. Compound **115** was not isolated in pure form. Instead, it was subjected to the condensation reaction after washing it with methanol, and the yield was only specified for **116** over two steps.

Unfortunately, this result was not reproducible, and another approach using the same reaction conditions resulted in a mass spectrum, which contained species with higher mass-to-charge ratios than **115** (**Figure 3.7B**). Although the spectrum was not well-resolved, signals at *m/z* 1194.580 and *m/z* 1320.652 suggested that condensation with excess protodeboronated **113** had occurred, corresponding to the one- (calcd for $(C_{85}H_{78}O_6)^+$: 1194.580) and two-fold (calcd for $(C_{95}H_{84}O_6)^+$: 1320.627) intermolecularly condensed compounds. Moreover, peaks at *m/z* 1176.633 and 1158.580, or *m/z* 1302.633 indicated further intramolecular condensations besides the intermolecular ones.

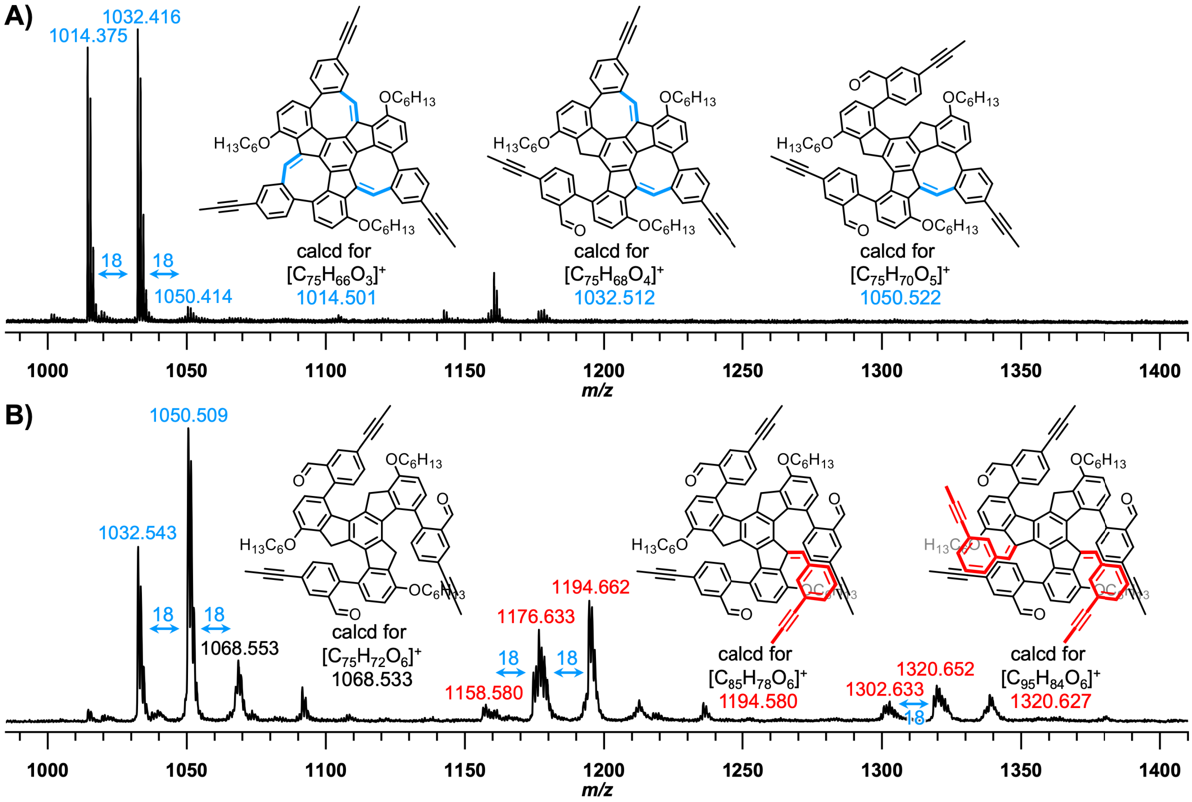

Figure 3.7: MALDI-TOF spectra of the Suzuki-Miyaura reaction to generate **115** showing **A)** intramolecular or **B)** intra- and intermolecular condensations as side reactions. Intramolecular condensations were highlighted in blue, intermolecular ones in red.

Due to the variety of byproducts, different bases (K_3PO_4, CsF, KF · 2 H_2O, Na_2CO_3), solvents (toluene, dioxane) and catalysts ($Pd_2(dba)_3$ with SPhos or $HP^tBu_3BF_4$, $Pd(PPh_3)_4$, $Pd(dppf)Cl_2$) were screened, but each attempt either ended in no conversion toward **115** or undesired side reactions. Given the lack of improvement, the original reaction conditions were reapplied with two modifications: the reaction time was reduced to 3 hours, and the amount of boronic ester **113** was limited to 3.3 equivalents in order to minimize intermolecularly condensed byproducts (**Scheme 3.11B**). After an aqueous work-up, aldehyde **115** was subjected to flash column chromatographic purification, which still did not provide the product in pure form.

Regardless, this material was submitted to the subsequent base-mediated condensation step. Initial approaches exploiting potassium hydroxide yielded the desired propyne monkey saddle **116** in 13% over two steps. Alternative bases (DBU, Cs_2CO_3, K_2CO_3, NEt_3) were explored as well, however no significant optimization was achieved with 16% yield for DBU, 15% for Cs_2CO_3, or 0% for both K_2CO_3 and NEt_3. Refining the purification process and applying DBU eventually delivered **116** in 18% yield over two steps (**Scheme**

3.11B). During the condensation, the yellow solution turned dark brown upon base addition, and the color persisted even after quenching the reaction with 6 M hydrochloric acid. Washing the flash chromatography column with ethyl acetate recovered the dark brown material, which did not exhibit any aromatic signals in ^1H NMR analysis. Hence, decomposition was assumed to be the primary cause of the reaction's low yields, and further optimization efforts were abandoned.

An analytically pure sample of propyne monkey saddle **116** was generated by silica gel-based high-performance liquid chromatography (HPLC). As previously mentioned, the protons H^a of the methine units give a characteristic singlet at $\delta = 8.28$ ppm in the ^1H NMR spectrum, which confirms the successful closure of the eight-membered rings (**Figure 3.8**). Since compound **116** is C_3-symmetrical, only five aromatic protons were observed. The two doublets at $\delta = 7.04$ and 6.95 ppm were assigned to the protons of the hexyloxy-substituted phenyl rings with H^b being upfield shifted compared to H^c because of the +M effect of the ether groups. Meanwhile, H^e of the propyne-functionalized benzene rings has coupling partners in *ortho*- and *meta*-position, causing the doublet of doublets at $\delta = 7.23$ ppm with $J = 8.0, 1.7$ Hz. The two remaining aromatic protons H^d and H^f appeared as doublets at $\delta = 6.74$ ppm and $\delta = 7.08$ ppm, respectively. Lastly, the methyl groups H^g capping the alkynes featured, as expected, a singlet at $\delta = 2.01$ ppm, integrating for nine protons in total (**Figure 3.8**).

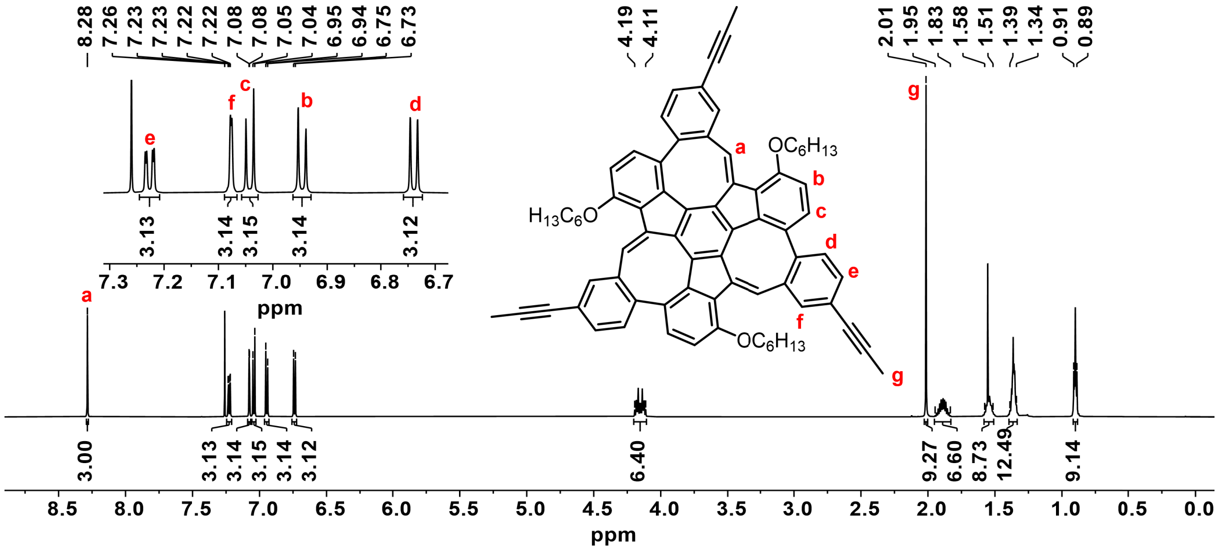

Figure 3.8: ^1H NMR spectrum (600 MHz, $CDCl_3$) of propyne monkey saddle **116** with assignment of distinctive protons.

Optical and Chiral Properties of Propyne Monkey Saddle 116

Investigating propyne monkey saddle **116** by UV/vis spectroscopy displayed the most intense absorption maximum in the UV region at $\lambda = 290$ nm and another, bathochromically shifted maximum at $\lambda = 408$ nm, which is responsible for the compound's yellow color (**Figure 3.9A**). Additionally, **116** exhibits a weak fluorescence at $\lambda_{em} = 539$ nm and thus a Stokes shift of $\tilde{\nu} = 5957$ cm^{-1}.

As monkey saddles are known to be chiral on account of the three biaryl axes in the molecule,[177, 184] chiral HPLC was used to separate the enantiomers of **116** (**Figure 3.9B**). After the material passed through a Chiralpak IE-column with a mixture of *n*-heptane and MTBE as eluent, the solvents were removed at 0 °C to prevent racemization of the enantiopure fractions. The isolated (S_a,S_a,S_a)- and (R_a,R_a,R_a)-enantiomers were analyzed by circular dichroism (CD) spectroscopy, showing mirror-image spectra with an opposite Cotton effect (**Figure 3.9C**). The most intense maximum is again located in the UV region at λ = 292 nm with a molar circular dichroism of ε = 215 M^{-1} cm^{-1}. To quantify the chiroptical response of chiral, optically active compounds, the dimensionless dissymmetry factor, g_{abs}, can be calculated as the ratio of the molar circular dichroism at a given wavelength to the corresponding extinction coefficient ($g_{abs} = \Delta\varepsilon(\lambda) / \varepsilon(\lambda)$).[257] Applying this equation to the data of **116** delivered the highest positive g_{abs} value of 2.06 × 10^{-3} at 254 nm and the lowest negative one of −2.69 × 10^{-3} at 452 nm. The observed dissymmetry factors are in the same order of magnitude (10^{-3}) as the previously reported monkey saddle series.[177, 184] Finally, TD-DFT calculations were used to predict the electronic circular dichroism (ECD) spectrum of (S_a,S_a,S_a)-**116**, which agreed with the experimental CD spectrum of the first eluted fraction, allowing the assignment of enantiomers (*cf.* **Figure 7.239** in the Appendix).

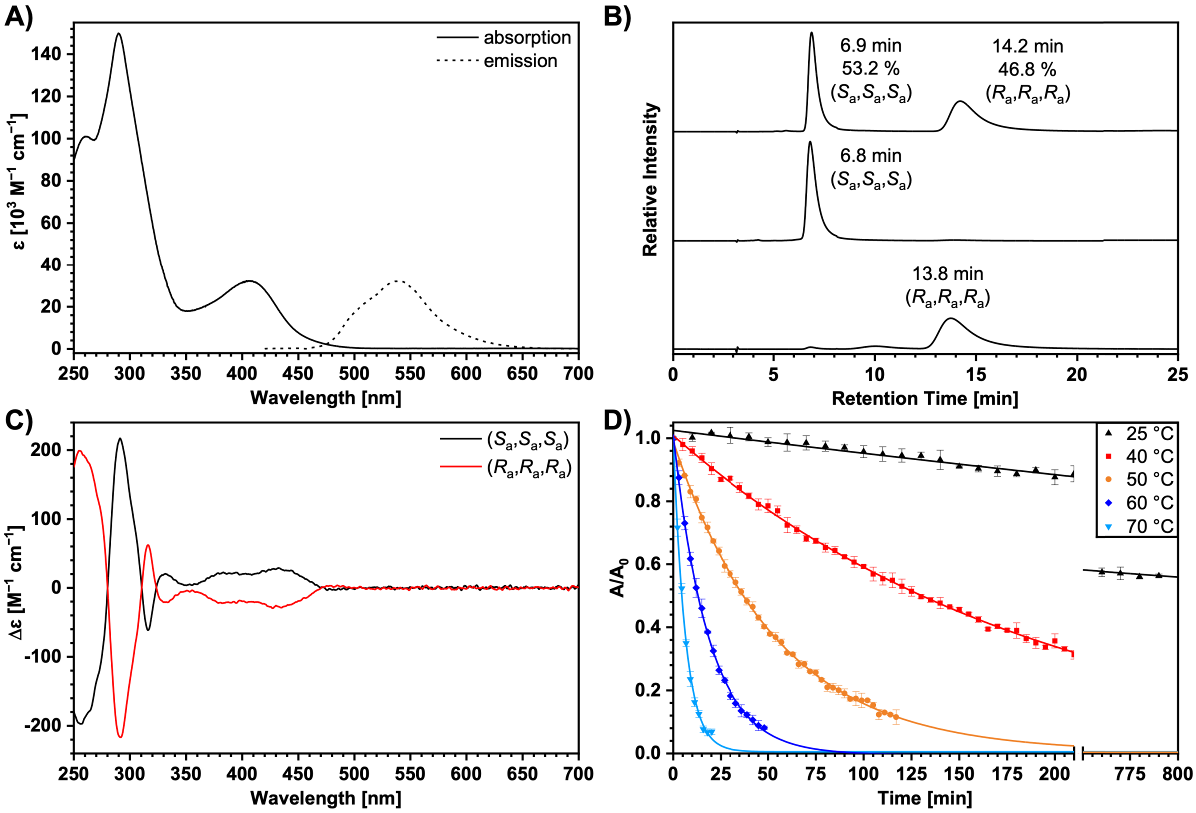

Figure 3.9: A) UV/vis absorption and emission spectrum of **116** both measured in CH_2Cl_2. An excitation wavelength of λ_{ex} = 403 nm was used to record the emission spectrum. **B)** Analytical chromatograms of **116** (IE column, *n*-heptane/MTBE (75:25 *v*:*v*), 1.0 mL min^{-1}, 30 °C, 300 nm) with assignment of the (S_a,S_a,S_a)- and (R_a,R_a,R_a)-enantiomer to the corresponding fraction. **C)** CD spectra of **116** (CH_2Cl_2, 20 °C). **D)** Decay of the CD signal intensity of (S_a,S_a,S_a)-**116** over time at different temperatures (*n*-heptane, 289 nm).

Moreover, the enantiopure material served to explore the conformational stability of **116**. Therefore, the (S_a,S_a,S_a)-enantiomer was subjected to kinetic CD measurements at five different temperatures ranging from 25 °C to 70 °C, with *n*-heptane as solvent to ensure comparability to the literature.[177, 184] Subsequently, the decay of the CD signal was plotted over time for the wavelength λ = 289 nm and fitted with an exponential function (**Figure 3.9D** and Appendix 7.12). This way, an inversion barrier of $\Delta G^{‡}$(25 °C) = 103 ± 1 kJ mol^{-1}

and a half-life of $t_{1/2}$(25 °C) = 15.3 ± 0.1 h could be determined. In comparison, the monkey saddle having no propyne groups exhibited an inversion barrier of $\Delta G^{\ddagger}$(25 °C) = 104 ± 2 kJ mol^{-1} and a half-life of $t_{1/2}$(25 °C) = 25 ± 0 h. Though, when raising the temperature to e.g., 70 °C, the half-life of **116** decreased drastically to $t_{1/2}$(70 °C) = 4.0 ± 0.1 minutes. Due to the lack of conformational stability, the use of enantiopure propyne monkey saddle **116** in chirality-assisted reactions is not a promising strategy, especially at elevated temperatures.

In conclusion, compound **116** aligns with the monkey saddle derivatives synthesized by Dr. Tobias Kirschbaum in its optical and chiroptical properties as well as inversion behavior, without deviating from expectations.[177, 184]

Alkyne Metathesis Catalyst Screening

The inherent curvature of propyne monkey saddle **116** combined with its C_3-symmetry provides an ideal pre-orientation for the formation of tetrahedral cage **76** (**Scheme 3.12A**). Although the alkyne metathesis catalyst does not require an exceptional functional group tolerance for converting **116**, a catalyst screening should still provide valuable insights owing to the precursor's considerable molecular size and the resulting steric demand. In collaboration with the group of Prof. Dr. Alois Fürstner at the Max-Planck-Institut (MPI) für Kohlenforschung in Mülheim an der Ruhr, five different catalyst systems were evaluated for their reactivity toward **116**. These included the trisamidomolybdenum(VI) propylidyne precatalyst **8**[104] with the silanol-based ligands **117**[67] or **12**,[107] alkylidyne complexes **15**[119] and **17**,[120] featuring a tripodal silanolate ligand framework, and catalyst **118**,[113] exhibiting a *p*-methoxybenzylidyne entity (**Scheme 3.12B**).

It has to be noted that the following screening was performed in the laboratory facilities of the MPI, whose mass department was not equipped for measuring molecules with a mass-to-charge ratio above 1000. Since the precursor **116** was found to give a signal at *m/z* 1014.5001, the reaction's progress could only be monitored on site by ^{1}H NMR spectroscopy and TLC. Consequently, reactions conditions had to be adjusted based on limited knowledge of **116**'s conversion. Meanwhile, each reaction attempt was stored in glass vials until they could be analyzed by the mass department at Heidelberg University using MALDI-TOF mass spectrometry. Additionally, each sample was submitted to gel permeation chromatography (GPC) in order to explore the size distribution of the generated species. Two representative GPC chromatograms are presented and discussed below.

All subsequent screening experiments were conducted in dry, degassed toluene under strict exclusion of moisture and oxygen. For reactions exceeding 48 hours, new catalyst loadings were added every two days. Observed fragments were designated by giving the **number** of **116** minus the **number** of released **2-butynes** in square brackets, for example the starting material **116** is referred to as [**1**-**0**], the dimer as [**2**-**1**], etc. The target cage **76** would be indicated as [**4**-**6**].

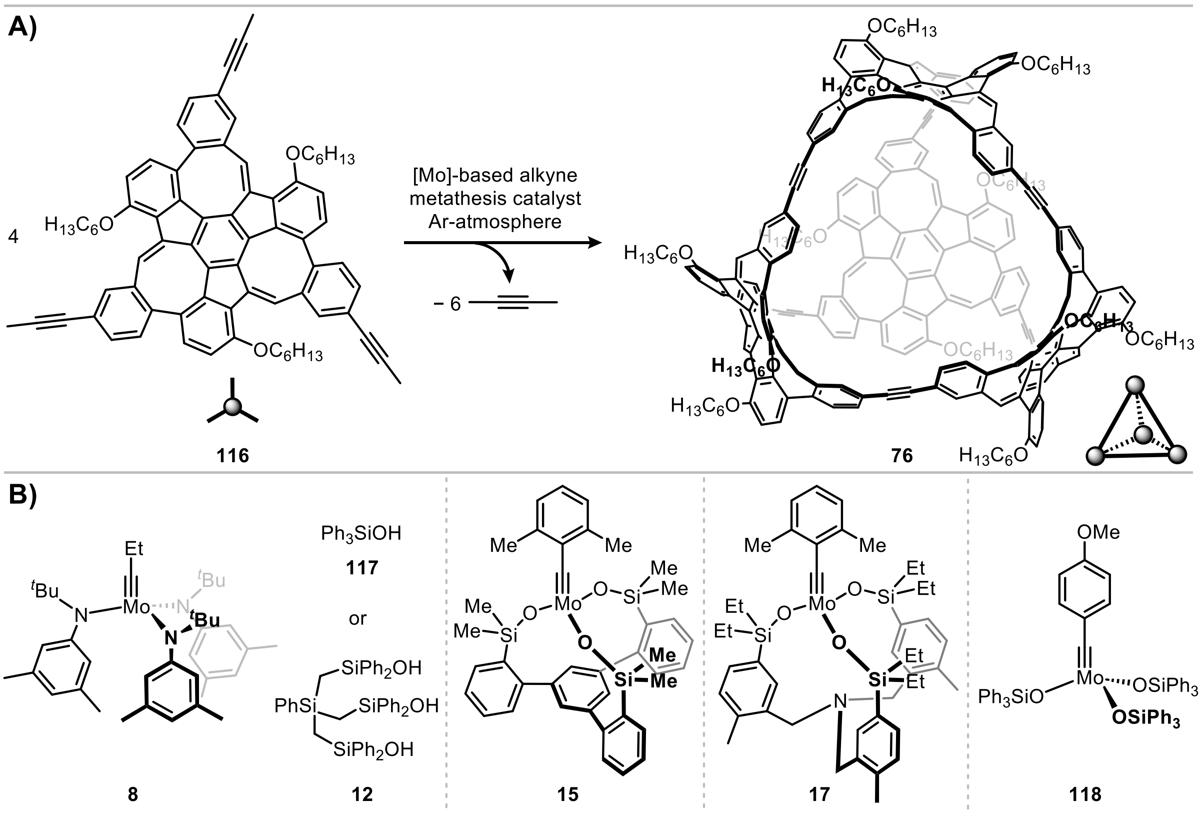

Scheme 3.12: A) General synthesis of tetrameric cage **76** using propyne monkey saddle **116** as precursor. **B)** Overview of screened [Mo]-based alkyne metathesis catalysts.

Starting with catalyst system **8**/**117**, a mixture of propyne monkey saddle **116** and powdered 5 Å molecular sieves was stirred at 70 °C for seven days (**Table 3.1**, Entry 1). ^{1}H NMR studies hinted at the formation of the dimer [**2**-**1**] alongside unreacted starting material, as the singlet at δ = 8.29 ppm – attributed to the COT protons of **116** – overlapped with another peak at δ = 8.30 ppm, likely corresponding to a newly generated monkey saddle species. MALDI-TOF mass spectrometry corroborated the incomplete consumption of **116** with a prominent peak at *m/z* 1015.356 (calcd for $(C_{75}H_{66}O_3)^+$: 1015.350). Additionally, the mass spectrum exhibited mass-to-charge ratios consistent with the dimer [**2**-**1**] at *m/z* 1976.798 (calcd for $(C_{146}H_{126}O_6)^+$: 1976.608), trimer [**3**-**2**] at *m/z* 2938.588 (calcd for $(C_{217}H_{186}O_9)^+$: 2937.866), and tetramer [**4**-**3**] at *m/z* 3899.913 (calcd for $(C_{288}H_{246}O_{12})^+$: 3899.124). Nevertheless, since the ^{1}H NMR spectrum primary displayed the presence of **116** despite the prolonged reaction time, the overall conversion was considered negligible.

Upon switching the ligand to silanol derivative **12** and stirring the reaction again at 70 °C for only 2 hours, no signals were detectable by either ^{1}H NMR or MALDI-TOF studies. It was assumed that compound **116** had undergone rapid polymerization until it precipitated as an insoluble solid, which was subsequently removed during filtration of the molecular sieves. In consequence, milder conditions were explored next by performing the reaction at room temperature. MALDI-TOF mass spectrometry included mass-to-charge ratios corresponding to monkey saddle species up to the tetramer [**4**-**3**], whereas ^{1}H NMR investigations showed signals of the monomer [**1**-**0**] and dimer [**2**-**1**] (**Table 3.1**, Entry 2-3).

Table 3.1: Summary of tested catalyst systems and reaction conditions to convert propyne monkey saddle **116** into tetrahedral cage **76** (*cf.* **Scheme 3.12**).[a]

Entry	**Catalyst**	**c [mM]**	**T [°C]**	**Time**	**5 Å MS**[b]	**Remark**	**^{1}H NMR of the crude**[c], [d]	**MALDI-TOF mass spectrometry**[c]
1	**8/117**	12	70	7 days	yes	–	mostly [**1**-**0**], [**2**-**1**]	[**1**-**0**], [**2**-**1**], [**3**-**2**], [**4**-**3**]
2	**8/12**	2	70	2 h	yes	solid in NMR	no signals	no signals
3	**8/12**	2	rt	2 h	yes	–	[**1**-**0**], [**2**-**1**]	[**1**-**0**], [**2**-**1**], [**3**-**2**], [**4**-**3**]
4	**15**	3.3	rt	2 days	no	–	[**1**-**0**]	[**1**-**0**]
5	**15**	2	120	18 h	yes	–	[**1**-**0**]	[**1**-**0**], [**2**-**1**], [**3**-**2**]
6	**17**	2	rt	13 h	no	–	[**1**-**0**]	[**1**-**0**]
7	**17**	2	70	50 min	yes	–	overlap of species	[**1**-**0**], [**2**-**1**], [**3**-**2**], [**3**-**3**], [**4**-**4**]
8	**118**	2	70	1 h	yes	–	no signals	no signals
9	**118**	2	rt	45 min	yes	–	no signals	no signals
10	**118**	2	rt	15 h	no	vacuum	[**1**-**0**]	[**1**-**0**]
11	**118**	2	40	13 h	no	vacuum	[**1**-**0**]	[**1**-**0**], [**2**-**1**]
12	**118**	2	70	3 h	no	–	overlap of species	[**1**-**0**], [**2**-**1**], [**3**-**2**], [**4**-**4**]
13	**118**	0.2	70	20 h	no	–	[**1**-**0**]	[**1**-**0**]
14	**118**	0.2	rt	20 h	yes	–	overlap of species	[**2**-**1**], [**3**-**3**]
15	**118**	0.2	rt	15 h	yes*	*pellets	[**1**-**0**]	[**1**-**0**]
16	**118**	0.2	rt	5.5 h	no	Ar-bubbling	[**1**-**0**], [**2**-**1**]	[**1**-**0**], [**2**-**1**], [**3**-**2**], [**4**-**3**]
17	**118**	2	70	20 h	yes	+ 0.2 equiv. diphenylacetylene	no signals	no signals
18[e]	**118**	2	rt	23 h	yes	+ 0.2 equiv. 2-octyne	[**1**-**0**]	[**1**-**0**]*, [**2**-**1**], [**3**-**2**], [**4**-**3**]

[a]: The reaction vessels were flame-dried with a Bunsen burner and set under argon before use. Starting material **116** (5.0 µmol, 5.1 mg) and the respective catalyst (20 mol%) were added and dissolved in dry, degassed toluene. All reactions were carried out under strict exclusion of moisture and oxygen. When molecular sieves were applied, the reaction was filtered over a pad of Celite, washed with CH_2Cl_2, and the solvents of the filtrate were removed under reduced pressure. When no molecular sieves were applied, a few drops of MeOH were added to quench any remaining catalyst, and the solvents were directly removed under reduced pressure.
[b]: MS: molecular sieves.
[c]: The designation of species was done as follows: [Number of starting molecules **116** – number of released **2-butynes**].
[d]: 'No signals' indicates that no monkey saddle-based signals were observed in the ^{1}H NMR spectrum, or that potential product peaks were obscured by signals of the used catalyst/ligand. 'Overlap of species' refers to spectra, in which broad signals appeared in the regions typically associated with the monkey saddle, but no clear distinction between compounds could be made.
[e]: (S_a, S_a, S_a)-**116** was used instead of the racemate.

At first glance, these findings suggest a significantly higher activity of **8**/**12** compared to **8**/**117**. However, it is important to consider that precatalyst **8** remains stable for merely a few days, even when stored in a glovebox.[62, 112, 115] Since ligand **117** was tested with an older batch of **8** and **12** with a freshly prepared one, the observed differences in catalytic performances may stem from the general lability of **8**. An improved stability of the catalyst should therefore deliver more reliable results.

Next in line were the alkylidyne complexes **15** and **17**, whose tripodal ligands endow the catalysts with excellent functional group tolerance, high activity, and good stability (**Scheme 3.12B**).[119-120] Remarkably, the pyridine adduct of **17** stayed intact for months even outside the glovebox.[120] Catalyst **15** was initially applied at room temperature, which led to the recovery of starting material **116** in pure form. Increasing the temperature to 120 °C, adding 5 Å molecular sieves and stirring the reaction for 18 h yielded the monomeric, dimeric and trimeric species according to MALDI-TOF MS. Yet ^{1}H NMR studies exclusively disclosed chemical shifts attributed to propyne monkey saddle **116**, showing that elevated temperatures did not enhance its consumption. The rigid structure of catalyst **15** appears to be incompatible with the steric demands of **116**, likely impeding efficient oligomerization (**Table 3.1**, Entry 4, 5).

In catalyst **17**, the design of the ligand framework was revised compared to **15** by incorporating a tris-benzylic amine instead of a central benzene ring.[120] This modification introduces additional degrees of rotational freedom, which are expected to accommodate space-filling substrates more effectively. Beginning again at room temperature, no reactivity could be monitored after treating **116** with catalyst **17** for 13 hours. The temperature was then elevated to 70 °C, 5 Å molecular sieves were added, and the mixture was stirred for 50 min (**Table 3.1**, Entry 6, 7). ^{1}H NMR analysis revealed broad peaks in the regions associated with monkey saddle protons, indicating a potential formation of oligomers. Furthermore, MALDI-TOF MS studies contained unprecedented mass-to-charge ratios at *m/z* 2884.595 and *m/z* 3846.092, which are consistent with trimer [**3**-**3**] (calcd for $(C_{213}H_{180}O_9)^+$: 2883.774) and tetramer [**4**-**4**] (calcd for $(C_{284}H_{240}O_{12})^+$: 3845.032), alongside the previously observed species [**2**-**1**], [**3**-**2**] as well as the starting material **116** (**Figure 3.10**). So far, catalyst **17** exhibited the most promising activity, because it not only supported an ordinary oligomerization, but also the generation of [**3**-**3**] and [**4**-**4**] – species in which one more triple bond was closed than required to create a trimeric or tetrameric structure.

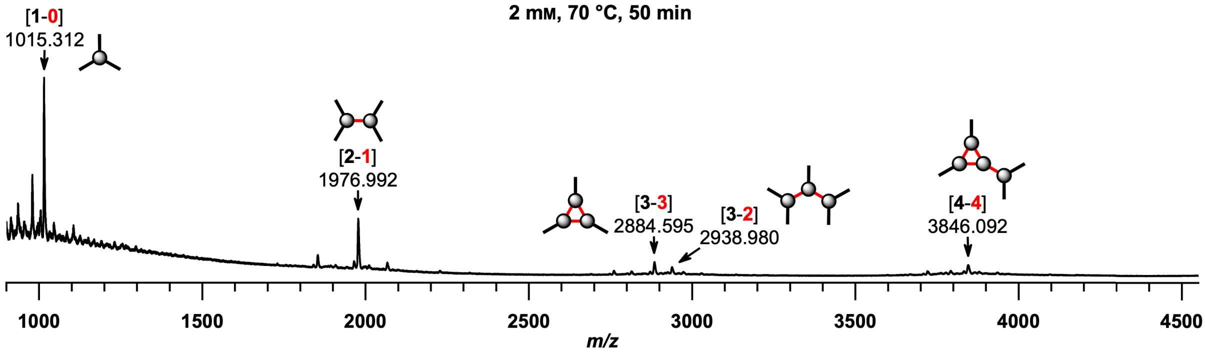

Figure 3.10: MALDI-TOF mass spectrum of **116** after treating it with catalyst **17** at 70 °C for 50 min. 5 Å Molecular sieves and a concentration of 2 mM were used (*cf.* **Table 3.1** Entry 7).

Lastly, the application of catalyst **118** was scrutinized. When the respective alkyne metatheses were conducted using 5 Å molecular sieves at either room temperature or 70 °C, one hour of reaction time sufficed to completely convert starting material **116** into novel compounds (**Table 3.1**, Entry 8, 9). Since neither ^{1}H NMR nor MALDI-TOF mass spectrometric investigations recorded any monkey saddle related signals, it was assumed that **116** had polymerized until it precipitated as an insoluble solid, which was then removed while filtering the molecular sieves off. In this case, **118** is even more active towards **116** than catalyst **17**, as the latter did not manage **116**'s exhaustive consumption within 1 hour at 70 °C.

Owing to **118**'s high activity, the reaction needed to be slowed down to avoid polymerization into insoluble material and simultaneously improve the ratio of intramolecular to intermolecular alkyne closures. To implement these considerations, the byproduct 2-butyne had to be removed less efficiently from the reaction mixture, for instance by applying vacuum instead of 5 Å molecular sieves. Hence, the metathesis was repeated under reduced pressure at 40 °C and room temperature (**Table 3.1**, Entry 10, 11). Analyzing both entries by ^{1}H NMR and mass spectrometry revealed **116** as the sole monkey saddle-based compound present. With the lack of conversion, vacuum was not a viable alternative.

Thermal removal was explored next because of the low boiling point (27 °C) of 2-butyne.[254] Therefore, precursor **116** and catalyst **118** were stirred at 70 °C for 3 hours (**Table 3.1**, Entry 12). Subsequent ^{1}H NMR studies disclosed broad signals in the region characteristic for monkey saddle protons, while MALDI-TOF mass spectrometry confirmed **116**'s oligomerization up to the tetrameric fragment [**4**-**4**]. Although the data point toward a moderated alkyne metathesis process, the degree of intramolecular closures did not increase compared to preceding attempts, implying that polymerization was only decelerated instead of redirected.

Another important parameter for cage synthesis is the concentration, as higher dilutions promote reactions within a molecule rather than between them. Correspondingly, the concentration was reduced by a factor of ten from 2 mM to 0.2 mM in the following. In this diluted state, elevated temperatures of 70 °C alone did not achieve a detectable transformation of **116** (**Table 3.1**, Entry 13). Thus, 5 Å molecular sieves were reintroduced at room temperature in both powder and pellet form. While the use of pellets resulted in no observable conversion, the powder enabled **116**'s oligomerization again up to the trimer [**3**-**3**] (**Table 3.1**, Entry 14, 15). As a final strategy to diminish the 2-butyne concentration, argon was continuously bubbled through the reaction mixture. However, this method is accompanied by solvent evaporation, necessitating regular refilling, and after 5.5 hours at room temperature, the MALDI-TOF mass spectrum detected a mixture of the species [**1**-**0**], [**2**-**1**], [**3**-**2**], and [**4**-**3**] (**Table 3.1**, Entry 16). Based on these findings, higher dilutions did not encourage additional intramolecular alkyne closures, which prompted a return to the original concentration of 2 mM.

The reversibility of this reaction could potentially also be enhanced by employing diphenylacetylene as an additive while scavenging 2-butyne with powdered 5 Å molecular sieves. After stirring this entry at 70 °C for 20 h, neither ^{1}H NMR nor MALDI-TOF MS studies contained any signals related to monkey saddles (**Table 3.1**, Entry 17). Nevertheless, GPC investigations still showed a dominant peak at 21.8 min (**Figure 3.11A**). According to records of prior GPC chromatograms, the starting material **116** typically elutes at 29.2 min, which means that this new species must exhibit a larger hydrodynamic radius than **116** due to the shorter retention time. After isolating the peak at 21.8 min by recycling GPC, the ^{1}H NMR spectrum displayed only a single resonance at $\delta = 0.07$ ppm, which can be attributed to grease. This signal originated either from the grease used during the alkyne metathesis reaction or from the GPC tubing. Moreover, no peaks were detected in the mass spectrum. Consequently, the peak observed in the GPC chromatogram at 21.8 min could simply correspond to grease, or, if another compound was present, its amount was too low to provide structural information.

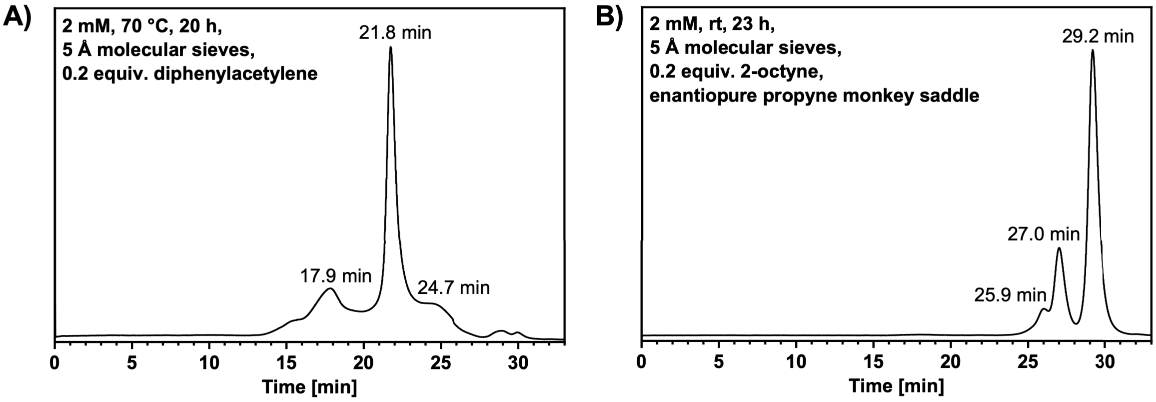

Figure 3.11: GPC chromatograms of reaction attempts toward tetrameric cage **76** using catalyst **118**. Both reaction entries employed a concentration of 2 mM and powdered 5 Å molecular sieves. **A)** 0.2 Equiv. diphenylacetylene were added to increase the reversibility of the reaction at 70 °C (**Table 3.1**, Entry 17). **B)** The reaction was set up with enantiopure propyne monkey saddle (S_a,S_a,S_a)-**116** at room temperature, and 0.2 equiv. 2-octyne were again added for reversibility (**Table 3.1**, Entry 18). The peaks could be assigned to **116** (R_t = 29.2 min), [**2**-**1**] (R_t = 27.0 min), and [**3**-**2**] (R_t = 25.9 min) based on MALDI-TOF mass spectrometric investigations.

Despite the variety of screened conditions and different approaches, the targeted cage synthesis could not be steered beyond nonselective oligomerization. As stated before, **116** consists of a mixture of (S_a,S_a,S_a)- and (R_a,R_a,R_a)-enantiomers, which should lead to the assembly of enantiopure as well as enantiomixed cages during alkyne metathesis. Though, reconsidering the pre-orientation of **116**'s alkyne groups, the question arises whether the construction of enantiomixed cages is generally possible. For a closer examination, models of the respective cage isomers were optimized at the B3LYP/6-31G(d) level of theory, revealing that the enantiopure cages are energetically favored over enantiomixed ones by up to 49 kJ mol^{-1} (**Figure 3.12**). Therefore, the issue of the targeted tetramerization might not lie in the choice of reaction conditions, but rather in the necessity of using enantiopure starting material, since the formation of enantiomixed cages is thermodynamically disfavored, if not unfeasible. Another important factor could be the entropic contribution of cage closure, as this reaction step would suppress racemization of the individual monkey saddle building blocks, thereby reducing the degrees of freedom and thus the configurational entropy.

As determined experimentally, propyne monkey saddle **116** has a racemization barrier of $\Delta G^{\ddagger}$(25 °C) = 103 ± 1 kJ mol^{-1} and a half-life of 15.3 ± 0.1 h at room temperature, which decreases drastically to 4 ± 0.1 min at 70 °C. Naturally, enantiopure **116** can still be applied for the synthesis of cage **76**, yet its limited conformational stability restricts the reaction temperature to 25 °C. Hence, a last attempt was carried out using (S_a,S_a,S_a)-**116**, catalyst **118**, 5 Å molecular sieves, and 2-octyne to enhance the reversibility (**Table 3.1**, Entry 18). After stirring the mixture for 23 hours at room temperature, MALDI-TOF mass spectrometry included mass-to-charge ratios of the species [**1**-**0**], [**2**-**1**], [**3**-**2**], and [**4**-**3**], but no significant conversion was evident based on ^{1}H NMR studies. The GPC chromatogram confirmed the predominance of unreacted starting material with a peak at 29.2 min (**Figure 3.11B**). Additionally, two other compounds with shorter retention times were detected and separated by recycling GPC, leading to the isolation of the dimer [**2**-**1**] (R_t = 27.0 min). It has to be noted that this product could only be obtained in a low quantity, which precluded further characterization by ^{13}C or 2D NMR techniques and accordingly, a definitive assignment of the aromatic protons.

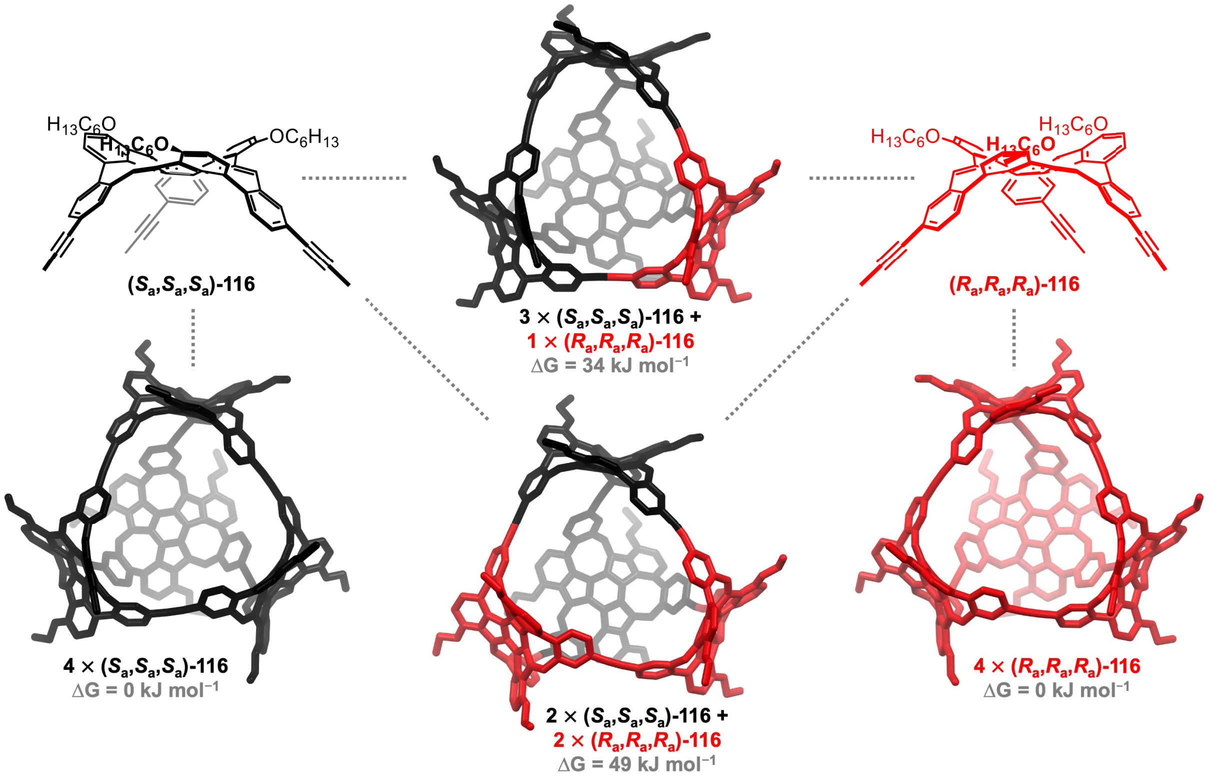

Figure 3.12: Illustration of the enantiomers (S_a,S_a,S_a)-**116** (black) and (R_a,R_a,R_a)-**116** (red) as well as the corresponding enantiopure and enantiomixed cages. The structures of the cages were optimized at the B3LYP/6-31G(d) level of theory.

Nevertheless, its ^{1}H NMR spectrum exhibited two distinctive features that supported dimerization (**Figure 3.13**). First, two overlapping singlets appeared at δ = 8.30 and 8.29 ppm – a region typical for the COT protons – reflecting the dimer's asymmetry and the altered chemical environment of the protons near to the newly formed triple bond. Second, the singlet at δ = 2.01 ppm, arising from the remaining propyne groups, showed a 2:1 integral ratio relative to the COT protons, as expected for [**2**-**1**]. In comparison, **116** displayed a 3:1 ratio, the trimer [**3**-**2**] would have approximately a 1.67:1 ratio, etc.

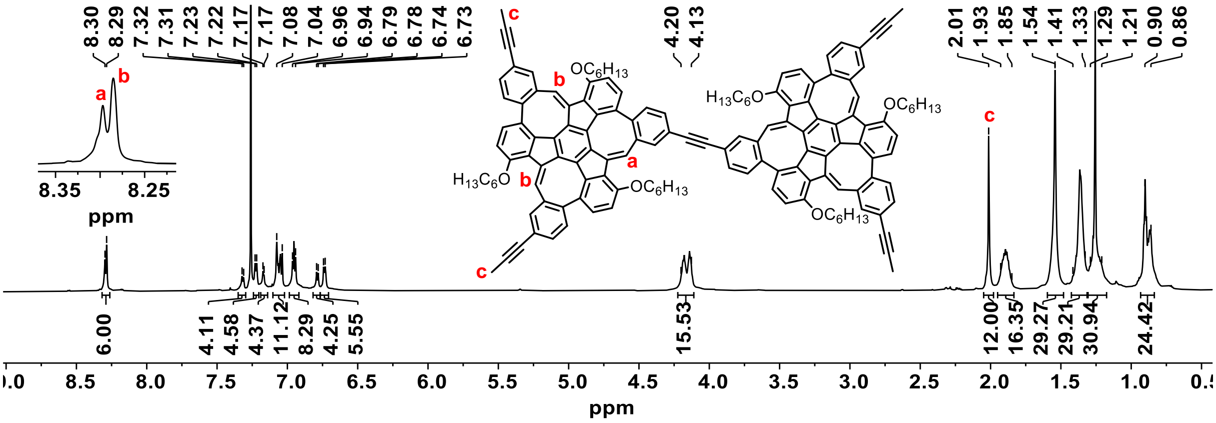

Figure 3.13: ^{1}H NMR spectrum (700 MHz, $CDCl_3$) of the dimeric species [**2**-**1**] after separation by recycling GPC. Distinct protons were assigned to their representative signals.

Interestingly, when the racemate had been subjected to very similar reaction conditions, it was polymerized into insoluble material within one hour at room temperature, whereas enantiopure **116** barely transformed into the dimeric species after 23 hours (compare **Table 3.1**, Entry 9 and 18). This outcome could indicate that the pre-orientation of the alkynes plays a crucial role in directing the reaction pathway toward the construction of the desired cage **76**. However, successful cage closure likely requires elevated temperatures (80-120 °C), which are incompatible with **116** due to its rapid racemization under these conditions.

Summary

In conclusion, the monkey saddle core was functionalized with three propyne groups to serve as a cage precursor for alkyne metathesis. The synthesis of **116** was accomplished in six steps, whereby the last one resulted in significant yield losses, which were presumably caused by substrate decomposition. After characterizing the propyne monkey saddle **116** and separating its enantiomers, the latter were examined by CD and TD-DFT. Furthermore, kinetic CD measurements using (S_a,S_a,S_a)-**116** delivered an inversion barrier of $\Delta G^‡(25\ °C) = 103 \pm 1\ \text{kJ mol}^{-1}$ and a half-life of $t_{1/2}(25\ °C) = 15.3 \pm 0.1\ \text{h}$.

Following, five different alkyne metathesis catalysts were tested on **116** in collaboration with Prof. Dr. Alois Fürstner at the MPI für Kohlenforschung. The performed catalyst screening showed that **15** had no considerable activity toward the designed monkey saddle building block, while **8**/**117**, **8**/**12**, and **17** exhibited low to moderate efficiency. The most active catalyst proved to be **118**, which polymerized **116** into insolubility within one hour at room temperature. Subsequent experiments investigated strategies (e.g., molecular sieves, vacuum, argon, temperature, concentration or additives) to decelerate polymerization and favor intramolecular alkyne metathesis. However, each attempt ultimately led to the recovery of the starting material or its polymerization, as confirmed by ^{1}H NMR and MALDI-TOF mass spectrometry.

These findings raised the question whether the use of the racemate was hindering cage formation. DFT calculations indeed proposed that the enantiomixed cages are energetically less favored compared to the enantiopure ones, rendering their generation probably unfeasible. Accordingly, a final alkyne metathesis attempt was carried out by treating (S_a,S_a,S_a)-**116** with catalyst **118**. Although small quantities of the dimeric compound were isolated, no substantial conversion could be observed, even after 23 hours at room temperature. The proper pre-orientation of the triple bonds with respect to **76**'s formation may have impeded straightforward polymerization, supporting the hypothesis that only the enantiopure cages are accessible.

Given the low conformational stability of **116**, pursuing alkyne metathesis at higher temperatures is not a viable approach, as the compound would revert to a racemic mixture within minutes. Therefore, a monkey saddle derivative is required that can retain its stereochemical integrity at elevated temperatures, which in turn would enable chirality-assisted syntheses. This objective will be further addressed in the following chapters.

3.4 Chromene Monkey Saddle

Parts of this chapter were previously published and can be found under: T. Kirschbaum[+]*, S. F. Ebel*[+]*, F. Rominger, M. Mastalerz, "Suppressing Inversion of a Chiral Polycyclic Aromatic Aza Monkey Saddle by Molecular Editing", Helv. Chim. Acta* ***2024****, 107, e202400158.* [+]*: equal contributions.*[186] *The synthesis of the functionalized aza monkey saddle* ***131*** *was performed by Sarah Schott as part of her bachelor's thesis under my supervision.*[258]

In 2020, Mastalerz and coworkers reported on a modified monkey saddle structure in which the CH units of **47** were replaced by nitrogen atoms (**Scheme 3.13**).[185] The obtained aza monkey saddle **56** did not only feature stabilized frontier molecular orbitals that tuned its optoelectronic properties, but also exhibited an increased inversion barrier of $\Delta G^{\ddagger}(25\ °\text{C}) = 115 \pm 8\ \text{kJ mol}^{-1}$, corresponding to a half-life of 7.7 ± 0.1 hours at 70 °C.[184-185] To improve the molecule's conformational stability even further, Dr. Tobias Kirschbaum explored the synthesis of the respective *N*-oxide by treating aza monkey saddle **56** with *meta*-chloroperoxybenzoic acid (*m*CPBA).[184, 186] Single-crystal X-ray diffraction of the resulting product **57** ultimately revealed that the oxygen atoms had been rearranged and inserted into the five-membered rings, forming carboximidate groups (**Scheme 3.13**). Based on investigations of the racemization behavior, chromene monkey saddle **57** can be considered inversion stable, as no decrease in *ee* was observed after heating the single enantiomers at 220 °C for 47 days.[186]

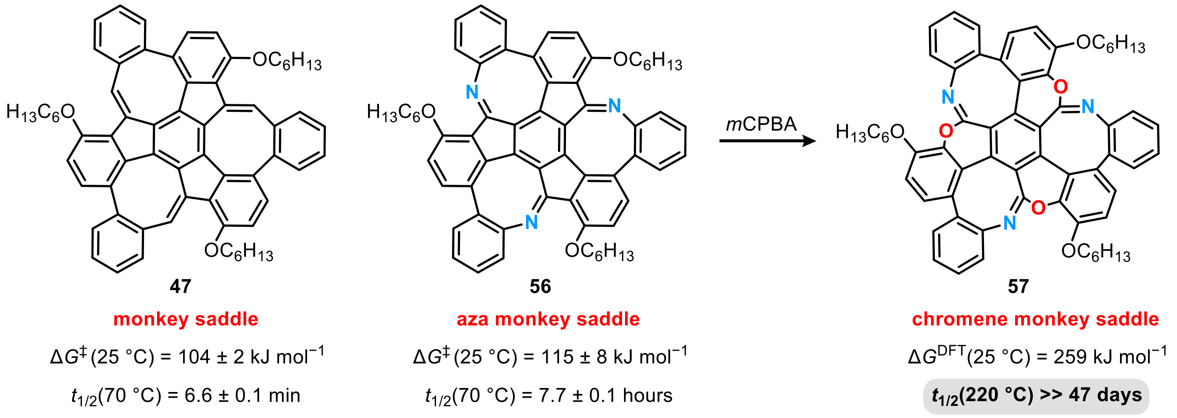

Scheme 3.13: Overview of previously synthesized monkey saddles with a summary of their racemization behavior. Chromene monkey saddle **57** showed no decrease in *ee* after heating the enantiomers at 220 °C for 47 days.

Owing to **57**'s exceptional conformational stability, the chromene monkey saddle core is a promising candidate for chirality-assisted syntheses,[259-260] provided that additional functional groups are introduced to enable further chemical transformations. Consequently, this chapter focuses on post- as well as prefunctionalization strategies for the chromene monkey saddle. Yet beforehand, the limited accessibility of the brominated trishexyloxytruxene **44**, which originates in its extensive purification, will be revisited, as this synthetic challenge also constrains the general availability of monkey saddles.

Improved Synthesis of the Chromene Monkey Saddle

The route toward monkey saddles usually starts with trishydroxytruxene **119**, which was supplied by the introductory organic chemistry practical course at Heidelberg University (**Scheme 3.14**). In the original procedure,[177] the hydroxy groups were first protected with hexyl chains to avoid future solubility issues, followed by a three-fold bromination. The latter produced a mixture of constitutional isomers, whose separation requires a tedious column chromatographic purification.[177] As discussed in chapter 3.3, approximately 20 L of eluent (petroleum ether/toluene 9:1) are consumed to isolate 2 grams of the desired product **44**, continuously restricting its available stock. Changing the protecting groups might offer a solution to improve the sustainability and efficiency of this step. For instance, if a sterically more demanding group such as isopropyl is employed, the generation of the unwanted isomer could potentially be minimized or the purification process simplified.

To examine this approach, trishydroxytruxene **119** was protected with isopropylbromide (**Scheme 3.14**). Initial conditions applied potassium carbonate in DMF at 100 °C and furnished the product **120** in an acceptable yield of 61%. However, this result was only reproducible on a 1.0 mmol (390 mg) scale of **119**. A three-fold scale-up already led to a significant drop in yield to 29%, which continued to decline with increasing amounts of starting material. Therefore, alternative conditions were tested, and the use of sodium hydroxide in a DMSO/H_2O-solvent mixture provided **120** in a reproducible yield of 54%, even on a 30 mmol (12 grams) scale of **119**. Single crystals suitable for X-ray diffraction analysis were obtained by slow diffusion of *n*-hexane into a solution of **120** in CH_2Cl_2, confirming its structure (**Figure 3.14A**).

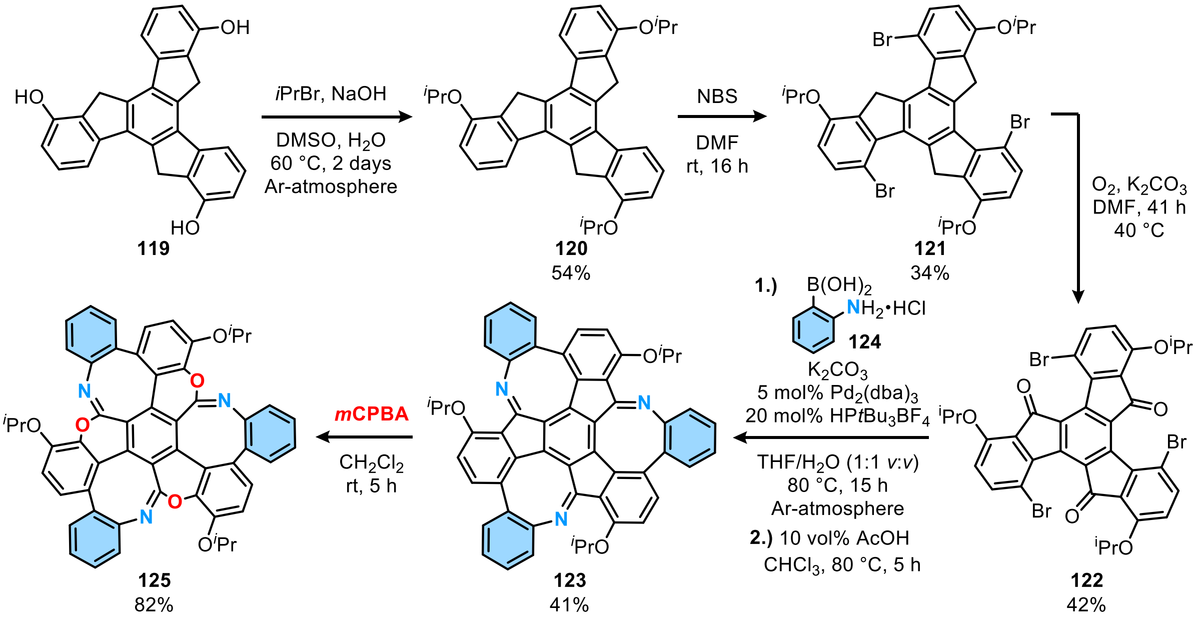

Scheme 3.14: Synthesis of chromene monkey saddle **125** using isopropyl protecting groups.

Next, **120** was brominated with 3.1 equiv. NBS in DMF to give product **121** in 34% yield after flash column chromatography (**Scheme 3.14**). Notably, the latter purification method proceeded more efficiently than for the hexyloxy derivative **44**, and the isolation of 5 grams of **121** required only around 5 L of eluent (petroleum ether/CH_2Cl_2 4:1). This outcome finally solved the limited accessibility issue of this building block. Subsequently, the methylene groups of the fluorene subunits were oxidized following the procedure reported by Kirschbaum *et al.*.[185] Thus, compound **121** was mixed with potassium carbonate under an oxygen atmosphere at 40 °C, delivering truxenone **122** in 42% yield as a brown-yellowish solid (**Scheme 3.14**). Single crystals of **122** were readily obtained by slow evaporation of a $CDCl_3$ solution of it (**Figure 3.14B**). Due to the steric repulsion between the bromine and carbonyl oxygen atoms ($d_{\text{Br-O}}$ = 3.1 Å), the truxene core adopted a contorted geometry featuring three helical substructures and causing the formation of the (*P*,*P*,*P*)- and (*M*,*M*,*M*)-enantiomers (**Figure 3.14C**).

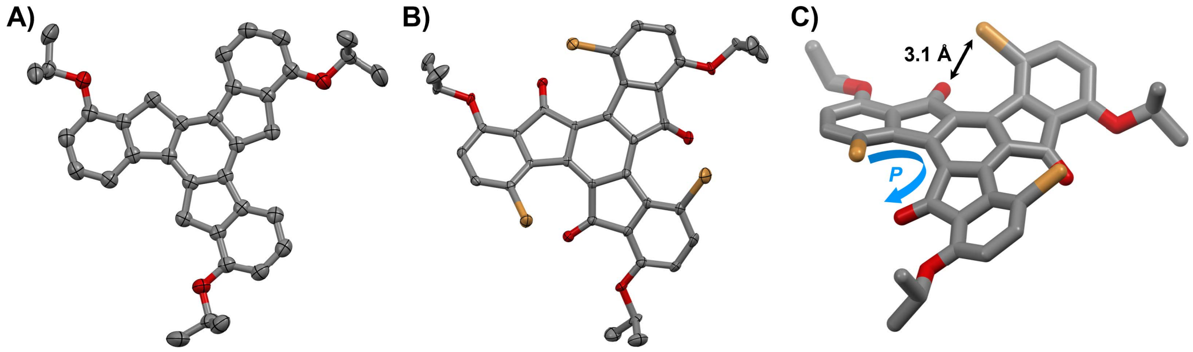

Figure 3.14: Single crystal structures of truxene derivatives **A) 120** and **B) 122** as ORTEP drawing with 50% probability of ellipsoids. **C)** Stick model of one (*P*,*P*,*P*)-enantiomer of **122**. Hydrogens were omitted for clarity. Grey = carbon, red = oxygen, brown = bromine.

In order to convert truxenone **122** into aza monkey saddle **123**, a three-fold Suzuki-Miyaura cross-coupling was carried out with boronic acid **124** and the catalyst system $Pd_2(dba)_3$/$HP^tBu_3BF_4$ (**Scheme 3.14**). After excess **124** was removed from the crude material by flash column chromatography, the coupled product was exposed to an acid-catalyzed condensation reaction to isolate the aza monkey saddle **123** as an orange solid in 41% yield over two steps. ^{1}H NMR analysis of **123** revealed a C_3-symmetrical compound, which has six chemically non-equivalent aromatic protons (**Figure 3.15A**). The doublets at δ = 7.39 and 7.06 ppm can be attributed to the isopropoxy-substituted benzene rings, with proton H^a shifted up-field owing to its *ortho*-position relative to the electron-donating alkoxy group. Besides, *ortho*-coupling of the protons H^c and H^f caused the two doublets of doublets (dd) at δ = 6.94 and 6.90 ppm, whereby their further assignment was possible by coupling between H^c and H^b in ^{1}H-^{1}H NOESY experiments. The remaining aromatic protons, H^d and H^e, each coupled with two *ortho* and one *meta* proton, resulting in the doublets of doublets of doublets (ddd) at δ = 7.30 and 7.12 ppm. Lastly, the isopropyl groups appeared with a characteristic septet at δ = 4.78 ppm and two doublets at δ = 1.44 and 1.38 ppm (**Figure 3.15A**). While the observed signals in the ^{1}H NMR spectrum are consistent with **123**, its structure was additionally confirmed by single crystal X-ray diffraction analysis, which is discussed in the next subchapter.

As discovered by Dr. Tobias Kirschbaum,[184, 186] the aza monkey saddle undergoes a rearrangement to the chromene monkey saddle upon treatment with *meta*-chloroperoxybenzoic acid (*m*CPBA) in dichloromethane at room temperature. Applying these conditions to **123** indeed delivered the rearranged product **125** as a colorless solid in 82% yield (**Scheme 3.14**). High-resolution MALDI-TOF mass spectrometry corroborated the incorporation of three oxygen atoms with a measured mass-to-charge ratio of *m/z* 825.2832 (calcd for $(C_{54}H_{39}N_3O_6)^+$: 825.2833) (**Figure 3.15C**). Moreover, ^{1}H NMR studies of **125** showed that proton H^b experienced the most pronounced chemical shift from $\delta = 7.39$ ppm to $\delta = 7.00$ ppm, thus agreeing with the expected *para*-insertion of the oxygen atoms relative to H^b (**Figure 3.15B**). Regarding the IR spectrum, the C=N stretching band shifted from $\tilde{\nu} = 1649$ cm^{-1} in **123** to $\tilde{\nu} = 1703$ cm^{-1} in **125**, which is indicative for a more electron-rich surrounding of the C=N double bond and can be found in such cyclic imidates.[261] These observations reaffirmed again the successful rearrangement of the oxygen atoms to their respective positions.

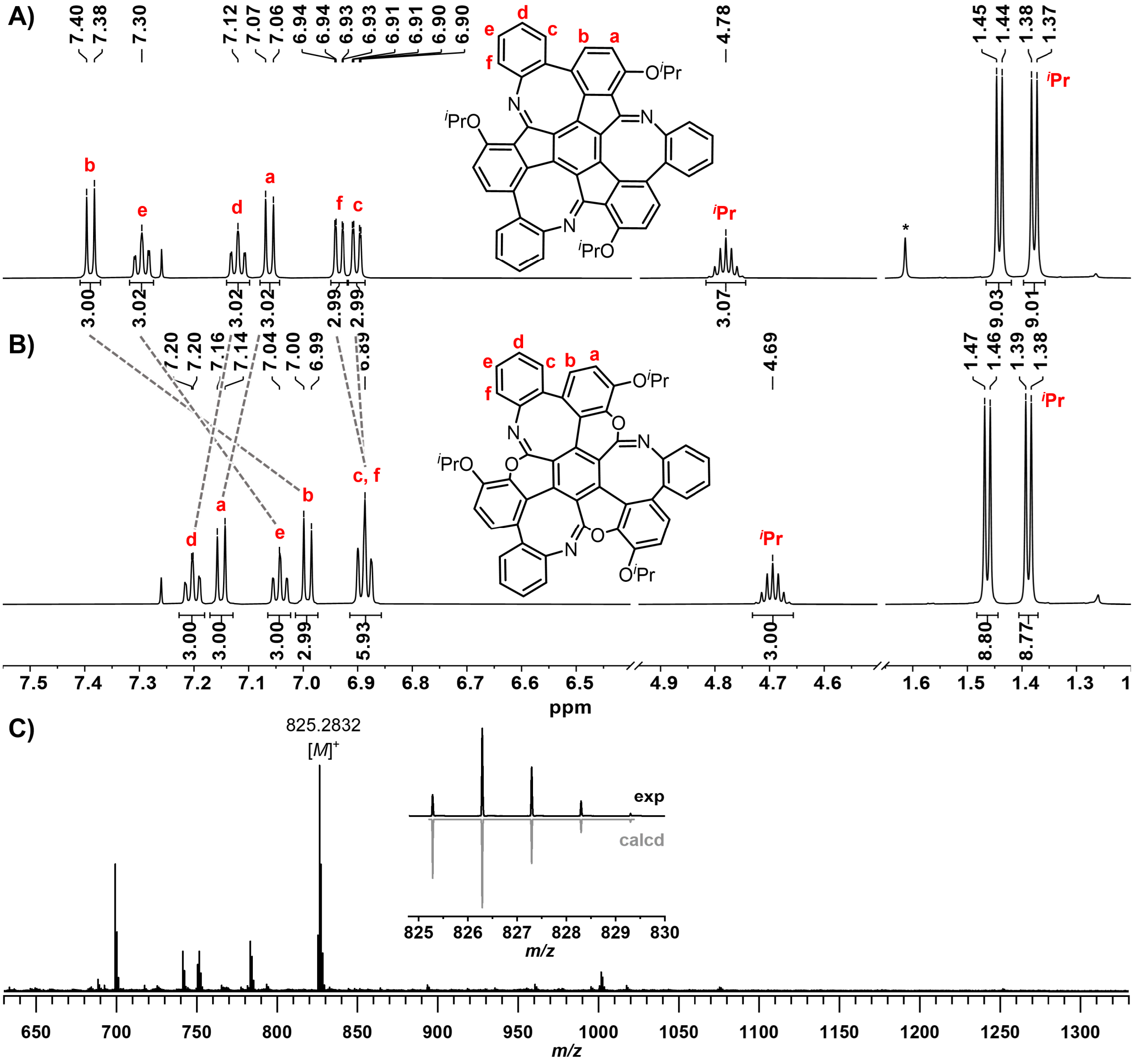

Figure 3.15: ^{1}H NMR spectra (600 MHz, $CDCl_3$) of **A)** aza monkey saddle **123** and **B)** chromene monkey saddle **125** with assignment of the protons. Residual solvent signals: *: H_2O. **C)** High-resolution MALDI mass spectrum of **125**. The measured isotopic pattern matches the calculated one. The figures **A**-**C)** were adapted from reference 186.

X-ray Structure Analysis of the Aza and Chromene Monkey Saddles 123 and 125

Slow diffusion of *n*-heptane into a solution of **123** in $CDCl_3$ provided suitable single crystals for X-ray diffraction analysis (**Figure 3.16A**). Aza monkey saddle **123** crystallized in the triclinic space group $P\overline{1}$ with eight molecules per unit cell, containing both the (S_a,S_a,S_a)- and (R_a,R_a,R_a)-enantiomer. On account of the three azocine subunits in the molecule, **123** adopts a contorted structure. The angles between the unsubstituted peripheral benzene rings (highlighted in blue in **Figure 3.16C**) and the central benzene ring (orange) thereby range from θ = 45-48°, while the angles between the isopropoxy-substituted benzene rings (red) and the central six-membered ring (orange) comprise φ = 29-35°. Another useful metric for specifying a ring's curvature is the nonplanarity, which is defined as the average distance of the atoms of one ring – in this case, the carbon and nitrogen atoms in the azocin – from a generated best-fit plane.[171-172] Accordingly, the average nonplanarity of **123**'s eight-membered rings was determined to be 0.364 Å, whereas a value of 0.000 Å would be obtained for perfectly planar systems.

Regarding the packing of **123**, homochiral layers formed along the crystallographic *a*-axis and alternated along the *b*-axis (**Figure 3.16E**). Between these layers, the (S_a,S_a,S_a)- and (R_a,R_a,R_a)-enantiomers interacted primarily through multiple face-to-edge CH···π interactions between the unsubstituted and alkoxy-substituted benzene rings ($d_{CH\cdots\pi}$ = 2.7-2.9 Å). Within a homochiral plane, three aza monkey saddle molecules always accumulated, interacting through several CH···π interactions of the isopropyl groups to the neighboring π-system ($d_{CH\cdots\pi}$ = 2.8-2.9 Å). Additionally, two edge-to-face CH···π interactions of the alkoxy-substituted benzene rings to the azocine subunits were observed ($d_{CH\cdots\pi}$ = 2.8 Å) as well as an interaction between the unsubstituted benzene ring and the nitrogen atom ($d_{CH\cdots N}$ = 2.7 Å) (**Figure 3.16E**).

Suitable single crystals of the chromene monkey saddle were obtained by layer-by-layer diffusion of methanol into a toluene solution of **125**. The compound crystallized as a racemate in the space group $P2_1/n$ with Z = 4 (**Figure 3.16B**). Notably, the rearrangement of the oxygen atoms into the five-membered rings caused **125**'s curvature to deepen even further compared to aza monkey saddle **123**. For instance, the angles θ and φ both significantly increased by around 26° for the unsubstituted benzene rings (θ = 45-48° for **123** vs. θ = 71-74° for **125**) and 13° for the alkoxy substituted rings (φ = 29-35° for **123** vs. φ = 41-48° for **125**) (*cf.* **Figure 3.16C**). Besides, the average nonplanarity of the eight-membered rings increased from 0.364 Å in **123** to 0.439 Å in **125**. Even the pyran ring was distorted from planarity despite its sp^2 hybridization and exhibited an average nonplanarity of 0.200 Å. By comparison, a structurally related pyran ring that was adjacent to a benzene ring and a heptagon on the other side featured a much lower nonplanarity of 0.042 Å.[262] Owing to the negative curvature, **125** also possesses two cavities with depths of 1.9 Å and 3.6 Å (**Figure 3.16D**). The values were determined by placing a centroid in the central benzene ring (highlighted in orange in **Figure 3.16C**) and a mean plane through the tips of the peripheral benzene rings (depicted in blue and red), followed by measuring the distance from each plane to the centroid.

Like **123**, compound **125** assembled into homochiral layers along the crystallographic *b*-axis, which alternated along the *c*-axis (**Figure 3.16F**). Within each homochiral layer, the molecules stacked on top of each other with a slight offset so that one isopropoxy group always pointed into the cavity of the monkey saddle above it (**Figure 3.16F**). This arrangement resulted in the formation of a homochiral chain, which aligned next to another chain consisting of the same enantiomer. Two of such chains interacted *via* edge-to-face CH···π interactions between the alkyloxy-substituted benzene rings ($d_{\mathrm{CH\cdots\pi}}$ = 2.8 Å) and interactions of the unsubstituted benzene rings to the oxygens of the pyran units ($d_{\mathrm{CH\cdots O}}$ = 2.4 Å). Between the homochiral planes, the (R_a,R_a,R_a) and (S_a,S_a,S_a) enantiomers showed edge-to-face CH···π interactions involving the unsubstituted benzene rings, with a distance of $d_{\mathrm{CH\cdots\pi}}$ = 2.8 Å (**Figure 3.16G**).

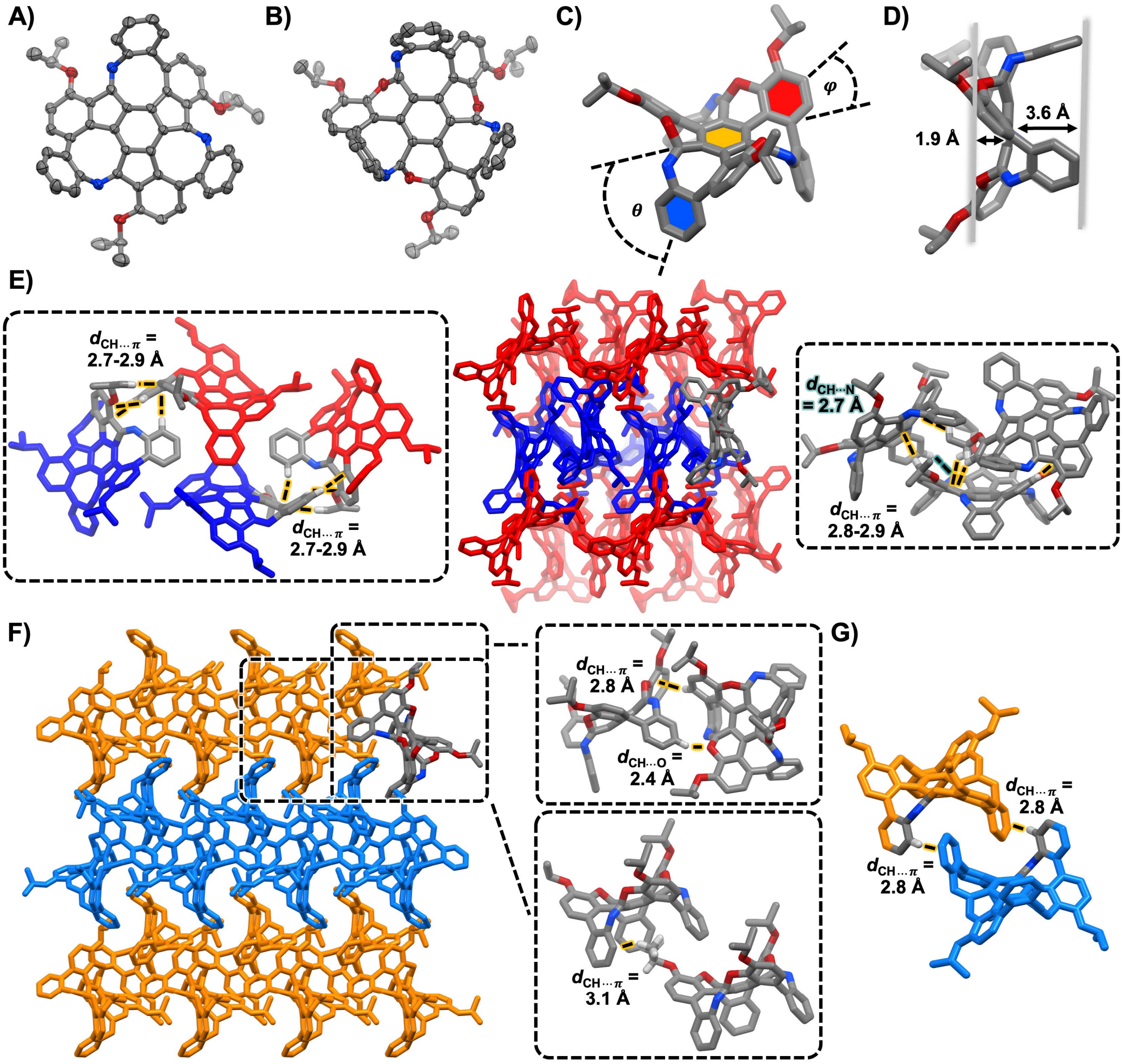

Figure 3.16: Single crystal structures of **123** (CCDC 2389439)[186] and **125** (CCDC 2389441).[186] Hydrogens were generally omitted for clarity. Grey = carbon, red = oxygen, blue = nitrogen, white = hydrogen. **A)** (S_a,S_a,S_a)-enantiomer of **123** and **B)** (S_a,S_a,S_a)-enantiomer of **125** as ORTEP drawings with 50% probability of ellipsoids. **C)** Side view of **125**. The colored benzene rings were used to calculate the angles θ (orange and blue) and $\boldsymbol{\varphi}$ (orange and red). **D)** Another side view of **125** to highlight the depths of its cavities. **E)** Packing of **123** with view along the crystallographic *c*-axis. For a better visualization, the (S_a,S_a,S_a)-enantiomers were colored in red, (R_a,R_a,R_a)-enantiomers in blue. Selected intermolecular interactions between homochiral layers (left) and within a homochiral layer (right) are shown enlarged. **F)** Packing of **125** with view along the crystallographic *a*-axis. For a better visualization, the (S_a,S_a,S_a)-enantiomers were colored in blue, (R_a,R_a,R_a)-enantiomers in orange. Selected intermolecular interactions within the homochiral layer are shown enlarged. **G)** Visualization of the intermolecular interactions between two homochiral planes. The figures **B)**, **C)**, **D)**, **F)**, and **G)** were reproduced from reference 186.

Optical and Chiral Properties of the Chromene Monkey Saddle 125

The ring expansions in chromene monkey saddle **125** influenced not only the curvature of its molecular structure, but also its optical properties. While precursor **123** exhibited absorption maxima at λ = 273, 319 and 414 nm – accounting for its bright orange color – chromene monkey saddle **125** solely displayed two maxima at λ = 284 and 304 nm, resulting in its colorless habit (**Figure 3.17A**). This change can be ascribed to a reduced conjugation between the benzene rings within the chromene monkey saddle framework. Quantum chemical calculations performed by Dr. Tobias Kirschbaum supported these findings and revealed an increased HOMO-LUMO gap for **125** (3.98 eV) compared to **123** (3.26 eV).[186]

The enantiomers of **125** were readily separable by chiral HPLC using a Chiralpak IE column and an *n*-heptane/CH_2Cl_2 (30:70) mixture as eluent. The CD spectra of enantiopure (S_a,S_a,S_a)-**125** and (R_a,R_a,R_a)-**125**, recorded in CH_2Cl_2 at 20 °C, showed mirror-imaged spectra with two intense maxima at λ = 239 and 321 nm (**Figure 3.17B**). The largest dissymmetry factors g_{abs} emerged at λ = 331 nm ($g_{abs} = 3.38\times10^{-3}$) and λ = 260 nm ($g_{abs} = -6.59\times10^{-4}$).

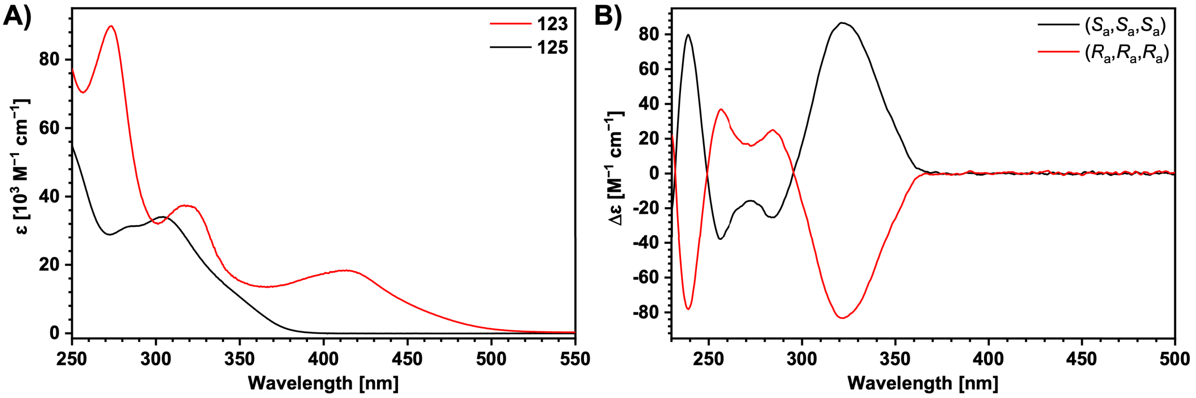

Figure 3.17: A) Comparison of UV/vis spectra of **123** (red) and **125** (black) recorded in CH_2Cl_2. **B)** CD spectra of enantiopure **125** measured in CH_2Cl_2 at 20 °C. TD-DFT calculations served for the assignment of the absolute stereochemistry.

Post-Functionalization Attempts of the Chromene Monkey Saddle

After successfully optimizing the synthesis of chromene monkey saddle **125**, different post-functionalization strategies were explored to introduce new functional groups to the monkey saddle core (see **Scheme 3.15**). Especially the three unsubstituted peripheral benzene rings are targeted, because these moieties of the molecule offer the opportunity to link the chromene monkey saddles to each other and thus to construct larger three-dimensional architectures such as cages.

At first, compound **125** was subjected to a bromination with 3.3 equiv. of NBS in DMF at room temperature to generate **126**. Since ^1H NMR studies of the crude material merely disclosed signals belonging to the starting material **125**, harsher reaction conditions were applied next, including 9.0 equiv. of NBS and a reaction temperature of 80 °C. Yet again, no conversion occurred according to ^1H NMR and MALDI-TOF mass spectrometric analyses (**Scheme 3.15**).

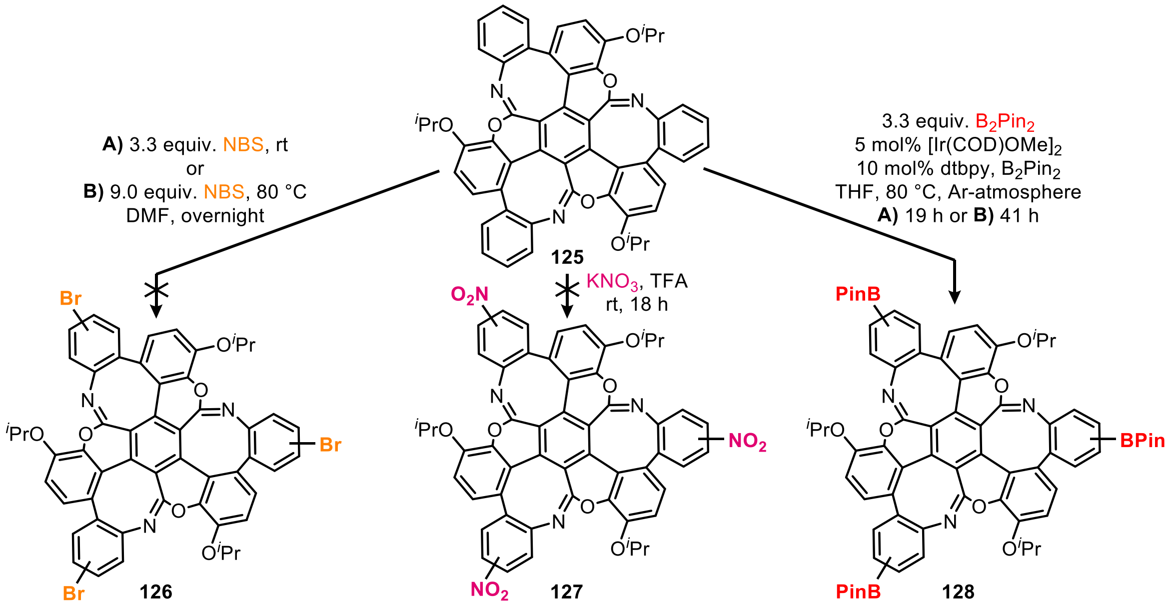

Scheme 3.15: Post-functionalization attempts of chromene monkey saddle **125**.

Another electrophilic substitution, namely a nitration toward derivative **127**, was attempted by mixing **125** with 3.3 equiv. of potassium nitrate in trifluoroacetic acid (TFA) at room temperature (**Scheme 3.15**). Upon addition of the acid, the solution adopted a dark brown color, which persisted even after the aqueous work-up. As the ^{1}H NMR spectrum of the crude material did not exhibit any signals in the aromatic region, it was concluded that compound **125** is chemically unstable under these conditions and decomposed during the reaction.

Lastly, the incorporation of three pinacol boronic esters, affording **128**, was investigated by an iridium-catalyzed C–H activation reaction[263] (**Scheme 3.15**). To this end, chromene monkey saddle **125** was stirred with 10 mol% of the active iridium-catalyst and 3.3 equiv. of B_2Pin_2 at 80 °C for 19 hours. The reaction progress was analyzed by MALDI-TOF mass spectrometry, exposing the presence of five distinct species, whose mass-to-charge ratios differed by increments of $\Delta m/z = 126$ (**Figure 3.18A**). This pattern is consistent with the stepwise substitution of hydrogen atoms by BPin groups. In consequence, the observed signals could be assigned to the unreacted starting material **125** at *m/z* 826.177(calcd for $(C_{54}H_{40}N_3O_6)^+$: 826.291) and the one-fold borylated species at *m/z* 952.285 (calcd for $(C_{60}H_{51}BN_3O_8)^+$: 952.376) up to the four-fold borylated derivative at *m/z* 1330.536 (calcd for $(C_{78}H_{84}B_4N_3O_{14})^+$: 1330.632).

Due to the incomplete conversion toward **128** after 19 hours, this entry was repeated with an extended reaction time of 41 hours, while keeping all other conditions constant. Although this adjustment enabled exhaustive consumption of **125**, MALDI-TOF MS studies of the crude product still revealed a mixture of borylated species (**Figure 3.18B**). The detected signals included the desired three-fold borylated product at *m/z* 1204.286 (calcd for $(C_{72}H_{73}B_3N_3O_{12})^+$: 1204.547), as well as the four-fold borylated compound at *m/z* 1330.362 (calcd for $(C_{78}H_{84}B_4N_3O_{14})^+$: 1330.632) and the five-fold borylated derivative at *m/z* 1456.388 (calcd for $(C_{84}H_{95}B_5N_3O_{16})^+$: 1456.717).

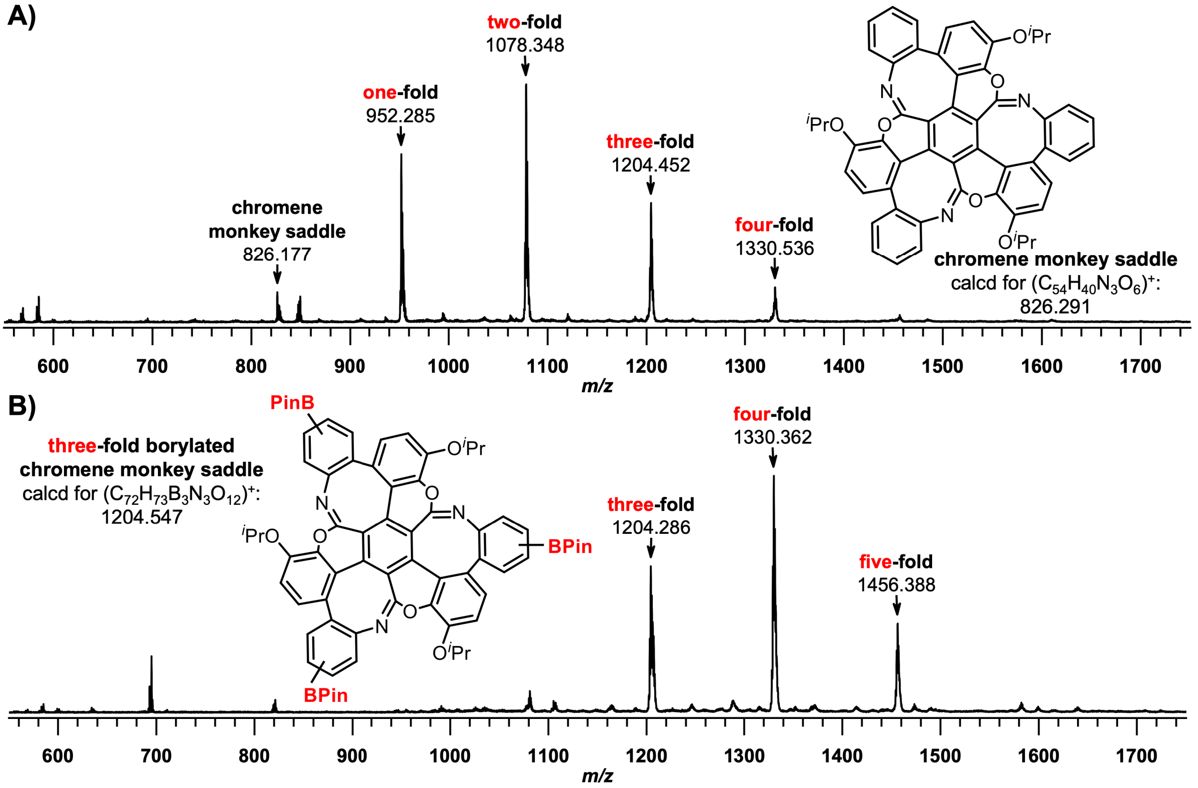

Figure 3.18: MALDI-TOF mass spectra after subjecting chromene monkey saddle **125** to an iridium-catalyzed borylation to yield **128** (*cf.* **Scheme 3.15**). The reactions were stirred for **A)** 19 hours and **B)** 41 hours.

All things considered, **125** can be functionalized by an iridium-catalyzed borylation, but the reaction lacks selectivity, and the chromene monkey saddle can likely be borylated up to six times with the corresponding amount of B_2Pin_2. However, the six-fold borylated derivative is not a suitable candidate for the intended follow-up chemistry. Additionally, given the variety of potential constitutional isomers and the anticipated challenges in purification – as aromatic compounds bearing boronic esters are often unstable on silica gel – the isolation of **128** was not pursued. Hence, synthetic strategies were redirected toward **125**'s pre-functionalization.

Pre-Functionalization Attempt of the Chromene Monkey Saddle

Recapping the synthesis of **125**, the use of a modified 2-aminophenylboronic acid or ester presented a promising opportunity to introduce new functional groups into the monkey saddle framework. The key advantage of such a pre-functionalization is the inherent selectivity of this approach, as it avoids the formation of constitutional isomers during the generation of the respective aza monkey saddle.

The experimental realization required a suitable boronic acid or ester derivative, whose direct purchase proved cost prohibitive. As a practical alternative, modified 2-bromoanilines were considered, especially since the bromide can be converted to the boronic acid pinacol ester in one step. Beside the accessibility of the bromide, the incorporated functional group needed to remain inert under the reaction conditions employed, including palladium-catalyzed cross-couplings as well as acidic and oxidative environments.

These stringent criteria significantly narrowed the pool of available candidates, and ultimately 2-bromo-4-nitroaniline (**129**) was selected as the most viable precursor.

The pre-functionalization sequence started with a Miyaura borylation of **129** (**Scheme 3.16**). Applying 5 mol% Pd(dppf)Cl_2 and potassium acetate as base delivered the product **130** as an orange solid in 80% yield. Subsequent coupling of **130** to the truxenone core would combine nitro, amino, carbonyl and isopropoxy groups within a single molecule, raising concerns about its solubility due to the expected high polarity. To circumvent this issue, the synthetic route was reverted to the hexyloxy truxene derivative. Hence, the fluorenyl positions of **44** were oxidized following a literature procedure,[185] and the truxenone **55** was obtained as a brown solid in 61% yield (**Scheme 3.16**).

Next, **55** and boronic acid pinacol ester **130** were subjected to a three-fold Suzuki-Miyaura cross-coupling. Based on ^{1}H NMR and MALDI-TOF mass spectrometric studies, it was concluded that a catalytic system comprising 10 mol% $Pd_2(dba)_3$ and 40 mol% $HP^tBu_3BF_4$ reliably produced the desired triply coupled product. Excess **130** was removed by flash column chromatography prior to exploring the condensation between the amino and carbonyl groups.

Initial experiments tested the same conditions used for generating the unmodified aza monkey saddle **123**. Yet, stirring the starting material in a mixture of acetic acid and chloroform at 80 °C did not lead to a detectable conversion toward aza monkey saddle **131**. Accordingly, a comprehensive screening of reaction parameters was conducted, including different acids (AcOH, TFA, H_2SO_4, *para*-toluenesulfonic acid), solvents ($CHCl_3$, ODCB, toluene, mesitylene) and temperatures (80, 120 and 160 °C). Despite these efforts, only trace amounts of **131** could be isolated. The most successful entry involved acetic acid in chloroform at 80 °C. After a purification by flash column chromatography and preparative HPLC, the product **131** was received as an orange solid in 2% yield over two steps (**Scheme 3.16**). This corresponded to a conversion of 507 mg of truxenone **55** to 13 mg of aza monkey saddle **131**.

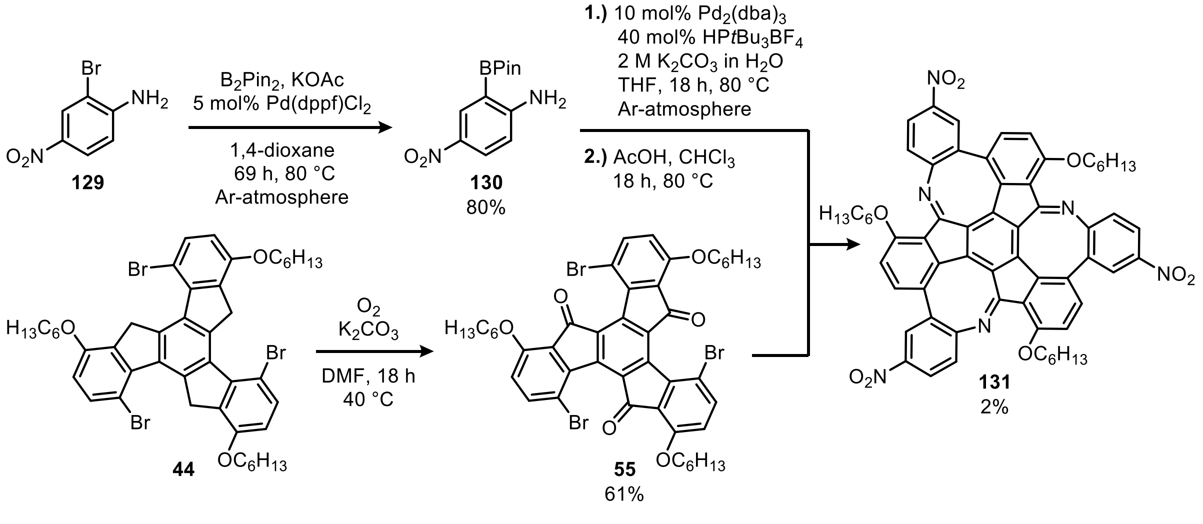

Scheme 3.16: Synthesis of the nitro-functionalized aza monkey saddle **131**.

Analyzing the ^{1}H NMR spectrum of **131** revealed five aromatic signals in a 1:1 integration ratio to each other, which is consistent with the molecule's symmetry (**Figure 3.19**). The *ortho*-coupled protons H^a and H^b, located near to the hexyloxy chains, belonged to the two doublets at δ = 7.56 and 7.14 ppm. H^d is the only aromatic proton flanked by both *ortho*- and *meta*-coupling partners, thus resulting in a characteristic doublet of doublets at δ = 8.14 ppm. The pronounced downfield shift of this signal can thereby be ascribed to the strong electron-withdrawing properties of the adjacent nitro group. The -M effect also applied to H^c (δ = 7.84 ppm), whereas H^e was not affected and appeared at δ = 7.04 ppm. This chemical shift assignment is in full agreement with aza monkey saddle **131**.

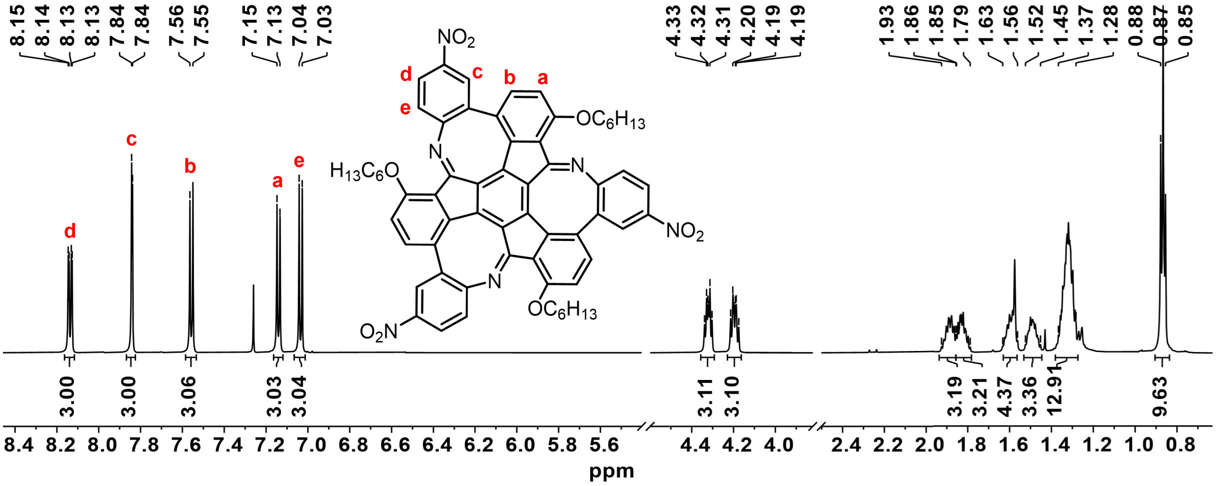

Figure 3.19: ^{1}H NMR spectrum (600 MHz, $CDCl_3$) of **131** with assignment of aromatic protons.

Furthermore, a slow layer-by-layer diffusion of *n*-heptane into a toluene solution of **131** yielded single crystals suitable for X-ray diffraction, unambiguously confirming its molecular structure (**Figure 3.20A**, **B**). Compound **131** crystallized as a racemate in the space group $P\bar{1}$ with eight molecules per unit cell. Compared to the unmodified aza monkey saddle **123**, the curvature of **131**'s azocin units was slightly diminished, as indicated by the lower average nonplanarity of 0.319 Å (vs. 0.364 Å for **123**). Besides, the dihedral angles between the nitro-substituted benzene rings and the central six-membered ring decreased from θ = 45-48° in **123** to θ = 36-42° in **131**, whereas the angles between the alkoxy-substituted benzene rings and the central ring remained constant (φ = 29-35° for **123** vs. φ = 32-33° for **131**).

Regarding the crystal packing, **131** formed homochiral columns along the crystallographic *a*-axis, whose chirality alternated along the *b*-axis (**Figure 3.20D**). Each homochiral column composed of stacked dimers with toluene molecules as separators. Within the dimer, the nitro-substituted benzene rings of one monkey saddle pointed toward the other monkey saddle and vice versa, while the hexyloxy groups extended outward from the dimer core. Notably, the two molecules packed quite tightly, whereby the centroids of their central benzene rings were only 3.6 Å apart. Multiple intermolecular interactions were observed within these homochiral pairs, for instance CH···O interactions between the aromatic protons and the nitro groups with distances of $d_{CH\cdots O}$ = 2.4-2.7 Å (**Figure 3.20E**). Similarly, columns of opposite chirality were linked by hydrogen bonding between the nitro groups of one enantiomer and the aromatic protons of the hexyloxy-substituted benzene rings of the other enantiomer with $d_{CH\cdots O}$ = 2.5-2.7 Å (**Figure 3.20C**).

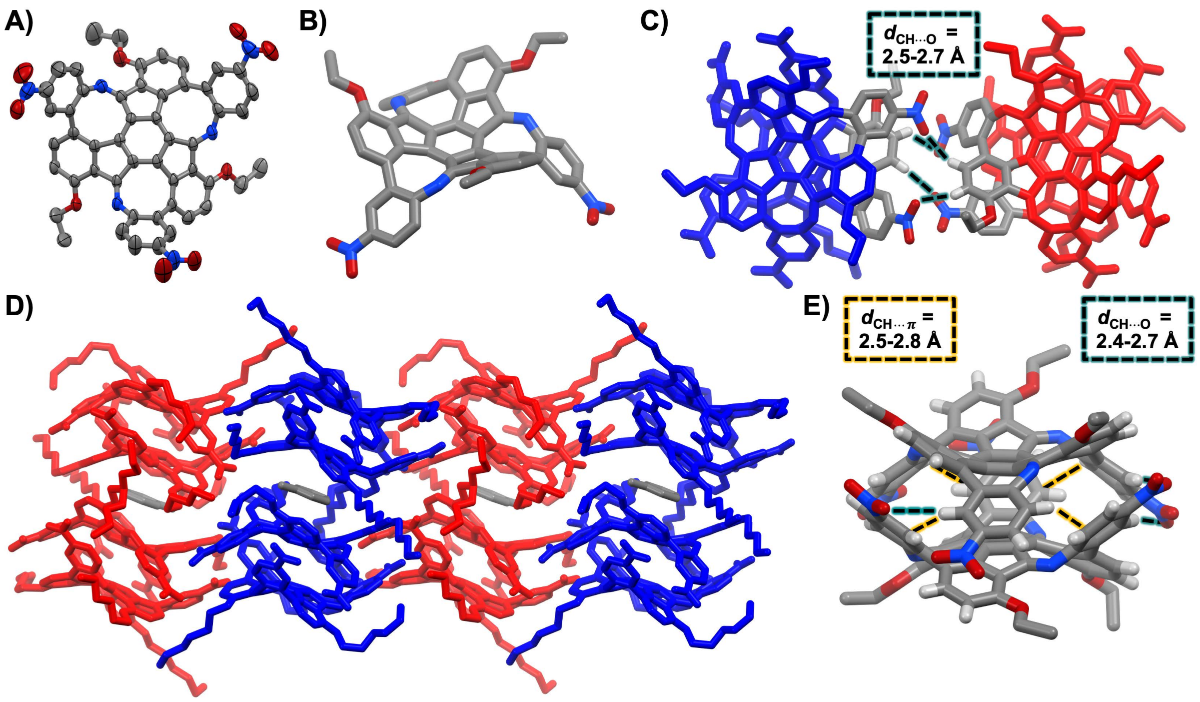

Figure 3.20: Single crystal structure of **131**. **A)** (R_a,R_a,R_a)-enantiomer of **131** as ORTEP drawing with 50% probability of ellipsoids. **B)** Side view of **131** as stick model. **C)** Visualization of intermolecular interactions between (R_a,R_a,R_a)-**131** (blue) and (S_a,S_a,S_a)-**131** (red). **D)** Packing of **131**. For a better visualization, the (R_a,R_a,R_a)-enantiomers were colored blue and the (S_a,S_a,S_a)-enantiomers red. The remaining grey molecules in between are toluene. **E)** Visualization of selected intermolecular interactions within a homochiral dimer of **131**. Hexyl chains were generally shortened to ethyl, and hydrogens were omitted for clarity. Grey = carbon, red = oxygen, blue = nitrogen, white = hydrogen.

Although the modified aza monkey saddle **131** was successfully generated and characterized, the poor yield of the condensation step precluded further synthetic efforts toward the corresponding chromene monkey saddle. Nevertheless, the pre-functionalization approach persists as a feasible route, despite its apparent incompatibility with nitro groups positioned *para* to the imine units within the aza monkey saddle framework.

Summary and Outlook

This chapter focused on the development of a functionalized, inversion stable monkey saddle that could serve as a potential candidate for chirality-assisted cage synthesis. For this objective, the production of the tribromotruxene was first revisited, as its challenging purification had limited the accessibility of monkey saddles. Replacing the hexyloxy substituents by isopropoxy groups proved advantageous, because this change rendered the purification process more efficient and sustainable. Subsequently, the synthesis of the isopropoxy-substituted chromene monkey saddle **125** was carried out, and its molecular structure was confirmed by single-crystal X-ray diffraction analysis.

With **125** in hand, several post-functionalization approaches were explored. For instance, a bromination with NBS resulted in the recovery of unreacted starting material, whereas a nitration using KNO_3 and TFA seemingly led to the decomposition of **125**. In contrast, an iridium-catalyzed C–H activation enabled **125**'s borylation, albeit in a non-selective manner. Given the estimated laborious and time-intense purification of the differently borylated species, efforts shifted toward the pre-functionalization strategy.

This alternative undertaking required a suitably functionalized boronic acid or ester. Accordingly, a nitro-substituted 2-bromoaniline derivative was purchased and transformed into the respective boronic acid pinacol ester. The subsequent Suzuki-Miyaura cross-coupling with truxenone **55** proceeded smoothly; however, the condensation of the amino groups with the truxenone carbonyls generated the desired aza monkey saddle **131** in merely 2% yield over two steps. Its structure was unambiguously confirmed by single-crystal X-ray diffraction. Due to the prohibitively low yield, the rearrangement of **131** into the chromene monkey saddle was not pursued.

Despite the modest outcome of this pre-functionalization attempt, it generally remains a promising approach, particularly since a variety of 2-bromoaniline derivatives bearing functional groups such as -OMe, -Me, -CF_3, or -CN are commercially available (**Scheme 3.17**). A systematic screening of these compounds could provide valuable insights into electronic effects, also in relation to the *meta* and *para* positioning of the substituent to the amino group. This, in turn, may eventually facilitate the formation of a functionalized chromene monkey saddle. Though, it should be emphasized that this screening would entail considerable synthetic efforts including the preparation of the boronic esters as well as the optimization of both the Suzuki-Miyaura cross-coupling and the condensation step.

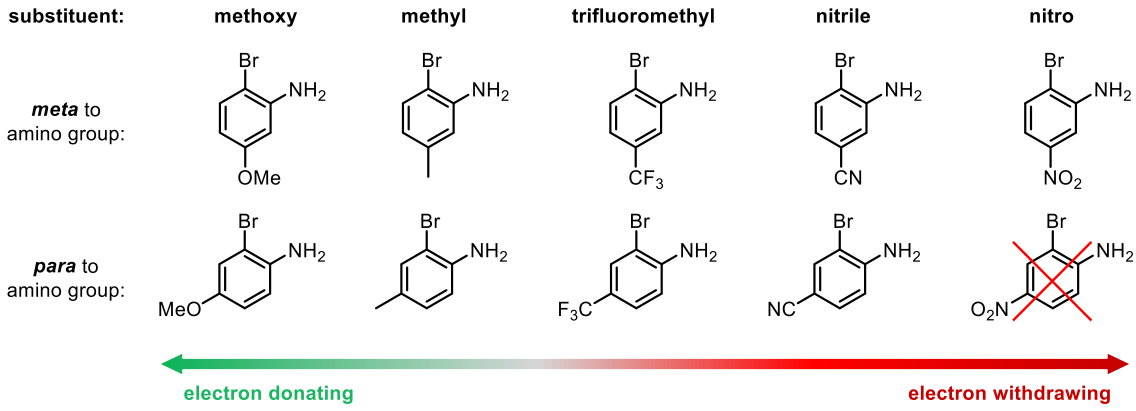

Scheme 3.17: Overview of commercially available 2-bomoaniline derivatives categorized by the electronic nature of the substituent. Screening these compounds for the generation of the aza monkey saddle could deliver valuable insights into the influence of electronic effects and overall synthetic feasibility. The crossed-out derivative was employed for the synthesis of aza monkey saddle **131** described in this chapter; however, it proved to be unsuitable for the intended goal.

3.5 Monkey Saddles – Substitution of the Eight-Membered Rings

*Some of the results presented within this chapter, namely the synthesis of **138**, **139**, **141**, and **142**, were first carried out by FRANZISKA MARTINA FIES (née DÜRR) as part of her bachelor's thesis under my supervision.*[264]

In the pursuit of a conformationally stable monkey saddle, whose distinctive scaffold and curvature offer great potential for the construction of elaborate, chiral architectures,[141-142, 265] it became clear that modification attempts of the chromene monkey saddle proved elusive (*Chapter 3.4*). On the other hand, a monkey saddle series of the CH-analog **47** was successfully synthesized, demonstrating its straightforward functionalization when suitable boronic esters were employed (*cf.* **Scheme 3.18**). For example, the incorporation of methoxy in **48**, dioxolane in **49** and TIPS-acetylene groups in **51** was accomplished by Dr. Tobias Kirschbaum during his doctoral studies, as well as the replacement of three benzene rings with thiophene units.[178, 184] Moreover, this work has presented another derivative featuring propyne substituents (see *Chapter 3.3*). Notably, all monkey saddle derivatives, except for the thiophene one **50**, exhibited inversion barriers between $\Delta G^{\ddagger}(25\ ^{\circ}C) = 103$ and $108\ kJ\ mol^{-1}$ and consequently half-lifes on the order of a few minutes at elevated temperatures, such as 70 °C (**Scheme 3.18**).[177-178, 184]

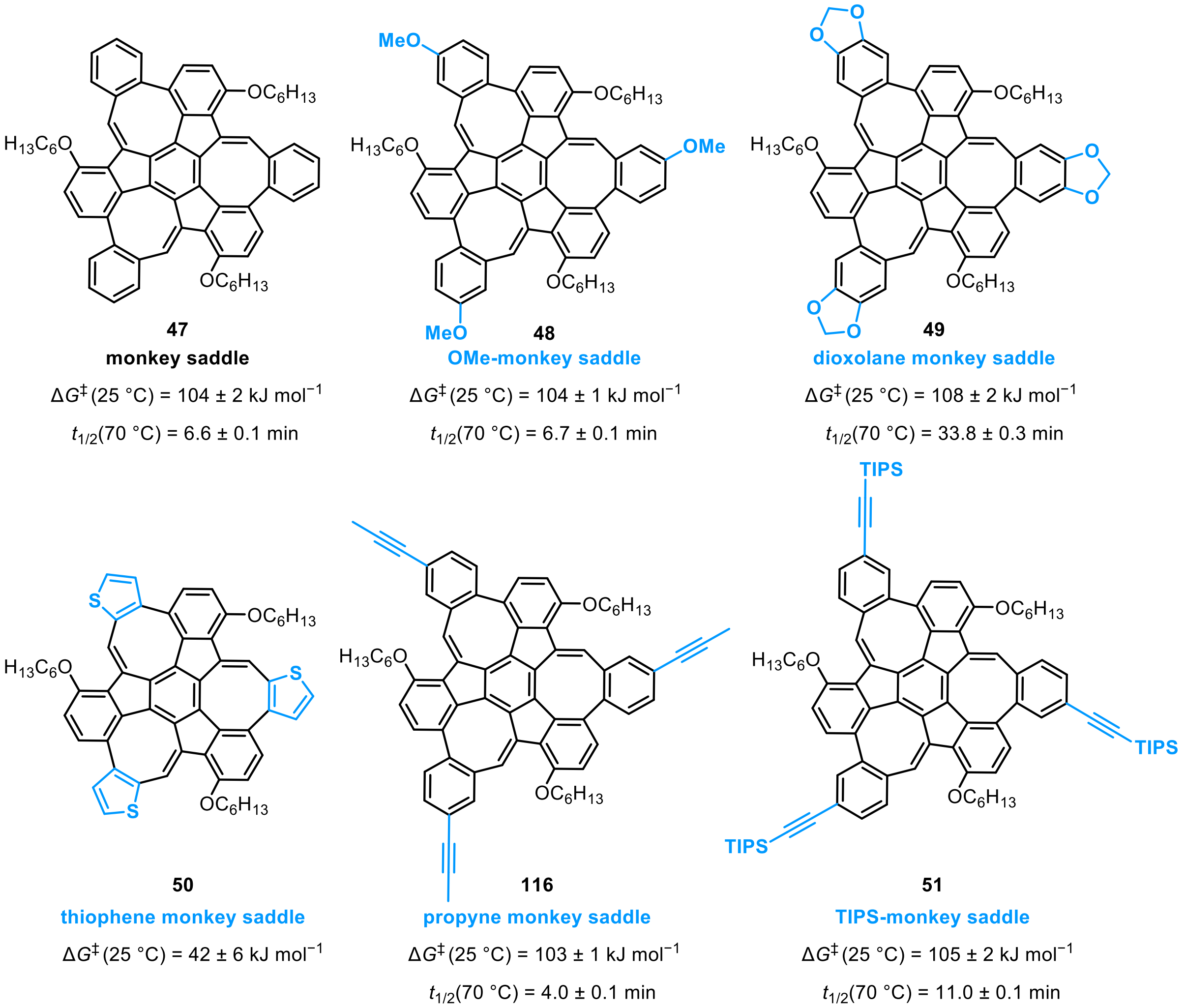

Scheme 3.18: Overview of synthesized monkey saddle derivatives, their inversion barriers, and the corresponding half-lifes at 70 °C.[177-178, 184]

Building on these established literature results, this chapter focuses on enhancing the conformational stability of the CH-analog monkey saddle **47**. To this end, quantum chemical calculations are first performed to gain insight into the racemization process and estimate the barrier heights. These theoretical studies shall serve as a foundation for identifying structural modifications that can significantly increase the inversion barrier. Subsequently, computational predictions are complemented by experimental investigations to validate the proposed strategy.

DFT Calculated Inversion Barriers of Monkey Saddles

Initial quantum chemical examinations on the racemization process of monkey saddles revealed a stepwise mechanism, in which the eight-membered rings undergo sequential flipping, leading to twisted transition structures (*cf.* **Figure 3.21**).[177] Dr. Tobias Kirschbaum computed the inversion barriers of the monkey saddle derivatives he had synthesized at the B3LYP/6-311G(d,p) level of theory.[177-178, 184] While this method was in excellent agreement with experimental data for **47** and the dioxolane monkey saddle **49**, deviations of 14 and 10 kJ mol^{-1} were obtained for the methoxy derivative **48** and TIPS-monkey saddle **51**, respectively. Hence, various computational methods are benchmarked in the following to determine the one that best reproduces the experimental values.

To begin, structure optimizations and frequency calculations were submitted using the PBEh-3c[266-269] method for the five monkey saddles **47**, **48**, **49**, **50**, and **51** and their respective two transition structures, which are critical for the barrier height. The validity of the located transition states (TS) was confirmed by visualizing the associated single imaginary frequency in *Chemcraft 1.8*. Afterwards, single point calculations were carried out. The methods benchmarked span different levels of computational cost and accuracy, comprising generalized-gradient-approximations- to double-hybrid functionals. These included PW6B95-D3(BJ),[270] B3LYP-D3(BJ),[271] M06-2X-D3Zero,[272] ωB97X-D4,[273] ωB97X-V,[274] B97M-D4,[273] TPSS0-D3(BJ),[275] revPBE0-D3(BJ),[276] RI-DSD-BLYP/2013-D3(BJ),[277] RI-DSD-PBEP86/2013-D3(BJ),[278-279] BLYP-D3(BJ),[280-282] r^{2}SCAN-3c,[283] RI-DSD-PBEB95-D3(BJ),[279] and RI-PWPB95-D3(BJ).[284] Depending on the method, the def2-QZVPP, def2-TZVPP, or def2-mTZVPP basis sets were employed.[283, 285] To account for solvent effects, the SMD solvation model[286] with *n*-heptane was applied based on the experimental conditions.

In the first benchmarking round, the inversion barriers of **47**, OMe-monkey saddle **48**, and thiophene compound **50** were calculated (see **Table 3.2**). It quickly became apparent that none of the tested methods was able to reach the experimental error margin of **50**. Nevertheless, they all captured the general trend, predicting barrier heights well below 100 kJ mol^{-1}. For **47** and **48**, the functionals M06-2X-D3Zero, ωB97x-D4 and ωB97X-V overestimated the molecules' conformational stability by at least 6 kJ mol^{-1}, whereas BLYP-D3(BJ) underestimated the barriers. Consequently, these four methods were excluded from further benchmarking. Remarkably, PW6B95-D3(BJ) and r^{2}SCAN-3c delivered barrier heights within the experimental error margin for both **47** and **48**, already demonstrating superior performance compared to the B3LYP/6-311G(d,p) level of theory. The remaining methods produced promising values as well, with deviations from the experimental error margins not exceeding 5 kJ mol^{-1}.

Table 3.2: Benchmarking of different methods for calculating the inversion barriers (ΔG^{DFT}) of the monkey saddles **47**, **48**, **49**, **50**, and **51** (for structures, see **Scheme 3.18**).[a] The experimental and B3LYP/6-311G(d,p)-calculated values were extracted from the references 177, 178, and 184. All values are given in kJ mol^{-1}.

	47		**48 (OMe)**		**50 (Thiophene)**		**49 (Dioxolane)**		**51 (TIPS)**	
Experimental	**104 ± 2**		**104 ± 1**		**42 ± 6**		**108 ± 2**		**105 ± 2**	
B3LYP/6-311G(d,p)	104		118		64		108		115	
Method	**TS1**	**TS2**	**TS1**	**TS2**	**TS1**	**TS2**	**TS1**	**TS2**	**TS1**	**TS2**
BLYP-D3(BJ)[b]	98	–	97	–	57	–	–	–	–	–
r^{2}SCAN-3c[c]	103	**104**	101	**103**	63	51	106	**108**	100	100
B97M-D4[b]	**103**	102	102	101	60	46	107	**107**	101	98
revPBE0-D3(BJ)[b]	105	107	103	106	63	51	109	112	103	**105**
B3LYP-D3(BJ)[b]	105	**106**	104	106	63	51	109	111	104	**104**
PW6B95-D3(BJ)[b]	102	**104**	101	**103**	61	49	106	**108**	101	102
TPSS0-D3(BJ)[b]	**102**	101	100	101	58	47	105	105	99	99
M06-2X-D3Zero[b]	112	–	111	–	70	–	–	–	–	–
ωB97X-D4[b]	118	–	117	–	75	–	–	–	–	–
ωB97X-V[b]	118	–	117	–	75	–	–	–	–	–
RI-DSD-BLYP/2013-D3(BJ)[d]	107	110	105	109	63	53	111	114	105	**107**
RI-DSD-PBEP86/2013-D3(BJ)[b]	107	110	105	109	64	53	111	115	105	**107**
RI-DSD-PBEB95-D3(BJ)[b]	107	110	106	110	65	54	111	116	105	109
RI-PWPB95-D3(BJ)[b]	106	107	103	107	63	52	108	113	103	**106**

[a]: TS stands for transition state. A dash signifies that the value was not calculated. Values falling within the experimental error margin are highlighted in bold and with a green box. Values deviating by only 1 kJ mol^{-1} from the experimental error margin were highlighted with a light green box.
[b]: def2-QZVPP basis set.
[c]: def2-mTZVPP basis set.
[d]: def2-TZVPP basis set.

The benchmarking study was then extended to the dioxolane-containing compound **49** and TIPS-monkey saddle **51** (**Table 3.2**). Comparison of the calculated and experimental inversion barriers once again identified PW6B95-D3(BJ) as the best-performing method, closely followed by B3LYP-D3(BJ). For each of these functionals, the deviation from the experimental error margin was no greater than 1 kJ mol^{-1} – excluding **50**. Though, r^{2}SCAN-3c should not be overlooked in this study, as it exhibited a surprisingly high accuracy and stands out as a computationally efficient alternative. Additionally, the double-hybrid functionals did not outperform the hybrid ones, thereby enabling the computation of monkey saddle inversion barriers with an excellent cost-to-accuracy ratio.

Having found a reliable method to reflect the experimental data, this approach was exploited to predict the inversion barriers of new monkey saddle derivatives to seek conformationally more stable candidates. Given that the cyclooctatetraene (COT) units flip sequentially during racemization, attaching bulkier substituents to the COT ring could significantly increase the barrier height due to an enhanced steric hindrance. To check this hypothesis, the COT-protons were replaced with methyl groups, and the inversion barrier was calculated at the PW6B95-D3(BJ)/def2-QZVPP+SMD(*n*-heptane)//PBEh-3 level of theory. Starting from the (S_a,S_a,S_a)-enantiomer, the first eight-membered ring reverses *via* formation of a twisted transition state and yields the (S_a,S_a,R_a)-isomer (**Figure 3.21**). This process is repeated with the other two COT rings in the molecule, ultimately generating the (R_a,R_a,R_a)-enantiomer. Relative to monkey saddle **47**, methyl substitution on the eight-membered rings increased the overall inversion barrier from 104 kJ mol^{-1} to 153 kJ mol^{-1}, placing this derivative at the threshold of conformational stability.[287] The latter implies that the corresponding species would be stable for 24 hours at 423 K.[287] Accordingly, the introduction of methyl groups emerges as an interesting strategy, and the experimental realization will be scrutinized in the subsequent discussion.

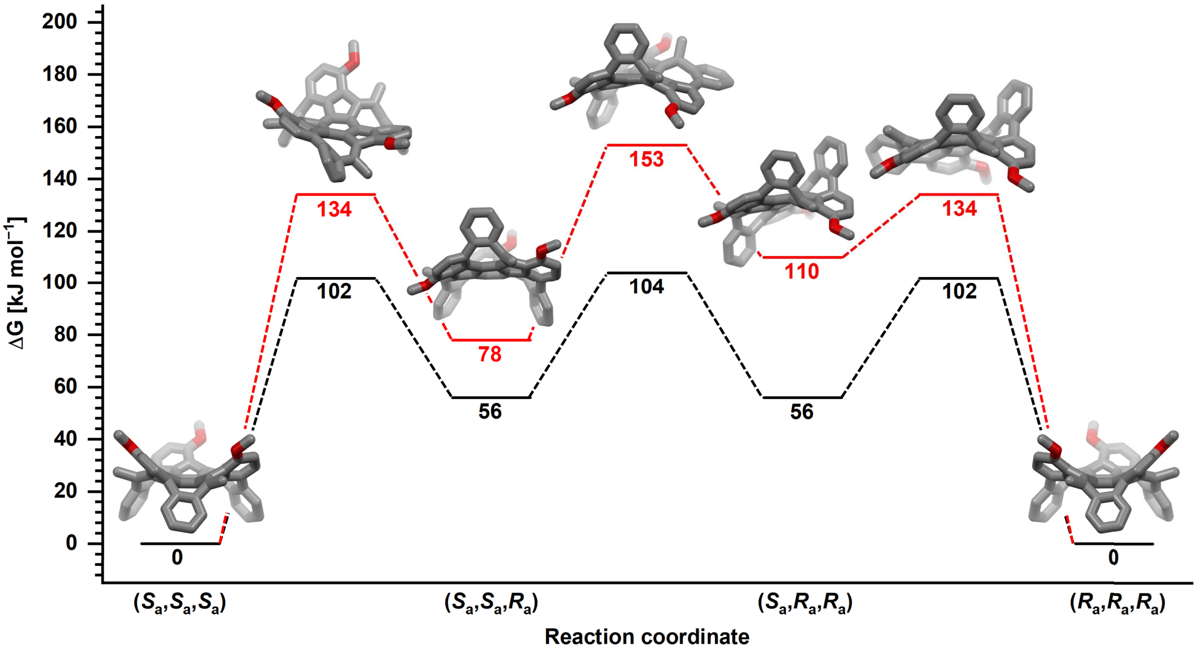

Figure 3.21: Comparison of inversion pathways of **47** (black) and the monkey saddle (red; depicted in figure), whose COT protons were substituted with methyl groups, calculated at the PW6B95-D3(BJ)/def2-QZVPP+SMD(*n*-heptane)//PBEh-3c level of theory. All values are given in kJ mol^{-1}. For simplicity, the hexyl groups were reduced to methyl groups. Grey = carbon, red = oxygen.

Prior Internal Work

The synthesis of a conformationally stable CH-monkey saddle, specifically through substitution of the eight-membered rings, has already been a sought-after topic within our research group. Therefore, prior internal work has to be considered. For one, Dr. Tobias Kirschbaum and his student Johannes Krieger conducted a screening of the Suzuki-Miyaura cross-coupling between tribromotruxene **44** and the methyl ketone **132**. Despite varying palladium-based catalyst systems, solvents, and concentrations, the coupled product **133** could not be detected (**Scheme 3.19A**).[184]

As an alternative approach, 2-cyanophenylboronic acid (**134**) was coupled to the truxene core. The resulting nitrile groups in substance **135** served to generate the desired ketones by a Grignard reaction, and indeed, treating **135** with 4-*tert*-butylphenylmagnesium bromide furnished compound **136** in 32% yield over two steps (**Scheme 3.19B**).[184] However, attempts to condense the ketones to the fluorenyl positions of the truxene subunit remained unfruitful. This outcome might be attributed to the steric bulk of the used *tert*-butylphenyl moieties, potentially rendering the formation of the target compound **137** unfeasible. Yet, the question persists whether ketone condensation inherently fails in such a system, or only under conditions of excessive steric hindrance. Since a viable route toward the ketone intermediate has been established, it will be applied to produce the sterically least demanding derivative, namely the methyl ketone, and the condensation step will be reassessed.

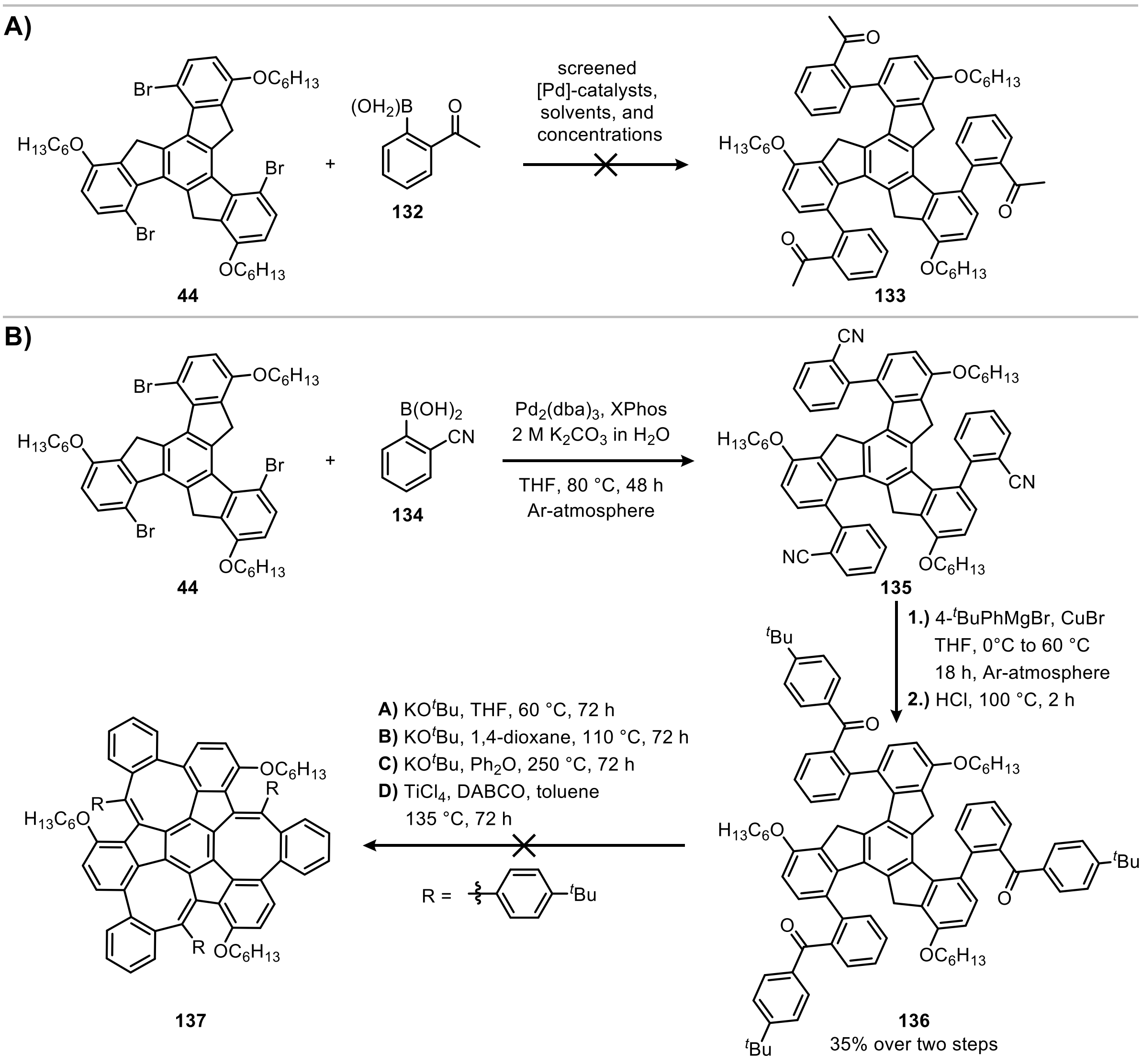

Scheme 3.19: Substitution attempts of the monkey saddle's eight-membered rings performed by Dr. Tobias Kirschbaum and his student Johannes Krieger.[184] **A)** Tested Suzuki-Miyaura cross-coupling to generate the methyl ketone **133**. **B)** Synthesis of the ketone **136**. Different condensation conditions (A) to D)) were explored, but none of them yielded the product **137**.

Condensation of the Methyl Ketone

Beginning with the isopropoxy-substituted tribromotruxene **121**, a Suzuki-Miyaura cross-coupling with boronic acid **134** was carried out according to the procedure of **135** (**Scheme 3.20**).[184] Consequently, the starting materials were mixed with the catalyst system $Pd_2(dba)_3$/XPhos, and the reaction was stirred at 80 °C overnight under the exclusion of oxygen. After an aqueous workup and purification by flash column chromatography, compound **138** was isolated as a beige solid in 46% yield. Next, the Grignard reaction was examined by subjecting an excess of methylmagnesium bromide to the starting material **138**. The reaction was heated at 80 °C overnight before being quenched with a sat. ammonium chloride solution to generate the corresponding ketones. Finally, a flash column chromatographic purification delivered the product **139** in 38% yield (**Scheme 3.20**). The successful conversion of the nitriles to ketones was confirmed by IR spectroscopy, among others. Precursor **138** exhibited a characteristic C≡N stretching band at $\tilde{\nu}$ = 2226 cm^{-1}, which completely vanished in the IR spectrum of **139**. Instead, carbonyl stretching bands were observed at $\tilde{\nu}$ = 1688 and 1674 cm^{-1}, matching expectations[288-289] (**Figure 3.22A**, **B**). Moreover, high-resolution MALDI-TOF mass spectrometry revealed a peak at *m/z* 870.3901, which belongs to the molecular ion $[M]^+$ of **139** (calcd for $(C_{60}H_{54}O_6)^+$: 870.3915) (**Figure 3.22C**).

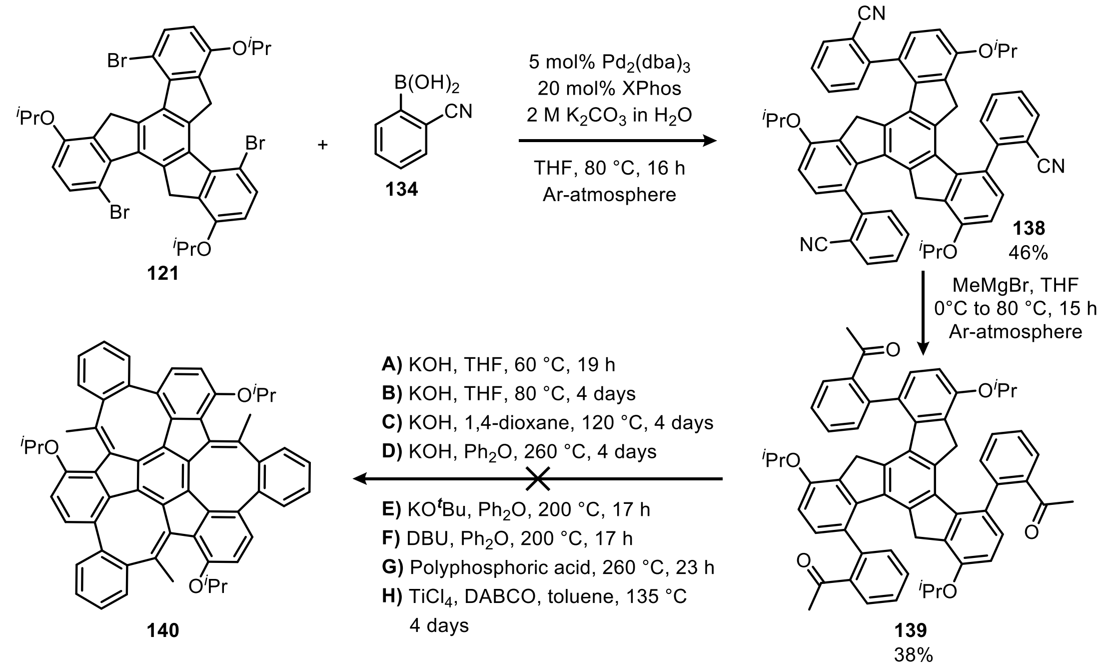

Scheme 3.20: Synthesis attempt of the methyl-substituted monkey saddle **140** by subjecting the methyl ketone **139** to a condensation reaction.

Continuing with the condensation step toward **140**, the monkey saddle framework is usually formed by exposing the aldehyde precursor to potassium hydroxide in THF solution at 60 °C. Hence, these conditions were initially applied to the methyl ketone **139**, and the reaction was stirred overnight (**Scheme 3.20**). Besides the starting material **139**, MALDI-TOF MS studies of the crude material disclosed a new signal at *m/z* 836.349, which might conform to the two-fold condensed product (calcd for $(C_{60}H_{51}O_4)^+$: 836.064). Nevertheless, TLC and ^{1}H NMR spectroscopy only showed the presence of unreacted **139**.

In consequence, increasingly harsher conditions were screened and included THF at 80 °C, 1,4-dioxane at 120 °C and diphenyl ether (Ph_2O) at 260 °C, while staying with potassium hydroxide as base (**Scheme 3.20**). All attempts led to the re-isolation of **139** without signs of product formation. Changing the base to potassium *tert*-butoxide or DBU in Ph_2O at 200 °C also proved ineffective, again resulting in the recovery of starting material.

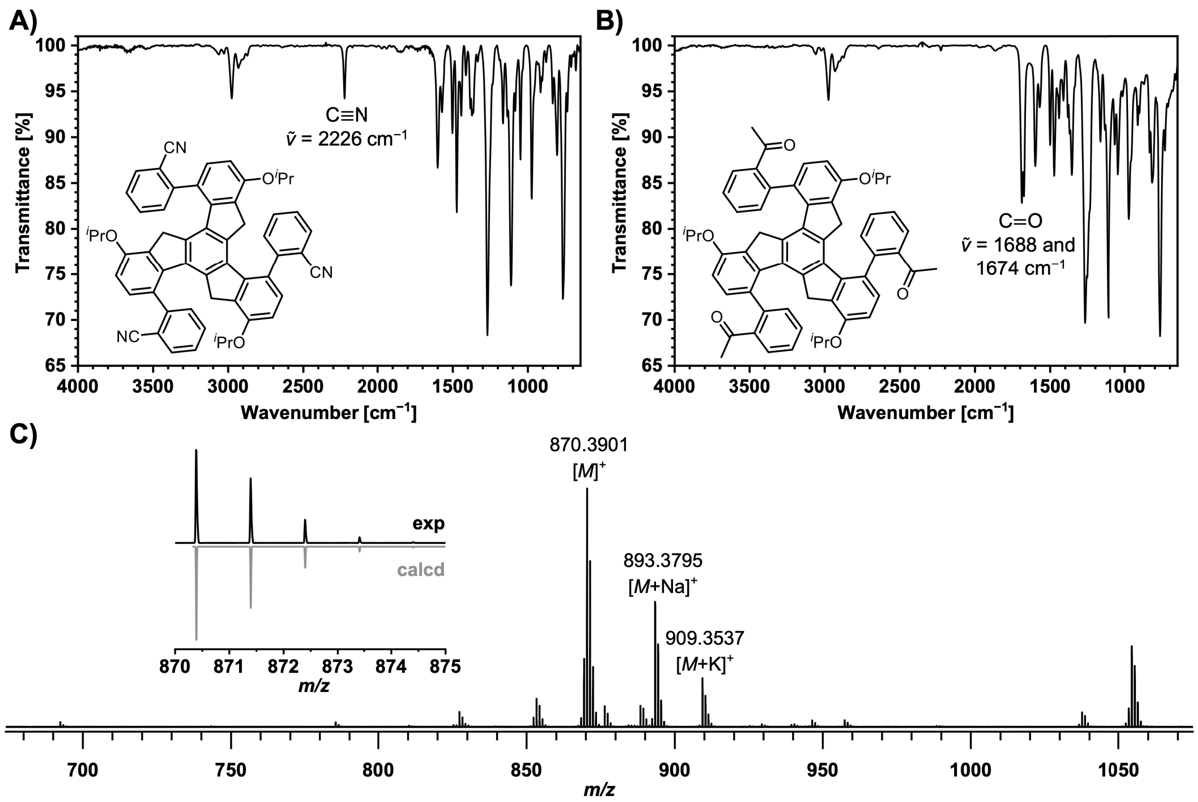

Figure 3.22: IR spectra of **A) 138** and **B) 139** with assignment of the characteristic bands. **C)** High-resolution MALDI-TOF mass spectrum of **139**. The measured isotopic pattern matches the calculated one.

Owing to the lack of conversion with the base-mediated approach, the condensation was also attempted under acidic conditions using polyphosphoric acid at 260 °C (**Scheme 3.20**). After the workup, ^{1}H NMR studies of the crude material no longer displayed any signals in the aromatic region, suggesting possible decomposition of **139**.

In the last experiment, a combination of the Lewis acid titanium tetrachloride and the base 1,4-diazabicyclo[2.2.2]octane (DABCO) was tested in toluene at 135 °C. Interestingly, MALDI-TOF MS measurements recorded mass-to-charge ratios at *m/z* 1715.289, 2550.231, 3402.925 and 4255.307, which correspond to the ranges for dimeric to pentameric species and may indicate the construction of oligomers by intermolecular condensation. However, the observed masses did not precisely match the calculated values for such oligomeric structures, leaving the reaction outcome ambiguous. Yet, it can still be concluded that the target monkey saddle **140** did not arise under any of the conditions explored in this chapter.

Direct Substitution of the Eight-Membered Rings

When researching synthetic methods to incorporate methyl groups into cyclooctatetraenes, it was found that a reaction between methyl bromide and the lithiated COT – prepared by halogen-lithium exchange – delivered methyl-cyclooctatetraene.[290] Beyond this report, other literature procedures describe the direct deprotonation of conjugated double bonds using *n*-butyllithium, whereby a subsequent treatment with methyl iodide also yielded the corresponding methylated double bonds.[291-295] In the context of monkey saddles, this could represent a promising approach, especially since the resulting anionic intermediates would be stabilized by π-conjugation with the adjacent aromatic rings.

To tackle this project, the monkey saddle **141** needed to be generated first (**Scheme 3.21**). Analogous to derivative **47**,[177] boronic acid **45** was coupled three-fold to tribromotruxene **121** by the catalyst system $Pd_2(dba)_3$/XPhos. After an aqueous workup, the crude material was purified by flash column chromatography, affording the product **142** in 44% yield. The aldehyde groups were then intramolecularly condensed to the fluorenyl positions by stirring **142** and potassium hydroxide in THF solution at 60 °C. This proceeding yielded monkey saddle **141** as a yellow solid in 72%. At this point, it is worth mentioning that the improved purification of tribromotruxene **121** enabled a substantial scale-up of subsequent reactions, for instance converting 713 mg of **142** to 418 mg of monkey saddle **141** in a single batch. Such a scale was not realizable with the hexyloxy derivative **44** due to its persistently limited availability.

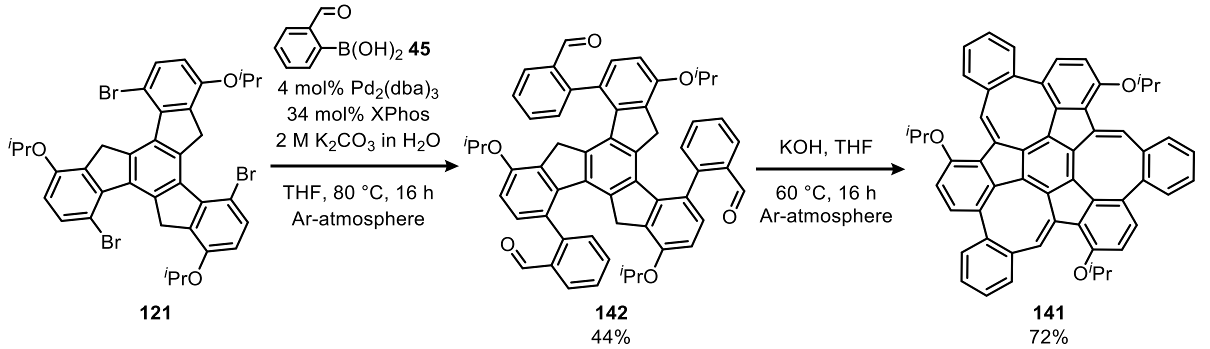

Scheme 3.21: Synthesis of the isopropoxy-substituted monkey saddle **141**.

In order to investigate the substitution of **141**'s eight-membered rings, the monkey saddle was dissolved in THF and cooled to 0 °C under the exclusion of moisture and oxygen (**Scheme 3.22**). Upon addition of 3.3 equiv. *n*-butyllithium, the color of the solution turned from yellow to dark red. Following, 6.0 equiv. methyl iodide were subjected to the mixture, and the reaction was stirred at room temperature overnight. Quenching with 1 M hydrochloric acid and an aqueous workup provided a brown solid, whose ^1H NMR spectrum consisted of undefined multiplets in both the aromatic and aliphatic regions.

Further examinations by MALDI-TOF mass spectrometry revealed a multitude of products, all exhibiting higher mass-to-charge ratios than the starting material **141** or the intended product **140** (see **Figure 3.23**). Calculations of the mass differences between the detected signals showed recurring values of $\Delta m/z = 14$ and $\Delta m/z = 58$. The former is thereby consistent with methylation, meaning the replacement of a hydrogen by a methyl group, whereas the latter corresponds to the mass of an *n*-butyl group. Based on this finding, the six distinct products **143** to **149** could be identified from the mass spectrum (**Scheme 3.22**). For example, the peaks at *m/z* 832.478 and 846.406 could be assigned to the compounds **143** and **144**, which each bear one *n*-butyl chain and either a proton or a methyl group at the other end of the former double bond (calcd for $(C_{61}H_{52}O_3)^+$: 832.392; calcd for $(C_{62}H_{54}O_3)^+$: 846.407). This pattern continued with species incorporating two or three *n*-butyl groups while being quenched with one, two, or even three methyl groups (*cf.* **Scheme 3.22** and **Figure 3.23**).

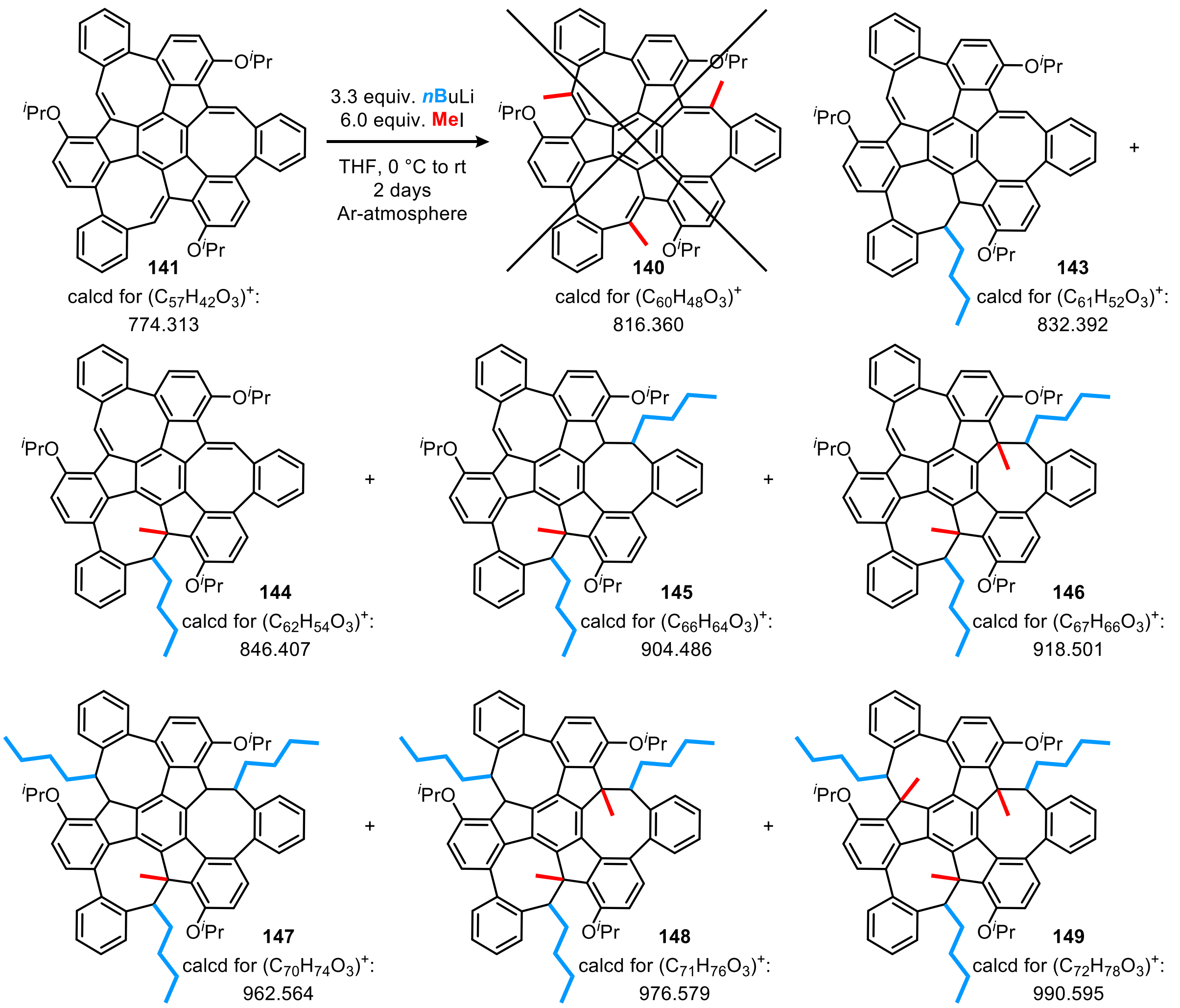

Scheme 3.22: Intended synthesis of **140** by treating monkey saddle **141** with *n*-butyllithium and methyl iodide. However, MALDI-TOF MS revealed a nucleophilic addition of the *n*-butyl anion to the double bonds, followed by quenching with methyl iodide or water.

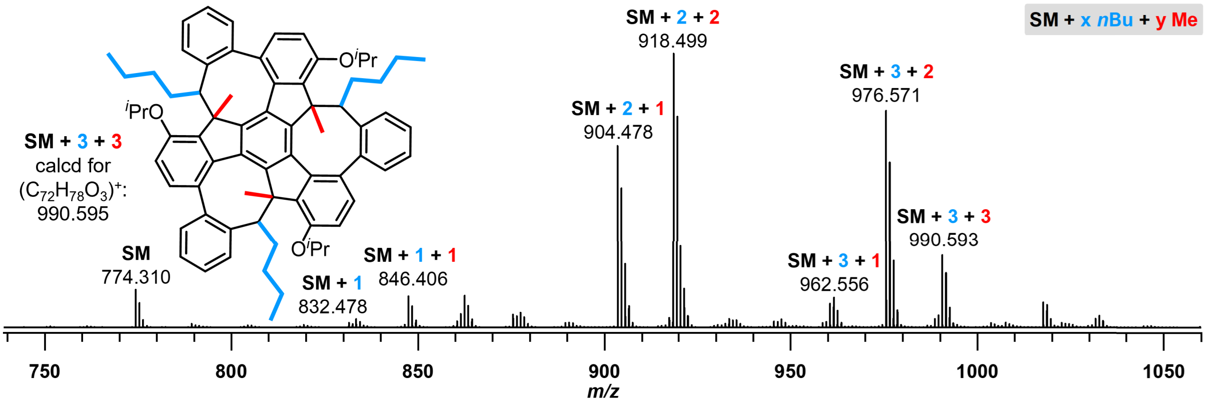

Figure 3.23: MALDI-TOF mass spectrum after treating the starting material (SM) **141** with *n*-butyllithium and methyl iodide (*cf.* **Scheme 3.22**). A mixture of species arose, which contained up to three added *n*-butyl chains and up to three methyl groups. One structure was exemplarily added to this spectrum to visualize the peak labeling.

Consequently, *n*-butyllithium did not fulfill its role as a base toward monkey saddle **141**, but as a nucleophile, adding itself to the cyclooctatetraene rings. This produced anionic intermediates that were quenched by either methyl iodide or water. Despite the unintended outcome, the observed reactivity could still offer synthetic merit because an oxidative dehydrogenation[296-297] of the proton-quenched species might be able to restore the double bonds in the eight-membered rings. This would yield a monkey saddle with COT units substituted by *n*-butyl instead of methyl groups. To ensure an exhaustive three-fold incorporation of *n*-butyl groups to the monkey saddle core, **141** was mixed with an increased amount of *n*-butyllithium – specifically 9.0 equivalents (**Scheme 3.23**). After stirring the reaction at 0 °C for 4 hours, it was quenched with 1 M HCl and worked up aqueously. Purification by flash column chromatography eventually delivered two fractions, both of which contained the product **150**. Though, ^{1}H and ^{13}C NMR investigations hinted at different molecular symmetries. For this reason, the fractions are referred to as **150-*anti*** (with the *n*-butyl groups oriented in opposite directions) and **150-*syn*** (with all *n*-butyl groups aligned in the same direction). Overall, **150** was isolated in 80% yield.

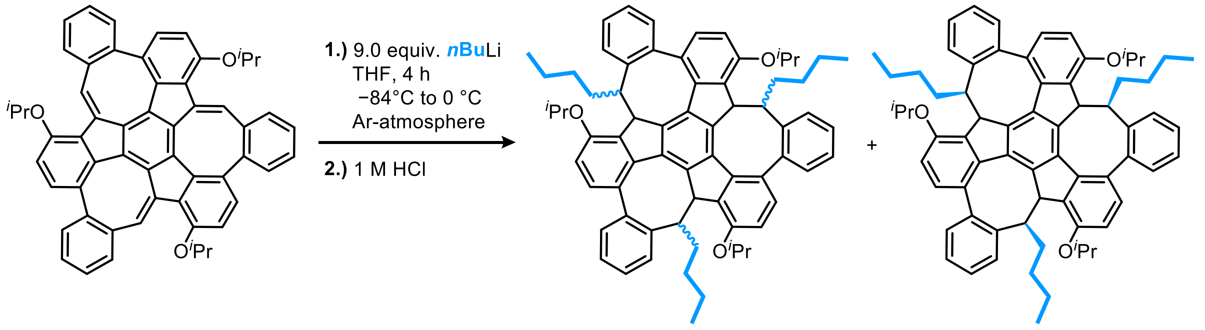

141

150-*anti*
53%

150-*syn*
27%

Scheme 3.23: Synthesis of **150**. Treatment of **141** with *n*-butyllithium led to a nucleophilic addition of *n*-butyl groups to the COT rings. The resulting anionic intermediate was quenched with acid. Compound **150** was isolated in two fractions, whereby NMR studies revealed differences in their molecular symmetries and therefore, the products are referred to as **150-*anti*** and **150-*syn***.

The ^{1}H NMR spectrum of **150-*anti*** clearly reflects its inherent asymmetry (**Figure 3.24A**). For example, three septets are observable at δ = 4.90, 4.83, and 4.78 ppm and correspond to the three chemically inequivalent CH protons of the isopropyl groups. Moreover, the addition of the *n*-butyl moieties gives rise to several multiplets between δ = 2.20 and 0.27 ppm. Among these, the three distinctive triplets at δ = 0.62, 0.44, and 0.27 ppm can be ascribed to the three terminal CH_3 groups of the *n*-butyl chains. The molecular asymmetry of **150-*anti*** is further highlighted by the protons attached to the positions of the former double bonds in the COTs. While proton H^b appears as three singlets at δ = 4.36, 4.18, and 3.99 ppm, H^a likewise causes three chemical shifts in the region δ = 4.01-3.60 ppm.

Each double bond in the starting material **141** generally exhibits two potential positions for the nucleophilic attack of the *n*-butyl anion, *i.e.*, at the methine units of the COTs or at the carbon C^b. In the latter case, C^b would not possess a proton, and C^a would transform to a CH_2 group. The absence of detected coupling between H^a and H^b in ^{1}H NMR studies, along with H^a's coupling to the *n*-butyl group, supports the incorporation of the *n*-butyl moieties to the methine units. The Karplus relationship can thereby rationalize the lacking H^a-H^b coupling as it predicts a near-zero $^{3}J_{H,H}$ coupling constant when the torsion angle between two vicinal protons approaches 90°.[298-299] Nevertheless, to unambiguously confirm that no CH_2 group had formed within the eight-membered rings, a DEPT-135 NMR spectrum was measured (**Figure 3.24B**). Ultimately, no negative-phase signals were observed for either C^a or C^b, identifying them both as CH carbons, and thus agreeing once more with **150-*anti***'s structure.

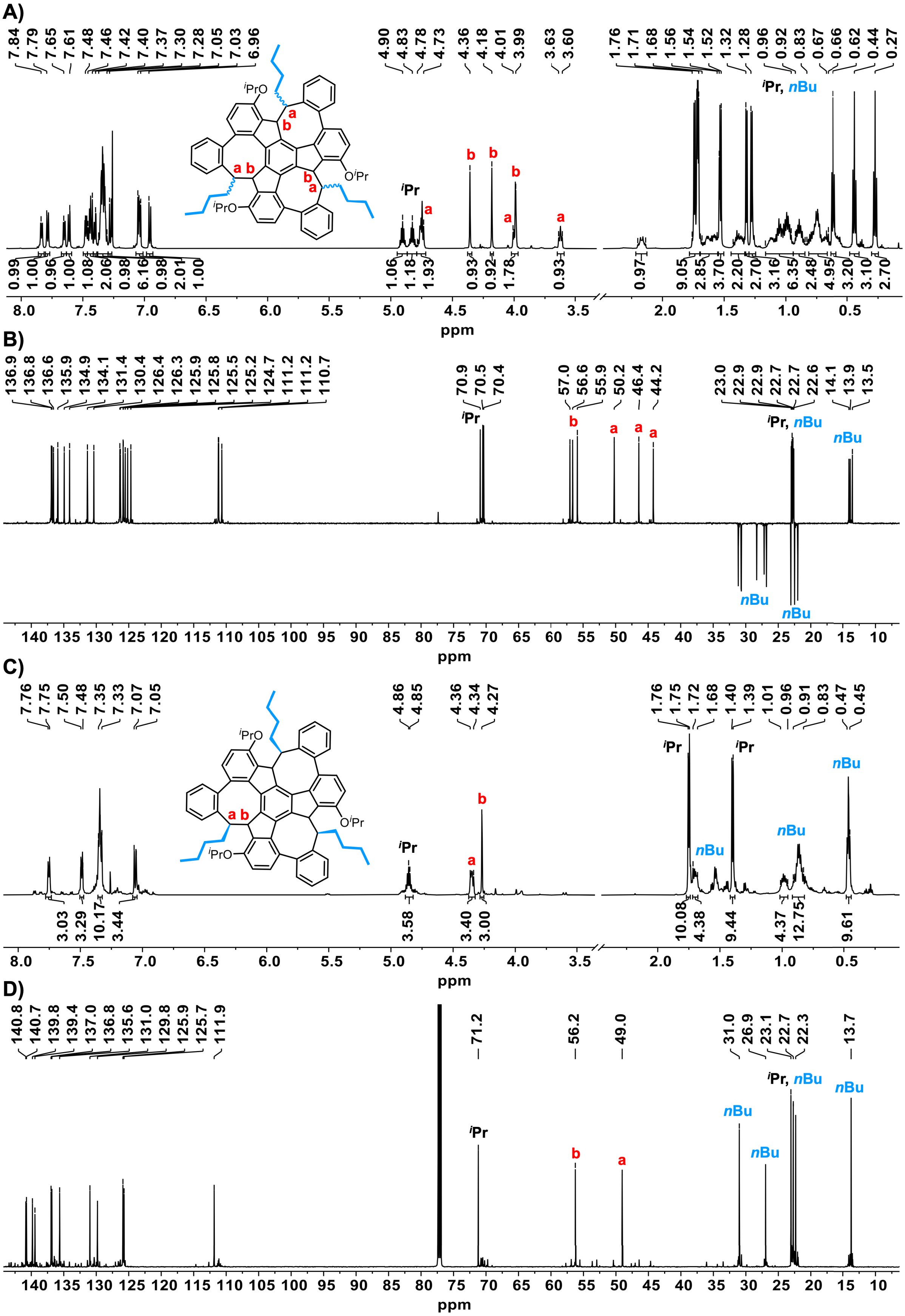

Figure 3.24: A) ^{1}H NMR spectrum (600 MHz, $CDCl_3$) of **150-*anti***. **B)** DEPT-135 NMR spectrum (150 MHz, $CDCl_3$) of **150-*anti***. **C)** ^{1}H NMR spectrum (600 MHz, $CDCl_3$) of **150-*syn***. **D)** ^{13}C NMR spectrum (150 MHz, $CDCl_3$) of **150-*syn*** illustrating its enhanced symmetry compared to **150-*anti***. In every spectrum, the signals in the aliphatic region were assigned to **150**.

As previously mentioned, the second fraction, **150-*syn***, contained more symmetrical isomers than **150-*anti***. For instance, in the ^{1}H NMR spectrum, the isopropyl CH protons produced a single septet at δ = 4.85 ppm, while H^b appeared as one singlet at δ = 4.27 ppm (**Figure 3.24C**). In addition, the terminal CH$_3$ protons of the newly inserted *n*-butyl groups gave one distinctive triplet at δ = 0.46 ppm instead of the three that were found for **150-*anti***. All these observations demonstrate the chemical equivalence of the corresponding protons in **150-*syn***. In the ^{13}C NMR spectrum, the dominant product species also showed only one signal each for C^a and C^b at δ = 49.0 ppm and δ = 56.2 ppm, respectively, whereas six peaks were obtained for **150-*anti*** (**Figure 3.24D**). Regarding the *n*-butyl substituents, the four chemical shifts at δ = 31.0, 26.9, 22.3, and 13.7 ppm indicate once again their chemical equivalence. Based on this insight, the alkyl chains are probably oriented in the same direction, so that the resulting molecule is effectively C_3-symmetrical. The ^{13}C NMR spectrum of **150-*syn*** features additional minor signals in the same regions associated with the product, which could belong to other, asymmetrical isomers of **150**. Further separation of the different isomers was however not attempted.

Besides increasing the complexity of the NMR spectra, saturation of the double bonds also had an influence on the optical properties. A comparison of the UV/vis spectra of **141** and **150-*anti*** revealed a hypsochromic shift of the lowest energy absorption band from λ = 403 nm for **141** to λ = 310 nm for **150-*anti***, which led to a visible color change from yellow to beige (**Figure 3.25A**). This shift can be attributed to a smaller conjugated system in **150**, in which the π-delocalization is limited to the benzene rings. Notably, **150-*anti*** and **150-*syn*** exhibited identical absorption maxima. Furthermore, the extinction coefficient of the most intense maximum decreased from $\varepsilon = 120 \times 10^3\ \mathrm{M^{-1}\ cm^{-1}}$ for **141** to $\varepsilon = 93 \times 10^3\ \mathrm{M^{-1}\ cm^{-1}}$ for **150-*anti*** and unlike **141**, no fluorescence could be detected for either batch of **150**.

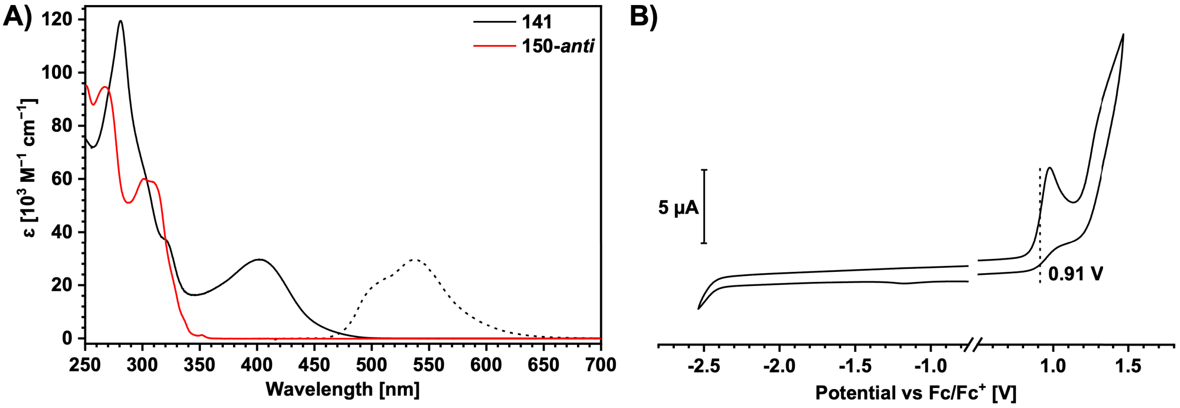

Figure 3.25: A) UV/vis absorption (solid lines) and emission spectra (dotted line) of **141** (black) and **150-*anti*** (red) measured in CH$_2$Cl$_2$. An excitation wavelength of λ_{ex} = 404 nm was used to record the emission spectrum of **141**. **B)** Cyclic voltammogram of **150-*anti*** (MeCN, 0.1 M NBu$_4$PF$_6$, scan rate: 100 mV s^{-1}, working electrode: Glassy carbon, counter electrode: Pt, pseudo-reference electrode: Ag/Ag$^+$) versus ferrocene as an internal reference.

An oxidative dehydrogenation toward monkey saddle **151** was investigated next using **150-*anti*** as the starting material, since it was the predominant product formed in the preceding nucleophilic addition reaction (**Scheme 3.24**). Initially, **150-*anti*** was mixed with DDQ in 1,4-dioxane at 70 °C overnight.[300] A subsequent aqueous work-up provided a dark brown solid, which did not display any signals in ^{1}H NMR studies. In a second attempt, potassium permanganate was employed as oxidant.[301] After stirring the reaction in acetonitrile at room temperature for 5 hours and an aqueous work-up, the crude product was examined by ^{1}H NMR spectroscopy, showing again no peaks in the aromatic region. These findings could hint at a possible decomposition of the starting material, though the precise outcome remains inconclusive.

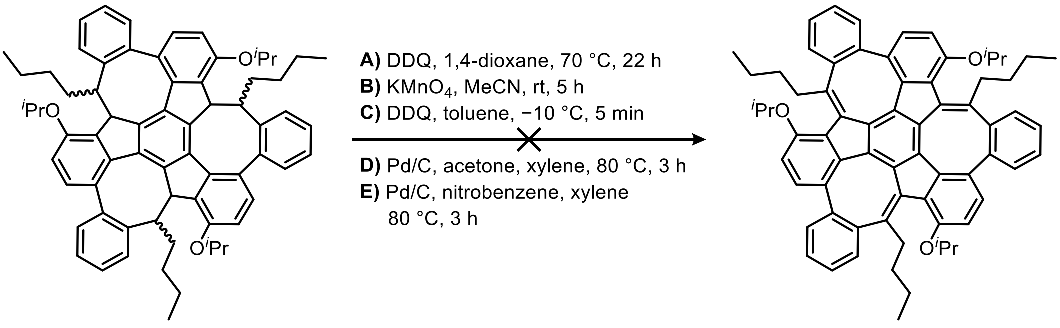

150-*anti* **151**

Scheme 3.24: Oxidative dehydrogenation attempts to restore the double bonds in the COT units of **150-*anti***.

Consequently, milder conditions were explored, such as DDQ in toluene at −10 °C for 5 minutes (**Scheme 3.24**).[302] MALDI-TOF MS analysis of the crude material included three new species at *m/z* 963.468, 979.467, and 955.487, whose mass-to-charge ratios are higher than that of the starting material **150-*anti*** (**Figure 3.26**). Moreover, the peaks feature mass differences of Δ*m/z* 16, which could imply an incorporation of oxygen atoms. Yet without additional experimental data, this assumption cannot be verified. The final approaches employed palladium on activated carbon with acetone or nitrobenzene as hydrogen acceptors.[303] Both reactions were stirred at 80 °C for 3 hours (**Scheme 3.24**). Since MALDI-TOF MS studies solely disclosed the same signals as the previous experiment (DDQ at −10 °C), the nature of the obtained product species remains undetermined.

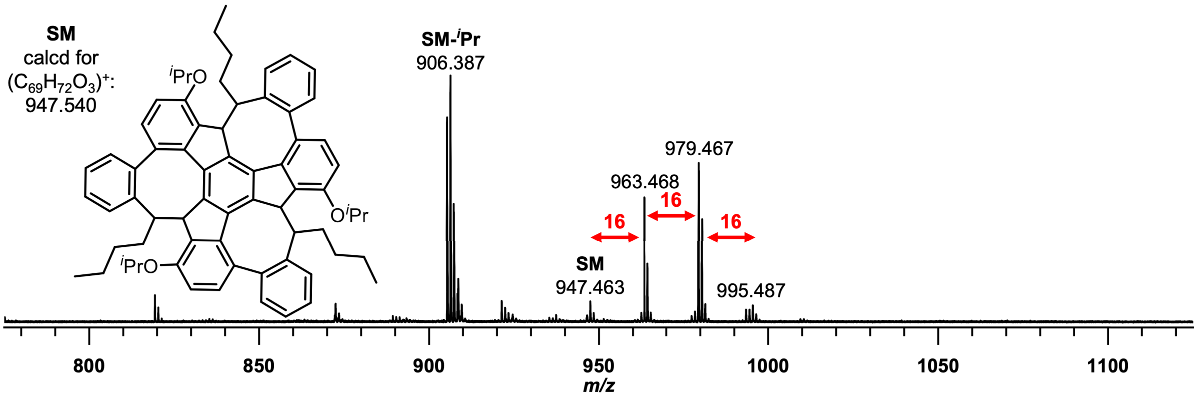

Figure 3.26: MALDI-TOF mass spectrum of **150-*anti*** after treating it with DDQ in toluene at −10 °C for 5 minutes.

With the lack of conversion toward monkey saddle **151**, the oxidizing agents tested may not have been sufficiently strong for the intended oxidative dehydrogenation. This hypothesis was scrutinized by recording the cyclic voltammogram of **150-*anti*** in CH_2Cl_2 with NBu_4PF_6 as the supporting electrolyte. However, no electrochemical features could be observed within the accessible potential window. For an extension of the solvent window, the measurement was repeated in acetonitrile with NBu_4PF_6, which revealed an irreversible oxidation at $E_{\mathrm{ox},1}$ = +0.91 V and no reduction (**Figure 3.25B**). Given that DDQ has a potential of E^0 = +0.13 V in acetonitrile,[304] it is not suited to oxidize **150-*anti***. In contrast, permanganate exhibits a redox potential of E^0 = +1.51 V vs. the aqueous standard hydrogen electrode (SHE)[305] and should in principle serve as an appropriate oxidizing agent. Nonetheless, the experiment using $KMnO_4$ probably led to the decomposition of the starting material **150-*anti*** rather than to product formation.

This finding highlights several key challenges. For one, any oxidant strong enough to promote the desired oxidative dehydrogenation may likewise induce **150-*anti***'s degradation instead of its productive consumption. On the other hand, even if **151** could be generated successfully under such conditions, the resulting monkey saddle would still require additional functional groups for subsequent transformations. Thus, the presented synthetic sequence would need to be repeated with a modified precursor – an approach that could impede the oxidative dehydrogenation anew due to an altered reactivity of the starting material.

Summary

This chapter focused on developing a strategy for improving the conformational stability of CH-monkey saddles, whereby DFT calculations on their inversion barriers were used to guide synthetic efforts.

In the beginning, the overlap between computational and experimental data was maximized by conducting a benchmark study, which comprised a scope of 14 different functionals in regard to the literature known monkey saddles **47**, **48**, **49**, **50**, and **51**. Among the tested functionals, the PW6B95-D3(BJ)/def2-QZVPP+SMD(*n*-heptane)//PBEh-3c level of theory agreed best with the experimental values, establishing it as standard method for predicting the inversion barriers of monkey saddles. Accordingly, it was found that methyl-substitution of the COT units would increase the barrier height from 104 kJ mol^{-1} to 153 kJ mol^{-1}, placing this monkey saddle derivative at the threshold of conformational stability.

Subsequently, two synthetic strategies were explored for the preparation of monkey saddle **140**, whose COT protons are replaced by methyl groups. In the first route, the methyl ketone **139** was generated in two steps starting from tribromotruxene **121**. Next followed the key step, which involved the condensation of the ketone functionalities to the truxene core. Various base-mediated condensation reactions were explored, resulting in the recovery of the starting material, whereas an acid-mediated entry with polyphosphoric acid probably decomposed **139**. The final approach employed a combination of titanium tetrachloride and DABCO. MALDI-TOF mass spectrometry indicated the formation of intermolecularly condensed species, though further experimental investigations are required to confirm this suggestion. In the second route, truxene **121** was first converted to the CH-monkey saddle **141**, which in turn was treated with *n*-BuLi and MeI to deprotonate its eight-membered rings and quench the anionic intermediates with methyl groups. Yet, instead of generating the methylated monkey saddle **140**, these conditions led to a one-, two-, and three-fold nucleophilic addition of the *n*-butyl anions to the COTs, which were quenched by either methyl iodide or water. Following, this reactivity was exploited for an exhaustive three-fold incorporation of the *n*-butyl moieties to **141**, and the intermediate was quenched with acid. Based on NMR studies, the product **150** was thereby obtained as a C_1- (**150-*anti***) and C_3-symmetrical (**150-*syn***) compound. Finally, the main product **150-*anti*** was submitted to an oxidative dehydrogenation to access the *n*-butyl modified monkey saddle **151**. While several reaction conditions were evaluated, none benefited the production of **151**. In consequence, the electrochemical properties of **150-*anti*** were examined by cyclic voltammetry, revealing an irreversible oxidation at $E_{\text{ox},1}$ = +0.91 V. This finding implied the necessity of a strong oxidant, whose prior use, however, left the synthesis of the target compound unattainable.

3.6 Monkey Saddles – Substitution of the Six-Membered Rings

This chapter was previously published and can be found under: S. F. Ebel, F. Rominger, M. Mastalerz, "Embedding a Planar Antiaromatic Cyclooctatetraene into a Truxene-Derived Polycyclic Aromatic Hydrocarbon", Org. Lett. ***2025****, 27, 7944-7949.*[306]

Reconsidering the inversion of a COT unit within the monkey saddle framework, it was perceived that the alkoxy- and unsubstituted benzene rings have to pass each other. This process appears feasible as long as both six-membered rings bear solely hydrogen atoms in the relevant moieties (see **Figure 3.27**). However, if one of these positions was substituted, e.g., by a hydroxy group, an increase of steric hindrance and consequently of the molecule's conformational stability would be expected. To verify this hypothesis, the inversion barrier of the corresponding OH-functionalized monkey saddle was calculated at the PW6B95-D3(BJ)/def2-QZVPP+SMD(*n*-heptane)//PBEh-3c level of theory. Compared to the unsubstituted monkey saddle, the barrier height indeed increased from 104 kJ mol^{-1} to 141 kJ mol^{-1} (**Figure 3.27**). This substantial elevation suggests that such a modification of the benzene rings is a promising alternative to the methylated monkey saddle, particularly since the latter has proven synthetically inaccessible (see *Chapter 3.5*).

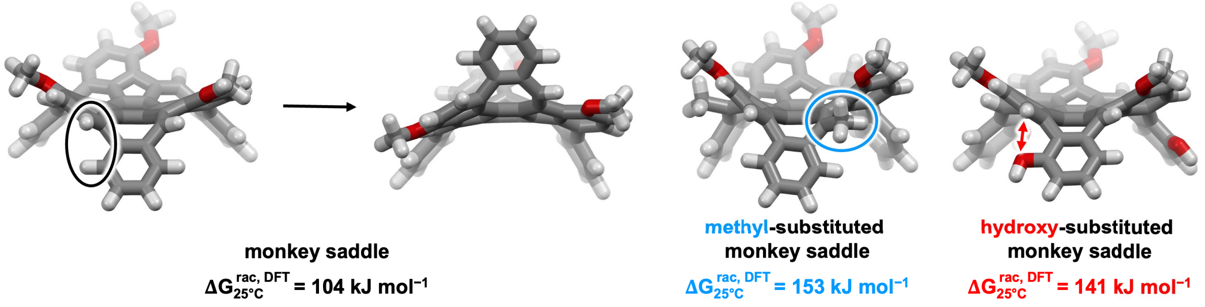

Figure 3.27: Illustration of the ring inversion of a COT unit within the monkey saddle during the racemization process. This inversion is impeded by substituents on either the eight-membered rings (e.g., Me group; highlighted in blue) or the six-membered rings (e.g., OH group). The expected steric hindrance for the OH-substituted monkey saddle is indicated with a red arrow. The inversion barriers were calculated at the PW6B95-D3(BJ)/def2-QZVPP+SMD(*n*-heptane)//PBEh-3c level of theory.

The introduction of hydroxy groups could provide some additional advantages. For instance, as an electron donating group, the OH-moieties offer the opportunity to post-functionalize the respective monkey saddle **152** by an *ortho*-selective electrophilic aromatic substitution ($\mathrm{S_EAr}$) (**Scheme 3.25A**). On the other hand, a protection of the alcohols could further increase the inversion barrier depending on the steric bulk of the chosen protecting group.

The synthesis of target compound **152** requires a bromobenzene derivative carrying both an aldehyde – for the condensation step – as well as a hydroxy group, each positioned *ortho* to the bromide (**Scheme 3.25B**). Accordingly, the route begins with the commercially available bromide **153**, whose hydroxy group should be protected to prevent interference during the palladium-catalyzed cross-couplings.[307] The protecting group must thereby fulfill three criteria: (1) it has to be stable under basic conditions, (2) it should exhibit a minimal steric demand to avoid impeding either the Suzuki-Miyaura cross-coupling or the subsequent condensation reaction, and (3) it should be readily cleavable in the presence of alkoxy groups and alkenes. Methoxymethyl (MOM) ethers were found to meet all these requirements,[308] rendering them well suited for the efficient production of **152**.

Based on the considerations outlined above, this chapter will explore the isolation of the hydroxy-functionalized monkey saddle **152**. Afterwards, this compound will be used to investigate the impact of the altered substitution pattern on the inversion barrier.

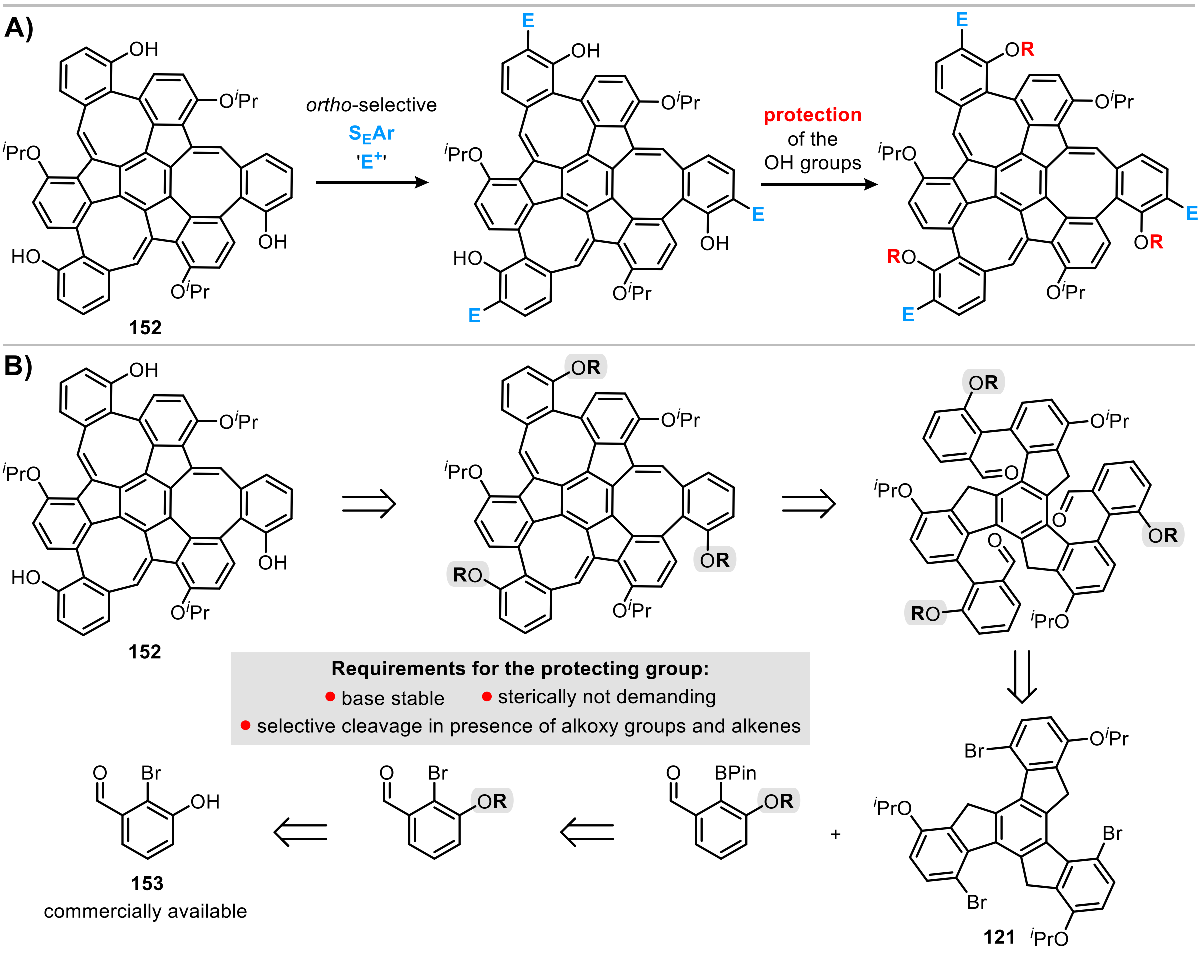

Requirements for the protecting group:
- base stable
- sterically not demanding
- selective cleavage in presence of alkoxy groups and alkenes

Scheme 3.25: A) Possible functionalization of the hydroxy-substituted monkey saddle **152**. **B)** Retrosynthesis of monkey saddle **152**. For the presented route, the commercially available bromide **153** needs a suitable protecting group that has to fulfill certain requirements.

Substitution of the Six-Membered Rings

The first step toward monkey saddle **152** consisted of **153**'s protection. Therefore, the hydroxy group was deprotonated with triethylamine, followed by its exposure to bromomethyl methyl ether (MOMBr).[309] After stirring the reaction at room temperature overnight, the product **154** was obtained as a colorless oil in 71% yield (**Scheme 3.26A**). Next, a Miyaura borylation[310] was performed to replace the aryl bromide with a boronic acid pinacol ester. To this end, a mixture of **154**, potassium acetate, bis(pinacolato)diboron (B_2Pin_2), and 10 mol% Pd(dppf)Cl_2 was stirred in 1,4-dioxane at 80 °C under an argon atmosphere. Monitoring the reaction progress by ^1H NMR spectroscopy showed that exhaustive consumption of the starting material was reached after three to six days, depending on **154**'s scale.

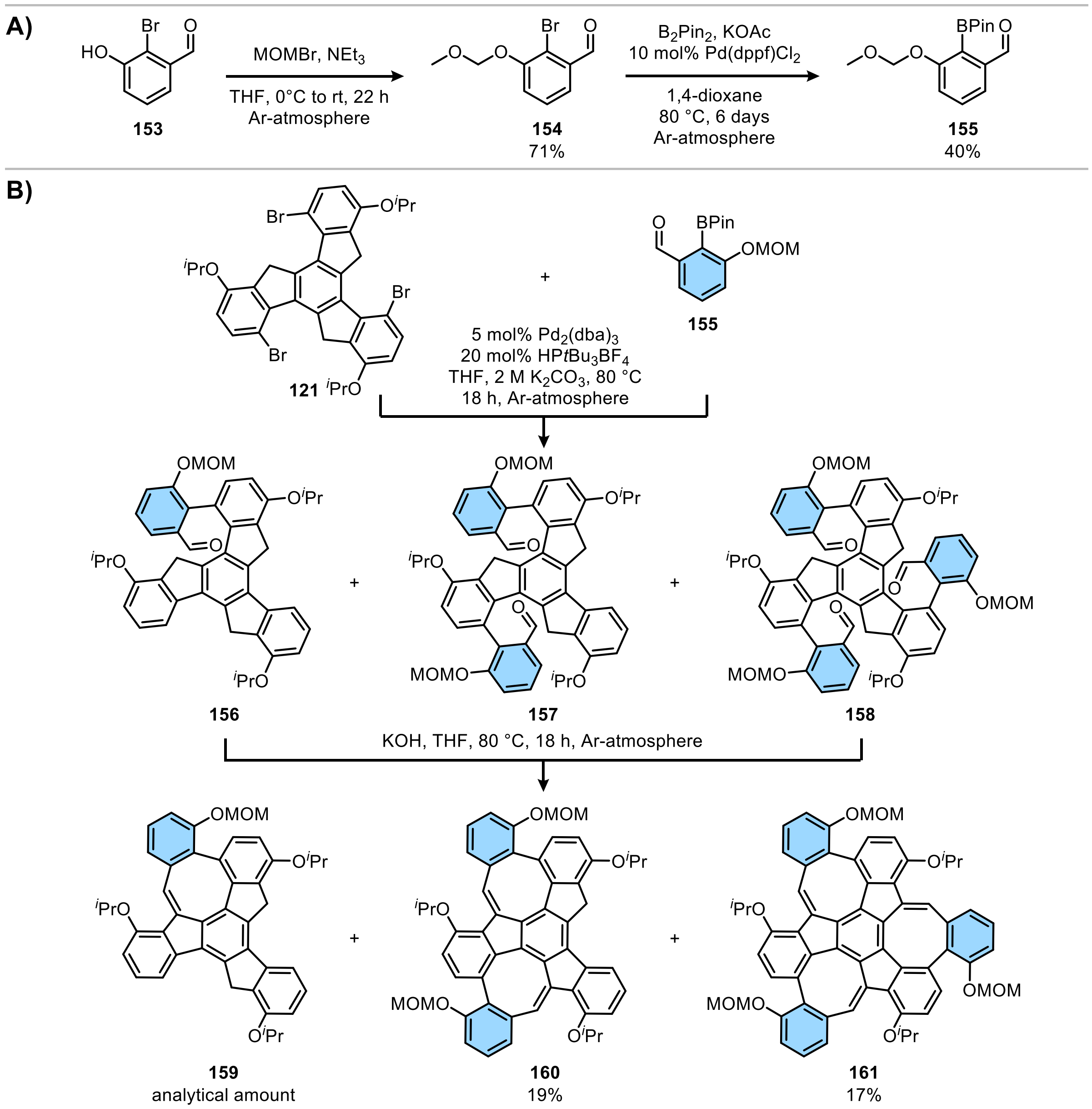

Scheme 3.26: A) Synthesis of the boronic ester derivative **155**. **B)** Synthesis of monkey saddle **161** and the truxene-derived PAHs **159** and **160**. Since the aldehyde species **156**-**158** were not separable by flash column chromatography, their mixture was subjected to the condensation reaction. The given yields refer to **121** over two steps.

Besides the boronic ester derivative **155**, ^{1}H NMR studies also revealed protodebromination of the starting material **154**, occurring in a 0.5:1 ratio relative to **155**. For purification, the two compounds were first separated by flash column chromatography before excess B_2Pin_2 was removed from the product fraction by sublimation. Finally, **155** was distilled *in vacuo* to isolate it as a colorless liquid in 40% yield. Since approximately 33% of the yield loss can be directly ascribed to the protodebromination of **154**, other solvents were explored for this Miyaura borylation. However, the use of toluene or DMSO led to even less favorable byproduct to product ratios of 0.7:1 and 1.1:1, respectively.

Eventually, boronic ester **155** and tribromotruxene **121** were subjected to a Suzuki-Miyaura cross-coupling (**Scheme 3.26B**). Initial conditions applied the catalyst $Pd_2(dba)_3$ with $HP^tBu_3BF_4$ as ligand in a THF/2 M $K_2CO_{3(aq)}$ solvent mixture, and the reaction was vigorously stirred at 80 °C overnight. MALDI-TOF mass spectrometry analysis of the crude material disclosed the formation of three new species at *m/z* 680.313, 844.359, and 1008.406, whose mass differences of Δ*m/z* = 164 correspond to **155**'s coupling to the truxene core (**Figure 3.28A**). Additionally, the isotope patterns illustrated the absence of bromine in all three structures, thus identifying the products as the one-, two-, and three-fold coupled as well as protodebrominated compounds **156** (calcd for $(C_{45}H_{44}O_6)^+$: 680.313), **157** (calcd for $(C_{54}H_{52}O_9)^+$: 844.361), and **158** (calcd for $(C_{63}H_{60}O_{12})^+$: 1008.408).

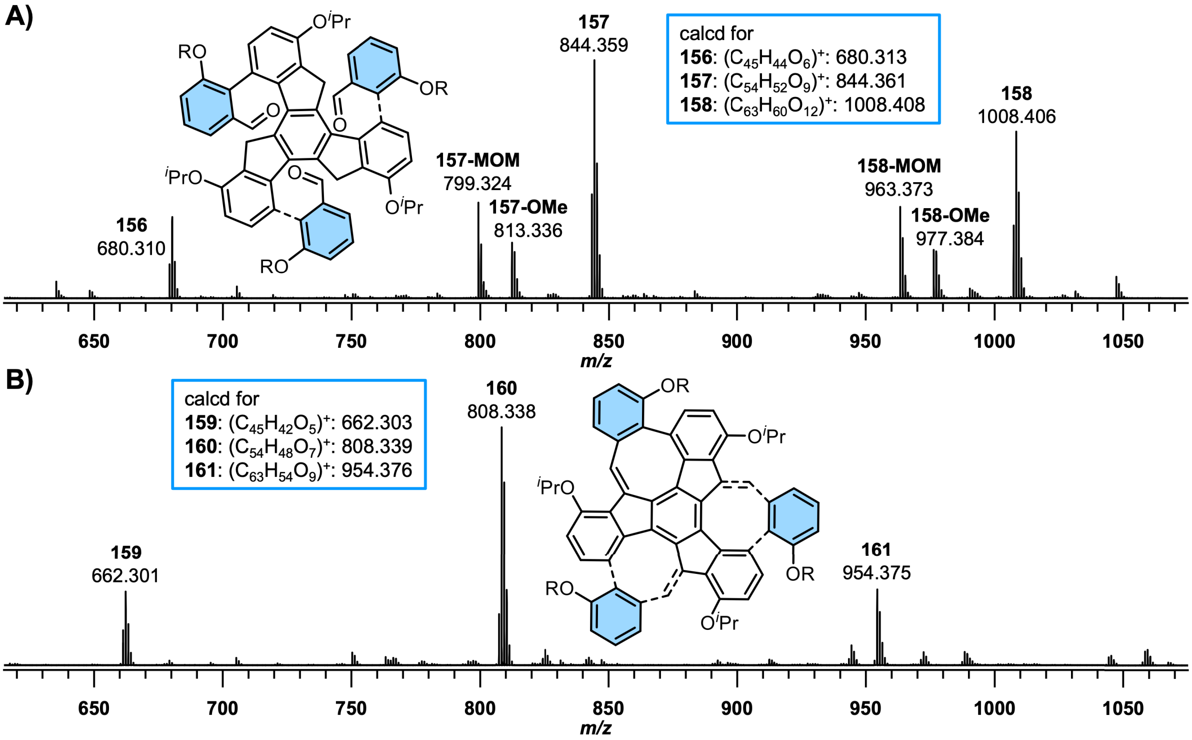

Figure 3.28: A) MALDI-TOF mass spectrum of the Suzuki-Miyaura cross-coupling between tribromotruxene **121** and boronic ester **155**. The crude product contained a mixture of the one-, two-, and three-fold coupled species **156**, **157**, and **158**. **B)** MALDI-TOF mass spectrum after subjecting a mixture of **156**-**158** to a base-mediated condensation, delivering the products **159**, **160** and **161**. The MOM group was abbreviated as R in the structures.

Increasing the equivalents of **155** progressively shifted the product distribution toward the targeted three-fold coupled derivative **158**. Yet, owing to **155**'s laborious purification process, minimizing its excess in the Suzuki-Miyaura cross-coupling was desirable. Consequently, a range of reaction conditions were screened, including various catalyst systems (Pd_2dba_3 with $HP^tBu_3BF_4$, SPhos, or XPhos, $Pd(dppf)Cl_2$, $Pd(PPh_3)_4$), bases (K_2CO_3, Cs_2CO_3, NaOH, K_3PO_4, NaH_2PO_4, Na_2HPO_4), solvents (THF, MTBE, toluene, DMF), temperatures, and concentrations. Despite these efforts, none of the alternative conditions outperformed the first setup and delivered at best comparable results. Moreover, closer examination of the different entries determined a rapid base-catalyzed protodeboronation[311-312] of **155** as the main limitation for the incomplete conversion. Ultimately, the initial conditions were accepted as optimum, and the synthesis proceeded with the condensation step.

As compounds **156**, **157**, and **158** could not be separated by flash column chromatography, their mixture was dissolved in THF and treated with potassium hydroxide (**Scheme 3.26B**). Upon heating the solution to 80 °C, its color changed from light yellow to dark brown. After 18 hours, the reaction was quenched with water, followed by an aqueous work-up. As expected, MALDI-TOF MS studies of the crude material displayed again three product species at *m/z* 662.301, 808.338, and 954.375, which matched the calculated masses of the intramolecularly condensed species **159** (calcd for $(C_{45}H_{42}O_5)^+$: 662.303), **160** (calcd for $(C_{54}H_{48}O_7)^+$: 808.339), and **161** (calcd for $(C_{63}H_{54}O_9)^+$: 954.376) (**Figure 3.28B**). At this stage, the products were separable by flash column chromatography; though due to the acid sensitivity of the MOM groups, 2 *vol%* NEt_3 had to be added to the eluent. The product fractions were further purified by suspending them in methanol and collecting the yellow-brownish solids by filtration. This procedure gave the two-fold MOM-substituted PAH (abbreviated as 2MOM-PAH) **160** in 19% and the MOM-substituted monkey saddle (abbreviated as MOM-MS) **161** in 17% yield over two steps, respectively. In contrast, compound **159** (abbreviated as 1MOM-PAH) was only obtained in trace amounts. Lastly, each of the isolated substances **159**-**161** still needed to be subjected to HPLC purification in order to gain analytically pure samples.

When the ^1H NMR spectrum of MOM-MS **161** was acquired in $CDCl_3$, additional signals beyond those of the target compound emerged within a few minutes and increased in intensity over time. This apparent chemical instability was attributed to trace amounts of acid in the deuterated chloroform, which had probably initiated the deprotection of the MOM-substituted hydroxy groups. Hence, all NMR investigations were carried out in CD_2Cl_2. The ^1H NMR spectrum of **161** confirmed its C_3-symmetry by disclosing five distinct aromatic peaks with equal integral ratios (**Figure 3.29A**). Furthermore, the formation of the COT units was supported by a singlet at $\delta = 8.35$ ppm, while the three MOM moieties appeared as two doublets at $\delta = 4.88$ and 4.79 ppm, corresponding to the chemically inequivalent CH_2 protons, and a singlet at $\delta = 3.26$ ppm for the MOM's terminal CH_3 protons.

In the final step, **161**'s deprotection was accomplished by treating it with 6 M $HCl_{(aq)}$ in *n*-heptane at 80 °C, followed by a flash column chromatographic purification, giving the target compound **152** as a brown solid in 34% yield (**Scheme 3.27**). Nevertheless, similar to substances **159**-**161**, the hydroxy-functionalized monkey saddle (abbreviated as OH-MS) **152** required additional HPLC purification for an analytically pure sample.

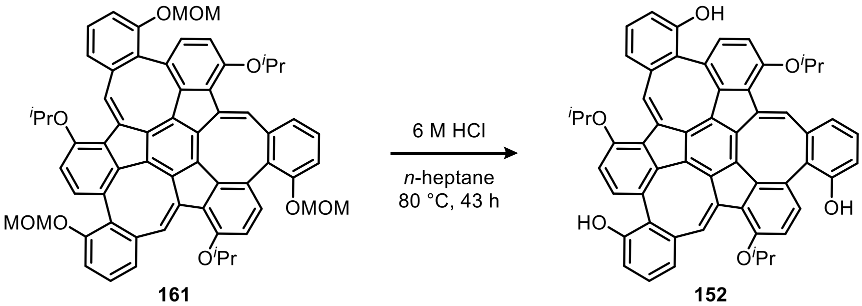

161

152
34%

Scheme 3.27: Synthesis of **152** by deprotecting the hydroxy groups of monkey saddle **161** with hydrochloric acid.

^{1}H NMR analysis of **152** verified the successful deprotection of precursor **161** for one by the disappearance of the three peaks previously associated with the MOM protecting groups (**Figure 3.29B**). In their place, a new singlet occurred at δ = 4.80 ppm, which can be attributed to **152**'s OH groups. Moreover, the strong electron-donating effect of the hydroxy moieties induced a slight up-field shift of the aromatic signals, whereby proton H^d experienced the most pronounced shift from δ = 7.03 ppm to δ = 6.89 ppm owing to its *ortho* position relative to the hydroxy group.

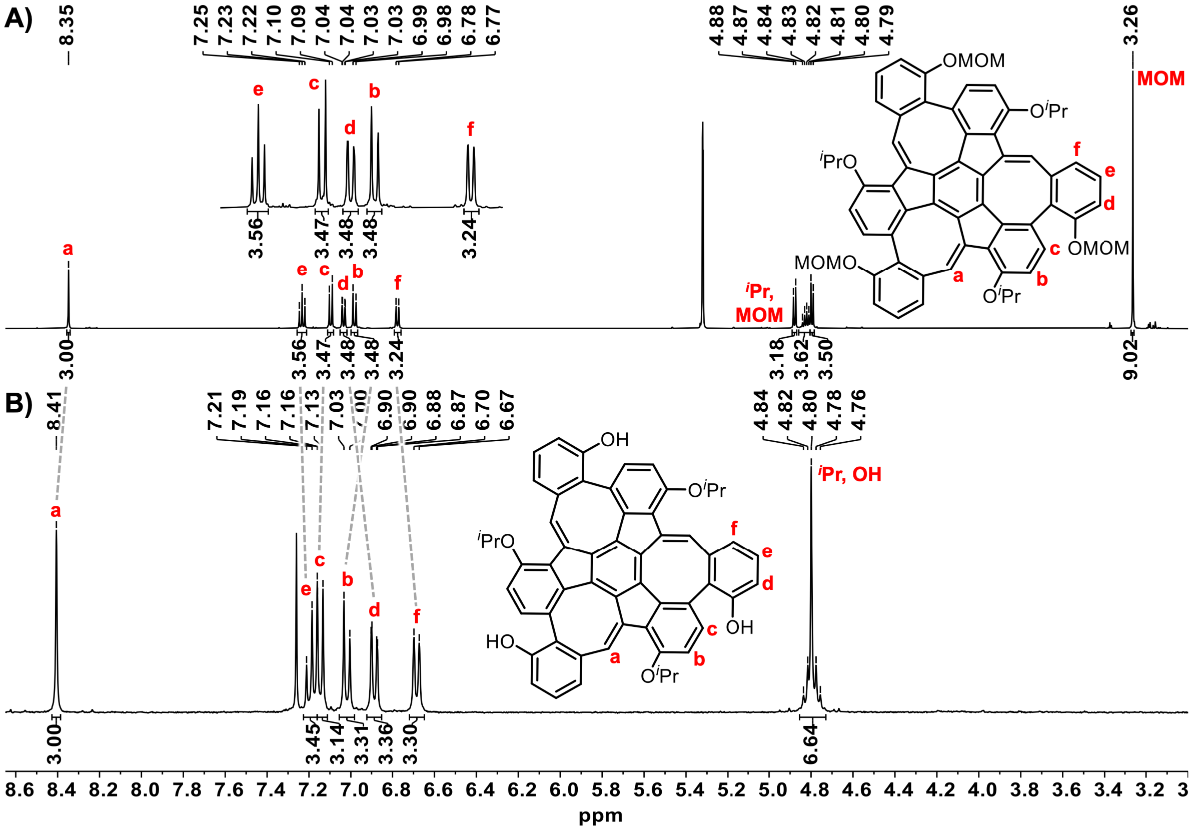

Figure 3.29: ^{1}H NMR spectra of the monkey saddles **A) 161** (600 MHz, CD_2Cl_2) and **B) 152** (600 MHz, $CDCl_3$) with assignment of the protons.

X-ray Structure Analysis of Monkey Saddle 161

X-ray diffraction analysis unambiguously confirmed the structure of compound **161** (**Figure 3.30A**). Suitable single crystals were obtained from a saturated solution of **161** in a CH_2Cl_2/*n*-heptane (80:20) mixture containing 1 vol% triethylamine. The monkey saddle crystallized in the triclinic space group $P\overline{1}$ with two molecules per unit cell, comprising one (S_a,S_a,S_a)- and one (R_a,R_a,R_a)-enantiomer. As commonly observed for monkey saddle derivatives,[177-178, 185-186] the incorporation of three cyclooctatetraene subunits in **161** results in a negatively curved framework, with dihedral angles of θ = 47-54° and φ = 27-33° (*cf.* **Figure 3.30B**). For comparison, the monkey saddle **47**, which lacks the OMOM groups, exhibits angles of θ = 41-53° and φ = 28-34°,[177] suggesting that the unprecedented substitution pattern does not deepen the overall curvature of the monkey saddle. Besides, similar nonplanarities were determined for **161**'s (0.348 Å) and **47**'s (0.341 Å) COTs,[177] reinforcing the conclusion that the OMOM substituents do not impose additional structural strain.

The crystal packing of **161** showed the formation of homochiral chains, whereby two chains of opposite chirality aligned in a way that one OMOM-substituted benzene ring of one enantiomer always pointed inside the cavity of the other enantiomer and vice versa (**Figure 3.30D**). Within each of these heterochiral pairs, several interactions were observed including CH···π interactions between the protons of the OMOM-substituted benzene ring and the π-system of the opposite enantiomer ($d_{\mathrm{CH\cdots\pi}}$ = 2.8 Å), as well as a CH···O interaction between two OMOM moieties with a distance of $d_{\mathrm{CH\cdots O}}$ = 2.6 Å (**Figure 3.30C**).

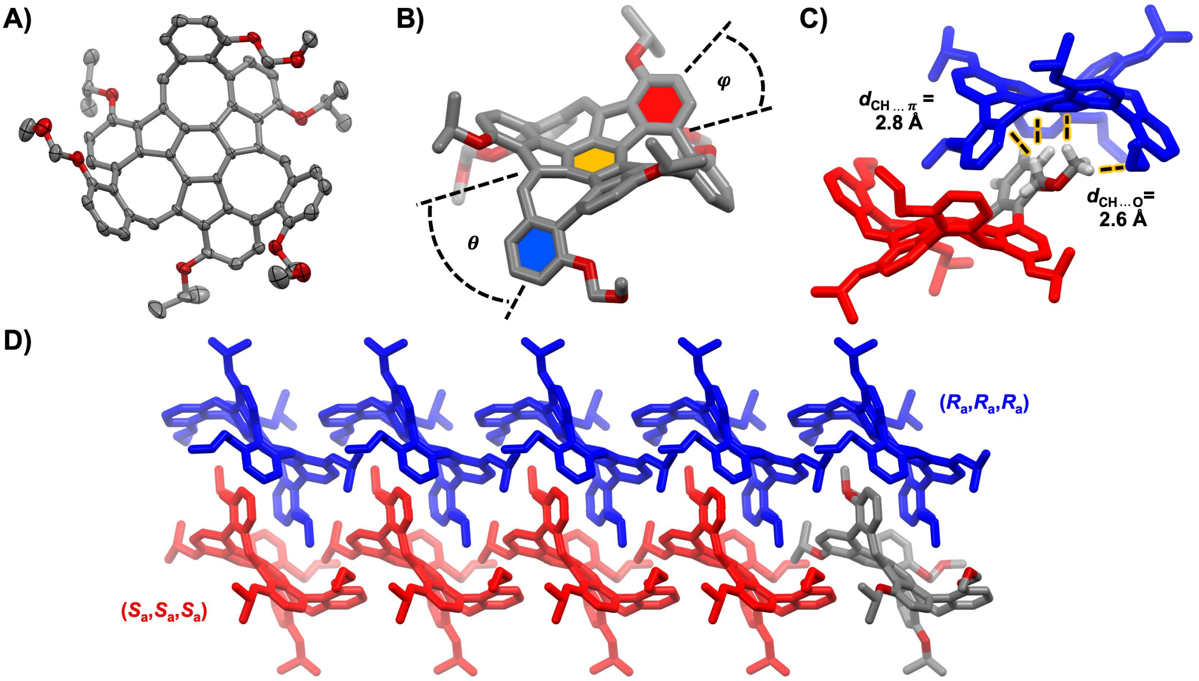

Figure 3.30: Single crystal structure of **161** (CCDC 2456924).[306] **A)** (S_a,S_a,S_a)-enantiomer of **161** as ORTEP drawing with 50% probability of ellipsoids. **B)** Side view of (S_a,S_a,S_a)-**161**. The colored benzene rings were used to calculate the angles θ (orange and blue) and $\boldsymbol{\varphi}$ (orange and red). **C)** Enlarged view of one (R_a,R_a,R_a)-**161** (blue) and one (S_a,S_a,S_a)-**161** (red) with illustration of selected intermolecular interactions. **D)** Packing of **161**. For a better visualization, the (S_a,S_a,S_a)-enantiomer was colored in red and the (R_a,R_a,R_a)-enantiomer in blue. Hydrogens were generally omitted for clarity. Grey = carbon, red = oxygen, white = hydrogen. The figures **A**-**C)** were adapted from the supporting information of reference 306.

Optoelectronic Properties

Investigating the optoelectronic properties of the four truxene-derived PAHs revealed that the MOM-MS **161** and OH-MS **152** exhibit very similar UV/vis spectra (**Figure 3.31A**, **Table 3.3**). Both compounds display their lowest energy absorption band at λ = 400 nm, along with two additional absorption maxima at λ = 281, 328 nm for **161** and λ = 278, 335 nm for **152**. Besides, they feature weak fluorescence emissions around λ_{em} = 535 nm, with Stokes shifts of $\tilde{\nu}$ = 6308 cm^{-1} for **161** and $\tilde{\nu}$ = 6273 cm^{-1} for **152**. Removing one or two wings from the monkey saddle framework reduces the conjugated system and consequently, leads to a hypsochromic shift of the lowest energy absorption band to λ = 374 nm for the 2MOM-PAH **160** or λ = 369 nm for the 1MOM-PAH **159**. No fluorescence was detectable for the latter two PAHs.

Table 3.3: Summary of photophysical and electrochemical properties of compounds (cmpd.) **159**-**161** and **152**.

Cmpd.	E_{LUMO}^{DFT} [eV][a]	E_{HOMO}^{DFT} [eV][a]	E_{gap}^{DFT} [eV][a]	E_{EA}^{CV} [eV][b]	E_{IP}^{CV} [eV][b]	E_{gap}^{CV} [eV]	λ_{max} [nm]	λ_{onset} [nm]	E_{gap}^{opt} [eV][c]	λ_{em} [nm][d]	$\nu_{Stockes}$ [cm^{-1}]
159	−1.78	−5.15	3.37	−2.68	−5.42	2.74	369	442	2.80	–	–
160	−1.82	−5.07	3.25	−2.69	−5.37	2.68	374	466	2.66	–	–
161	−1.67	−5.03	3.36	−2.71	−5.46	2.75	400	447	2.77	535	6308
152	−1.73	−5.09	3.36	–	−5.56	–	400	450	2.76	534	6273

[a]: Calculated at the B3LYP/6-311G* level of theory.
[b]: E^{CV}= −($E_{1/2}$ + 4.8 eV). CH_2Cl_2, 0.1 M NBu_4PF_6, scanrate: 100 mV s^{-1}, Fc/Fc$^+$ was used as an internal reference.
[c]: Estimated from the onset of the corresponding UV/vis absorption spectrum (E_{gap}^{opt} = 1240/λ_{onset}).
[d]: The most intense emission maximum was specified.

The cyclic voltammograms of the OMOM-substituted compounds **159**-**161** all showed a reversible reduction (**159**: $E_{red,1}$ = −2.12 V, **160**: $E_{red,1}$ = −2.11 V, **161**: $E_{red,1}$ = −2.09 V) and an irreversible oxidation (**159**: $E_{ox,1}$ = +0.62 V, **160**: $E_{ox,1}$ = +0.57 V, **161**: $E_{ox,1}$ = +0.66 V) (**Figure 3.31B**). In contrast, OH-MS **152** disclosed only one irreversible oxidation at a higher potential ($E_{ox,1}$ = +0.76 V) compared to MOM-MS **161**. Based on these measurements, 1MOM-PAH **159** and MOM-MS **161** have nearly identical electrochemical band gaps of $E_{CV,gap}$ = 2.74 V and $E_{CV,gap}$ = 2.75 V, respectively, while 2MOM-PAH **160** exhibits a slightly smaller band gap of $E_{CV,gap}$ = 2.68 V. This trend is consistent with the observed optical band gaps and DFT calculated HOMO-LUMO gaps (**Table 3.3**).

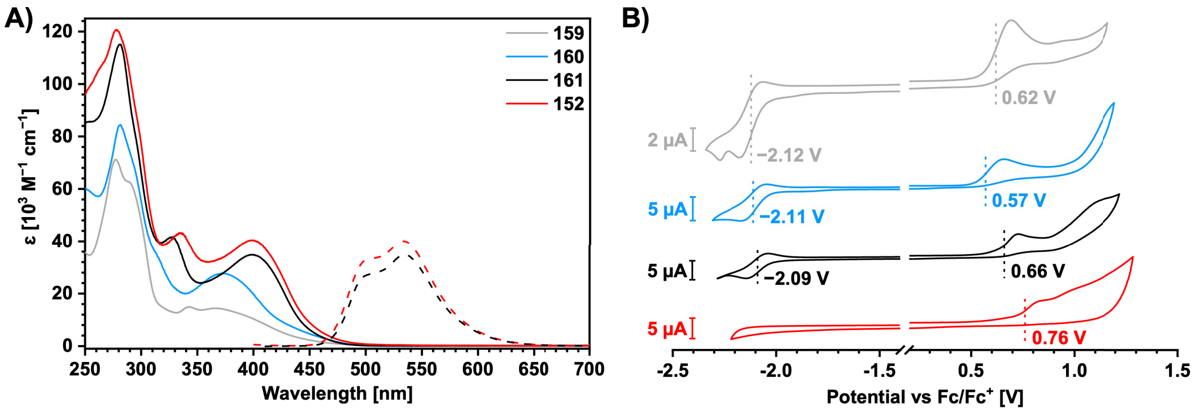

Figure 3.31: A) UV/vis absorption (solid line) and emission spectra (dotted line) of 1MOM-PAH **159**, 2MOM-PAH **160**, MOM-MS **161**, and OH-MS **152**. Used excitation wavelengths: λ_{ex} = 400 nm for **161**; λ_{ex} = 277 nm for **152**. **B)** Cyclic voltammograms of **159** (grey), **160** (blue), **161** (black), and **152** (red) (CH_2Cl_2, 0.1 M NBu_4PF_6, scan rate: 100 mV s^{-1}, working electrode: Glassy carbon, counter electrode: Pt, pseudo-reference electrode: Ag/Ag$^+$) vs. ferrocene as internal reference.

Investigations of the Inversion Barriers

As previously discussed, the substitution pattern in monkey saddles **161** and **152** was designed to improve their conformational stability. Due to an incomplete conversion during the Suzuki-Miyaura cross-coupling step, compounds **159** and **160**, which lack two or one wings of the monkey saddle framework, were unanticipatedly furnished as well, completing this series of truxene-derived PAHs. Prior to experimental studies, the inversion barriers of the obtained products were investigated by DFT calculations at the PW6B95-D3(BJ)/def2-QZVPP+SMD(*n*-heptane)//PBEh-3c level of theory.

Although the eight-membered rings undergo a sequential instead of simultaneous conformational flipping,[177] it was found that the total number of embedded COT units significantly affects the barrier height (**Figure 3.32**). For instance, 1MOM-PAH **159** has a relatively low inversion barrier of 97 kJ mol^{-1}, while the second eight-membered ring in 2MOM-PAH **160** raises its conformational stability by 15 kJ mol^{-1}. The incorporation of a third COT moiety increased the barrier by another 31 kJ mol^{-1} relative to **160**, giving a total inversion barrier of 143 kJ mol^{-1} for MOM-MS **161**. In contrast, replacing the MOM-protecting groups with hydrogen atoms has no relevant effect on the inversion barrier, lowering it by merely 2 kJ mol^{-1}. This observation can likely be ascribed to the ability of the MOM groups to rotate out of the way, thereby minimizing their apparent influence on the COT's inversion process.

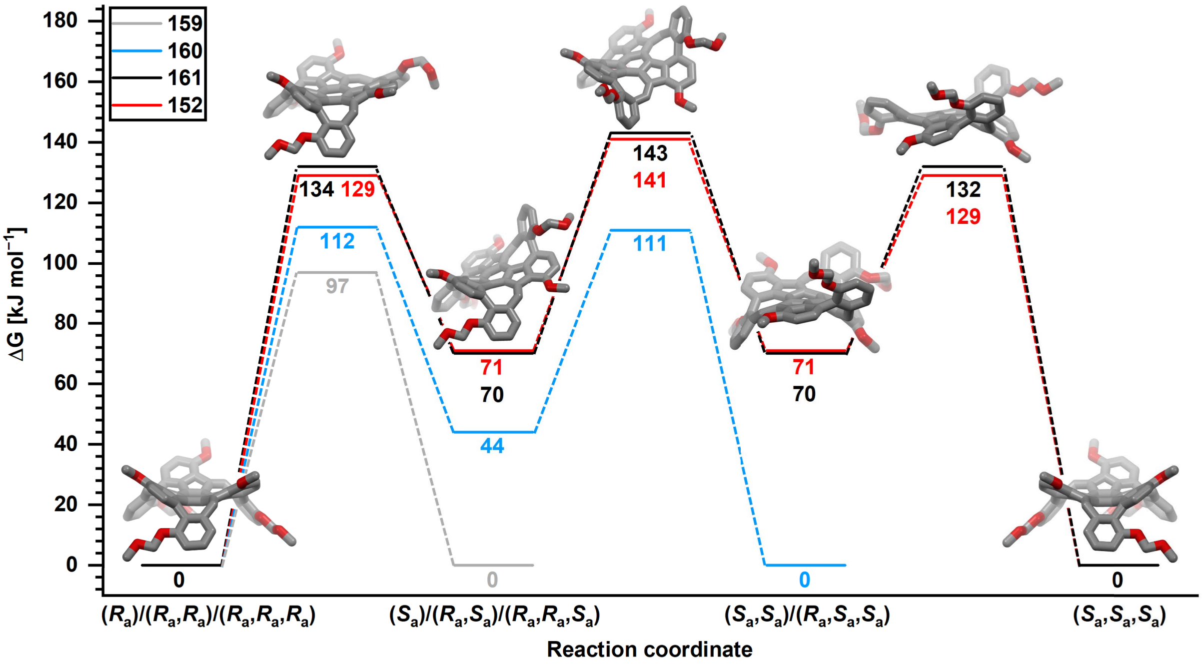

Figure 3.32: Comparison of DFT calculated inversion pathways of 1MOM-PAH **159** (grey), 2MOM-PAH **160** (blue), MOM-MS **161** (black), and OH-MS **152** (red) calculated at the PW6B95-D3(BJ)/def2-QZVPP+SMD(*n*-heptane)//PBEh-3c level of theory. Monkey saddle **161** was pictured exemplary for the inversion pathway. For simplicity, the isopropoxy groups of all four molecules were shortened to methoxy groups.

Experimentally, the enantiomers of **159**-**161** and **152** were first separated by chiral HPLC using either a Chiralpak IB or IE column. For compounds **160** and **161**, a compromise between solubility and peak separation precluded the enantiopure isolation of the second enantiomer, despite repeated injections of the respective fraction into the chiral HPLC (*cf.* **Figure 3.33A** for **160**). Hence, kinetic CD measurements were exclusively performed with the first eluted enantiomer, which, according to TD-DFT calculations, could be assigned to (R_a,R_a)-**160** and (R_a,R_a,R_a)-**161**, respectively. Meanwhile, 1MOM-PAH **159** featured a baseline separation, which however did not provide the (R_a)- and (S_a)-fractions enantiopure. This outcome was attributed to the low inversion barrier predicted for **159**, leading to its rapid racemization, and thus examinations of **159**'s chiral properties and inversion barrier were not pursued.

Next, the decay of CD signal intensity of the 2MOM-PAH (R_a,R_a)-**160** was recorded at four different temperatures ranging from 50 °C to 80 °C (**Figure 3.33B**). This study delivered an experimental inversion barrier of $\Delta G^{\ddagger}$(25 °C) = 111 ± 2 kJ mol^{-1}, which agrees with the calculated value of 112 kJ mol^{-1}. In terms of half-lifes, this represents a significant increase compared to the unsubstituted monkey saddle **47** (e.g., **160**: $t_{1/2}$(50 °C) = 14.3 ± 0.2 h vs. **47**: $t_{1/2}$(50 °C) = 57.8 ± 0.4 min),[177] already demonstrating the superiority of the modified substitution pattern on the conformational stability. This effect is expected to be even more pronounced in **161** and **152** because of the incorporation of the third COT moiety.

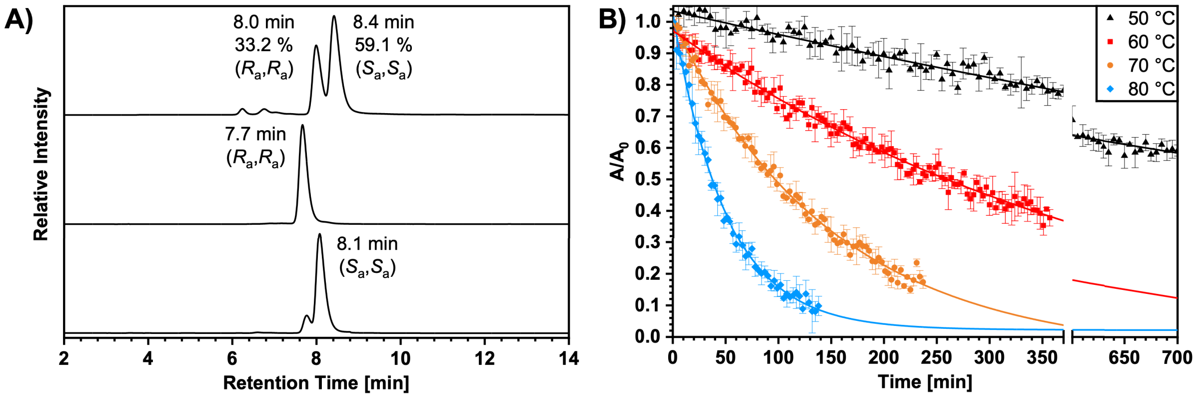

Figure 3.33: A) Analytical chromatograms of 2MOM-PAH **160** (IB column, *n*-heptane/CH_2Cl_2/MTBE (80/10/10 *v*/*v*/*v*), 1.0 mL min^{-1}, 30 °C, 300 nm) with assignment of the (R_a,R_a)- and (S_a,S_a)-enantiomer to the corresponding fraction. **B)** Decay of CD signal intensity of (R_a,R_a)-**160** over time at different temperatures (*n*-heptane, 219 nm).

Initial measurements of the MOM-MS (R_a,R_a,R_a)-**161** were conducted in *n*-decane at 125 °C. Surprisingly, after approximately 90 minutes, the recorded CD spectra no longer corresponded to (R_a,R_a,R_a)-**161** (**Figure 3.34A**). In addition, when the normalized decay of the CD signal intensity was plotted over time for the maximum at 252 nm, a value of −0.2 was reached before gradually approaching zero (**Figure 3.34B**). This behavior contradicts racemization, as in that case the CD peaks would simply diminish and eventually vanish. The emergence of new signals rather indicates that at least one other chiral compound arose during the heating process.

To further analyze this chemical instability, the samples were reinjected into the analytical HPLC after heating, and the chromatograms were compared to that of the applied starting material (**Figure 3.34C**). Moreover, milder conditions were explored, beginning with heating (R_a,R_a,R_a)-**161** in *n*-heptane at 80 °C overnight. This entry provided a mixture of unconsumed (R_a,R_a,R_a)-**161** at a retention time of 4.8 min and a new compound eluting at 3.2 min. Remarkably, the amount of the (S_a,S_a,S_a)-enantiomer did not increase during this measurement, indirectly confirming a significant increase of the racemization barrier, especially compared to the unsubstituted monkey saddle **47**, which completely racemizes within 40 min at 70 °C.[177] In another approach, (R_a,R_a,R_a)-**161** was heated again in *n*-decane at 120 °C overnight, giving an unresolved mixture of various compounds or isomers (**Figure 3.34C**). Following, the OH-MS (R_a,R_a,R_a)-**152** was subjected to kinetic CD measurements, whereby the prepared samples were heated in *n*-decane at 120 °C overnight and at 160 °C for two days, respectively. Subsequent injections of the solutions into the analytical HPLC revealed once more the formation of new compounds eluting at 3.3 min, with no detectable traces of (R_a,R_a,R_a)-**152** or its racemate (**Figure 3.34D**). These observed chemical instabilities prohibited the experimental determination of the inversion barriers for both **161** and **152**.

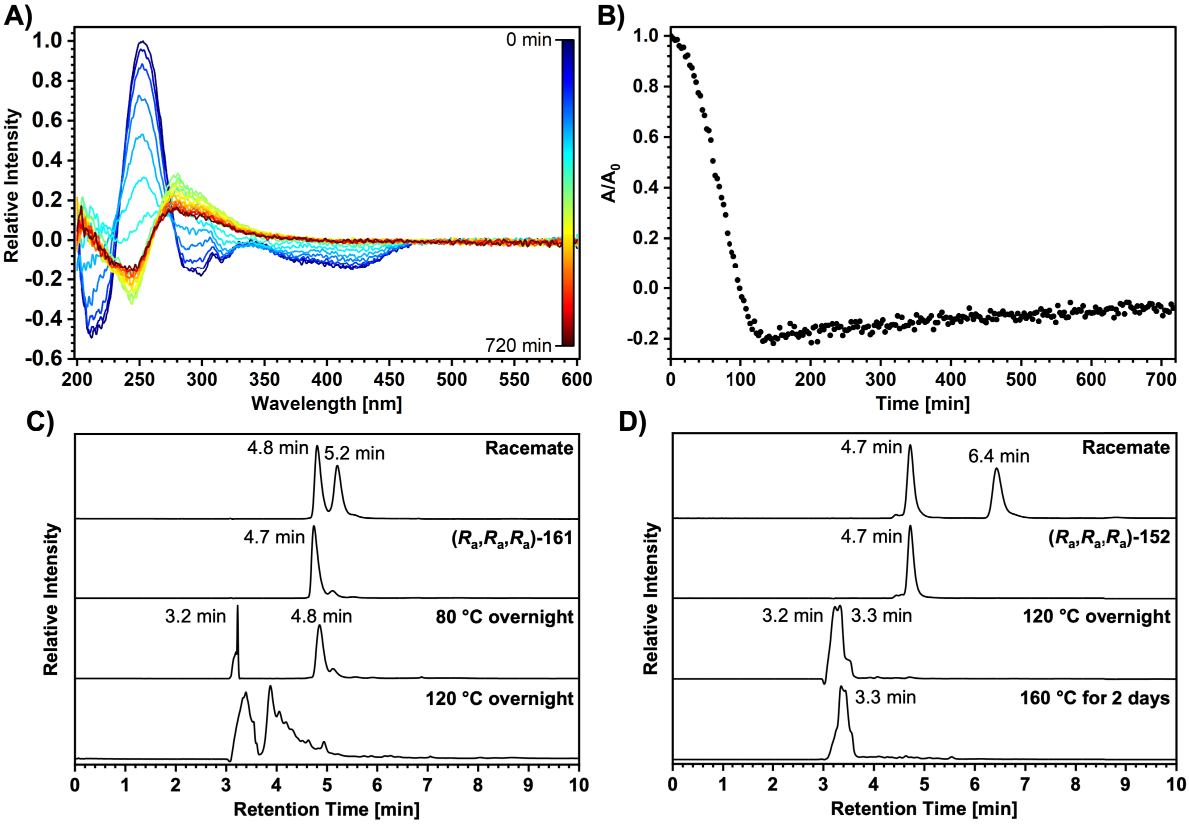

Figure 3.34: A) Normalized change of the CD spectrum of the MOM-MS (R_a,R_a,R_a)-**161** when heated in *n*-decane at 125 °C for 720 min. **B)** Decay of the CD signal intensity of (R_a,R_a,R_a)-**161** at 125 °C (*n*-decane, 252 nm). **C)** Analytical chromatograms (IE column, *n*-heptane/CH_2Cl_2 (50:50 *v*/*v*), 1 mL min^{-1}, 30 °C, 280 nm) of **161**'s racemate, (R_a,R_a,R_a)-**161**, and (R_a,R_a,R_a)-**161** heated in *n*-heptane at 80 °C overnight and in *n*-decane at 120 °C overnight, respectively. **D)** Analytical chromatograms (IE column, *n*-heptane/EA (70:30 *v*/*v*), 1 mL min^{-1}, 30 °C, 280 nm) of the racemate of OH-MS **152**, (R_a,R_a,R_a)-**152**, and (R_a,R_a,R_a)-**152** heated in *n*-decane at 120 °C overnight and at 160 °C for two days, respectively. The figures **A**-**D)** were adapted from the supporting information of reference 306.

The unknown reactivity that the OMOM- and OH-substituted monkey saddles seemingly prefer over racemization, was scrutinized by heating around 10 mg of MOM-MS **161** in 1.0 mL of solvent (*n*-heptane, THF, chloroform, toluene, DMSO, or *n*-decane) at 80-120 °C for one to seven days. Unfortunately, each entry consistently resulted in the isolation of either the starting material **161** or the deprotected species **152** according to ^{1}H NMR and MALDI-TOF MS analysis. Hence, no insights could be gained into the processes occurring during the kinetic CD measurements. Similarly, heating a solution of OH-MS **152** in *n*-heptane at 80 °C for one week solely led to the recovery of unreacted starting material. Owing to the limited availability of **152**, further studies of its potential reactivity could not be carried out.

Summary and Outlook

This chapter presented an alternative strategy for improving the conformational stability of monkey saddles. Based on prior computational examinations, it was proposed that a specific substitution pattern on the six-membered rings could increase the inversion barrier by at least 37 kJ mol^{-1}. For the experimental realization, hydroxy groups were selected as they offer promising opportunities to post-functionalize the corresponding OH-MS **152**.

The synthesis route started with the preparation of the boronic ester **155**, which was then coupled to the tribromotruxene **121**. This Suzuki-Miyaura reaction delivered a mixture of the one-, two-, and three-fold coupled products **156**-**158**, whose separation could not be achieved by flash column chromatography. Thus, an extensive screening was performed to optimize the conversion toward **158**, yet none of the tested conditions outperformed the initial setup. In consequence, the mixture consisting of **156**-**158** was directly subjected to the condensation step, giving the series of 1MOM-PAH **159**, 2MOM-PAH **160**, and MOM-MS **161**. The structure of the latter was unambiguously confirmed by X-ray diffraction analysis. Ultimately, the deprotection of **161** using hydrochloric acid provided OH-MS **152**.

Following, the optoelectronic properties of all four compounds **159**-**161** and **152** were investigated. Regarding the UV/vis spectra, the reduction of the conjugated system in **159** and **160** led to a hypsochromic shift of the lowest energy absorption band relative to **161**. In contrast, the presence of either OMOM or OH groups in **161** and **152** had minimal influence on their optical characteristics. The electrochemical properties were studied by cyclic voltammetry, which revealed a reversible reduction and an irreversible oxidation for the OMOM-substituted derivatives **159**-**161**, whereas **152** exhibited only an irreversible oxidation.

Next, the racemization barriers were assessed both computationally and experimentally. DFT calculations suggested that the number of incorporated COT units in the structure has a pronounced effect on the barrier height (*cf.* 97 kJ mol^{-1} for 1MOM-PAH **159** vs. 143 kJ mol^{-1} for MOM-MS **161**), while replacing the MOM groups with hydrogen resulted in a negligible decrease of 2 kJ mol^{-1}. Experimentally, an inversion barrier of $\Delta G^{‡}$(25 °C) = 111 ± 2 kJ mol^{-1} was obtained for 2MOM-PAH **160**, agreeing with the computed value of 112 kJ mol^{-1}. However, attempts to determine the racemization barrier of **161** and **152** furnished an unexpected chemical reactivity, the nature of which could not be elucidated through subsequent experiments. Nonetheless, one notable entry still contained non-racemized (R_a,R_a,R_a)-**161** after heating the enantiomer at 80 °C overnight – indirectly confirming the effectiveness of the substitution pattern in regard to the monkey saddle's conformational stability.

Overall, the proposed strategy remains a compelling approach. The instability of **161** and **152** was likely caused by the general reactivity of hydroxy groups and the lability of the MOM protecting groups, respectively. To test this hypothesis, a more robust protecting group, namely methyl, was briefly explored. Yet, this approach was not pursued due to the poor solubility of the respective OMe-substituted monkey saddle. Considering these findings, the introduction of simple alkyl chains may resolve the chemical instability as well as solubility issues. For instance, the commercially available salicylaldehyde **162** could serve as a convenient starting point for synthesizing such a modified monkey saddle (**Scheme 3.28A**). The transformation of **162** into the boronic ester **163** could begin with the protection of the hydroxy group using allyl bromide, followed by a Cope rearrangement.[313] To avoid undesired side reactions, the alkene could then be hydrogenated yielding a propyl chain. Finally, conversion of the hydroxy group to the triflate and a subsequent Miyaura borylation could deliver precursor **163**. Alternatively, the project could benefit from employing phenol derivative **164** (**Scheme 3.28B**). A sequential Friedel-Crafts alkylation and formylation would insert an alkyl chain and an aldehyde in the *ortho* positions relative to the hydroxy group. Afterwards, triflation and a Miyaura borylation could generate the desired boronic ester **165**. Both **163** and **165** represent promising candidates for achieving the goal of a conformationally stable monkey saddle, while also providing functional groups for post-synthetic modifications.

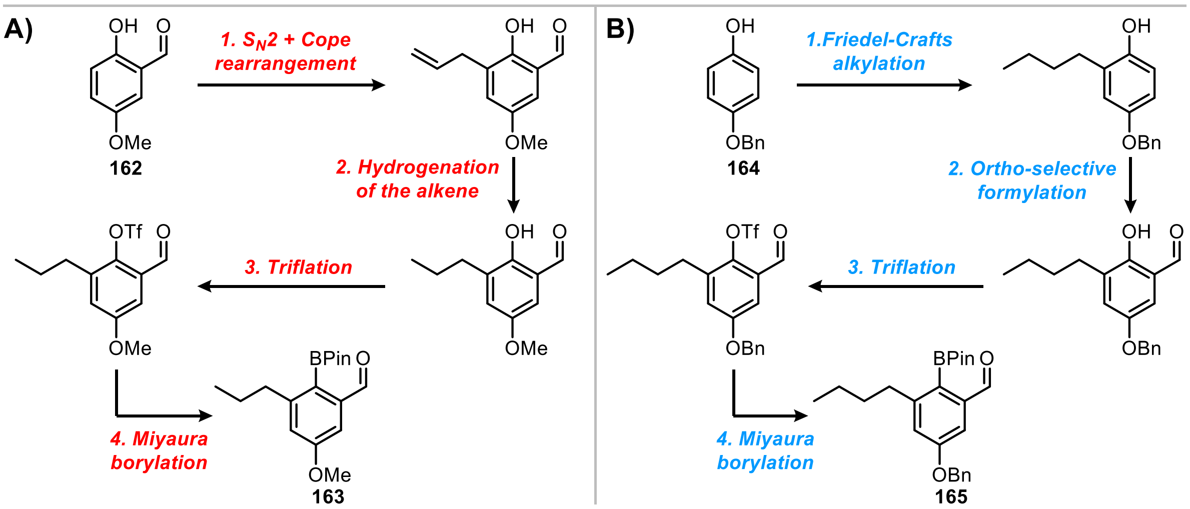

Scheme 3.28: Alternative boronic esters, which could be used to synthesize a conformational more stable as well as functionalized monkey saddle. **A)** Proposed synthesis route toward boronic ester **163**. **B)** Proposed synthesis route toward boronic ester **165**.

3.7 Planar Antiaromatic Cyclooctatetraene Derivative

This chapter was previously published and can be found under: S. F. Ebel, F. Rominger, M. Mastalerz, "Embedding a Planar Antiaromatic Cyclooctatetraene into a Truxene-Derived Polycyclic Aromatic Hydrocarbon", Org. Lett. ***2025****, 27, 7944-7949.*[306]

The preceding chapter 3.6 dealt with the synthesis of monkey saddles featuring six-membered rings with additional OMOM or OH substituents. Though, upon heating, these derivatives underwent unexpected transformations rather than the anticipated racemization, and efforts to elucidate the underlying reactivity remained unfruitful. In contrast, the inversion barrier of 2MOM-PAH **160** – isolated as the second major product alongside MOM-MS **161** – was determined without difficulties. Besides, **160** proved generally more stable than **161**; e.g., a solution of **160** in deuterated chloroform remained unchanged for at least one day, while **161** displayed new signals within minutes. To better understand the chemical behavior of **161** and **152** under thermal conditions, this chapter will explore the deprotection of **160** and whether the resulting hydroxy-substituted derivative also exhibits an unanticipated reactivity.

Synthesis of a Planar Cyclooctatetraene Derivative

The MOM groups of **160** were cleaved by treating a THF solution with 6 M hydrochloric acid at 60 °C (**Scheme 3.29**). During the three-hour reaction time, product **166** precipitated as a red solid and was obtained in 60% yield after an aqueous work-up and flash column chromatographic purification.

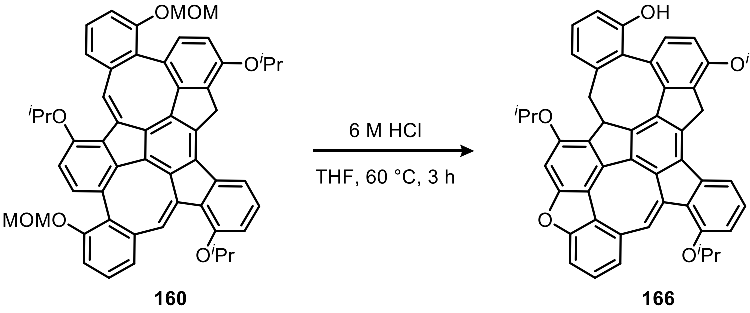

160

166
60%

Scheme 3.29: Deprotection of **160** using hydrochloric acid, which resulted in the generation of compound **166**.

Subsequent high-resolution MALDI-TOF mass spectrometry supported successful deprotection of **160** with a mass-to-charge ratio of m/z 720.2880 (calcd. for $(C_{50}H_{40}O_5)^+$: 720.2870), but ^1H NMR studies indicated a more complex structural outcome (**Figure 3.35A**, **B**). For example, the starting material shows two characteristic singlets at δ = 8.71 and 8.23 ppm, corresponding to the chemically inequivalent protons of the two eight-membered rings, whereas the deprotected species exhibits only one singlet at δ = 8.44 ppm. Yet, in place of the missing proton, a CH_2 group appeared at δ = 3.46 and 2.94 ppm, which couples to a CH unit at δ = 3.41 ppm, as confirmed by ^1H-^1H COSY analysis. In the aromatic region of **166**, proton H^e emerged as a singlet at δ = 6.70 ppm, and an overall integration reveals the lack of one aromatic proton. These spectroscopic changes suggest the formation of a dibenzofuran unit, thereby eliminating the coupling partner of H^e, and the hydrogenation of one of the COT's double bonds. This modification still leaves four possible isomers, as there are two positions in **160** for both the generation of the dibenzofuran unit and the hydrogenation of the double bond (*cf.* **Figure 3.35D**). A distinct coupling between H^e and C^d in the ^1H-^{13}C HMBC spectrum, however, identifies **166** as the sole product of this reaction (**Figure 3.35C**).

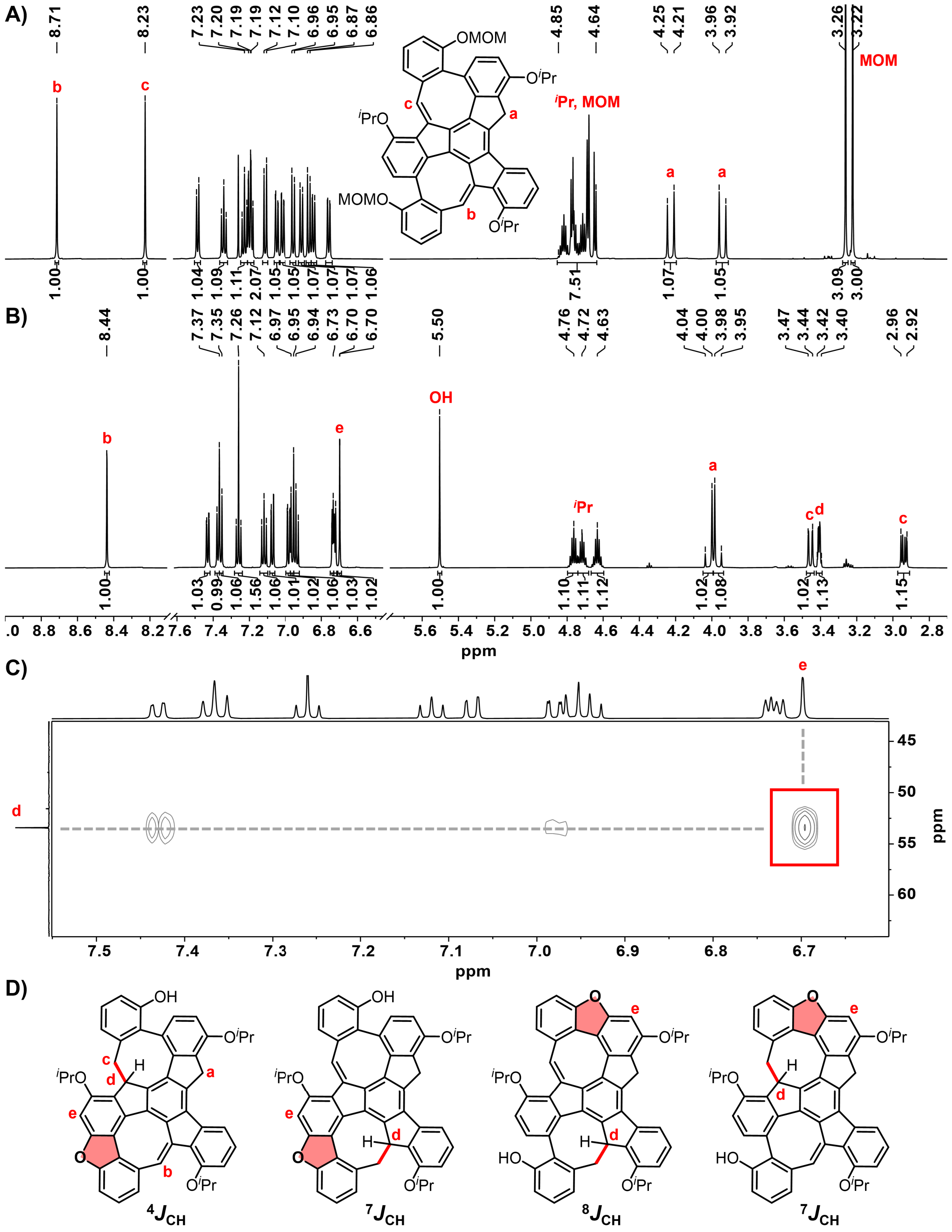

Figure 3.35: ^1H NMR spectra (600 MHz, $CDCl_3$) of **A)** precursor **160** and **B)** product **166** with assignment of designated protons. **C)** ^1H-^{13}C HMBC spectrum (600 MHz, $CDCl_3$) of **166** with emphasis on the coupling between H^e and C^d. **D)** Potential products, which could have formed during the deprotection of **160**. The coupling between H^e and C^d in the ^1H-^{13}C HMBC spectrum eliminates three of these structures and leaves the first one as the sole product of this deprotection reaction. The figures **A**-**C)** were adapted from reference 306 with kind permission from the American Chemical Society and Copyright Clearance Center.

X-Ray Structure Analysis

Suitable single crystals of **166** were obtained by layer-by-layer diffusion of toluene into a saturated DMSO solution, unambiguously confirming its structure. Compound **166** crystallized in the space group *C2/c* with 32 molecules per unit cell, comprising a racemic mixture of (*R*)- and (*S*)-enantiomers. The generation of the dibenzofuran unit thereby enforced a planar conformation of the neighboring cyclooctatetraene, while the double bond of the other COT unit was indeed hydrogenated during the deprotection reaction (**Figure 3.36A**). Bond length analysis of the planar COT showed that bonds shared with the adjacent six-membered rings measured 1.39-1.40 Å, which is consistent with benzene rings.[314-315] The double bond between the pentagon and the methine unit exhibited a slightly elongated length of 1.38 Å, suggesting expansion of the conjugated π-system. The longest bonds (1.48-1.49 Å) annulated to the five-membered rings correspond to typical C_{sp2}-C_{sp2} single bonds (1.48 Å).[315]

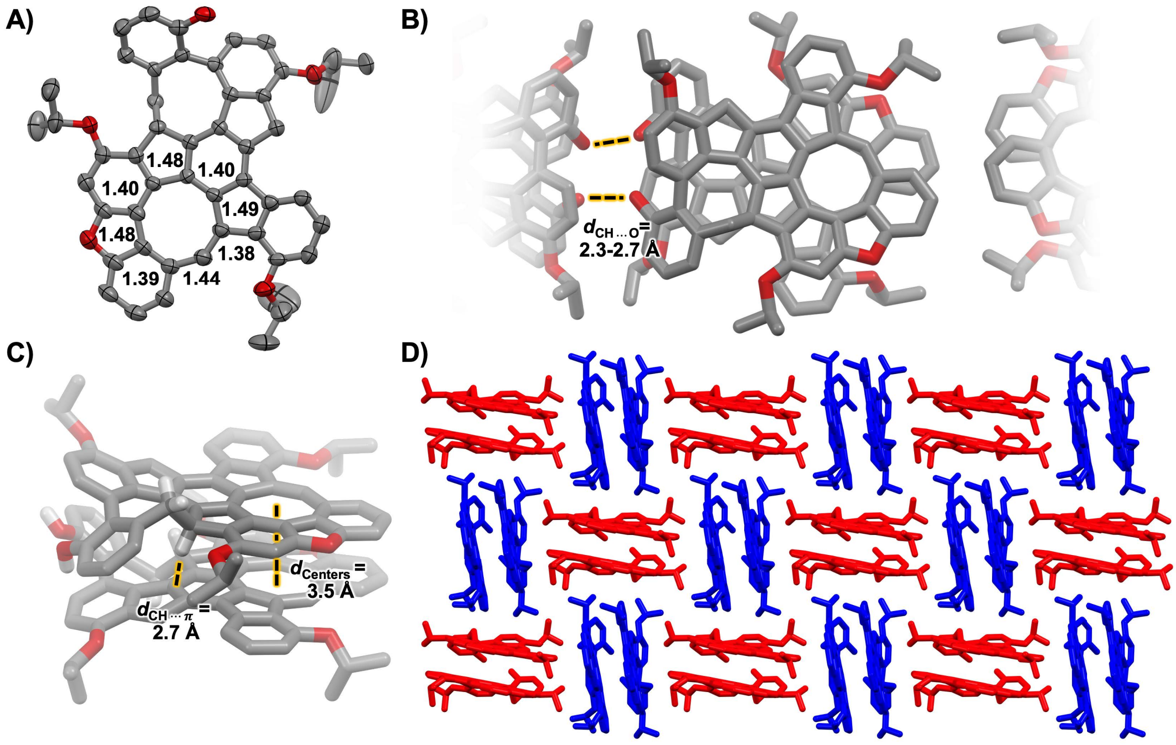

Figure 3.36: Single crystal structure of **166** (CCDC 2456925).[306] Hydrogens were omitted for clarity. Gray = carbon, red = oxygen, white = hydrogen. **A)** (*R*)-**166** as ORTEP drawing with 50% probability of ellipsoids. The bond lengths of the planar COT are given in Å. **B)** Stacking of (*S*)-enantiomers forming a homochiral line with visualization of the interactions between the OH groups. **C)** Dimeric unit consisting of two (*S*)-**166** with visualization of an intermolecular interaction and distance between the COT-centers. **D)** Packing of **166** with view along the crystallographic *c*-axis. The (*R*)-enantiomer was colored in blue and the (*S*)-enantiomer in red. The figure was adapted from reference 306 with kind permission from the American Chemical Society and Copyright Clearance Center.

In terms of packing, **166** formed homochiral dimers in which the dibenzofuran units arranged themselves on opposite sides (**Figure 3.36C**). The planar octagons, on the other hand, stacked directly on top of one another, with the centers being 3.5 Å apart. These dimers assembled into homochiral chains, where the hydroxy groups faced each other and engaged in hydrogen bonds with distances of $d_{CH\cdots O}$ = 2.3-2.7 Å (**Figure 3.36B**). Along the crystallographic *c*-axis, the dimers of the (*S*)-enantiomer aligned horizontally and were surrounded by vertically aligned dimers of the (*R*)-enantiomer. This resulted in a chessboard-like packing (**Figure 3.36D**).

Optoelectronic and Chiral Properties

Unlike the characteristic yellow coloration usually observed for monkey saddles[184] or the OMOM-substituted PAH series **159**-**161**, compound **166** displays an intensive red color (**Figure 3.37A**). This change is attributed to the planarization of the octagon, which effectively extends the conjugated system relative to its precursor **160**. As a result, its UV/vis spectrum discloses a significant bathochromic shift of the lowest energy absorption band from λ = 374 nm in **160** to λ = 556 nm in **166**.

Cyclic voltammetry analysis of **166** revealed a reversible reduction at $E_{\mathrm{red},1}$ = −1.93 V and two irreversible oxidations at $E_{\mathrm{ox},1}$ = +0.49 V and $E_{\mathrm{ox},2}$ = +0.98 V (**Figure 3.37B**). Furthermore, differential pulse voltammetry (DPV) identified two more oxidation processes at $E_{\mathrm{ox},3}$ = +1.13 V and $E_{\mathrm{ox},4}$ = +1.18 V. According to these redox features, **166** has an electrochemical band gap of $E_{\mathrm{CV,gap}}$ = 2.4 eV, which is around 0.3 eV lower than that of the curved OMOM-series **159**-**161**. This trend is also consistent with the optical band gap ($E_{\mathrm{opt,gap}}$ = 2.16 eV for **166** vs. $E_{\mathrm{opt,gap}}$ = 2.66 eV for **160**) and the HOMO-LUMO gap calculated at the B3LYP/6-311G* level of theory ($E_{\mathrm{DFT,gap}}$ = 2.91 eV for **166** vs. $E_{\mathrm{DFT,gap}}$ = 3.25 eV for **160**).

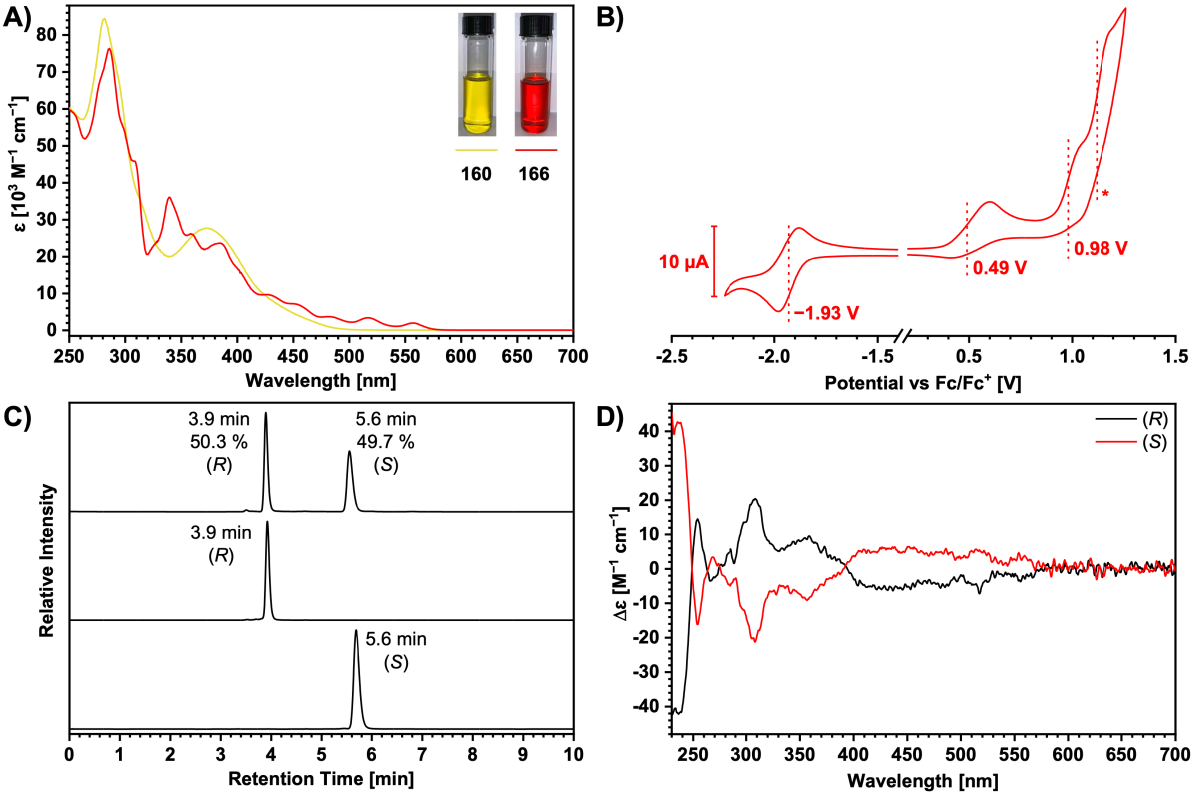

Figure 3.37: A) Comparison of UV/vis absorption spectra of **160** (yellow) and **166** (red). **B)** Cyclic voltammogram of **166** (CH_2Cl_2, 0.1 M NBu_4PF_6, scan rate: 100 mV s^{-1}, working electrode: Glassy carbon, counter electrode: Pt, pseudo-reference electrode: Ag/Ag$^+$) vs. ferrocene as internal reference. The asterisk (*) marks an oxidation at the edge of the solvent window, which is not resolved in the CV. However, DPV of **166** revealed to two more oxidations at +1.13 V and +1.18 V. **C)** Analytical chromatograms of **166** (IE column, CH_2Cl_2, 1.0 mL min^{-1}, 30 °C, 270 nm) with assignment of the (*R*)- and (*S*)-enantiomer to the corresponding fraction. **D)** CD spectra of **166** (CH_2Cl_2, 20 °C).

Hydrogenation of the double bonds introduced a stereocenter in **166**, yielding a racemic mixture of (*R*)- and (*S*)-enantiomers. Their separation was readily manageable by chiral HPLC using a Chiralpak IE column with dichloromethane as mobile phase (**Figure 3.37C**). CD spectroscopy of the isolated fractions showed a positive Cotton effect for the (S)-enantiomer, but since **166** contains only one stereocenter as sole chiral element in the structure, the single enantiomers exhibited a low molar circular dichroism and correspondingly an even smaller absorption dissymmetry factor (g_{abs}) on the order of 10^{-5} (**Figure 3.37D**).

Investigations of the COT's Antiaromatic Character

To study the potential antiaromatic character of the planar eight-membered ring in **166**, NICS values[208] and ACID plots[210] were computed at the HF/6-31+G(d)//B3LYP/6-311G(d,p) level of theory and compared to its precursor **160**. Consistent with previous observations for monkey saddle type structures,[184] **160** features aromatic benzene rings with NICS(1)$_{\text{av}}$ values ranging from −10.5 ppm to −8.5 ppm, while its pentagons and octagons show near-zero NICS(1)$_{\text{av}}$ values (−1.9 to 1.8 ppm), indicative for a nonaromatic character (**Figure 3.38A**). The ACID plot corroborated this conclusion by illustrating diatropic ring currents localized within the benzene units. Consequently, the five- and eight-membered rings are excluded from the conjugated system (**Figure 3.38B**).

For compound **166**, the NICS values imply that the benzene rings as well as the furan unit contribute to the aromatic system (NICS(1)$_{\text{av}}$ = −10.3 ppm to −6.5 ppm) (**Figure 3.38E**). The pentagons within the truxene core can be considered nonaromatic, as the NICS(1)$_{\text{av}}$ values are again close to zero (−2.4 to −1.2 ppm). Finally, a positive NICS(1)$_{\text{av}}$ value of +7.4 ppm revealed the antiaromatic character of the planarized cyclooctatetraene unit. The ACID plot supports this finding by displaying a paratropic ring current in the planar octagon, which facilitates π-conjugation between the dibenzofuran moiety and the central benzene ring, thereby extending the overall conjugated system compared to **160** (**Figure 3.38F**).

Since the planar COT in **166** contains a methine proton, its chemical environment is expected to be influenced by the ring's antiaromatic character. Specifically, the predicted paratropic ring current should induce a shielding effect, which in turn should lead to an upfield shift of the proton's signal in ^{1}H NMR experiments. Regarding other reports on the magnetic antiaromaticity of planar COTs,[202, 316-317] e.g., by Nishinaga and coworkers, the authors observed an experimental upfield shift of approximately $\Delta\delta = -1.5$ ppm for the olefinic protons of a planar COT monoannulated with dithieno[3,4-*b*:3',4'-*d*]thiophene.[202] However, in the case of **166**, an upfield shift of merely $\Delta\delta = -0.27$ ppm was detected.

To assess whether the proposed antiaromaticity of the planar COT should have a more pronounced impact, the ^{1}H NMR chemical shifts of **160** and **166** were computed at the B3LYP/IGLO-II,CPCM($CHCl_3$)//PBEh-3c level of theory. The calculations accurately reproduced the distinct chemical shifts of **160**'s COT protons (**Figure 3.38C**). Yet for compound **166**, the computed shifts of the methine proton surprisingly exhibit a marginal downfield shift ($\Delta\delta = +0.02$ ppm) despite the simulated paratropic ring current (**Figure 3.38G**). When considering this proton's proximity to the oxygen of the adjacent isopropoxy group, this outcome becomes more comprehensible as the two atoms probably form an intramolecular hydrogen bond, which deshields the proton. This kind of hydrogen bonds are also apparent in precursor **160**, whose DFT-optimized structures features distances of 2.2 Å and 2.3 Å between the COT protons and the nearest oxygens (*cf.* **Figure 3.38A**). This slight variation in distance already provides a notable difference in the chemical shifts of $\Delta\delta = 0.48$ ppm experimentally and $\Delta\delta = 0.47$ ppm theoretically. In compound **166**, the planarization of the COT reduced this distance to 2.0 Å in the calculated structure (2.1 Å in the X-ray structure), indicating a stronger hydrogen bonding and conversely a more deshielded proton (*cf.* **Figure 3.38E**). This assumption was verified by recalculating the chemical shifts of **160** and **166** with one isopropoxy group replaced with a hydrogen atom. In the absence of the oxygen atom, the respective COT proton in **160** experienced an upfield shift of $\Delta\delta = -0.86$ ppm, while the proton of **166** was shifted upfield by $\Delta\delta = -1.57$ ppm. According to this finding, the COT proton in **166** is exposed to two opposing effects, namely deshielding because of an intramolecular hydrogen bond and shielding due to the antiaromatic character of the planar COT, ultimately resulting in a relatively small experimental shift, from $\delta = 8.71$ ppm to $\delta = 8.44$ ppm.

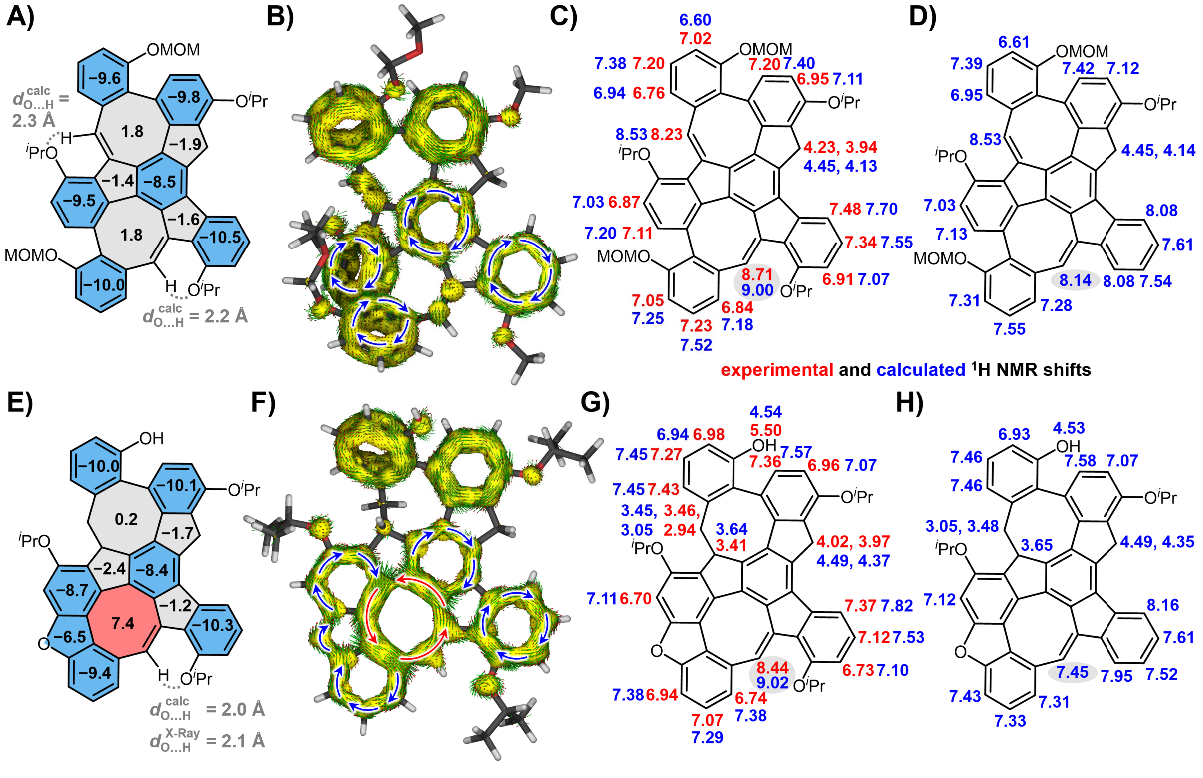

Figure 3.38: A) NICS(1)$_{av}$ values of **160**. **B)** ACID plot (isovalue: 0.035) of **160**. **C)** Experimental and calculated ^{1}H NMR shifts of **160**. **D)** Calculated ^{1}H NMR shifts of **160**, with one O^{i}Pr group replaced by a hydrogen atom. **E)** NICS(1)$_{av}$ values of **166**. **F)** ACID plot (isovalue: 0.035) of **166**. **G)** Experimental and calculated ^{1}H NMR shifts of **166**. **H)** Calculated ^{1}H NMR shifts of **166**, with one O^{i}Pr group replaced by a hydrogen atom. NICS values and ACID plots were calculated at the HF/6-31+G(d)//B3LYP/6-311G(d,p) level of theory. For a better visualization, aromatic rings were highlighted in blue, non-aromatic in grey and the antiaromatic COT ring in red. In the ACID plots, diatropic ring currents were indicated with blue arrows, paratropic with red ones. ^{1}H NMR chemical shifts were calculated at the B3YLP/IGLO-II,CPCM(CHCl$_3$)//PBEh-3c level of theory. The figure was reproduced from reference 306 with kind permission from the American Chemical Society and Copyright Clearance Center.

Mechanistic Studies

To gain a deeper insight into the formation of **166**, deuteration experiments were conducted, identifying the positions of deuterium incorporation and consequently, the reactive sites involved in the mechanism. Initially, **160** was deprotected using deuterium chloride (36% in D_2O) in THF-d_8 and undeuterated THF, respectively (**Scheme 3.30A**). Both attempts delivered similar ^{1}H NMR spectra, in which the integral values of the former double bond (H^a and H^b) and the dibenzofuran unit (H^c) were reduced from one to around 0.5

(**Figure 3.39A**). This observation is a first indication for a partial deuteration of these positions. Further analysis by ^{2}H NMR spectroscopy disclosed two doublets at δ = 3.47 and 1.73 ppm, likely belonging to the coupling pair D^a and D^b, as well as a broad singlet at δ = 6.98 ppm, attributed to the dibenzofuran proton D^c (**Figure 3.39B**). Finally, MALDI-TOF MS measurements confirmed the inclusion of three deuterium atoms with a mass-to-charge ratio of *m/z* 723.215 (calcd. for $(C_{50}H_{37}D_3O_5)^+$: 723.306) (**Figure 3.39C**).

In a third experiment, **160** was stirred in a mixture of hydrochloric acid (6 M in H_2O) and THF-d_8 at 60 °C for 1.5 hours to undoubtedly rule out any involvement of the THF in the generation of **166-d_3** (**Scheme 3.30A**). ^{1}H NMR studies of the reaction outcome showed integral values of one for each of H$^{a\text{-}c}$, while MALDI-TOF mass spectrometry recorded a peak at *m/z* 720.199 (calcd. for $(C_{50}H_{40}O_5)^+$: 720.288). Hence, both methods affirmed the isolation of the undeuterated compound **166** and, by extension, exclude THF as a participant in the formation of **166-d_3**. All findings considered, the acid must play a key role in the hydrogenation of the double bond. Moreover, the incorporation of deuterium in the dibenzofuran unit (D^c) suggests that this position also takes part in the mechanism.

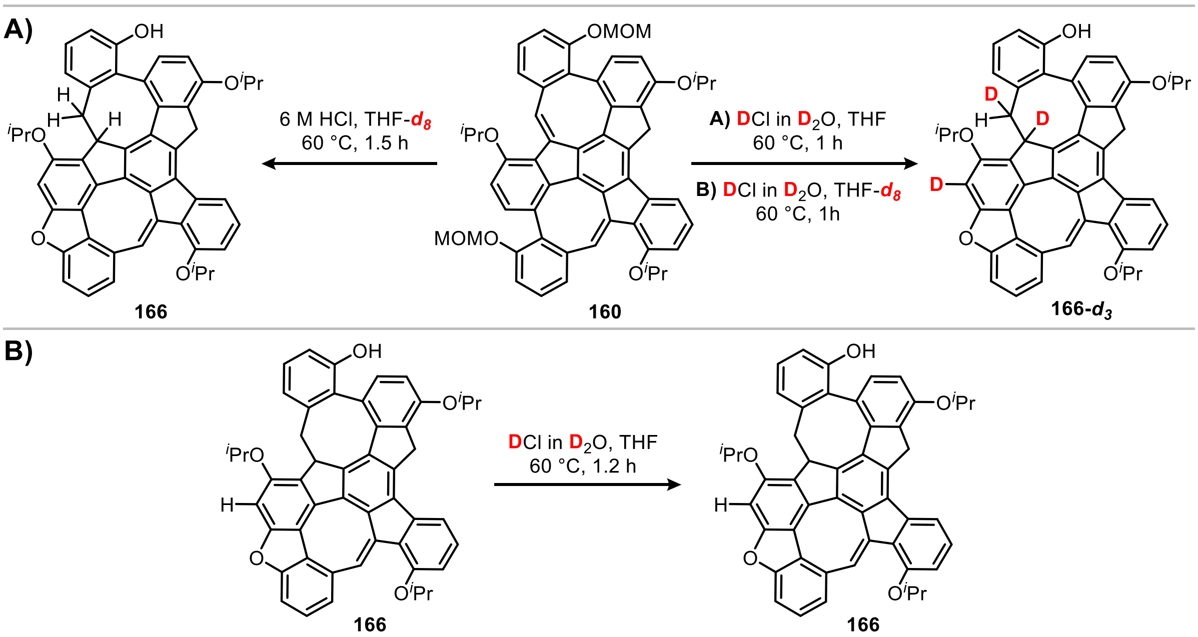

Scheme 3.30: A) Generation of **166** and **166-d_3** using deuterium chloride, deuterated THF or both. **B)** Hydrogen-deuterium exchange experiment of **166**. No hydrogen was exchanged with deuterium after stirring **166** in deuterium chloride for 1.2 hours.

Lastly, to check whether one of the deuterium atoms D$^{a\text{-}c}$ originated from a simple hydrogen-deuterium exchange, **166** was exposed to a mixture of DCl (36% in D_2O) in THF at 60 °C for 1.2 hours (**Scheme 3.30B**). ^{1}H NMR analysis of the crude material revealed the absence of deuterium, since the integral values of all proton signals matched those expected for **166**. Besides, MALDI-TOF mass spectrometry only detected a peak at *m/z* 720.286 (calcd. for $(C_{50}H_{40}O_5)^+$: 720.288), which corroborates the lack of H/D exchange under the conditions employed.

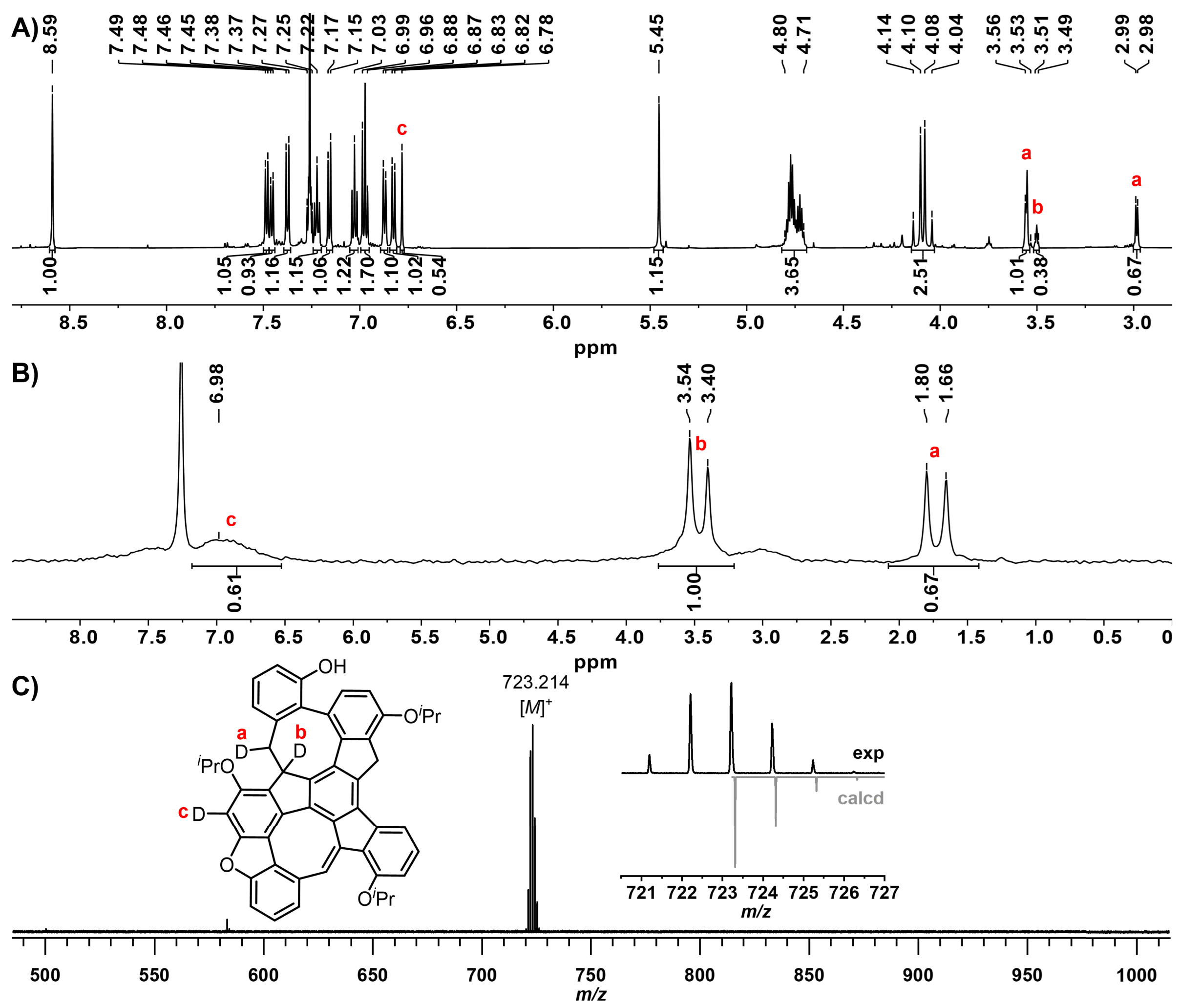

Figure 3.39: A) ^{1}H NMR spectrum (600 MHz, CDCl$_3$) of **166-*d*$_3$**, showing decreased integral values for H$^{a\text{-}c}$. The reaction was performed using DCl (36% in D$_2$O) and THF-*d*$_8$. **B)** ^{2}H NMR spectrum (92 MHz, CHCl$_3$/CDCl$_3$) of **166-*d*$_3$**. **C)** MALDI-TOF mass spectrum of **166-*d*$_3$**. Since positions a-c contain deuterium and hydrogen in roughly a 1:1 ratio, the species with one, two, and three deuterium atoms overlap in the mass spectrum, causing the isotope pattern to differ from the calculated one. This figure was reproduced from the supporting information of reference 306.

Overall, there are several possible pathways to convert **160** into **166**. Assuming that the cleavage of the MOM groups initially resulted in the expected deprotected species **167**, the next step probably consists of the addition of a proton (**Scheme 3.31**). Three positions are plausible for this electrophilic attack, including the O^{i}Pr-substituted benzene ring and the two double bonds in **167**. The contributing structures of intermediates **168** and **169** allow positioning of the positive charge at the site susceptible to the subsequent nucleophilic attack by the oxygen atom, thus promoting the furan ring closure. Additionally, both compounds align with the prior deuterium labeling experiments, whereas intermediate **170** does not agree with the experimental results nor mechanistic considerations.

Subsequent structure optimizations of **168** and **169**, performed at the PW6B95-D3(BJ)/def2-QZVPP+SMD(THF)//PBEh-3c level of theory, showed that **169** is energetically favored over **168** by 84 kJ mol^{-1}. In the next step, the furan ring was likely constructed, leading to the isomers **171** or **172**. However, DFT calculations failed to locate stable minima for either structure, and only the respective deprotonated species, **173** and **174**, were successfully optimized. Among these, **174** was found to be more stable than **173** by 65 kJ mol^{-1}. Hence, calculations indicate that the reaction pathway probably proceeds by protonation of the double bond rather than the aromatic ring. At last, a hydride shift in **174** could furnish the final product **166**.

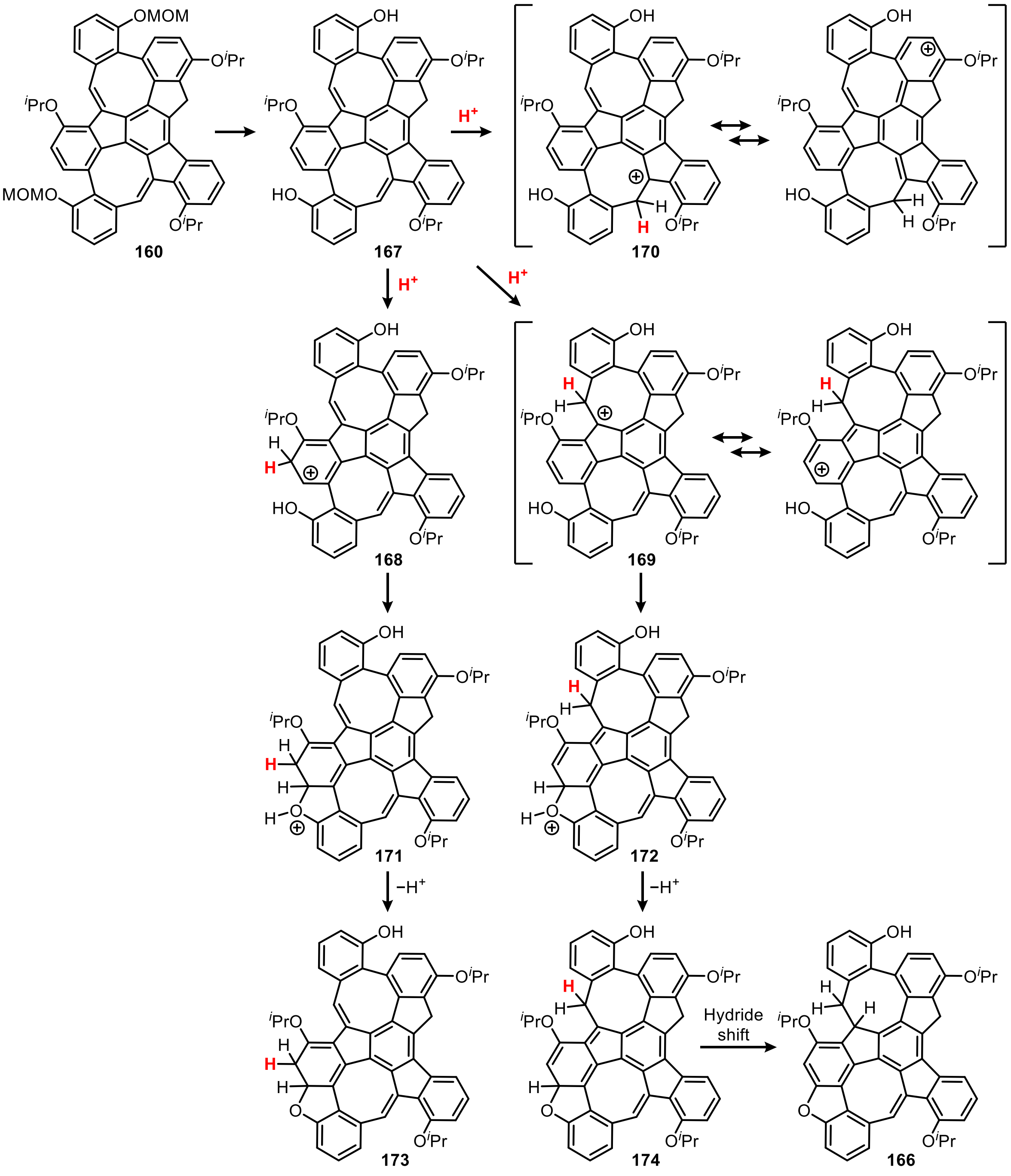

Scheme 3.31: Mechanistic proposal of the formation of **166**. This scheme was adapted from the supporting information of reference 306.

Summary

This chapter presented a detailed examination of **160**'s deprotection, which unexpectedly provided the planar cyclooctatetraene derivative **166** instead of the hydroxy-functionalized analog **167**. Product **166** was generated in 60% yield through formation of a dibenzofuran moiety and hydrogenation of the double bond in the second COT unit, ultimately giving a racemic mixture of (*R*)-**166** and (*S*)-**166**. The structure was unambiguously confirmed by single-crystal X-ray diffraction analysis. Owing to the planarized octagon, **166** discloses a larger conjugated system compared to its precursor **160**. Accordingly, its UV/vis absorption spectrum showed a bathochromic shift of 182 nm, while cyclic voltammetry recorded a reduction in the electrochemical band gap by around 0.3 eV relative to the OMOM-substituted PAH series **159**-**161**.

Subsequent NICS and ACID calculations suggested that the planar octagon in **166** exhibits an antiaromatic character, yet ^{1}H NMR studies detected only an upfield shift of $\Delta\delta = -0.27$ ppm for the proton attached to the planar COT ring. To assess whether this experimental observation is still in agreement with the proposed antiaromaticity, the ^{1}H NMR chemical shifts were calculated for the compounds **160** and **166**. Surprisingly, the computed data predicted a marginal downfield shift ($\Delta\delta = +0.02$ ppm) of the COT proton upon planarization of the eight-membered ring. Further investigations revealed that this apparent discrepancy stems from a hydrogen bond between the COT proton and the adjacent O^{i}Pr-group, which deshields the proton and thus masks the shielding effect of the paratropic ring current.

Lastly, the formation mechanism of **166** was further examined through deuterium labeling experiments, complemented with computational studies. It was proposed that the mechanism starts with a protonation of the double bond in the deprotected intermediate **167**. Following, the O^{i}Pr-substituted benzene ring undergoes a nucleophilic attack of the oxygen, constructing the furan ring. A deprotonation and final hydride shift could then deliver the product **166**.

The original aim of deprotecting **160** was to explore whether the hydroxy-functionalized species **167** would display an unexpected reactivity. While this was indeed the case, the extent to which this behavior is transferable to the unidentified transformations of monkey saddles **161** and **152** remains unclear. Nevertheless, the findings provided in this chapter strongly indicate that the presence of highly reactive OH groups in the corresponding positions is a key factor contributing to the observed chemical instability.

4 Summary and Outlook

The research presented in this dissertation addressed two primary objectives: (1) the synthesis of shape-persistent organic cage compounds by alkyne metathesis and (2) the development of a conformationally stable and functionalized monkey saddle.

Investigations related to the first topic necessitated the preparation of a highly active alkyne metathesis catalyst based on synthetic procedures known to the literature (**Scheme 4.1A**). Specifically, molybdenum(V) chloride (**83**) was converted into precatalyst **8** over six steps, and the tris(2-hydroxylbenzyl)methane-based ligand **11** was generated in eight steps starting from 2-isopropylphenol (**87**). The route toward **11** was significantly optimized by changing the protecting group from benzyl to methyl. This modification allowed the execution of each step on a gram scale without any substantial yield losses.

For the initial target cage **74**, the triptycene scaffold was functionalized with four propyne and two hexyl groups, giving precursor **75** in eight steps from hexabromotriptycene **95** (**Scheme 4.1B**). The catalyst system **8/11** was then tested on the trimerization of intermediate **101** and successfully enabled the synthesis of the two hexadehydro[12]annulene isomers **103a** and **103b**, which represent structural subunits of cage **74**. However, all subsequent alkyne metathesis attempts with precursor **75** consistently led to undesired polymerization. Since the formation of **74** requires reversible reaction conditions to correct misaligned subunits, scrambling experiments were performed using the partially deuterated analogs **101-*d*$_8$** and **103-*d*$_{24}$**. This study revealed that the catalyst **8/11** does not promote reversible subunit closure, effectively preventing the assembly of cage **74**. Nevertheless, compound **103b**, or more precisely its hydroxy-functionalized derivative **104**, remains a promising building block for alternative cages, such as those constructed by boronic acid condensations.

Another potential building block was developed from CH-monkey saddle **47**, whose framework was substituted with three propyne moieties in six steps starting from trishexyloxytruxene **114** (**Scheme 4.1C**). The resulting precursor **116** was obtained as a racemic mixture of (R_a,R_a,R_a)- and (S_a,S_a,S_a)-enantiomers, which proved conformationally unstable even at room temperature, as confirmed by kinetic CD measurements. In collaboration with the Fürstner group at the Max-Planck-Institut für Kohlenforschung, five different alkyne metathesis catalysts were screened for the transformation of **116** into the target cage **76**. Though, similar to triptycene precursor **75**, oligomerization of **116** occurred instead of the desired tetrahedral cage architecture. To gain a deeper understanding of this outcome, DFT calculations were performed on the structures of both the enantiopure and enantiomixed cage isomers, indicating that the latter are thermodynamically disfavored. In addition, cage closing would suppress further racemization of the monkey saddle core, thereby reducing the entropic driving force. Consequently, the success of this reaction likely depends on the use of a single, conformationally stable monkey saddle enantiomer.

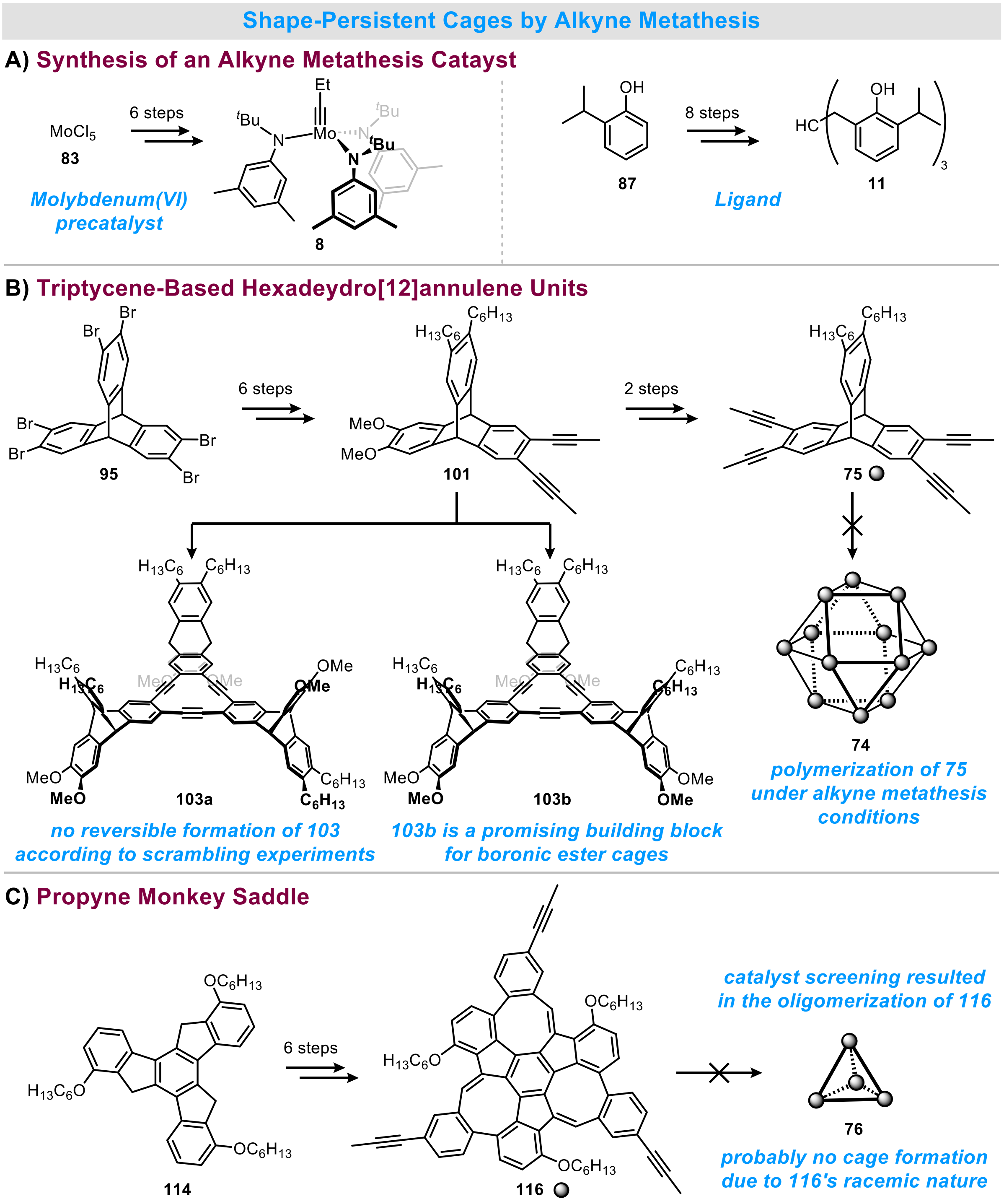

Scheme 4.1: Summary of projects performed on the topic of alkyne metathesis. **A)** Synthesis of an alkyne metathesis catalyst. **B)** Synthesis of the triptycene-based building block **75** to generate cage **74** by alkyne metathesis. However, scrambling experiments with the cage subunit **103** showed that the hexadeydro[12]annulenes are not formed reversibly under the conditions employed. **C)** Synthesis of propyne monkey saddle **116** for the generation of the tetrahedral cage **76**. This alkyne metathesis probably failed owing to the racemic nature of **116**.

This conclusion led to the second major objective of this thesis: the development of a conformationally stable, functionalized monkey saddle. Considering prior research on monkey saddles, the chromene monkey saddle was found to be an inversion-stable candidate; yet its core still required functionalization to enable further synthetic elaborations. In addition, the original route toward monkey saddles contained a key limitation: the isolation, or more specifically, the purification of tribromotruxene **44**. To address this issue, the hexyloxy moieties in **44** were replaced by isopropoxy groups. This modification facilitated a more efficient and sustainable purification of the corresponding bromide species **121**, ultimately eliminating the previous synthetic constraint. Using this improved route, chromene monkey saddle **125** was prepared in six steps from trishydroxytruxene **119** (**Scheme 4.2A**). Afterwards, the introduction of new groups was investigated through post- and pre-functionalization strategies, with the latter providing the nitro-substituted aza monkey saddle **131** (**Scheme 4.2A**). However, due to substantial material loss during the condensation step as well as lack of optimization prospects, this project was not pursued.

In contrast, several CH-monkey saddle derivatives have been synthesized, all of which completely racemize within one hour at elevated temperatures (up to 90 °C). To identify substitution patterns capable of preventing racemization, 14 different computational methods were first benchmarked to ensure maximum consistency between theoretical predictions and available experimental data. Afterwards, calculations on monkey saddle **140**, whose eight-membered rings each bear a methyl group, were carried out, suggesting an increase in the inversion barrier to the threshold of conformational stability. Accordingly, two synthetic routes toward **140** were explored (**Scheme 4.2B**). The first approach involved condensation of methyl ketones onto the truxene core, but this step failed owing to either a lack of conversion or decomposition of the starting material. In the second route, direct methylation of CH-monkey saddle **141** was attempted. Yet, instead of deprotonation, *n*-butyllithium acted as a nucleophile toward the COT units, producing compound **150** upon aqueous work-up (**Scheme 4.2B**). Subsequent attempts to restore the double bonds in **150**'s eight-membered rings by an oxidative dehydrogenation remained unfruitful. Cyclic voltammetry, combined with results from a previous attempt at this reaction, indicated that the starting material would not withstand the strong oxidant and harsh reaction conditions required for the intended conversion.

As an alternative approach, substitution of the monkey saddle's six-membered rings in a modified pattern was proposed (**Scheme 4.2C**). The synthetic realization of the respective hydroxy-functionalized monkey saddle **152** began with a Suzuki-Miyaura cross-coupling between tribromotruxene **121** and boronic ester **155**, which delivered the one-, two-, and three-fold coupled and protodebrominated species. This mixture was then subjected to a base-mediated condensation to give the OMOM-decorated PAH series **159**-**161**. Final cleavage of the MOM groups from **161** provided the target monkey saddle **152**. Experimentally, the racemization barriers of this new series were investigated by kinetic CD measurements. Upon heating MOM-MS **161** and OH-MS **152**, both compounds showed unexpected transformations; the exact nature of which could not be elucidated with additional studies. It is hypothesized that the presence of labile MOM protecting groups and highly reactive hydroxy groups in the corresponding positions contributed to the degradation of the two monkey saddles during these measurements.

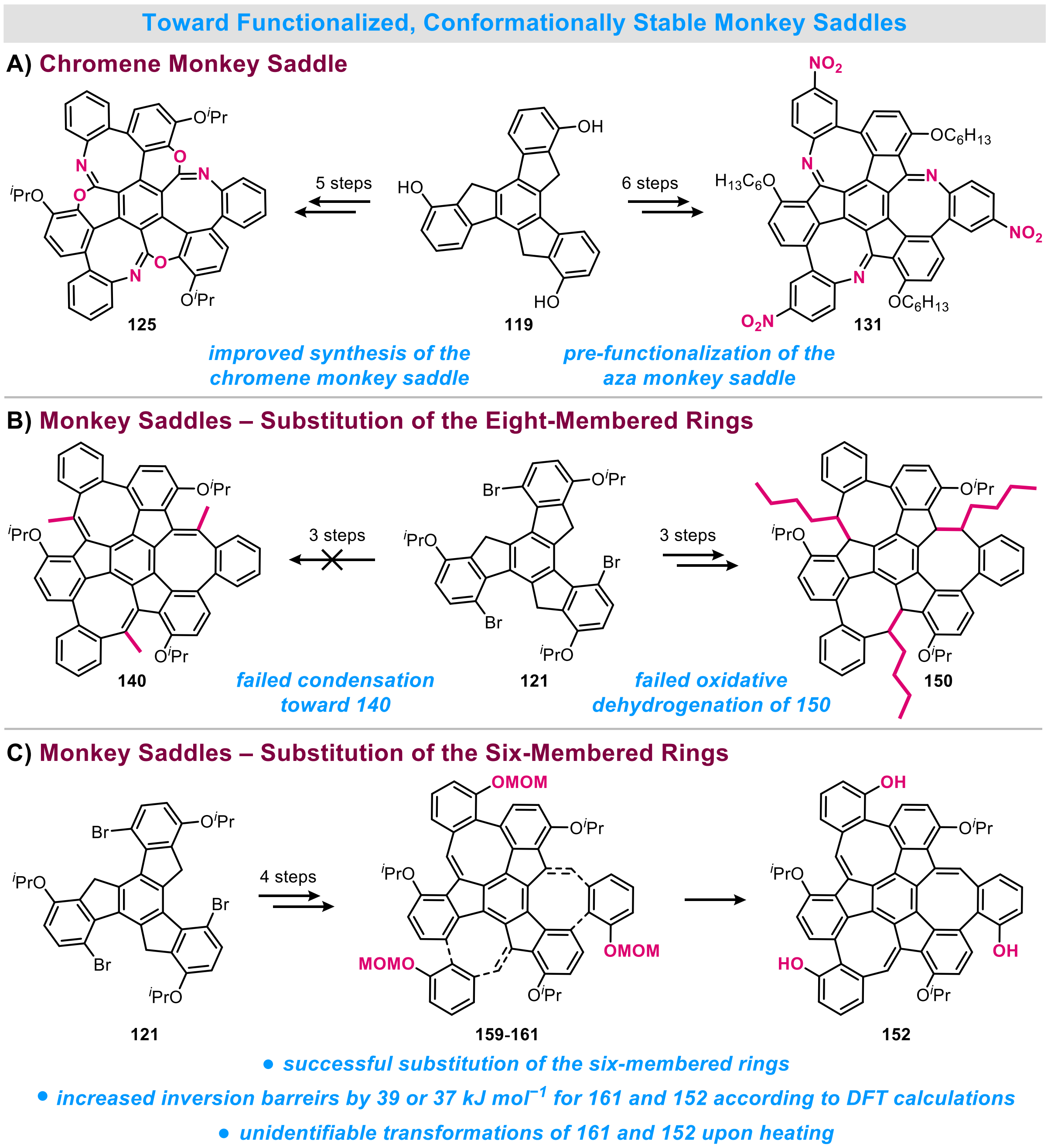

Scheme 4.2: Summary of projects performed on the topic of monkey saddles. **A)** Improved synthesis of the chromene monkey saddle and prefunctionalization of the aza monkey saddle. **B)** Attempts to substitute the eight-membered ring of the monkey saddle. **C)** Substitution of the monkey saddle's six-membered rings to enhance the conformational stability of the framework.

Given the greater overall stability of 2MOM-PAH **160**, it was also deprotected to assess whether the resulting hydroxy-functionalized analog **167** would exhibit unprecedented reactivity. Interestingly, this deprotection reaction generated compound **166** as the sole product (**Scheme 4.3**). The formation of a dibenzofuran moiety thereby forced the adjacent cyclooctatetraene into a planar conformation, while the double bond of the other eight-membered ring was hydrogenated in the process. Single-crystal X-ray analysis unambiguously confirmed the structure of **166**. Because of the octagon's planarization, the conjugated system in **166** experienced an extension, which was reflected in the optoelectronic properties by a red-shifted absorption and a reduced electrochemical band gap compared to **160**. NICS and ACID calculations suggested an antiaromatic character of the planar COT, although the shielding effect of the expected paratropic ring current was partially masked in the ^{1}H NMR spectrum on account of an intramolecular hydrogen bond between the COT proton and the oxygen atom of the neighboring isopropoxy group. Lastly, the formation mechanism of **166** was examined by deuterium labeling experiments and complemented by computational studies.

The outcome of **160**'s deprotection strongly indicates that the instability observed for MOM-MS **161** and OH-MS **152** originates from the presence of the hydroxy groups. Nevertheless, the strategy of substituting the six-membered rings is still a conceptually valuable approach as long as alternative, less reactive groups (e.g., alkyl chains) are introduced in future attempts.

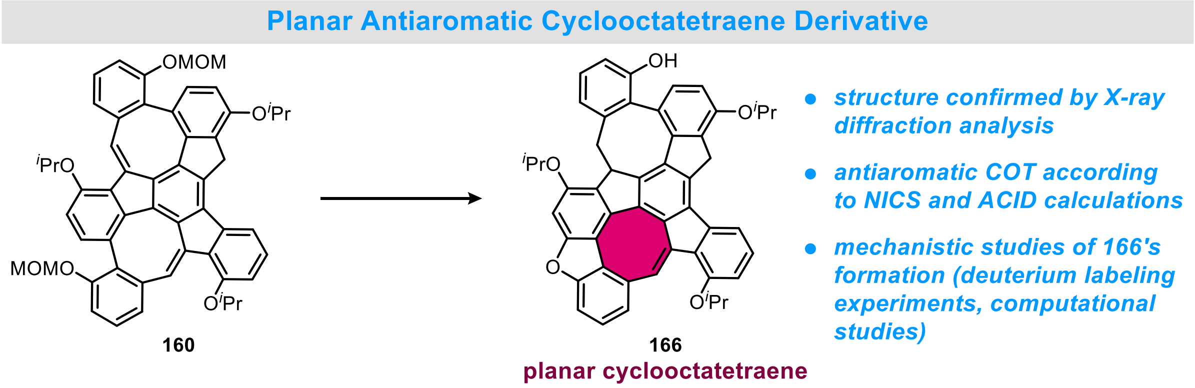

Scheme 4.3: Overview of the deprotection reaction of **160**, yielding the planar cyclooctatetraene derivative **166**.

In summary, the potential of triptycene- and monkey saddle-based building blocks for the preparation of organic cages by alkyne metathesis was investigated, with each approach encountering its own distinct challenges. For the monkey saddle structure, additional modifications were required to achieve conformational stability and thus enable its enantiopure use in the design of complex, chiral architectures. Subsequent studies on this topic provided several promising strategies that merit further explorations in future projects.

5 Experimental Section

5.1 General Remarks

Chemicals were purchased from Honeywell, Sigma-Aldrich, BLDpharm, Deutero, TCI, Acros Organics, VWR Chemicals, Alfa Aesar, Fisher Scientific, Thermo Fisher, Eurisotop, Grüssing, Carl Roth, Carbolution, Merck, or Air Liquide (for detailed information see Appendix 7.2). Hexabromotriptycene **95** and trishydroxytruxene **119** were provided from the introductory organic chemistry practical course based on literature procedures.[177, 241] The truxene derivatives **44** and **55** were synthesized according to literature procedures.[177, 185] If not stated otherwise, chemicals were used without further purification. Dry acetonitrile, toluene, dichloromethane, tetrahydrofuran, and diethyl ether were obtained from an MB SPS-800 system. Dry 1,1-dichloropropane, ethanol, pentane, TCE-d_2, tetrachloromethane, triethylamine, toluene-d_8, and xylene were prepared by storing them over activated molecular sieves (3 Å or 4 Å) for at least 24 h before use. Solvents were degassed either by three freeze-pump-thaw cycles (Et_2O, THF, pentane, toluene) or by bubbling argon through the liquid for at least 30 min (MeCN, CCl_4, H_2O, 2 M K_2CO_3 in H_2O, TCE-d_2). Molecular sieves (3 Å, 4 Å, powdered 5 Å) were activated at 280 °C and $1{\times}10^{-2}$ mbar for 24 h, then they were stored in a Schlenk ampoule under an argon atmosphere before use. Unless noted otherwise, all reactions were performed under standard conditions (25 °C, 1013 mbar). Inert conditions were achieved with standard Schlenk techniques and an argon atmosphere. In the case of moisture-sensitive reactions, all glassware was flame-dried *in vacuo* with a Bunsen burner before use.

Thin layer and flash column chromatography: Thin layer chromatography (TLC) was carried out on fluorescent-labeled silica gel 60 coated aluminum plates from Macherey-Nagel. Spots were visualized under UV light at λ_{ex} = 254 and 366 nm. Flash column chromatography was performed using silica gel 60 (40-63 µm) from Macherey-Nagel GmbH & Co. KG.

High-performance liquid chromatography (HPLC): Preparative HPLC was performed with a Shimadzu LC-20A Prominence recycling HPLC system with a normal-phase column (SiO_2, 5 µm particle size) from Restek at a flow rate of 15 mL min^{-1}. Only HPLC-grade solvents were used as eluents.

Chiral HPLC: Analytical chiral HPLC was conducted using a Shimadzu LC-40 Nexera HPLC system, and semi-preparative HPLC was performed with a Shimadzu LC-20A Prominence recycling HPLC system. Chiral stationary phases included Chiralpak® IB (cellulose tris(3,5-dimethylphenylcarbamate)) and IE (amylose tris(3,5-dichlorophenylcarbamate)) columns from Daicel. Only HPLC-grade solvents were used as the mobile phase.

Recycling gel permeation chromatography (r-GPC): Recycling GPC was carried out with a Shimadzu CBM-20A communication bus module, DGU-20A3R degassing unit, LC-20AD pump unit, SIL-20AHT autosampler, SPD-M20A diode array detector, CTO-20A column oven, and FRC-10A fraction collector, using HPLC-grade chloroform as the solvent.

Melting point analysis (M.p.): Melting points of solid samples were determined in open glass capillaries using a Büchi Melting Point B-540 or B-565 device.

Nuclear magnetic resonance (NMR) spectroscopy: NMR spectra were recorded with a Bruker Avance III 300 (300 MHz), Bruker Avance DRX 300 (300 MHz), Bruker Fourier 300 (300 MHz), Bruker Avance III 400 (400 MHz), Bruker Avance III 500 (500 MHz), Bruker Avance III 600 (600 MHz), or Bruker Avance Neo 700 (700 MHz). The latter four instruments were exclusively operated by the NMR department of the Institute of Organic Chemistry at Heidelberg University. Chemical shifts (δ) are reported in parts per million (ppm). ^{1}H and ^{13}C NMR spectra were referenced to residual solvent signals ($CDCl_3$: 7.26 / 77.2 ppm; CD_2Cl_2: 5.32 / 53.8 ppm; toluene-d_8: 2.08 / 20.4 ppm; DMSO-d_6: 2.50 / 39.5 ppm).[318] ^{2}H NMR spectra were acquired in $CHCl_3$ with a small amount of $CDCl_3$, added for referencing to the deuterated solvent ($CDCl_3$: 7.26 ppm). ^{19}F NMR spectra were not calibrated. Coupling constants (J) are reported in Hertz (Hz). NMR signal multiplicities are abbreviated as: s = singlet, d = doublet, t = triplet, q = quartet, sept = septet, m = multiplet, dd = doublet of doublets, ddd = doublet of doublets of doublets, and td = triplet of doublets. For literature-unknown compounds, ^{1}H and ^{13}C NMR signals were assigned to the respective atoms with the aid of 2D NMR spectra (^{1}H-^{1}H COSY, ^{1}H-^{1}H NOESY, ^{1}H-^{13}C HSQC, ^{1}H-^{13}C HMBC). If a signal could not be unambiguously assigned to one atom, the potential assignments were separated by a slash; if one signal corresponded to multiple atoms, the assignments were separated by a comma. All ^{13}C NMR spectra were acquired with ^{1}H decoupling.

Infrared spectroscopy (IR): Fourier transform infrared (FT-IR) spectra were recorded with a Bruker Tensor 27 spectrometer equipped with a ZnSe crystal. Absorption bands ($\tilde{\nu}$) are reported in cm^{-1}, with their intensities characterized as: s = strong, m = medium, w = weak, and br = broad.

UV/vis and fluorescence spectroscopy: UV/vis absorption spectra were measured with a Jasco V-730-ST UV/vis spectrometer, and fluorescence emission spectra were recorded with a Jasco FP-8300 fluorescence spectrometer.

Mass Spectrometry (MS): Mass spectra were measured with a Bruker timsTOFfleX, Bruker Autoflex speed MALDI-TOF, or a JEOL AccuTOF GCx instrument. MALDI-MS analyses used DCTB (*trans*-2-[3-(4-*tert*-butylphenyl)-2-methyl-2-propenylidene]malononitrile) as the matrix. All measurements were conducted by the Mass Spectrometry Facility of Heidelberg University under the supervision of Dr. Jürgen H. Gross.

Elemental analysis: Elemental compositions (C, H, N) were determined using a vario MICRO cube device from Elementar. All measurements were performed by the microanalytical laboratory of the chemical institutes of Heidelberg University.

Optical rotation: Optical rotations were measured in dichloromethane at λ = 578 and 546 nm using a Perkin-Elmer 341 polarimeter equipped with a mercury lamp. Specific rotations were calculated according to the Biot equation: $[\alpha]_{\lambda}^{T} = \frac{\alpha \cdot 100}{l \cdot c}$ with T = temperature (°C), λ = wavelength (nm), α = measured rotation (°), l = cuvette path length = 1 dm, and c = concentration (grams/100 mL).

Circular dichroism spectroscopy (CD): CD spectra were recorded with a Jasco J-1500 CD spectrometer.

Cyclic voltammetry (CV): Cyclic voltammetry and differential pulse voltammetry (DPV) were performed with a Metrohm Autolab PGSTAT101 potentiostat with a glassy carbon working electrode, Pt counter electrode and Ag/Ag$^+$ pseudo-reference electrode. Ferrocene/Ferrocenium (Fc/Fc$^+$) was used as an internal standard for calibration. Measurements were conducted in a 0.1 M tetrabutylammonium hexafluorophosphate solution in degassed HPLC-grade solvents and analyte concentrations of 1 mM. Cyclic voltammograms were recorded at a scan rate of 100 mV s^{-1}. Differential pulse voltammograms were recorded with a step size of 0.005 V, modulation amplitude of 0.025 V, modulation time of 0.05 s, and interval time of 0.5 s.

X-ray crystal structure analysis: Single-crystal X-ray diffraction measurements were performed at the X-ray facility of Heidelberg University using either a Bruker APEX-II Quazar diffractometer (MoK$_\alpha$ radiation, λ = 0.71073 Å) or a Stoe Stadivari (CuK$_\alpha$ radiation, λ = 1.54178 Å). Structure solution and refinements were carried out by Dr. Frank Rominger (Institute of Organic Chemistry, Heidelberg University). Intensities were corrected for Lorentz and polarization effects, and empirical scaling and absorption corrections were applied using SADABS[319] or X-Area LANA 2.7.5.0 based on the Laue symmetry of the reciprocal space. Structures were solved with SHELXT-2014 (Sheldrick 2014) or SHELXT-2018/2 (Sheldrick 2015)[320] and refined against F^2 with a Full-matrix least-squares algorithm using the SHELXL-2018/3, SHELXL-2019/1, or SHELXL-2019/2 software.[321] Hydrogen atoms were treated using appropriate riding models.

Software: This thesis was written with Microsoft Word for Mac (version 16.62) and Microsoft Word for Windows 11 (version 2507). Chemical structures were drawn with ChemDraw 22.2.0 (PerkinElmer). NMR spectra were processed and plotted using MestReNova (v14.0.1-23559, Mestrelab Research S.L). Graphs were plotted in OriginPro (OriginLab Corporation). IR spectra were processed with ACD/Spectrus Processor 2017.2 (Advanced Chemistry Development, Inc.). Kinetic data were evaluated with Excel 365 and OriginPro. X-ray structures were analyzed and visualized using Mercury 2023.2.0. References were managed with Endnote 21. The AI tools ChatGPT-4/ChatGPT-5 and Grammarly (free version) were used for minor sentence rephrasing, as well as for grammar, wording, and punctuation review.

Computational Details: DFT and TD-DFT calculations were performed using ORCA (version 5.0.4).[322] Molecular structures were visualized and edited with Chemcraft[323] and Avogadro.[324] Computational resources were provided by the bwForCluster JUSTUS2 at Ulm University within the Baden-Württemberg High Performance Computing program. Support by the state of Baden-Württemberg through bwHPC and the German Research Foundation is gratefully acknowledged.

All structure optimizations and frequency calculations were carried out with the PBEh-3c method.[266-269] Equilibrium structures were confirmed to possess only positive Hessian matrix eigenvalues. Transition structures were optimized using the keyword `OptTS` to obtain a single negative Hessian matrix eigenvalue (one imaginary frequency). The correctness of the located transition structures was verified by visualizing the corresponding imaginary frequency in Chemcraft.

Following structure optimization, single point calculations were performed. Solvent effects were included using the SMD solvation model.[286] The electronic energy from the higher computation level was combined with the thermal correction from the frequency calculations on the lower computation level (PBEh-3c). Enthalpies were calculated at 298.15 K. According to the rigid-rotor-harmonic-oscillator approximation (QRRHO) of Grimme,[325] the enthalpy values were combined with the vibrational entropy terms to obtain the Gibbs free energies.

Inversion barriers of the various monkey saddles were benchmarked using the functionals: PW6B95-D3(BJ),[270] B3LYP-D3(BJ),[271] M06-2X-D3Zero,[272] ωB97x-D4,[273] ωB97X-V,[274] B97M-D4,[273] TPSS0-D3(BJ),[275] re-vPBE0-D3(BJ),[276] RI-DSD-BLYP/2013-D3(BJ),[277] RI-DSD-PBEP86/2013-D3(BJ),[278-279] BLYP-D3(BJ),[280-282] r^{2}SCAN-3c,[283] RI-DSD-PBEB95-D3(BJ),[279] and RI-PWPB95-D3(BJ).[284] The def2-QZVPP, def2-TZVPP, or def2-mTZVPP basis sets were thereby employed.[283, 285] In agreement with experimental work, *n*-heptane was chosen as solvent. PW6B95-D3(BJ)/def2-QZVPP provided the best agreement with experimental data and was therefore applied as the standard method for subsequent calculations.

Time-dependent density functional theory (TD-DFT) calculations were performed to predict excited state properties and electronic circular dichroism (ECD) spectra. The PBE0[276], B3LYP[326], and range-separated CAM-B3LYP[327] hybrid functionals were used with the def2-TZVP basis set.[285] Unless stated otherwise, the 100 energetically lowest singlet excitations were computed. Solvent effects were included with the CPCM model[328] for dichloromethane as it is implemented in Orca 5.0.4. The resulting absorption and CD spectra were processed in Avogadro with Orca 4.1 support, exported, and plotted in OriginPro.

Absolute isotropic chemical shieldings were calculated using the gauge-independent atomic orbital (GIAO) method,[329-332] as implemented in ORCA 5.0.4, with the B3LYP functional,[326] and Kutzelnigg's individual gauge for localized orbitals (IGLO) IGLO-II basis set.[333-334] Solvent effects were incorporated using the CPCM(Chloroform) key word.[328] NMR chemical shifts were obtained by subtracting the calculated isotropic shieldings from reference data obtained from tetramethylsilane (TMS). The structure of TMS was optimized as described above prior to GIAO-DFT calculations.

Nucleus-independent chemical shifts (NICS) and the anisotropy of the induced current density (ACID) calculations were performed using the Gaussian16 program package.[335] At first, structure optimizations and frequency calculations were submitted at the B3LYP/6-311G* level of theory.[326, 336-343] The ground state exhibited no imaginary frequency. NICS(0) and NICS(1) values were obtained from the optimized structures by placing ghost atoms at the ring center and 1 Å above and below it, followed by Hartree-Fock[344-351] single point calculations with the 6-31+G(d)[340, 352-358] basis set using the GIAO method to obtain the NMR shielding tensors.[329, 332, 359-361] Ring-current analysis was accomplished by carrying out a single point calculation with the CSGT[361-363] method on the HF/6-31+G(d) level. The π-orbitals were extracted with Multiwfn,[364-365] and the ring currents were visualized using the ACID program package from the Herges group.[210, 366]

5.2 Synthetic Procedures

Compounds of Chapter 3.1

The molybdenum complexes **4**, **8**, and **84**-**86** described in the following procedures are highly sensitive toward air and moisture.[112] Hence, their synthesis was carried out under a strict argon atmosphere in flame-dried glassware using standard Schlenk techniques. Furthermore, only dry and degassed solvents were used (compare *Chapter 5.1 General Remarks*).

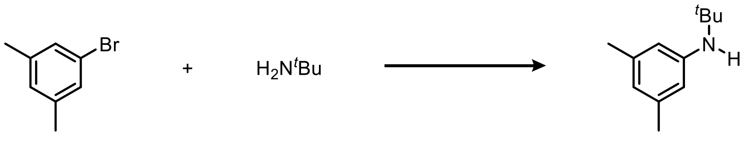

81 **82** **80**

Compound 80:[100, 112] Under argon, sodium *tert*-butoxide (510 mg, 5.30 mmol), 2-(dicyclohexylphosphino)biphenyl (42.0 mg, 120 µmol), $Pd_2(dba)_3$ (55.0 mg, 60.0 µmol), dry toluene (5.00 mL), *tert*-butylamine (**82**) (500 µL, 4.70 mmol) and 5-bromo-*m*-xylene (**81**) (407 µL, 3.00 mmol) were filled in a flame-dried Schlenk flask. The mixture was stirred for 21 h at 80 °C under an argon atmosphere. After cooling to room temperature, water (20 mL) was added, and the aqueous phase was extracted with MTBE (4×20 mL). The combined organic layers were washed with water (50 mL), a sat. sodium chloride solution (50 mL) and concentrated under reduced pressure. Subsequently, the residue was purified by flash column chromatography (SiO_2, PE/EA 10:1, $R_f = 0.42$), followed by an *in vacuo* distillation (1×10^{-1} mbar, oil bath temperature 80 °C) to give compound **80** as a colorless liquid in 64% yield (341 mg, 1.92 mmol).

Refractive index: $n_D^{20} = 1.5170$; **^{1}H NMR** (300 MHz, $CDCl_3$): δ (ppm) = 6.42 (s, 1H), 6.39 (s, 2H), 2.23 (s, 6H), 1.33 (s, 9H).

The analytical data conforms to the literature.[100]

$$\underset{\mathbf{83}}{MoCl_5} \longrightarrow \underset{\mathbf{84}}{MoCl_4(CH_3CN)_2} \longrightarrow \underset{\mathbf{85}}{MoCl_4(THF)_2} \longrightarrow \underset{\mathbf{86}}{MoCl_3(THF)_3}$$

Compound 86:[112, 367] Molybdenum(V) chloride (**83**) (4.40 g, 16.0 mmol) was filled in a flame-dried Schlenk flask. Acetonitrile (25.0 mL) was added, and the reaction was stirred for 16 h at room temperature. The formed brown solid was collected by filtration, rinsed carefully with acetonitrile (5.00 mL), and dried *in vacuo* to give $MoCl_4(CH_3CN)_2$ (**84**) as a brown solid in 85% yield (4.37 g, 13.7 mmol). Following, **84** was dispersed in THF (20.0 mL) and stirred for 3 h at room temperature. The resulting solid was filtered off, washed with pentane (10.0 mL), and dried *in vacuo* to give $MoCl_4(THF)_2$ (**85**) as an orange-brown solid in 84% yield (4.44 g, 11.6 mmol). Subsequently, **85** was mixed with THF (30.0 mL) and tin shots (8.90 g, 75.0 mmol). The reaction was stirred for an additional 30 min at room temperature before stirring was discontinued. The suspension was then decanted while swirling it manually in order to leave excess tin shots at the bottom of the flask. The remaining solid was collected by filtration, washed with pentane (10.0 mL), and dried *in vacuo* to give compound **86** as an orange solid in 80% yield (3.90 g, 9.30 mmol).

Elemental analysis calcd (%) for $MoCl_4(CH_3CN)_2$: C 15.02, H 1.89, N 8.76; found: C 14.72, H 2.08, N 8.67.

Elemental analysis calcd (%) for $MoCl_4(C_4H_8O)_2$: C 25.16, H 4.22; found: C 25.77, H 4.22.

Elemental analysis calcd (%) for $MoCl_3(C_4H_8O)_3$: C 34.43, H 5.78; found: C 33.18, H 5.38.

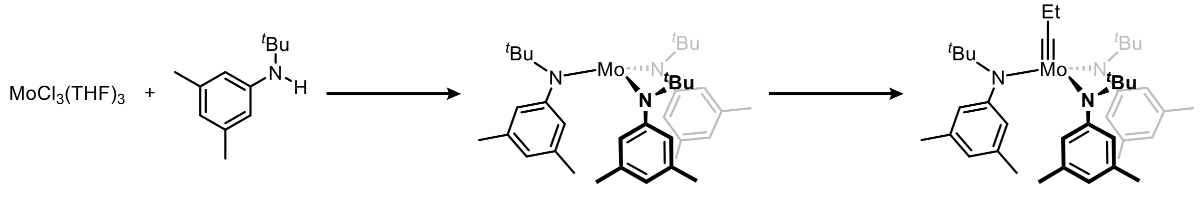

86 **80** **4** **8**

Compound 8:[100, 104, 112, 222] In a flame-dried Schlenk flask, a solution of amine **80** (802 mg, 4.50 mmol) in diethyl ether (15.0 mL) was cooled to −78 °C. *n*-Butyllithium (2.50 M in hexanes, 2.88 mL, 4.60 mmol) was added dropwise, causing the precipitation of a colorless solid. The suspension was stirred for 20 min at −78 °C, then it was allowed to warm to −30 °C. $MoCl_3(THF)_3$ (**86**) (942 mg, 2.25 mmol) and diethyl ether (20.0 mL) were added, and the reaction was stirred for another 3 h while warming to room temperature. After filtering the suspension and washing the solid with diethyl ether (5.00 mL), the filtrate was concentrated under reduced pressure. The residue was dissolved in diethyl ether (5.00 mL) and cooled to −78 °C, leading to the precipitation of a dark red solid. The supernatant was decanted, and the solid was dried *in vacuo* to furnish **4** as a dark red solid in 77% yield (727 mg, 1.16 mmol). Subsequently, complex **4** (727 mg, 1.16 mmol) was mixed with THF (22.0 mL), magnesium turnings (352 mg, 14.5 mmol) and 1,1-dichloropropane (230 µL, 2.32 mmol). After stirring the suspension for 3.5 h at room temperature, it was filtered removing excess magnesium, and the solvent of the filtrate was removed *in vacuo*. The residue was suspended in pentane (8.00 mL) and cooled to −78 °C for 2 h before the supernatant was removed by cannula transfer. Finally, the remaining brown solid was dried *in vacuo* to give compound **8** in 50%* yield (386 mg, 580 µmol). **Note: ^{1}H NMR analysis revealed the presence of approximately one equivalent of free ligand **80**. Nevertheless, the precatalyst **8** was used without further purification.*

^{1}H NMR (300 MHz, toluene-*d$_8$*): δ (ppm) = 6.63 (s, 3H), 5.99 (br. s, 6H), 3.04 (br. s, 3H), 2.11 (s, 18H), 1.42 (s, 30H).

The analytical data is in accordance with the literature.[104, 112]

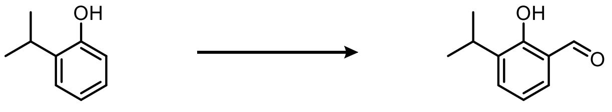

87 **88**

Compound 88:[222-223] Under argon, paraformaldehyde (6.8 g, 0.23 mol) and anhydrous magnesium chloride (14 g, 0.15 mol) were suspended in dry acetonitrile (300 mL) and dry triethylamine (38 mL). After stirring the mixture for 15 min at room temperature, 2-isopropylphenol (**87**) (10 mL, 75 mmol) was added. The reaction was stirred for 3 h at 80 °C under argon, then it was cooled to room temperature. Next, 1 M hydrochloric acid (300 mL) was added, and stirring was continued for another 30 min at room temperature. The aqueous phase was then extracted with diethyl ether (3×300 mL), and the combined organic layers were washed with 1 M hydrochloric acid (2×500 mL) and a sat. sodium chloride solution (500 mL). After drying the organic phase over $MgSO_4$ and filtering it, the solvents were removed under reduced pressure. The remaining oil was purified by flash column chromatography (SiO_2, PE/EA 8:1, R_f = 0.54) to give compound **88** as a yellow liquid in 88% yield (11 g, 66 mmol).

R

R_f = 0.54 (PE/EA 8:1); **refractive index:** n_D^{20} = 1.541; **^{1}H NMR** (300 MHz, $CDCl_3$): δ (ppm) = 11.37 (s, 1H), 9.88 (s, 1H), 7.47 (dd, *J* = 7.6 Hz, *J* = 1.7 Hz, 1H), 7.40 (dd, *J* = 7.7 Hz, *J* = 1.7 Hz, 1H), 6.99 (t, *J* = 7.6 Hz, 1H), 3.38 (sept, *J* = 6.9 Hz, 1H), 1.25 (d, *J* = 6.9 Hz, 6H).

The analytical data is in accordance with the literature.[223]

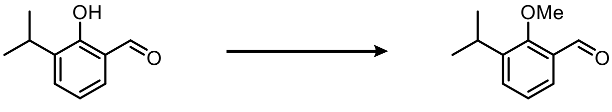

88 89

Compound 89:[224] Under argon, a solution of alcohol **88** (20.6 g, 126 mmol) in DMF (126 mL) was mixed with potassium carbonate (35.0 g, 252 mmol) and iodomethane (11.7 mL, 189 mmol). The reaction was stirred for 19 h at room temperature under an argon atmosphere. Subsequently, water (200 mL) was added, and the aqueous phase was extracted with diethyl ether (3×200 mL). The combined organic layers were washed with water (2×500 mL) and a sat. sodium chloride solution (500 mL), dried over $MgSO_4$, and filtered. Removal of the solvent under reduced pressure gave compound **89** as a yellow liquid in 98% yield (22.1 g, 124 mmol).

Refractive index: n_D^{20} = 1.526; **^{1}H NMR** (300 MHz, $CDCl_3$): δ (ppm) = 10.38 (s, 1H), 7.70 (dd, *J* = 7.6, 1.8 Hz, 1H), 7.54 (dd, *J* = 7.7, 1.8 Hz, 1H), 7.22 (t, *J* = 7.7 Hz, 1H), 3.90 (s, 3H), 3.46-3.32 (m, 1H), 1.26 (d, *J* = 7.0 Hz, 6H).

The analytical data is in accordance with the literature.[224]

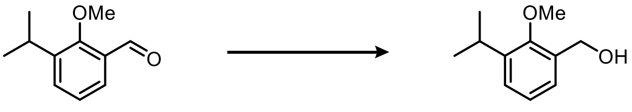

89 90

Compound 90:[225] Under argon, a solution of aldehyde **89** (5.8 g, 30 mmol) in dry ethanol (75 mL) was cooled to 0 °C. Sodium borohydride (1.1 g, 30 mmol) was added in portions, then the reaction was stirred for 1.5 h at 0 °C. After the mixture was quenched carefully with water (100 mL), the aqueous phase was extracted with CH_2Cl_2 (3×100 mL). The combined organic layers were washed with water (300 mL) and a sat. sodium chloride solution (300 mL), dried over $MgSO_4$, and filtered. Removal of the solvent under reduced pressure gave compound **90** as a light-yellow liquid in 96% yield (5.2 g, 29 mmol).

Refractive index: n_D^{20} = 1.514; **^{1}H NMR** (300 MHz, $CDCl_3$): δ (ppm) = 7.25-7.18 (m, 2H), 7.11 (t, *J* = 7.5 Hz, 1H), 4.73 (d, *J* = 6.0 Hz, 2H), 3.81 (s, 3H), 3.34 (sept, *J* = 6.9 Hz, 1H), 1.24 (d, *J* = 6.9 Hz, 6H).

The analytical data is in accordance with the literature.[368]

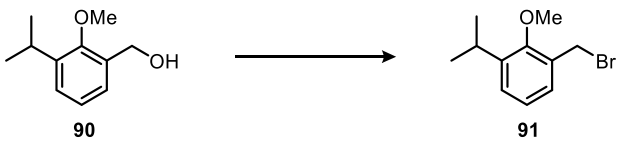

Compound 91:[226] Under argon, a solution of benzyl alcohol **90** (19.8 g, 110 mmol) in dry diethyl ether (700 mL) was cooled to 0 °C. After phosphorus tribromide (10.0 mL, 110 mmol) was added dropwise, the reaction was stirred for 65 h at room temperature under an argon atmosphere. Next, the mixture was quenched with water (500 mL), the aqueous phase was extracted with CH_2Cl_2 (3×400 mL), and the combined organic layers were washed with water (800 mL) and a sat. sodium chloride solution (800 mL). Removing the solvents on a rotary evaporator and purifying the residue by flash column chromatography (SiO_2, PE/EA 40:1, R_f = 0.42) delivered compound **91** as a light-yellow liquid in 79% yield (21.2 g, 87.0 mmol).

***R*f** = 0.42 (PE/EA 40:1); **refractive index:** n_D^{20} = 1.543; **^{1}H NMR** (300 MHz, $CDCl_3$): δ (ppm) = 7.25-7.23 (m, 2H), 7.10 (dd, *J* = 8.2, 7.0 Hz, 1H), 4.60 (s, 2H), 3.89 (s, 3H), 3.33 (sept, *J* = 6.9 Hz, 1H), 1.23 (d, *J* = 6.9 Hz, 6H). The analytical data is in accordance with the literature.[226]

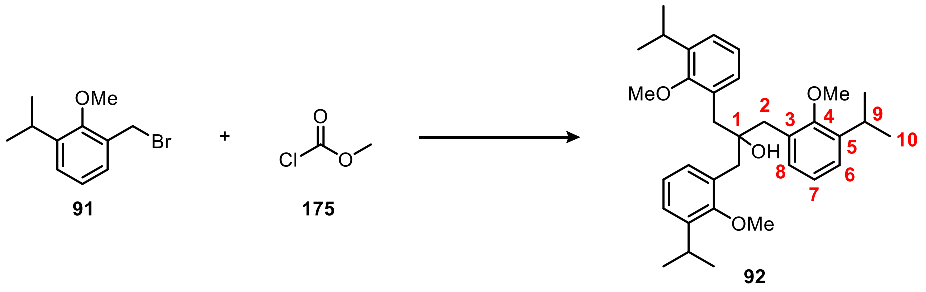

Compound 92: Magnesium turnings were activated before use by stirring them overnight under an argon atmosphere. Dry THF (70 mL) and magnesium turnings (34 g, 1.4 mol) were filled in a Schlenk flask under argon. 1,2-Dibromoethane (2.8 mL) was added dropwise, and the mixture was stirred for 30 min at room temperature. Subsequently, a solution of benzyl bromide **91** (17 g, 70 mmol) in dry THF (70 mL) was added dropwise over 45 min, and the reaction was stirred for another 2 h at room temperature. The resulting black solution was then drawn into a syringe, leaving the excess magnesium turnings in the flask, and it was transferred into another Schlenk flask under argon. Next, a solution of methyl chloroformate (**175**) (1.6 mL, 21 mmol) in dry THF (30 mL) was added dropwise. After stirring the reaction for 19 h at room temperature, it was quenched with 1 M hydrochloric acid (100 mL), and the aqueous phase was extracted with CH_2Cl_2 (3×100 mL). The combined organic layers were washed with water (300 mL) and a sat. sodium chloride solution (300 mL), dried over $MgSO_4$, and filtered. Removal of the solvent under reduced pressure and purification by flash column chromatography (SiO_2, PE/CH_2Cl_2 1:1, R_f = 0.38) gave compound **92** as a colorless oil in 82% yield (9.0 g, 17 mmol).

***R*f** = 0.38 (PE/CH_2Cl_2 1:1); **^{1}H NMR** (400 MHz, $CDCl_3$): δ (ppm) = 7.23 (dd, *J* = 7.4, 1.8 Hz, 3H, H-8), 7.13 (dd, *J* = 7.7, 1.8 Hz, 3H, H-6), 7.04 (t, *J* = 7.6 Hz, 3H, H-7), 3.48 (s, 9H, OCH_3), 3.35-3.23 (m, 3H, H-9), 2.82 (s, 6H, H-2), 1.20 (d, *J* = 6.9 Hz, 18H, H-10); **^{13}C NMR** (100 MHz, $CDCl_3$): δ (ppm) = 156.4 (C-4), 141.7 (C-5), 131.6 (C-3), 130.3 (C-8), 124.9 (C-6), 124.2 (C-7), 75.9 (C-1), 61.2 (OCH_3), 39.6 (C-2), 26.6 (C-9), 24.1 (C-10); **FT-IR** (ATR):

$\tilde{\nu}$ (cm^{-1}) **=** 3487 (w, br), 3067 (w), 2961 (m), 2935 (m), 2868 (w), 2828 (w), 1742 (w), 1589 (w), 1460 (s), 1427 (m), 1383 (m), 1362 (w), 1327 (w), 1283 (w), 1254 (m), 1202 (s), 1165 (m), 1103 (m), 1049 (s), 1009 (s), 964 (w), 943 (w), 885 (w), 798 (s), 766 (s), 702 (w), 679 (w), 644 (w), 617 (w); **HRMS** (MALDI$^+$, DCTB): *m/z* calcd for $C_{34}H_{46}O_4$+Na$^+$: 541.3288 [*M*+Na]$^+$; found: 541.3296; *m/z* calcd for $C_{34}H_{46}O_4$+K$^+$: 557.3028 [*M*+K]$^+$; found: 557.3032; **elemental analysis** calcd (%) for $C_{34}H_{46}O_4$+H_2O: C 76.08, H 9.01; found: C 76.54, H 8.81.

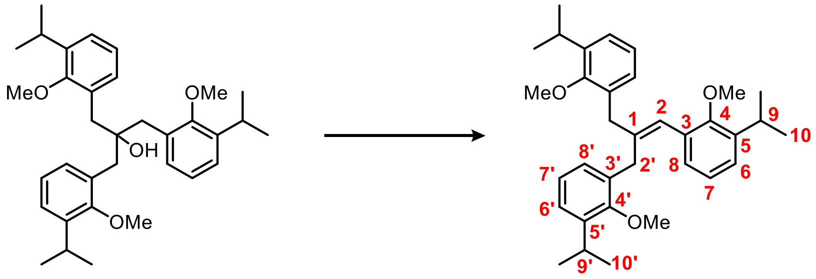

92 **93**

Compound 93: A solution of tribenzylmethanol **92** (6.99 g, 13.4 mmol) in dry toluene (80.0 mL) and pyridine (74.0 mL) was cooled to 0 °C under argon. Phosphoryl trichloride (14.0 mL, 150 mmol) was added dropwise, then the cooling bath was exchanged by an oil bath. After the reaction was stirred for 19 h at 70 °C under an argon atmosphere, the brown solution was cooled to room temperature. Following, it was quenched with water (200 mL), and the aqueous phase was extracted with CH_2Cl_2 (3×200 mL). The combined organic layers were washed with water (500 mL) and a sat. sodium chloride solution (500 mL), then concentrated under reduced pressure. Lastly, the residue was purified by flash column chromatography (SiO_2, PE/EA 40:1, R_f = 0.34) to give compound **93** as a colorless oil in 74% yield (4.99 g, 9.96 mmol).

$\boldsymbol{R_f}$ = 0.34 (PE/EA 40:1); **^{1}H NMR** (600 MHz, $CDCl_3$): δ (ppm) = 7.18-7.06 (m, 8H, H-6, 8, 6', 7', 8'), 6.98 (t, *J* = 7.6 Hz, 1H, H-7), 6.51 (s, 1H, H-2), 3.72 (s, 2H, H-2'), 3.69 (s, 3H, OCH_3), 3.61 (s, 3H, OCH_3), 3.57 (s, 3H, OCH_3), 3.50 (s, 2H, H-2'), 3.39-3.29 (m, 3H, H-9, 9'), 1.26-1.22 (m, 18H, H-10, 10'); **^{13}C NMR** (150 MHz, $CDCl_3$): δ (ppm) = 156.2 (C-4'), 155.6 (C-4), 142.0 (C_q), 141.9 (C_q), 141.7 (C_q), 140.1 (C_q), 132.7 (C_q), 132.6 (C_q), 131.4 (C_q), 128.7 (C^{Ph}-H), 127.2 (C^{Ph}-H), 127.1 (C^{Ph}-H), 125.4 (C-2), 125.2 (C^{Ph}-H), 125.0 (C^{Ph}-H), 124.7 (C^{Ph}-H), 124.5 (C^{Ph}-H), 124.3 (C^{Ph}-H), 123.9 (C-7), 61.6 (OCH_3), 61.5 (OCH_3), 61.2 (OCH_3), 37.2 (C-2'), 31.6 (C-2'), 26.6 (C-9/9'), 26.5 (C-9/9'), 26.5 (C-9/9'), 24.1 (C-10'), 23.9 (C-10); **FT-IR** (ATR): $\tilde{\nu}$ (cm^{-1}) = 3064 (w), 2960 (m), 2868 (w), 2825 (w), 2011 (w), 1928 (w), 1865 (w), 1650 (w), 1589 (w), 1458 (s), 1423 (m), 1382 (w), 1361 (w), 1334 (w), 1305 (w), 1251 (m), 1201 (m), 1164 (m), 1091 (m), 1049 (m), 1010 (s), 964 (w), 948 (w), 864 (w), 856 (w), 796 (s), 763 (s), 738 (w), 642 (w); **HRMS** (MALDI$^+$, DCTB): *m/z* calcd for $C_{34}H_{44}O_3^{+}$: 500.3285 [*M*]$^+$; found: 500.3293; calcd for $C_{34}H_{44}O_3$+K$^+$: 539.2922 [*M*+K]$^+$, found: 539.2932; **elemental analysis** calcd (%) for $C_{34}H_{44}O_3$: C 81.56, H 8.86; found: C 81.27, H 8.98.

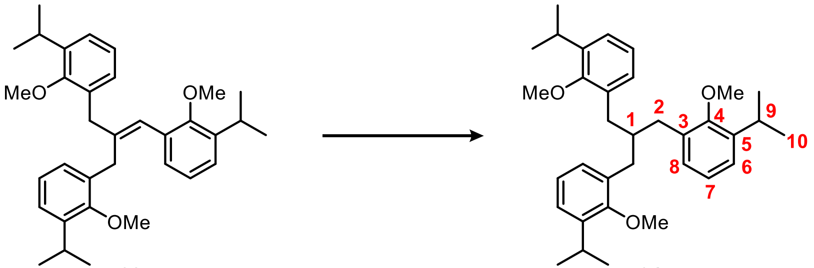

93 **94**

Compound 94: Palladium on carbon (5 *wt*%, 1.00 g) was added to a solution of **93** (4.99 g, 9.96 mmol) in ethyl acetate (142 mL). The mixture was bubbled through with hydrogen gas for 5 min, then it was stirred for 16 h at room temperature under a hydrogen atmosphere. Subsequently, the reaction was filtered over a pad of Celite, and the solvent was removed under reduced pressure. The residue was purified by flash column chromatography (SiO_2, PE/EA 30:1, R_f = 0.35) to give compound **94** as a colorless oil in 95% yield (4.80 g, 9.54 mmol).

$\boldsymbol{R_f}$ = 0.35 (PE/EA 30:1); **^{1}H NMR** (300 MHz, $CDCl_3$): δ (ppm) = 7.10-7.07 (m, 3H, H-6), 7.05-6.98 (m, 6H, H-7, 8), 3.43 (s, 9H, OCH_3), 3.31 (sept, J = 6.9 Hz, 3H, H-9), 2.57 (s, 7H, H-1, 2), 1.21 (d, J = 6.9 Hz, 18H, H-10); **^{13}C NMR** (75 MHz, $CDCl_3$): δ (ppm) = 156.3 (C-4), 141.9 (C-5), 134.5 (C-3), 128.7 (C-8), 124.4 (C-6), 124.1 (C-7), 61.2 (OCH_3), 40.9 (C-1), 35.5 (C-2), 26.4 (C-9), 24.2 (C-10); **FT-IR** (ATR): $\tilde{\nu}$ (cm^{-1}) = 3064 (w), 2960 (m), 2937 (m), 2868 (w), 2825 (w), 2013 (w), 1922 (w), 1861 (w), 1801 (w), 1589 (w), 1461 (s), 1425 (m), 1382 (w), 1361 (w), 1336 (w), 1319 (w), 1253 (m), 1203 (m), 1166 (m), 1097 (m), 1049 (m), 1010 (s), 943 (w), 881 (w), 796 (s), 763 (s), 680 (w), 630 (w); **HRMS** (MALDI$^+$, DCTB): *m/z* calcd for $C_{34}H_{46}O_3^{+}$: 502.3441 [*M*]$^+$; found: 502.3451; *m/z* calcd for $C_{34}H_{46}O_3$+Na$^+$: 525.3339 [*M*+Na]$^+$; found: 525.3349; *m/z* calcd for $C_{34}H_{46}O_3$+K$^+$: 541.3079 [*M*+K]$^+$; found: 541.3086; **elemental analysis** calcd (%) for $C_{34}H_{46}O_3$+0.5 H_2O: C 79.80, H 9.26; found: C 80.00, H 9.23.

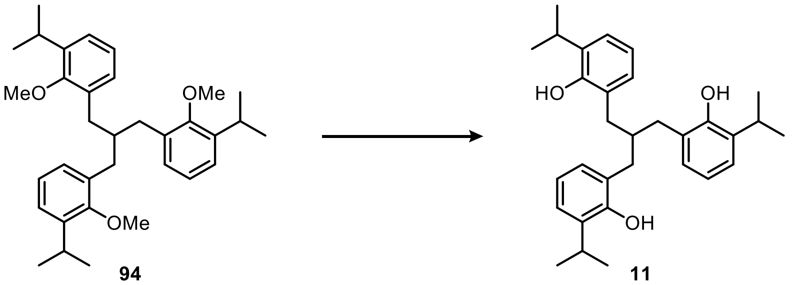

94 **11**

Compound 11: Under argon, a solution of tribenzylmethane **94** (4.80 g, 9.54 mmol) in dry CH_2Cl_2 (95.0 mL) was cooled to 0 °C. Boron tribromide (5.00 mL, 52.7 mmol) was added dropwise, and the reaction was stirred for 19 h at room temperature. The resulting orange solution was poured carefully onto ice water (150 mL), and the aqueous phase was extracted with CH_2Cl_2 (3×150 mL). The combined organic layers were washed with 1 M hydrochloric acid (500 mL), a sat. $NaHCO_3$ solution (500 mL), and a sat. sodium chloride solution (500 mL), dried over $MgSO_4$, and filtered. After the filtrate was concentrated under reduced pressure, the residue was purified by flash column chromatography (SiO_2, PE/EA 20:1, R_f = 0.08) to give compound **11** as a colorless solid in 87% yield (3.85 g, 8.35 mmol).

***R*$_f$** = 0.08 (PE/EA 20:1); **m.p.** 105-109 °C; **^{1}H NMR** (300 MHz, CDCl$_3$): δ (ppm) = 7.07 (dd, *J* = 7.6, 1.7 Hz, 3H), 6.93 (dd, *J* = 7.5, 1.7 Hz, 3H), 6.83 (t, *J* = 7.5 Hz, 3H), 4.54 (s, 3H), 3.13 (sept, *J* = 6.9 Hz, 3H), 2.64 (d, *J* = 7.0 Hz, 6H), 2.34 (sept, *J* = 6.9 Hz, 1H), 1.23 (d, *J* = 6.9 Hz, 18H).

The analytical data is in accordance with the literature.[71]

Compounds of Chapter 3.2

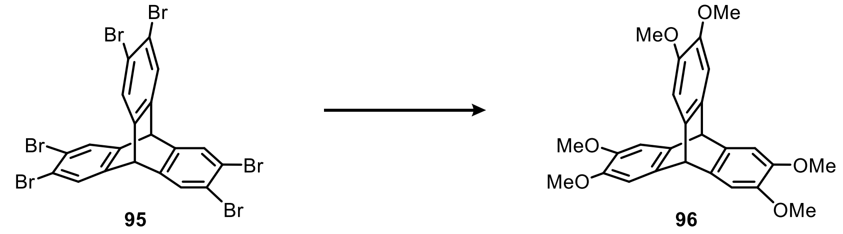

Compound 96:[222, 241] Under argon, a solution of hexabromotriptycene **95** (10.2 g, 14.0 mmol) in dry toluene (100 mL) and ethyl acetate (13 mL) was treated with sodium methoxide in methanol (25 *wt*%, 100 mL) and copper(I) bromide (1.20 g, 8.40 mmol). The reaction was stirred for 18 h at 120 °C under an argon atmosphere. After cooling to room temperature, water (200 mL) was added, and the aqueous phase was extracted with CH$_2$Cl$_2$ (3×150 mL). The combined organic layers were washed with a sat. sodium chloride solution (500 mL) and water (500 mL), dried over MgSO$_4$, filtered, and the solvent was removed under reduced pressure. The residue was purified by flash column chromatography (SiO$_2$, PE/EA 2:3, *R*$_f$ = 0.34) to give hexamethoxytriptycene **96** as a colorless solid in 90% yield (5.48 g, 12.6 mmol).

***R*$_f$** = 0.34 (PE/EA 2:3); **m.p.** 287-289 °C (lit. 250-253 °C[241]); **^{1}H NMR** (400 MHz, CDCl$_3$): δ (ppm) = 7.01 (s, 6H), 5.19 (s, 2H), 3.84 (s, 18H); **HRMS** (EI): *m/z* calcd for $C_{26}H_{26}O_6^+$: 434.17294 [*M*]$^+$; found: 434.17399; **elemental analysis** calcd (%) for $C_{26}H_{26}O_6$: C 71.87, H 6.03; found: C 71.95, H 6.15.

The analytical data is in accordance with the literature.[241]

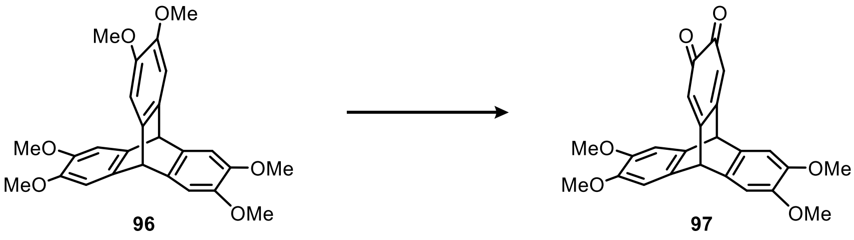

Compound 97:[222, 243] A solution of hexamethoxytriptycene **96** (4.35 g, 10.0 mmol) in CH$_2$Cl$_2$ (30.0 mL) and acetic acid (30.0 mL) was cooled to 0 °C. 64-66% Nitric acid (0.44 M, 1.88 mL) was added, causing a color change to dark red. After stirring the reaction for 5 min at 0 °C, it was quenched with ice water (100 mL), and the aqueous phase was extracted with CH$_2$Cl$_2$ (3×100 mL). The combined organic layers were washed with a sat. NaHCO$_3$ solution (2×300 mL), dried over MgSO$_4$, and filtered. Finally, the solvent was removed on a rotary evaporator to give quinone **97** as a dark red solid in 99% yield (4.87 g, 9.95 mmol), which still contained 1.0 equiv. CH$_2$Cl$_2$ according to ^{1}H NMR studies.

M.p. 239-242 °C; **^{1}H NMR** (500 MHz, CDCl$_3$): δ (ppm) = 6.98 (s, 4H), 6.28 (s, 2H), 4.99 (s, 2H), 3.98 (s, 12H).

The analytical data is in accordance with the literature.[243]

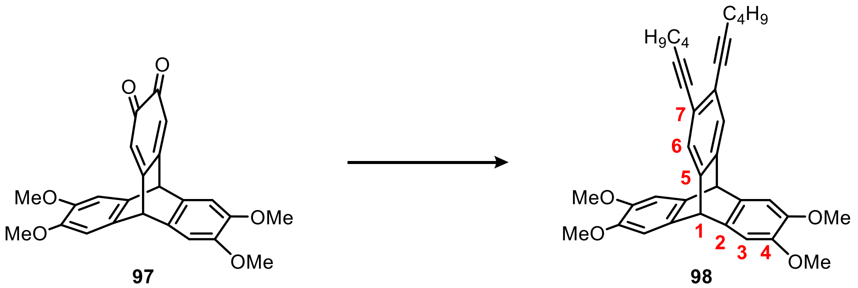

97 **98**

Compound 98:[222, 244] Under argon, a solution of quinone **97** (7.34 g, 15.0 mmol) in dry THF (94.0 mL) was cooled to −78 °C. In another reaction vessel, a solution of 1-hexyne (4.93 g, 60.0 mmol) in dry THF (84.0 mL) was also cooled to −78 °C under argon. Next, *n*-butyllithium (2.5 M in hexanes, 24.0 mL, 60.0 mmol) was added dropwise to the solution of 1-hexyne. After stirring the lithiation reaction for 45 min at −78 °C, it was added dropwise to the solution of quinone **97**. While the reaction was stirred for another 17 h, it was allowed to warm to room temperature. Subsequently, water (200 mL) was added, the aqueous phase was extracted with CH_2Cl_2 (4×200 mL), and the solvents of the combined organic layers were removed under reduced pressure. The residual brown oil was redissolved in THF (103 mL) and acetic acid (107 mL), then tin(II) chloride dihydrate (16.9 g, 75.0 mmol) was added. After stirring the mixture for 5.5 h at room temperature, water (200 mL) was added, and the aqueous phase was extracted with CH_2Cl_2 (3×250 mL). The combined organic layers were washed with 1 M hydrochloric acid (400 mL), water (400 mL), and a sat. $NaHCO_3$ solution (400 mL). Removal of the solvents under reduced pressure and purification of the residue by flash column chromatography (SiO_2, PE/EA 3:1, R_f = 0.26) delivered the triptycene derivative **98** as a brown solid in 84% yield (6.59 g, 12.3 mmol).

R

R_f = 0.26 (PE/EA 3:1); **m.p.** 78-81 °C; **^{1}H NMR** (400 MHz, $CDCl_3$): δ (ppm) = 7.35 (s, 2H, H-6), 6.97 (s, 4H, H-3), 5.18 (s, 2H, H-1), 3.83 (s, 12H, OCH_3), 2.44-2.40 (m, 4H, hexyne-H-3), 1.61-1.53 (m, 4H, hexyne-H-4), 1.52-1.44 (m, 4H, hexyne-H-5), 0.95-0.92 (m, 6H, hexyne-H-6); **^{13}C NMR** (100 MHz, $CDCl_3$): δ (ppm) = 146.2 (C-4), 145.2 (C-5), 137.9 (C-2), 126.4 (C-6), 123.1 (C-7), 108.6 (C-3), 93.1 (hexyne-C-2), 80.0 (hexyne-C-1), 56.4 (OCH_3), 53.0 (C-1), 31.0 (hexyne-C-4), 22.0 (hexyne-C-5), 19.4 (hexyne-C-3), 13.8 (hexyne-C-6); **FT-IR** (ATR): $\tilde{\nu}$ (cm^{-1}) = 2954 (w), 2930 (w), 2860 (w), 2829 (w), 1612 (w), 1603 (w), 1587 (w), 1485 (m), 1464 (s), 1439 (m), 1404 (w), 1282 (s), 1221 (s), 1184 (m), 1155 (w), 1148 (w), 1084 (s), 1024 (w), 986 (w), 895 (w), 860 (w), 808 (w), 760 (m), 744 (m), 650 (w), 611 (s); **HRMS** (MALDI$^+$, DCTB): *m/z* calcd for $C_{36}H_{38}O_4^+$: 534.2765 $[M]^+$; found: 534.2764; **elemental analysis** calcd (%) for $C_{36}H_{38}O_4$+0.5 H_2O: C 79.53, H 7.23; found: C 79.93, H 7.23. The analytical data is in accordance with the literature.[244]

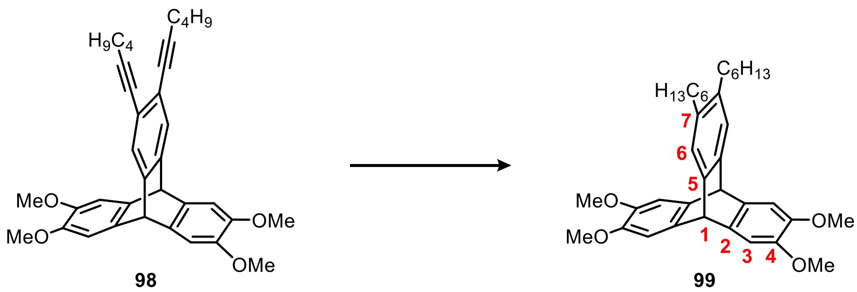

98 99

Compound 99:[222, 244] Palladium on carbon (5 *wt*%, 238 mg) was added to a solution of triptycene **98** (730 mg, 1.36 mmol) in diethyl ether (10.0 mL). The black suspension was bubbled through with hydrogen gas for 5 min, then it was stirred for 17 h at room temperature under a hydrogen atmosphere. Subsequently, the reaction mixture was filtered over a pad of Celite, and the solvent was removed under reduced pressure. The residue was purified by flash column chromatography (SiO_2, PE/EA 5:1, R_f = 0.18) to give compound **99** as a yellow solid in 93% yield (693 mg, 1.28 mmol).

***R*$_f$** = 0.18 (PE/EA 5:1); **m.p.** 154-155 °C; **^{1}H NMR** (700 MHz, $CDCl_3$): δ (ppm) = 7.15 (s, 2H, H-6), 7.00 (s, 4H, H-3), 5.20 (s, 2H, H-1), 3.84 (s, 12 H, OCH_3), 2.50-2.48 (m, 4H, hexyl-H-1), 1.53-1.49 (m, 4H, hexyl-H-2), 1.39-1.36 (m, 4H, hexyl-H-3), 1.35-1.28 (m, 8H, hexyl-H-4, 5), 0.91-0.89 (m, 6H, hexyl-H-6); **^{13}C NMR** (176 MHz, $CDCl_3$): δ (ppm) = 145.8 (C-4), 143.5 (C-5), 138.9 (C-2), 136.9 (C-7), 123.9 (C-6), 108.5 (C-3), 56.3 (OCH_3), 53.2 (C-1), 32.8 (hexyl-C-1), 31.8 (hexyl-C-4/5), 31.5 (hexyl-C-2), 29.7 (hexyl-C-3), 22.7 (hexyl-C-4/5), 14.2 (hexyl-C-6); **FT-IR** (ATR): $\tilde{\nu}$ (cm^{-1}) = 2999 (w), 2949 (w), 2928 (m), 2854 (m), 2829 (w), 1607 (w), 1487 (s), 1462 (m), 1439 (m), 1406 (w), 1283 (s), 1223 (s), 1182 (m), 1159 (w), 1090 (s), 1038 (w), 987 (m), 897 (w), 881 (m), 864 (m), 854 (m), 760 (m), 744 (m), 721 (m), 609 (m); **HRMS** (MALDI$^+$, DCTB): *m/z* calcd for $C_{36}H_{46}O_4^+$: 542.3391 $[M]^+$; found: 542.3384; **elemental analysis** calcd for $C_{34}H_{46}O_4$: C 79.67, H 8.54; found: C 79.50, H 8.43.

The analytical data is in accordance with the literature.[244]

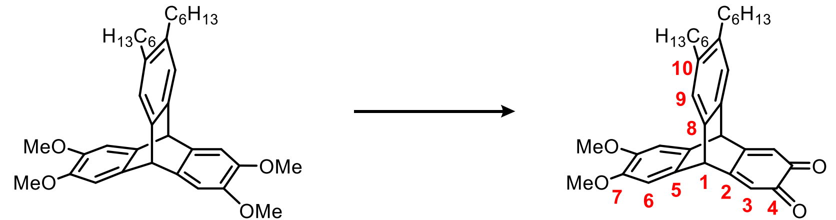

99 100

Compound 100:[222] A solution of tetramethoxytriptycene **99** (2.30 g, 4.24 mmol) in CH_2Cl_2 (25.0 mL) and acetic acid (25.0 mL) was cooled to 0 °C. 64-66% Nitric acid (0.36 M, 1.27 mL) was added dropwise, causing a color change to dark red. After stirring the reaction for 5 min at 0 °C, cold water (100 mL) was added, and the aqueous phase was extracted with CH_2Cl_2 (3×100 mL). The combined organic layers were washed with a sat. $NaHCO_3$ solution (2×300 mL), dried over $MgSO_4$, and filtered. Removing the solvent under reduced pressure delivered the quinone **100** as a dark red solid in 99% yield (2.17 g, 4.23 mmol).

M.p. 231-232 °C; **^{1}H NMR** (400 MHz, $CDCl_3$): δ (ppm) = 7.19 (s, 2H, H-9), 6.97 (s, 2H, H-6), 6.28 (s, 2H, H-3), 4.98 (s, 2H, H-1), 3.89 (s, 6H, OCH_3), 2.59-2.55 (m, 4H, hexyl-H-1), 1.58-1.50 (m, 4H, hexyl-H-2), 1.41-1.36 (m, 4H, hexyl-H-3), 1.34-1.27 (m, 8H, hexyl-H-4, 5), 0.91-0.87 (m, 6H, hexyl-H-6); **^{13}C NMR** (100 MHz, $CDCl_3$):

δ (ppm) = 180.5 (C-4), 153.4 (C-2), 149.3 (C-7), 141.0 (C-10), 136.3 (C-8), 131.5 (C-5), 125.0 (C-9), 120.8 (C-3), 108.4 (C-6), 56.4 (OCH_3), 51.6 (C-1), 32.9 (hexyl-C-1), 31.9 (hexyl-C-4/5), 31.4 (hexyl-C-2), 29.7 (hexyl-C-3), 22.8 (hexyl-C-4/5), 14.2 (hexyl-C-6); **FT-IR** (ATR): $\tilde{\nu}$ (cm^{-1}) = 3055 (w), 2998 (w), 2955 (m), 2923 (m), 2854 (m), 1677 (m), 1656 (s), 1602 (m), 1583 (s), 1502 (m), 1479 (m), 1464 (m), 1442 (m), 1415 (w), 1366 (m), 1333 (w), 1289 (s), 1263 (s), 1227 (s), 1198 (m), 1129 (w), 1087 (s), 1055 (w), 1034 (w), 992 (m), 882 (m), 836 (w), 813 (w), 792 (w), 751 (m), 725 (w), 688 (m), 636 (m), 618 (m); **UV/vis** (CH_2Cl_2): λ_{max} (lg ε) = 286 (4.75), 397 (4.69), 437 (4.68), 581 nm (3.85); **MS** (MALDI$^+$, DCTB): *m/z* calcd for $C_{34}H_{40}O_4^{+}$: 512.293 [*M*]$^+$; found: 512.182; **elemental analysis** calcd (%) for $C_{34}H_{40}O_4$+0.5 H_2O: C 78.28, H 7.92; found: C 78.64, H 7.94.

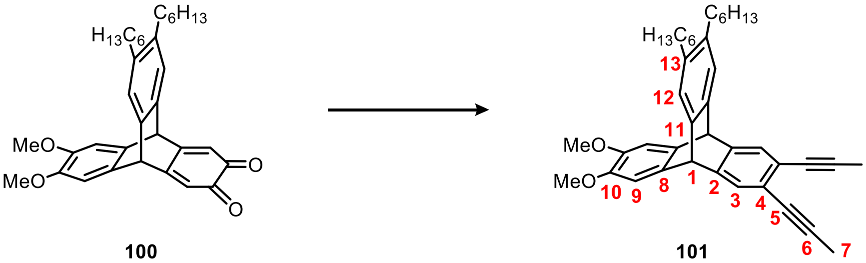

100 **101**

Compound 101:[222] In a flame-dried Schlenk flask, propyne (~1.0 M in THF, 39.0 mL, 39.0 mmol) was cooled to −78 °C under argon. *n*-Butyllithium (1.60 M in hexanes, 18.0 mL, 29.0 mmol) was added dropwise, and the mixture was stirred for 1 h at −78 °C. Next, a solution of quinone **100** (2.51 g, 4.90 mmol) in dry THF (25.0 mL) was added dropwise. The reaction was stirred for another 15 h under an argon atmosphere while it was allowed to warm to room temperature. Water (150 mL) and 1 M hydrochloric acid (50 mL) were added, and the aqueous phase was extracted with CH_2Cl_2 (3×150 mL). The solvents of the combined organic layers were removed on a rotary evaporator, leaving a brown solid, which was redissolved in THF (34.0 mL) and acetic acid (34.0 mL). After tin(II) chloride dihydrate (4.42 g, 19.6 mmol) was added, the reaction was stirred for 4 h at room temperature. Subsequently, 1 M hydrochloric acid (200 mL) was added, and the aqueous layer was extracted with CH_2Cl_2 (3×200 mL). The combined organic layers were washed with a sat. $NaHCO_3$ solution (500 mL) and a sat. sodium chloride solution (500 mL), dried over $MgSO_4$, and filtered. At last, the solvents were removed under reduced pressure, and the residue was purified by flash column chromatography (SiO_2, PE/CH_2Cl_2 1:1, R_f = 0.15) to give the triptycene derivative **101** as a yellow solid in 78% yield (2.15 g, 3.85 mmol).

***R*$_\mathbf{f}$** = 0.15 (PE/CH_2Cl_2 1:1); **m.p.** 64-68 °C; **^{1}H NMR** (400 MHz, $CDCl_3$): δ (ppm) = 7.33 (s, 2H, H-3), 7.12 (s, 2H, H-12), 6.96 (s, 2H, H-9), 5.18 (s, 2H, H-1), 3.82 (s, 6H, OCH_3), 2.50-2.46 (m, 4H, hexyl-H-1), 2.07 (s, 6H, H-7), 1.55-1.46 (m, 4H, hexyl-H-2), 1.37-1.28 (m, 12H, hexyl-H-3, 4, 5), 0.90-0.87 (m, 6H, hexyl-H-6); **^{13}C NMR** (100 MHz, $CDCl_3$): δ (ppm) = 146.3 (C-10), 145.4 (C-2), 142.4 (C-11), 137.9 (C-8), 137.5 (C-13), 126.8 (C-3), 124.3 (C-12), 122.9 (C-4), 108.8 (C-9), 88.4 (C-6), 79.1 (C-5), 56.4 (OCH_3), 53.1 (C-1), 32.8 (hexyl-C-1), 31.9 (hexyl-C-3/4/5), 31.5 (hexyl-C-2), 29.7 (hexyl-C-3/4/5), 22.8 (hexyl-C-3/4/5), 14.3 (hexyl-C-6), 4.9 (C-7); **FT-IR** (ATR): $\tilde{\nu}$ (cm^{-1}) = 3002 (w), 2953 (m), 2925 (m), 2855 (m), 2368 (w), 2356 (w), 2336 (w), 2237 (w), 2229 (w), 1605 (w), 1501 (m), 1478 (s), 1464 (s), 1439 (m), 1406 (m), 1376 (w), 1289 (s), 1220 (s), 1183 (m), 1156 (w), 1098 (m), 1084 (s), 1025 (m), 988 (w), 896 (m), 859 (w), 810 (w), 751 (m), 723 (w), 673 (w), 654 (w), 615 (m); **UV/vis** (CH_2Cl_2): λ_{max} (lg ε) = 276 (4.11), 293 (4.15), 305 (3.85), 317 nm (3.48); **HRMS** (MALDI$^+$, DCTB): *m/z* calcd for $C_{40}H_{46}O_2^{+}$: 558.3492 [*M*]$^+$; found: 558.3493; **elemental analysis** calcd (%) for $C_{40}H_{46}O_2$+0.5 H_2O: C 84.61, H 8.34; found: C 84.63, H 8.18.

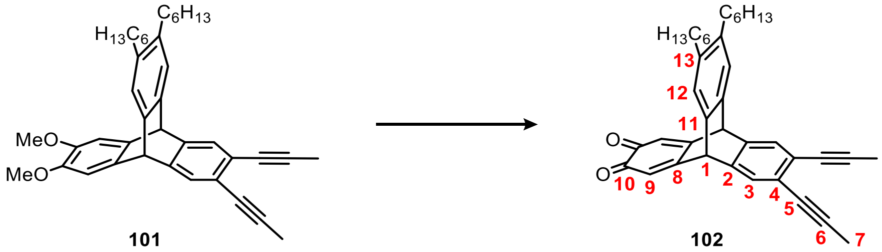

Compound 102:[222] A solution of dimethoxytriptycene **101** (56 mg, 0.10 mmol) in CH_2Cl_2 (1.0 mL) and acetic acid (1.0 mL) was cooled to 0 °C. 64-66% Nitric acid (2.0 M, 0.29 mL) was added, causing the solution to turn red. After stirring for 15 min at 0 °C, water (10 mL) was added, and the aqueous phase was extracted with CH_2Cl_2 (3×10 mL). The combined organic layers were washed with a sat. $NaHCO_3$ solution (30 mL), dried over $MgSO_4$, and filtered. The solvent was then removed under reduced pressure, and the residue was purified by flash column chromatography (SiO_2, CH_2Cl_2, R_f = 0.26) to give the quinone **102** as a red solid in 74% yield (39 mg, 74 µmol).

R

$\boldsymbol{R_f}$ = 0.26 (CH_2Cl_2); **m.p.** 97-100 °C; **^{1}H NMR** (300 MHz, $CDCl_3$): δ (ppm) = 7.40 (s, 2H, H-3), 7.17 (s, 2H, H-12), 6.29 (s, 2H, H-9), 4.97 (s, 2H, H-1), 2.59-2.53 (m, 4H, hexyl-H-1), 2.10 (s, 6H, H-7), 1.58-1.48 (m, 4H, hexyl-H-2), 1.39-1.26 (m, 12H, hexyl-H-3, 4, 5), 0.91-0.86 (m, 6H, hexyl-H-6); **^{13}C NMR** (100 MHz, $CDCl_3$): δ (ppm) = 180.1 (C-10), 152.9 (C-8), 141.3 (C-13), 138.2 (C-2), 135.5 (C-11), 127.9 (C-3), 126.1 (C-4), 125.2 (C-12), 121.6 (C-9), 90.7 (C-6), 78.4 (C-5), 51.5 (C-1), 32.8 (hexyl-C-1), 31.8 (hexyl-C-3/4/5), 31.4 (hexyl-C-2), 29.6 (hexyl-C-3/4/5), 22.7 (hexyl-C-3/4/5), 14.2 (hexyl-C-6), 4.9 (C-7); **FT-IR** (ATR): $\tilde{\nu}$ (cm^{-1}) = 2955 (m), 2924 (m), 2855 (m), 2229 (w), 1720 (w), 1684 (m), 1662 (s), 1601 (m), 1576 (w), 1468 (m), 1414 (w), 1360 (m), 1259 (s), 1189 (w), 1145 (w), 1102 (w), 1072 (w), 987 (w), 901 (m), 862 (m), 810 (w), 790 (w), 729 (m), 686 (m), 647 (w), 635 (w); **UV/vis** (CH_2Cl_2): λ_{max} (lg ε) = 275 (4.11), 400 nm (3.62); **MS** (MALDI$^+$, DCTB): *m/z* calcd for $C_{38}H_{40}O_2$+Na$^+$: 551.292 [*M*+Na]$^+$; found: 551.243; **elemental analysis** calcd (%) for $C_{38}H_{40}O_2$+H_2O: C 83.48, H 7.74; found: C 82.41, H 7.55.

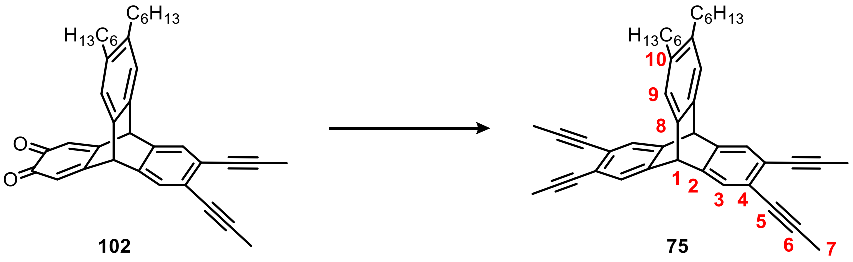

Compound 75:[222] In a flame-dried Schlenk flask, propyne (~1 M in THF, 1.6 mL, 1.6 mmol) was cooled to −78 °C under argon. *n*-Butyllithium (2.5 M in hexanes, 0.75 mL, 1.2 mmol) was added dropwise, and the mixture was stirred for 1 h at −78 °C. Next, a solution of quinone **102** (0.11 g, 0.20 mmol) in dry THF (1.0 mL) was added dropwise, and the reaction was stirred for another 16 h while it was allowed to warm to room temperature. Water (10 mL) and 1 M hydrochloric acid (5 mL) were added, and the aqueous phase

was extracted with CH_2Cl_2 (3×10 mL). The solvents of the combined organic layers were removed under reduced pressure. After adding THF (1.4 mL), acetic acid (1.4 mL), and tin(II) chloride dihydrate (0.18 g, 0.80 mmol) to the residual brown solid, the reaction was stirred for 4 h at room temperature. Following, 1 M hydrochloric acid (20 mL) was added, and the aqueous phase was extracted with CH_2Cl_2 (3×20 mL). The combined organic layers were washed with 1 M hydrochloric acid (50 mL), water (50 mL) and again 1 M hydrochloric acid (50 mL), dried over $MgSO_4$, and filtered. Removal of the solvents on a rotary evaporator and purification of the residue by flash column chromatography (SiO_2, CH_2Cl_2/hexane 1:2, R_f = 0.52) delivered the triptycene derivative **75** as a light-yellow solid in 44% yield (51 mg, 88 µmol).

R_f = 0.52 (CH_2Cl_2/hexane 1:2); **m.p.** 77-81 °C; **^{1}H NMR** (600 MHz, $CDCl_3$): δ (ppm) = 7.32 (s, 4H, H-3), 7.10 (s, 2H, H-9), 5.17 (s, 2H, H-1), 2.49-2.46 (m, 4H, hexyl-H-1), 2.07 (s, 12H, H-7), 1.50-1.45 (m, 4H, hexyl-H-2), 1.36-1.31 (m, 4H, hexyl-H-3), 1.30-1.26 (m, 8H, hexyl-H-4, 5), 0.89-0.87 (m, 6H, hexyl-H-6); **^{13}C NMR** (150 MHz, $CDCl_3$): δ (ppm) = 144.2 (C-2), 141.2 (C-8), 137.9 (C-10), 127.1 (C-3), 124.6 (C-9), 123.2 (C-4), 88.7 (C-6), 78.9 (C-5), 52.8 (C-1), 32.8 (hexyl-C-1), 31.9 (hexyl-C-4/5), 31.5 (hexyl-C-2), 29.7 (hexyl-C-3), 22.8 (hexyl-C-4/5), 14.3 (hexyl-C-6), 4.9 (C-7); **FT-IR** (ATR): $\tilde{\nu}$ (cm^{-1}) = 2954 (m), 2917 (m), 2853 (m), 2357 (w), 2341 (w), 2239 (w), 1734 (w), 1625 (w), 1541 (w), 1488 (s), 1466 (w), 1407 (w), 1375 (w), 1255 (w), 1179 (w), 1158 (w), 1105 (w), 1065 (w), 1023 (w), 964 (w), 927 (m), 899 (w), 797 (w), 723 (w) 670 (w), 649 (w); **UV/vis** (CH_2Cl_2): λ_{max} (lg ε) = 254 (4.93), 274 (4.30), 304 (3.59), 318 nm (3.61); **HRMS** (MALDI$^+$, DCTB): *m/z* calcd for $C_{44}H_{46}^+$: 574.3594 [*M*]$^+$; found: 574.3598; **elemental analysis** calcd (%) for $C_{44}H_{46}$+0.5 H_2O: C 90.52, H 8.11; found: C 90.24, H 8.36.

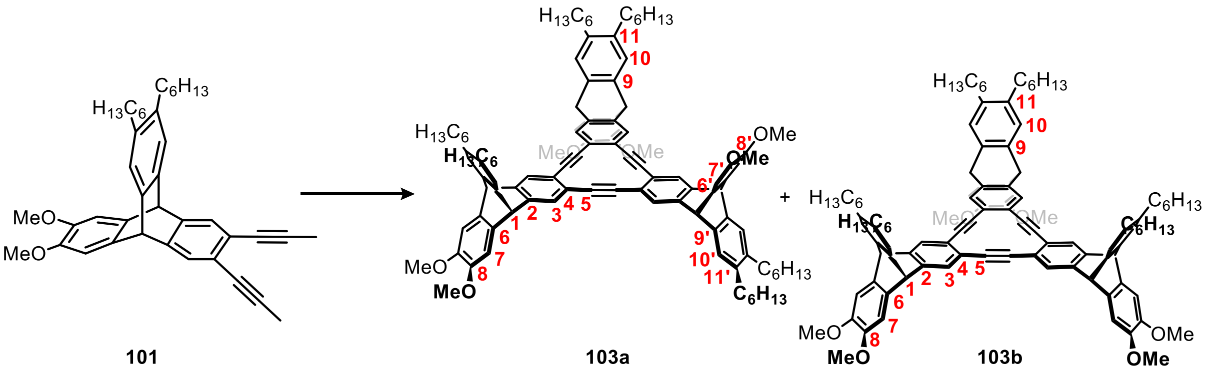

Compound 103a and 103b:[222] Under argon, a solution of precatalyst **8** (17 mg, 20 µmol) and ligand **11** (9.2 mg, 20 µmol) in dry tetrachloromethane (2.0 mL) was stirred for 30 min at room temperature. Meanwhile, triptycene derivative **101** (0.11 g, 0.20 mmol), powdered 5 Å molecular sieves (0.30 g), and dry tetrachloromethane (4.0 mL) were filled in a flame-dried Schlenk flask under argon. After adding the catalyst solution to **101**, the flask was sealed, and the reaction was stirred for 17 h at 80 °C under an argon atmosphere. Afterwards, the suspension was filtered over a pad of Celite, and the solvent was removed under reduced pressure. The residue was purified by flash column chromatography (SiO_2, CH_2Cl_2/hexane 5:1, R_f = 0.18, 0.05), separating the isomers **103a** (R_f = 0.18) and **103b** (R_f = 0.05). Each compound was further purified by precipitating it from a CH_2Cl_2 (1.0 mL) solution with methanol (1.0 mL). The precipitates were collected by filtration, washed with methanol (2.0 mL), and dried *in vacuo* to give **103a** as a yellow-brownish solid in 53% yield (54 mg, 35 µmol) and **103b** as a brown solid in 20% yield (21 mg, 13 µmol).

Compound 103a

R_f = 0.18 (CH_2Cl_2/hexane 5:1); **m.p.** 171-174 °C; **^{1}H NMR** (700 MHz, $CDCl_3$): δ (ppm) = 7.16 (s, 6H, H-3), 7.12 (s, 6H, H-10, 10'), 6.97 (s, 6H, H-7, 7'), 5.15 (s, 2H, H-1), 3.84 (s, 18H, OCH_3), 2.50-2.48 (m, 12H, hexyl-H-1), 1.52-1.47 (m, 12H, hexyl-H-2), 1.38-1.34 (m, 12H, hexyl-H-3), 1.31-1.29 (m, 24H, hexyl-H-4, 5), 0.90-0.88 (m, 18 H, hexyl-H-6); **^{13}C NMR** (176 MHz, $CDCl_3$): δ (ppm) = 146.4 (C-2), 146.3 (C-8, 8'), 141.89 (C-9), 141.88 (C-9'), 137.5 (C-11, 11'), 137.4 (C-6'), 137.3 (C-6), 126.4 (C-3), 124.3 (C-10, 10'), 123.9 (C-4), 108.6 (C-7, 7'), 92.6 (C-5), 56.3 (OCH_3), 53.0 (C-1), 32.8 (hexyl-C-1), 31.8 (hexyl-C-4/5), 31.5 (hexyl-C-2), 29.7 (hexyl-C-3), 22.7 (hexyl-C-4/5), 14.2 (hexyl-C-6); **FT-IR** (ATR): $\tilde{\nu}$ (cm^{-1}) = 2952 (m), 2926 (s), 2855 (m), 1718 (w), 1605 (w), 1501 (m), 1477 (s), 1439 (m), 1410 (w), 1377 (w), 1339 (w), 1290 (s), 1221 (s), 1184 (m), 1146 (m), 1085 (s), 1025 (m), 985 (m), 895 (m), 858 (w), 829 (w), 798 (w), 749 (m), 723 (m), 656 (w), 616 (m); **UV/vis** (CH_2Cl_2): λ_{max} (lg ε) = 299 (5.04), 311 nm (5.26); **fluorescence** (CH_2Cl_2): λ_{ex} = 315 nm, λ_{em} = 492, 530, 545 nm; **HRMS** ($MALDI^+$, DCTB): *m/z* calcd for $C_{108}H_{120}O_6^{+}$: 1512.9085 $[M]^+$; found: 1512.9079.

Compound 103b

R_f = 0.05 (CH_2Cl_2/hexane 5:1); **m.p.** 180-182 °C; **^{1}H NMR** (700 MHz, $CDCl_3$): δ (ppm) = 7.15 (s, 6H, H-3), 7.11 (s, 6H, H-10), 6.96 (s, 6H, H-7), 5.14 (s, 2H, H-1), 3.83 (s, 18H, OCH_3), 2.49-2.47 (m, 12H, hexyl-H-1), 1.51-1.46 (m, 12H, hexyl-H-2), 1.37-1.34 (m, 12H, hexyl-H-3), 1.32-1.26 (m, 24H, hexyl-H-4, 5), 0.89-0.87 (m, 18H, hexyl-H-6); **^{13}C NMR** (176 MHz, $CDCl_3$): δ (ppm) = 146.4 (C-2), 146.3 (C-8), 141.9 (C-9), 137.5 (C-11), 137.3 (C-6), 126.4 (C-3), 124.3 (C-10), 123.9 (C-4), 108.6 (C-7), 92.6 (C-5), 56.3 (OCH_3), 53.0 (C-1), 32.8 (hexyl-C-1), 31.9 (hexyl-C-4/5), 31.5 (hexyl-C-2), 29.7 (hexyl-C-3), 22.7 (hexyl-C-4/5), 14.3 (hexyl-C-6), **FT-IR** (ATR): $\tilde{\nu}$ (cm^{-1}) = 2953 (m), 2927 (m), 2855 (m), 1684 (w), 1605 (w), 1543 (w), 1500 (m), 1477 (s), 1440 (m), 1410 (w), 1377 (w), 1290 (s), 1221 (m), 1183 (w), 1146 (w), 1085 (s), 1026 (m), 985 (w), 896 (m), 857 (w), 831 (w), 807 (w), 751 (m), 725 (w), 691 (w), 659 (w), 613 (m); **UV/vis** (CH_2Cl_2): λ_{max} (lg ε) = 300 (5.05), 311 nm (5.23); **fluorescence** (CH_2Cl_2): λ_{ex} = 311 nm, λ_{em} = 421, 490, 531, 544 nm; **HRMS** ($MALDI^+$, DCTB): *m/z* calcd for $C_{108}H_{120}O_6^{+}$: 1512.9085 $[M]^+$; found: 1512.9079.

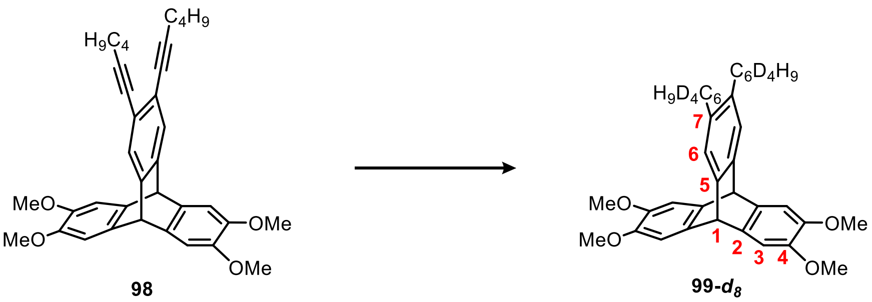

98 **99-*d*$_8$**

Compound 99-*d*$_8$: Under argon, a flame-dried Schlenk tube was charged with triptycene derivative **98** (0.26 g, 0.50 mmol), dry toluene (10 mL), and $RhCl(PPh_3)_3$ (42 mg, 45 µmol). The flask was evacuated until the solvent started boiling and backfilled with deuterium gas. After this procedure was repeated two times, the reaction was stirred for 23 h at room temperature under a deuterium atmosphere. Following, the mixture was filtered over a pad of Celite, and the solvent was removed on a rotary evaporator. Purification of the residue by flash column chromatography (SiO_2, PE/EA 4:1, R_f = 0.21) gave compound **99-d_8** as a yellow solid in 87% yield (0.24 g, 0.44 mmol).

R_f = 0.21 (PE/EA 4:1); **m.p.** 156 °C; **^{1}H NMR** (700 MHz, $CDCl_3$): δ (ppm) = 7.13 (s, 2H, H-6), 6.99 (s, 4H, H-3), 5.19 (s, 2H, H-1), 3.83 (s, 12H, OCH_3), 1.35-1.32 (m, 4H, hexyl-H-3), 1.31-1.27 (m, 8H, hexyl-H-4, 5), 0.90-0.88 (m, 6H, hexyl-H-6); **^{2}H NMR** (92 MHz, $CHCl_3/CDCl_3$): δ (ppm) = 2.45 (s, 4D), 1.46 (s, 4D); **^{13}C NMR** (176 MHz, $CDCl_3$): δ (ppm) = 145.8 (C-4), 143.5 (C-5), 138.9 (C-2), 136.9 (C-7), 123.9 (C-6), 108.5 (C-3), 56.3 (OCH_3), 53.2 (C-1), 31.8 (hexyl-C-4/5), 29.5 (hexyl-C-3), 22.8 (hexyl-C-4/5), 14.2 (hexyl-C-6); **FT-IR** (ATR): $\tilde{\nu}$ (cm^{-1}) = 2999 (w), 2950 (w), 2916 (w), 2855 (w), 2829 (w), 2202 (w), 2121 (w), 1606 (w), 1487 (m), 1462 (m), 1438 (m), 1404 (w), 1379 (w), 1283 (s), 1223 (w), 1182 (m), 1158 (w), 1088 (s), 1038 (m), 990 (m), 897 (m), 881 (m), 866 (m), 761 (m), 744 (m), 644 (w), 609 (m); **UV/vis** (CH_2Cl_2): λ_{max} (lg ε) = 299 nm (4.23); **HRMS** ($MALDI^+$, DCTB): *m/z* calcd for $C_{36}H_{38}D_8O_4^+$: 550.3893 $[M]^+$; found: 550.3866; *m/z* calcd for $C_{36}H_{38}D_8O_4+Na^+$: 573.3790 $[M+Na]^+$; found: 573.3771; **elemental analysis** calcd (%) for $C_{36}H_{38}D_8O_4$: C 78.50, H+D 8.43; found: C 78.54, H+D 8.36.

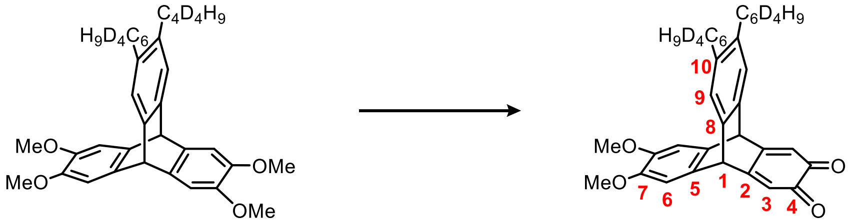

99-d_8 **100-d_8**

Compound 100-d_8: A solution of tetramethoxytriptycene **99-d_8** (65.0 mg, 110 µmol) in CH_2Cl_2 (660 µL) and acetic acid (660 µL) was cooled to 0 °C. 64-66% Nitric acid (0.36 M, 34.0 µL, 470 µmol) was added, causing a color change to dark red. After the reaction was stirred for 5 min at 0 °C, water (10 mL) was added, and the aqueous phase was extracted with CH_2Cl_2 (3×10 mL). The combined organic layers were washed with water (30 mL) and a sat. $NaHCO_3$ solution (30 mL), dried over $MgSO_4$, and filtered. Lastly, the solvent was removed under reduced pressure to give the quinone **100-d_8** as a dark red solid in 98% yield (57.0 mg, 109 µmol).

M.p. = 232-234 °C; **^{1}H NMR** (400 MHz, $CDCl_3$): δ (ppm) = 7.18 (s, 2H, H-9), 6.96 (s, 2H, H-6), 6.28 (s, 2H, H-3), 4.97 (s, 2H, H-1), 3.89 (s, 6H, OCH_3), 1.39-1.33 (m, 4H, hexyl-H-3), 1.32-1.26 (m, 8H, hexyl-H-4, 5), 0.91-0.87 (hexyl-H-6); **^{2}H NMR** (92 MHz, $CHCl_3/CDCl_3$): δ (ppm) = 2.53 (s, 4D), 1.50 (s, 4D); **^{13}C NMR** (100 MHz, $CDCl_3$): δ (ppm) = 180.4 (C-4), 153.3 (C-2), 149.2 (C-7), 141.0 (C-10), 136.2 (C-8), 131.4 (C-5), 125.0 (C-9), 120.8 (C-3), 108.4 (C-6), 56.4 (OCH_3), 51.6 (C-1), 31.8 (hexyl-C-4/5), 29.4 (hexyl-C-3), 22.7 (hexyl-C-4/5), 14.2 (hexyl-C-6); **FT-IR** (ATR): $\tilde{\nu}$ (cm^{-1}) = 3053 (w), 2999 (w), 2955 (w), 2918 (m), 2870 (w), 2851 (w), 2205 (w), 2102 (w), 1676 (m), 1655 (s), 1626 (w), 1601 (m), 1583 (m), 1502 (s), 1477 (m), 1464 (m), 1443 (m), 1412 (w), 1366 (m), 1333 (w), 1288 (s), 1263 (s), 1227 (s), 1198 (m), 1130 (w), 1088 (s), 1034 (w), 993 (m), 903 (w), 881 (m), 837 (w), 806 (w), 793 (w), 752 (m), 731 (w), 687 (m), 660 (w), 633 (w), 615 (w); **HRMS** ($MALDI^+$, DCTB): *m/z* calcd for $C_{34}H_{32}D_8O_4^+$: 520.3423 $[M]^+$; found: 520.3424; *m/z* calcd for $C_{34}H_{32}D_8O_4+Na^+$: 543.3321 $[M+Na]^+$; found:

543.3323; *m/z* calcd for $C_{34}H_{32}D_8O_4$+K^+: 559.3060 [*M*+K]$^+$; found: 559.3067; **elemental analysis** calcd (%) for $C_{34}H_{32}D_8O_4$+0.25 H_2O: C 77.75, H+D 7.78; found: C 77.75, H+D 7.44.

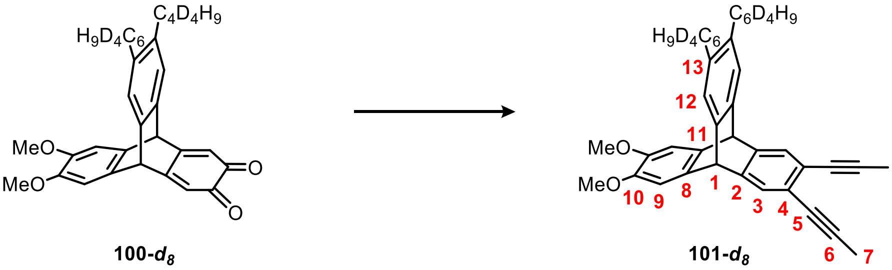

100-*d₈* **101-*d₈***

Compound 101-*d₈*: In a flame-dried Schlenk flask, propyne (~1.0 M in THF, 20.0 mL, 20.0 mmol) was cooled to −78 °C under argon. *n*-Butyllithium (2.5 M in hexanes, 5.20 mL, 13.0 mmol) was added dropwise, and the resulting colorless suspension was stirred for 1 h at −78 °C. Next, a solution of the quinone **100-*d₈*** (1.73 g, 3.25 mmol) in dry THF (15.0 mL) was added dropwise, and the reaction was stirred for 17 h while being allowed to warm to room temperature. Subsequently, 1 M hydrochloric acid (50 mL) was added, and the aqueous phase was extracted with CH_2Cl_2 (3×50 mL). The combined organic layers were washed with 1 M hydrochloric acid (150 mL), and the solvent was removed under reduced pressure. The resulting orange solid was redissolved in THF (22.0 mL) and acetic acid (22.0 mL), and tin(II) chloride dihydrate (3.67 g, 16.3 mmol) was added. After the reaction was stirred for 4 h at room temperature, 1 M hydrochloric acid (50 mL) was added, and the aqueous phase was extracted with CH_2Cl_2 (3×50 mL). The combined organic layers were washed with water (150 mL) and a sat. sodium chloride solution (150 mL), dried over $MgSO_4$, and filtered. Finally, the solvents were removed on a rotary evaporator, and the residue was purified by flash column chromatography (SiO_2, PE/CH_2Cl_2 1:1, R_f = 0.13) to give compound **101-*d₈*** as a light-yellow solid in 74% yield (1.38 g, 2.43 mmol).

$\boldsymbol{R_f}$ = 0.13 (PE/CH_2Cl_2 1:1); **m.p.** 68-70 °C; **^{1}H NMR** (400 MHz, $CDCl_3$): δ (ppm) = 7.36 (s, 2H, H-3), 7.13 (s, 2H, H-12), 6.98 (s, 2H, H-9), 5.20 (s, 2H, H-1), 3.83 (s, 6H, OCH_3), 2.08 (s, 6H, H-7), 1.35-1.29 (m, 12H, hexyl-H-3, 4, 5), 0.92-0.88 (m, 6H, hexyl-H-6); **^{2}H NMR** (92 MHz, $CHCl_3$/$CDCl_3$): δ (ppm) = 2.44 (s, 4D), 1.45 (s, 4D); **^{13}C NMR** (100 MHz, $CDCl_3$): δ (ppm) = 146.3 (C-10), 145.3 (C-2), 142.3 (C-11), 137.8 (C-8), 137.3 (C-13), 126.7 (C-3), 124.3 (C-12), 122.9 (C-4), 108.7 (C-9), 88.4 (C-6), 79.0 (C-5), 56.3 (OCH_3), 53.0 (C-1), 31.8 (hexyl-C-3/4/5), 29.4 (hexyl-C-3/4/5), 22.7 (hexyl-C-3/4/5), 14.2 (hexyl-C-6), 4.8 (C-7); **FT-IR** (ATR): $\tilde{\nu}$ (cm^{-1}) = 2999 (w), 2953 (m), 2916 (m), 2853 (m), 2205 (w), 2104 (w), 1605 (w), 1503 (m), 1476 (m), 1476 (s), 1464 (s), 1439 (m), 1404 (m), 1377 (w), 1329 (w), 1288 (s), 1221 (s), 1184 (s), 1155 (w), 1150 (w), 1084 (s), 1026 (m), 991 (m), 924 (w), 895 (m), 860 (m), 795 (w), 752 (m), 671 (w), 648 (w), 608 (m); **UV/vis** (CH_2Cl_2): λ_{max} (lg ε) = 277 (4.17), 293 (4.19), 305 (3.97), 318 nm (3.72); **HRMS** (MALDI$^+$, DCTB): *m/z* calcd for $C_{40}H_{38}D_8O_2^+$: 566.3994 [*M*]$^+$; found: 566.3992; *m/z* calcd for $C_{40}H_{38}D_8O_2$+Na^+: 589.3892 [*M*+Na]$^+$; found: 589.3889; **elemental analysis** calcd for $C_{40}H_{38}D_8O_2$: C 84.76, H+D 8.19; found: C 84.92, H+D 8.17.

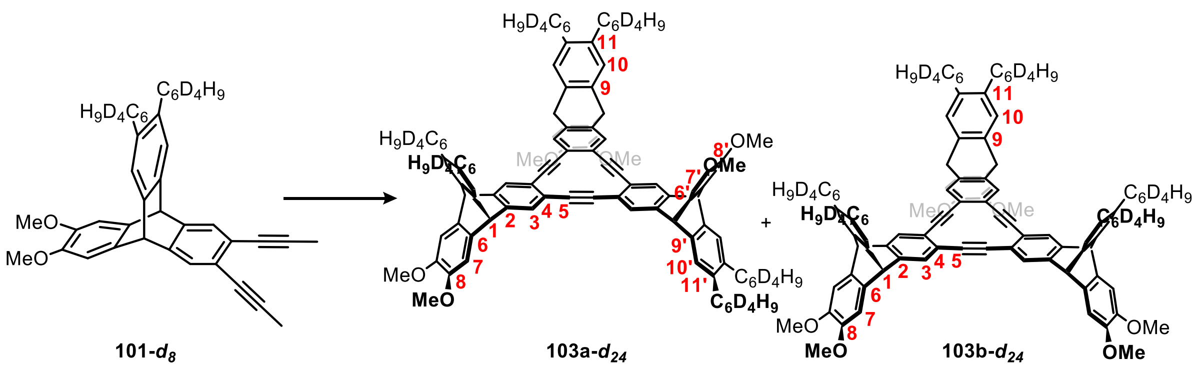

Compound 103a-d_{24} and 103b-d_{24}: Under argon, a solution of precatalyst **8** (29 mg, 30 µmol) and ligand **11** (16 mg, 30 µmol) in dry tetrachloromethane (3.0 mL) was stirred for 30 min at room temperature. Meanwhile, triptycene derivative **101-d_8** (0.19 g, 0.34 mmol), powdered 5 Å molecular sieves (0.51 g), and dry tetrachloromethane (7.0 mL) were filled in a flame-dried Schlenk flask under argon. Following, the catalyst solution was added, and the reaction was stirred for 4 days at 80 °C under an argon atmosphere. After cooling to room temperature, the mixture was filtered over a pad of Celite, and the solvent was removed *in vacuo*. The crude residue was subjected to flash column chromatography (SiO_2, PE/CH_2Cl_2 1:6, R_f = 0.35, 0.03), separating the isomers **103a-d_{24}** and **103b-d_{24}**. Each compound was further purified by precipitation from a CH_2Cl_2 (2.0 mL) solution with methanol (2.0 mL). The respective precipitates were then collected by filtration, washed with methanol (2.0 mL), and dried *in vacuo* to give **103a-d_{24}** as a yellow solid in 56% yield (98 mg, 63 µmol) and **103b-d_{24}** as a brown solid in 38% yield (67 mg, 43 µmol).

Compound 103a-d_{24}

R_f = 0.35 (PE/CH_2Cl_2 1:6); **m.p.** 175 °C (dec.); **^{1}H NMR** (600 MHz, $CDCl_3$): δ (ppm) = 7.16 (s, 6H, H-3), 7.11 (s, 6H, H-10, 10'), 6.96 (s, 6H, H-7, 7'), 5.14 (s, 2H, H-1), 3.83 (s, 18H, OCH_3), 1.34-1.31 (m, 12H, hexyl-H-3), 1.30-1.27 (m, 24H, hexyl-H-4, 5), 0.89-0.87 (m, 18H, hexyl-H-6); **^{2}H NMR** (92 MHz, $CHCl_3$/$CDCl_3$): δ (ppm) = 2.46 (s, 12D), 1.46 (s, 12D); **^{13}C NMR** (150 MHz, $CDCl_3$): δ (ppm) = 146.4 (C-2), 146.3 (C-8, 8'), 141.9 (C-9), 141.9 (C-9'), 137.5 (C-11, 11'), 137.4 (C-6'), 137.4 (C-6), 126.4 (C-3), 124.3 (C-10, 10'), 123.9 (C-4), 108.6 (C-7, 7'), 92.6 (C-5), 56.3 (OCH_3), 53.0 (C-1), 31.8 (hexyl-C-4/5), 29.4 (hexyl-C-3), 22.8 (hexyl-C-4/5), 14.2 (hexyl-C-6); **FT-IR** (ATR): $\tilde{\nu}$ (cm^{-1}) = 2999 (w), 2954 (m), 2921 (m), 2853 (m), 2203 (w), 2111 (w), 1606 (w), 1502 (m), 1477 (s), 1439 (m), 1409 (m), 1377 (w), 1339 (w), 1290 (s), 1222 (s), 1186 (s), 1147 (m), 1085 (s), 1026 (m), 986 (m), 954 (w), 895 (m), 859 (m), 828 (m), 806 (w), 795 (w), 765 (w), 750 (m), 730 (m), 651 (w), 612 (s); **UV/vis** (CH_2Cl_2): λ_{max} (lg ε) = 298 (5.05), 311 nm (5.26); **fluorescence** (CH_2Cl_2): λ_{ex} = 311 nm, λ_{em} = 493, 530, 544 nm; **HRMS** (MALDI$^+$, DCTB): *m/z* calcd for $C_{108}H_{96}D_{24}O_6^+$: 1537.0586 [*M*]$^+$; found: 1537.0549.

Compound 103b-d_{24}

R_f = 0.03 (PE/CH_2Cl_2 1:6); **m.p.** 183 °C (dec.); **^{1}H NMR** (700 MHz, $CDCl_3$): δ (ppm) = 7.15 (s, 6H, H-3), 7.11 (s, 6H, H-10), 6.96 (s, 6H, H-7), 5.14 (s, 2H, H-1), 3.83 (s, 18H, OCH_3), 1.34-1.32 (m, 12H, hexyl-H-3), 1.31-1.27 (m, 24H, hexyl-H-4, 5), 0.89-0.87 (m, 18H, hexyl-H-6); **^{2}H NMR** (92 MHz, $CHCl_3$/$CDCl_3$): δ (ppm) = 2.48 (s, 12D), 1.46 (s, 12D); **^{13}C NMR** (176 MHz, $CDCl_3$): δ (ppm) = 146.4 (C-2), 146.4 (C-8), 141.9 (C-9), 137.5 (C-11), 137.4 (C-6), 126.4 (C-3), 124.3 (C-10), 123.9 (C-4), 108.7 (C-7), 92.6 (C-5), 56.4 (OCH_3), 53.0 (C-1), 31.8 (hexyl-

C-4/5), 29.4 (hexyl-C-3), 22.8 (hexyl-C-4/5), 14.2 (hexyl-C-6); **FT-IR** (ATR): $\tilde{\nu}$ (cm^{-1}) = 2999 (w), 2954 (m), 2920 (m), 2853 (m), 2203 (w), 1605 (w), 1499 (m), 1476 (s), 1466 (s), 1439 (m), 1408 (w), 1377 (w), 1337 (w), 1290 (s), 1263 (w), 1222 (s), 1186 (m), 1147 (m), 1085 (s), 1026 (m), 988 (w), 850 (m), 857 (w), 824 (w), 796 (w), 750 (m), 613 (m), 606 (m); **UV/vis** (CH_2Cl_2): λ_{max} (lg ε) = 298 (4.94), 311 nm (5.06); **fluorescence** (CH_2Cl_2): λ_{ex} = 310 nm, λ_{em} = 421, 487, 531, 544 nm; **HRMS** (MALDI$^+$, DCTB): *m/z* calcd for $C_{108}H_{96}D_{24}O_6^{+}$: 1537.0586 [*M*]$^+$; found: 1537.0562.

Compounds of Chapter 3.3

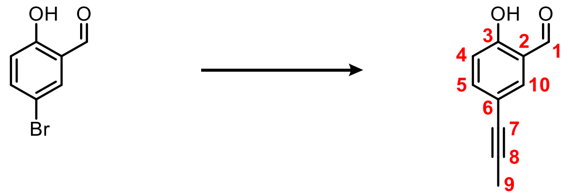

110 **111**

Compound 111:[256] The batch size described below was carried out twice, and the batches were combined for the aqueous work-up. Compound **110** (5.03 g, 25.0 mmol), copper(I) iodide (143 mg, 750 µmol), and Pd(dppf)Cl_2 (549 mg, 750 µmol) were placed under an argon atmosphere. The solids were then dissolved in propyne (~1 M in THF, 50.0 mL, 50.0 mmol) and triethylamine (50.0 mL), and the reaction vessels were sealed. Each reaction was stirred for 16 h at 80 °C under an argon atmosphere. After cooling to room temperature, the two batches were combined and quenched with water (100 mL). The aqueous phase was extracted with CH_2Cl_2 (3×100 mL), and the combined organic layers were washed with 1 M hydrochloric acid (2×200 mL), dried over $MgSO_4$, and filtered. The solvents were removed under reduced pressure, and the residue was purified by flash column chromatography (SiO_2, PE/EA 20:1, R_f = 0.38) to give compound **111** as a yellow solid in 97% yield (7.78 g, 48.5 mmol).

***R*$_f$** = 0.38 (PE/EA 20:1); **m.p.** 111 °C; **^{1}H NMR** (300 MHz, $CDCl_3$): δ (ppm) = 11.02 (s, 1H, OH), 9.84 (s, 1H, H-1), 7.59 (d, *J* = 2.2 Hz, 1H, H-10), 7.52 (dd, *J* = 8.6, 2.2 Hz, 1H, H-5), 6.91 (d, *J* = 8.6 Hz, 1H, H-4), 2.04 (s, 3H, H-9); **^{13}C NMR** (75 MHz, $CDCl_3$): δ (ppm) = 196.3 (C-1), 161.0 (C-3), 140.0 (C-5), 136.8 (C-10), 120.5 (C-2), 118.0 (C-4), 116.2 (C-6), 85.4 (C-8), 78.1 (C-7), 4.4 (C-9); **FT-IR** (ATR): $\tilde{\nu}$ (cm^{-1}) = 3020 (w), 2879 (w), 1665 (m), 1649 (m), 1614 (w), 1590 (m), 1553 (w), 1478 (m), 1435 (w), 1413 (w), 1369 (m), 1336 (w), 1314 (w), 1287 (m), 1259 (m), 1219 (m), 1174 (m), 1159 (m), 1130 (w), 1035 (w), 1000 (w), 971 (w), 909 (m), 894 (m), 844 (s), 787 (w), 766 (m), 733 (s), 715 (vs), 662 (m), 644 (m), 615 (m); **HRMS** (EI$^+$): *m/z* calcd for $C_{10}H_8O_2^{+}$: 160.05188 [*M*]$^+$; found: 160.05186; **elemental analysis** calcd (%) for $C_{10}H_8O_2$: C 74.99, H 5.03; found: C 75.09, H 5.04.

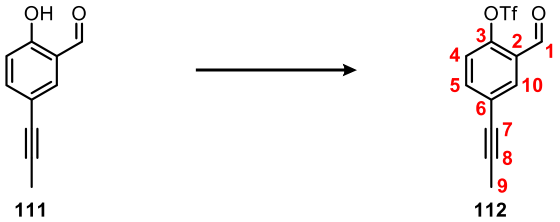

Compound 112:[256] In a flame-dried Schlenk flask, a solution of **111** (7.7 g, 48 mmol) in dry CH_2Cl_2 (150 mL) was cooled to 0 °C under argon. Triethylamine (13 mL, 96 mmol) and triflic anhydride (14 mL, 84 mmol) were added sequentially, and the mixture was stirred for 5 min at 0 °C. After removing the cooling bath and stirring the reaction for an additional 1 h at room temperature, it was quenched with 1 M hydrochloric acid (200 mL). The aqueous phase was extracted with CH_2Cl_2 (3×200 mL), and the combined organic layers were washed with a sat. sodium chloride solution (500 mL). Finally, the solvents of the organic phase were removed under reduced pressure, and the remaining dark brown liquid was purified by flash column chromatography (SiO_2, PE/EA 40:1, R_f = 0.23) to give compound **112** as a yellow liquid in 77% yield (10 g, 37 mmol).

R_f = 0.23 (PE/EA 40:1); **^{1}H NMR** (400 MHz, $CDCl_3$): δ (ppm) = 10.19 (s, 1H, H-1), 7.94 (d, *J* = 2.2 Hz, 1H, H-10), 7.65 (dd, *J* = 8.6, 2.3 Hz, 1H, H-5), 7.31 (d, *J* = 8.6 Hz, 1H, H-4), 2.06 (s, 3H, H-9); **^{19}F NMR** (282 MHz, $CDCl_3$): δ (ppm) = 72.8 (CF_3); **^{13}C NMR** (100 MHz, $CDCl_3$): δ (ppm) = 186.1 (C-1), 148.5 (C-3), 138.4 (C-5), 133.9 (C-10), 128.5 (C-2), 125.9 (C-6), 122.6 (C-4), 123.6-114.0 (q, CF_3), 90.1 (C-8), 77.2 (C-7), 4.4 (C-9); **FT-IR** (ATR): $\tilde{\nu}$ (cm^{-1}) = 2236 (w), 1701 (m), 1644 (w), 1597 (w), 1580 (w), 1482 (m), 1427 (s), 1318 (w), 1294 (w), 1246 (m), 1208 (s), 1160 (s), 1134 (s), 1111 (m), 1086 (s), 1029 (w), 1003 (w), 954 (w), 940 (w), 897 (s), 850 (s), 831 (s), 793 (w), 779 (m), 748 (s), 720 (m), 699 (m), 643 (m), 608 (s); **MS** (APCI$^+$): *m/z* calcd for $C_{11}H_7F_3O_4S+H^+$: 293.0090 $[M+H]^+$; found: 293.0089; **elemental analysis** calcd (%) for $C_{11}H_7F_3O_4S+0.5\ H_2O$: C 43.86, H 2.68; found: C 43.60, H 2.71.

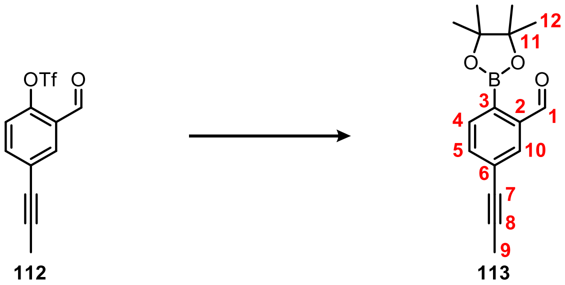

Compound 113:[256] The batch size described below was carried out twice, and the two batches were combined for the aqueous work-up. In a flame-dried Schlenk tube, potassium acetate (5.45 g, 55.5 mmol) was dried *in vacuo* at 250 °C for 5 min. After cooling to room temperature, compound **112** (5.41 g, 18.5 mmol), B_2Pin_2 (5.64 g, 22.2 mmol), Pd(dppf)Cl_2 (406 mg, 55.5 µmol), and dry dioxane (60.0 mL) were added. The solutions were degassed by bubbling argon through them for 10 min, then the Schlenk tubes were sealed, and the reactions were stirred for 63 h at 80 °C under an argon atmosphere. After cooling to room temperature, the combined reactions were mixed with water (150 mL), and the aqueous phase was extracted with

CH_2Cl_2 (3×200 mL). The combined organic layers were washed with a sat. sodium chloride solution (600 mL) and concentrated under reduced pressure, leaving a dark brown solid. The crude material was suspended in *n*-hexane (40 mL), ultrasonicated for 5 min, and filtered over a pad of $MgSO_4$. The filtrate was concentrated under reduced pressure, then excess B_2Pin_2 was removed by sublimation at 1.0×10^{-3} mbar and 120 °C. The residue was suspended again in *n*-hexane (30 mL), ultrasonicated for 5 min, and filtered over a pad of $MgSO_4$. Lastly, the filtrate was concentrated once more under reduced pressure and purified by an *in vacuo* distillation (1.0×10^{-3} mbar, 140 °C oil bath temperature) to give compound **113** as a colorless solid in 40% yield (4.08 g, 15.1 mmol).

M.p. 70 °C; **^{1}H NMR** (300 MHz, $CDCl_3$): δ (ppm) = 10.51 (s, 1H, H-1), 7.95 (d, J = 1.9 Hz, 1H, H-10), 7.78 (d, J = 7.6 Hz, 1H, H-4), 7.57 (dd, J = 7.7, 1.7 Hz, 1H, H-5), 2.07 (s, 3H, H-9), 1.38 (s, 12H, H-12); **^{13}C NMR** (75 MHz, $CDCl_3$): δ (ppm) = 194.2 (C-1), 141.4 (C-2), 135.7 (C-4), 135.5 (C-5), 130.8 (C-10), 127.0 (C-6), 88.8 (C-8), 84.6 (C-11), 79.0 (C-7), 25.0 (C-12), 4.5 (C-9); **FT-IR** (ATR): $\tilde{\nu}$ (cm^{-1}) = 2977 (w), 2921 (w), 2231 (w), 1692 (s), 1657 (w), 1602 (m), 1539 (w), 1499 (w), 1480 (w), 1471 (w), 1447 (w), 1393 (w), 1380 (s), 1372 (m), 1346 (vs), 1322 (s), 1294 (m), 1269 (s), 1234 (w), 1215 (m), 1173 (m), 1142 (s), 1117 (s), 1066 (s), 1013 (w), 1004 (w), 963 (m), 910 (m), 887 (w), 856 (s), 843 (s), 828 (m), 814 (m), 741 (w), 707 (m), 670 (m), 651 (s), 602 (w); **MS** (EI$^+$): *m/z* calcd for $C_{16}H_{19}BO_3^{+}$: 270.14218 [M]$^+$; found: 270.14169; **elemental analysis** calcd (%) for $C_{16}H_{19}BO_3$: C 71.14, H 7.09; found: C 70.96, H 6.95.

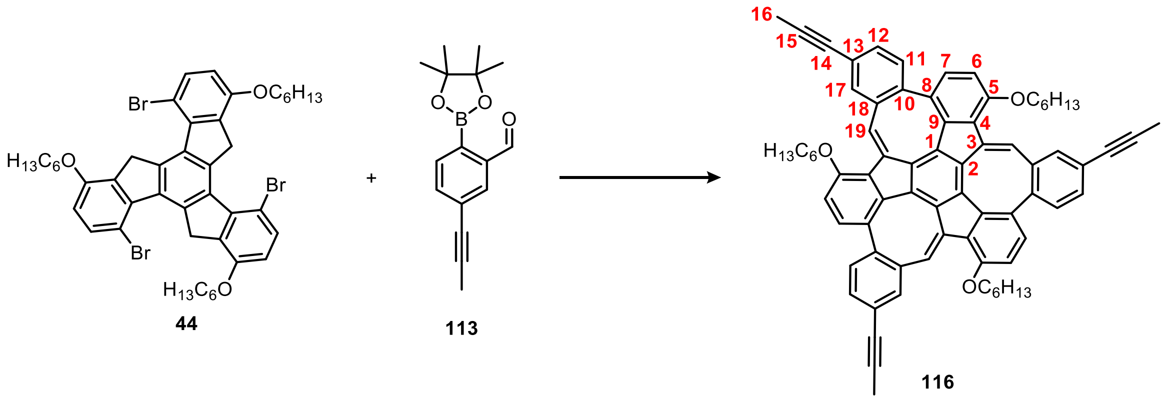

Compound 116:[256] Under argon, $Pd_2(dba)_3$ (11.0 mg, 12.5 µmol), XPhos (24.0 mg, 50.0 µmol), and boronic ester **113** (223 mg, 825 µmol) were dissolved in degassed THF (2.50 mL) and a degassed potassium carbonate solution (2.0 M in H_2O, 1.25 mL). The mixture was stirred for 5 min at room temperature, then tribromotruxene **44** (220 mg, 250 µmol) was added, and the reaction vessel was sealed. The reaction was stirred vigorously for 3 h at 80 °C under an argon atmosphere. After cooling to room temperature, water (10 mL) was added, and the aqueous phase was extracted with CH_2Cl_2 (3×10 mL). The combined organic layers were washed with water (30 mL), 1 M hydrochloric acid (30 mL), and a sat. sodium chloride solution (10 mL), dried over $MgSO_4$, and filtered. Concentrating the filtrate under reduced pressure left a brown-orange solid, which was suspended in methanol (10 mL), ultrasonicated for 10 min, and collected by filtration. The orange solid was further washed with methanol (2 mL) and dried *in vacuo*. Next, it was transferred into a Schlenk tube under argon, and dry THF (10.0 mL) and DBU (10.0 µL, 45.0 µmol) were added. The

resulting dark brown solution was stirred for 6 h at 60 °C before 6 M hydrochloric acid (1.00 mL) was added, and stirring was continued for an additional 15 min at 60 °C. After cooling to room temperature, 1 M hydrochloric acid (10 mL) was added, and the aqueous phase was extracted with CH_2Cl_2 (3×15 mL). The combined organic layers were washed with water (50 mL) and a sat. sodium chloride solution (50 mL), dried over $MgSO_4$, and filtered. Subsequently, the solvents were removed under reduced pressure, and the remaining dark brown solid was purified by flash column chromatography (SiO_2, PE/CH_2Cl_2 4:1, R_f = 0.13) to give the propyne monkey saddle **116** as a yellow-brownish solid in 18% yield (47.0 mg, 46.2 µmol). For an analytically pure sample, **116** was further purified by recycling HPLC (SiO_2, *n*-heptane/CH_2Cl_2 2:1).

R

$\boldsymbol{R_f}$ = 0.13 (PE/CH_2Cl_2 4:1); **m.p.** 186 °C (dec.); **^{1}H NMR** (600 MHz, $CDCl_3$): δ (ppm) = 8.28 (s, 3H, H-19), 7.23 (dd, *J* = 8.0, 1.7 Hz, 3H, H-12), 7.08 (d, *J* = 1.8 Hz, 3H, H-17), 7.04 (d, *J* = 8.4 Hz, 3H, H-7), 6.95 (d, *J* = 8.4 Hz, 3H, H-6), 6.74 (d, *J* = 8.1 Hz, 3H, H-11), 4.19-4.11 (m, 6H, hexyloxy-H-1), 2.01 (s, 9H, H-16), 1.95-1.83 (m, 6H, hexyloxy-H-2), 1.58-1.51 (m, 6H, hexyloxy-H-3), 1.39-1.34 (m, 12H, hexyloxy-H-4, 5), 0.91-0.89 (m, 9H, hexyloxy-H-6); **^{13}C NMR** (150 MHz, $CDCl_3$): δ (ppm) = 154.1 (C-5), 142.5 (C_q), 142.2 (C_q), 142.1 (C_q), 139.9 (C_q), 138.2 (C_q), 134.6 (C_q), 134.5 (C-11), 134.0 (C-17), 132.9 (C_q), 132.3 (C-7), 132.0 (C_q), 131.7 (C-19), 130.8 (C-12), 123.0 (C-13), 112.5 (C-6), 86.6 (C-15), 79.2 (C-14), 68.6 (hexyloxy-C-1), 31.7 (hexyloxy-C-4/5), 29.4 (hexyloxy-C-2), 26.2 (hexyloxy-C-3), 22.8 (hexyloxy-C-4/5), 14.2 (hexyloxy-C-6), 4.5 (C-16); **FT-IR** (ATR): $\tilde{\nu}$ (cm^{-1}) = 2951 (m), 2926 (m), 2853 (m), 2359 (w), 2232 (w), 1585 (m), 1555 (m), 1506 (w), 1483 (s), 1466 (s), 1377 (w), 1337 (m), 1306 (w), 1271 (s), 1252 (s), 1219 (m), 1119 (w), 1097 (m), 1061 (m), 1020 (m), 997 (m), 899 (m), 876 (w), 833 (m), 804 (s), 781 (m), 762 (m), 737 (m); **UV/vis** (CH_2Cl_2): λ_{max} (lg ε) = 260 (5.00), 290 (5.17), 408 nm (4.50); **fluorescence** (CH_2Cl_2): λ_{ex} = 403 nm, λ_{em} = 539 nm; **HRMS** (MALDI$^+$, DCTB): *m/z* calcd for $C_{75}H_{66}O_3^+$: 1014.5006 [*M*]$^+$; found: 1014.5001; **elemental analysis** calcd (%) for $C_{75}H_{66}O_3$+0.25 H_2O: C 88.30, H 6.57; found: C 88.14, H 6.51.

The enantiomers of **116** were separated by chiral HPLC (Chiralpak® IE, *n*-heptane/MTBE 75:25 (*v/v*), R_t: 6.9 min (S_a,S_a,S_a), 14.2 min (R_a,R_a,R_a)). (S_a,S_a,S_a)-**116**: **M.p.** 178 °C; $[\boldsymbol{\alpha}]_{\mathbf{D}}^{\mathbf{20}}$ = +727.1 (in CH_2Cl_2). (R_a,R_a,R_a)-**116**: **M.p.** 182 °C; $[\boldsymbol{\alpha}]_{\mathbf{D}}^{\mathbf{20}}$ = −882.7 (in CH_2Cl_2).

Compounds of Chapter 3.4

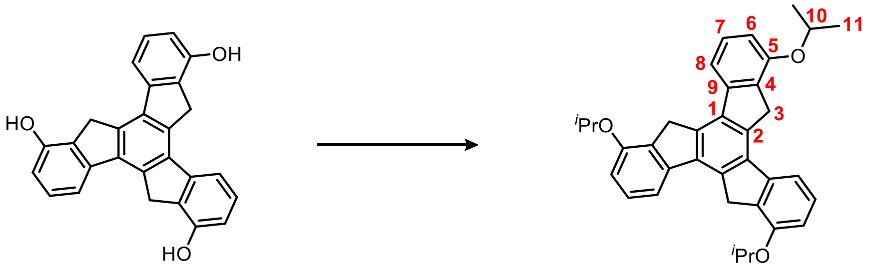

119 120

Compound 120:[186] In a Schlenk flask, trishydroxytruxene **119** (5.86 g, 15.0 mmol) and powdered sodium hydroxide (3.78 g, 94.5 mmol) were dissolved in DMSO (50.0 mL) and water (4.50 mL). The solution was stirred for 30 min at room temperature while bubbling argon through it, then 2-bromopropane (25.0 mL, 270 mmol) was added. The reaction was stirred for 4 days at 60 °C under an argon atmosphere. After cooling to room temperature, it was quenched with 1 M hydrochloric acid (100 mL), and the aqueous phase was extracted with CH_2Cl_2 (3×150 mL). The combined organic layers were washed with 1 M hydrochloric acid (500 mL) followed by removal of the solvents under reduced pressure. Lastly, the crude material was purified by flash column chromatography (SiO_2, PE/CH_2Cl_2 4:1 to 1:1) to give truxene derivative **120** as a beige solid in 54% yield (4.15 g, 8.03 mmol).

R_f = 0.21 (PE/CH_2Cl_2 3:1); **m.p.** 285 °C; **^{1}H NMR** (600 MHz, $CDCl_3$): δ (ppm) = 7.66 (d, J = 7.4 Hz, 3H, H-8), 7.46 (t, J = 7.8 Hz, 3H, H-7), 6.93 (d, J = 8.1 Hz, 3H, H-6), 4.76 (sept, J = 6.1 Hz, 3H, H-10), 4.22 (s, 6H, H-3), 1.48 (d, J = 6.1 Hz, 18H, H-11); **^{13}C NMR** (150 MHz, $CDCl_3$): δ (ppm) = 154.9 (C-5), 143.8 (C-9), 137.4 (C-1), 135.7 (C-2), 132.4 (C-4), 128.5 (C-7), 114.9 (C-8), 111.1 (C-6), 70.3 (C-10), 34.1 (C-3), 22.6 (C-11); **FT-IR** (ATR): $\tilde{\nu}$ (cm^{-1}) = 3076 (w), 2974 (w), 2932 (w), 2881 (w), 2363 (w), 1605 (m), 1580 (m), 1483 (m), 1450 (w), 1408 (w), 1381 (m), 1371 (m), 1354 (w), 1331 (w), 1275 (s), 1256 (s), 1169 (w), 1134 (m), 1113 (s), 1076 (w), 1053 (m), 970 (s), 926 (w), 908 (w), 868 (w), 843 (w), 812 (w), 787 (s), 743 (s), 719 (m), 698 (w), 669 (w), 656 (w), 631 (w); **UV/vis** (CH_2Cl_2): λ_{max} (lg ε) = 278 (4.88), 292 nm (4.74); **HRMS** (MALDI$^+$, DCTB): m/z calcd for $C_{36}H_{36}O_3^+$: 516.2659 $[M]^+$; found: 516.2668; **elemental analysis** calcd (%) for $C_{36}H_{36}O_3$: C 83.69, H 7.02; found: C 83.99, H 7.23.

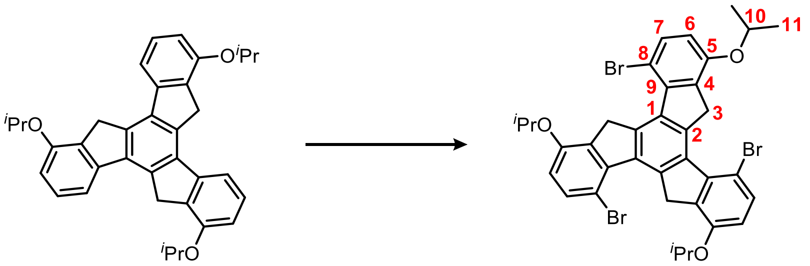

120 121

Compound 121:[186] Truxene derivative **120** (9.78 g, 18.9 mmol) and NBS (10.4 g, 58.5 mmol) were stirred in DMF (180 mL) for 16 h at room temperature. Afterwards, MTBE (300 mL) and water (500 mL) were added to the resulting grey-purple suspension, the layers were separated, and the aqueous phase was extracted with MTBE (2×200 mL). The combined organic layers were then washed with water (2×500 mL), followed by removing the solvent under reduced pressure. Lastly, the residue was purified by flash column chromatography (SiO_2, PE/CH_2Cl_2 4:1, R_f = 0.19) to give compound **121** as a colorless solid in 34% yield (4.84 g, 6.43 mmol).

***R*~f~** = 0.19 (PE/CH_2Cl_2 4:1); **m.p.** 138 °C; **^{1}H NMR** (600 MHz, $CDCl_3$): δ(ppm) = 7.60 (d, *J* = 8.5 Hz, 3H, H-7), 6.76 (d, *J* = 8.6 Hz, 3H, H-6), 4.75 (s, 6H, H-3), 4.63 (sept, *J* = 6.0 Hz, 3H, H-10), 1.43 (d, *J* = 6.1 Hz, 18H, H-11); **^{13}C NMR** (150 MHz, $CDCl_3$): δ(ppm) = 153.4 (C-5), 141.9 (C-9), 138.8 (C-1/2), 138.5 (C-1/2), 137.6 (C-4), 134.4 (C-7), 113.5 (C-6), 105.8 (C-8), 71.1 (C-10), 41.2 (C-3), 22.5 (C-11); **FT-IR** (ATR): $\tilde{\nu}$ (cm^{-1}) = 2970 (m), 2930 (w), 1595 (m), 1560 (m), 1464 (s), 1404 (w), 1385 (m), 1364 (s), 1271 (s), 1258 (s), 1207 (m), 1167 (m), 1134 (m), 1123 (s), 1109 (s), 1051 (m), 1041 (m), 978 (s), 970 (s), 951 (m), 906 (m), 885 (m), 833 (m), 806 (s), 793 (s), 743 (m), 733 (w), 656 (w), 644 (w), 633 (w), 604 (m); **UV/vis** (CH_2Cl_2): λ_{max} (lg ε) = 286 (4.75), 296 nm (4.68); **HRMS** (MALDI$^+$, DCTB): *m/z* calcd for $C_{36}H_{33}Br_3O_3^{+}$: 749.9974 [*M*]$^+$; found: 749.9953; **elemental analysis** calcd (%) for $C_{36}H_{33}Br_3O_3$+0.5 H_2O: C 56.72, H 4.50; found: C 56.90, H 4.17.

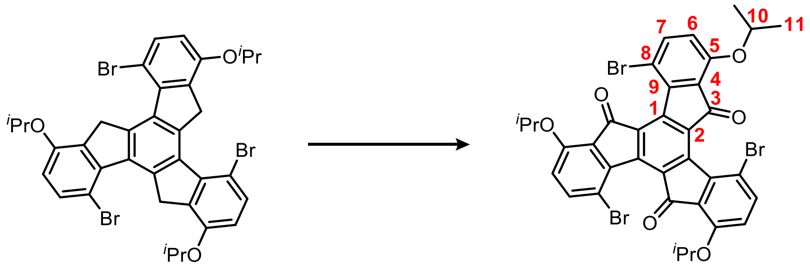

121 **122**

Compound 122:[186] In a 100 mL round-bottom flask, tribromotruxene **121** (1.13 g, 1.50 mmol) and potassium carbonate (1.24 g, 9.00 mmol) were suspended in DMF (90 mL). Oxygen gas was bubbled through the suspension for 5 min, then the reaction was stirred for 41 h at 40 °C under an oxygen atmosphere. Subsequently, the solvent was removed using a rotary evaporator (20 mbar, 60 °C water bath temperature), and the remaining dark brown solid was purified by flash column chromatography (SiO_2, CH_2Cl_2/EA 80:1, R_f = 0.63, 0.53, 0.22) to give the truxenone **122** as a brown-yellowish solid in 42% yield (500 mg, 629 µmol).

***R*~f~** = 0.22 (CH_2Cl_2/EA 80:1); **m.p.** 290 °C (dec.); **^{1}H NMR** (600 MHz, $CDCl_3$): δ(ppm) = 7.69 (d, *J* = 8.9 Hz, 3H, H-7), 6.94 (d, *J* = 9.0 Hz, 3H, H-6), 4.72 (sept, *J* = 6.1 Hz, 3H, H-10), 1.44 (d, *J* = 6.0 Hz, 18H, H-11); **^{13}C NMR** (150 MHz, $CDCl_3$): δ(ppm) = 184.8 (C-3), 156.2 (C-5), 144.8 (C-9), 144.6 (C-1), 141.0 (C-7), 135.7 (C-2), 127.4 (C-4), 120.6 (C-6), 112.9 (C-8), 73.7 (C-10), 22.3 (C-11); **FT-IR** (ATR): $\tilde{\nu}$ (cm^{-1}) = 2976 (w), 2930 (w), 1705 (s), 1595 (m), 1580 (m), 1564 (s), 1462 (s), 1371 (m), 1337 (w), 1306 (w), 1271 (s), 1215 (m), 1182 (m), 1163 (s), 1136 (m), 1103 (s), 1061 (s), 970 (s), 908 (s), 872 (w), 841 (m), 814 (s), 806 (s), 764 (w), 741 (w), 723 (s), 700 (m), 673 (m), 660 (m); **UV/vis** (CH_2Cl_2): λ_{max} (lg ε) = 305 (4.78), 400 (4.37), 437 nm (3.91); **HRMS** (MALDI$^-$, DCTB): *m/z* calcd for $C_{36}H_{27}Br_3O_6^{-}$: 791.9363 [*M*]$^-$; found: 791.9348; **elemental analysis** calcd (%) for $C_{36}H_{27}Br_3O_6$: C 54.37, H 3.42; found: C 54.49, H 3.37.

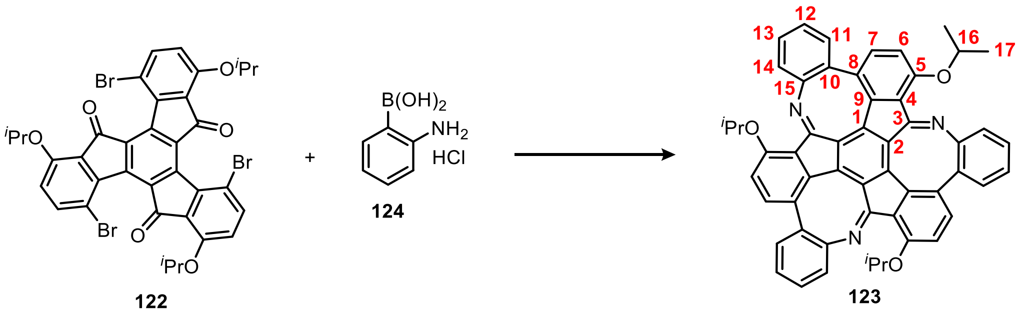

Compound 123:[186] Boronic acid **124** (468 mg, 2.70 mmol), potassium carbonate (870 mg, 6.30 mmol), $Pd_2(dba)_3$ (13.7 mg, 15.0 µmol), and $HP^tBu_3BF_4$ (17.4 mg, 60.0 µmol) were filled in an 8 mL vial under argon. Degassed THF (1.50 mL) and degassed water (1.50 mL) were added, and the mixture was stirred for 5 min at room temperature. Following, compound **122** (239 mg, 300 µmol) was added, the vial was sealed, and the reaction was stirred vigorously for 15 h at 80 °C under an argon atmosphere. After cooling to room temperature, water (10 mL) was added, and the aqueous phase was extracted with CH_2Cl_2 (3×10 mL). The combined organic layers were concentrated under reduced pressure, and the residue was purified by flash column chromatography (SiO_2, CH_2Cl_2/EA 1:1, R_f = 0.16) to give a red solid, which was dissolved in $CHCl_3$ (9.00 mL) and acetic acid (900 µL). The red solution was stirred for 5 h at 80 °C. After cooling to room temperature, a sat. $NaHCO_3$ solution (10 mL) was added, and the aqueous phase was extracted with CH_2Cl_2 (3×10 mL). Finally, the combined organic layers were concentrated under reduced pressure, and the residue was purified by flash column chromatography (SiO_2, CH_2Cl_2, R_f = 0.48) to give the aza monkey saddle **123** as an orange solid in 41% yield (95.0 mg, 122 µmol).

R_f = 0.48 (CH_2Cl_2); **m.p.** 326 °C (dec.); **^{1}H NMR** (600 MHz, $CDCl_3$): δ (ppm) = 7.39 (d, J = 8.5 Hz, 3H, H-7), 7.30 (ddd, J = 8.4, 7.2, 1.5 Hz, 3H, H-13), 7.12 (ddd, J = 7.5, 7.4, 1.4 Hz, 3H, H-12), 7.06 (d, J = 8.5 Hz, 3H, H-6), 6.94 (dd, J = 8.1, 1.3 Hz, 3H, H-14), 6.90 (dd, J = 7.8, 1.5 Hz, 3H, H-11), 4.78 (sept, J = 6.1 Hz, 3H, H-16), 1.44 (d, J = 6.1 Hz, 9H, H-17), 1.38 (d, J = 6.1 Hz, 9H, H-17); **^{13}C NMR** (150 MHz, $CDCl_3$): δ (ppm) = 165.8 (C-3), 155.1 (C-5), 149.8 (C-15), 147.4 (C-1), 144.3 (C-9), 135.4 (C-7), 134.5 (C-11), 133.3 (C-4), 131.8 (C-8), 130.8 (C-2), 128.8 (C-10), 128.2 (C-13), 126.3 (C-14), 125.2 (C-12), 119.3 (C-6), 73.3 (C-16), 22.6 (C-17), 22.5 (C-17); **FT-IR** (ATR): $\tilde{\nu}$ (cm^{-1}) = 3053 (w), 2972 (w), 2927 (w), 1649 (m), 1582 (s), 1501 (m), 1474 (s), 1383 (m), 1346 (w), 1281 (s), 1261 (s), 1167 (m), 1109 (s), 1057 (m), 989 (m), 918 (m), 885 (m), 837 (m), 810 (s), 762 (vs), 739 (s), 727 (s), 700 (s), 640 (s), 608 (s); **UV/vis** (CH_2Cl_2): λ_{max} (lg ε) = 273 (4.95), 319 (4.57), 414 nm (4.26); **HRMS** (MALDI$^+$, DCTB): *m/z* calcd for $C_{54}H_{39}N_3O_3-H^+$: 776.2908 $[M-H]^+$; found: 776.2901; **elemental analysis** calcd (%) for $C_{54}H_{39}N_3O_3$+0.5 H_2O: C 82.42, H 5.12, N 5.34; found: C 82.03, H 5.09, N 5.22.

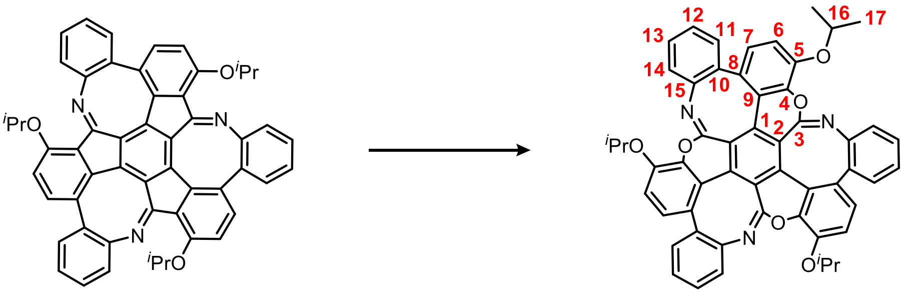

123 **125**

Compound 125:[186] A solution of **123** (98 mg, 0.12 mmol) and *m*CPBA (75 *wt*%, 96 mg, 0.42 mmol) in CH_2Cl_2 (5.7 mL) was stirred for 5 h at room temperature. Afterwards, the reaction was quenched with a sat. $NaHCO_3$ solution (20 mL), and the aqueous phase was extracted with CH_2Cl_2 (3×20 mL). The combined organic layers were dried over $MgSO_4$, filtered, and concentrated under reduced pressure. Lastly, the residue was subjected to a flash column chromatographic purification (SiO_2, CH_2Cl_2, R_f = 0.63, 0.47) to give the chromene monkey saddle **125** as an off-white solid in 82% yield (85 mg, 0.10 mmol).

R$_\mathbf{f}$ = 0.63 (CH_2Cl_2); **m.p.** 390 °C (dec.); **^{1}H NMR** (600 MHz, $CDCl_3$): δ (ppm) = 7.20 (td, *J* = 7.7, 1.5 Hz, 3H, H-12), 7.15 (d, *J* = 8.5 Hz, 3H, H-6), 7.04 (td, *J* = 7.5, 1.3 Hz, 3H, H-13), 6.99 (d, *J* = 8.4 Hz, 3H, H-7), 6.90-6.87 (m, 6H, H-11, 14), 4.69 (sept, *J* = 6.1 Hz, 3H, H-16), 1.46 (d, *J* = 6.1 Hz, 9H, H-17), 1.39 (d, *J* = 6.0 Hz, 9H, H-17); **^{13}C NMR** (150 MHz, $CDCl_3$): δ (ppm) = 155.7 (C-3), 146.0 (C-5), 143.6 (C_q), 143.2 (C_q), 137.1 (C_q), 131.7 (C-11/14), 130.6 (C_q), 130.5 (C_q), 128.9 (C_q), 128.7 (C-12), 125.2 (C-13), 125.2 (C-7), 124.4 (C_q), 122.0 (C-11/14), 118.2 (C-6), 72.4 (C-16), 22.4 (C-17), 22.1 (C-17); **FT-IR** (ATR): $\tilde{\nu}$ (cm^{-1}) = 2976 (w), 2930 (w), 1703 (s), 1597 (w), 1564 (w), 1545 (m), 1502 (w), 1477 (m), 1445 (w), 1416 (w), 1369 (m), 1312 (m), 1281 (m), 1211 (w), 1178 (w), 1136 (s), 1107 (s), 1078 (s), 1057 (s), 1038 (m), 939 (s), 868 (w), 808 (s), 764 (vs), 725 (s), 646 (s); **UV/vis** (CH_2Cl_2): λ_{max} (lg ε) = 284 (4.49), 304 nm (4.53); **HRMS** (MALDI$^+$, DCTB): *m/z* calcd for $C_{54}H_{39}N_3O_6^+$: 825.2833 $[M]^+$; found: 825.2832; **elemental analysis** calcd (%) for $C_{54}H_{39}N_3O_6$+0.25 H_2O: C 78.10, H 4.79, N 5.06; found: C 78.09, H 4.93, N 5.17.

The enantiomers of **125** were separated by chiral HPLC (Chiralpak® IE, *n*-heptane/CH_2Cl_2 30:70 (*v*/*v*), R_t: 3.6 min (S_a,S_a,S_a), 4.3 min (R_a,R_a,R_a)). (S_a,S_a,S_a)-**125**: **M.p.** 377 °C (dec.); $[\boldsymbol{\alpha}]_\mathbf{D}^{\mathbf{20}}$ = +409.9 (in CH_2Cl_2). (R_a,R_a,R_a)-**125**: **M.p.** 380 °C (dec.); $[\boldsymbol{\alpha}]_\mathbf{D}^{\mathbf{20}}$ = −417.5 (in CH_2Cl_2).

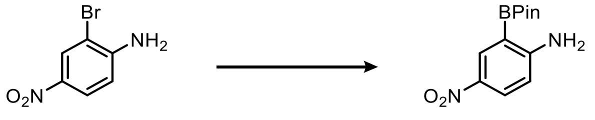

129 **130**

Compound 130:[258] Under argon, a flame-dried Schlenk flask was charged with potassium acetate (735 mg, 7.50 mmol), B_2Pin_2 (952 mg, 3.75 mmol), Pd(dppf)Cl_2 (91.5 mg, 125 µmol), and the bromide **129** (543 mg, 2.50 mmol). Dry dioxane (11.0 mL) was added to the solids, the flask was sealed, and the reaction was stirred for 69 h at 80 °C under an argon atmosphere. After cooling to room temperature, water (20 mL) was added, and the aqueous phase was extracted with CH_2Cl_2 (3×20 mL). The combined organic layers were washed with water (50 mL), dried over $MgSO_4$, filtered, and concentrated under reduced pressure. The residue was further purified by flash column chromatography (SiO_2, CH_2Cl_2, R_f = 0.39) before remaining B_2Pin_2 was removed from the obtained orange solid by sublimation (1×10^{-3} mbar, 80 °C) to give compound **130** as an orange solid in 80% yield (532 mg, 2.01 mmol).

R

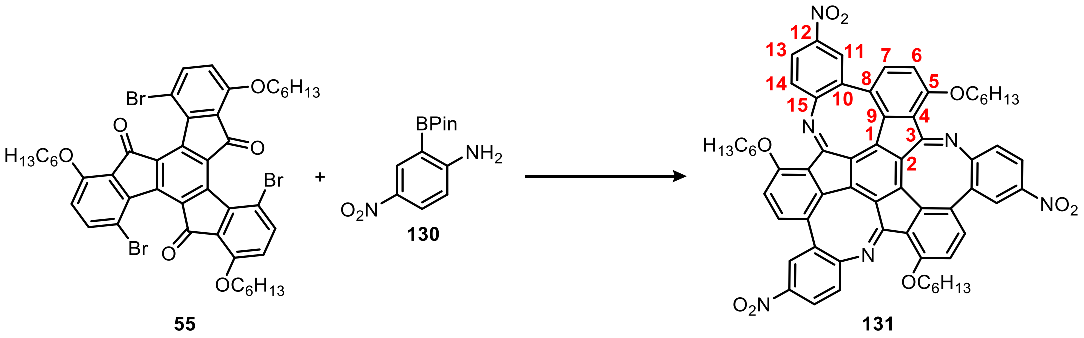

Compound 131:[258] Under argon, an 8 mL vial was charged with boronic ester **130** (1.31 g, 4.95 mmol), $Pd_2(dba)_3$ (50.4 mg, 60.0 µmol), and $HP^tBu_3BF_4$ (63.8 mg, 220 µmol). Degassed THF (1.50 mL) and a degassed potassium carbonate solution (2 M in H_2O, 1.50 mL) were added, and the mixture was stirred for 5 min at room temperature. Subsequently, the truxenone **55** (507 mg, 550 µmol) was added, the vial was sealed, and the reaction was stirred vigorously for 18 h at 80 °C under an argon atmosphere. After cooling to room temperature, water (50 mL) was added, and the aqueous phase was extracted with CH_2Cl_2 (3×50 mL). The combined organic layers were dried over $MgSO_4$, filtered, and concentrated under reduced pressure. The dark brown residue was then submitted to a plug of silica using CH_2Cl_2 (200 mL) to remove excess amine **130**. Following, the silica-plug was flushed with ethyl acetate (200 mL), and the solvent of this fraction was removed under reduced pressure. The remaining red solid was dissolved in $CHCl_3$ (15 mL) and acetic acid (5 mL), and the red solution was stirred for 18 h at 80 °C in a sealed tube. After cooling to room temperature, water (50 mL) was added, and the aqueous phase was extracted with CH_2Cl_2 (3×50 mL). The combined organic layers were washed with a sat. $NaHCO_3$ solution (100 mL), dried over $MgSO_4$, filtered, and concentrated under reduced pressure. Finally, the residue was purified by flash column chromatography (SiO_2, PE/CH_2Cl_2 1:1, R_f = 0.08) and then by chiral HPLC (Chiralpak® IB, *n*-heptane/CH_2Cl_2/THF 75:20:5 (*v*/*v*/*v*), R_t: 6.2 min, 7.5 min) to give the aza monkey saddle derivative **131** as an orange solid in 2% yield (13.0 mg, 12.5 µmol).

$\boldsymbol{R_f}$ = 0.08 (PE/CH_2Cl_2 1:1); **m.p.** 260 °C (dec.); **^{1}H NMR** (600 MHz, $CDCl_3$): δ (ppm) = 8.14 (dd, *J* = 8.9, 2.6 Hz, 3H, H-13), 7.84 (d, *J* = 2.6 Hz, 3H, H-11), 7.56 (d, *J* = 8.5 Hz, 3H, H-7), 7.14 (d, *J* = 8.6 Hz, 3H, H-6), 7.03 (d, *J* = 8.8 Hz, 3H, H-14), 4.32 (dt, *J* = 9.5, 5.9 Hz, 3H, hexyloxy-H-1), 4.19 (dt, *J* = 9.5, 6.8 Hz, 3H, hexyloxy-H-1), 1.93-1.86 (m, 3H, hexyloxy-H-2), 1.85-1.79 (m, 3H, hexyloxy-H-2), 1.63-1.56 (m, 3H, hexyloxy-H-3), 1.52-1.45 (m, 3H, hexyloxy-H-3), 1.37-1.28 (m, 12H, hexyloxy-H-4, 5), 0.87 (t, *J* = 7.0 Hz, 9H, hexyloxy-H-6); **^{13}C NMR** (150 MHz, $CDCl_3$): δ (ppm) = 166.4 (C-3), 157.0 (C-5), 155.3 (C_q), 147.5 (C-12), 144.9 (C_q), 144.3 (C_q), 136.3 (C-7), 131.4 (C_q), 131.1 (C_q), 130.0 (C-11), 129.4 (C_q), 128.7 (C_q), 126.8 (C-14), 123.4 (C-13), 116.2 (C-6), 69.6 (hexyloxy-C-1), 31.6 (hexyloxy-C-4/5), 29.1 (hexyloxy-C-2), 25.7 (hexyloxy-C-3), 22.7 (hexyloxy-C-4/5), 14.1 (hexyloxy-C-6); **FT-IR** (ATR): $\tilde{\nu}$ (cm^{-1}) = 2957 (m), 2922 (m), 2872 (w), 2854 (m), 1734 (w), 1715 (w), 1703 (w), 1695 (w), 1649 (m), 1583 (m), 1558 (m), 1541 (m), 1520 (m), 1499 (s), 1466 (m), 1402 (w), 1393 (w), 1377 (m), 1337 (s), 1288 (s), 1256 (s), 1211 (m), 1171 (m), 1159 (m), 1113 (s), 1094 (m), 1057 (m), 1038 (m), 1014 (m), 986 (w), 962 (m), 953 (m), 933 (w), 905 (m), 856 (m), 835 (s), 822 (m), 808 (m), 791 (m), 770 (m), 748 (m), 723 (m), 706 (m), 675 (w), 654 (w), 619 (w); **UV/vis** (CH_2Cl_2): λ_{max} (lg ε) = 271 (4.92), 325 (4.84), 418 nm (4.43); **HRMS** ($MALDI^+$, DCTB): *m/z* calcd for $C_{63}H_{54}N_6O_9^+$: 1038.3947 $[M]^+$; found: 1038.3917.

Compounds of Chapter 3.5

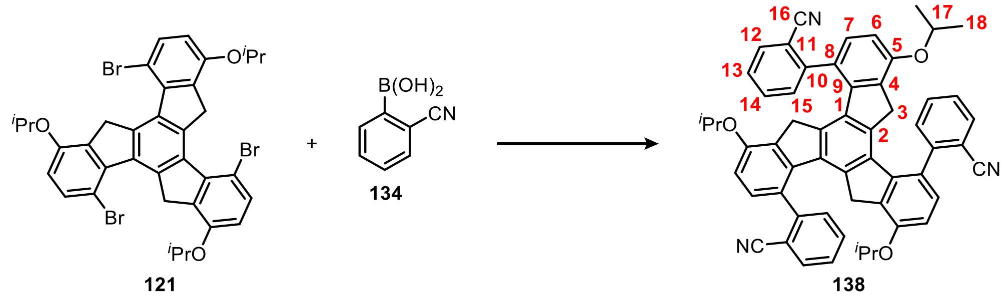

Compound 138:[184, 264] Under argon, boronic acid **134** (2.8 g, 19 mmol), XPhos (0.30 g, 0.63 mmol), and $Pd_2(dba)_3$ (0.15 g, 0.16 mmol) were dissolved in a mixture of degassed THF (32 mL) and a degassed potassium carbonate solution (2.0 M in H_2O, 16 mL). The solution was stirred for 5 min at room temperature, then tribromotruxene **121** (2.4 g, 3.2 mmol) was added, and the reaction was further stirred at 80 °C for 16 h under an argon atmosphere. After cooling to room temperature, water (70 mL) was added, and the aqueous phase was extracted with CH_2Cl_2 (3×70 mL). The combined organic layers were washed with water (2×100 mL) and a sat. sodium chloride solution (100 mL), dried over $MgSO_4$, and filtered. Removal of the solvent under reduced pressure left an orange solid, which was purified by flash column chromatography (SiO_2, PE/CH_2Cl_2 1:10, R_f = 0.38, 0.12) to give compound **138** as a beige solid in 46% yield (1.2 g, 1.5 mmol). ***R***$_{\mathbf{f}}$ = 0.38, 0.12 (PE/CH_2Cl_2 1:10); **m.p.** 226 °C (dec.); **^{1}H NMR** (600 MHz, $CDCl_3$): δ (ppm) = 7.99-7.98 (m, H-12/15), 7.95-7.92 (m, H-12/15), 7.80-7.80 (m, H-12/15), 7.73 (d, *J* = 7.8 Hz, H-12/15), 7.57-7.44 (m, H-13, 14), 7.35-7.33 (m, H-7, H-12/15), 7.30-7.28 (m, H-7), 7.14 (d, *J* = 8.3 Hz, H-7), 6.86-6.80 (m, H-6), 4.64-4.57 (m, H-17), 3.17 (d, *J* = 22.8 Hz, H-3), 3.06 (d, *J* = 22.4 Hz, H-3), 3.02 (d, *J* = 22.4 Hz, H-3), 2.96 (d, *J* = 22.8 Hz, H-3), 2.46 (d, *J* = 22.2 Hz, H-3), 2.42 (d, *J* = 22.4 Hz, H-3), 2.29 (d, *J* = 22.8 Hz, H-3), 2.20 (d, *J* = 22.8 Hz, H-3), 1.42-1.36 (m, H-18); **^{13}C NMR** (150 MHz, $CDCl_3$): δ (ppm) = 153.9-153.8 (C-5), 148.5-147.9 (C_q), 141.2-140.8 (C_q), 139.0 (C_q), 138.9 (C_q), 138.8 (C_q), 138.7 (C_q), 138.7 (C_q), 138.6 (C_q), 138.3 (C_q), 134.3-134.1 (C-12/15), 133.8-133.6 (C-12/15), 133.2 (C-12/15), 132.6-132.4 (C-13/14), 132.1 (C-13/14), 131.7 (C-12/15), 131.4-131.2 (C-7), 127.8-127.5 (C_q), 125.7-125.5 (C_q), 118.8-118.3 (CN), 114.3(C_q), 112.9 (C_q), 112.8 (C_q), 110.4-109.8 (C-6), 70.0-69.6 (C-17), 36.1-36.0 (C-3), 22.9-22.3 (C-18); **FT-IR** (ATR): $\tilde{\nu}$ (cm^{-1}) = 2976 (w), 2932 (w), 2226 (w), 1601 (m), 1572 (w), 1502 (m), 1474 (m), 1443 (w), 1412 (w), 1383 (w), 1371 (w), 1364 (w), 1335 (w), 1269 (s), 1188 (w), 1165 (w), 1136 (w), 1113 (s), 1084 (w), 1049 (m), 974 (m), 933 (w), 916 (w), 905 (w), 879 (w), 835 (w),

806 (m), 768 (s), 739 (w), 712 (w), 698 (w), 681 (w), 644 (w), 608 (w); **HRMS** (MALDI$^+$, DCTB): *m/z* calcd for $C_{57}H_{45}N_3O_3^+$: 819.3455 [*M*]$^+$; found: 819.3453; **elemental analysis** calcd (%) for $C_{57}H_{45}N_3O_3$+0.50 H_2O: C 82.58, H 5.59, N 5.07; found: C 82.75, H 5.88, N 4.95.

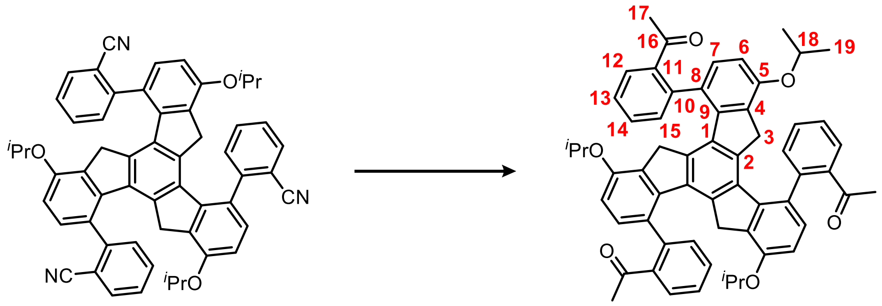

138 **139**

Compound 139:[264] In a flame-dried Schlenk tube, a suspension of nitrile **138** (325 mg, 396 µmol) in dry, degassed THF (3.50 mL) was cooled to 0 °C under argon, then methylmagnesium bromide (3 M in Et_2O, 2.50 mL, 7.50 mmol) was added dropwise. The Schlenk tube was sealed and stirring was continued for 15 h at 80 °C. After cooling to room temperature, the reaction was quenched with a saturated NH_4Cl solution (50 mL), and the aqueous layer was extracted with CH_2Cl_2 (3×20 mL). The combined organic layers were washed with a sat. sodium chloride solution (50 mL), dried over $MgSO_4$, filtered, and the solvents were removed under reduced pressure. Lastly, the residue was purified by flash column chromatography (SiO_2, CH_2Cl_2/MeOH 100:1, R_f = 0.33, 0.17, 0.02) to give compound **139** as a beige solid in 38% yield (131 mg, 150 µmol).

***R*$_f$** = 0.33, 0.17 (CH_2Cl_2/MeOH 100:1); **m.p.** 190 °C; **^{1}H NMR** (700 MHz, $CDCl_3$): δ (ppm) = 7.89-7.88 (m, H^{Ph}), 7.84 (d, *J* = 7.9 Hz, H^{Ph}), 7.69 (d, *J* = 7.8 Hz, H^{Ph}), 7.65 (t, *J* = 7.4 Hz, H^{Ph}), 7.61 (d, *J* = 7.4 Hz, H^{Ph}), 7.54-7.44 (m, H^{Ph}), 7.42-7.36 (m, H^{Ph}), 7.32-7.29 (m, H^{Ph}), 7.12 (d, *J* = 8.2 Hz, H-7), 6.95 (d, *J* = 8.3 Hz, H-7), 6.80-6.77 (m, H-6), 6.74-6.70 (m, H-6), 4.62-4.52 (m, H-18), 3.30 (d, *J* = 23.0 Hz, H-3), 3.18 (d, *J* = 23.2 Hz, H-3), 3.11 (d, *J* = 23.0 Hz, H-3), 3.01 (d, *J* = 23.1 Hz, H-3), 2.76 (d, *J* = 23.1 Hz, H-3), 2.64 (d, *J* = 23.1 Hz, H-3), 2.63 (d, *J* = 23.1 Hz, H-3), 2.61 (d, *J* = 23.1 Hz, H-3), 2.34-2.32 (m, H-17), 2.29-2.25 (m, H-17), 2.22-2.16 (m, H-17), 1.86-1.80 (m, H-17), 1.40-1.30 (m, H-19); **^{13}C NMR** (176 MHz, $CDCl_3$): δ (ppm) = 203.9-203.3 (C-16), 153.4-153.2 (C-5), 143.2-143.0 (C_q), 141.6 (C_q), 141.4 (C_q), 140.5-140.1 (C_q), 139.0 (C_q), 138.8 (C_q), 138.8-138.5 (C_q), 134.5-134.0 (C_q), 132.9-132.3 (C^{Ph}-H), 131.4-131.3 (C-7), 130.7-130.6 (C^{Ph}-H), 129.3 (C_q), 129.0 (C^{Ph}-H), 129.0 (C^{Ph}-H), 128.4 (C^{Ph}-H), 128.3-128.2 (C^{Ph}-H), 128.0 (C^{Ph}-H), 127.8 (C^{Ph}-H), 127.7 (C^{Ph}-H), 110.2-109.8 (C-6), 69.7-69.5 (C-18), 36.5-36.1 (C-3), 30.9-29.9 (C-17), 22.6-22.3 (C-19); **FT-IR** (ATR): $\tilde{\nu}$ (cm^{-1}) = 2974 (w), 2932 (w), 2874 (w), 1688 (m), 1674 (m), 1599 (m), 1570 (w), 1501 (m), 1474 (m), 1441 (w), 1412 (w), 1383 (w), 1371 (m), 1356 (m), 1267 (s), 1254 (s), 1665 (m), 1136 (w), 1111 (s), 1067 (m), 1045 (m), 1013 (w), 972 (s), 914 (w), 903 (w), 872 (w), 835 (m), 818 (m), 766 (s), 733 (m), 714 (w), 683 (w), 662 (w), 644 (w), 609 (w); **HRMS** (MALDI$^+$, DCTB): *m/z* calcd for $C_{60}H_{54}O_6$–H$^+$: 869.3837 [*M*–H]$^+$; found: 869.3830; *m/z* calcd for $C_{60}H_{54}O_6$+Na$^+$: 893.3813 [*M*+Na]$^+$; found: 893.3795; *m/z* calcd for $C_{60}H_{54}O_6$+K$^+$: 909.3552 [*M*+K]$^+$; found: 909.3537.

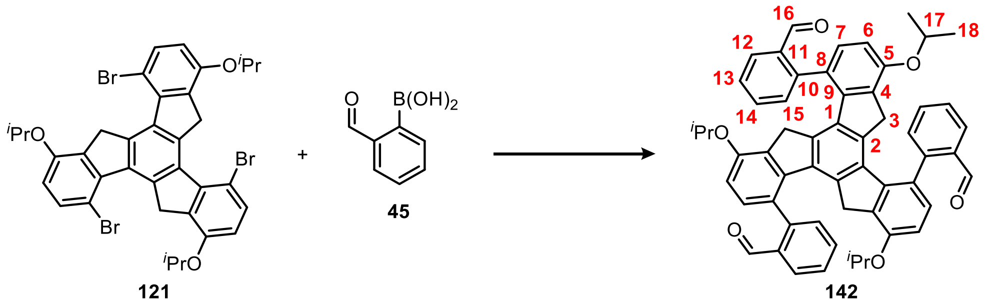

Compound 142:[184, 264] Under argon, boronic acid **45** (632 mg, 4.22 mmol), XPhos (114 mg, 240 µmol), $Pd_2(dba)_3$ (28.2 mg, 30.8 µmol), and tribromotruxene **121** (533 mg, 707 µmol) were dissolved in degassed THF (7.00 mL) and a degassed potassium carbonate solution (2.0 M in H_2O, 3.50 mL). The reaction was stirred for 16 h at 80 °C under an argon atmosphere. After cooling to room temperature, CH_2Cl_2 (50 mL) was added, and the organic phase was washed with water (20 mL), 1 M hydrochloric acid (20 mL), and a sat. sodium chloride solution (20 mL). The solvents of the organic layer were removed under reduced pressure, leaving an orange solid, which was purified by flash column chromatography (SiO_2, toluene/EA 100:1, R_f = 0.27, 0.20). The resulting yellow solid was dried *in vacuo* at 100 °C overnight to give compound **142** in 44% yield (255 mg, 308 µmol).

***R*$_\mathbf{f}$** = 0.27, 0.20 (Toluene/EA 100:1); **m.p.** 205 °C; **^{1}H NMR** (600 MHz, $CDCl_3$): δ (ppm) = 10.39 (s, C-16), 10.24 (s, C-16), 10.18 (s, C-16), 9.85 (s, C-16), 8.27 (dd, J = 7.8, 1.5 Hz, H^{Ph}), 8.20 (td, J = 7.5, 1.5 Hz, H^{Ph}), 7.78 (td, J = 7.5, 1.5 Hz, H^{Ph}), 7.69 (dd, J = 7.7, 1.2 Hz, H^{Ph}), 7.64-7.55 (m, H^{Ph}), 7.52-7.49 (m, H^{Ph}), 7.44 (dd, J = 7.1, 1.8 Hz, H^{Ph}), 7.36 (dd, J = 7.6, 1.3 Hz, H^{Ph}), 7.15 (d, J = 8.13 Hz, H-17), 7.08 (d, J = 7.8 Hz, H-7), 7.07 (d, J = 7.2 Hz, H-7), 6.79 (d, J = 8.3 Hz, H-6), 6.77 (d, J = 8.4, H-6), 6.77 (d, J = 8.4, H-6), 4.63-4.54 (m, H-17), 2.98 (d, J = 23.1 Hz, H-3), 2.91 (d, J = 23.2 Hz, H-3), 2.84 (d, J = 23.2 Hz, H-3), 2.79 (d, J = 23.1 Hz, H-3), 2.59 (d, J = 23.1 Hz, H-3), 2.54 (d, J = 23.2 Hz, H-3), 2.49 (d, J = 23.2 Hz, H-3), 2.42 (d, J = 23.0 Hz, H-3), 1.39-1.33 (m, H-18); **^{13}C NMR** (150 MHz, $CDCl_3$): δ (ppm) = 193.1-192.7 (C-16), 153.6-153.5 (C-5), 148.2-148.0 (C_q), 141.9-141.1 (C_q), 138.8-138.6 (C_q), 134.8 (C_q), 134.6 (C_q), 134.5-134.4 (C^{Ph}-H), 134.3 (C_q), 133.9 (C_q), 133.9 (C^{Ph}-H), 133.6 (C^{Ph}-H), 133.3 (C-7), 133.2 (C-7), 133.0 (C^{Ph}-H), 132.9-132.8 (C^{Ph}-H), 132.4 (C^{Ph}-H), 132.3 (C-7), 128.3-128.0 (C^{Ph}-H), 127.9-127.8 (C^{Ph}-H), 127.0 (C^{Ph}-H), 124.6-124.5 (C_q), 110.0-109.6 (C-6), 69.8-69.6 (C-17), 36.6-36.2 (C-3), 22.6-22.2 (C-18); **FT-IR** (ATR): $\tilde{\nu}$ (cm^{-1}) = 2974 (m), 2930 (m), 2897 (m), 2837 (m), 2745 (m), 1691 (s), 1597 (s), 1570 (m), 1499 (m), 1472 (s), 1448 (m), 1408 (m), 1385 (m), 1371 (m), 1362 (m), 1335 (m), 1265 (s), 1194 (s), 1165 (m), 1136 (m), 1111 (s), 1082 (m), 1049 (s), 1005 (m), 972 (s), 914 (m), 903 (m), 881 (m), 824 (s), 810 (s), 770 (s), 741 (s), 714 (m), 702 (m), 642 (m), 604 (m); **HRMS** (MALDI$^+$, DCTB): m/z calcd for $C_{57}H_{48}O_6^+$: 828.3445 $[M]^+$; found: 828.3436; **elemental analysis** calcd (%) for $C_{57}H_{48}O_6$: C 82.58, H 5.84; found: C 82.20, H 5.87.

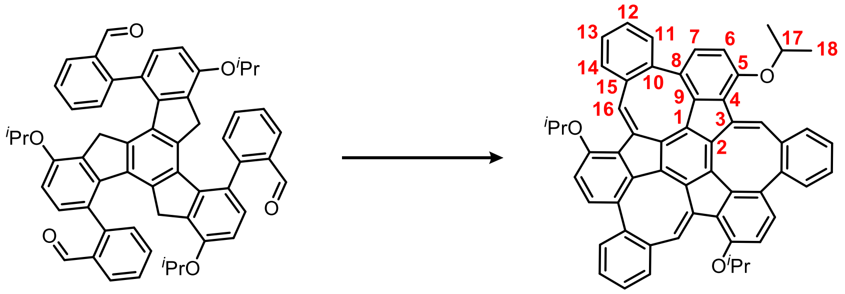

142 141

Compound 141:[184, 264] Under argon, trisaldehyde **142** (713 mg, 861 µmol) and potassium hydroxide (284 mg, 5.06 mmol) were filled in a flame-dried Schlenk flask. Dry, degassed THF (90 mL) was added, the flask was sealed, and the reaction was stirred for 16 h at 60 °C under an argon atmosphere. Subsequently, the reaction was acidified by addition of 6 M hydrochloric acid (10 mL), and the mixture was stirred for an additional 15 min at 60 °C. After cooling to room temperature, water (50 mL) was added, and the aqueous phase was extracted with CH_2Cl_2 (3×50 mL). The combined organic layers were dried over $MgSO_4$, filtered, and the solvents were removed under reduced pressure. The remaining dark brown solid was purified by flash column chromatography (SiO_2, PE/CH_2Cl_2 2:1, R_f = 0.26). Following, the obtained yellow solid was suspended in methanol (25 mL), ultrasonicated for 15 min, and collected by filtration. At last, washing the yellow solid with methanol (10 mL) and drying it *in vacuo* delivered the monkey saddle **141** in 72% yield (418 mg, 620 µmol).

R_f = 0.26 (PE/CH_2Cl_2 2:1); **m.p.** 330-333 °C (dec.); **^{1}H NMR** (700 MHz, $CDCl_3$): δ (ppm) = 8.38 (s, 3H, H-16), 7.25-7.22 (m, 6H, H-12, 13), 7.07 (d, J = 8.3 Hz, 3H, H-7), 7.02-7.01 (m, 3H, H-14), 6.97 (d, J = 8.4 Hz, 3H, H-6), 6.85-6.84 (m, 3H, H-11), 4.78 (sept, J = 6.1 Hz, 3H, H-17), 1.50 (d, J = 6.0 Hz, 9H, H-18), 1.41 (d, J = 6.0 Hz, 9H, H-18); **^{13}C NMR** (176 MHz, $CDCl_3$): δ (ppm) = 152.6 (C-5), 142.5 (C_q), 142.5 (C_q), 142.1 (C_q), 140.6 (C_q), 138.3 (C_q), 134.7 (C_q), 134.6 (C-11), 133.7 (C_q), 132.6 (C_q), 132.2 (C-16), 132.1 (C-7), 131.0 (C-14), 128.0 (C-12/13), 127.1 (C-12/13), 114.1 (C-6), 70.7 (C-17), 22.7 (C-18), 22.3 (C-18); **FT-IR** (ATR): $\tilde{\nu}$ (cm^{-1}) = 3053 (w), 3022 (w), 2974 (w), 2928 (w), 2870 (w), 1626 (w), 1578 (m), 1504 (m), 1481 (s), 1450 (w), 1433 (w), 1383 (m), 1371 (m), 1333 (m), 1304 (w), 1261 (s), 1225 (m), 1173 (w), 1161 (w), 1136 (w), 1107 (s), 1059 (w), 1040 (w), 982 (m), 959 (m), 951 (m), 937 (w), 918 (m), 889 (m), 862 (w), 849 (w), 824 (w), 808 (m), 783 (m), 752 (s), 735 (m), 694 (w), 677 (w), 654 (w), 642 (w), 635 (w), 625 (w), 608 (w); **UV/vis** (CH_2Cl_2): λ_{max} (lg ε) = 281 (5.08), 321 (4.56), 403 nm (4.47); **fluorescence** (CH_2Cl_2): λ_{ex} = 404 nm, λ_{em} = 537 nm; **HRMS** (MALDI$^+$, DCTB): *m/z* calcd for $C_{57}H_{42}O_3^+$: 774.3128 [*M*]$^+$; found: 774.3118; **elemental analysis** calcd (%) for $C_{57}H_{42}O_3$+H_2O: C 86.34, H 5.59; found: C 86.71, H 5.55.

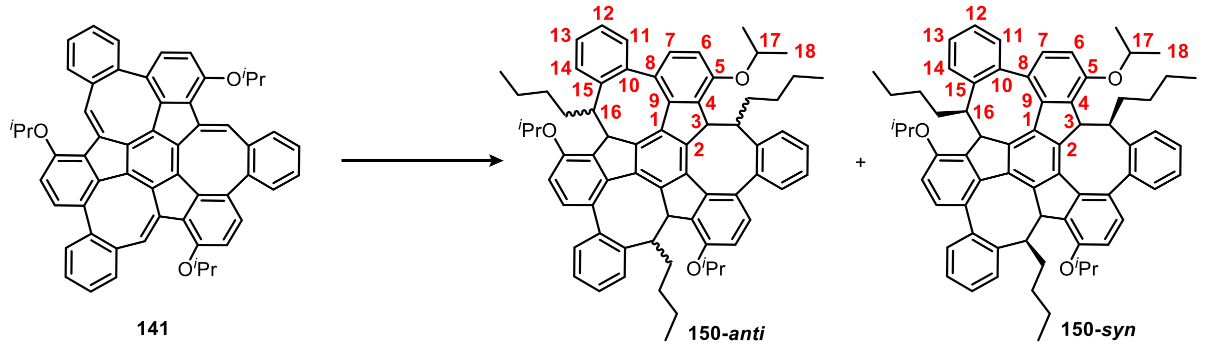

Compound 150: A flame-dried Schlenk tube was charged with monkey saddle **141** (271 mg, 350 µmol) and dry THF (21.0 mL) under argon. After the yellow solution was cooled to −84 °C using an ethyl acetate/N$_{2(l)}$ cooling bath, *n*-butyllithium (2.5 M in hexanes, 1.26 mL, 3.15 mmol) was added dropwise, upon which the solution turned dark red. The reaction was stirred for 4 h while being allowed to warm to 0 °C, then it was quenched with 1 M hydrochloric acid (50 mL), and the aqueous phase was extracted with CH$_2$Cl$_2$ (3×50 mL). The combined organic layers were washed with a sat. NaHCO$_3$ solution (100 mL), dried over MgSO$_4$, and filtered. Concentrating the filtrate under reduced pressure provided a brown solid, which was purified by flash column chromatography (SiO$_2$, PE/toluene 3:1, R_f = 0.22, 0.07), yielding two fractions of possible stereoisomers of **150**. The first fraction (R_f = 0.22) contained C_1-symmetrical isomers (denoted **150-*anti***) as a beige solid in 53% yield (179 mg, 188 µmol). The second fraction (R_f = 0.07) predominantly contained the C_3-symmetrical stereoisomers (denoted **150-*syn***) as a brown solid in 27% yield (92.0 mg, 96.9 µmol). Further separation of the C_3-symmetrical isomers from C_1-symmetrical ones in the **150-*syn***-fraction was not achieved. Thus, only the signals assignable to the C_3-symmetrical **150-*syn*** were considered in subsequent NMR analysis.

Compound 150-*anti*

***R*$_f$** = 0.22 (PE/toluene 3:1); **m.p.** 178-180 °C; **^{1}H NMR** (600 MHz, CDCl$_3$): δ (ppm) = 7.84 (dd, J = 6.8, 2.4 Hz, 1H, H-14), 7.79 (d, J = 7.7 Hz, 1H, H-11), 7.65 (dd, J = 7.2, 2.0 Hz, 1H, H-14), 7.61 (dd, J = 7.8, 1.4 Hz, 1H, H-14), 7.48 (dd, J = 6.8, 2.2 Hz, 1H, H-11), 7.46-7.42 (m, 2H, H-7, 12), 7.40 (dd, J = 7.1, 2.0 Hz, 1H, H-11), 7.37-7.30 (m, 6H, H-7, 12, 13), 7.28 (d, J = 8.5 Hz, 1H, H-7), 7.05-7.03 (m, 2H, H-6), 6.96 (d, J = 8.6 Hz, 1H, H-6), 4.90 (sept, J = 6.2 Hz, 1H, H-17), 4.83 (sept, J = 6.0 Hz, 1H, H-17), 4.78-4.73 (m, 2H, H-16, 17), 4.36 (s, 1H, H-3), 4.18 (s, 1H, H-3), 4.01-3.99 (m, 2H, H-3, 16), 3.62 (ddd, J = 9.1, 6.7, 2.6 Hz, 1H, H-16), 2.20-2.14 (m, 1H, *n*Bu-1), 1.76-1.71 (m, 9H, H-18), 1.68-1.56 (m, 3H, *n*Bu-1), 1.54-1.52 (m, 3H, H-18), 1.43-1.32 (m, 2H, *n*Bu-1), 1.32 (d, J = 6.0 Hz, 3H, H-18), 1.28 (d, J = 6.1 Hz, 3H, H-18), 1.17-0.96 (m, 6H, *n*Bu-2), 0.92-0.84 (m, 2H, *n*Bu-3), 0.83-0.66 (m, 4H, *n*Bu-3), 0.62 (t, J = 7.3 Hz, 3H, *n*Bu-4), 0.44 (t, J = 7.3 Hz, 3H, *n*Bu-4), 0.27 (t, J = 7.2 Hz, 3H, *n*Bu-4); **^{13}C NMR** (150 MHz, CDCl$_3$): δ (ppm) = 154.1 (C$_q$, C-5), 153.7 (C$_q$, C-5), 153.5 (C$_q$, C-5), 148.5 (C$_q$), 147.3 (C$_q$), 147.2 (C$_q$), 144.7 (C$_q$), 142.7 (C$_q$), 142.1 (C$_q$), 140.8 (C$_q$), 140.7 (C$_q$), 140.7 (C$_q$), 140.6 (C$_q$), 140.0 (C$_q$), 139.1 (C$_q$), 139.0 (C$_q$), 137.7 (C$_q$), 137.5 (C$_q$), 136.9 (C-7), 136.8 (C-11), 136.6 (C-7), 136.3 (C$_q$), 136.1 (C$_q$), 135.9 (C-7), 134.9 (C-11), 134.1 (C-14), 132.9 (C$_q$), 131.4 (C-14), 130.4 (C-14), 130.3 (C$_q$), 130.2 (C$_q$), 129.8 (C$_q$), 126.4 (C-12/13), 126.3 (C-12), 125.9 (C-12/13), 125.8 (C-12/13), 125.5 (C-12/13), 125.2 (C-12/13), 124.7 (C-11), 111.2 (C-6), 111.2 (C-6), 110.7 (C-6), 70.9 (C-17), 70.5 (C-17), 70.4 (C-17), 57.0 (C-3), 56.6 (C-3), 55.9 (C-3), 50.2 (C-16), 46.4 (C-16), 44.2 (C-16), 31.1 (*n*Bu-2), 30.7 (*n*Bu-2), 30.7 (*n*Bu-2), 28.3 (*n*Bu-1), 27.2 (*n*Bu-1), 26.8 (*n*Bu-1), 23.1 (*n*Bu-3), 23.0 (C-18), 22.9 (C-18), 22.9 (C-18), 22.7 (C-18), 22.7 (C-18), 22.6 (C-18), 22.5 (*n*Bu-3), 22.0 (*n*Bu-3), 14.1 (*n*Bu-4), 13.9 (*n*Bu-4), 13.5 (*n*Bu-4); **FT-IR** (ATR): $\tilde{\nu}$ (cm^{-1}) = 3055 (w), 2972 (w), 2955 (w), 2926 (w), 2868 (w), 2856 (w), 1591 (m), 1560 (w), 1479 (s), 1466 (m), 1383 (m), 1371 (m), 1333 (w), 1265 (s), 1219 (w), 1163 (m), 1113 (s), 1067 (w), 1055 (w), 1034 (w), 1001 (m), 936 (m), 912 (w), 829 (w), 806 (m), 777 (w), 756 (s), 667 (w); **UV/vis** (CH_2Cl_2): λ_{max} (lg ε) = 267 (4.97), 301 (4.77), 310 nm (4.76); **HRMS** (MALDI$^+$, DCTB): *m/z* calcd for $C_{69}H_{72}O_3^+$: 948.5476 [*M*]$^+$; found: 948.5458; **elemental analysis** calcd (%) for $C_{69}H_{72}O_3$: C 87.30, H 7.64; found: C 87.25, H 8.01.

Compound 150-*syn*

***R*$_f$** = 0.07 (PE/Toluene 3:1); **m.p.** 156-158 °C (dec.); **^{1}H NMR** (600 MHz, $CDCl_3$): δ (ppm) = 7.76-7.75 (m, 3H, H-14), 7.50-7.48 (m, 3H, H-11), 7.35-7.33 (m, 9H, H-7, 12, 13), 7.07-7.05 (m, 3H, H-6), 4.85 (sept, *J* = 6.1 Hz, 3H, H-17), 4.36-4.34 (m, 3H, H-16), 4.27 (s, 3H, H-3), 1.75 (d, *J* = 6.2 Hz, 9H, H-18), 1.72-1.68 (m, 3H, *n*Bu-1), 1.40 (d, *J* = 6.2 Hz, 9H, H-18), 1.01-0.96 (m, 3H, *n*Bu-1), 0.91-0.82 (m, 12H, *n*Bu-2, 3), 0.47-0.45 (m, 9H, *n*Bu-4); **^{13}C NMR** (150 MHz, $CDCl_3$): δ (ppm) = 153.7 (C-5), 147.5 (C_q), 140.8 (C_q), 140.7 (C_q), 139.8 (C_q), 139.4 (C_q), 137.0 (C_q), 136.8 (C-7), 135.6 (C-11), 131.0 (C-14), 129.8 (C_q), 125.9 (C-12/13), 125.7 (C-12/13), 111.9 (C-6), 71.2 (C-17), 56.2 (C-3), 49.0 (C-16), 31.0 (*n*Bu-2), 26.9 (*n*Bu-1), 23.1 (C-18), 22.7 (C-18), 22.3 (*n*Bu-3), 13.7 (*n*Bu-4); **FT-IR** (ATR): $\tilde{\nu}$ (cm^{-1}) = 3051 (w), 3026 (w), 2972 (m), 2957 (m), 2926 (m), 2870 (w), 2854 (w), 1591 (m), 1560 (w), 1493 (w), 1479 (s), 1466 (m), 1383 (m), 1371 (m), 1333 (w), 1267 (s), 1223 (w), 1165 (m), 1113 (s), 1070 (w), 1051 (w), 1032 (w), 1003 (m), 976 (w), 937 (m), 827 (w), 806 (m), 775 (w), 754 (s), 731 (m); **UV/vis** (CH_2Cl_2): λ_{max} (lg ε) = 267 (4.83), 304 nm (4.61); **HRMS** (MALDI$^+$, DCTB): *m/z* calcd for $C_{69}H_{72}O_3{-}H^+$: 947.5398 [*M*–H]$^+$; found: 947.5374; **elemental analysis** calcd (%) for $C_{69}H_{72}O_3$+0.5 H_2O: C 86.48, H 7.68; found: C 86.37, H 7.21.

Compounds of Chapter 3.6

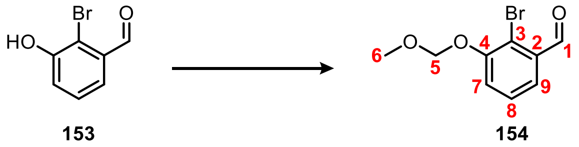

Compound 154: Based on a literature procedure,[309] a 250 mL Schlenk flask was flame dried and placed under an argon atmosphere. Benzaldehyde **153** (10 g, 50 mmol) and dry THF (125 mL) were added. The yellow solution was cooled to 0 °C before dry triethylamine (35 mL, 0.25 mol) was added. Subsequently, bromomethyl methyl ether (9.0 mL, 0.10 mol) was added dropwise, causing the precipitation of a colorless solid. Next, the cooling bath was removed, and the reaction was stirred for 22 h at room temperature under an argon atmosphere. The suspension was then mixed with water (300 mL), and the aqueous phase was extracted with CH_2Cl_2 (3×200 mL). The combined organic layers were dried over $MgSO_4$, filtered, and concentrated under reduced pressure. Lastly, the remaining light brown liquid was purified by flash column chromatography (SiO_2, PE/CH_2Cl_2 1:1, R_f = 0.19) to give compound **154** as a colorless oil in 71% yield (8.7 g, 35 mmol).

R_f = 0.19 (PE/CH_2Cl_2 1:1); **^{1}H NMR** (400 MHz, $CDCl_3$): δ (ppm) = 10.43 (d, *J* = 0.8 Hz, 1H, H-1), 7.58 (dd, *J* = 7.2, 2.0 Hz, 1H, H-9), 7.40-7.33 (m, 2H, H-7, 8), 5.29 (s, 2H, H-5), 3.54 (s, 3H, H-6); **^{13}C NMR** (100 MHz, $CDCl_3$): δ (ppm) = 192.2 (C-1), 154.4 (C-4), 135.1 (C-2), 128.5 (C-8), 123.0 (C-9), 121.4 (C-7), 118.2 (C-3), 95.5 (C-5), 56.7 (C-6); **FT-IR** (ATR): $\tilde{\nu}$ (cm^{-1}) = 2959 (w), 2905 (w), 2858 (w), 2827 (w), 1732 (w), 1691 (vs), 1568 (s), 1462 (m), 1437 (m), 1404 (w), 1383 (m), 1308 (w), 1292 (w), 1259 (vs), 1238 (s), 1205 (m), 1153 (vs), 1103 (m), 1086 (s), 1032 (s), 1009 (vs), 922 (s), 895 (vs), 785 (s), 771 (s), 708 (m), 654 (w); **MS** (APCI$^+$): *m/z* calcd for $C_9H_9BrO_3$+H$^+$: 244.9808 [*M*+H]$^+$; found: 244.9805; **elemental analysis** calcd (%) for $C_9H_9BrO_3$: C 44.11, H 3.70; found: C 44.34, H 3.82.

The analytical data is in accordance with the literature.[370]

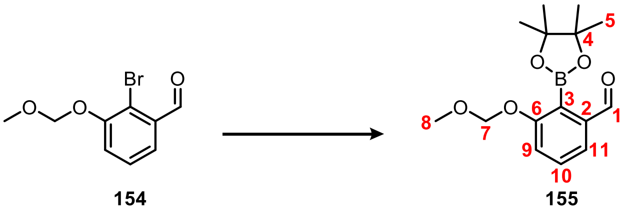

154 **155**

Compound 155:[306] A 250 mL Schlenk flask was flame dried and placed under an argon atmosphere. Potassium acetate (9.83 g, 100 mmol), B_2Pin_2 (11.9 g, 46.8 mmol), Pd(dppf)Cl_2 (2.44 g, 3.34 mmol), compound **154** (8.18 g, 33.4 mmol), and dry 1,4-dioxane (100 mL) were added. The flask was sealed, and the reaction was stirred for 6 days at 80 °C under an argon atmosphere. After cooling to room temperature, water (400 mL) was added, and the aqueous phase was extracted with CH_2Cl_2 (3×250 mL). The combined organic layers were washed with a sat. sodium chloride solution (500 mL), dried over $MgSO_4$, and filtered. Removal of the solvents under reduced pressure delivered a dark brown oil, which was first purified by flash column chromatography (SiO_2, CH_2Cl_2, R_f = 0.09). Excess B_2Pin_2 was subsequently removed *in vacuo* at 1×10^{-3} mbar and 120 °C before the product was distilled *in vacuo* at 1×10^{-3} mbar and 140 °C, giving compound **155** as a colorless liquid in 40% yield (3.89 g, 13.3 mmol).

R_f = 0.09 (CH_2Cl_2); **^{1}H NMR** (700 MHz, $CDCl_3$): δ (ppm) = 9.93 (s, 1H, H-1), 7.48-7.44 (m, 2H, H-10, 11), 7.30 (dd, *J* = 7.3, 1.7 Hz, 1H, H-9), 5.19 (s, 2H, H-7), 3.47 (s, 3H, H-8), 1.45 (s, 12H, H-5); **^{13}C NMR** (176 MHz, $CDCl_3$): δ (ppm) = 193.1 (C-1), 160.6 (C-6), 141.2 (C-2), 130.9 (C-10), 125.9 (C-11), 119.7 (C-9), 94.3 (C-7), 84.4 (C-4), 56.2 (C-8), 25.0 (C-5); **FT-IR** (ATR): $\tilde{\nu}$ (cm^{-1}) = 2976 (m, br), 2932 (w), 2827 (w), 1697 (s), 1597 (m), 1572 (m), 1474 (m), 1458 (m), 1391 (m), 1371 (m), 1337 (vs), 1308 (s), 1271 (m), 1246 (s), 1215 (m), 1144 (vs), 1109 (s), 1092 (m), 1059 (s), 1038 (s), 962 (m), 937 (vs), 856 (s), 825 (m), 789 (m), 746 (s), 731 (m), 677 (s); **MS** (APCI$^+$): *m/z* calcd for $C_{15}H_{21}BO_5$+H$^+$: 293.1555 [*M*+H]$^+$; found: 293.1558; **elemental analysis** calcd (%) for $C_{15}H_{21}BO_5$: C 61.67, H 7.25; found: C 61.28, H 7.47.

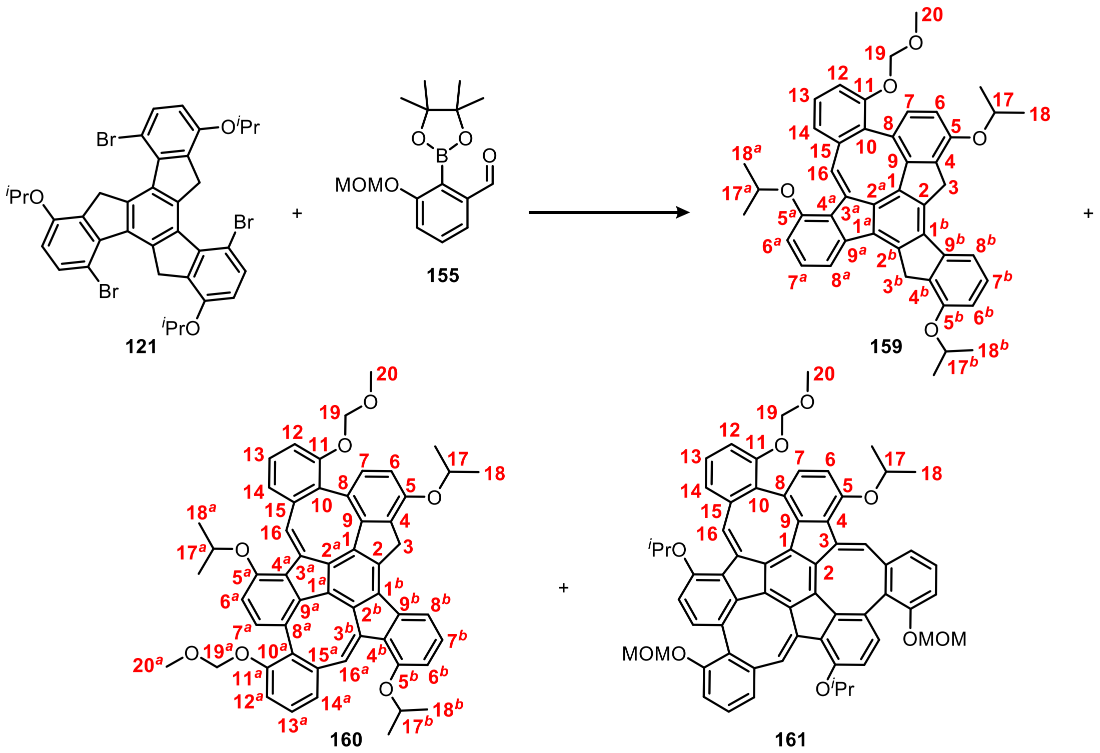

Compound 159, 160, and 161:[306] Boronic ester **155** (1.48 g, 5.00 mmol) was weighed in the reaction vessel. $Pd_2(dba)_3$ (45.8 mg, 50.0 µmol) and HP^{t}Bu$_3$BF$_4$ (58.0 mg, 200 µmol) were added, and the substances were placed under an argon atmosphere. Next, degassed THF (7.0 mL) and a degassed potassium carbonate solution (2.0 M in H_2O, 7.0 mL) were added, and the mixture was stirred for 5 min at room temperature. Tribromotruxene **121** (753 mg, 1.00 mmol) was added, the reaction vessel was sealed, and the reaction was stirred vigorously for 18 h at 80 °C under an argon atmosphere. After cooling to room temperature, water (10 mL) was added, and the aqueous phase was extracted with CH_2Cl_2 (3×20 mL). The combined organic layers were dried over $MgSO_4$, filtered, and the solvents were removed under reduced pressure. Following, the crude material was purified by flash column chromatography (SiO_2, CH_2Cl_2/NEt_3 100:2, R_f = 0.86, 0.79, 0.71, 0.65), furnishing an orange oil, which was suspended in methanol (25 mL) and ultrasonicated for a total of 45 min. After cooling the suspension to 0 °C, the precipitated light-yellow solid was collected by filtration, washed with methanol (5.0 mL), and dried *in vacuo*. The filtered solid was then transferred into a Schlenk tube under argon, and dry THF (66 mL) and potassium hydroxide (327 mg, 5.83 mmol) were added. The tube was sealed, and the reaction was stirred for 18 h at 80 °C under an argon atmosphere. Afterwards, water (75 mL) was added, and the mixture was stirred for an additional 40 min at 80 °C before cooling to room temperature. A sat. sodium chloride solution (40 mL) was added, and aqueous phase was extracted with CH_2Cl_2 (3×100 mL). The combined organic layers were dried over $MgSO_4$, filtered, and the solvents were removed under reduced pressure. The resulting dark brown solid was purified by flash column chromatography (SiO_2, PE/CH_2Cl_2 5:1 + 2% NEt_3 to 4:1 + 2% NEt_3, R_f = 0.28, 0.18, 0.10), yielding three fractions. Each fraction was suspended in methanol (15 mL), ultrasonicated for 15 min, filtered, and the solids were washed again with methanol (2 mL). Finally, drying the solids *in vacuo* gave compound **160** (R_f = 0.18) as a yellow solid in 19% yield (159 mg, 196 µmol) and monkey saddle **161** (R_f = 0.10) as a yellow solid in 17% yield (167 mg, 174 µmol). The first fraction (R_f = 0.28) contained minor amounts of **159**; an analytically pure sample of **159** was obtained only after further purification by chiral HPLC (Chiralpak® IE, *n*-heptane/EA/NEt_3 90:10:1 (*v*:*v*:*v*)).

Compound 159

$\boldsymbol{R_f}$ = 0.28 (PE/CH_2Cl_2 4:1 + 2% NEt_3); **m.p.** 155 °C (dec.); ^{1}**H NMR** (700 MHz, $CDCl_3$): δ (ppm) = 8.70 (s, 1H, H-16), 7.61 (d, *J* = 7.4 Hz, 1H, H-8^b), 7.50 (d, *J* = 7.4 Hz, 1H, H-8^a), 7.44 (t, *J* = 7.8 Hz, 1H, H-7^b), 7.31 (t, *J* = 7.8 Hz, 1H, H-7^a), 7.22 (d, *J* = 8.3 Hz, 1H, H-7), 7.20 (t, *J* = 7.9 Hz, 1H, H-13), 7.04 (d, *J* = 7.8 Hz, 1H, H-12), 6.93 (t, *J* = 7.0 Hz, 2H, H-6^a, 6^b), 6.89 (d, *J* = 8.2 Hz, 1H, H-6), 6.85 (d, *J* = 7.7 Hz, 1H, H-14), 4.82 (sept, *J* = 6.7 Hz, 1H, H-17), 4.72 (sept, *J* = 6.1 Hz, 2H, H-17^a, 17^b), 4.58 (d, *J* = 6.5 Hz, 1H, H-19), 4.55 (d, *J* = 6.3 Hz, 1H, H-19), 4.29 (d, *J* = 21.9 Hz, 1H, H-3), 4.20 (d, *J* = 21.8 Hz, 1H, H-3^b), 4.09 (d, *J* = 21.9 Hz, 1H, H-3^b), 3.98 (d, *J* = 21.8 Hz, 1H, H-3), 3.26 (s, 3H, H-20), 1.55 (d, *J* = 6.0 Hz, 3H, H-18), 1.47-1.44 (m, 12H, H-18^a, 18^b), 1.39 (d, *J* = 6.0 Hz, 3H, H-18); ^{13}**C NMR** (176 MHz, $CDCl_3$): δ (ppm) = 157.0 (C-11), 154.8 (C-5^b), 154.2 (C-5^a), 153.8 (C-5), 145.2 (C_q), 143.3 (C_q), 141.6 (C_q), 141.4 (C_q), 141.0 (C_q), 141.0 (C_q), 139.8 (C_q), 137.3 (C_q), 137.0 (C_q), 136.4 (C_q), 135.5 (C-7), 134.4 (C_q), 134.3 (C-16), 133.0 (C_q), 132.6 (C_q), 131.6 (C_q), 129.5 (C_q), 128.6 (C-7^b), 128.3 (C-7^a), 128.3 (C-13), 128.1 (C-14), 125.5 (C_q), 118.6 (C-12), 115.1 (C-8^b), 114.7 (C-8^a), 112.2 (C-6), 112.2 (C-6^a/6^b), 111.5 (C-6^a/6^b), 96.4 (C-19), 70.5 (C-17^b), 70.5 (C-17^a), 70.4 (C-17), 56.3 (C-20), 34.7 (C-3), 34.5 (C-3^b), 22.8 (C-18), 22.6 (C-18^a/18^b), 22.6 (C-18^a/18^b), 22.4 (C-18^a/18^b), 22.4 (C-18); **FT-IR** (ATR): $\tilde{\nu}$ (cm^{-1}) = 2972 (m), 2927 (w), 2898 (w), 2360 (s), 2341 (m), 1577 (s), 1480 (s), 1467 (m), 1449 (m), 1436 (m), 1381 (m), 1370 (m), 1271 (s), 1255 (s), 1243 (s), 1150 (m), 1136 (m), 1110 (s), 1061 (s), 1039 (s), 1017 (m), 982 (s), 969 (s), 934 (m), 909 (m), 786 (m), 738 (s), 721 (m); **UV/vis** (CH_2Cl_2): λ_{max} (lg ε) = 277 (4.85), 289 (4.79), 343 (4.17), 369 nm (4.15); **HRMS** (MALDI$^+$, DCTB): *m/z* calcd for $C_{45}H_{42}O_5^{+}$: 662.3027 [*M*]$^+$; found: 662.3027.

The enantiomers of **159** were separated by chiral HPLC (Chiralpak® IE, *n*-heptane/EA 90:10 (*v*/*v*), R_t: 6.0 min, 7.0 min). For separating the enantiomers by preparative HPLC, 1 *vol*% NEt_3 was added to the eluent.

Compound 160

$\boldsymbol{R_f}$ = 0.18 (PE/CH_2Cl_2 4:1 + 2% NEt_3); **m.p.** 215 °C (dec.); ^{1}**H NMR** (600 MHz, $CDCl_3$): δ (ppm) = 8.71 (s, 1H, H-16^a), 8.23 (s, 1H, H-16), 7.48 (d, *J* = 7.5 Hz, 1H, H-8^b), 7.34 (t, *J* = 7.8 Hz, 1H, H-7^b), 7.23 (t, *J* = 7.9 Hz, 1H, H-13/13^a), 7.21-7.18 (m, 2H, H-7, H-13/13^a), 7.11 (d, *J* = 8.4 Hz, 1H, H-7^a), 7.05 (dd, *J* = 8.1, 1.2 Hz, 1H, H-12/12^a), 7.02 (dd, *J* = 8.0, 1.2 Hz, 1H, H-12/12^a), 6.95 (d, *J* = 8.5 Hz, 1H, H-6), 6.91 (d, *J* = 8.2 Hz, 1H, H-6^b), 6.87 (d, *J* = 8.5 Hz, 1H, H-6^a), 6.84 (d, *J* = 7.3 Hz, 1H, H-14/14^a), 6.76 (dd, *J* = 7.9, 1.2 Hz, 1H, H-14/14^a), 4.85-4.64 (m, 7H, H-17, 17^a, 17^b, 19, 19^a), 4.23 (d, *J* = 22.1 Hz, 1H, H-3), 3.94 (d, *J* = 22.1 Hz, 1H, H-3), 3.26 (s, 3H, H-20/20^a), 3.22 (s, 3H, H-20/20^a), 1.54 (d, *J* = 6.0 Hz, 3H, H-18^b), 1.48 (d, *J* = 6.0 Hz, 3H, H-18/18^a), 1.47 (d, *J* = 6.0 Hz, 3H, H-18/18^a), 1.44 (d, *J* = 6.0 Hz, 3H, H-18^b), 1.40 (d, *J* = 6.1 Hz, 3H, H-18/18^a), 1.38 (d, *J* = 6.0 Hz, 3H, H-18/18^a); ^{13}**C NMR** (150 MHz, $CDCl_3$): δ (ppm) = 156.7 (C-11), 156.6 (C-11^a), 154.3 (C-5^b), 153.7 (C-5), 152.1 (C-5^a), 144.7 (C_q), 144.3 (C_q), 144.2 (C_q), 144.0 (C_q), 142.4 (C_q), 142.3 (C_q), 141.2 (C_q), 140.4 (C_q), 140.4 (C_q), 138.6 (C_q), 137.4 (C_q), 136.2 (C_q), 135.1 (C_q), 135.0 (C-7), 134.8 (C-16^a), 134.7 (C-7^a), 134.4 (C_q), 134.0 (C_q), 131.3 (C_q), 130.5 (C_q), 130.1 (C-16), 129.1 (C_q), 128.5 (C-7^b), 128.5 (C-13/13^a), 128.1 (C-13/13^a), 126.6 (C-14/14^a), 126.3 (C-14/14^a), 126.0 (C$_q$), 125.6 (C$_q$), 117.5 (C-12/12^a), 117.1 (C-12/12^a), 115.3 (C-8^b), 112.9 (C-6^a), 112.5 (C-6), 112.2 (C-6^b), 96.2 (C-19/19^a), 96.1 (C-19/19^a), 70.7 (H-17/17^a/17^b), 70.4 (C-17/17^a/17^b), 70.4 (C-17/17^a/17^b), 56.3 (C-20/20^a), 56.2 (C-20/20^a), 35.3 (C-3), 22.8 (C-18/18^a/18^b), 22.7 (C-18/18a/18^b), 22.4 (C-18/18^a/18^b), 22.3 (C-18/18^a/18^b); **FT-IR** (ATR): $\tilde{\nu}$ (cm^{-1}) = 2971 (m), 2928 (w), 2899 (w), 2822 (w), 2361 (s), 2341 (m), 1579 (s), 1498 (m), 1468 (m), 1443 (s), 1403 (w), 1383 (m), 1371 (m), 1333 (m), 1307 (w), 1240 (s), 1206 (m), 1150 (s), 1106 (s), 1082 (s), 1048 (s), 1034 (s), 976 (s), 959 (s), 923 (s), 898 (m), 879 (m), 807 (m), 780 (m), 765 (w), 735 (s); **UV/vis** (CH_2Cl_2): λ_{max} (lg ε) = 281 (4.92), 374 nm (4.44); **HRMS** (MALDI$^+$, DCTB): *m/z* calcd for $C_{54}H_{48}O_7^+$: 808.3395 [*M*]$^+$; found: 808.3377; **elemental analysis** calcd (%) for $C_{54}H_{48}O_7$+H_2O: C 78.43, H 6.09; found: C 78.32, H 6.03.

The enantiomers of **160** were separated by chiral HPLC (Chiralpak® IB, *n*-heptane/CH_2Cl_2/MTBE 80:10:10 (*v/v/v*), R_t: 7.7 min (R_a,R_a), 8.1 min (S_a,S_a)). For separating the enantiomers by preparative HPLC, 1 *vol*% NEt_3 was added to the eluent. (R_a,R_a)-**160**: **M.p.** 199 °C; $[\alpha]_D^{20}$ = +599.5 (in CH_2Cl_2). (S_a,S_a)-**160**: **M.p.** 195 °C; $[\alpha]_D^{20}$ = −435.9 (in CH_2Cl_2).

Compound 161

***R*$_f$** = 0.10 (PE/CH_2Cl_2 4:1 + 2% NEt_3); **m.p.** 242-244 °C (dec.); **^{1}H NMR** (600 MHz, CD_2Cl_2): δ (ppm) = 8.35 (s, 3H, H-16), 7.23 (t, *J* = 7.9 Hz, 3H, H-13), 7.10 (d, *J* = 8.6 Hz, 3H, H-7), 7.03 (dd, *J* = 8.1, 1.2 Hz, 3H, H-12), 6.98 (d, *J* = 8.5 Hz, 3H, H-6), 6.78 (d, *J* = 7.7 Hz, 3H, H-14), 4.88 (d, *J* = 6.5 Hz, 3H, H-19), 4.83 (sept, *J* = 6.0 Hz, 3H, H-17), 4.79 (d, *J* = 6.5 Hz, 3H, H-19), 3.26 (s, 9H, H-20), 1.51 (d, *J* = 6.1 Hz, 9H, H-18), 1.39 (d, *J* = 6.0 Hz, 9H, H-18); **^{13}C NMR** (150 MHz, CD_2Cl_2): δ (ppm) = 156.6 (C-11), 152.5 (C-5), 143.7 (C$_q$), 143.4 (C$_q$), 143.0 (C$_q$), 141.0 (C$_q$), 135.2 (C$_q$), 134.5 (C-7), 134.4 (C$_q$), 131.3 (C-16), 129.9 (C$_q$), 128.6 (C-13), 126.0 (C$_q$), 124.9 (C-14), 116.0 (C-12), 113.3 (C-6), 96.0 (C-19), 70.9 (C-17), 56.4 (C-20), 22.7 (C-18), 22.2 (C-18); **FT-IR** (ATR): $\tilde{\nu}$ (cm^{-1}) = 2971 (m), 2928 (w), 2899 (w), 2361 (s), 2341 (m), 1579 (s), 1498 (m), 1468 (m), 1443 (s), 1383 (m), 1371 (m), 1333 (m), 1240 (s), 1206 (m), 1150 (s), 1106 (s), 1082 (s), 1048 (s), 1034 (s), 976 (s), 959 (s), 923 (s), 898 (m), 879 (m), 807 (m), 780 (m), 765 (w), 735 (s); **UV/vis** (CH_2Cl_2): λ_{max} (lg ε) = 281 (5.06), 328 (4.61), 400 nm (4.54); **fluorescence** (CH_2Cl_2): λ_{ex} = 400 nm, λ_{em} = 503, 535 nm; **HRMS** (MALDI$^+$, DCTB): *m/z* calcd for $C_{63}H_{54}O_9^+$: 954.3762 [*M*]$^+$; found: 954.3756; **elemental analysis** calcd (%) for $C_{63}H_{54}O_9$: C 79.23, H 5.70; found: C 79.00, H 5.79.

The enantiomers of **161** were separated by chiral HPLC (Chiralpak® IE, *n*-heptane/CH_2Cl_2 50:50 (*v/v*), R_t: 4.7 min (R_a,R_a,R_a), 5.2 min (S_a,S_a,S_a)). For separating the enantiomers by preparative HPLC, 1 *vol*% NEt_3 was added to the eluent. (R_a,R_a,R_a)-**161**: **M.p.** 220 °C (dec.); $[\alpha]_D^{20}$ = +660.9 (in CH_2Cl_2). (S_a,S_a,S_a)-**161**: **M.p.** 215 °C (dec.); $[\alpha]_D^{20}$ = −586.4 (in CH_2Cl_2).

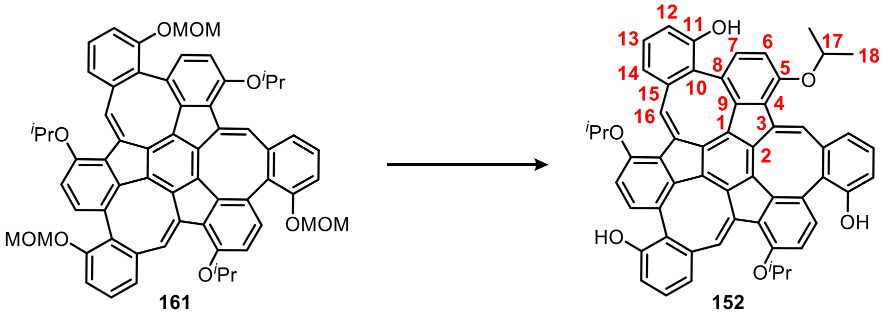

161 **152**

Compound 152:[306] Monkey saddle **161** (27 mg, 28 µmol) was suspended in *n*-heptane (5.0 mL) and 6 M hydrochloric acid (0.50 mL). The mixture was ultrasonicated for 5 min, then it was stirred for 43 h at 80 °C. After removal of the solvents under reduced pressure, the remaining brown solid was purified by flash column chromatography (SiO_2, CH_2Cl_2, R_f = 0.51) to give monkey saddle **152** as a brown solid in 34% yield (8.0 mg, 9.7 µmol). An analytically pure sample of **152** was obtained by recycling HPLC (SiO_2, CH_2Cl_2).

***R*$_f$** = 0.51 (CH_2Cl_2); **m.p.** 280 °C (dec.); **^{1}H NMR** (600 MHz, $CDCl_3$): δ (ppm) = 8.41 (s, 3H, H-16), 7.17 (t, *J* = 7.5 Hz, 3H, H-13), 7.15 (d, *J* = 7.7 Hz, 3H, H-7), 7.02 (d, *J* = 8.4 Hz, 3H, H-6), 6.89 (dd, *J* = 8.0, 1.3 Hz, 3H, H-12), 6.69 (d, *J* = 7.6 Hz, 3H, H-14), 4.80 (s, 3H, OH), 4.80 (sept, *J* = 6.1 Hz, 3H, H-17), 1.53 (d, *J* = 6.0 Hz, 9H, H-18), 1.40 (d, *J* = 6.0 Hz, 9H, H-18); **^{13}C NMR** (150 MHz, $CDCl_3$): δ (ppm) = 154.6 (C_q, C-11), 152.8 (C_q, C-5), 144.5 (C_q, C-9), 142.7 (C_q, C-1), 141.8 (C_q, C-2), 139.7 (C_q, C-15), 135.6 (C_q, C-3), 135.3 (C_q, C-4), 132.9 (C-16), 130.8 (C-7), 129.0 (C-13), 125.1 (C_q, C-10), 123.7 (C_q, C-8), 123.3 (C-14), 115.7 (C-12), 113.9 (C-6), 70.9 (C-17), 22.7 (C-18), 22.1 (C-18); **FT-IR** (ATR): $\tilde{\nu}$ (cm^{-1}) = 3522 (w), 2972 (m), 2928 (w), 2363 (w), 2359 (w), 2339 (w), 1716 (w), 1575 (s), 1500 (w), 1477 (m), 1439 (s), 1384 (m), 1371 (m), 1334 (m), 1258 (s), 1241 (s), 1160 (m), 1136 (m), 1103 (s), 1078 (m), 1044 (m), 1021 (m), 957 (s), 933 (w), 914 (m), 897 (m), 876 (w), 866 (m), 805 (m), 776 (s), 744 (m), 732 (s), 607 (m); **UV/vis** (CH_2Cl_2): λ_{max} (lg ε) = 278 (5.08), 335 (4.63), 400 nm (4.60); **fluorescence** (CH_2Cl_2): λ_{ex} = 277 nm, λ_{em} = 504, 534 nm; **HRMS** (MALDI$^+$, DCTB): *m/z* calcd for $C_{57}H_{42}O_6^+$: 822.2976 [*M*]$^+$; found: 822.2983; **elemental analysis** calcd (%) for $C_{57}H_{42}O_6$+H_2O: C 81.41, H 5.27; found: C 81.02, H 4.87.

The enantiomers of **152** were separated by chiral HPLC (Chiralpak® IE, *n*-heptane/EA 70:30 (*v/v*), R_t: 4.7 min (R_a,R_a,R_a), 6.3 min (S_a,S_a,S_a)). (R_a,R_a,R_a)-**152**: **M.p.** 270 °C (dec.); $[\boldsymbol{\alpha}]_{\mathbf{D}}^{\mathbf{20}}$ = +1012.9 (in CH_2Cl_2). (S_a,S_a,S_a)-**152**: **M.p.** 273 °C (dec.); $[\boldsymbol{\alpha}]_{\mathbf{D}}^{\mathbf{20}}$ = −1052.5 (in CH_2Cl_2).

Compounds of Chapter 3.7

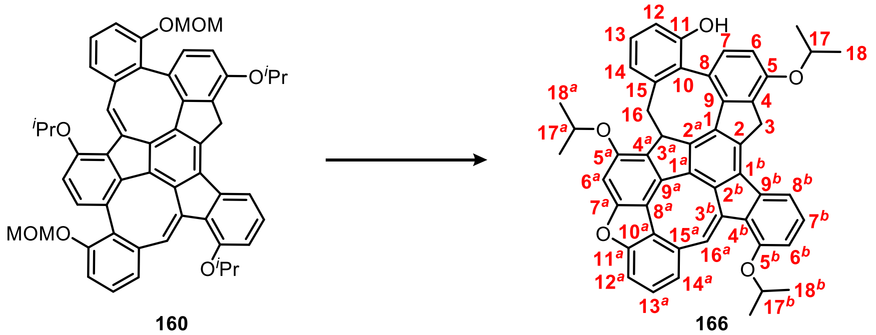

160 **166**

Compound 166:[306] A solution of compound **160** (0.13 g, 0.16 mmol) in THF (5.0 mL) was mixed with 6 M hydrochloric acid (2.5 mL). The reaction was stirred for 3 h at 60 °C, during which a red suspension formed. After cooling to room temperature, water (10 mL) was added, and the aqueous phase was extracted with CH_2Cl_2 (3×20 mL). The combined organic layers were washed with water (50 mL), dried over $MgSO_4$, and filtered. Concentrating the filtrate under reduced pressure left a red oil, which was purified by flash column chromatography (SiO_2, PE/CH_2Cl_2 1:1, R_f = 0.17). The obtained red solid was suspended in methanol (10 mL), ultrasonicated for 15 min, and collected by filtration. Finally, washing the red solid with methanol (5.0 mL) and drying it *in vacuo* delivered compound **166** in 60% yield (70 mg, 97 µmol).

$\boldsymbol{R_f}$ = 0.17 (PE/CH_2Cl_2 1:1); **m.p.** 245 °C (dec.); **^{1}H NMR** (600 MHz, $CDCl_3$): δ (ppm) = 8.44 (s, 1H, H-16^a), 7.43 (dd, J = 7.6, 1.4 Hz, 1H, H-14), 7.37 (d, J = 8.2 Hz, 1H, H-7/8^b), 7.36 (d, J = 8.4 Hz, 1H, H-7/8^b), 7.27 (t, J = 7.8 Hz, 1H, H-13), 7.12 (t, J = 7.7 Hz, 1H, H-7^b), 7.07 (dd, J = 7.8, 7.8 Hz, 1H, H-13^a), 6.98 (dd, J = 8.0, 1.3 Hz, 1H, H-12), 6.96 (d, J = 8.4 Hz, 1H, H-6), 6.94 (t, J = 7.8 Hz, 1H, H-12^a), 6.74-6.73 (m, 1H, H-14^a), 6.73-6.72 (m, 1H, H-6^b), 6.70 (s, 1H, H-6^a), 5.50 (s, 1H, OH), 4.76 (sept, J = 6.1 Hz, 1H, H-17), 4.72 (sept, J = 6.0 Hz, 1H, H-17^a), 4.63 (sept, J = 6.1 Hz, 1H, H-17^b), 4.02 (d, J = 22.2 Hz, 1H, H-3), 3.97 (d, J = 22.2 Hz, 1H, H-3), 3.46 (dd, J = 13.3, 1.7 Hz, 1H, H-16), 3.41 (m, 1H, H-3^a), 2.94 (m, 1H, H-16), 1.64 (d, J = 6.1 Hz, 3H, H-18^a), 1.56 (d, J = 6.0 Hz, 3H, H-18^a), 1.56 (d, J = 6.0 Hz, 3H, H-18), 1.47 (d, J = 6.1 Hz, 3H, H-18), 1.46 (d, J = 6.0 Hz, 3H, H-18^b), 1.42 (d, J = 6.0 Hz, 3H, H-18^b); **^{13}C NMR** (150 MHz, $CDCl_3$): δ (ppm) = 158.0 (C_q, C-7^a), 156.1 (C_q, C-11^a),155.4 (C_q, C-5^a), 156.4 (C_q, C-5^b), 156.4 (C_q, C-11), 153.8 (C_q,C-5), 146.2 (C_q, C-15), 143.7 (C_q), 142.5 (C_q, C-9), 140.9 (C_q, C-9^b), 139.0 (C_q, C-1), 137.5 (C_q, C-1^b), 137.4 (C_q), 136.9 (C_q), 135.8 (C_q, C-4), 135.5 (C_q), 135.4 (C_q), 134.4 (C_q), 133.0 (C-7/8^b), 132.1 (C_q), 131.9 (C_q), 131.4 (C-14^a), 131.3 (C_q), 129.0 (C_q, C-4^b), 128.0 (C-13), 127.6 (C-7^b), 126.5 (C_q, C-10), 125.7 (C-12^a), 122.7 (C_q, C-10^a), 121.8 (C_q), 121.7 (C-14), 114.7 (C-7/8^b), 114.0 (C-12), 112.6 (C-13^a), 112.5 (C-6^b), 112.2 (C_q), 111.1 (C-6), 95.0 (C-6^a), 70.8 (C-17^a), 70.6 (C-17^b), 70.4 (C-17), 53.4 (C-3^a), 35.0 (C-3), 33.7 (C-16), 22.8 (C-18/18^a/18^b), 22.8 (C-18/18^a/18^b), 22.7 (C-18/18^a/18^b), 22.6 (C-18/18^a/18^b), 22.5 (C-18/18^a/18^b), 22.5 (C-18/18^a/18^b); **FT-IR** (ATR): $\tilde{\nu}$ (cm^{-1}) = 3391 (w), 2973 (m), 2929 (m), 2868 (w), 2084 (w), 1626 (m), 1592 (m), 1578 (s), 1483 (m), 1452 (s), 1380 (s), 1371 (m), 1357 (m), 1290 (s), 1272 (s), 1257 (m), 1243 (s), 1173 (m), 1159 (m), 1136 (m), 1113 (s), 1072 (m), 1065 (m), 1030 (m), 1014 (m), 1004 (m), 957 (m), 915 (m), 809 (m), 782 (s), 753 (s), 741 (s), 728 (m); **UV/vis** (CH_2Cl_2): λ_{max} (lg ε) = 286 (4.88), 339 (4.56), 360 (4.42), 386 (4.37), 430 (3.98), 453 (3.85), 486 (3.55), 518 (3.53), 556 nm (3.29); **HRMS** (MALDI$^+$, DCTB): *m/z* calcd for $C_{50}H_{40}O_5^+$: 720.2870 [*M*]$^+$; found: 720.2880; **elemental analysis** calcd (%) for $C_{50}H_{40}O_5$+0.5 H_2O: C 82.28, H 5.66; found: C 82.18, H 5.71.

The enantiomers of **166** were separated by chiral HPLC (Chiralpak® IE, CH_2Cl_2, R_t: 3.9 min (*R*), 5.6 min (*S*)).
(*R*)-**166**: **M.p.** 202 °C; (*S*)-**166**: **M.p.** 207 °C.

6 References

[1] J. Rouquerol, D. Avnir, C. W. Fairbridge, D. H. Everett, J. M. Haynes, N. Pernicone, J. D. F. Ramsay, K. S. W. Sing, K. K. Unger, *Pure Appl. Chem.* **1994**, *66*, 1739-1758.

[2] X. Yang, Z. Ullah, J. F. Stoddart, C. T. Yavuz, *Chem. Rev.* **2023**, *123*, 4602-4634.

[3] D. Hu, J. Zhang, M. Liu, *Chem. Commun.* **2022**, *58*, 11333-11346.

[4] A. U. Czaja, N. Trukhan, U. Müller, *Chem. Soc. Rev.* **2009**, *38*, 1284-1293.

[5] I. I. Ivanova, E. E. Knyazeva, *Chem. Soc. Rev.* **2013**, *42*, 3671-3688.

[6] W. Hölderich, M. Hesse, F. Näumann, *Angew. Chem. Int. Ed.* **1988**, *27*, 226-246.

[7] F. Schwochow, L. Puppe, *Angew. Chem. Int. Ed.* **1975**, *14*, 620-628.

[8] S. L. James, *Chem. Soc. Rev.* **2003**, *32*, 276-288.

[9] O. M. Yaghi, H. Li, *J. Am. Chem. Soc.* **1995**, *117*, 10401-10402.

[10] H. Li, M. Eddaoudi, T. L. Groy, O. M. Yaghi, *J. Am. Chem. Soc.* **1998**, *120*, 8571-8572.

[11] H. Li, M. Eddaoudi, M. O'Keeffe, O. M. Yaghi, *Nature* **1999**, *402*, 276-279.

[12] O. K. Farha, I. Eryazici, N. C. Jeong, B. G. Hauser, C. E. Wilmer, A. A. Sarjeant, R. Q. Snurr, S. T. Nguyen, A. Ö. Yazaydın, J. T. Hupp, *J. Am. Chem. Soc.* **2012**, *134*, 15016-15021.

[13] M. Mastalerz, *Angew. Chem. Int. Ed.* **2008**, *47*, 445-447.

[14] S.-Y. Ding, W. Wang, *Chem. Soc. Rev.* **2013**, *42*, 548-568.

[15] M. S. Lohse, T. Bein, *Adv. Funct. Mater.* **2018**, *28*, 1705553.

[16] H. M. El-Kaderi, J. R. Hunt, J. L. Mendoza-Cortés, A. P. Côté, R. E. Taylor, M. O'Keeffe, O. M. Yaghi, *Science* **2007**, *316*, 268-272.

[17] J.-M. Lehn, *Chem. Eur. J.* **1999**, *5*, 2455-2463.

[18] S. J. Rowan, S. J. Cantrill, G. R. L. Cousins, J. K. M. Sanders, J. F. Stoddart, *Angew. Chem. Int. Ed.* **2002**, *41*, 898-952.

[19] P. T. Corbett, J. Leclaire, L. Vial, K. R. West, J.-L. Wietor, J. K. M. Sanders, S. Otto, *Chem. Rev.* **2006**, *106*, 3652-3711.

[20] J.-M. Lehn, *Chem. Soc. Rev.* **2007**, *36*, 151-160.

[21] A. P. Côté, A. I. Benin, N. W. Ockwig, M. O'Keeffe, A. J. Matzger, O. M. Yaghi, *Science* **2005**, *310*, 1166-1170.

[22] M. Mastalerz, *Angew. Chem. Int. Ed.* **2010**, *49*, 5042-5053.

[23] M. Mastalerz, *Chem. Eur. J.* **2012**, *18*, 10082-10091.

[24] G. Zhang, M. Mastalerz, *Chem. Soc. Rev.* **2014**, *43*, 1934-1947.

[25] F. Beuerle, B. Gole, *Angew. Chem. Int. Ed.* **2018**, *57*, 4850-4878.

[26] Z. Xu, Y. Ye, Y. Liu, H. Liu, S. Jiang, *Chem. Commun.* **2024**, *60*, 2261-2282.

[27] S.-D. Guo, T. Jiao, D.-S. Guo, K. Cai, *Smart Mol.* **2025**, *3*, e20240038.

[28] T. Tozawa, J. T. A. Jones, S. I. Swamy, S. Jiang, D. J. Adams, S. Shakespeare, R. Clowes, D. Bradshaw, T. Hasell, S. Y. Chong, C. Tang, S. Thompson, J. Parker, A. Trewin, J. Bacsa, A. M. Z. Slawin, A. Steiner, A. I. Cooper, *Nat. Mater.* **2009**, *8*, 973-978.

[29] T. Hasell, A. I. Cooper, *Nat. Rev. Mater.* **2016**, *1*, 16053.

[30] J. C. Lauer, A. S. Bhat, C. Barwig, N. Fritz, T. Kirschbaum, F. Rominger, M. Mastalerz, *Chem. Eur. J.* **2022**, *28*, e202201527.

[31] M. Holsten, S. Feierabend, S. M. Elbert, F. Rominger, T. Oeser, M. Mastalerz, *Chem. Eur. J.* **2021**, *27*, 9383-9390.

[32] A. G. Slater, A. I. Cooper, *Science* **2015**, *348*, aaa8075.

[33] Q. Song, S. Jiang, T. Hasell, M. Liu, S. Sun, A. K. Cheetham, E. Sivaniah, A. I. Cooper, *Adv. Mater.* **2016**, *28*, 2629-2637.

[34] S. Wuttke, D. D. Medina, J. M. Rotter, S. Begum, T. Stassin, R. Ameloot, M. Oschatz, M. Tsotsalas, *Adv. Funct. Mater.* **2018**, *28*, 1801545.

[35] J. T. A. Jones, T. Hasell, X. Wu, J. Bacsa, K. E. Jelfs, M. Schmidtmann, S. Y. Chong, D. J. Adams, A. Trewin, F. Schiffman, F. Cora, B. Slater, A. Steiner, G. M. Day, A. I. Cooper, *Nature* **2011**, *474*, 367-371.

[36] M. Liu, L. Zhang, M. A. Little, V. Kapil, M. Ceriotti, S. Yang, L. Ding, D. L. Holden, R. Balderas-Xicohténcatl, D. He, R. Clowes, S. Y. Chong, G. Schütz, L. Chen, M. Hirscher, A. I. Cooper, *Science* **2019**, *366*, 613-620.

[37] S. Yu, S. Yang, M. Yang, J. Yang, Z. Song, D. Hu, H. Ji, Z. Jia, M. Liu, *Angew. Chem. Int. Ed.* **2025**, *64*, e202420086.

[38] M. L. C. Quan, D. J. Cram, *J. Am. Chem. Soc.* **1991**, *113*, 2754-2755.

[39] X. Liu, Y. Liu, G. Li, R. Warmuth, *Angew. Chem. Int. Ed.* **2006**, *45*, 901-904.

[40] X. Liu, R. Warmuth, *J. Am. Chem. Soc.* **2006**, *128*, 14120-14127.

[41] K. E. Jelfs, X. Wu, M. Schmidtmann, J. T. A. Jones, J. E. Warren, D. J. Adams, A. I. Cooper, *Angew. Chem. Int. Ed.* **2011**, *50*, 10653-10656.

[42] M. Mastalerz, M. W. Schneider, I. M. Oppel, O. Presly, *Angew. Chem. Int. Ed.* **2011**, *50*, 1046-1051.

[43] S. Klotzbach, T. Scherpf, F. Beuerle, *Chem. Commun.* **2014**, *50*, 12454-12457.

[44] S. M. Elbert, F. Rominger, M. Mastalerz, *Chem. Eur. J.* **2014**, *20*, 16707-16720.

[45] G. Zhang, O. Presly, F. White, I. M. Oppel, M. Mastalerz, *Angew. Chem. Int. Ed.* **2014**, *53*, 5126-5130.

[46] G. Zhang, O. Presly, F. White, I. M. Oppel, M. Mastalerz, *Angew. Chem. Int. Ed.* **2014**, *53*, 1516-1520.

[47] S. Klotzbach, F. Beuerle, *Angew. Chem. Int. Ed.* **2015**, *54*, 10356-10360.

[48] K. Tian, S. M. Elbert, X.-Y. Hu, T. Kirschbaum, W.-S. Zhang, F. Rominger, R. R. Schröder, M. Mastalerz, *Adv. Mater.* **2022**, *34*, 2202290.

[49] P. H. Kirchner, L. Schramm, S. Ivanova, K. Shoyama, F. Würthner, F. Beuerle, *J. Am. Chem. Soc.* **2024**, *146*, 5305-5315.

[50] D. Shao, L. Feng, W. Wang, K. Su, D. Yuan, *Angew. Chem. Int. Ed.* **2025**, e202514219.

[51] Y. Jin, Q. Wang, P. Taynton, W. Zhang, *Acc. Chem. Res.* **2014**, *47*, 1575-1586.

[52] T. P. Moneypenny, N. P. Walter, Z. Cai, Y.-R. Miao, D. L. Gray, J. J. Hinman, S. Lee, Y. Zhang, J. S. Moore, *J. Am. Chem. Soc.* **2017**, *139*, 3259-3264.

[53] F. Pennella, R. L. Banks, G. C. Bailey, *Chem. Commun.* **1968**, 1548-1549.

[54] A. Mortreux, M. Blanchard, *J. Chem. Soc., Chem. Commun.* **1974**, 786-787.

[55] T. J. Katz, J. McGinnis, *J. Am. Chem. Soc.* **1975**, *97*, 1592-1594.

[56] P. Jean-Louis Hérisson, Y. Chauvin, *Makromol. Chem.* **1971**, *141*, 161-176.

[57] W. Zhang, J. S. Moore, *Adv. Synth. Catal.* **2007**, *349*, 93-120.

[58] J. H. Wengrovius, J. Sancho, R. R. Schrock, *J. Am. Chem. Soc.* **1981**, *103*, 3932-3934.

[59] S. F. Pedersen, R. R. Schrock, M. R. Churchill, H. J. Wasserman, *J. Am. Chem. Soc.* **1982**, *104*, 6808-6809.

[60] R. R. Schrock, *Acc. Chem. Res.* **1986**, *19*, 342-348.

[61] W. Zhang, J. S. Moore, *J. Am. Chem. Soc.* **2004**, *126*, 12796.

[62] J. Heppekausen, R. Stade, R. Goddard, A. Fürstner, *J. Am. Chem. Soc.* **2010**, *132*, 11045-11057.

[63] A. Fürstner, *Angew. Chem. Int. Ed.* **2013**, *52*, 2794-2819.

[64] C. C. Pattillo, M. M. Cencer, J. S. Moore, *Org. Synth.* **2018**, *95*, 231-239.

[65] W. Zhang, S. Kraft, J. S. Moore, *J. Am. Chem. Soc.* **2004**, *126*, 329-335.

[66] Q. Wang, C. Zhang, B. C. Noll, H. Long, Y. Jin, W. Zhang, *Angew. Chem. Int. Ed.* **2014**, *53*, 10663-10667.

[67] S. Lee, A. Yang, T. P. Moneypenny, J. S. Moore, *J. Am. Chem. Soc.* **2016**, *138*, 2182-2185.

[68] T. P. Moneypenny, A. Yang, N. P. Walter, T. J. Woods, D. L. Gray, Y. Zhang, J. S. Moore, *J. Am. Chem. Soc.* **2018**, *140*, 5825-5833.

[69] C. C. Pattillo, J. S. Moore, *Chem. Sci.* **2019**, *10*, 7043-7048.

[70] H. Yang, Z. Liu, W. Zhang, *Adv. Synth. Catal.* **2013**, *355*, 885-890.

[71] Y. Du, H. Yang, C. Zhu, M. Ortiz, K. D. Okochi, R. Shoemaker, Y. Jin, W. Zhang, *Chem. Eur. J.* **2016**, *22*, 7959-7963.

[72] M. Cui, W. Bai, H. H. Y. Sung, I. D. Williams, G. Jia, *J. Am. Chem. Soc.* **2020**, *142*, 13339-13344.

[73] S. Lee, E. Chénard, D. L. Gray, J. S. Moore, *J. Am. Chem. Soc.* **2016**, *138*, 13814-13817.

[74] X. Jiang, S. D. Laffoon, D. Chen, S. Pérez-Estrada, A. S. Danis, J. Rodríguez-López, M. A. Garcia-Garibay, J. Zhu, J. S. Moore, *J. Am. Chem. Soc.* **2020**, *142*, 6493-6498.

[75] A. J. Greenlee, H. Chen, C. I. Wendell, J. S. Moore, *J. Org. Chem.* **2022**, *87*, 8429-8436.

[76] A. Mortreux, N. Dy, M. Blanchard, *J. Mol. Catal.* **1976**, *1*, 101-109.

[77] A. Mortreux, J. C. Delgrange, M. Blanchard, B. Lubochinsky, *J. Mol. Catal.* **1977**, *2*, 73-82.

[78] A. Bencheick, M. Petit, A. Mortreux, F. Petit, *J. Mol. Catal.* **1982**, *15*, 93-101.

[79] D. Villemin, P. Cadiot, *Tetrahedron Lett.* **1982**, *23*, 5139-5140.

[80] J. A. K. Du Plessis, H. C. M. Vosloo, *J. Mol. Catal.* **1991**, *65*, 21-24.

[81] K. Naotake, H. Ken, A. Shin-ichi, U. Motokazu, M. Miwako, *Chem. Lett.* **1995**, *24*, 1055-1056.

[82] K. Naotake, H. Tomoe, M. Miwako, *Chem. Lett.* **1995**, *24*, 627-628.

[83] H. C. M. Vosloo, J. A. K. du Plessis, *J. Mol. Catal. A. Chem.* **1998**, *133*, 205-211.

[84] L. Kloppenburg, D. Song, U. H. F. Bunz, *J. Am. Chem. Soc.* **1998**, *120*, 7973-7974.

[85] K. Grela, J. Ignatowska, *Org. Lett.* **2002**, *4*, 3747-3749.

[86] G. Brizius, U. H. F. Bunz, *Org. Lett.* **2002**, *4*, 2829-2831.

[87] V. Huc, R. Weihofen, I. Martin-Jimenez, P. Oulié, C. Lepetit, G. Lavigne, R. Chauvin, *New J. Chem.* **2003**, *27*, 1412-1414.

[88] V. Sashuk, J. Ignatowska, K. Grela, *J. Org. Chem.* **2004**, *69*, 7748-7751.

[89] V. Maraval, C. Lepetit, A.-M. Caminade, J.-P. Majoral, R. Chauvin, *Tetrahedron Lett.* **2006**, *47*, 2155-2159.

[90] R. Schrock, S. Rocklage, J. Wengrovius, G. Rupprecht, J. Fellmann, *J. Mol. Catal.* **1980**, *8*, 73-83.

[91] J. H. Wengrovius, R. R. Schrock, M. R. Churchill, J. R. Missert, W. J. Youngs, *J. Am. Chem. Soc.* **1980**, *102*, 4515-4516.

[92] R. R. Schrock, D. N. Clark, J. Sancho, J. H. Wengrovius, S. M. Rocklage, S. F. Pedersen, *Organometallics* **1982**, *1*, 1645-1651.

[93] M. L. Listemann, R. R. Schrock, *Organometallics* **1985**, *4*, 74-83.

[94] R. R. Schrock, *Polyhedron* **1995**, *14*, 3177-3195.

[95] A. Fürstner, O. Guth, A. Rumbo, G. Seidel, *J. Am. Chem. Soc.* **1999**, *121*, 11108-11113.

[96] A. Fürstner, T. Dierkes, *Org. Lett.* **2000**, *2*, 2463-2465.

[97] V. V. Vintonyak, M. E. Maier, *Angew. Chem. Int. Ed.* **2007**, *46*, 5209-5211.

[98] M. G. Nilson, R. L. Funk, *Org. Lett.* **2010**, *12*, 4912-4915.

[99] A. Fürstner, C. Mathes, C. W. Lehmann, *J. Am. Chem. Soc.* **1999**, *121*, 9453-9454.

[100] A. Fürstner, C. Mathes, C. W. Lehmann, *Chem. Eur. J.* **2001**, *7*, 5299-5317.

[101] C. C. Cummins, *Chem. Commun.* **1998**, 1777-1786.

[102] J. C. Peters, A. L. Odom, C. C. Cummins, *Chem. Commun.* **1997**, 1995-1996.

[103] T. Agapie, P. L. Diaconescu, C. C. Cummins, *J. Am. Chem. Soc.* **2002**, *124*, 2412-2413.

[104] W. Zhang, S. Kraft, J. S. Moore, *Chem. Commun.* **2003**, 832-833.

[105] K. Jyothish, W. Zhang, *Angew. Chem. Int. Ed.* **2011**, *50*, 3435-3438.

[106] K. Jyothish, Q. Wang, W. Zhang, *Adv. Synth. Catal.* **2012**, *354*, 2073-2078.

[107] S. Schaubach, K. Gebauer, F. Ungeheuer, L. Hoffmeister, M. K. Ilg, C. Wirtz, A. Fürstner, *Chem. Eur. J.* **2016**, *22*, 8494-8507.

[108] Y. Ge, S. Huang, Y. Hu, L. Zhang, L. He, S. Krajewski, M. Ortiz, Y. Jin, W. Zhang, *Nat. Commun.* **2021**, *12*, 1136.

[109] W. Zhang, J. S. Moore, *Macromolecules* **2004**, *37*, 3973-3975.

[110] W. Zhang, J. S. Moore, *J. Am. Chem. Soc.* **2005**, *127*, 11863-11870.

[111] W. Zhang, S. M. Brombosz, J. L. Mendoza, J. S. Moore, *J. Org. Chem.* **2005**, *70*, 10198-10201.

[112] W. Zhang, Y. Lu, J. S. Moore, G. Seidel, A. Fürstner, *Org. Synth.* **2007**, *84*, 163-176.

[113] J. Heppekausen, R. Stade, A. Kondoh, G. Seidel, R. Goddard, A. Fürstner, *Chem. Eur. J.* **2012**, *18*, 10281-10299.

[114] H. Ehrhorn, M. Tamm, *Chem. Eur. J.* **2019**, *25*, 3190-3208.

[115] A. Fürstner, *J. Am. Chem. Soc.* **2021**, *143*, 15538-15555.

[116] J. Groos, P. M. Hauser, M. Koy, W. Frey, M. R. Buchmeiser, *Organometallics* **2021**, *40*, 1178-1184.

[117] Y. Ge, Y. Hu, G. Duan, Y. Jin, W. Zhang, *Trends Chem.* **2022**, *4*, 540-553.

[118] B. Haberlag, M. Freytag, C. G. Daniliuc, P. G. Jones, M. Tamm, *Angew. Chem. Int. Ed.* **2012**, *51*, 13019-13022.

[119] J. Hillenbrand, M. Leutzsch, E. Yiannakas, C. P. Gordon, C. Wille, N. Nöthling, C. Copéret, A. Fürstner, *J. Am. Chem. Soc.* **2020**, *142*, 11279-11294.

[120] J. N. Korber, C. Wille, M. Leutzsch, A. Fürstner, *J. Am. Chem. Soc.* **2023**, *145*, 26993-27009.

[121] C. Zhang, Q. Wang, H. Long, W. Zhang, *J. Am. Chem. Soc.* **2011**, *133*, 20995-21001.

[122] Q. Wang, C. Yu, H. Long, Y. Du, Y. Jin, W. Zhang, *Angew. Chem. Int. Ed.* **2015**, *54*, 7550-7554.

[123] S. Huang, Z. Lei, Y. Jin, W. Zhang, *Chem. Sci.* **2021**, *12*, 9591-9606.

[124] X. Yang, S. Huang, M. Ortiz, X. Wang, Y. Cao, O. Kareem, Y. Jin, F. Huang, X. Wang, W. Zhang, *Org. Chem. Front.* **2021**, *8*, 4723-4729.

[125] K. Tashiro, T. Aida, *Chem. Soc. Rev.* **2007**, *36*, 189-197.

[126] G. Gil-Ramírez, S. D. Karlen, A. Shundo, K. Porfyrakis, Y. Ito, G. A. D. Briggs, J. J. L. Morton, H. L. Anderson, *Org. Lett.* **2010**, *12*, 3544-3547.

[127] W. Meng, B. Breiner, K. Rissanen, J. D. Thoburn, J. K. Clegg, J. R. Nitschke, *Angew. Chem. Int. Ed.* **2011**, *50*, 3479-3483.

[128] Y. Jin, B. A. Voss, R. D. Noble, W. Zhang, *Angew. Chem. Int. Ed.* **2010**, *49*, 6348-6351.

[129] Y. Jin, B. A. Voss, A. Jin, H. Long, R. D. Noble, W. Zhang, *J. Am. Chem. Soc.* **2011**, *133*, 6650-6658.

[130] J. Wu, K. Müllen, All-benzenoid Polycyclic Aromatic Hydrocarbons: Synthesis, Self-assembly and Applications in Organic Electronics. In *Carbon-Rich Compounds*, Prof. Michael M. Haley, P. R. R. Tykwinski, Eds. Wiley-VCH Verlag GmbH & Co. KGaA: **2006**; pp 90-139.

[131] M. Rickhaus, M. Mayor, M. Juríček, *Chem. Soc. Rev.* **2017**, *46*, 1643-1660.

[132] E. Fawcett, J. Trotter, *Proc. R. Soc. A: Math. Phys. Eng. Sci.* **1966**, *289*, 366-376.

[133] J. C. Hanson, C. E. Nordman, *Acta Crystallogr. B* **1976**, *32*, 1147-1153.

[134] Y. Chen, L. Zhang, *Acc. Chem. Res.* **2025**, *58*, 762-776.

[135] C. N. Feng, W. C. Hsu, J. Y. Li, M. Y. Kuo, Y. T. Wu, *Chem. Eur. J.* **2016**, *22*, 9198-9208.

[136] I. R. Márquez, S. Castro-Fernández, A. Millán, A. G. Campaña, *Chem. Commun.* **2018**, *54*, 6705-6718.

[137] S. H. Pun, Q. Miao, *Acc. Chem. Res.* **2018**, *51*, 1630-1642.

[138] Chaolumen, I. A. Stepek, K. E. Yamada, H. Ito, K. Itami, *Angew. Chem. Int. Ed.* **2021**, *60*, 23508-23532.

[139] G. González Miera, S. Matsubara, H. Kono, K. Murakami, K. Itami, *Chem. Sci.* **2022**, *13*, 1848-1868.

[140] H. A. Schwarz, *Gesammelte mathematische Abhandlungen*. Springer Berlin: 1890.

[141] A. L. Mackay, H. Terrones, *Nature* **1991**, *352*, 762-762.

[142] T. Lenosky, X. Gonze, M. Teter, V. Elser, *Nature* **1992**, *355*, 333-335.

[143] D. Vanderbilt, J. Tersoff, *Phys. Rev. Lett.* **1992**, *68*, 511-513.

[144] J. Spengler, Y. Wagenhäuser, F. Würthner, *Chem* **2025**, 102658.

[145] L. C. Felix, C. F. Woellner, D. S. Galvao, *Carbon* **2020**, *157*, 670-680.

[146] P. O. Krasnov, G. S. Shkaberina, S. P. Polyutov, *Comput. Mater. Sci.* **2022**, *209*, 111410.

[147] D. Damasceno Borges, D. S. Galvao, *MRS Adv.* **2018**, *3*, 115-120.

[148] J. Jiang, S. I. Sandler, *J. Am. Chem. Soc.* **2005**, *127*, 11989-11997.

[149] D. Odkhuu, D. H. Jung, H. Lee, S. S. Han, S.-H. Choi, R. S. Ruoff, N. Park, *Carbon* **2014**, *66*, 39-47.

[150] M. Tagami, Y. Liang, H. Naito, Y. Kawazoe, M. Kotani, *Carbon* **2014**, *76*, 266-274.

[151] M.-Z. Huang, W. Y. Ching, T. Lenosky, *Phys. Rev. B* **1993**, *47*, 1593-1606.

[152] H. Nishihara, T. Kyotani, *Chem. Commun.* **2018**, *54*, 5648-5673.

[153] E. Braun, Y. Lee, S. M. Moosavi, S. Barthel, R. Mercado, I. A. Baburin, D. M. Proserpio, B. Smit, *Proc. Natl. Acad. Sci.* **2018**, *115*, E8116-E8124.

[154] E. E. Taylor, K. Garman, N. P. Stadie, *Chem. Mater.* **2020**, *32*, 2742-2752.

[155] K. Kawasumi, Q. Zhang, Y. Segawa, L. T. Scott, K. Itami, *Nat. Chem.* **2013**, *5*, 739-744.

[156] R. Scholl, J. Mansfeld, *Chem. Ber.* **1910**, *43*, 1734-1746.

[157] Y. Zhang, S. H. Pun, Q. Miao, *Chem. Rev.* **2022**, *122*, 14554-14593.

[158] J. Janata, J. Gendell, C.-Y. Ling, W. E. Barth, L. Backes, H. B. Mark, R. G. Lawton, *J. Am. Chem. Soc.* **1967**, *89*, 3056-3058.

[159] C. Bruno, R. Benassi, A. Passalacqua, F. Paolucci, C. Fontanesi, M. Marcaccio, E. A. Jackson, L. T. Scott, *J. Phys. Chem. B* **2009**, *113*, 1954-1962.

[160] Y. Yang, F. Arias, L. Echegoyen, L. P. F. Chibante, S. Flanagan, A. Robertson, L. J. Wilson, *J. Am. Chem. Soc.* **1995**, *117*, 7801-7804.

[161] J. M. Farrell, V. Grande, D. Schmidt, F. Würthner, *Angew. Chem. Int. Ed.* **2019**, *58*, 16504-16507.

[162] M. A. Medel, R. Tapia, V. Blanco, D. Miguel, S. P. Morcillo, A. G. Campaña, *Angew. Chem. Int. Ed.* **2021**, *60*, 6094-6100.

[163] H. Isla, J. Crassous, *C. R. Chim.* **2016**, *19*, 39-49.

[164] Y. Yang, B. Rice, X. Shi, J. R. Brandt, R. Correa da Costa, G. J. Hedley, D.-M. Smilgies, J. M. Frost, I. D. W. Samuel, A. Otero-de-la-Roza, E. R. Johnson, K. E. Jelfs, J. Nelson, A. J. Campbell, M. J. Fuchter, *ACS Nano* **2017**, *11*, 8329-8338.

[165] Z. Ma, T. Winands, N. Liang, D. Meng, W. Jiang, N. L. Doltsinis, Z. Wang, *Sci. China Chem.* **2020**, *63*, 208-214.

[166] Y. Zhang, D. Yang, S. H. Pun, H. Chen, Q. Miao, *Precis. Chem.* **2023**, *1*, 107-111.

[167] J. P. Mora-Fuentes, M. D. Codesal, M. Reale, C. M. Cruz, V. G. Jiménez, A. Sciortino, M. Cannas, F. Messina, V. Blanco, A. G. Campaña, *Angew. Chem. Int. Ed.* **2023**, *62*, e202301356.

[168] S. M. Elbert, O. T. A. Paine, T. Kirschbaum, M. P. Schuldt, L. Weber, F. Rominger, M. Mastalerz, *J. Am. Chem. Soc.* **2024**, *146*, 27324-27334.

[169] B. Borrisov, G. M. Beneventi, Y. Fu, Z.-l. Qiu, H. Komber, Q.-s. Deng, P. M. Greißel, A. Cadranel, D. M. Guldi, J. Ma, X. Feng, *J. Am. Chem. Soc.* **2024**, *146*, 27335-27344.

[170] Y. Sakamoto, T. Suzuki, *J. Am. Chem. Soc.* **2013**, *135*, 14074-14077.

[171] R. W. Miller, A. K. Duncan, S. T. Schneebeli, D. L. Gray, A. C. Whalley, *Chem. Eur. J.* **2014**, *20*, 3705-3711.

[172] K. Y. Cheung, X. Xu, Q. Miao, *J. Am. Chem. Soc.* **2015**, *137*, 3910-3914.

[173] J. M. Fernández-García, P. J. Evans, S. Medina Rivero, I. Fernández, D. García-Fresnadillo, J. Perles, J. Casado, N. Martín, *J. Am. Chem. Soc.* **2018**, *140*, 17188-17196.

[174] M. A. Medel, C. M. Cruz, D. Miguel, V. Blanco, S. P. Morcillo, A. G. Campaña, *Angew. Chem. Int. Ed.* **2021**, *60*, 22051-22056.

[175] B. Ejlli, F. Rominger, J. Freudenberg, U. H. F. Bunz, K. Müllen, *Chem. Eur. J.* **2023**, *29*, e202203735.

[176] S.-N. Lei, L. Zhu, N. Xue, X. Xiao, L. Shi, D.-C. Wang, Z. Liu, X.-R. Guan, Y. Xie, K. Liu, L.-R. Hu, Z. Wang, J. F. Stoddart, Q.-H. Guo, *Angew. Chem. Int. Ed.* **2024**, *63*, e202402255.

[177] T. Kirschbaum, F. Rominger, M. Mastalerz, *Angew. Chem. Int. Ed.* **2020**, *59*, 270-274.

[178] T. Kirschbaum, C. Daiber, J. A. Esteves, B. P. Benke, F. Rominger, S. M. Elbert, M. Mastalerz, *Asian J. Org. Chem.* **2025**, *14*, e202500394.

[179] T. E. Cecil, P. J. Ryan, *Am. Math. Mon.* **1986**, *93*, 380-382.

[180] W. K. L. C. Cross, *Pure Appl. Chem.* **1976**, *45*, 11-30.

[181] R. S. Cahn, C. Ingold, V. Prelog, *Angew. Chem. Int. Ed.* **1966**, *5*, 385-415.

[182] V. Prelog, G. Helmchen, *Angew. Chem. Int. Ed.* **1982**, *21*, 567-583.

[183] G. P. Moss, *Pure Appl. Chem.* **1996**, *68*, 2193-2222.

[184] T. Kirschbaum, *Chirale polyzyklische aromatische Kohlenwasserstoffe mit Affensattel-Topologie*, Dissertation, Ruprecht-Karls-Universität Heidelberg, Heidelberg, **2022**.

[185] T. Kirschbaum, F. Rominger, M. Mastalerz, *Chem. Eur. J.* **2020**, *26*, 14560-14564.

[186] T. Kirschbaum, S. F. Ebel, F. Rominger, M. Mastalerz, *Helv. Chim. Acta* **2024**, *107*, e202400158.

[187] J. H. Dopper, H. Wynberg, *Tetrahedron Lett.* **1972**, *13*, 763-766.

[188] Y. Miyake, H. Shinokubo, *Chem. Commun.* **2020**, *56*, 15605-15614.

[189] T. Hensel, N. N. Andersen, M. Plesner, M. Pittelkow, *Synlett* **2016**, *27*, 498-525.

[190] K. Yamamoto, T. Harada, M. Nakazaki, T. Naka, Y. Kai, S. Harada, N. Kasai, *J. Am. Chem. Soc.* **1983**, *105*, 7171-7172.

[191] X. Xiong, C.-L. Deng, B. F. Minaev, G. V. Baryshnikov, X.-S. Peng, H. N. C. Wong, *Chem. Asian J.* **2015**, *10*, 969-975.

[192] C. Maeda, S. Nomoto, K. Akiyama, T. Tanaka, T. Ema, *Chem. Eur. J.* **2021**, *27*, 15699-15705.

[193] T. Nishinaga, T. Ohmae, M. Iyoda, *Symmetry* **2010**, *2*, 76-97.

[194] H. Erdtman, H. E. Högberg, *Chem. Commun.* **1968**, 773-774.

[195] H. Erdtman, H. E. Högberg, *Tetrahedron Lett.* **1970**, *11*, 3389-3392.

[196] H.-E. Högberg, *Acta Chem. Scand.* **1972**, *26*, 2752-2758.

[197] H. Erdtman, H.-E. Högberg, *Tetrahedron* **1979**, *35*, 535-540.

[198] C. B. Nielsen, T. Brock-Nannestad, T. K. Reenberg, P. Hammershøj, J. B. Christensen, J. W. Stouwdam, M. Pittelkow, *Chem. Eur. J.* **2010**, *16*, 13030-13034.

[199] T. Brock-Nannestad, C. B. Nielsen, M. Schau-Magnussen, P. Hammershøj, T. K. Reenberg, A. B. Petersen, D. Trpcevski, M. Pittelkow, *Eur. J. Org. Chem.* **2011**, *2011*, 6320-6325.

[200] T. Hensel, D. Trpcevski, C. Lind, R. Grosjean, P. Hammershøj, C. B. Nielsen, T. Brock-Nannestad, B. E. Nielsen, M. Schau-Magnussen, B. Minaev, G. V. Baryshnikov, M. Pittelkow, *Chem. Eur. J.* **2013**, *19*, 17097-17102.

[201] S. K. Pedersen, V. B. R. Pedersen, F. S. Kamounah, L. M. Broløs, G. V. Baryshnikov, R. R. Valiev, K. Ivaniuk, P. Stakhira, B. Minaev, N. Karaush-Karmazin, H. Ågren, M. Pittelkow, *Chem. Eur. J.* **2021**, *27*, 11609-11617.

[202] K. Aita, T. Ohmae, M. Takase, K. Nomura, H. Kimura, T. Nishinaga, *Org. Lett.* **2013**, *15*, 3522-3525.

[203] J. A. N. F. Gomes, R. B. Mallion, *Chem. Rev.* **2001**, *101*, 1349-1384.

[204] D. Rabinovich, Z. Shakked, *Acta Crystallogr. B* **1975**, *31*, 819-825.

[205] Y. Nie, H. Wadepohl, C. Hu, T. Oeser, W. Siebert, *J. Organomet. Chem.* **2009**, *694*, 1884-1889.

[206] V. Kotlyar, *J. Org. Chem.* **1997**, *62*, 7512-7515.

[207] M. Hudlicky, *J. Fluor. Chem.* **1986**, *32*, 441-452.

[208] P. v. R. Schleyer, C. Maerker, A. Dransfeld, H. Jiao, N. J. R. van Eikema Hommes, *J. Am. Chem. Soc.* **1996**, *118*, 6317-6318.

[209] P. v. R. Schleyer, M. Manoharan, Z.-X. Wang, B. Kiran, H. Jiao, R. Puchta, N. J. R. van Eikema Hommes, *Org. Lett.* **2001**, *3*, 2465-2468.

[210] D. Geuenich, K. Hess, F. Köhler, R. Herges, *Chem. Rev.* **2005**, *105*, 3758–3772.

[211] S. Akahori, A. Kaga, J. Kim, H. Yorimitsu, D. Kim, H. Shinokubo, Y. Miyake, *Chem. Asian J.* **2022**, *17*, e202200244.

[212] V. B. Pedersen, S. K. Pedersen, Z. Jin, N. Kofod, B. W. Laursen, G. V. Baryshnikov, C. Nuckolls, M. Pittelkow, *Angew. Chem. Int. Ed.* **2022**, *61*, e202212293.

[213] F. Chen, Y. S. Hong, S. Shimizu, D. Kim, T. Tanaka, A. Osuka, *Angew. Chem. Int. Ed.* **2015**, *54*, 10639-10642.

[214] Y. Morimoto, F. Chen, Y. Matsuo, K. Kise, T. Tanaka, A. Osuka, *Chem. Asian J.* **2021**, *16*, 648-655.

[215] B. Lousen, S. K. Pedersen, P. Bols, K. H. Hansen, M. R. Pedersen, O. Hammerich, S. Bondarchuk, B. Minaev, G. V. Baryshnikov, H. Ågren, M. Pittelkow, *Chem. Eur. J.* **2020**, *26*, 4935-4940.

[216] S. Kato, Y. Serizawa, D. Sakamaki, S. Seki, Y. Miyake, H. Shinokubo, *Chem. Commun.* **2015**, *51*, 16944-16947.

[217] S. Kato, S. Akahori, Y. Serizawa, X. Lin, M. Yamauchi, S. Yagai, T. Sakurai, W. Matsuda, S. Seki, H. Shinokubo, Y. Miyake, *J. Org. Chem.* **2020**, *85*, 62-69.

[218] Y. Serizawa, S. Akahori, S. Kato, H. Sakai, T. Hasobe, Y. Miyake, H. Shinokubo, *Chem. Eur. J.* **2017**, *23*, 6948-6952.

[219] K. Y. Chernichenko, V. V. Sumerin, R. V. Shpanchenko, E. S. Balenkova, V. G. Nenajdenko, *Angew. Chem. Int. Ed.* **2006**, *45*, 7367-7370.

[220] A. Nakagawa, W. Ota, T. Ehara, Y. Matsuo, K. Miyata, K. Onda, T. Sato, S. Seki, T. Tanaka, *Chem. Commun.* **2024**, *60*, 14770-14773.

[221] H. Murase, Y. Nagata, S. Akahori, H. Shinokubo, Y. Miyake, *Chem. Asian J.* **2020**, *15*, 3873-3877.

[222] S. F. Ebel, *The Synthesis of a Triptycene-based Organic Cage via an Alkyne Metathesis Approach*, Master thesis, Ruprecht-Karls-Universität, Heidelberg (Germany), **2021**.

[223] R. F. M. Elshaarawy, Z. H. Kheiralla, A. A. Rushdy, C. Janiak, *Inorg. Chim. Acta* **2014**, *421*, 110-122.

[224] S. Goncalves, S. Santoro, M. Nicolas, A. Wagner, P. Maillos, F. Himo, R. Baati, *J. Org. Chem.* **2011**, *76*, 3274-3285.

[225] X.-J. Zou, Z.-X. Jin, H.-Y. Yang, F. Wu, Z.-H. Ren, Z.-H. Guan, *Angew. Chem. Int. Ed.* **2024**, *63*, e202406226.

[226] R. Chahboun, J. M. Botubol-Ares, M. J. Durán-Peña, F. Jiménez, R. Alvarez-Manzaneda, E. Alvarez-Manzaneda, *J. Org. Chem.* **2021**, *86*, 8742-8754.

[227] C.-F. Chen, *Chem. Commun.* **2011**, *47*, 1674-1688.

[228] M. Mastalerz, *Acc. Chem. Res.* **2018**, *51*, 2411-2422.

[229] G. Preda, A. Nitti, D. Pasini, *ChemistryOpen* **2020**, *9*, 719-727.

[230] J. C. Lauer, B. Kohl, F. Braun, F. Rominger, M. Mastalerz, *Eur. J. Org. Chem.* **2022**, e202101317.

[231] C.-F. Chen, Y. Han, *Acc. Chem. Res.* **2018**, *51*, 2093-2106.

[232] C. Zhang, C.-F. Chen, *J. Org. Chem.* **2007**, *72*, 9339-9341.

[233] H. Li, F. Chen, X. Guan, J. Li, C. Li, B. Tang, V. Valtchev, Y. Yan, S. Qiu, Q. Fang, *J. Am. Chem. Soc.* **2021**, *143*, 2654-2659.

[234] C. Yu, H. Li, Y. Wang, J. Suo, X. Guan, R. Wang, V. Valtchev, Y. Yan, S. Qiu, Q. Fang, *Angew. Chem. Int. Ed.* **2022**, *61*, e202117101.

[235] Z. Li, G. Xu, C. Zhang, S. Ma, Y. Jiang, H. Xiong, G. Tian, Y. Wu, Y. Wei, X. Chen, Y. Yang, F. Wei, *J. Am. Chem. Soc.* **2024**, *146*, 4327-4332.

[236] P. Chandrasekhar, A. Mukhopadhyay, G. Savitha, J. N. Moorthy, *J. Mater. Chem. A* **2017**, *5*, 5402-5412.

[237] J. Lv, W. Li, J. Li, Z. Zhu, A. Dong, H. Lv, P. Li, B. Wang, *Angew. Chem.* **2023**, *135*, e202217958.

[238] B. S. Ghanem, K. J. Msayib, N. B. McKeown, K. D. M. Harris, Z. Pan, P. M. Budd, A. Butler, J. Selbie, D. Book, A. Walton, *Chem. Commun.* **2007**, 67-69.

[239] B. S. Ghanem, R. Swaidan, E. Litwiller, I. Pinnau, *Adv. Mater.* **2014**, *26*, 3688-3692.

[240] F. Ishiwari, Y. Shoji, C. J. Martin, T. Fukushima, *Polym. J.* **2024**, *56*, 791-818.

[241] B. S. Ghanem, M. Hashem, K. D. M. Harris, K. J. Msayib, M. Xu, P. M. Budd, N. Chaukura, D. Book, S. Tedds, A. Walton, N. B. McKeown, *Macromolecules* **2010**, *43*, 5287-5294.

[242] J.-M. Zhao, H.-Y. Lu, J. Cao, Y. Jiang, C.-F. Chen, *Tetrahedron Lett.* **2009**, *50*, 219-222.

[243] C. Bourguignon, D. Schindler, G. Zhou, F. Rominger, M. Mastalerz, *Org. Chem. Front.* **2021**, *8*, 3668-3674.

[244] D. Schindler, *Triptycenbasierte Bausteine für organische Käfigmoleküle*, Master thesis, Ruprecht-Karls-Universität, Heidelberg (Germany), **2015**.

[245] C. Bourguignon, *Synthese von vierfach ortho-formylierten Triptycenen und deren Verwendung zum Aufbau neuartiger Käfigmoleküle*, Dissertation, Ruprecht-Karls-Universität, Heidelberg (Germany), **2021**.

[246] M. L. Josien, N. Fuson, J. M. Lebas, T. M. Gregory, *J. Chem. Phys.* **1953**, *21*, 331-340.

[247] I. Horiuti, M. Polanyi, *Trans. Faraday Soc.* **1934**, *30*, 1164-1172.

[248] B. Mattson, W. Foster, J. Greimann, T. Hoette, N. Le, A. Mirich, S. Wankum, A. Cabri, C. Reichenbacher, E. Schwanke, *J. Chem. Educ.* **2013**, *90*, 613-619.

[249] J. Young, J. Osborn, F. Jardine, G. Wilkinson, *Chem. Commun.* **1965**, 131-132.

[250] J. R. Morandi, H. B. Jensen, *J. Org. Chem.* **1969**, *34*, 1889-1891.

[251] J. Halpern, T. Okamoto, A. Zakhariev, *J. Mol. Catal.* **1977**, *2*, 65-68.

[252] J. Luo, A. G. Oliver, J. Scott McIndoe, *Dalton Trans.* **2013**, *42*, 11312-11318.

[253] E. Tyrode, J. Hedberg, *J. Phys. Chem. C* **2012**, *116*, 1080-1091.

[254] I. Aracil, R. Font, J. A. Conesa, *Environ. Sci. Technol.* **2010**, *44*, 4169-4175.

[255] M. Hähsler, M. Mastalerz, *Chem. Eur. J.* **2021**, *27*, 233-237.

[256] J. A. Guenther, *The Synthesis of a Monkey Saddle Precursor to Assemble Organic Cages via Alkyne Metathesis*, Bachelor Thesis, Ruprecht-Karls-Universität Heidelberg, Heidelberg, **2022**.

[257] H. Tanaka, Y. Inoue, T. Mori, *ChemPhotoChem* **2018**, *2*, 386-402.

[258] S. Schott, *Synthese eines funktionalisierten, truxenbasierten Aza-Affensattel-PAKs*, Bachelor Thesis, Ruprecht-Karls-Universität Heidelberg, Heidelberg, **2024**.

[259] X. Liu, Z. J. Weinert, M. Sharafi, C. Liao, J. Li, S. T. Schneebeli, *Angew. Chem. Int. Ed.* **2015**, *54*, 12772-12776.

[260] M. Mastalerz, *Angew. Chem. Int. Ed.* **2016**, *55*, 45-47.

[261] H. L. Goering, *J. Am. Chem. Soc.* **1951**, *73*, 4737-4741.

[262] Y. Liu, L. Huang, F. Xie, X. Chen, Y. Hu, *Org. Biomol. Chem.* **2011**, *9*, 2680-2684.

[263] T. Ishiyama, J. Takagi, K. Ishida, N. Miyaura, N. R. Anastasi, J. F. Hartwig, *J. Am. Chem. Soc.* **2002**, *124*, 390-391.

[264] F. M. Dürr, *Erforschung der Synthese eines truxenbasierten Affensattel-PAKs mit erhöhter Inversionsbarriere*, Bachelor Thesis, Ruprecht-Karls-Universität Heidelberg, Heidelberg, **2023**.

[265] N. Park, M. Yoon, S. Berber, J. Ihm, E. Osawa, D. Tománek, *Phys. Rev. Lett.* **2003**, *91*, 237204.

[266] S. Grimme, J. G. Brandenburg, C. Bannwarth, A. Hansen, *J. Chem. Phys.* **2015**, *143*, 054107.

[267] H. Kruse, S. Grimme, *J. Chem. Phys.* **2012**, *136*, 154101.

[268] S. Grimme, J. Antony, S. Ehrlich, H. Krieg, *J. Chem. Phys.* **2010**, *132*, 154104.

[269] S. Grimme, S. Ehrlich, L. Goerigk, *J. Comput. Chem.* **2011**, *32*, 1456-1465.

[270] Y. Zhao, D. G. Truhlar, *J. Phys. Chem. A* **2005**, *109*, 5656-5667.

[271] P. J. Stephens, F. J. Devlin, C. F. Chabalowski, M. J. Frisch, *J. Phys. Chem.* **1994**, *98*, 11623–11627.

[272] Y. Zhao, D. G. Truhlar, *Theor. Chem. Acc.* **2008**, *120*, 215-241.

[273] A. Najibi, L. Goerigk, *J. Comput. Chem.* **2020**, *41*, 2562-2572.

[274] N. Mardirossian, M. Head-Gordon, *Phys. Chem. Chem. Phys.* **2014**, *16*, 9904-9924.

[275] S. Grimme, *J. Phys. Chem. A* **2005**, *109*, 3067-3077.

[276] C. Adamo, V. Barone, *J. Chem. Phys.* **1999**, *110*, 6158-6170.

[277] S. Kozuch, D. Gruzman, J. M. L. Martin, *J. Phys. Chem. C* **2010**, *114*, 20801-20808.

[278] S. Kozuch, J. M. Martin, *Phys. Chem. Chem. Phys.* **2011**, *13*, 20104-20107.

[279] S. Kozuch, J. M. Martin, *J. Comput. Chem.* **2013**, *34*, 2327-2344.

[280] A. D. Becke, *Phys. Rev. A* **1988**, *38*, 3098-3100.

[281] C. Lee, W. Yang, R. G. Parr, *Phys. Rev. B* **1988**, *37*, 785.

[282] B. Miehlich, A. Savin, H. Stoll, H. Preuss, *Chem. Phys. Lett.* **1989**, *157*, 200-206.

[283] S. Grimme, A. Hansen, S. Ehlert, J.-M. Mewes, *J. Chem. Phys.* **2021**, *154*, 064103.

[284] L. Goerigk, S. Grimme, *J. Chem. Theory Comput.* **2011**, *7*, 291-309.

[285] F. Weigend, R. Ahlrichs, *Phys. Chem. Chem. Phys.* **2005**, *7*, 3297-3305.

[286] A. V. Marenich, C. J. Cramer, D. G. Truhlar, *J. Phys. Chem. B* **2009**, *113*, 6378-6396.

[287] P. J. Canfield, I. M. Blake, Z.-L. Cai, I. J. Luck, E. Krausz, R. Kobayashi, J. R. Reimers, M. J. Crossley, *Nat. Chem.* **2018**, *10*, 615-624.

[288] R. E. Kitson, N. E. Griffith, *Anal. Chem.* **1952**, *24*, 334-337.

[289] N. Fuson, M.-L. Josien, E. M. Shelton, *J. Am. Chem. Soc.* **1954**, *76*, 2526-2533.

[290] J. Gasteiger, G. E. Gream, R. Huisgen, W. E. Konz, U. Schnegg, *Chem. Ber.* **1971**, *104*, 2412-2419.

[291] A. R. Katritzky, J. Li, N. Malhotra, *Liebigs Ann. Chem.* **1992**, 843-853.

[292] P. H. Mason, N. D. Emslie, *Tetrahedron* **1995**, *51*, 2673-2678.

[293] M. Dankova, R. L. Kravchenko, A. P. Cole, R. M. Waymouth, *Macromolecules* **2002**, *35*, 2882-2891.

[294] K. Amsharov, N. Abdurakhmanova, S. Stepanow, S. Rauschenbach, M. Jansen, K. Kern, *Angew. Chem. Int. Ed.* **2010**, *49*, 9392-9396.

[295] S. El Rayes, A. Linden, K. Abou-Hadeed, H.-J. Hansen, *Helv. Chim. Acta* **2010**, *93*, 1894-1911.

[296] P. P. Fu, R. G. Harvey, *Chem. Rev.* **1978**, *78*, 317-361.

[297] S. Hati, U. Holzgrabe, S. Sen, *Beilstein J. Org. Chem.* **2017**, *13*, 1670-1692.

[298] M. Karplus, *J. Am. Chem. Soc.* **1963**, *85*, 2870-2871.

[299] M. J. Minch, *Concepts Magn. Reson.* **1994**, *6*, 41-56.

[300] M. Aghazade Tabrizi, P. G. Baraldi, M. Guarneri, S. Manfredini, G. P. Pollini, D. Simoni, *Tetrahedron Lett.* **1991**, *32*, 683-686.

[301] I. Mohammadpoor-Baltork, M. A. Zolfigol, M. Abdollahi-Alibeik, *Tetrahedron Lett.* **2004**, *45*, 8687-8690.

[302] S. Prateeptongkum, K. M. Driller, R. Jackstell, A. Spannenberg, M. Beller, *Chem. Eur. J.* **2010**, *16*, 9606-9615.

[303] T. Eicher, W. Freihoff, *Synthesis* **1986**, *1986*, 908-916.

[304] N. G. Connelly, W. E. Geiger, *Chem. Rev.* **1996**, *96*, 877-910.

[305] J. E. Nutting, J. B. Gerken, A. G. Stamoulis, D. L. Bruns, S. S. Stahl, *J. Org. Chem.* **2021**, *86*, 15875-15885.

[306] S. F. Ebel, F. Rominger, M. Mastalerz, *Org. Lett.* **2025**, *27*, 7944-7949.

[307] N. Miyaura, A. Suzuki, *Chem. Rev.* **1995**, *95*, 2457-2483.

[308] P. G. M. Wuts, *Greene's Protective Groups in Organic Synthesis*. 5th ed.; John Wiley & Sons, Inc.: Hoboken, New Jersey, **2014**.

[309] M. Biosca, O. Pàmies, M. Diéguez, *J. Org. Chem.* **2019**, *84*, 8259-8266.

[310] T. Ishiyama, M. Murata, N. Miyaura, *J. Org. Chem.* **1995**, *60*, 7508-7510.

[311] A. J. J. Lennox, G. C. Lloyd-Jones, *Chem. Soc. Rev.* **2014**, *43*, 412-443.

[312] J. Lozada, Z. Liu, D. M. Perrin, *J. Org. Chem.* **2014**, *79*, 5365-5368.

[313] A. Tobiasz, S. Walas, B. Trzewik, P. Grzybek, M. M. Zaitz, M. Gawin, H. Mrowiec, *Microchem. J.* **2009**, *93*, 87-92.

[314] E. G. Cox, *Rev. Mod. Phys.* **1958**, *30*, 159-162.

[315] F. H. Allen, O. Kennard, D. G. Watson, L. Brammer, A. G. Orpen, R. Taylor, *J. Chem. Soc., Perkin Trans. 2* **1987**, S1-S19.

[316] C. Wilcox Jr, J. Uetrecht, K. Grohman, *J. Am. Chem. Soc.* **1972**, *94*, 2532-2533.

[317] I. Willner, M. Rabinovitz, *J. Org. Chem.* **1980**, *45*, 1628-1633.

[318] G. R. Fulmer, A. J. M. Miller, N. H. Sherden, H. E. Gottlieb, A. Nudelman, B. M. Stoltz, J. E. Bercaw, K. I. Goldberg, *Organometallics* **2010**, *29*, 2176-2179.

[319] L. Krause, R. Herbst-Irmer, G. M. Sheldrick, D. Stalke, *J. Appl. Cryst.* **2015**, *48*, 3-10.

[320] G. M. Sheldrick, *Acta Cryst. A* **2015**, *71*, 3-8.

[321] G. M. Sheldrick, *Acta Crystallogr. C* **2015**, *71*, 3-8.

[322] F. Neese, *WIREs Comput Mol Sci.* **2022**, *12*, e1606.

[323] G. A. Andrienko, *Chemcraft - graphical software for visualization of quantum chemistry computations*, Version 1.8; https://www.chemcraftprog.com (accessed 2025).

[324] M. D. Hanwell, D. E. Curtis, D. C. Lonie, T. Vandermeersch, E. Zurek, G. R. Hutchison, *J. Cheminformatics* **2012**, *4*, 17.

[325] S. Grimme, *Chem. Eur. J.* **2012**, *18*, 9955-9964.

[326] A. D. Becke, *J. Chem. Phys.* **1993**, *98*, 5648-5652.

[327] T. Yanai, D. P. Tew, N. C. Handy, *Chem. Phys. Lett.* **2004**, *393*, 51-57.

[328] V. Barone, M. Cossi, *J. Phys. Chem. A* **1998**, *102*, 1995-2001.

[329] F. London, *J. Phys. Radium* **1937**, *8*, 397-409.

[330] H. F. Hameka, *Mol. Phys.* **1958**, *1*, 203-215.

[331] R. Ditchfield, *J. Chem. Phys.* **1972**, *56*, 5688-5691.

[332] K. Wolinski, J. F. Hinton, P. Pulay, *J. Am. Chem. Soc.* **1990**, *112*, 8251-8260.

[333] W. Kutzelnigg, *Isr. J. Chem.* **1980**, *19*, 193-200.

[334] M. Schindler, W. Kutzelnigg, *J. Chem. Phys.* **1982**, *76*, 1919-1933.

[335] M. J. Frisch, G. W. Trucks, H. B. Schlegel, G. E. Scuseria, M. A. Robb, J. R. Cheeseman, G. Scalmani, V. Barone, G. A. Petersson, H. Nakatsuji, X. Li, M. Caricato, A. V. Marenich, J. Bloino, B. G. Janesko, R. Gomperts, B. Mennucci, H. P. Hratchian, J. V. Ortiz, A. F. Izmaylov, J. L. Sonnenberg, D. Williams-Young, F. Ding, F. Lipparini, F. Egidi, J. Goings, B. Peng, A. Petrone, T. Henderson, D. Ranasinghe, V. G. Zakrzewski, J. Gao, N. Rega, G. Zheng, W. Liang, M. Hada, M. Ehara, K. Toyota, R. Fukuda, J. Hasegawa, M. Ishida, T. Nakajima, Y. Honda, O. Kitao, H. Nakai, T. Vreven, K. Throssell, J. A. Montgomery Jr., J. E. Peralta, F. Ogliaro, M. J. Bearpark, J. J. Heyd, E. N. Brothers, K. N. Kudin, V. N. Staroverov, T. A. Keith, R. Kobayashi, J. Normand, K. Raghavachari, A. P. Rendell, J. C. Burant, S. S. Iyengar, J. Tomasi, M. Cossi, J. M. Millam, M. Klene, C. Adamo, R. Cammi, J. W. Ochterski, R. L. Martin, K. Morokuma, O. Farkas, J. B. Foresman, D. J. Fox, *Gaussian 16*, Revision C.01, Gaussian, Inc., Wallingford CT, **2016**.

[336] C. Lee, W. Yang, R. G. Parr, *Phys. Rev. B* **1988**, *37*, 785-789.

[337] S. H. Vosko, L. Wilk, M. Nusair, *Can. J. Phys.* **1980**, *58*, 1200-1211.

[338] R. Krishnan, J. S. Binkley, R. Seeger, J. A. Pople, *J. Chem. Phys.* **1980**, *72*, 650-654.

[339] A. McLean, G. Chandler, *J. Chem. Phys.* **1980**, *72*, 5639-5648.

[340] M. M. Francl, W. J. Pietro, W. J. Hehre, J. S. Binkley, M. S. Gordon, D. J. DeFrees, J. A. Pople, *J. Chem. Phys.* **1982**, *77*, 3654-3665.

[341] L. A. Curtiss, M. P. McGrath, J. P. Blaudeau, N. E. Davis, R. C. Binning Jr, L. Radom, *J. Chem. Phys.* **1995**, *103*, 6104-6113.

[342] M. N. Glukhovtsev, A. Pross, M. P. McGrath, L. Radom, *J. Chem. Phys.* **1995**, *103*, 1878-1885.

[343] J.-P. Blaudeau, M. P. McGrath, L. A. Curtiss, L. Radom, *J. Chem. Phys.* **1997**, *107*, 5016-5021.

[344] J. Gaunt, *Math. Proc. Camb. Philos. Soc.* **1928**, *24*, 328-342.

[345] D. R. Hartree, *Math. Proc. Camb. Philos. Soc.* **1928**, *24*, 111-132.

[346] J. C. Slater, *Phys. Rev.* **1928**, *32*, 339.

[347] V. Fock, *Z. Phys.* **1930**, *61*, 126-148.

[348] V. Fock, *Z. Phys.* **1930**, *62*, 795-805.

[349] J. C. Slater, *Phys. Rev.* **1930**, *35*, 210.

[350] D. R. Hartree, W. Hartree, *Proc. R. Soc. Lond. A* **1935**, *150*, 9-33.

[351] C. C. J. Roothaan, *Rev. Mod. Phys.* **1951**, *23*, 69.

[352] R. Ditchfield, W. J. Hehre, J. A. Pople, *J. Chem. Phys.* **1971**, *54*, 724-728.

[353] W. J. Hehre, R. Ditchfield, J. A. Pople, *J. Chem. Phys.* **1972**, *56*, 2257-2261.

[354] P. C. Hariharan, J. A. Pople, *Theor. Chem. Acc.* **1973**, *28*, 213-222.

[355] M. S. Gordon, J. S. Binkley, J. A. Pople, W. J. Pietro, W. J. Hehre, *J. Am. Chem. Soc.* **1982**, *104*, 2797-2803.

[356] T. Clark, J. Chandrasekhar, G. W. Spitznagel, P. V. R. Schleyer, *J. Comput. Chem.* **1983**, *4*, 294-301.

[357] J. D. Dill, J. A. Pople, *J. Chem. Phys.* **1975**, *62*, 2921-2923.

[358] G. W. Spitznagel, T. Clark, P. von Ragué Schleyer, W. J. Hehre, *J. Comput. Chem.* **1987**, *8*, 1109-1116.

[359] R. McWeeny, *Phys. Rev.* **1962**, *126*, 1028.

[360] R. Ditchfield, *Mol. Phys.* **1974**, *27*, 789-807.

[361] J. R. Cheeseman, G. W. Trucks, T. A. Keith, M. J. Frisch, *J. Chem. Phys.* **1996**, *104*, 5497-5509.

[362] T. Keith, R. Bader, *Chem. Phys. Lett.* **1992**, *194*, 1-8.

[363] T. A. Keith, R. F. Bader, *Chem. Phys. Lett.* **1993**, *210*, 223-231.

[364] T. Lu, F. Chen, *J. Comput. Chem.* **2012**, *33*, 580-592.

[365] T. Lu, Q. Chen, *Theor. Chem. Acc.* **2020**, *139*, 25.

[366] R. Herges, D. Geuenich, *J. Phys. Chem. A* **2001**, *105*, 3214–3220.

[367] F. Stoffelbach, D. Saurenz, R. Poli, *Eur. J. Inorg. Chem.* **2001**, *2001*, 2699-2703.

[368] J. W. Anthis, I. Filippov, D. E. Wigley, *Inorg. Chem.* **2004**, *43*, 716-724.

[369] M. R. Smith, III, R. Bisht, C. Haldar, G. Pandey, J. E. Dannatt, B. Ghaffari, R. E. Maleczka, Jr., B. Chattopadhyay, *ACS Catal.* **2018**, *8*, 6216-6223.

[370] F. Kaiser, L. Schwink, J. Velder, H.-G. Schmalz, *Tetrahedron* **2003**, *59*, 3201-3217.

[371] M. Rickhaus, L. Jundt, M. Mayor, *Chimia* **2016**, *70*, 192.

7 Appendix

7.1 List of Abbreviations

[9]CPP	[9]Cycloparaphenylene
3DMM2O	3D Matter Made to Order
ACID	Anisotropy of the induced current density
AI	Artificial intelligence
ATR	Attenuated total reflection
B_2Pin_2	Bis(pinacolato)diboron
BOC	*tert*-Butyloxycarbonyl
br	Broad
calcd	Calculated
CCl_4	Tetrachloromethane
CD	Circular dichroism
$CDCl_3$	Chloroform-*d*
CH_2Cl_2	Dichloromethane
CIP	Cahn-Ingold-Prelog
Cmpd.	Compound
COFs	Covalent organic frameworks
COSY	Correlation (NMR) spectroscopy
COT	Cyclooctatetraene
CPCM	Conductor-like polarizable continuum model
CSGT	Continuous set of gauge transformations
CV	Cyclic voltammetry
d	Doublet
DABCO	1,4-Diazabicyclo[2.2.2]octane
dba	Dibenzylideneacetone
DBU	1,8-Diazabicyclo[5.4.0]undec-7-ene
DCC	Dynamic covalent chemistry
DCTB	Trans-2-[3-(4-*tert*-butylphenyl)-2-methyl-2-propenylidene]malononitrile
dd	Doublet of doublets
ddd	Doublet of doublets of doublets
DDQ	2,3-Dichloro-5,6-dicyano-1,4-benzoquinone
DEPT	Distortionless enhancement by polarization transfer
DFG	Deutsche Forschungsgemeinschaft
DFT	Density functional theory
DMF	Dimethylformamide
DMSO	Dimethyl sulfoxide
dppf	1,1'-Bis(diphenylphosphino)ferrocene
DPV	Differential pulse voltammetry
dtbpy	4,4'-Di-*tert*-butyl-2,2'-dipyridyl
EA	Ethyl acetate
ECD	Electronic circular dichroism
equiv.	Equivalents
Et	Ethyl
FT	Fourier transform
GIAO	Gauge-independent atomic orbital
GPC	Gel permeation chromatography
HBC	Hexa-*peri*-hexabenzocoronene
HMBC	Heteronuclear multiple-bond correlation (NMR) spectroscopy
HOMO	Highest occupied molecular orbital
HPLC	High performance liquid chromatography
HR	High-resolution
HSQC	Heteronuclear single-quantum correlation (NMR) spectroscopy
Hz	Hertz
IGLO	Individual gauge for localized orbitals
^{i}Pr	Isopropyl
IR	Infrared
IUPAC	International Union of Pure and Applied Chemistry
LUMO	Lowest occupied molecular orbital
M	Molar (mol L^{-1})
m	Multiplet (NMR), medium (IR)
M.p.	Melting point

m/z Mass-to-charge ratio
MALDI Matrix-assisted laser desorption/ionization
***m*CPBA** *meta*-Chloroperoxybenzoic acid
Me Methyl
MOFs Metal-organic frameworks
MOM Methoxymethyl
MOMBr Bromomethyl methyl ether
MPI Max-Planck-Institut
MS Mass spectrometry
MS Monkey saddle
MTBE Methyl *tert*-butyl ether
NBS *N*-Bromosuccinimide
***n*-Bu** *n*-Butyl
NICS Nucleus-independent chemical shifts
NMR Nuclear magnetic resonance
NOESY Nuclear Overhauser effect (NMR) spectroscopy
o.n. Overnight
OB8C Octabenzo[8]circulene
ODCB *ortho*-Dichlorobenzene
OLED Organic light-emitting diode
PAH Polycyclic aromatic hydrocarbon
Pd/C Palladium on carbon
PE Petroleum ether
Ph$_2$O Diphenyl ether
Ph$_3$SiOH Triphenylsilanol
Pin Pinacol (as ligand)
PPG Precipitating group
ppm Parts per million
q Quartet
QRRHO Quasi-rigid-rotor-harmonic-oscillator
rec Recycling
rt Room temperature
s Singlet (NMR), strong (IR)
sat. Saturated
S$_E$Ar Electrophilic aromatic substitution
sept Septet
SHE Standard hydrogen electrode
SM Starting material
SMD Solvation model based on density
SPhos Dicyclohexyl(2′,6′-dimethoxy[1,1′-biphenyl]-2-yl)phosphane
SPS Solvent purification system
t Triplet
TBDMS *tert*-Butyldimethylsilyl
TBS *tert*-Butyldimethylsilyl
TBTQ Tribenzo triquinacene
^{t}Bu *tert*-Butyl
TCE 1,1,2,2-Tetrachloroethane
td Triplet of doublets
TD-DFT Time-dependent density functional theory
TFA Trifluoroacetic acid
THF Tetrahydrofuran
TIPS Triisopropylsilyl
TLC Thin layer chromatography
TMS Tetramethylsilane
TOF Time of flight
TRAM Terminal ring-closing alkyne metathesis
TS Transition state
UV/vis Ultraviolet/visible
w Weak
XPhos Dicyclohexyl[2′,4′,6′-tris(propan-2-yl)[1,1′-biphenyl]-2-yl]phosphane

7.2 List of Chemicals

Substance	**Supplier**	**Purity**
Acetic acid	Honeywell	≥ 99%
Acetone	Thermo Fisher	99%
Acetonitrile	Sigma-Aldrich	≥ 99.9%
Acetonitrile (SPS)	Honeywell	≥ 99.8%
2-Aminophenylboronic acid hydrochloride	BLDpharm	97%
L-Ascorbic acid	Sigma-Aldrich	reagent grade
Benzene-*d*$_6$	Deutero	99.5%
Benzene-1,4-diboronic acid	Sigma Aldrich	≥ 95.0%
Benzene-1,3,5-triyltriboronic acid	BLDpharm	98.30%
(2-Biphenyl)dicyclohexylphosphine	Sigma-Aldrich	97%
[1,1’-Bis(diphenylphosphino)ferrocene]dichloropalladium(II)	BLDpharm	99.4%
Bis(pinacolato)diboron	BLDpharm	99.97%
Bis(triphenylphosphine)palladium(II) dichloride	Sigma-Aldrich	–
Boron tribromide (1.0 M in CH_2Cl_2)	Sigma-Aldrich	–
2-Bromo-3-hydroxybenzaldehyde	BLDpharm	98.33%
Bromomethyl methyl ether	Thermo Fisher	90%
2-Bromo-4-nitroaniline	BLDpharm	98.2%
2-Bromopropane	Thermo Fisher	99%
5-Bromosalicylaldehyde	BLDpharm	99.43%
N-Bromosuccinimide	Sigma-Aldrich	99%
5-Bromo-*m*-xylene	TCI	> 98.0%
tert-Butylamine	Sigma-Aldrich	98%
n-Butyllithium (2.5 M or 1.6 M in hexanes)	Acros Organics	–
Celite® 545	VWR Chemicals	–
Chloroform (HPLC, EtOH stabilized)	Thermo Fisher	99%
Chloroform-*d* (99.8% D)	Sigma-Aldrich	–
meta-Chloroperoxybenzoic acid	Thermo Fisher	70-75%
Copper(I) bromide	Alfa Aesar	98%
Copper(I) iodide	Sigma-Aldrich	≥ 99.5%

Substance	**Supplier**	**Purity**
(2-Cyanophenyl)boronic acid	BLDpharm	97%
n-Decane	Sigma-Aldrich	analytical standard
n-Decane (dry)	Sigma-Aldrich	99.8%
1,2-Dibromoethane	Sigma-Aldrich	≥ 98.0%
Dichloromethane	Sigma-Aldrich	≥ 99.9%
Dichloromethane (HPLC, amylene stabilized)	Fisher scientific	99.8%
Dichloromethane (SPS)	Honeywell	≥ 99.8%
Dichloromethane-d_2 (99.8% D)	Eurisotop	–
1,2-Dichloropropane	Sigma-Aldrich	97%
Diethyl ether	Honeywell	–
Diethyl ether (SPS)	Honeywell	ACS reagent
N,*N*-Dimethylformamide	Fisher Scientific	≥ 99%
Dimethylsulfoxide	Grüssing	99%
Dioxane (dry, BHT stabilized)	Thermo Fisher	99.5%
Ethanol (denaturated with 1% MEK)	VWR Chemicals	99.5%
Ethanol (HPLC)	Fisher scientific	99.8%
Ethyl acetate	Fisher scientific	≥ 99%
Ethyl acetate (HPLC)	Honeywell	≥ 99.7%
2-Formylphenylboronic acid	BLDpharm	98%
n-Heptane (HPLC)	Honeywell	≥ 99%
n-Hexane	Honeywell	≥ 95%
1-Hexyne	Acros Organics	–
Hydrochloric acid (fuming 36.5-38%)	Honeywell	–
Iodomethane	Thermo Fisher	99%
2-Isopropylphenol	Sigma-Aldrich	98%
Lithium aluminum hydride (1 M in THF)	Acros Organics	–
Magnesium chloride, anhydrous	Sigma-Aldrich	≥ 98%
Magnesium sulfate	Honeywell	≥ 97%
Magnesium turnings	Carl Roth	≥ 99.9%
Manganese(II) chloride, 80 mesh, anhydrous	Acros Organics	99%

Substance	**Supplier**	**Purity**
Methanol	Fisher scientific	≥ 99.5%
Methyl *tert*-butyl ether (HPLC)	Honeywell	≥ 99.8%
Methyl chloroformate	Sigma-Aldrich	99%
Methylmagnesium bromide (3 M in Et_2O)	Sigma-Aldrich	–
Molecular sieves 3 Å	Carl Roth	–
Molecular sieves 4 Å	Carl Roth	–
Molecular sieves 5 Å, powder < 50 micrometer	Acros Organics	–
Molybdenum(V) chloride	Carbolution	99.5%
Nitric acid (64-66%)	Sigma-Aldrich	–
Palladium on carbon (5 *wt*% loading)	Sigma-Aldrich	–
Paraformaldehyde, extra pure	Merck	–
n-Pentane	Honeywell	≥ 99%
Petroleum ether (PE) (bp 40-60 °C)	Fisher scientific	–
Phosphorus(V) oxychloride	Sigma-Aldrich	99%
Phosphorus pentoxide	Thermo Fisher	≥ 99%
Phosphorus tribromide	Sigma-Aldrich	97%
Piperidine	Merck	≥ 99%
Potassium acetate	Grüssing	99%
Potassium carbonate	Grüssing	99%
Potassium hydroxide (powder)	Sigma-Aldrich	synthesis grade
2-Propanol	Honeywell	≥ 99.8%
Propyne (~1 M in THF)	TCI	–
Pyridine	Grüssing	99%
Sand	Fisher scientific	–
Sodium bicarbonate	Grüssing	99%
Sodium borohydride	Thermo Fisher	98%
Sodium *tert*-butoxide	Merck	~98%
Sodium chloride	Honeywell	≥ 99.5%
Sodium hydroxide (pellets)	Fisher scientific	98.9%
Sodium methoxide solution (25 *wt*% in MeOH)	Sigma-Aldrich	–

Substance	**Supplier**	**Purity**
Sodium sulfate	Grüssing	99%
1,1,2,2-Tetrachlorethane-d_2 (99.5% D)	Deutero	–
Tetrachloromethane	Sigma-Aldrich	≥ 99.9%
Tetrahydrofuran	Acros Organics	99.6%
Tetrahydrofuran (HPLC, BHT stabilized)	Fisher scientific	–
Tetrahydrofuran (SPS, inhibitor free)	Honeywell	≥ 99.9%
Tetrahydrofuran-d_8 (99.5% D)	Eurisotop	–
Tin(II) chloride dihydrate	Grüssing	99%
Tin shot, 3 mm	Sigma-Aldrich	99.8%
Toluene	Sigma-Aldrich	≥ 99.7%
Toluene (SPS)	Honeywell	≥ 99.9%
Toluene-d_8	Deutero	99%
Tri-*tert*-butylphosphonium tetrafluoroborate	Carbolution	97%
Triethylamine	Sigma-Aldrich	≥ 99.5%
Triethylamine (HPLC)	Fisher scientific	≥ 99.5%
Triflic anhydride	Carbolution	98%
Tris(dibenzylideneacetone)dipalladium(0)	Acros Organics	97%
Tris(triphenylphosphine)rhodium(I) chloride	Sigma-Aldrich	99.9%
XPhos	Sigma-Aldrich	97%
Xylene (isomeric mixture)	Grüssing	99%

7.3 NMR Spectra

^{1}H and ^{13}C NMR spectra of compounds **120**, **121**, **122**, **123**, and **125** can be found in reference 186; those of **154**, **155**, **159**, **160**, **161**, **152**, and **166** are reported in reference 306.

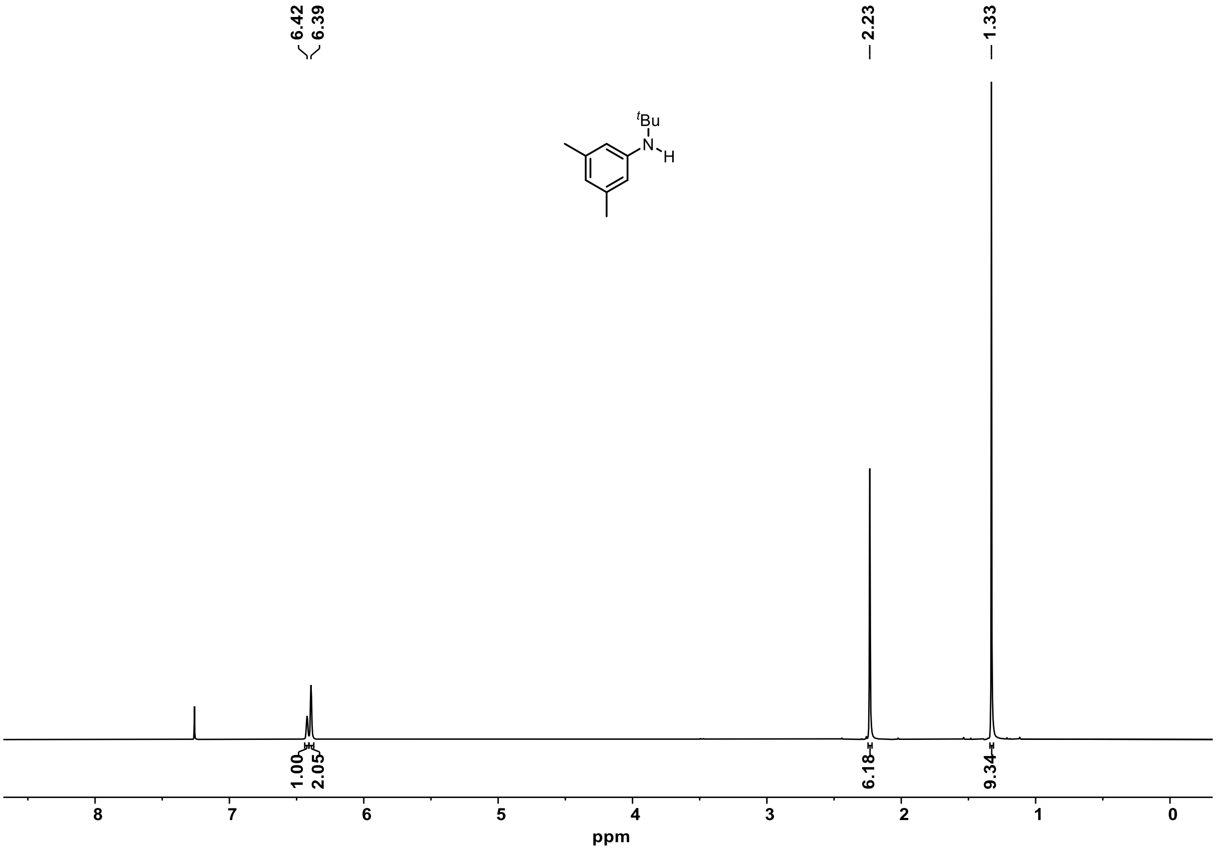

Figure 7.1: ^{1}H NMR spectrum of **80** (300 MHz, $CDCl_3$).

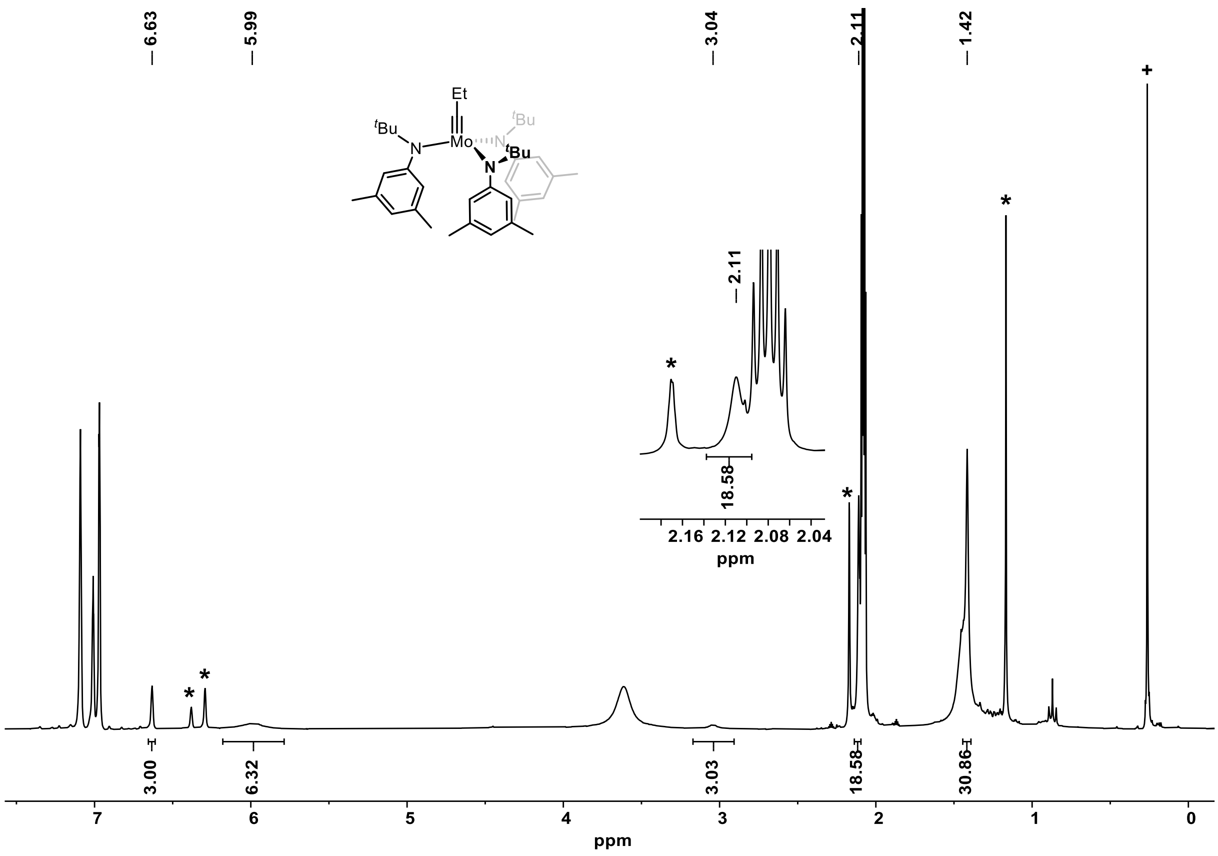

Figure 7.2: ^{1}H NMR spectrum of **8** (300 MHz, toluene-d_8). Residual signals: *: free ligand **80**, +: grease.

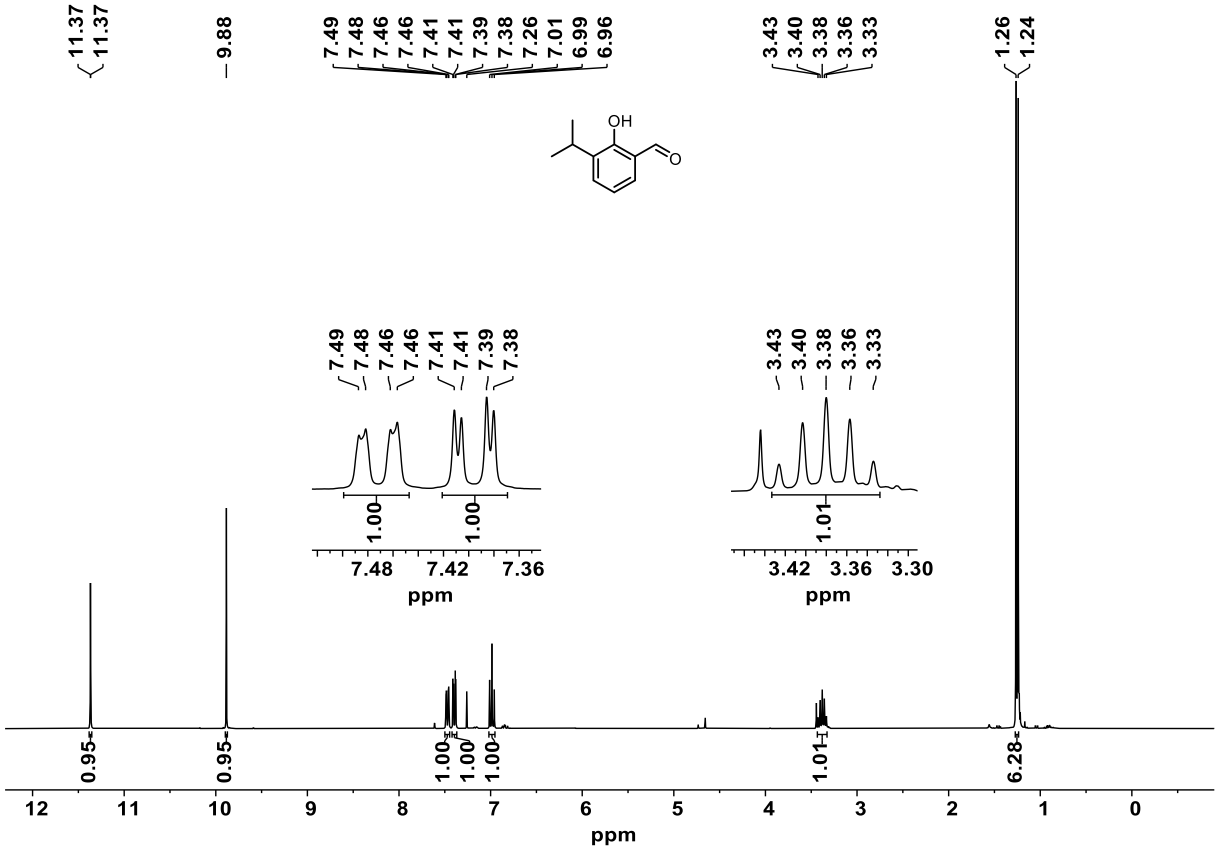

Figure 7.3: ^{1}H NMR spectrum of **88** (300 MHz, CDCl$_3$).

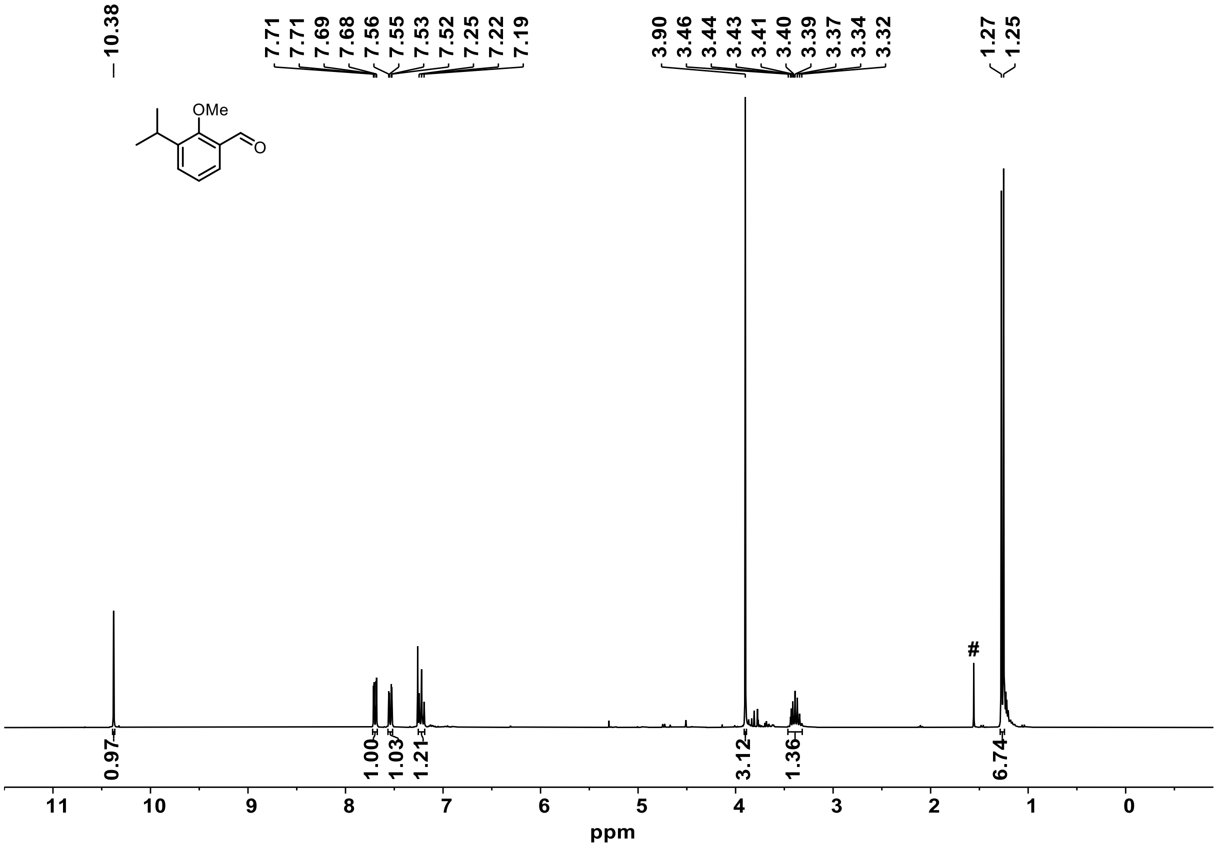

Figure 7.4: ^{1}H NMR spectrum of **89** (300 MHz, CDCl$_3$). #: water.

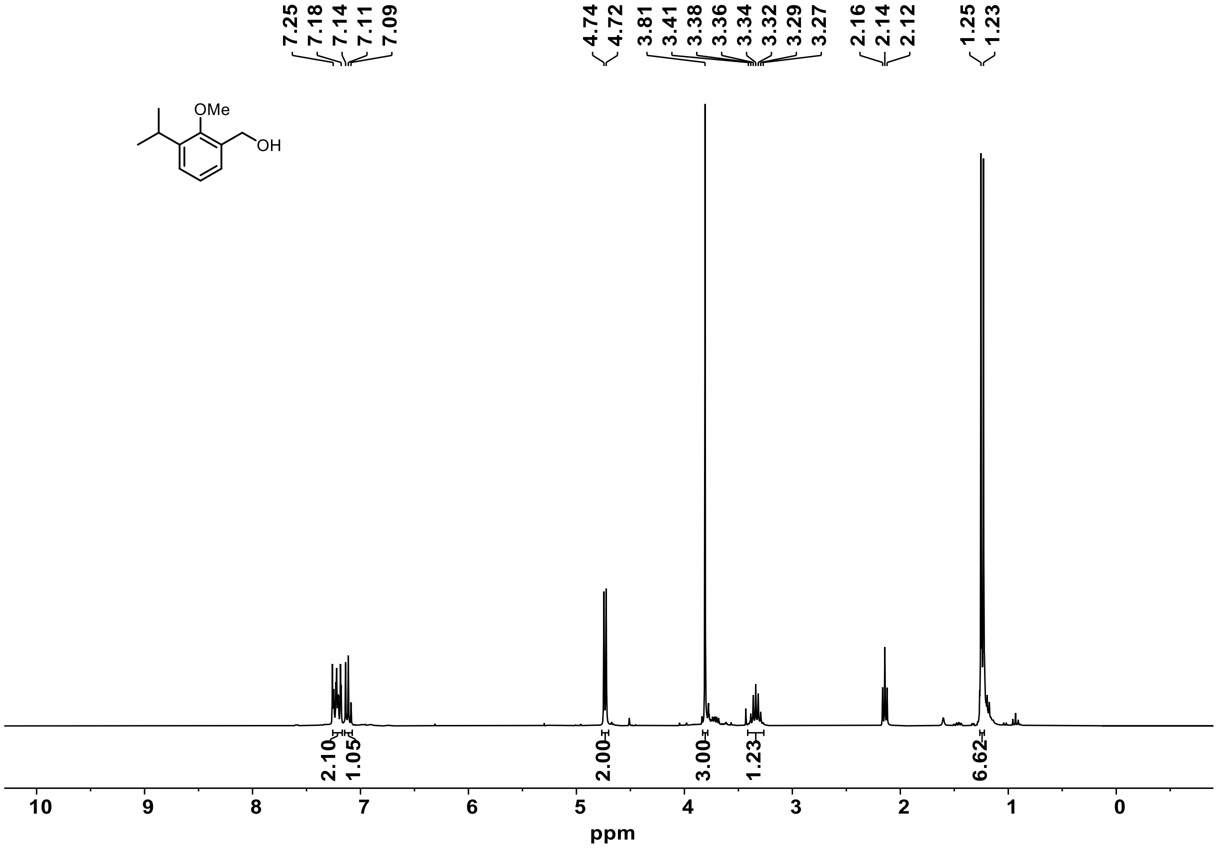

Figure 7.5: ^{1}H NMR spectrum of **90** (300 MHz, CDCl$_3$).

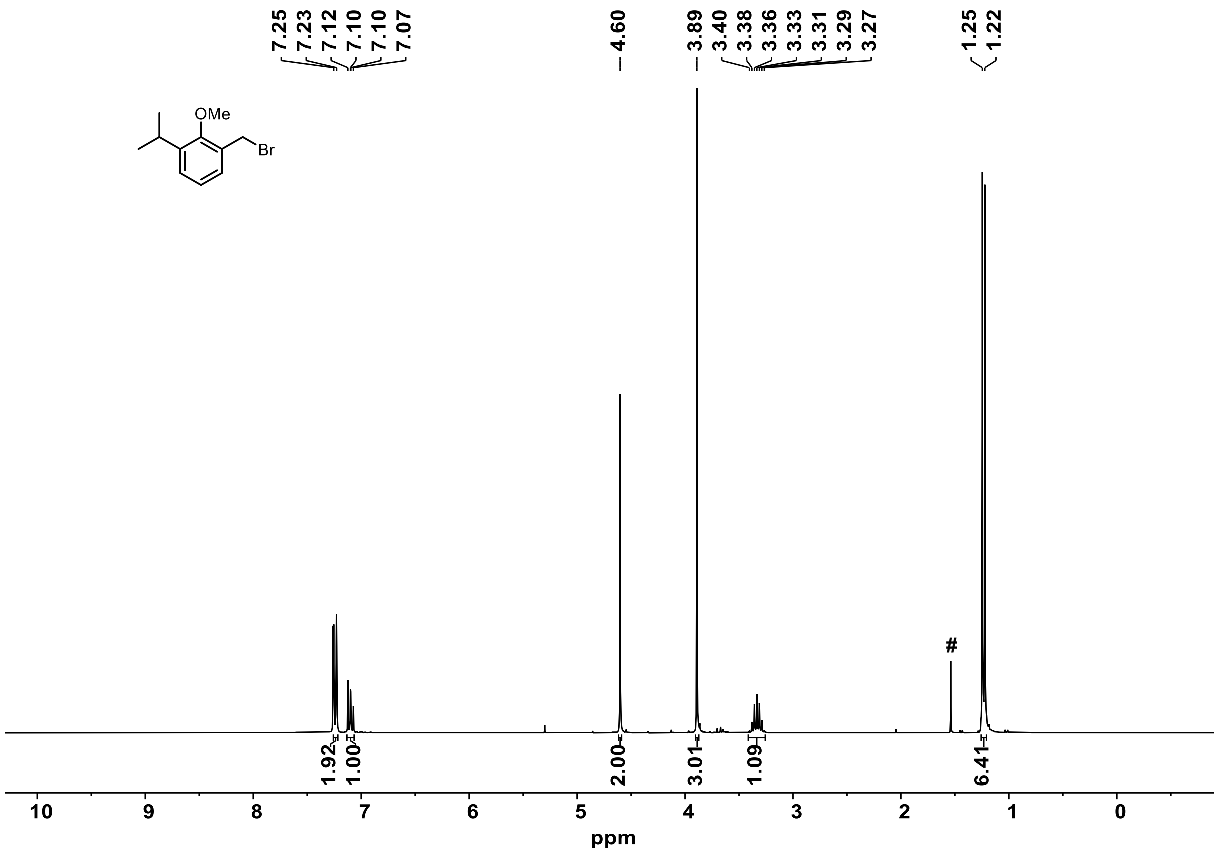

Figure 7.6: ^{1}H NMR spectrum of compound **91** (300 MHz, CDCl$_3$). #: water.

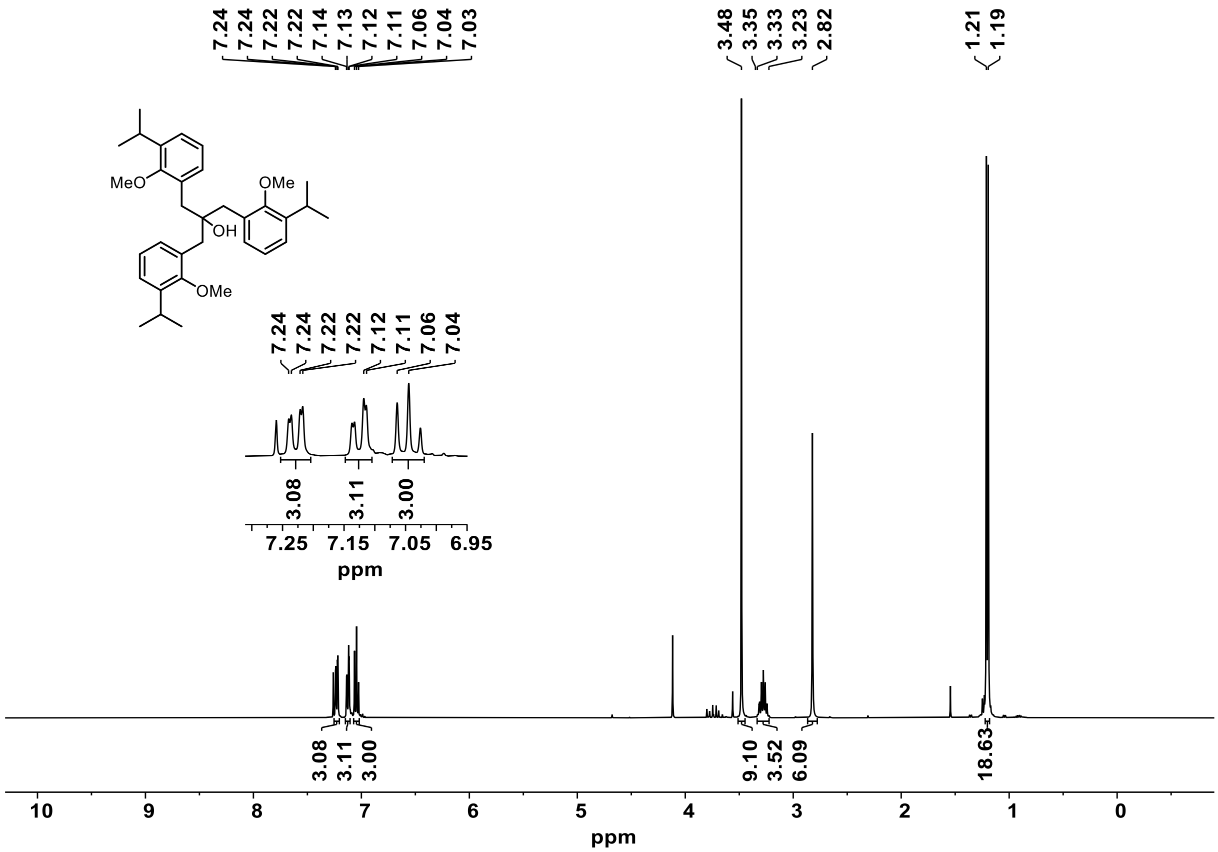

Figure 7.7: ^{1}H NMR spectrum of **92** (400 MHz, CDCl$_3$).

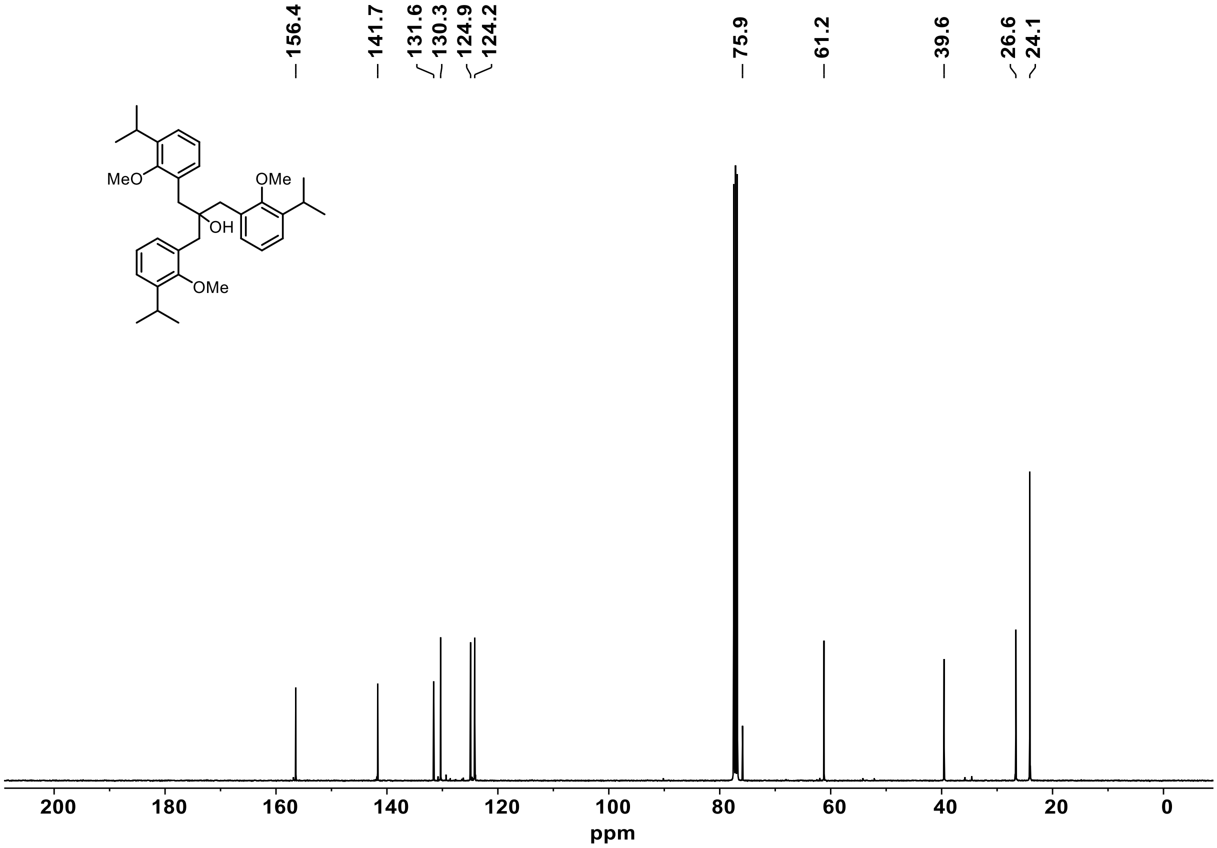

Figure 7.8: ^{13}C NMR spectrum of **92** (100 MHz, $CDCl_3$).

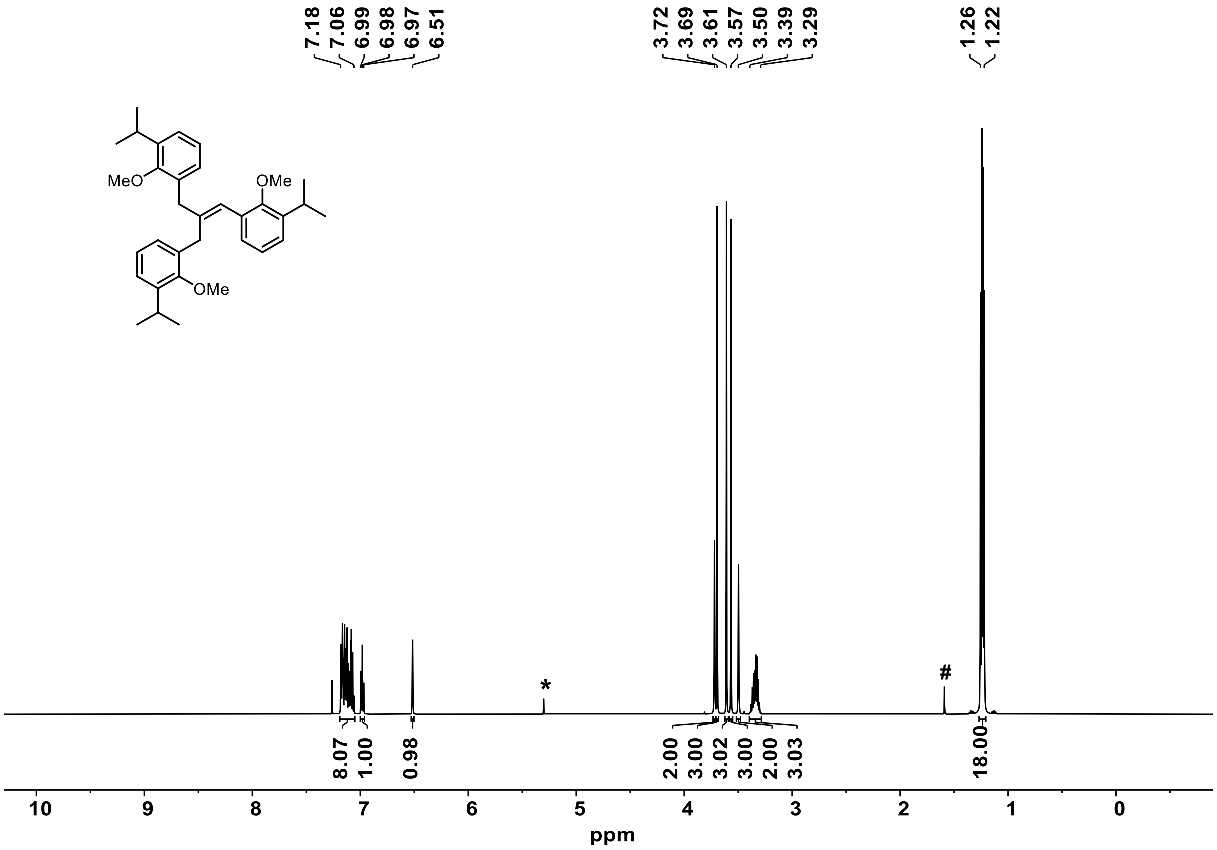

Figure 7.9: ^{1}H NMR spectrum of **93** (600 MHz, $CDCl_3$). #: H_2O, *: CH_2Cl_2.

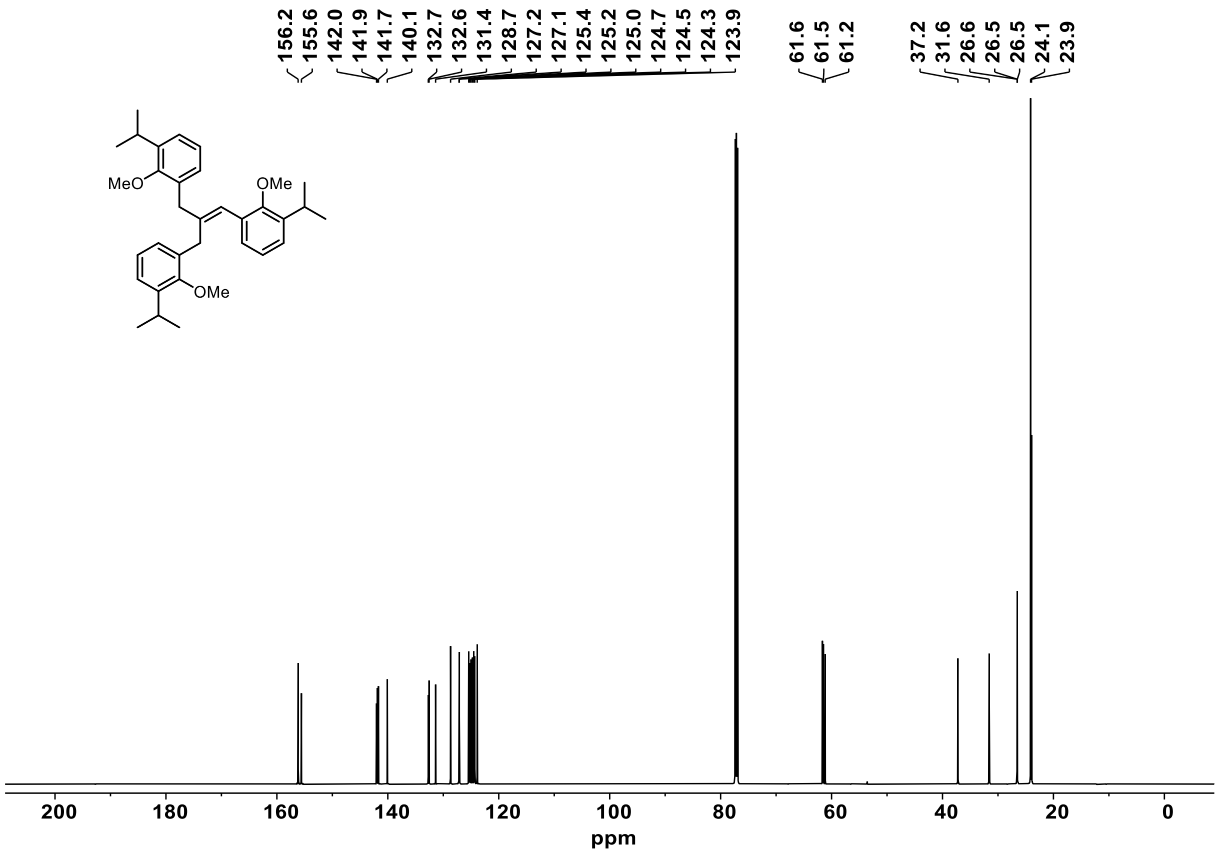

Figure 7.10: ^{13}C NMR spectrum of **93** (150 MHz, $CDCl_3$).

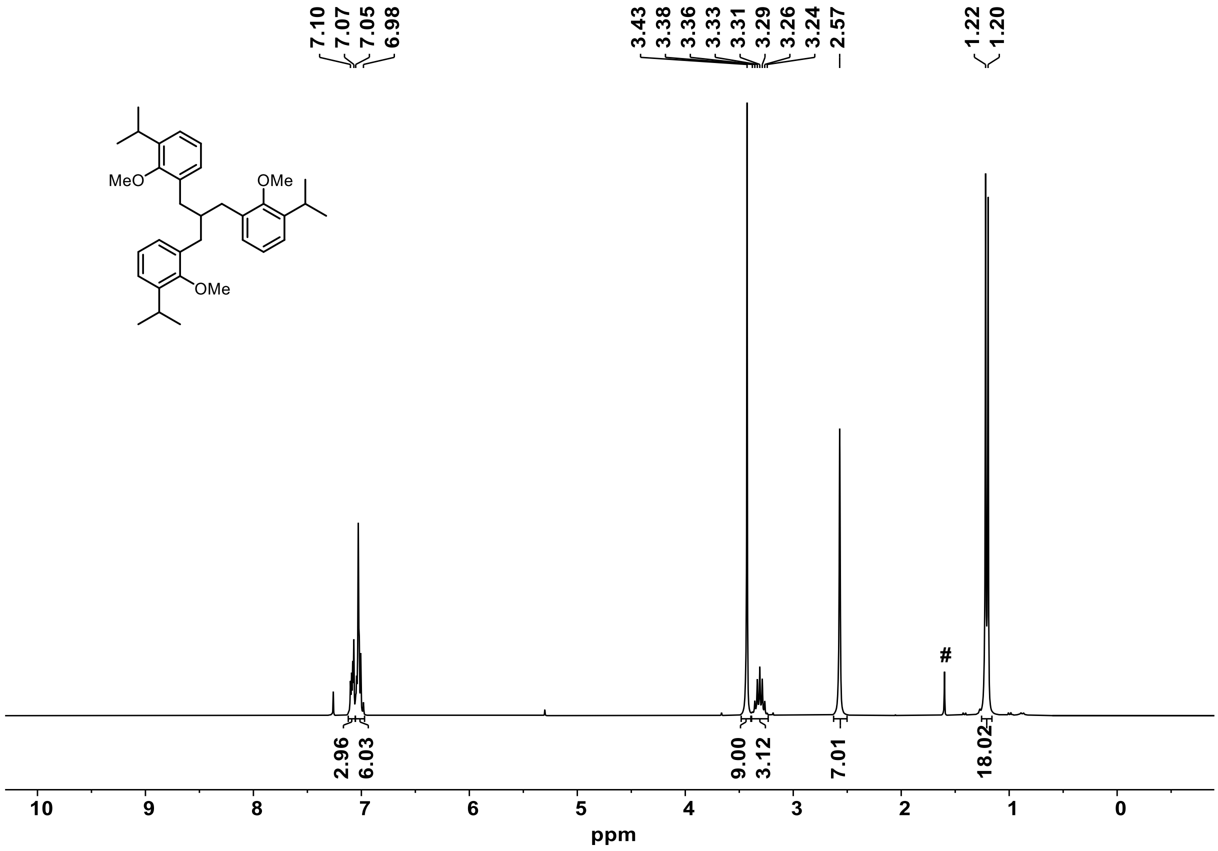

Figure 7.11: ^{1}H NMR spectrum of **94** (300 MHz, $CDCl_3$). #: H_2O.

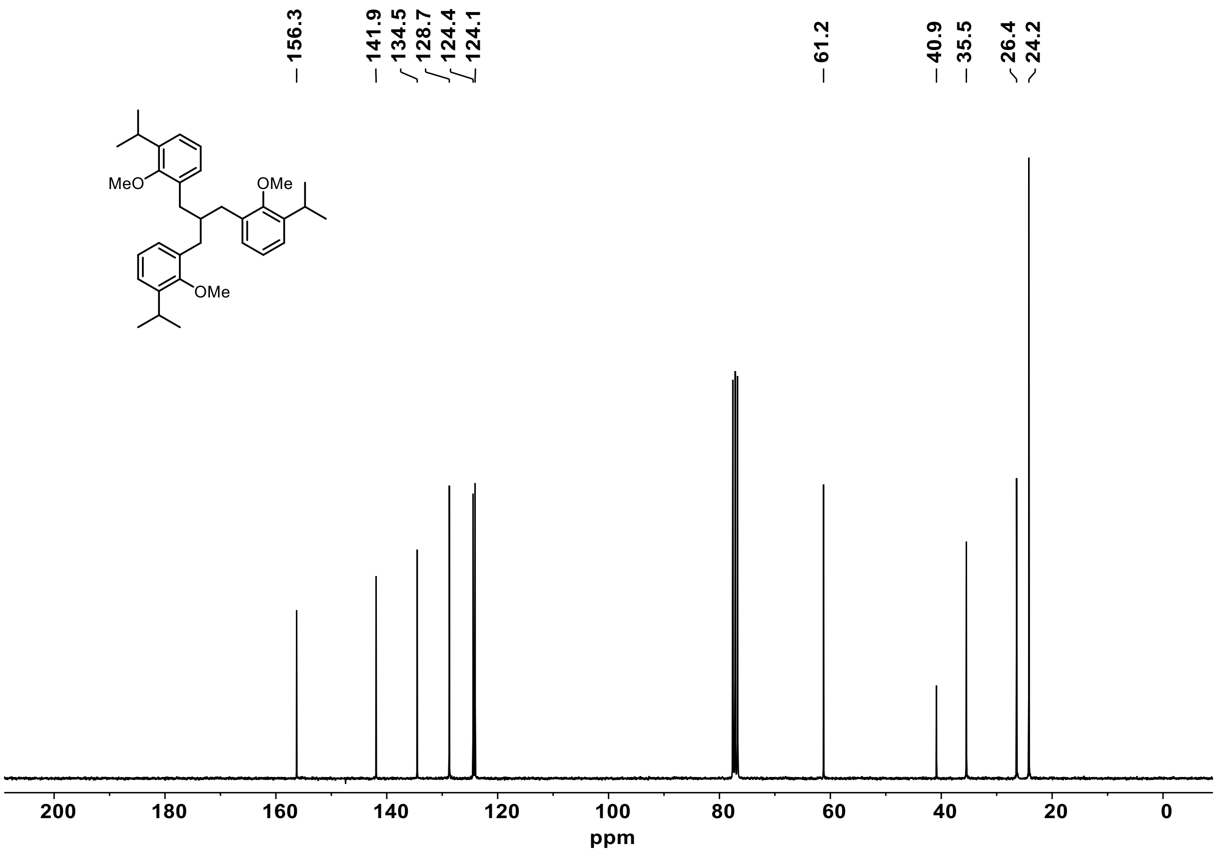

Figure 7.12: ^{13}C NMR spectrum of **94** (75 MHz, CDCl$_3$).

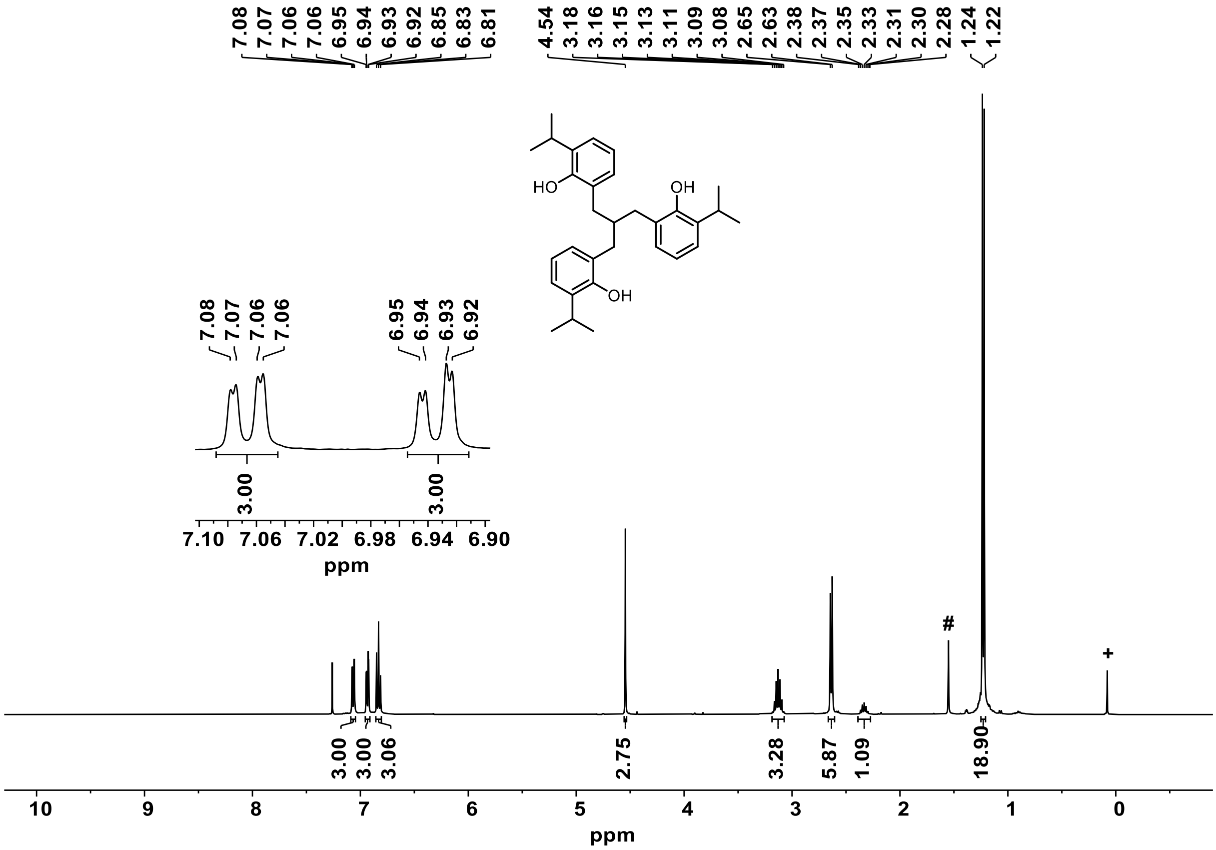

Figure 7.13: ^{1}H NMR spectrum of **11** (300 MHz, CDCl$_3$). #: H_2O, +: grease.

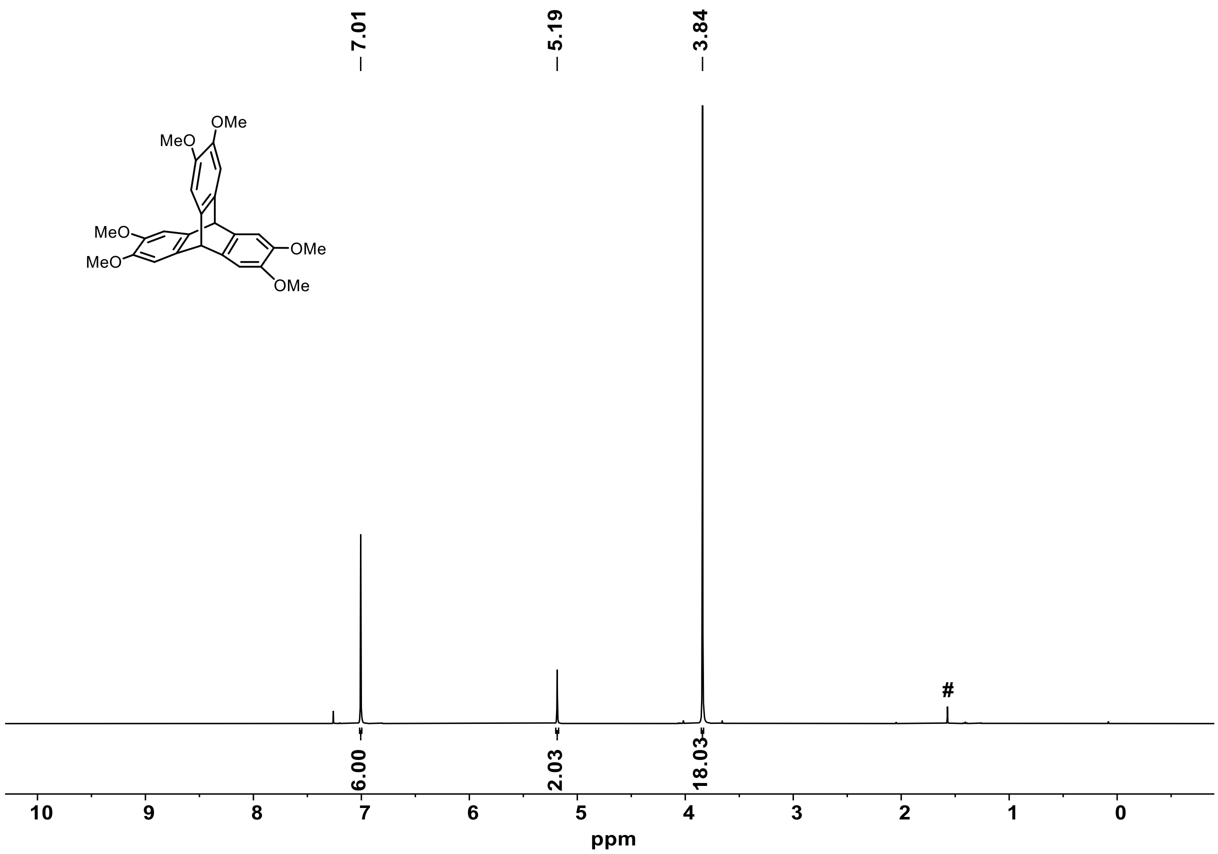

Figure 7.14: ^{1}H NMR spectrum of compound **96** (400 MHz, $CDCl_3$). Residual solvent signals: #: H_2O.

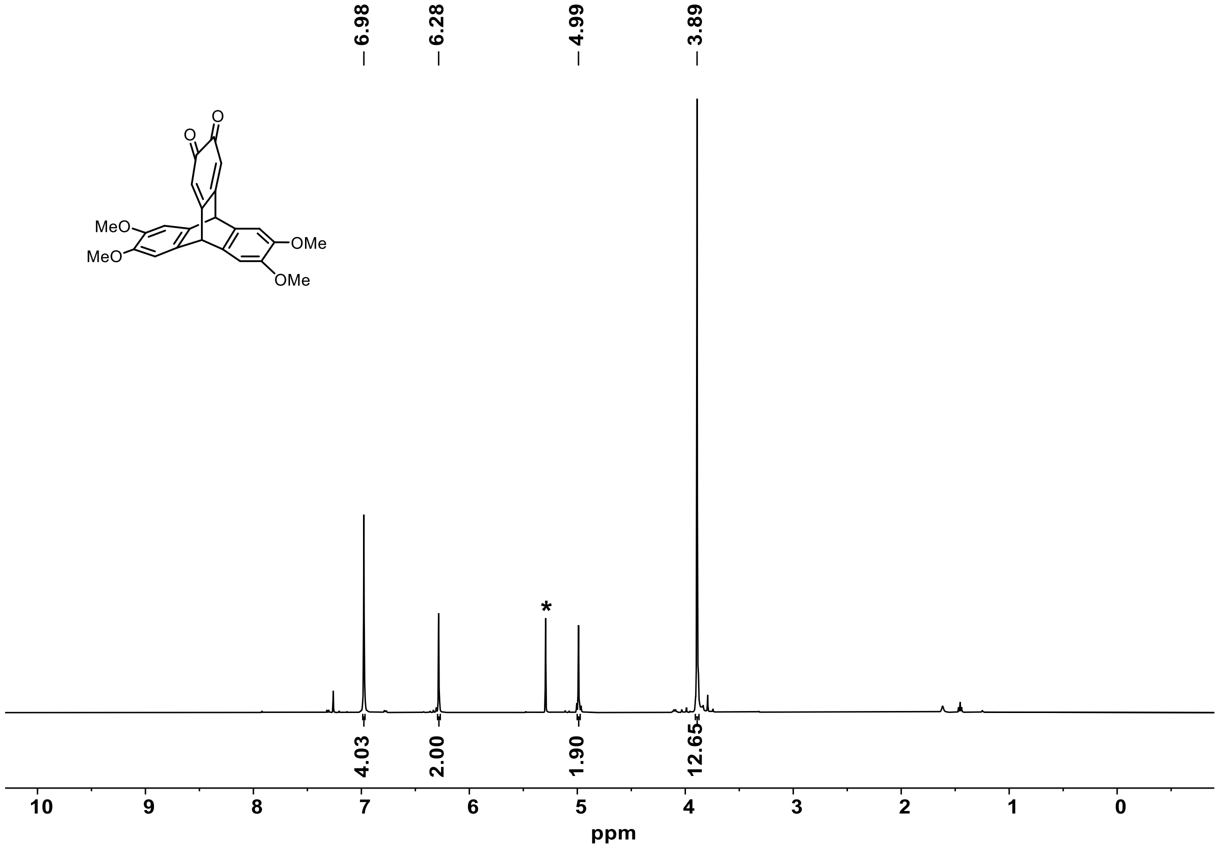

Figure 7.15: ^{1}H NMR spectrum of **97** (500 MHz, $CDCl_3$). Residual solvent signals: *: CH_2Cl_2.

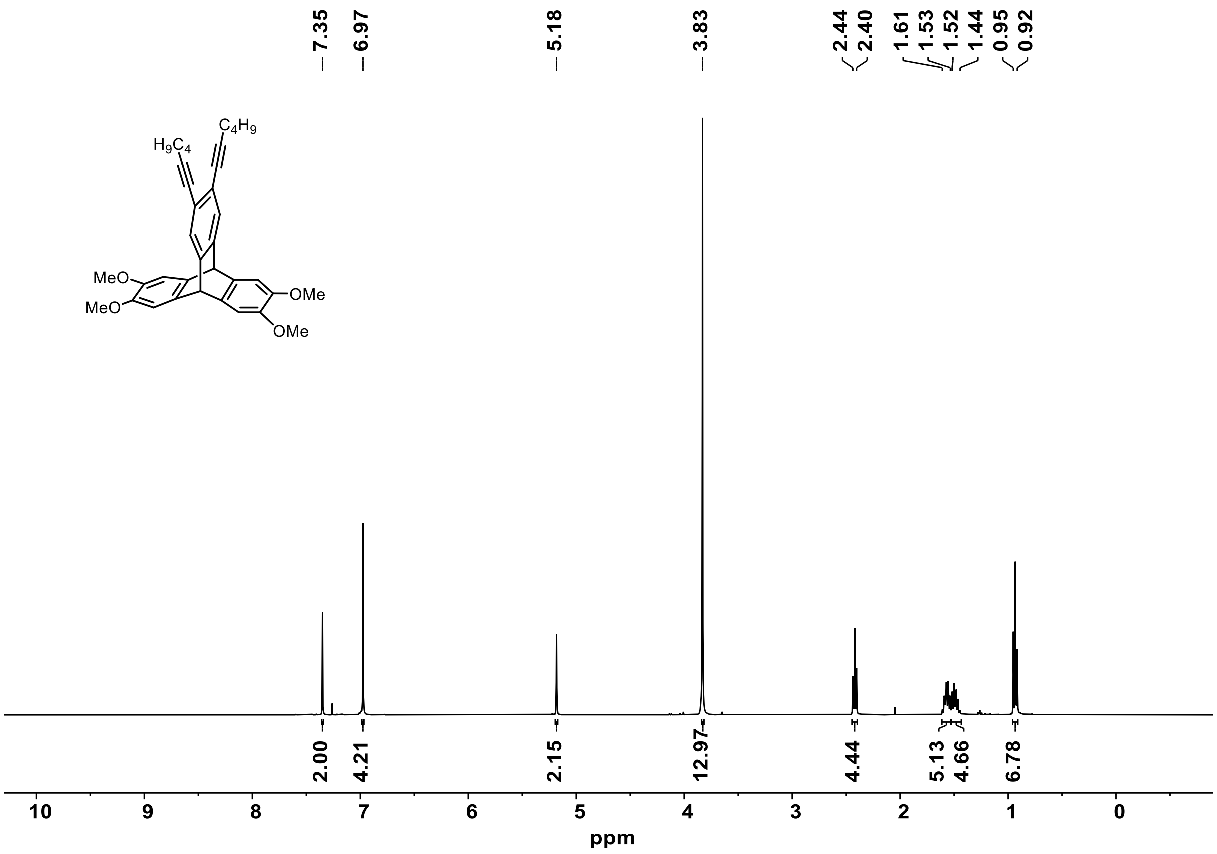

Figure 7.16: ^{1}H NMR spectrum of **98** (400 MHz, CDCl$_3$).

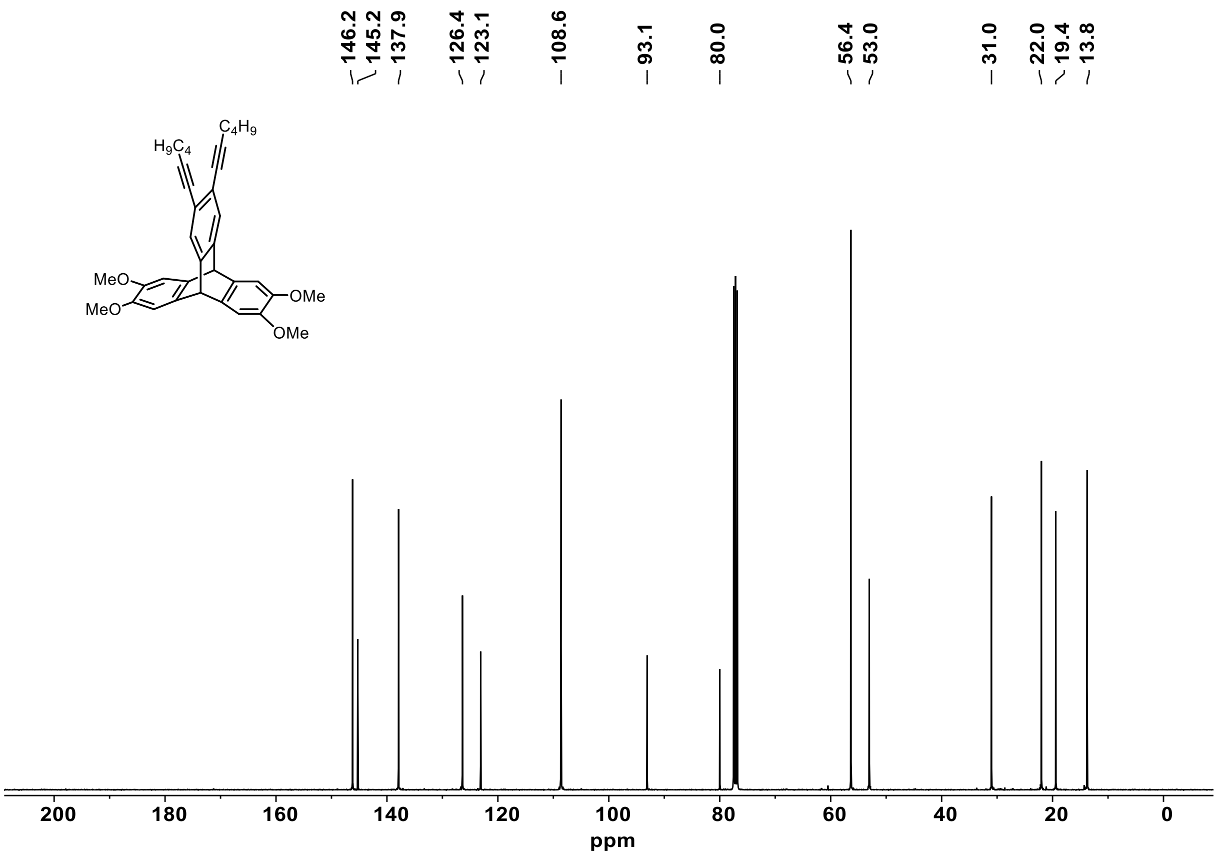

Figure 7.17: ^{13}C NMR spectrum of **98** (100 MHz, CDCl$_3$).

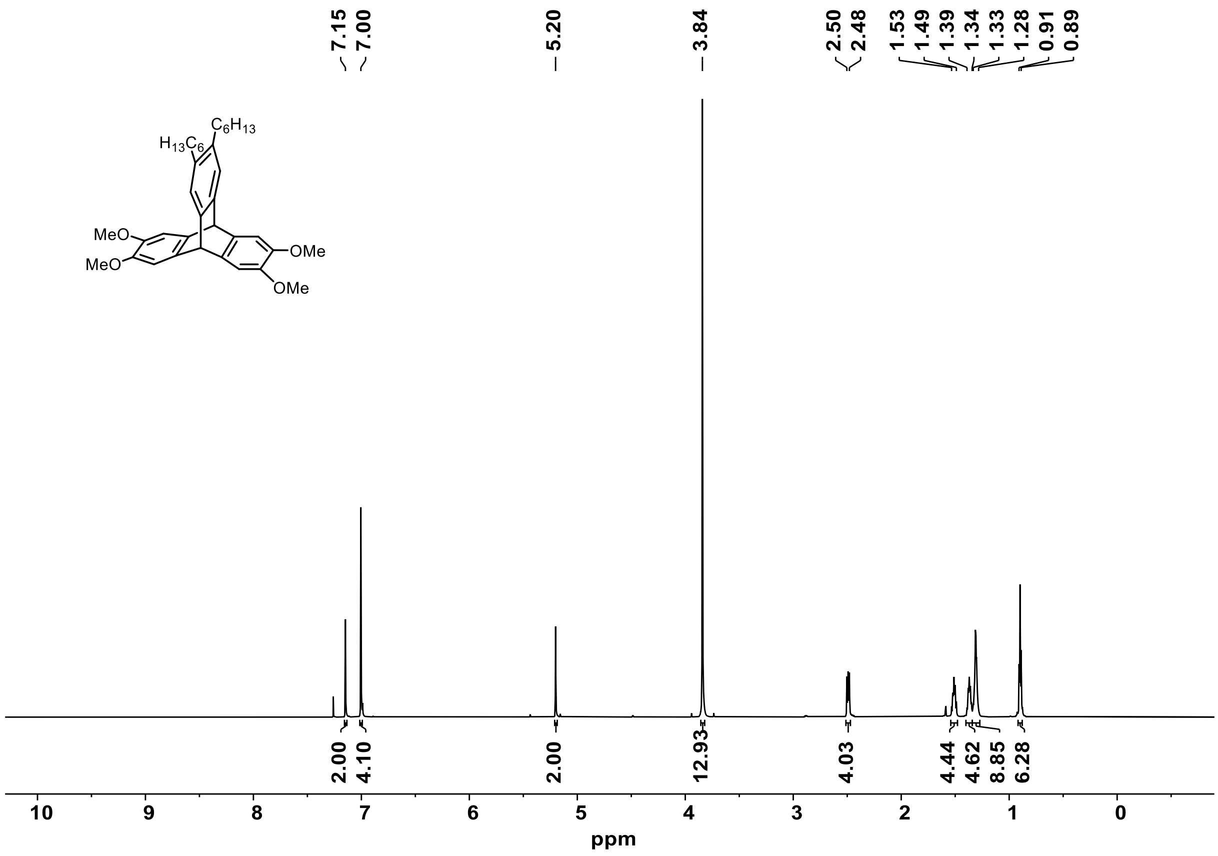

Figure 7.18: ^{1}H NMR spectrum of **99** (700 MHz, $CDCl_3$).

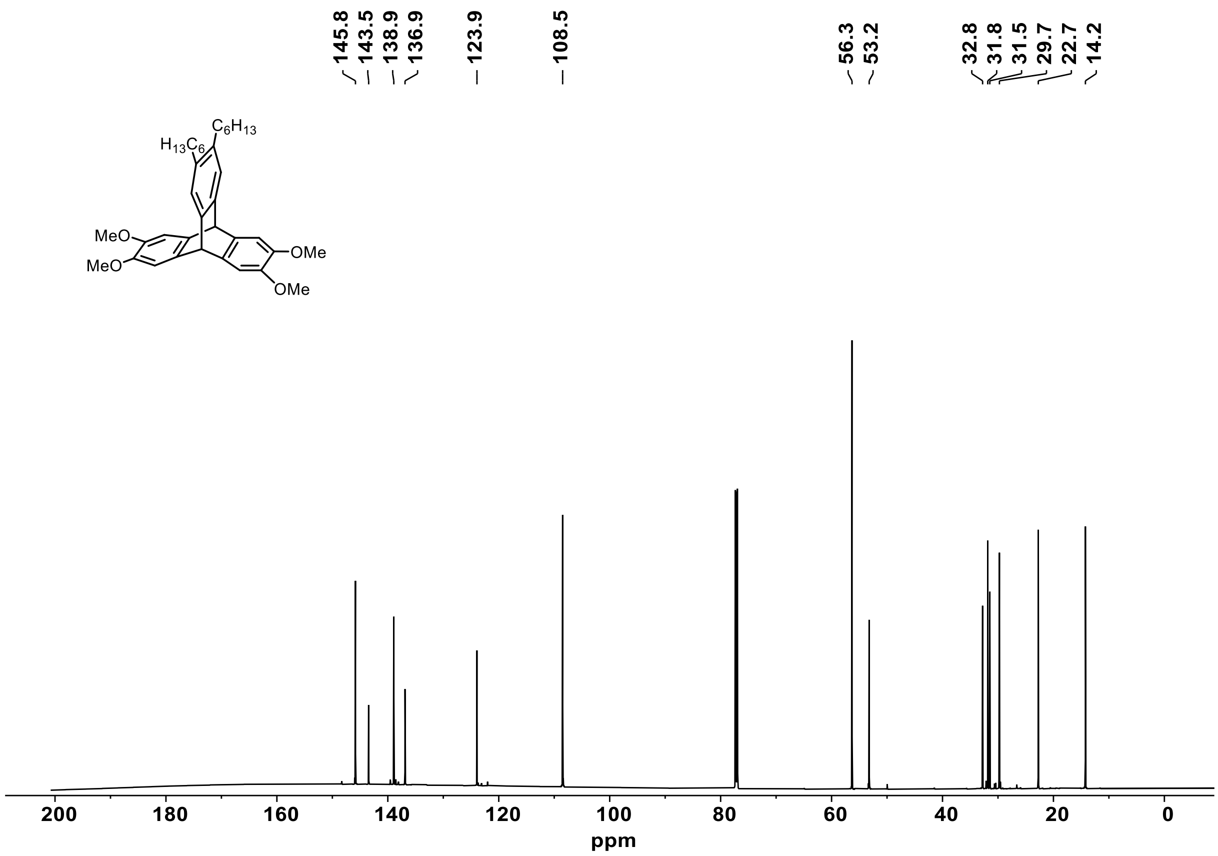

Figure 7.19: ^{13}C NMR spectrum of **99** (176 MHz, $CDCl_3$).

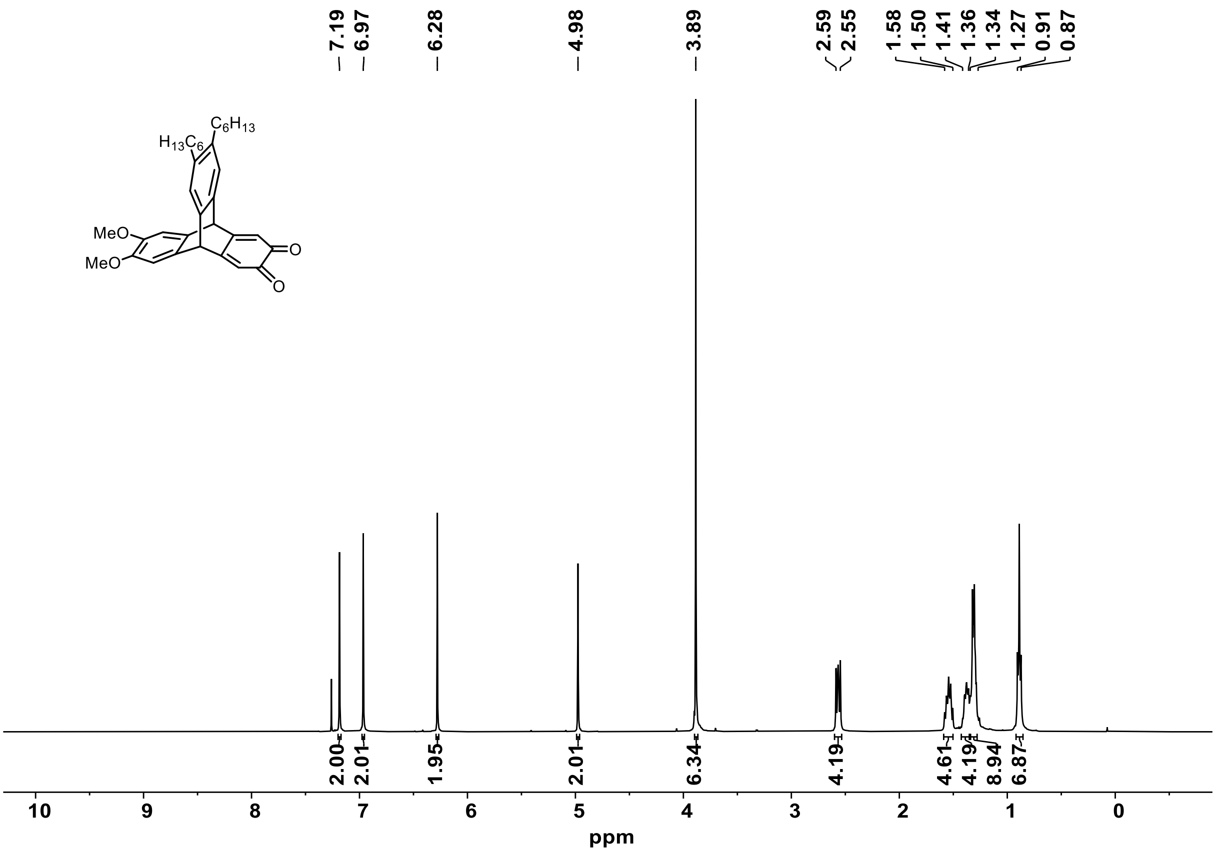

Figure 7.20: ^{1}H NMR spectrum of **100** (400 MHz, CDCl$_3$).

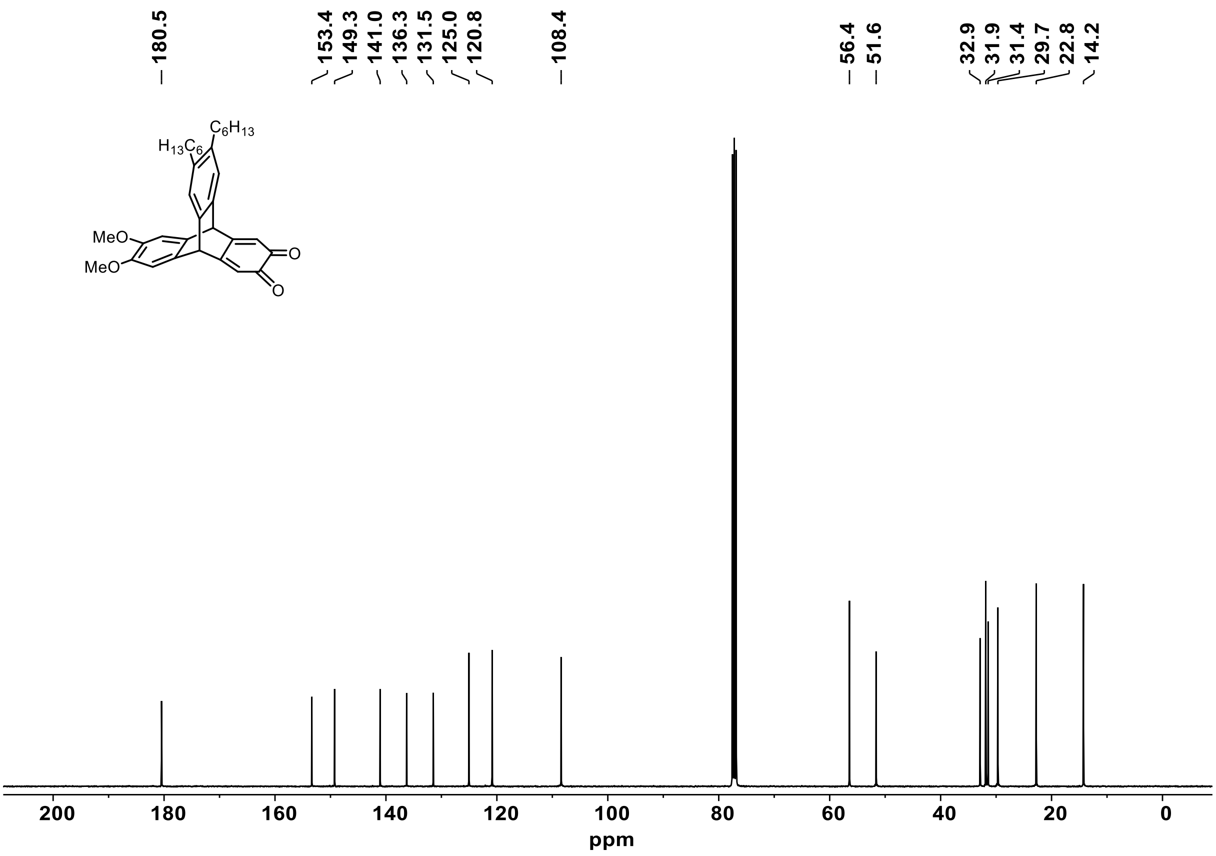

Figure 7.21: ^{13}C NMR spectrum of **100** (100 MHz, CDCl$_3$).

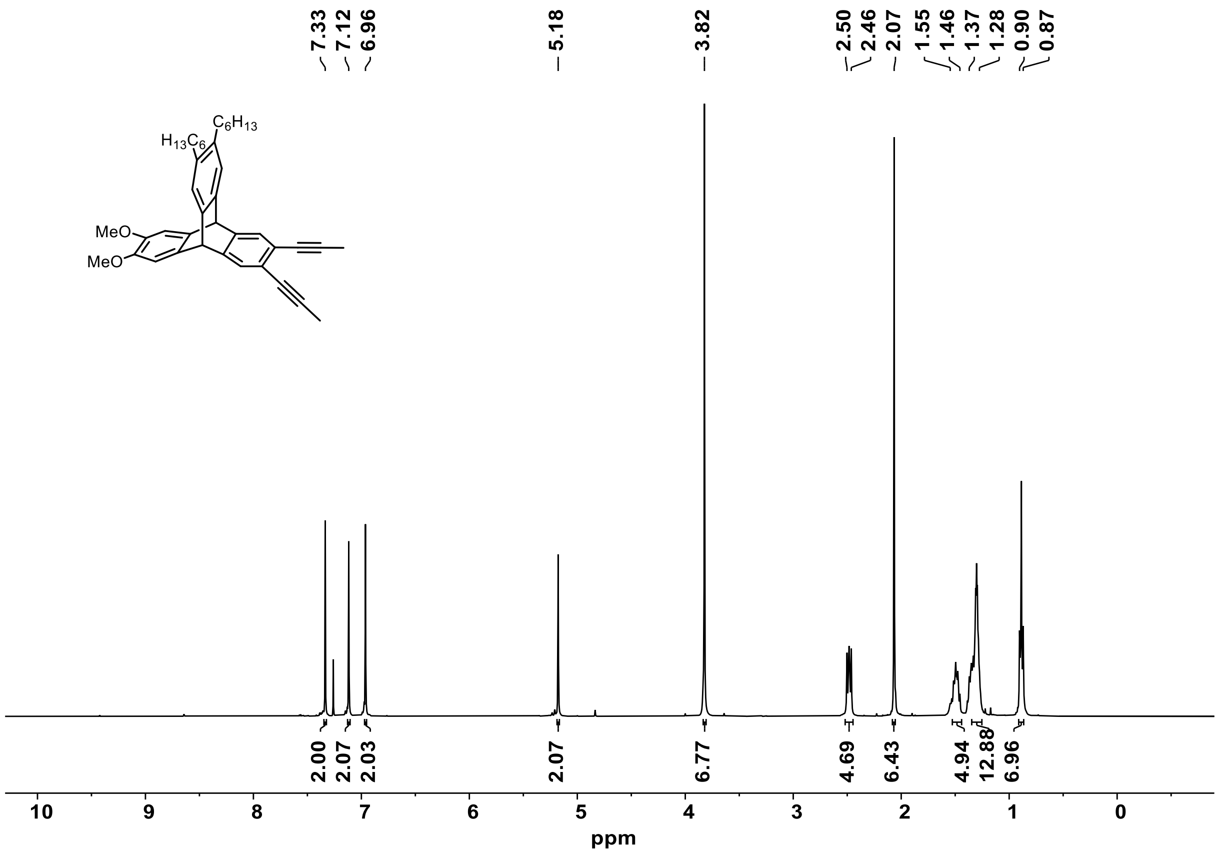

Figure 7.22: ^{1}H NMR spectrum of **101** (400 MHz, CDCl$_3$).

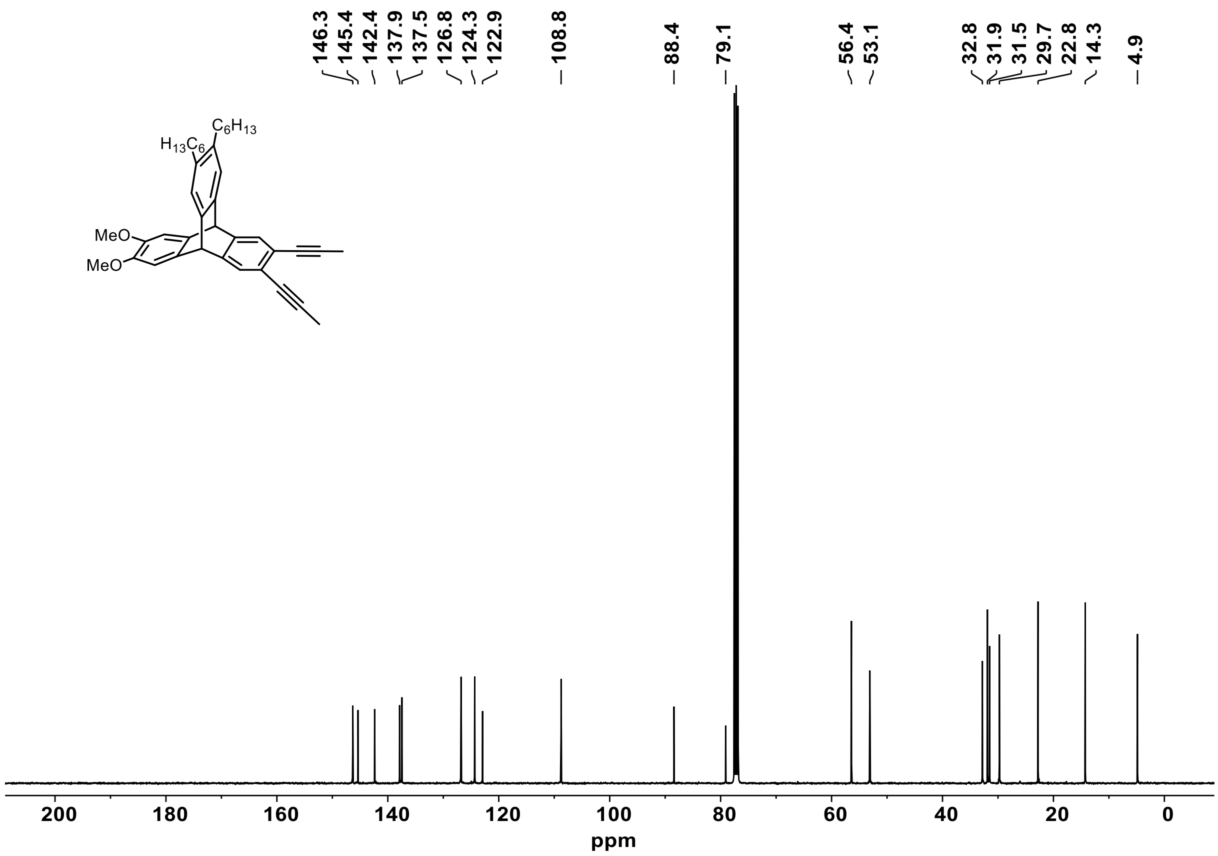

Figure 7.23: ^{13}C NMR spectrum of **101** (100 MHz, CDCl$_3$).

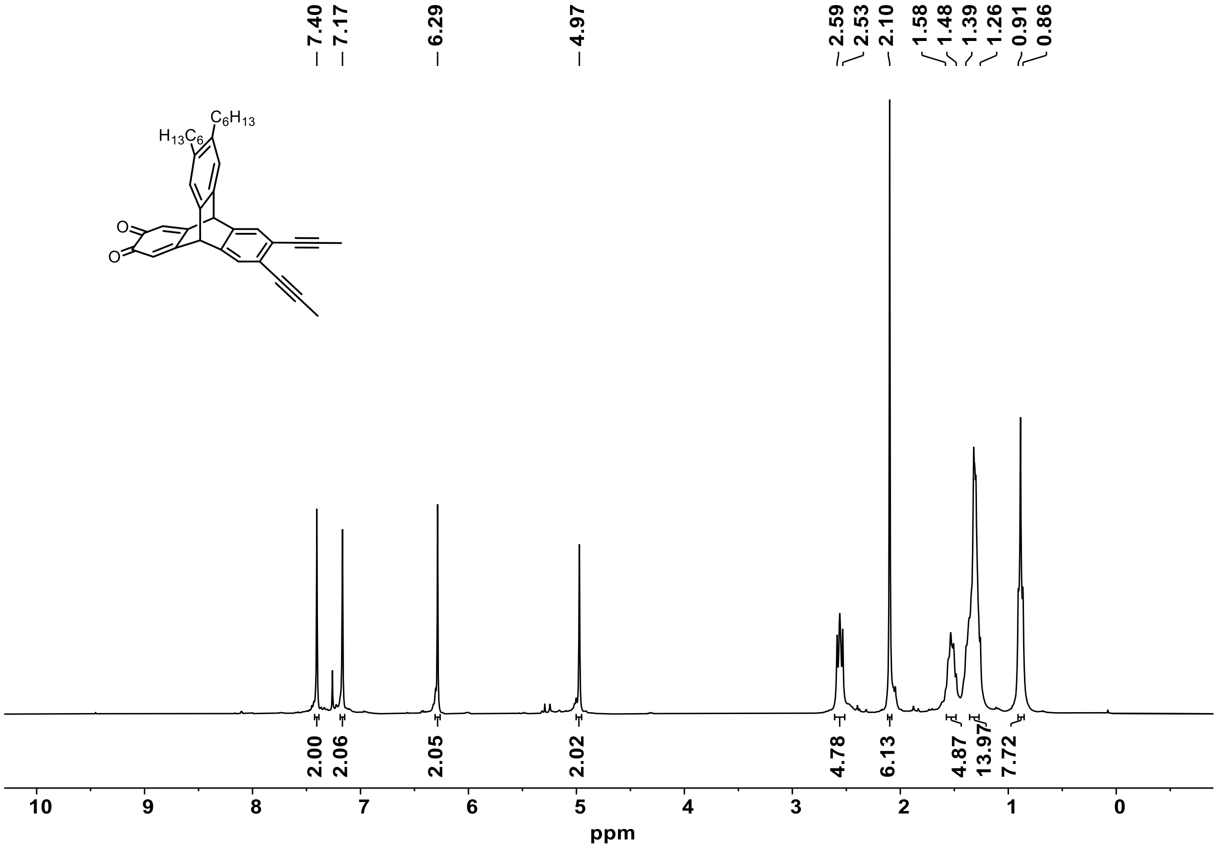

Figure 7.24: ^{1}H NMR spectrum of **102** (300 MHz, $CDCl_3$).

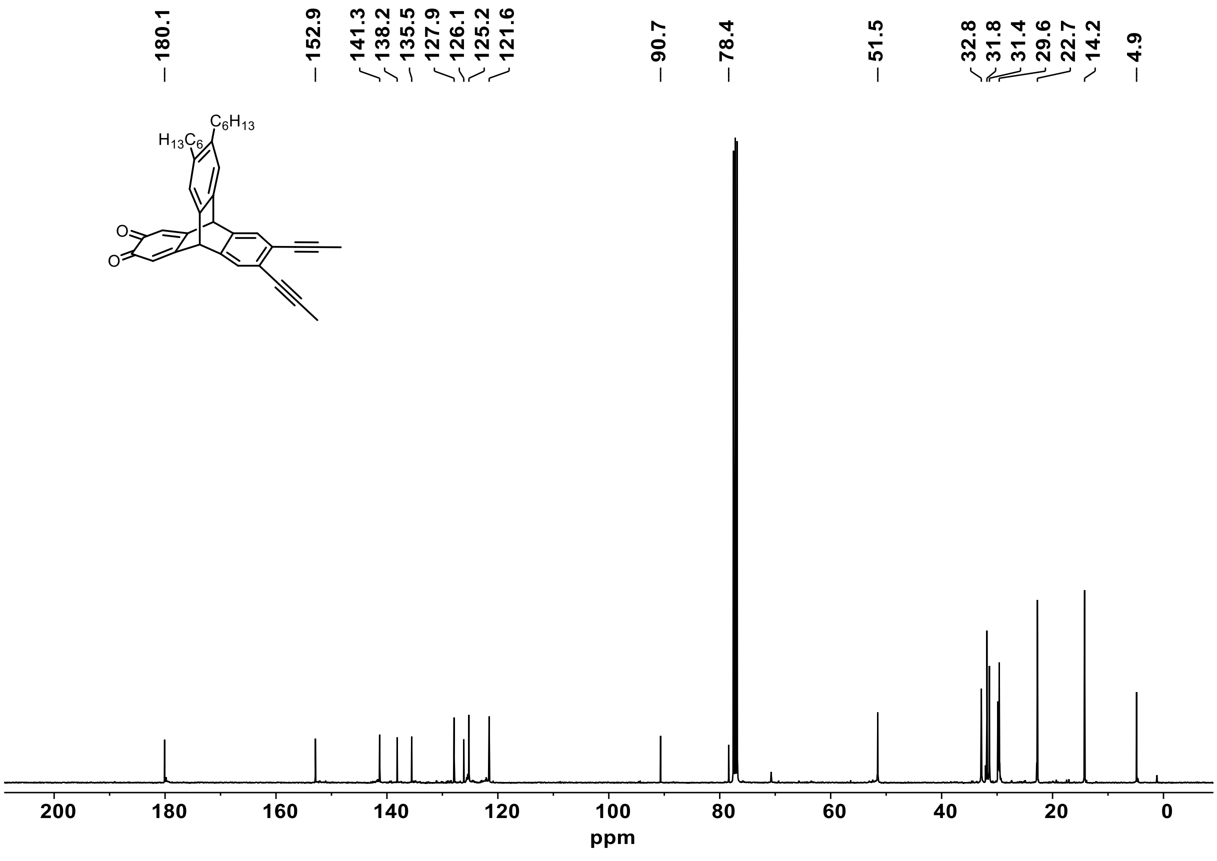

Figure 7.25: ^{13}C NMR spectrum of **102** (100 MHz, $CDCl_3$).

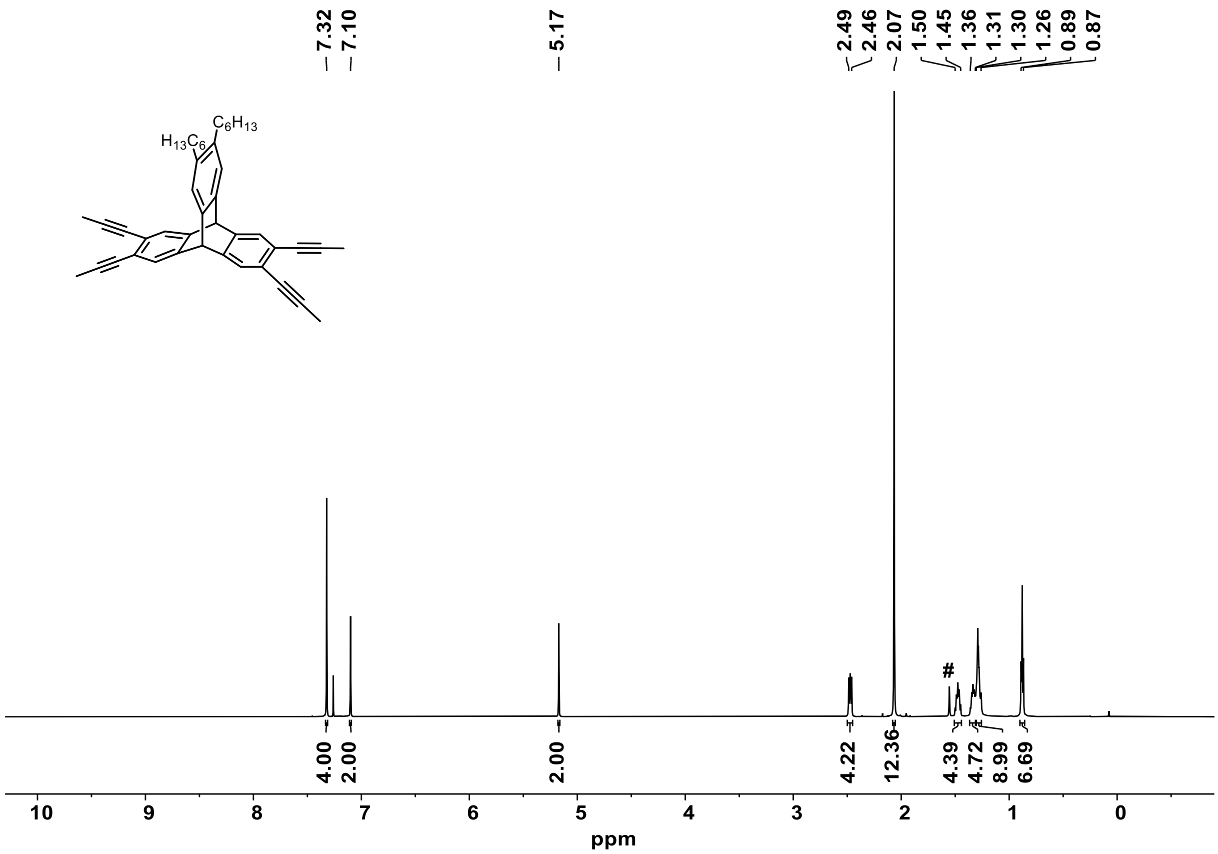

Figure 7.26: ^{1}H NMR spectrum of **75** (600 MHz, $CDCl_3$). #: H_2O.

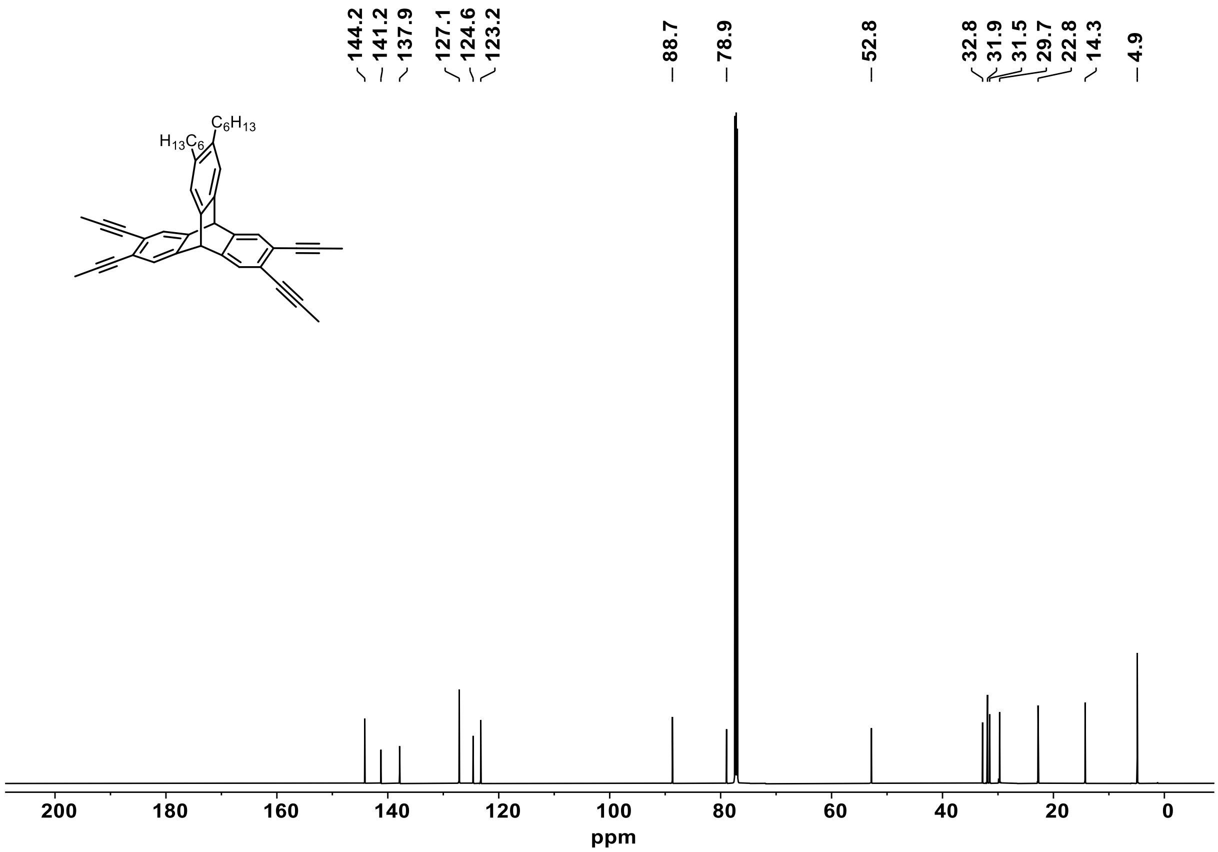

Figure 7.27: ^{13}C NMR spectrum of **75** (150 MHz, $CDCl_3$).

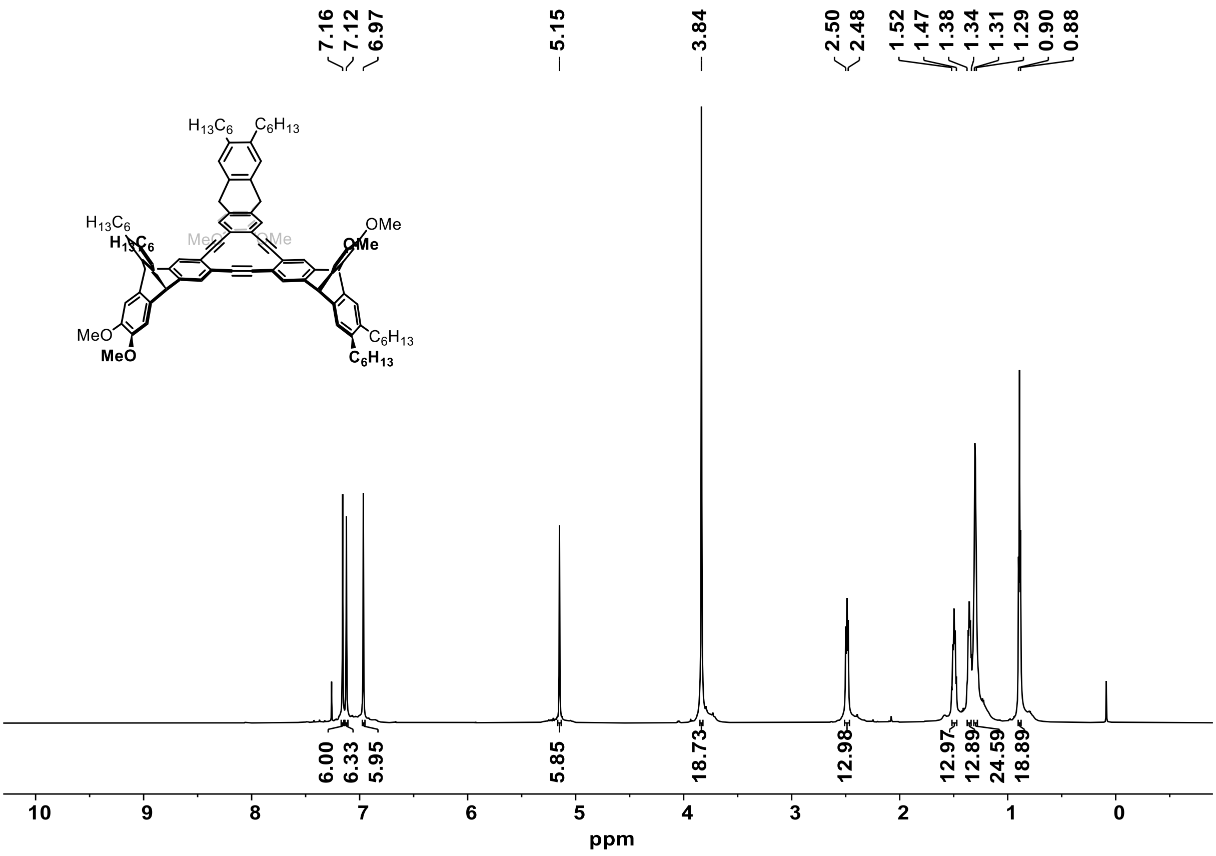

Figure 7.28: ^{1}H NMR spectrum of **103a** (700 MHz, $CDCl_3$).

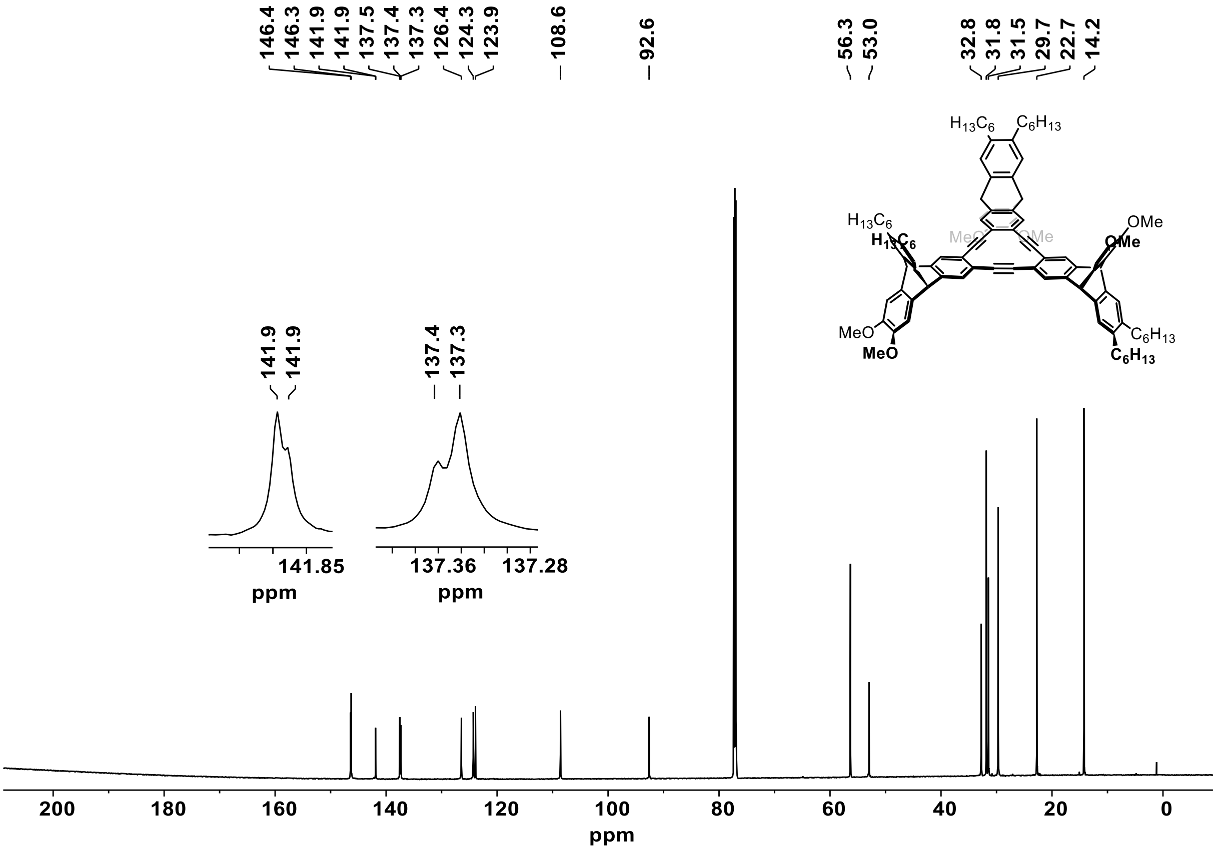

Figure 7.29: ^{13}C NMR spectrum of **103a** (176 MHz, $CDCl_3$).

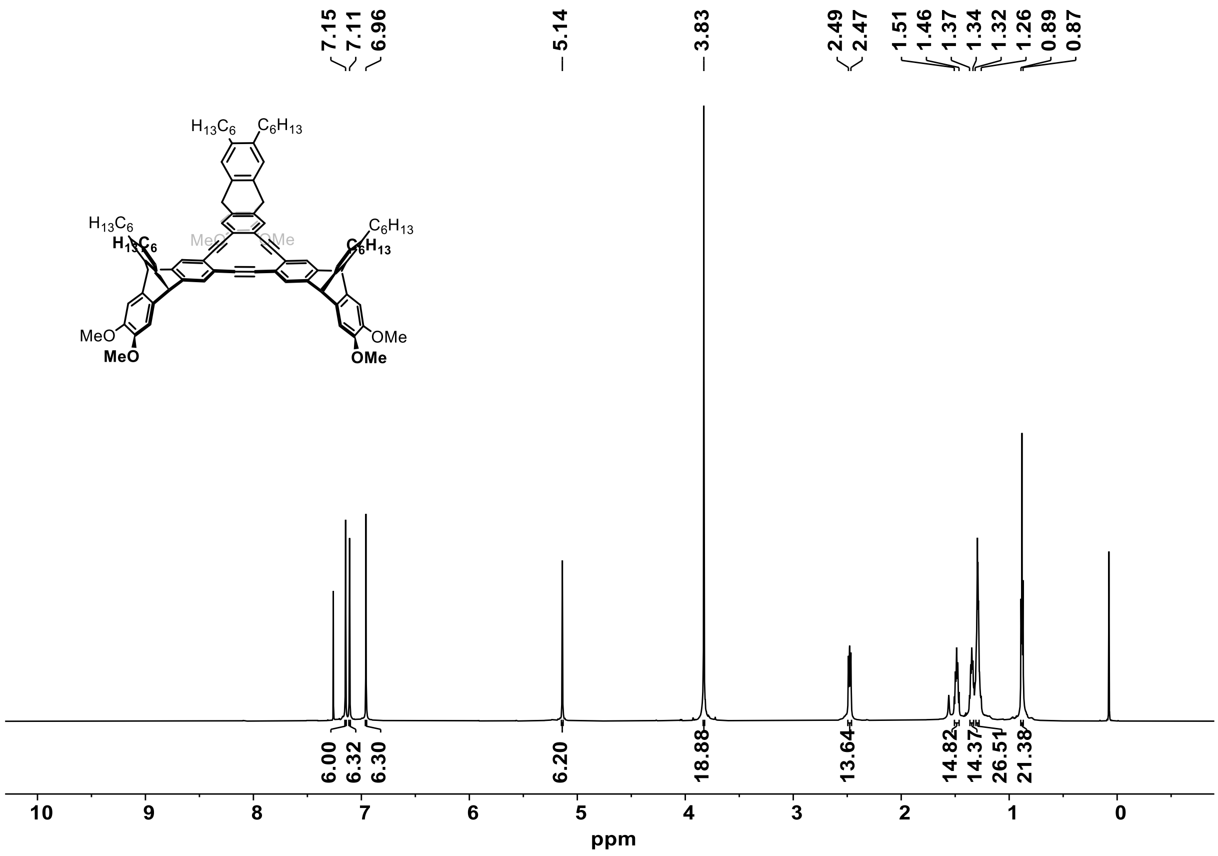

Figure 7.30: ^{1}H NMR spectrum of **103b** (700 MHz, $CDCl_3$).

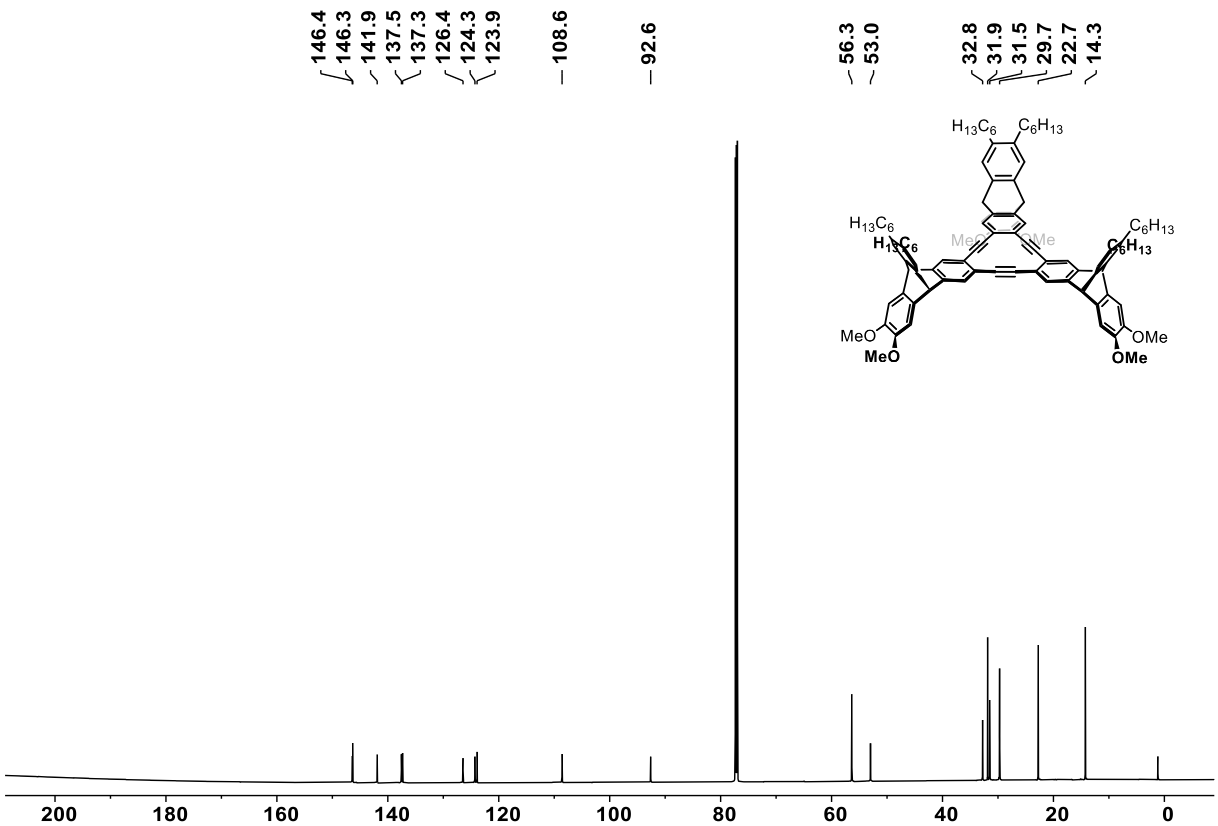

Figure 7.31: ^{13}C NMR spectrum of **103b** (176 MHz, $CDCl_3$).

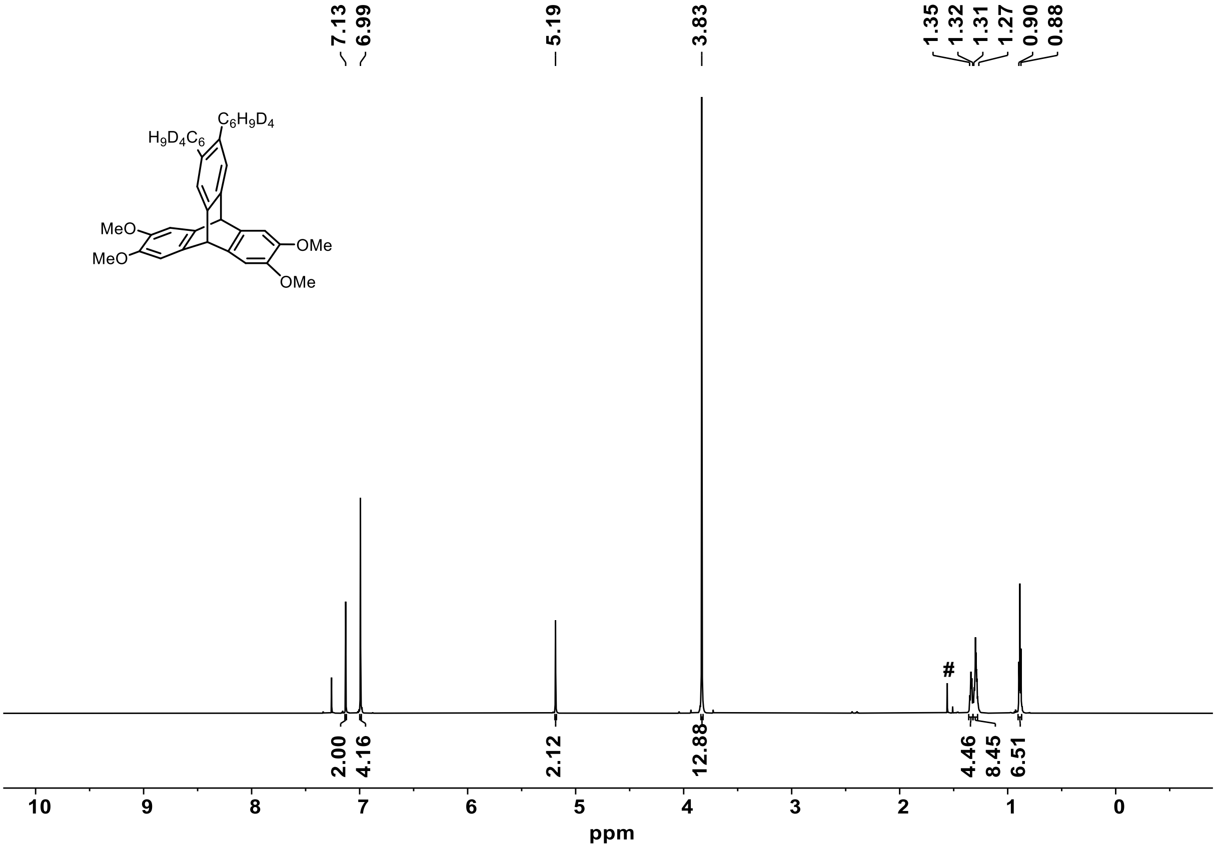

Figure 7.32: ^{1}H NMR spectrum of **99-*d*$_8$** (700 MHz, $CDCl_3$). #: H_2O.

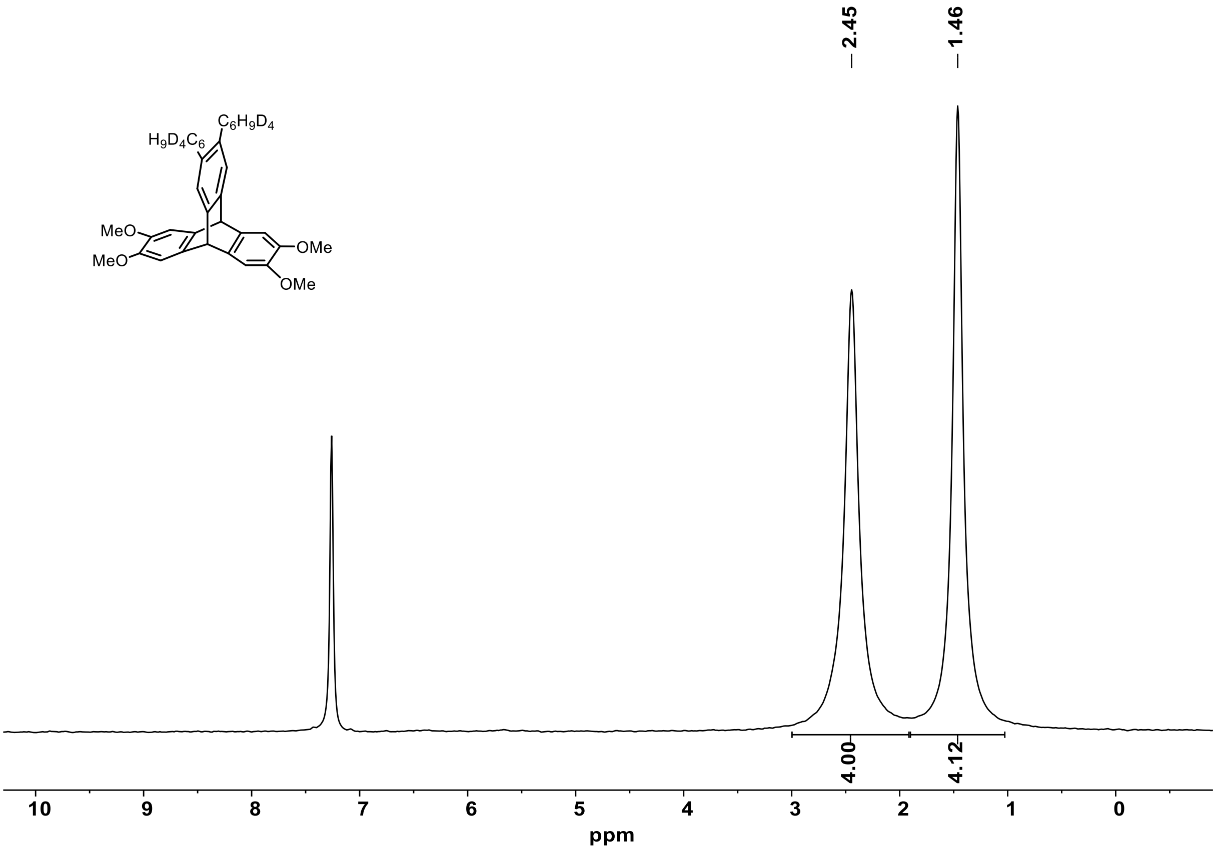

Figure 7.33: ^{2}H NMR spectrum of **99-*d*$_8$** (92 MHz, $CHCl_3$/$CDCl_3$).

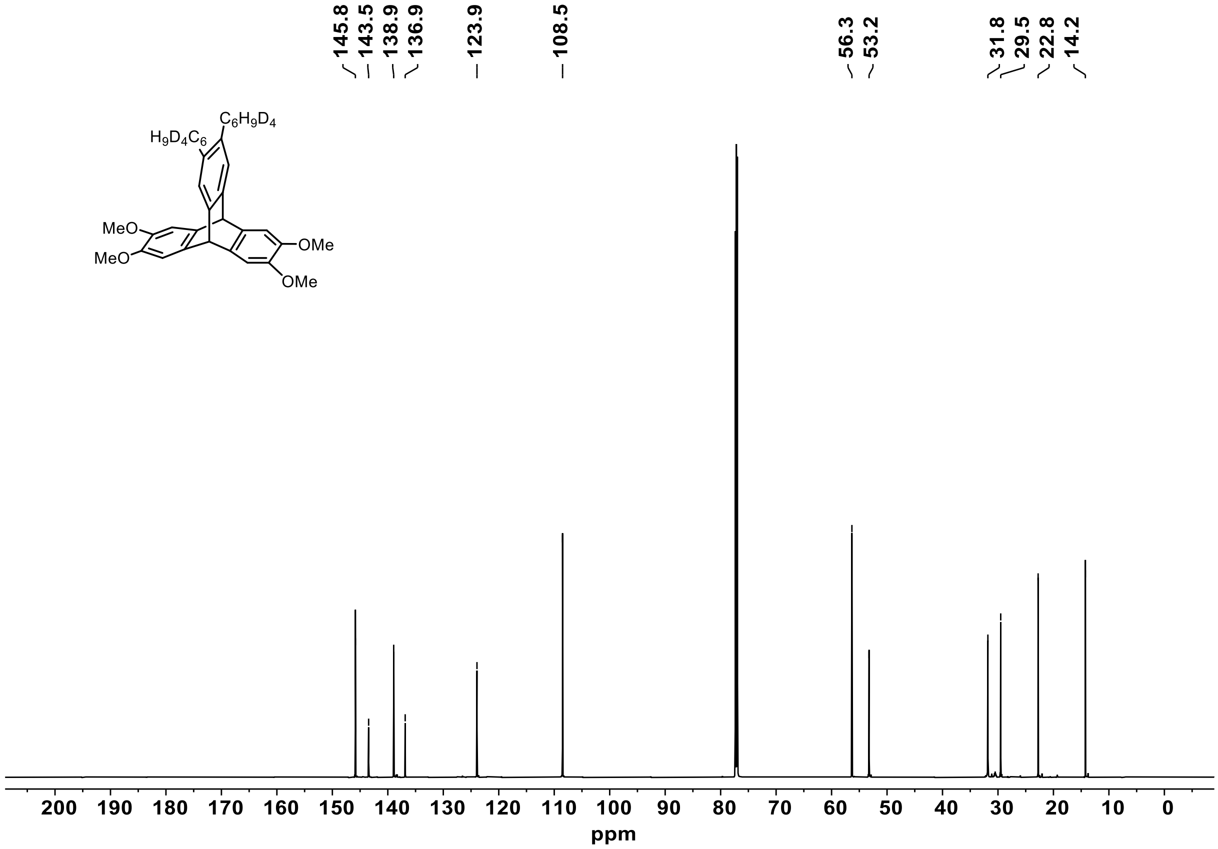

Figure 7.34: ^{13}C NMR spectrum of **99-*d*$_8$** (176 MHz, CDCl$_3$).

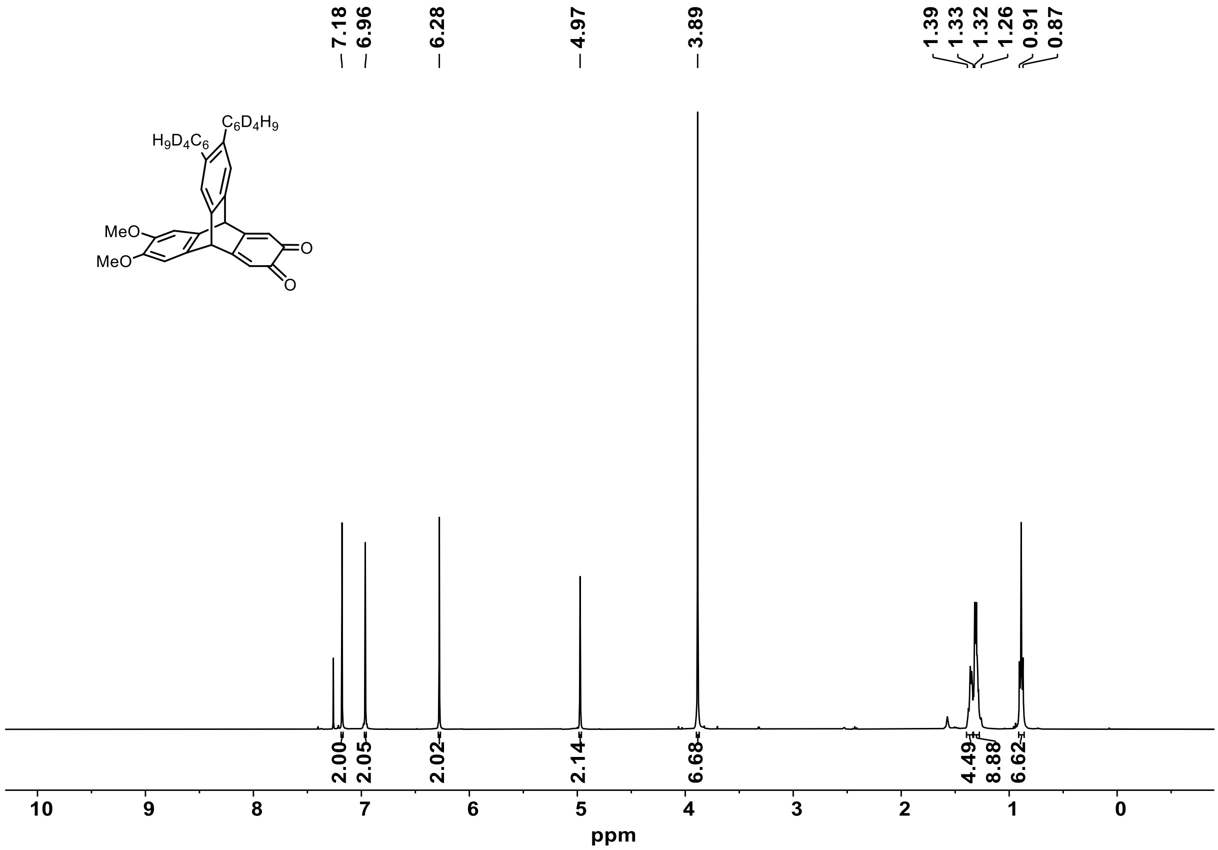

Figure 7.35: ^{1}H NMR spectrum of **100-*d*$_8$** (400 MHz, CDCl$_3$).

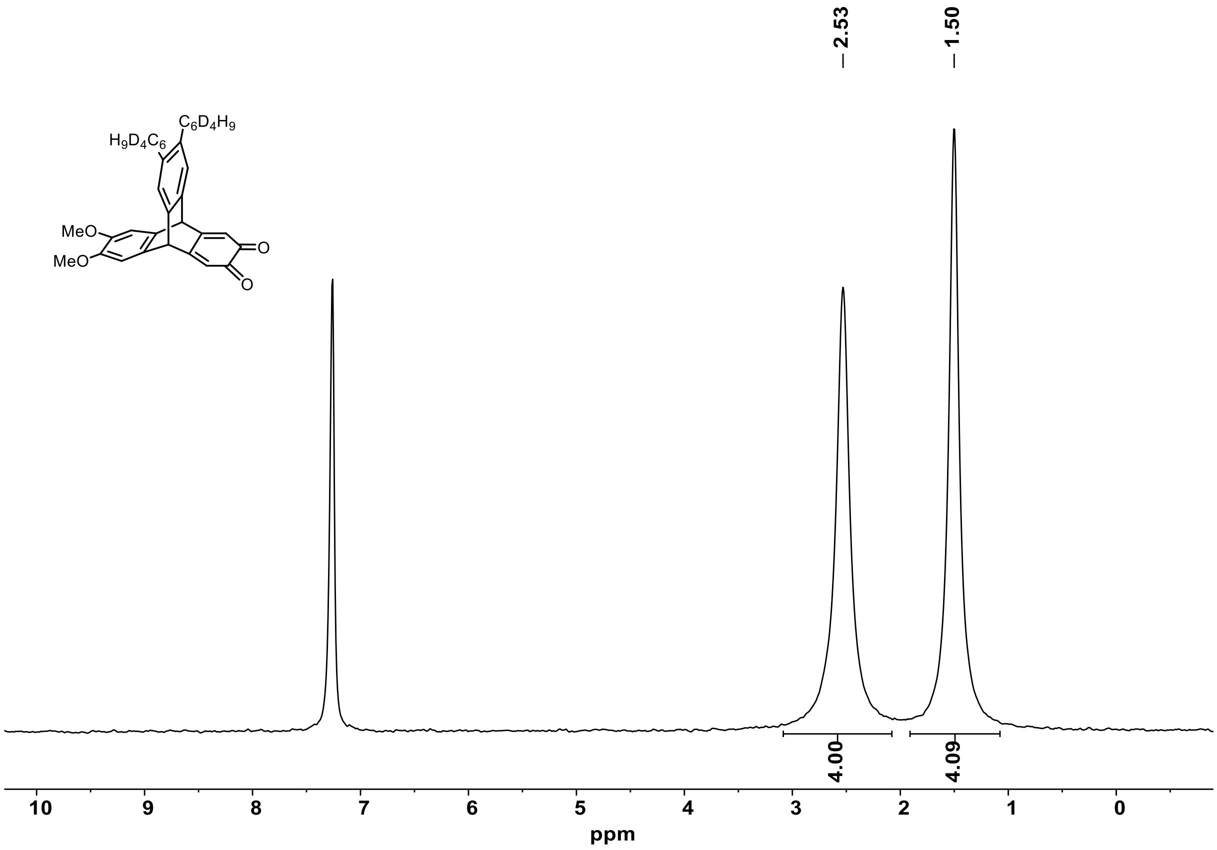

Figure 7.36: ^{2}H NMR spectrum of **100-d_8** (92 MHz, $CHCl_3/CDCl_3$).

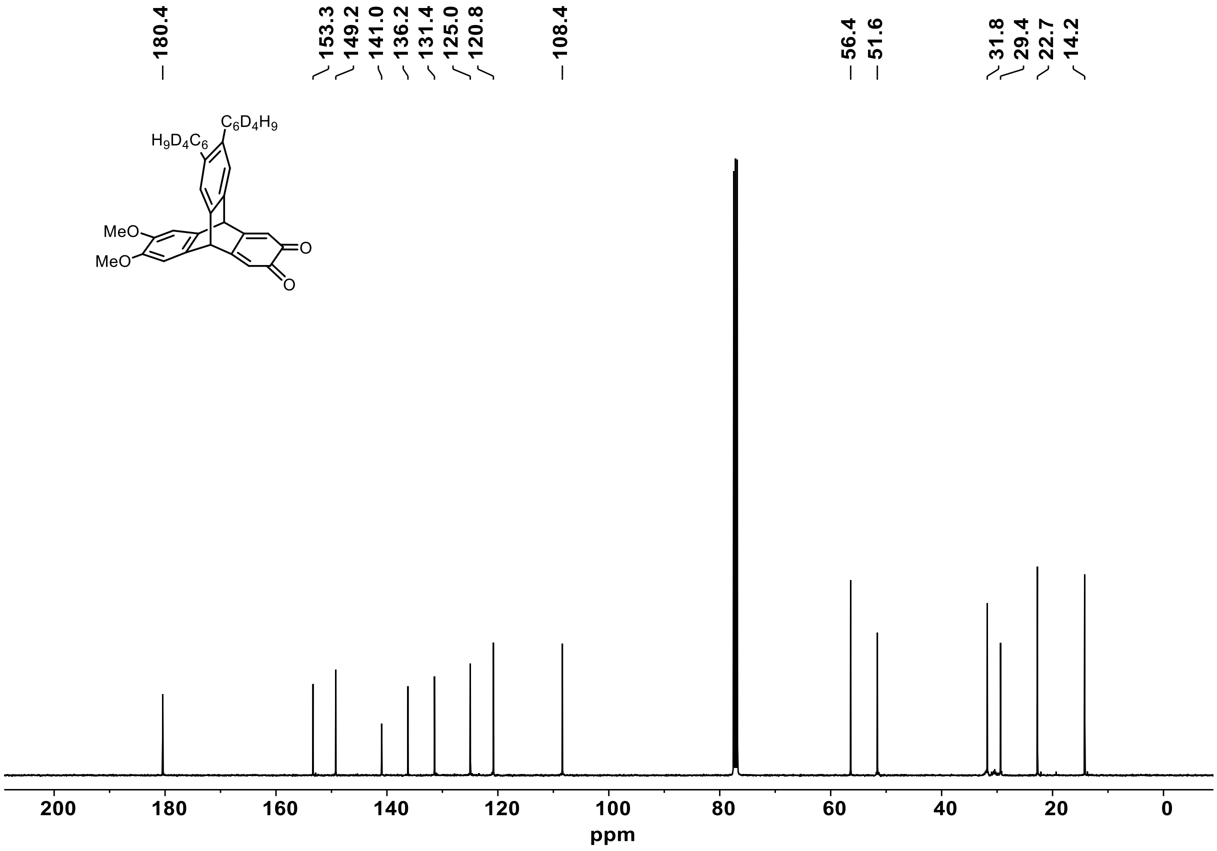

Figure 7.37: ^{13}C NMR spectrum of **100-d_8** (100 MHz, $CDCl_3$).

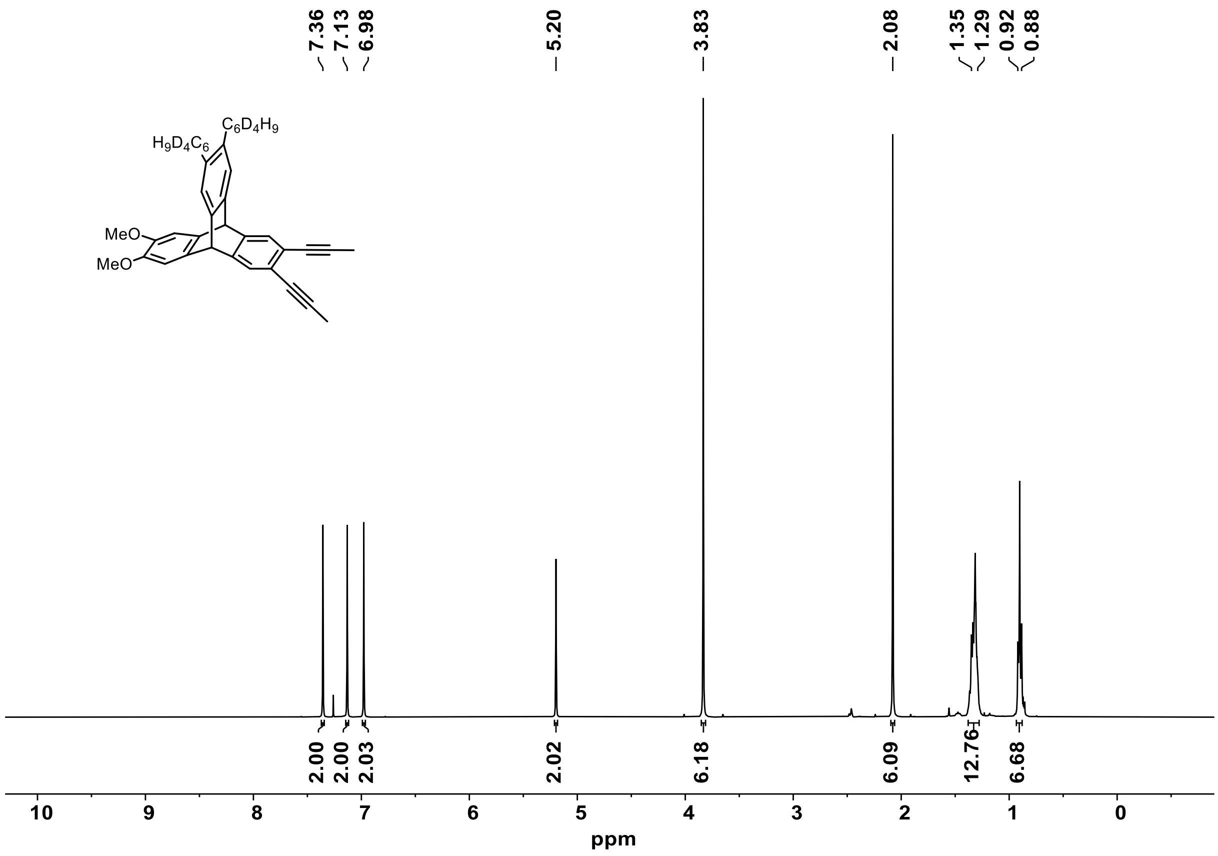

Figure 7.38: ^{1}H NMR spectrum of **101-*d*$_8$** (400 MHz, $CDCl_3$).

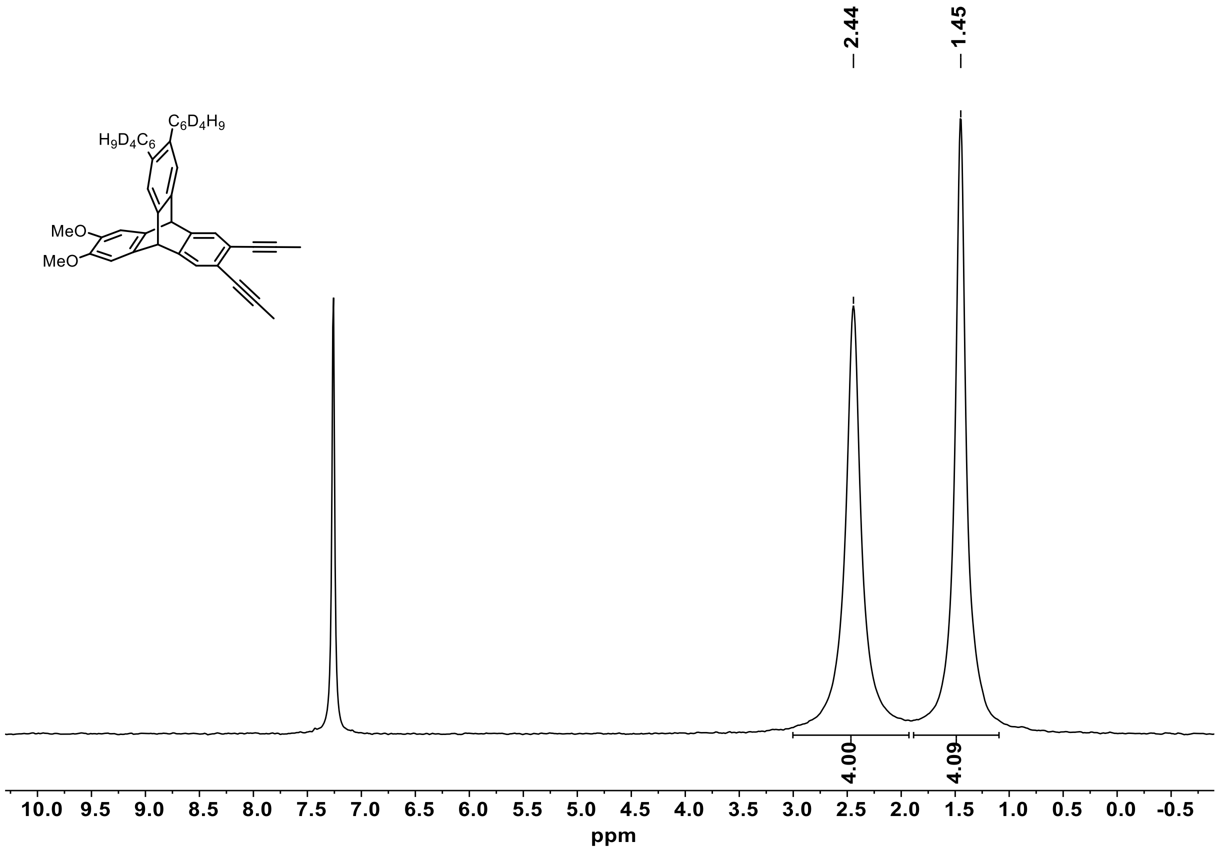

Figure 7.39: ^{2}H NMR spectrum of **101-*d*$_8$** (92 MHz, $CHCl_3$/$CDCl_3$).

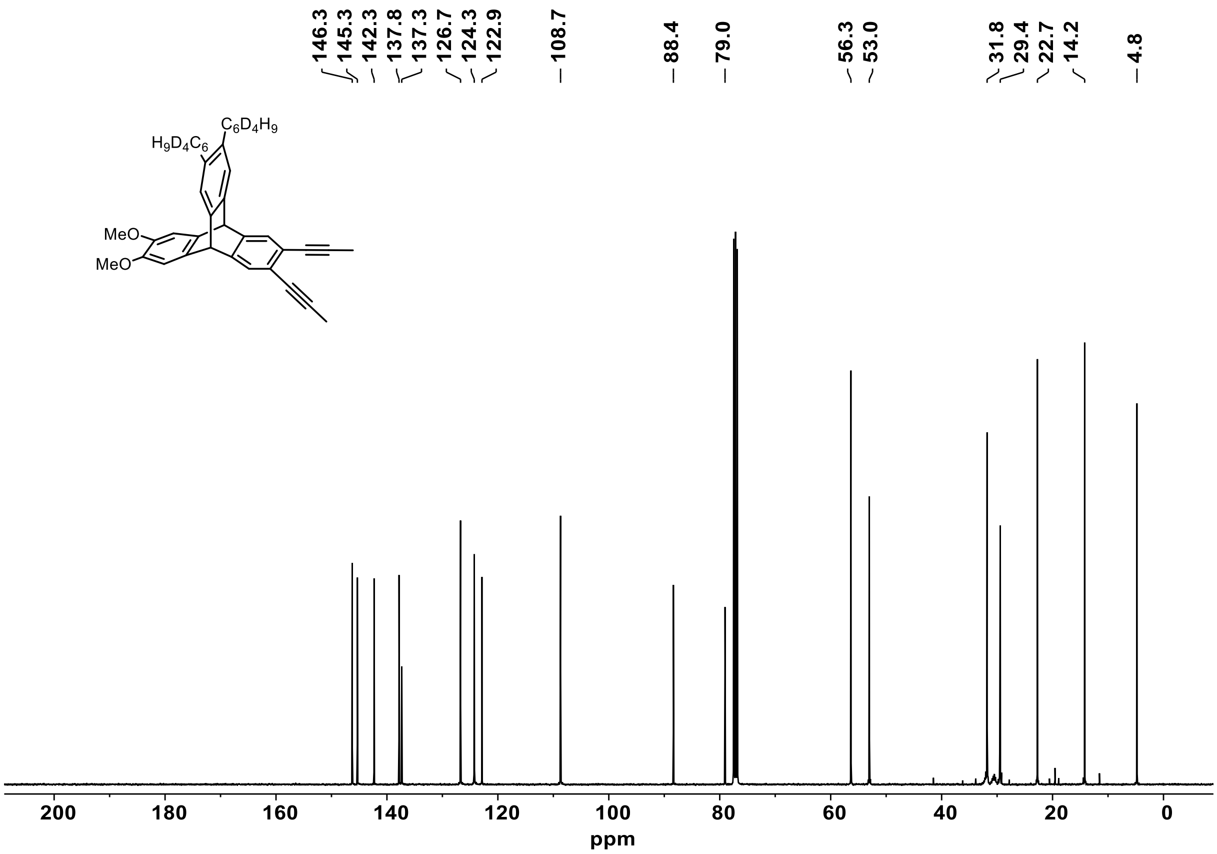

Figure 7.40: ^{13}C NMR spectrum of **101-*d*$_8$** (100 MHz, CDCl$_3$).

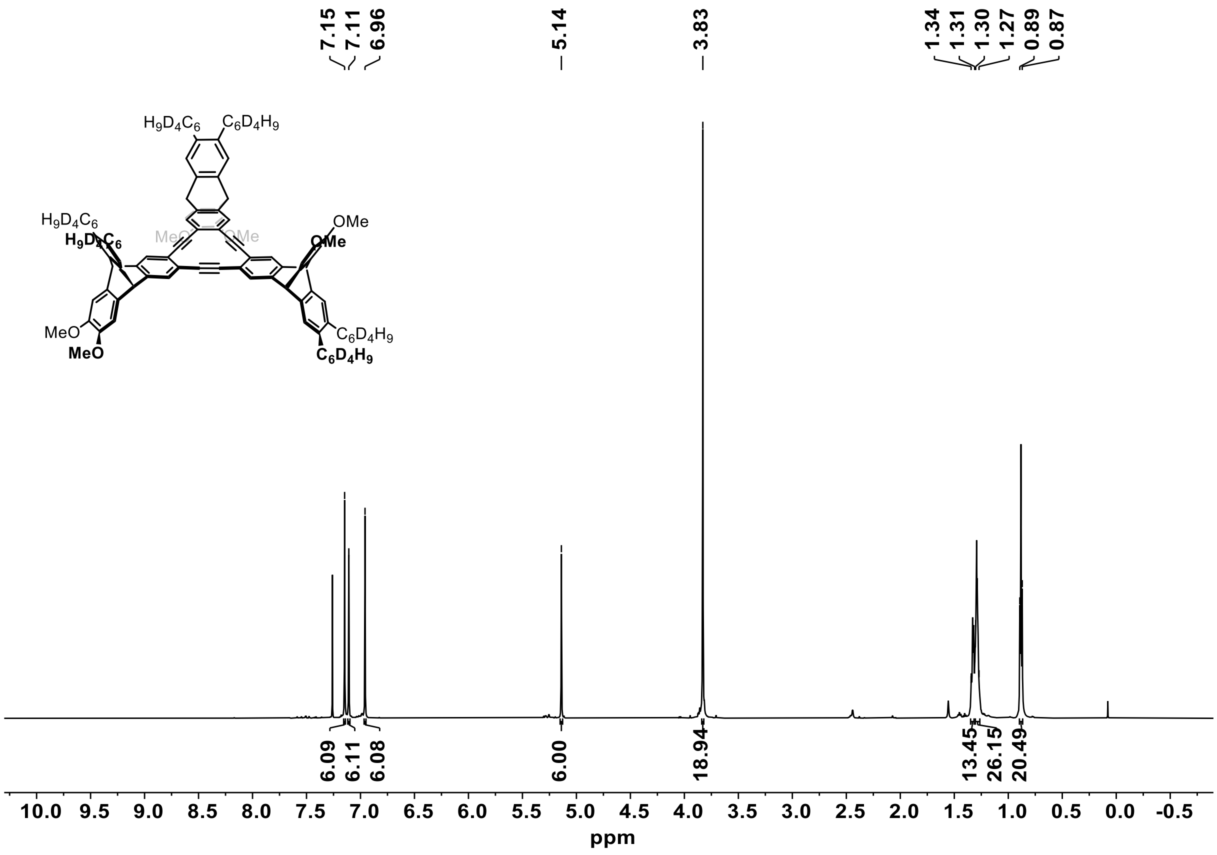

Figure 7.41: ^{1}H NMR spectrum of **103a-*d*$_{24}$** (600 MHz, CDCl$_3$).

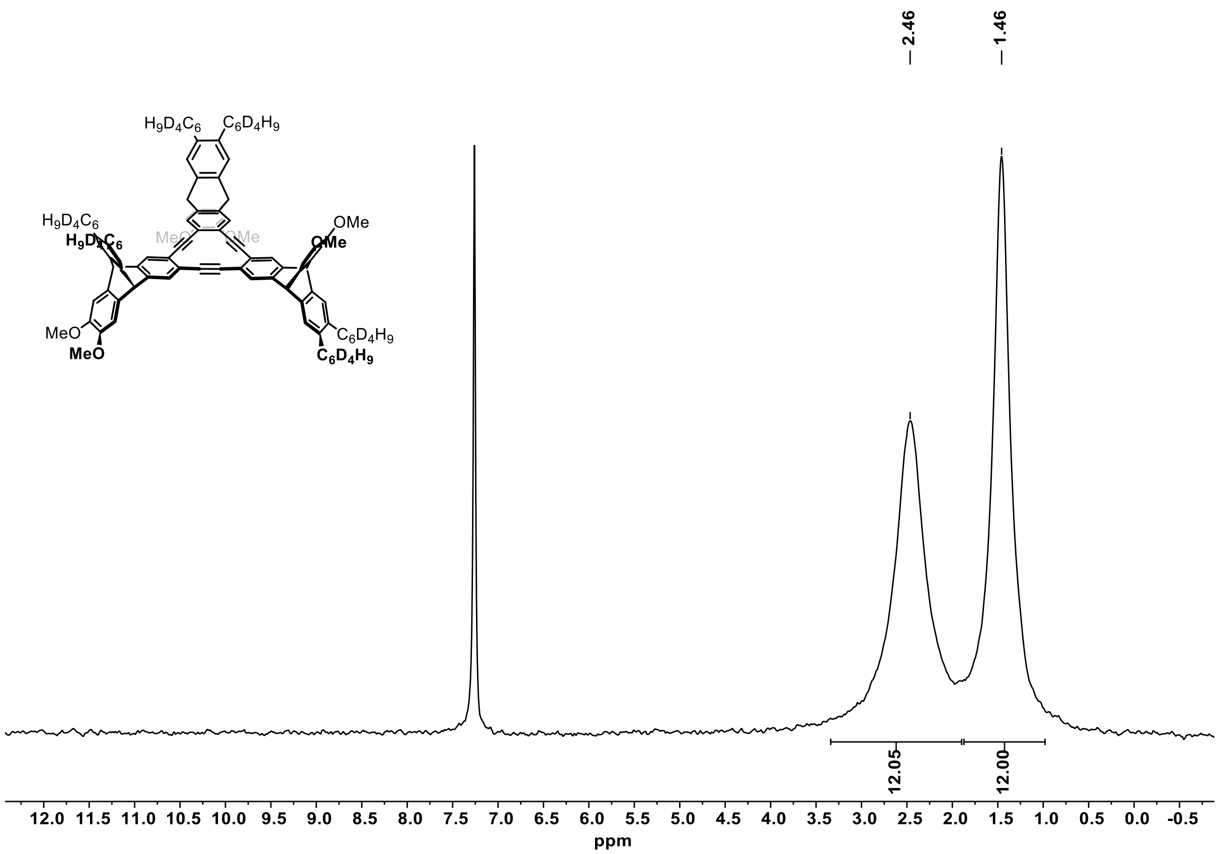

Figure 7.42: ^{2}H NMR spectrum of **103a-*d*$_{24}$** (92 MHz, CHCl$_3$/CDCl$_3$).

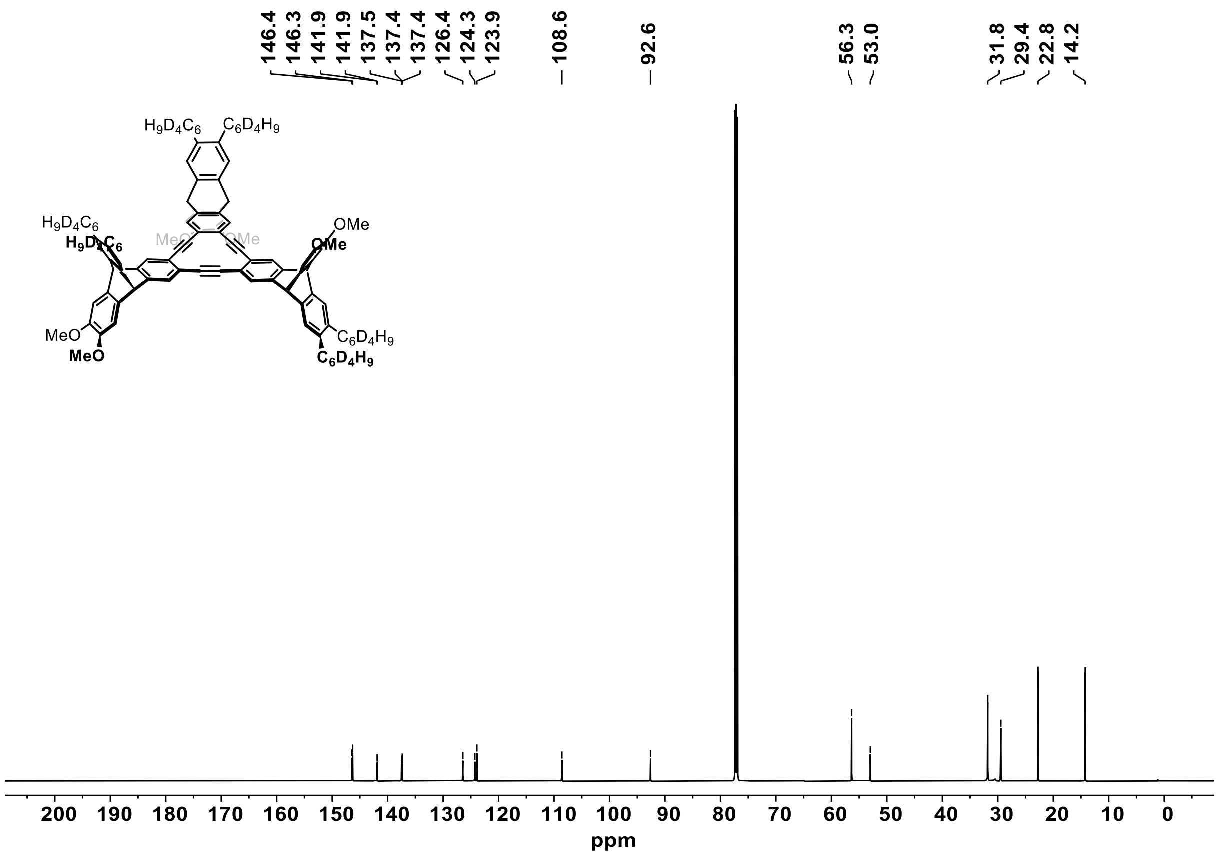

Figure 7.43: ^{13}C NMR spectrum of **103a-*d*$_{24}$** (150 MHz, CDCl$_3$).

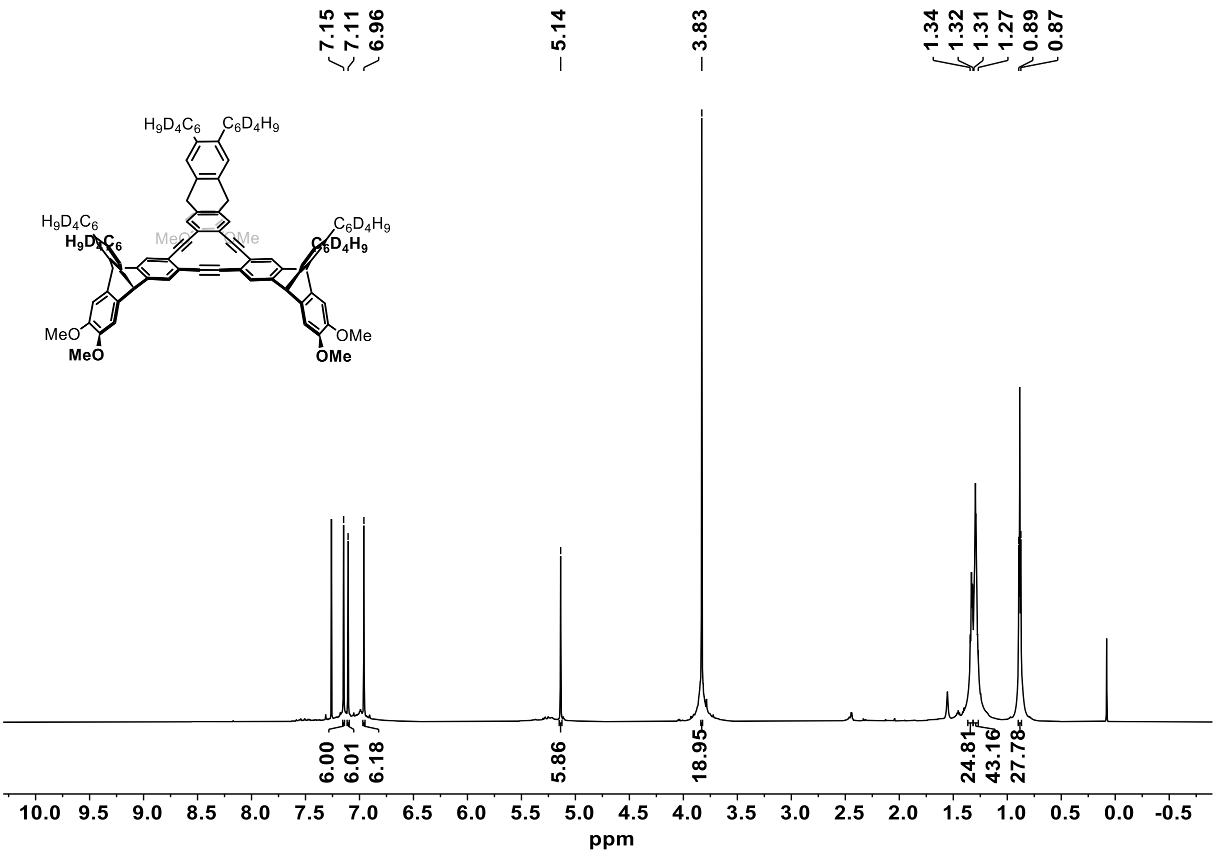

Figure 7.44: ^{1}H NMR spectrum of **103b-*d*$_{24}$** (700 MHz, CDCl$_3$).

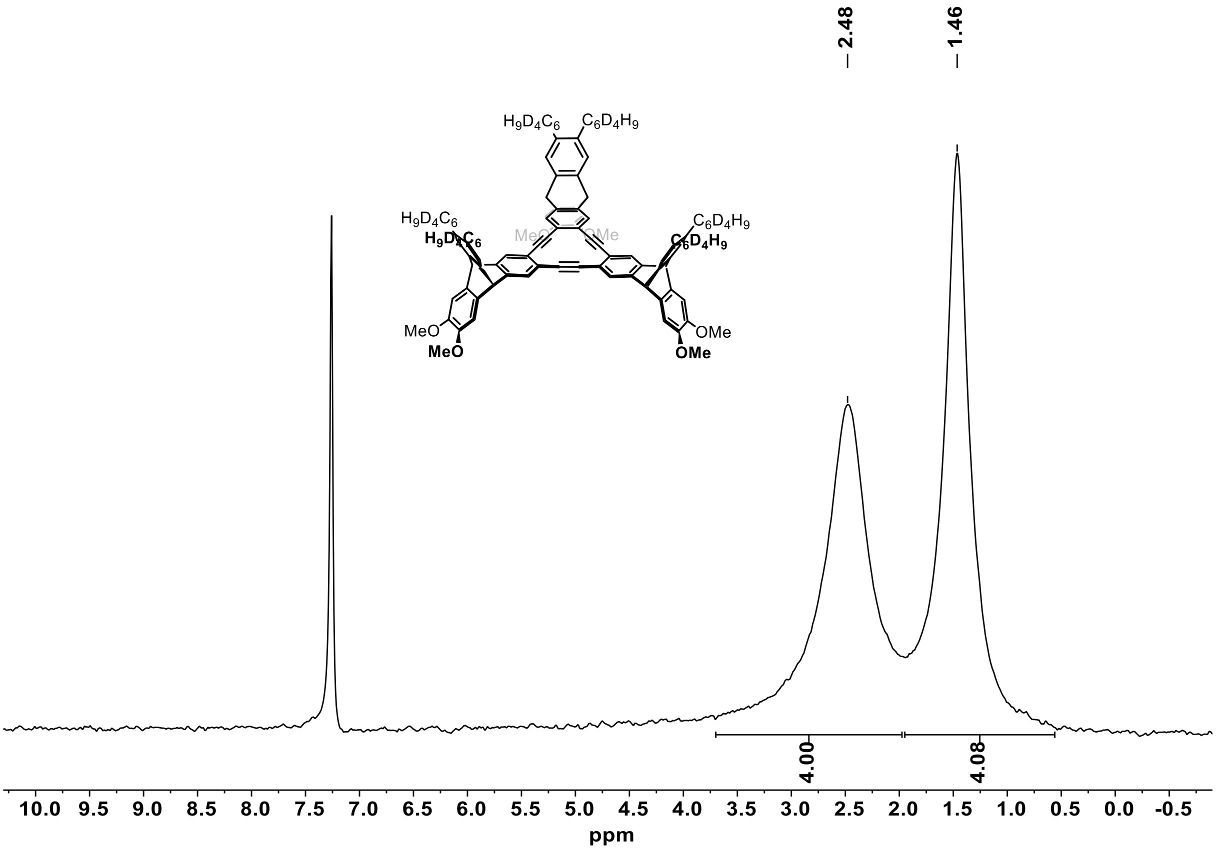

Figure 7.45: ^{2}H NMR spectrum of **103b-*d*$_{24}$** (92 MHz, CHCl$_3$/CDCl$_3$).

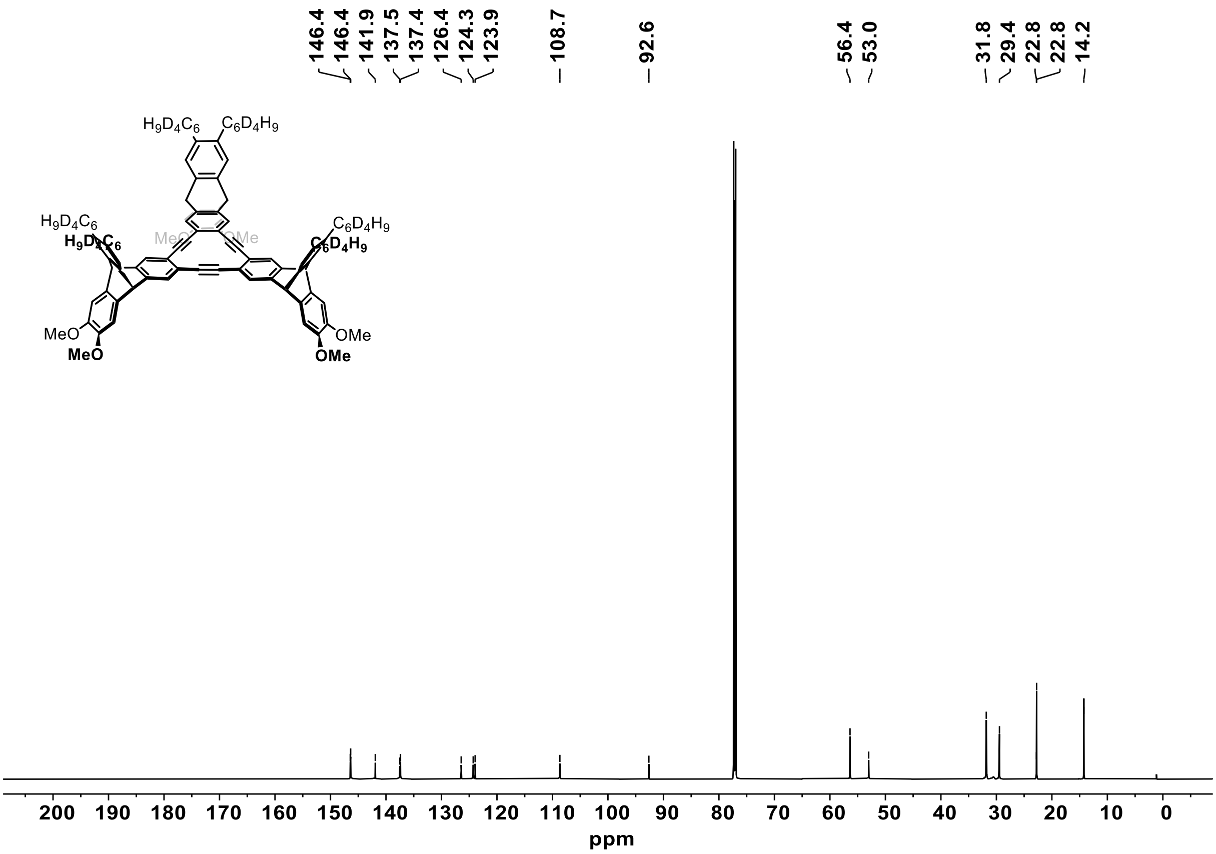

Figure 7.46: ^{13}C NMR spectrum of **103b-*d*$_{24}$** (176 MHz, CDCl$_3$).

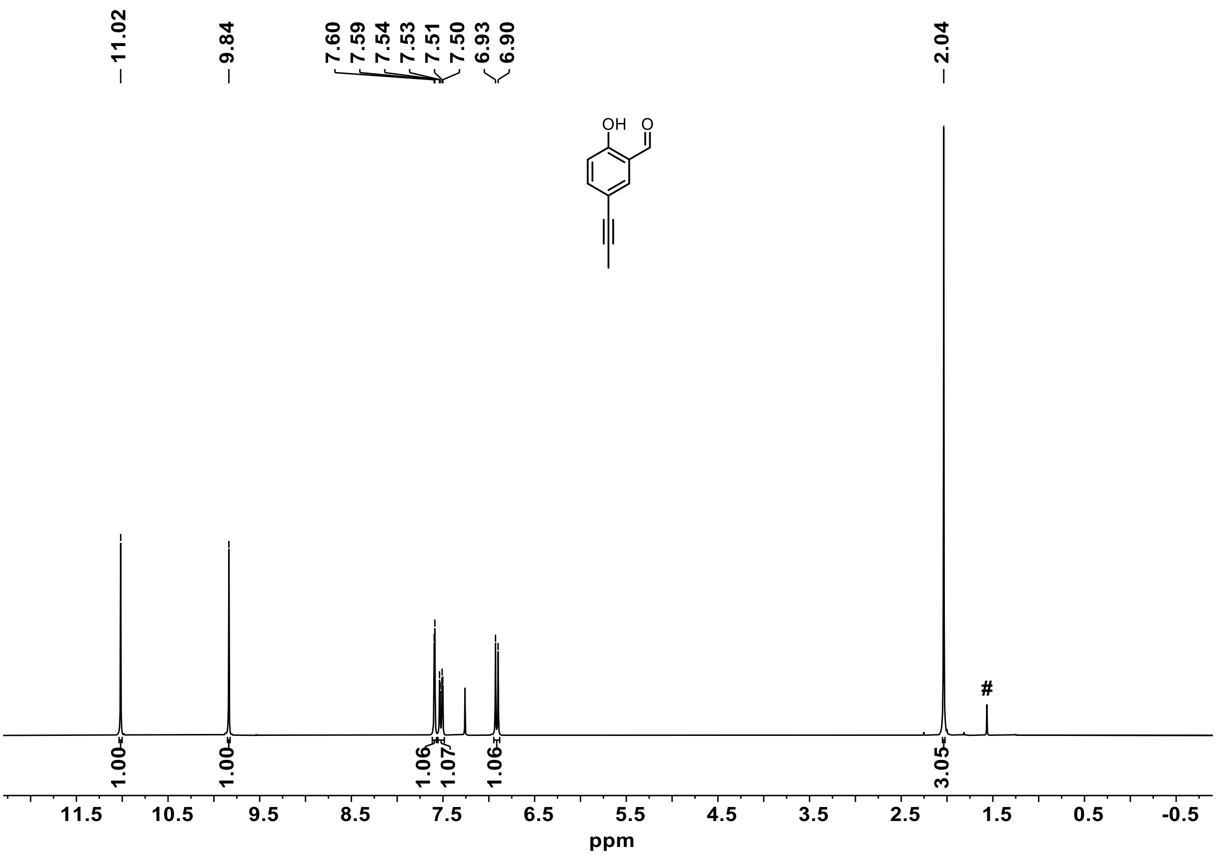

Figure 7.47: ^{1}H NMR spectrum of **111** (300 MHz, CDCl$_3$). #: H$_2$O.

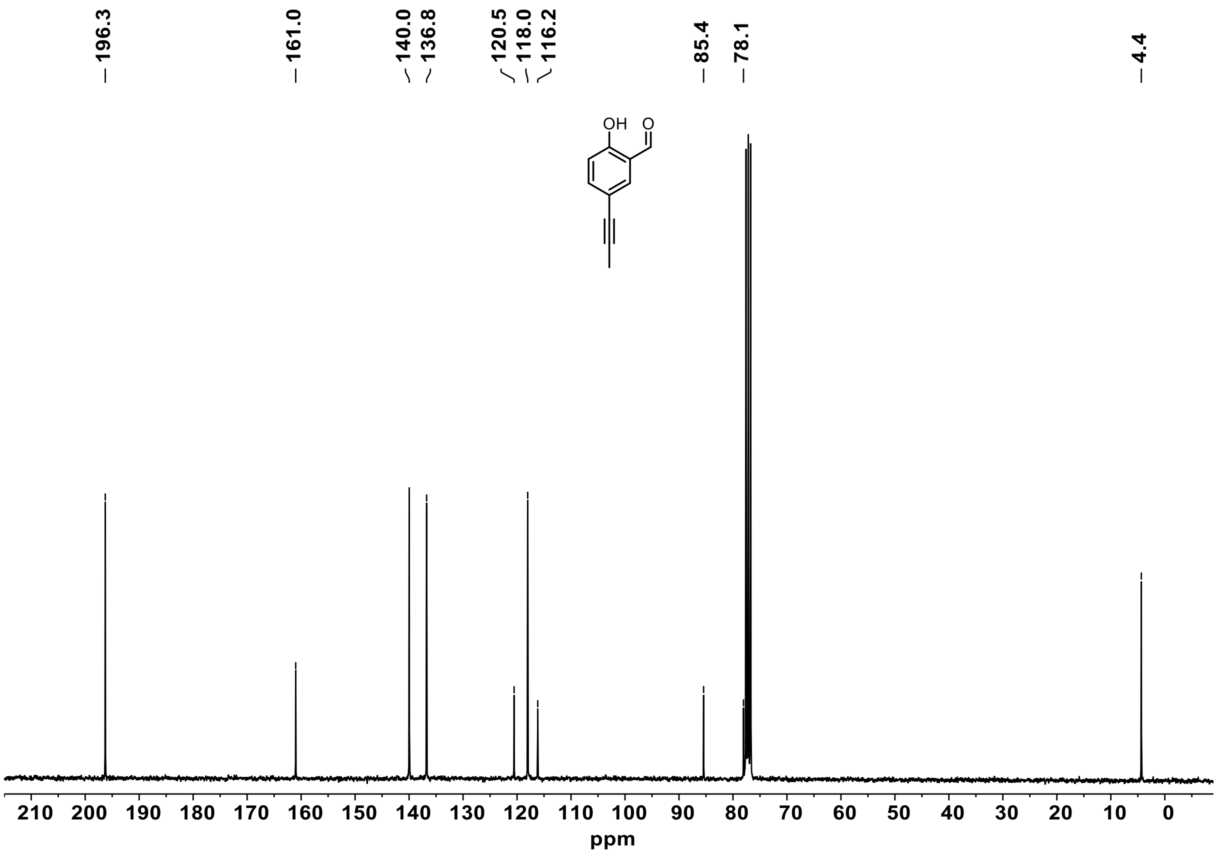

Figure 7.48: ^{13}C NMR spectrum of **111** (75 MHz, CDCl$_3$).

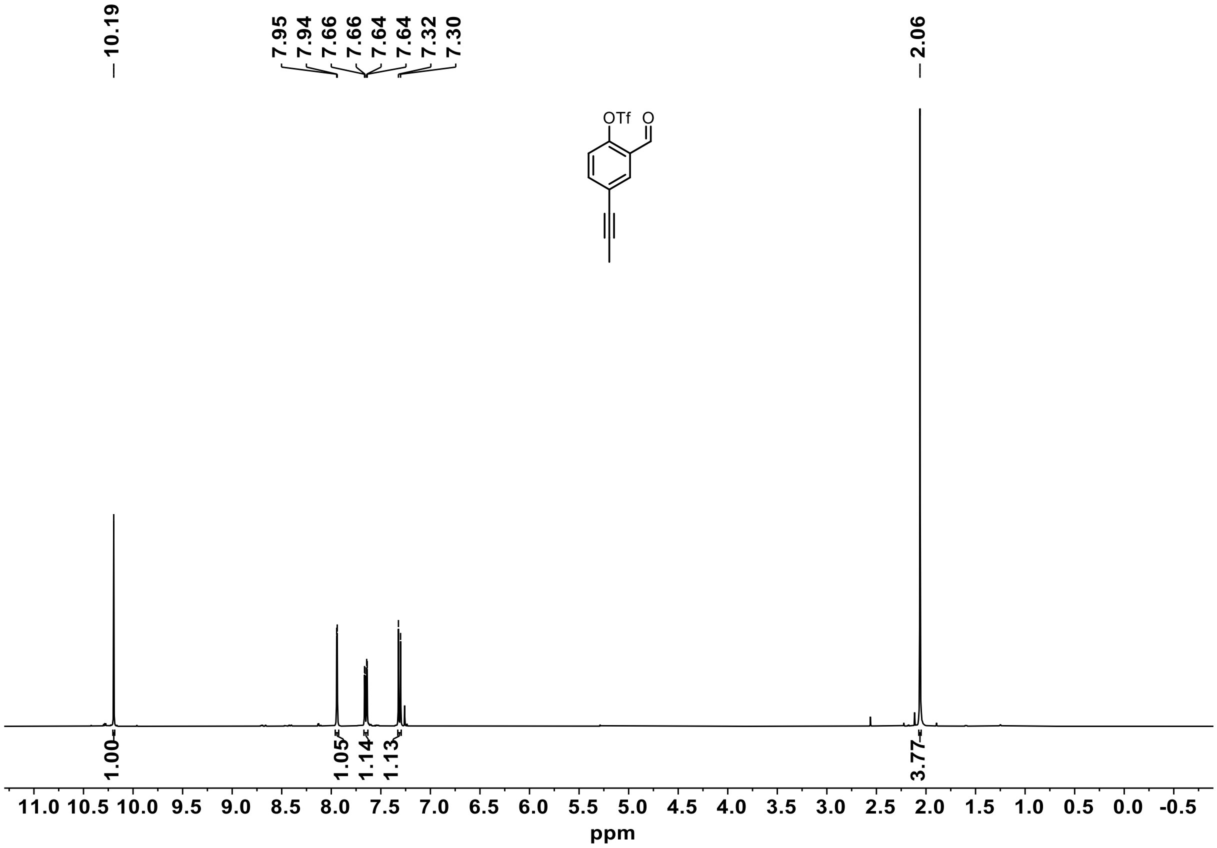

Figure 7.49: ^{1}H NMR spectrum of **112** (400 MHz, CDCl$_3$).

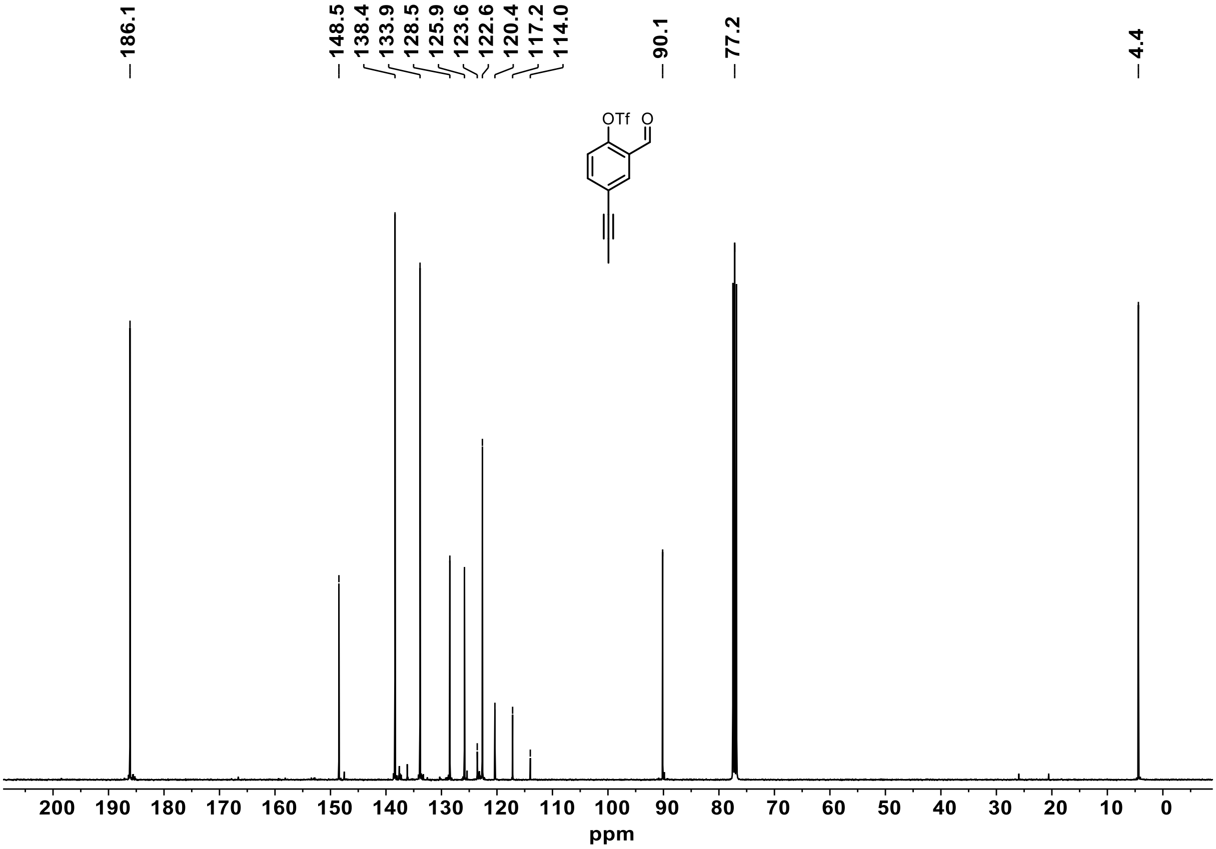

Figure 7.50: ^{13}C NMR spectrum of **112** (100 MHz, CDCl$_3$).

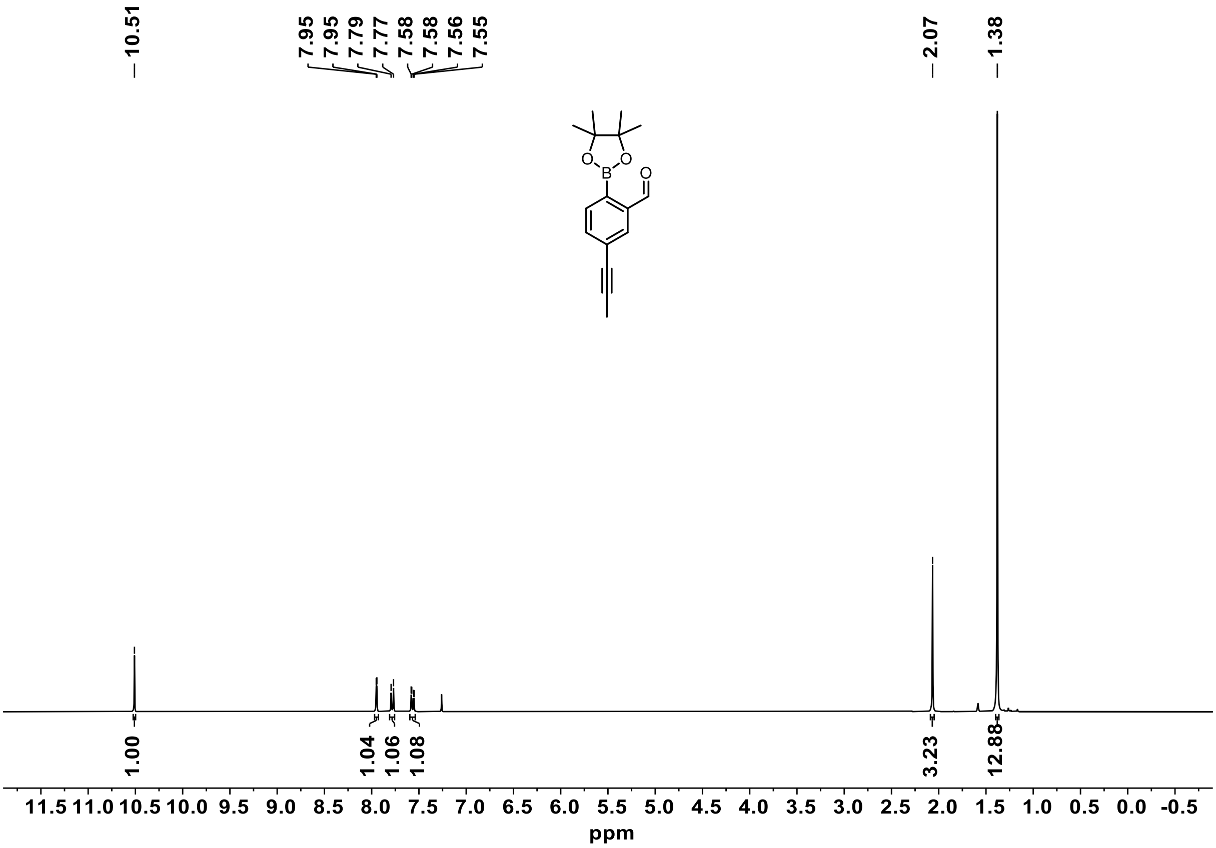

Figure 7.51: ^{1}H NMR spectrum of **113** (300 MHz, CDCl$_3$).

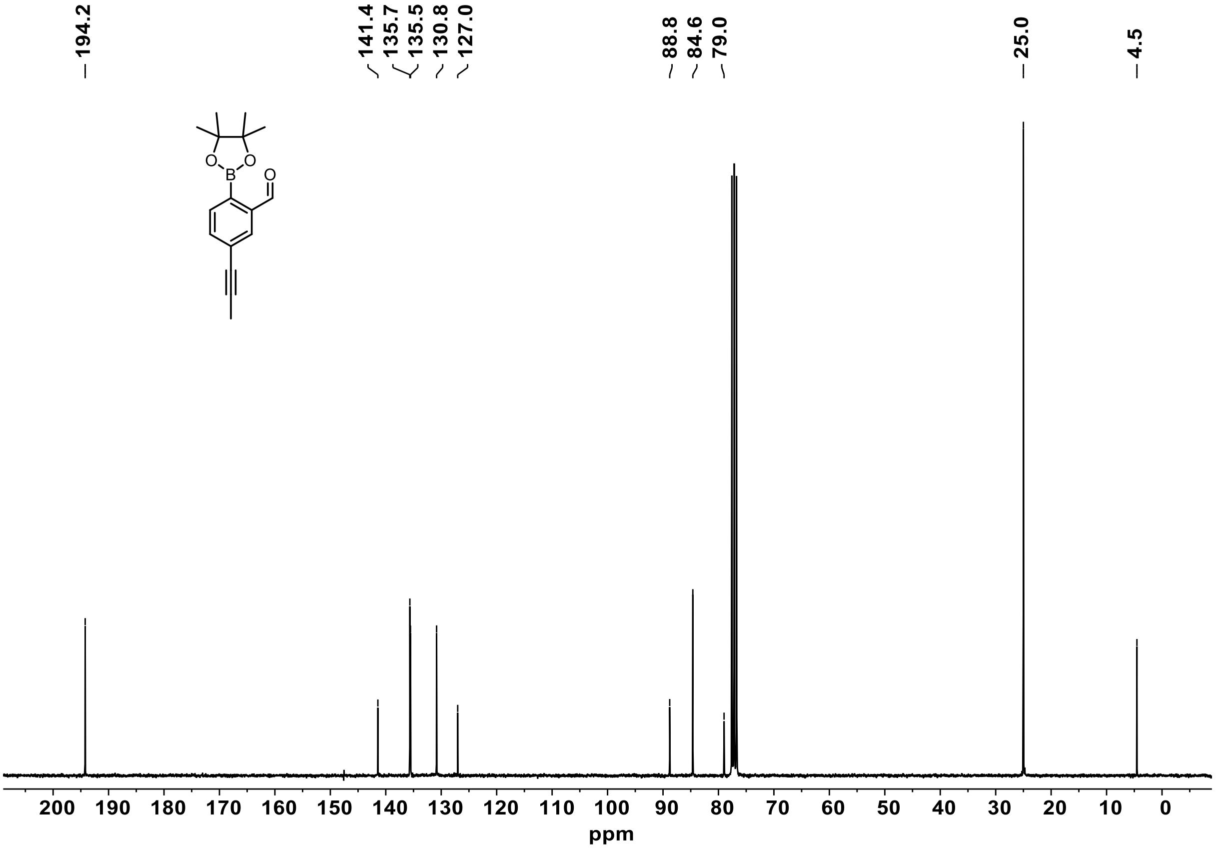

Figure 7.52: ^{13}C NMR spectrum of **113** (75 MHz, CDCl$_3$).

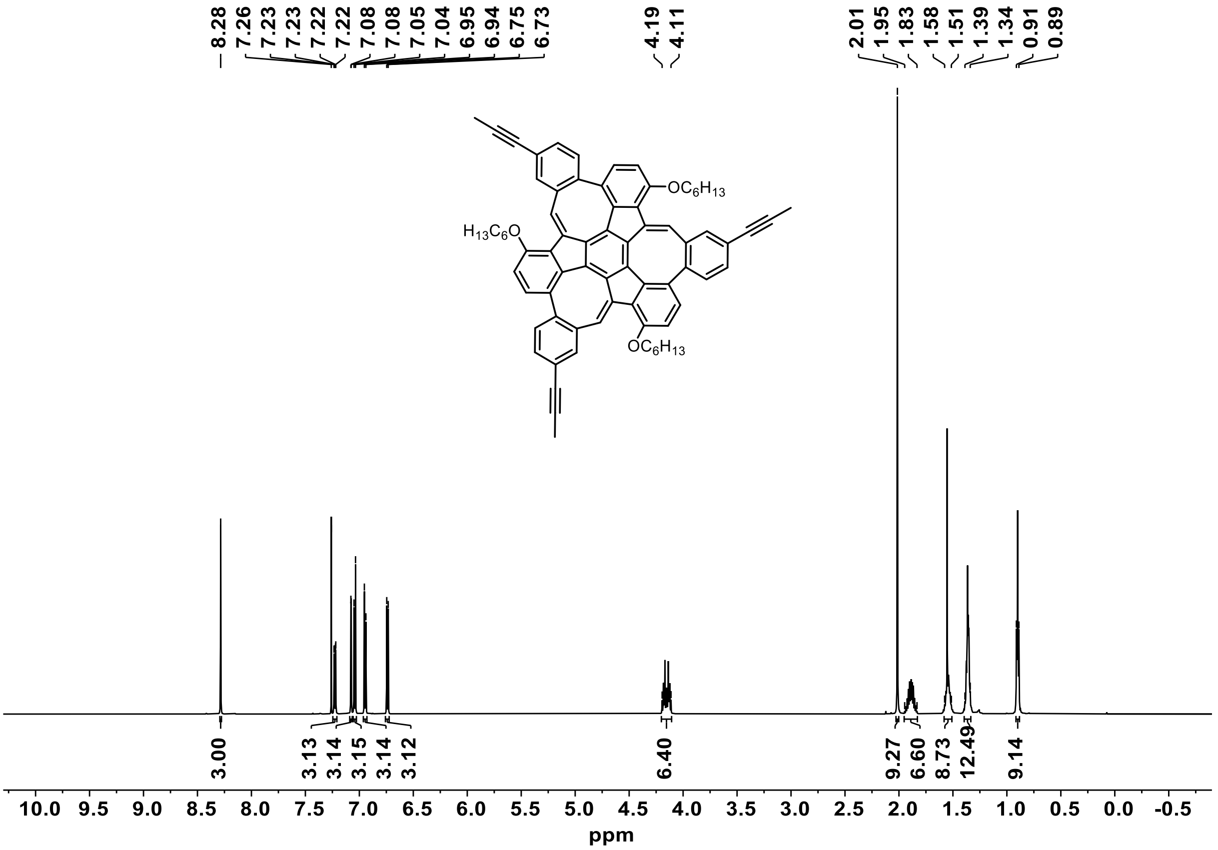

Figure 7.53: ^{1}H NMR spectrum of **116** (600 MHz, CDCl$_3$).

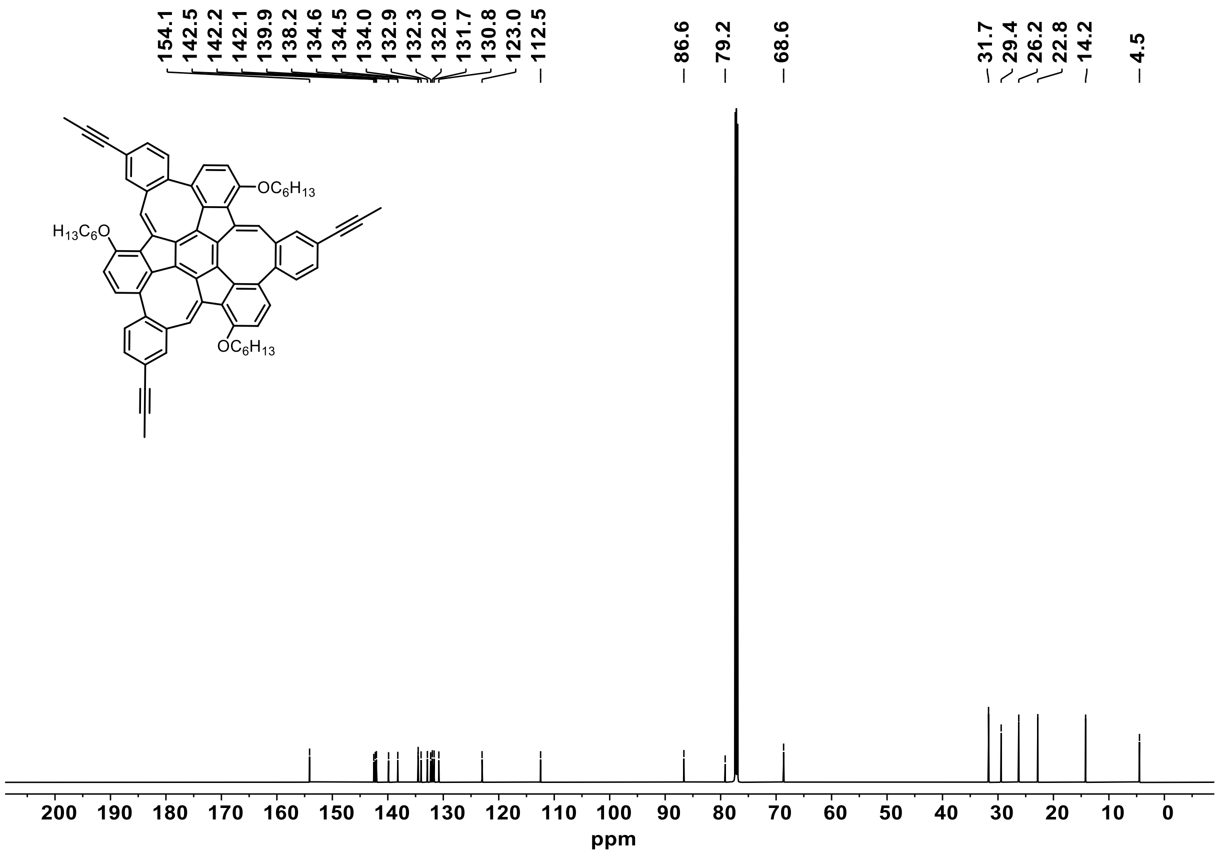

Figure 7.54: ^{13}C NMR spectrum of **116** (150 MHz, $CDCl_3$).

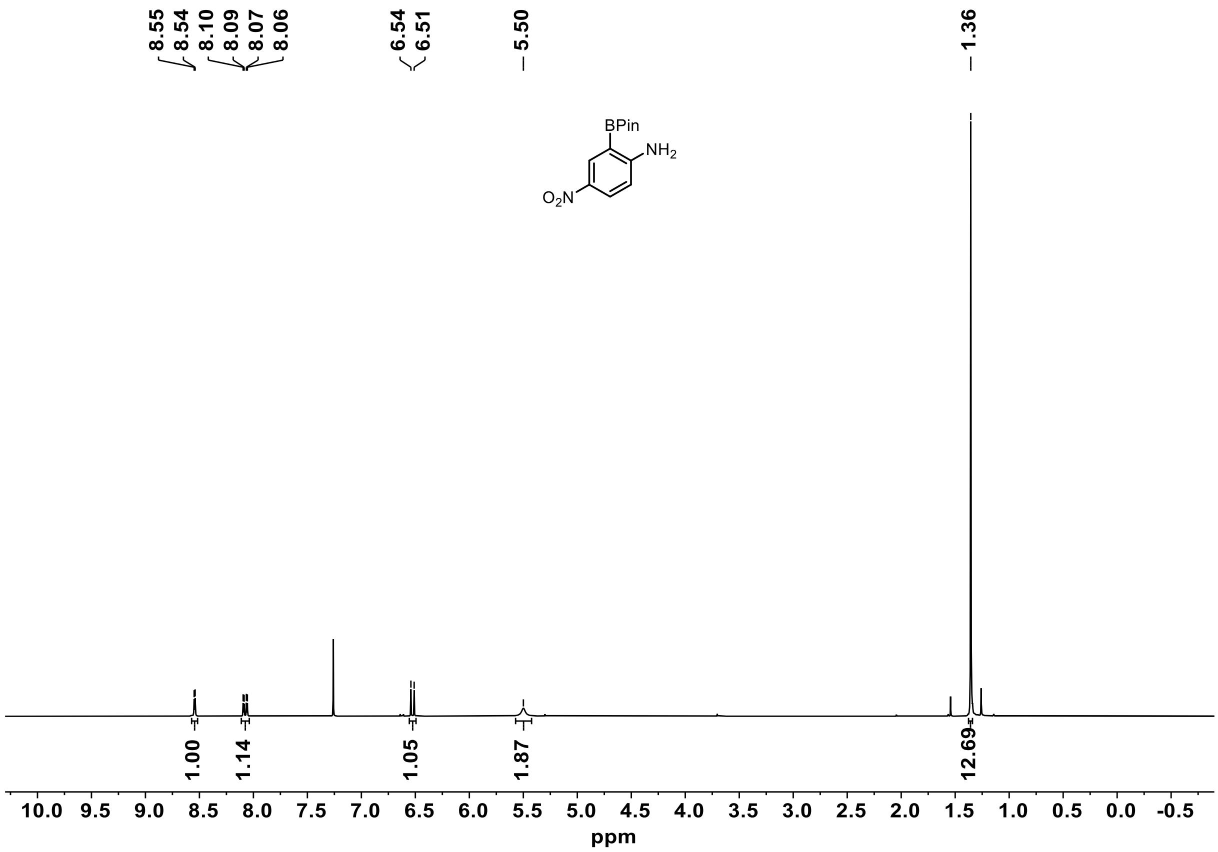

Figure 7.55: ^{1}H NMR spectrum of **130** (300 MHz, $CDCl_3$).

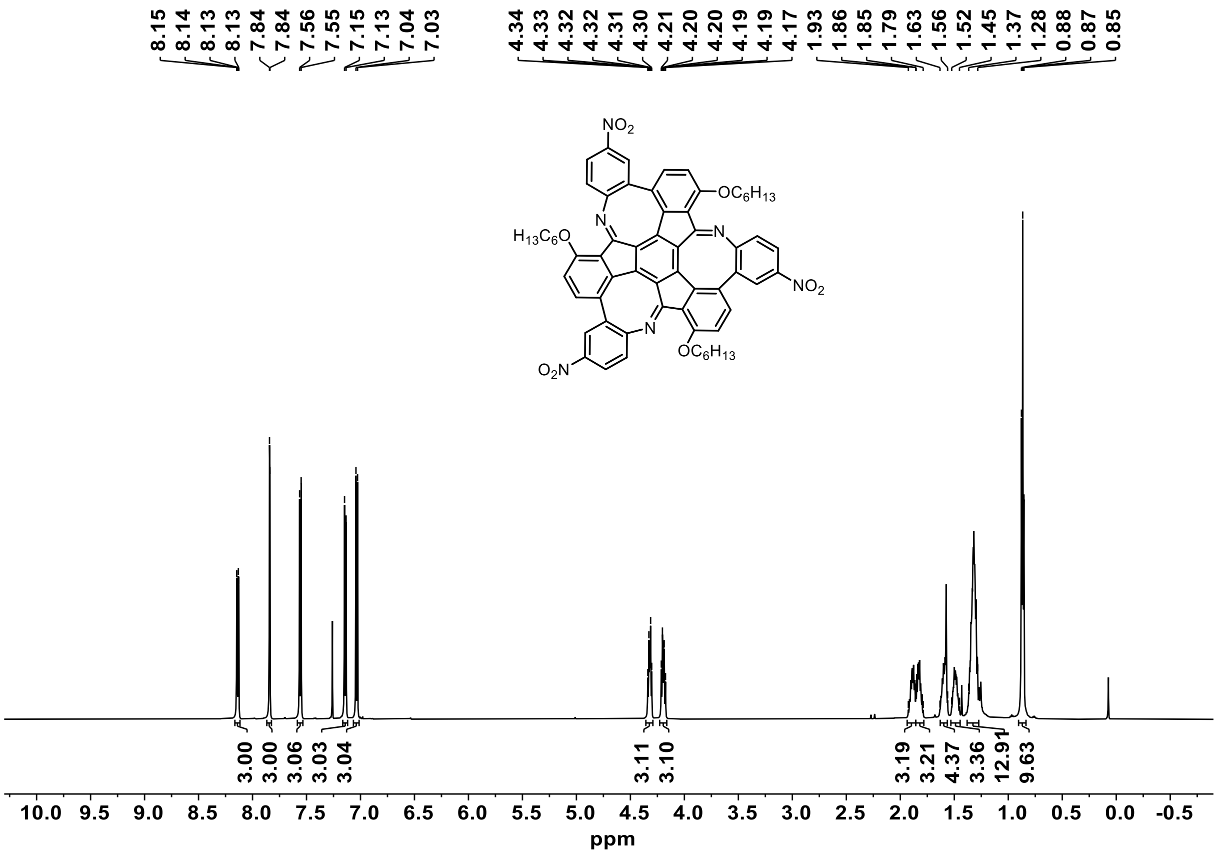

Figure 7.56: ^{1}H NMR spectrum of **131** (600 MHz, CDCl$_3$).

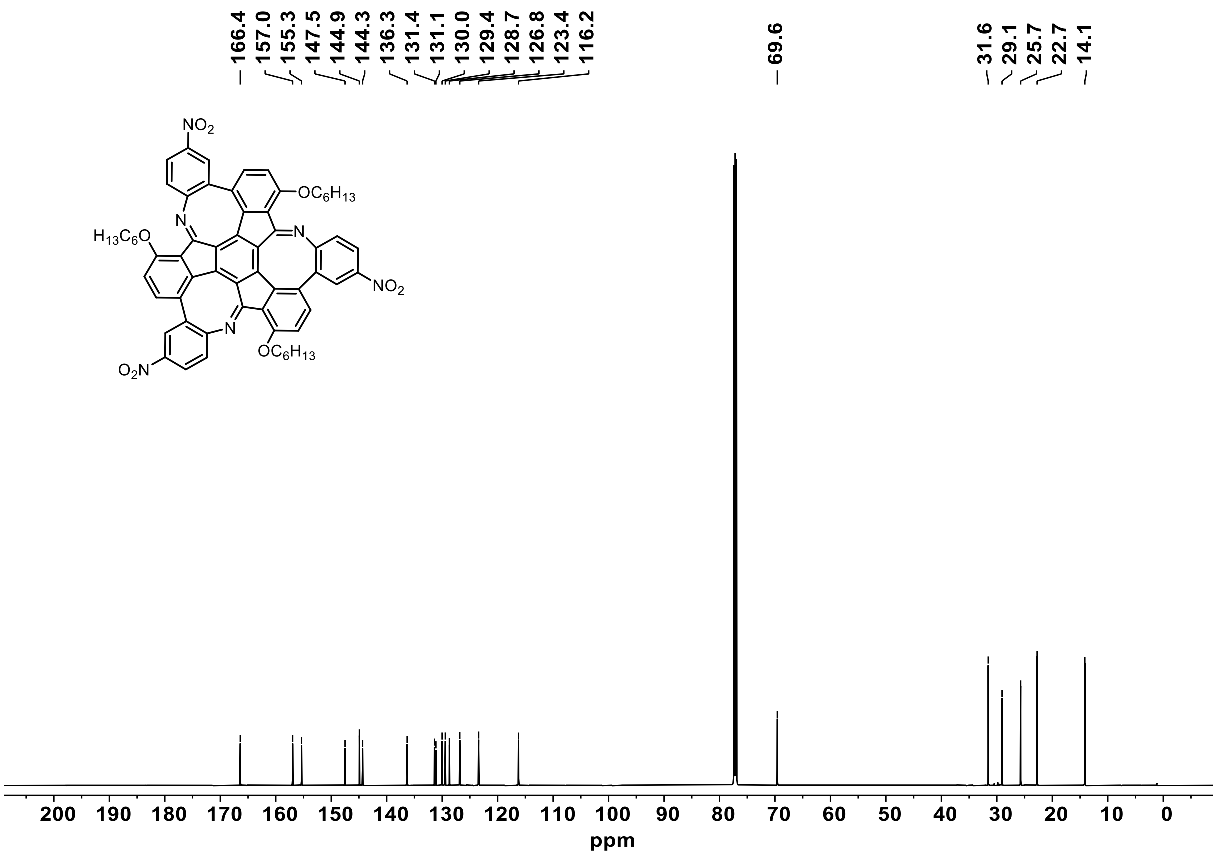

Figure 7.57: ^{13}C NMR spectrum of **131** (150 MHz, CDCl$_3$).

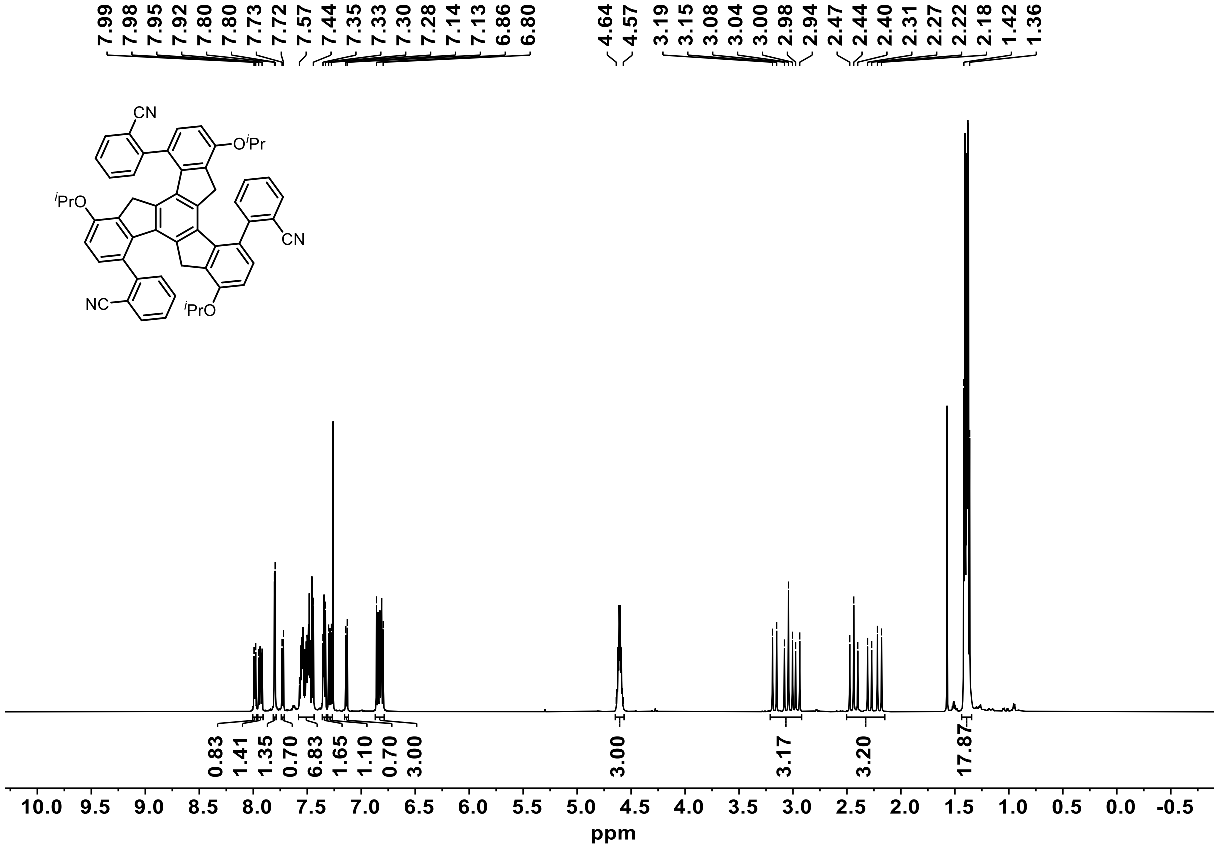

Figure 7.58: ^{1}H NMR spectrum of **138** (600 MHz, CDCl$_3$).

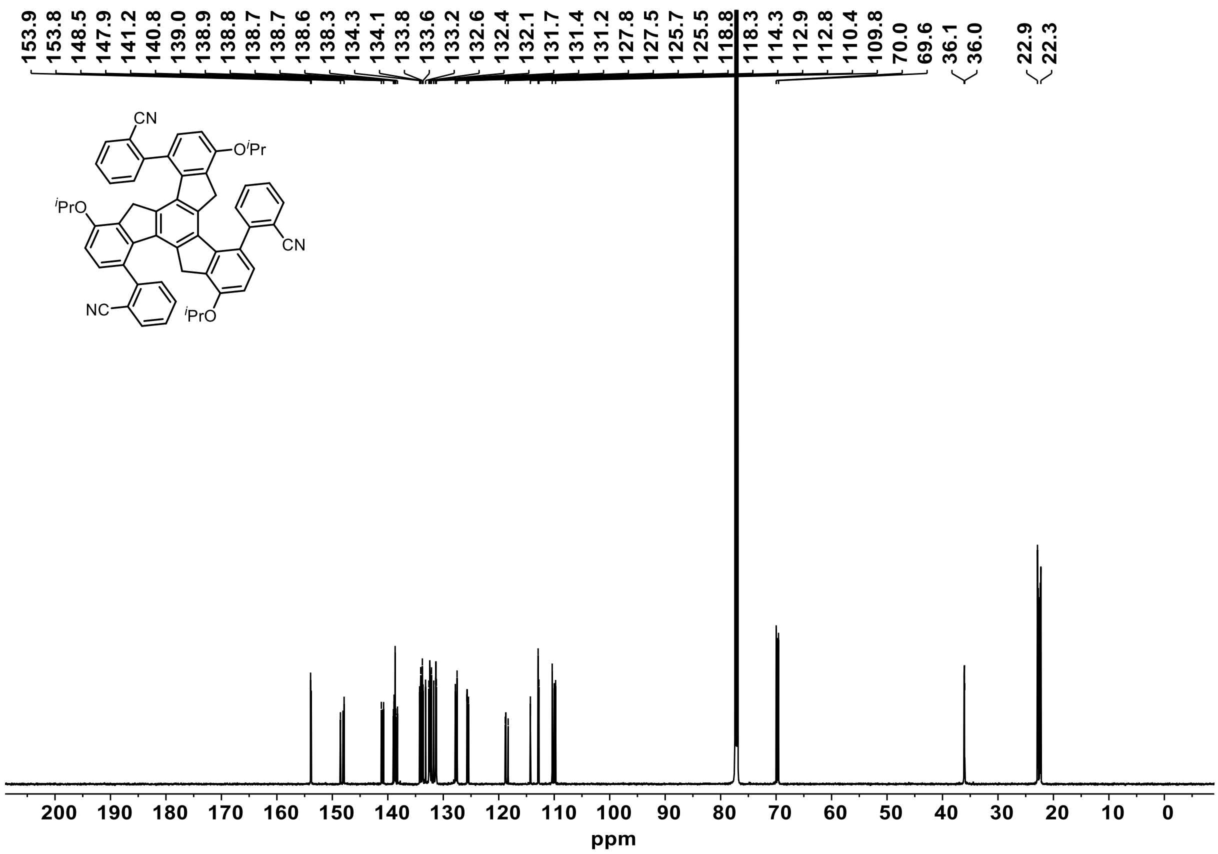

Figure 7.59: ^{13}C NMR spectrum of **138** (150 MHz, CDCl$_3$).

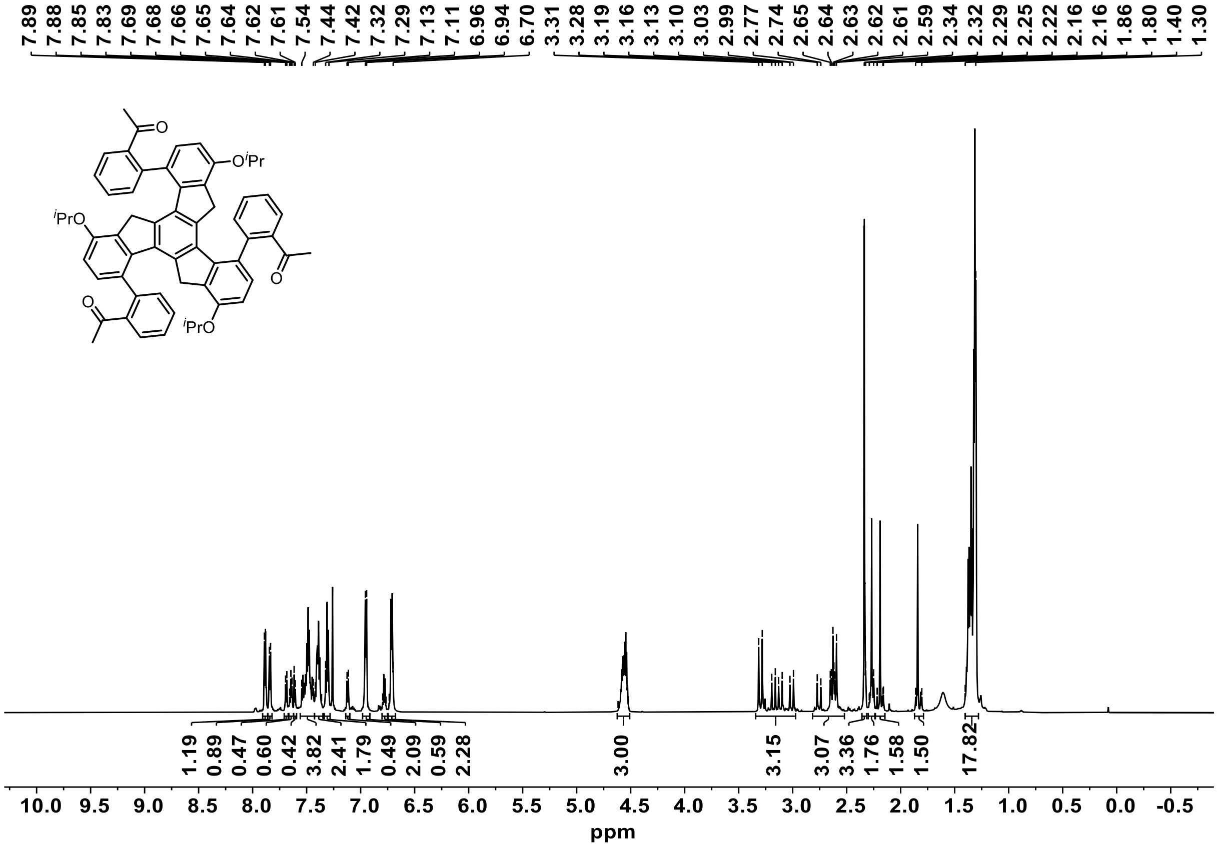

Figure 7.60: ^{1}H NMR spectrum of **139** (700 MHz, CDCl$_3$).

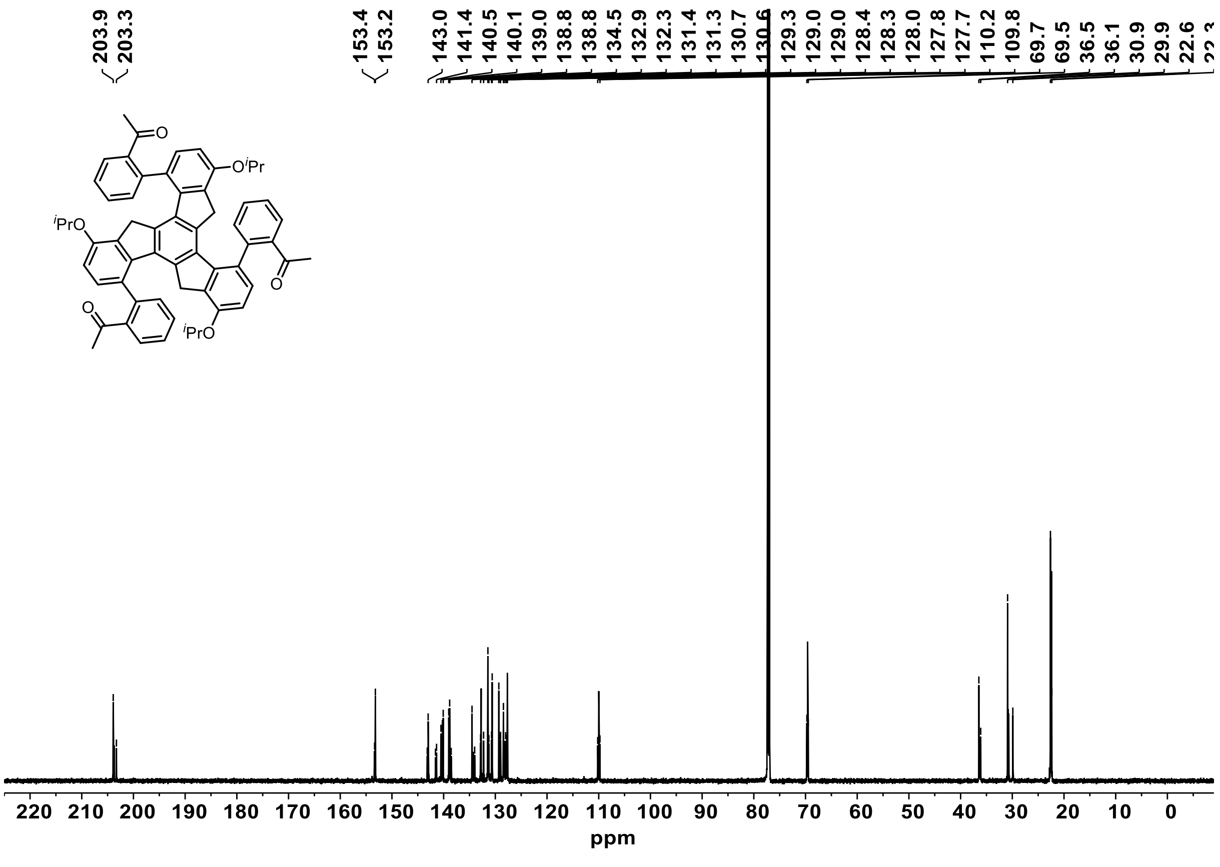

Figure 7.61: ^{13}C NMR spectrum of **139** (176 MHz, CDCl$_3$).

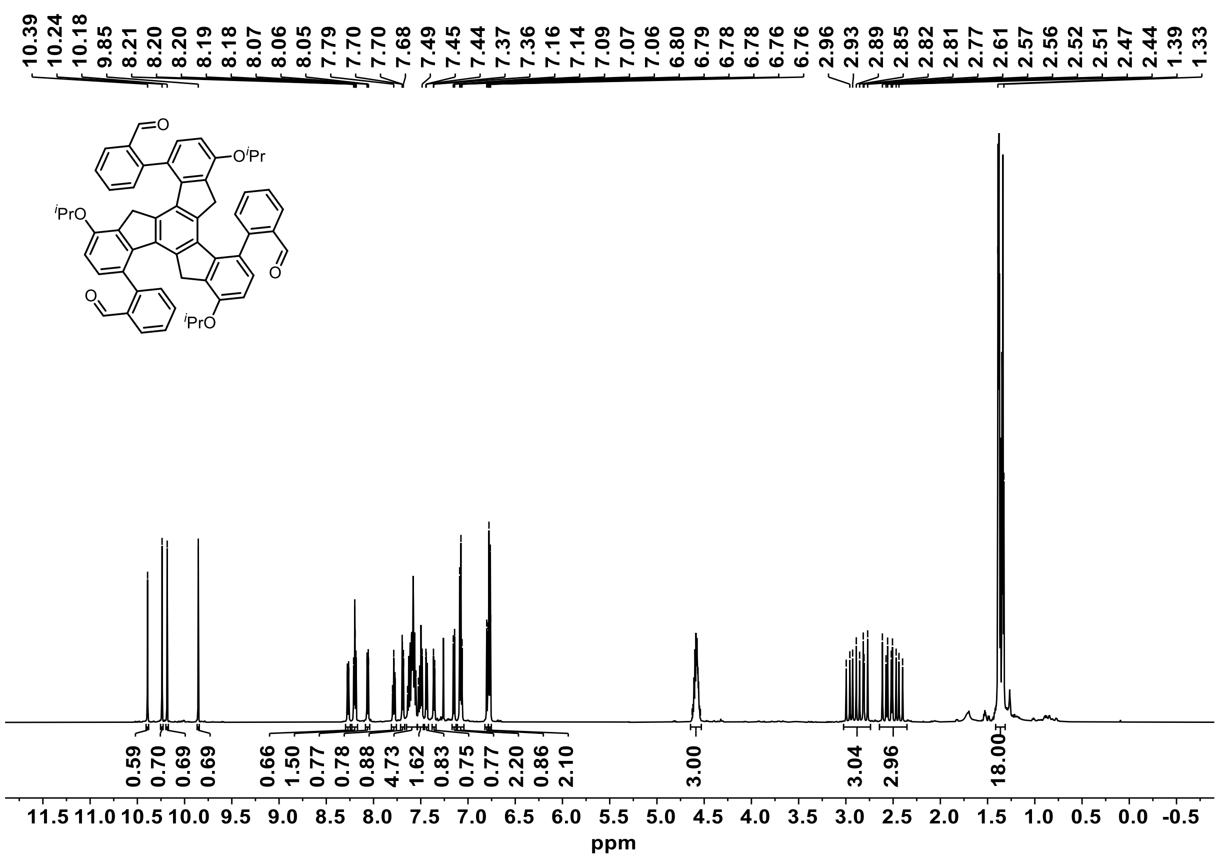

Figure 7.62: ^{1}H NMR spectrum of **142** (600 MHz, $CDCl_3$).

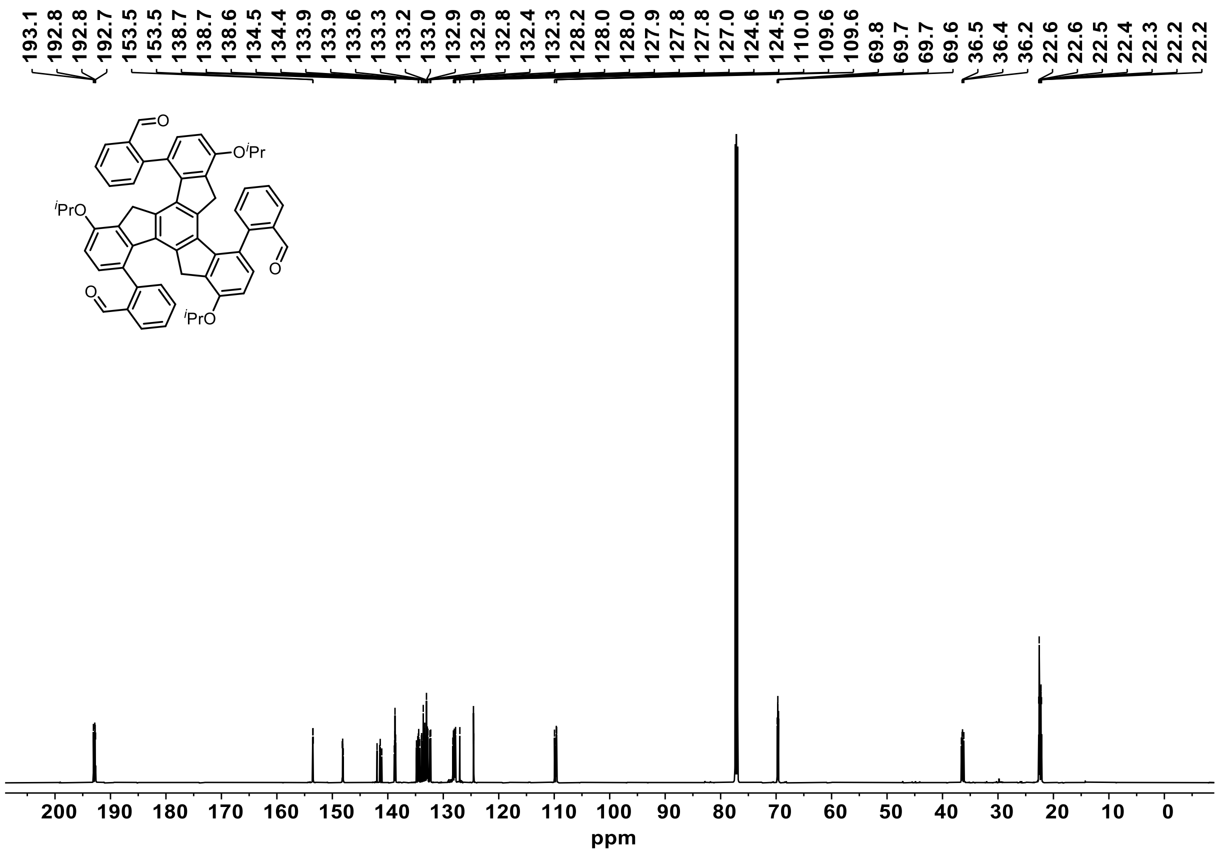

Figure 7.63: ^{13}C NMR spectrum of **142** (150 MHz, $CDCl_3$).

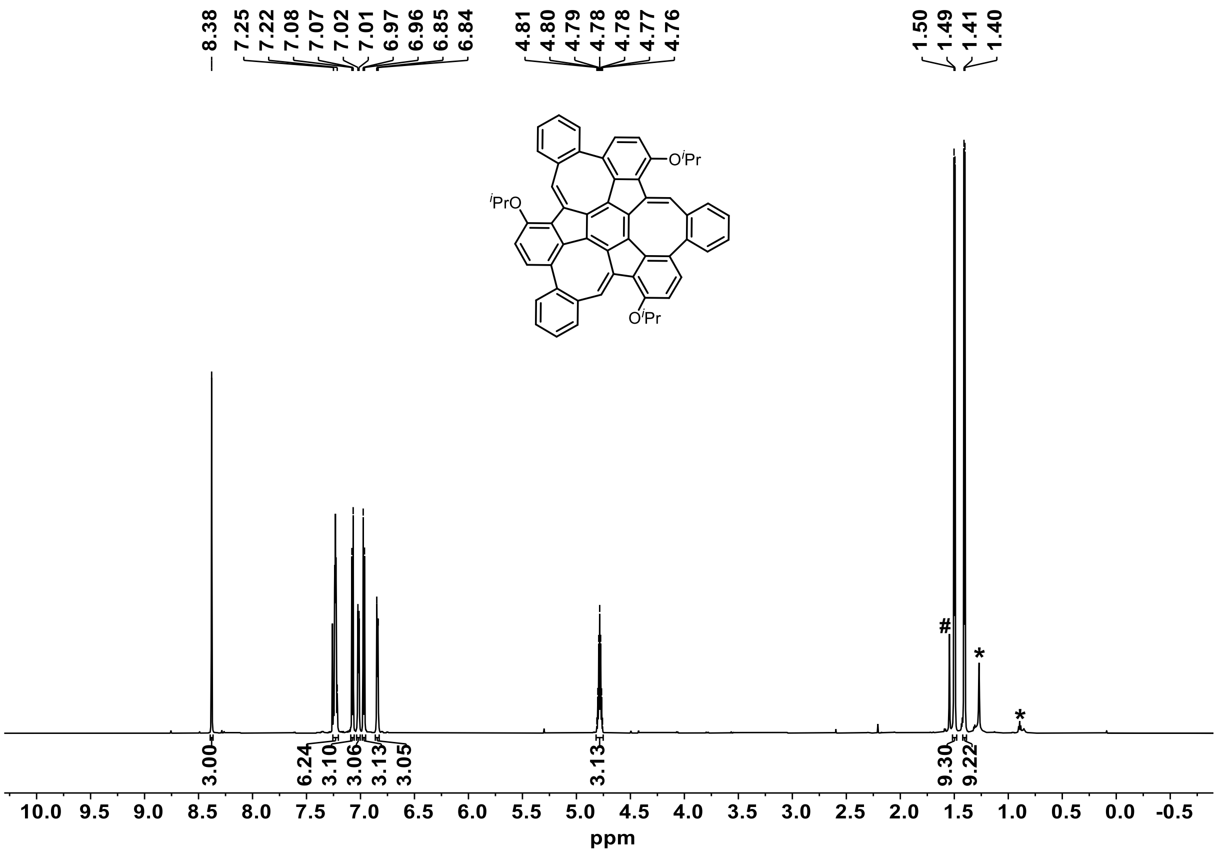

Figure 7.64^{1}H NMR spectrum of **141** (700 MHz, $CDCl_3$). #: H_2O; *: hexane.

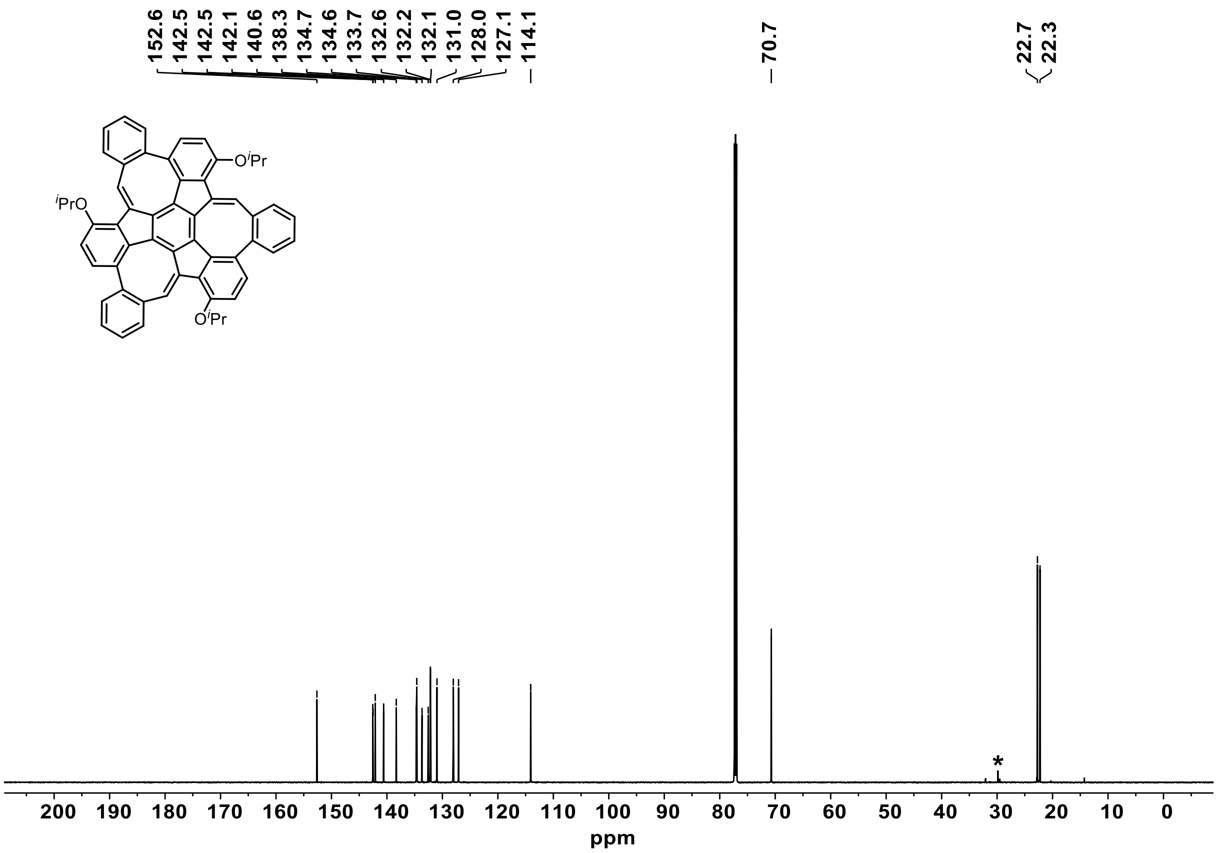

Figure 7.65: ^{13}C NMR spectrum of **141** (176 MHz, $CDCl_3$). *: hexane.

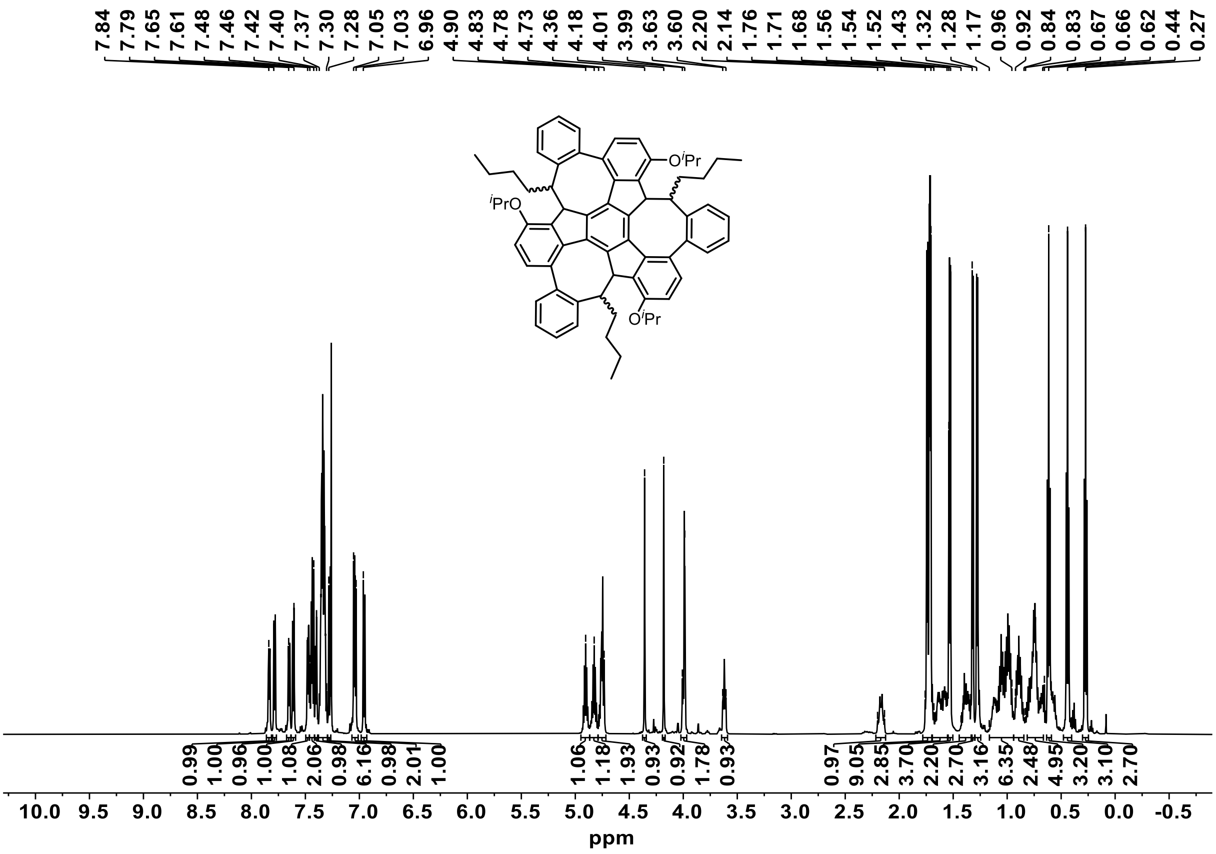

Figure 7.66: ^{1}H NMR spectrum of **150-*anti*** (600 MHz, $CDCl_3$).

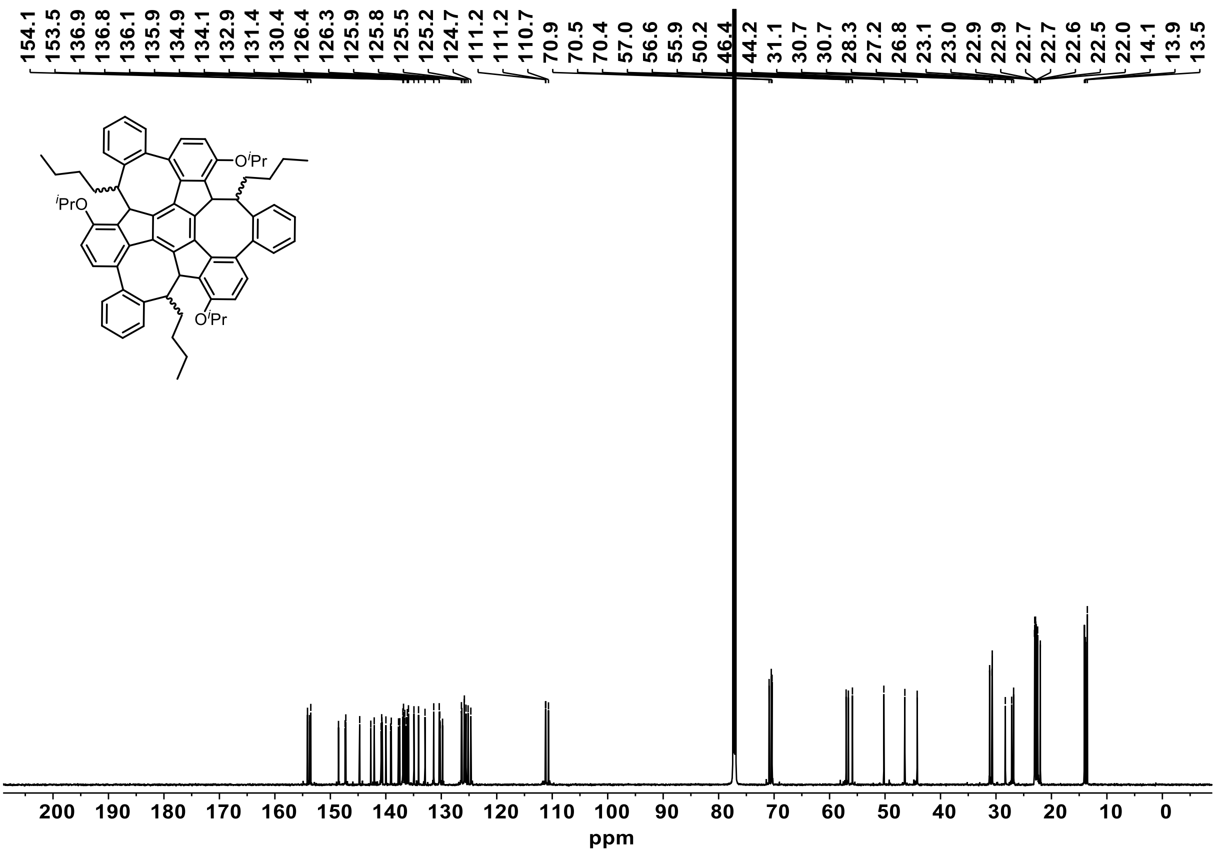

Figure 7.67: ^{13}C NMR spectrum of **150-*anti*** (150 MHz, $CDCl_3$).

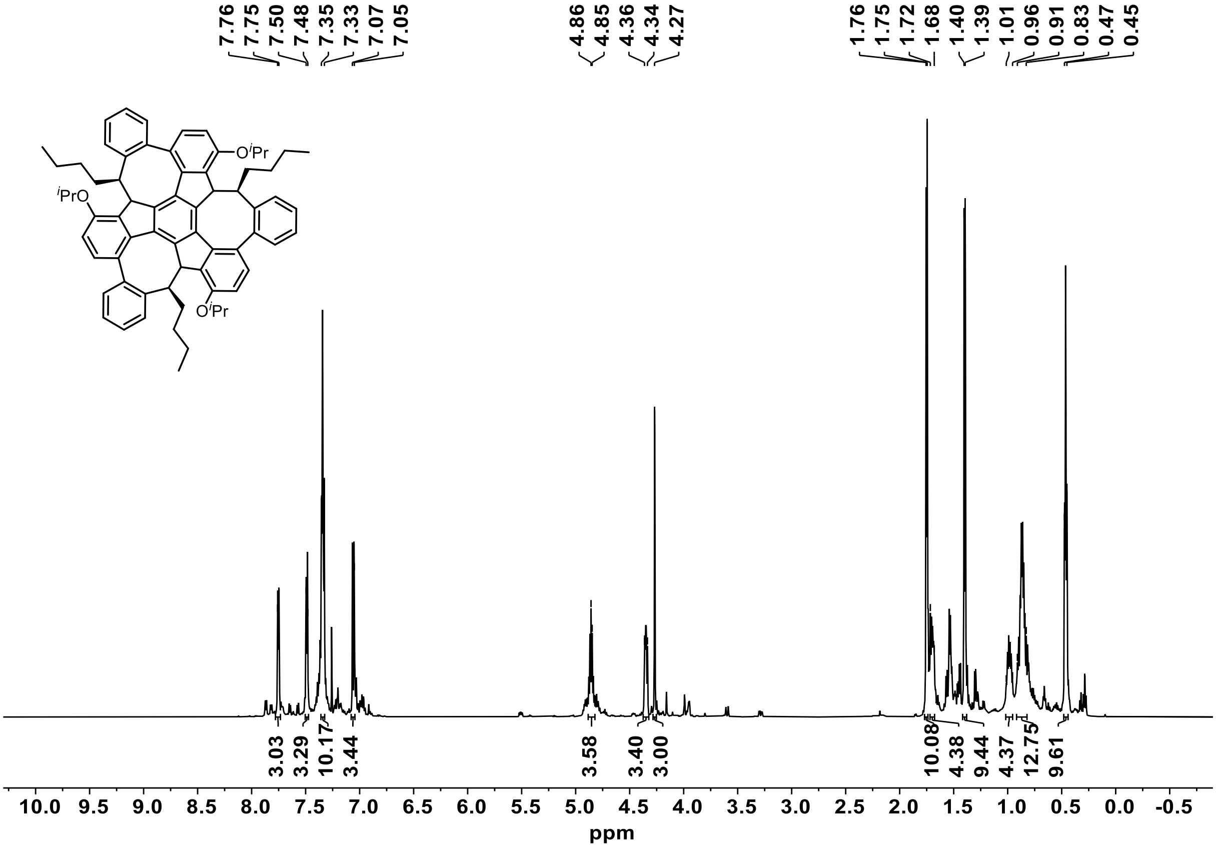

Figure 7.68: ^{1}H NMR spectrum of **150-*syn*** (600 MHz, $CDCl_3$). Only signals of the C_3-symmetrical stereoisomers were picked.

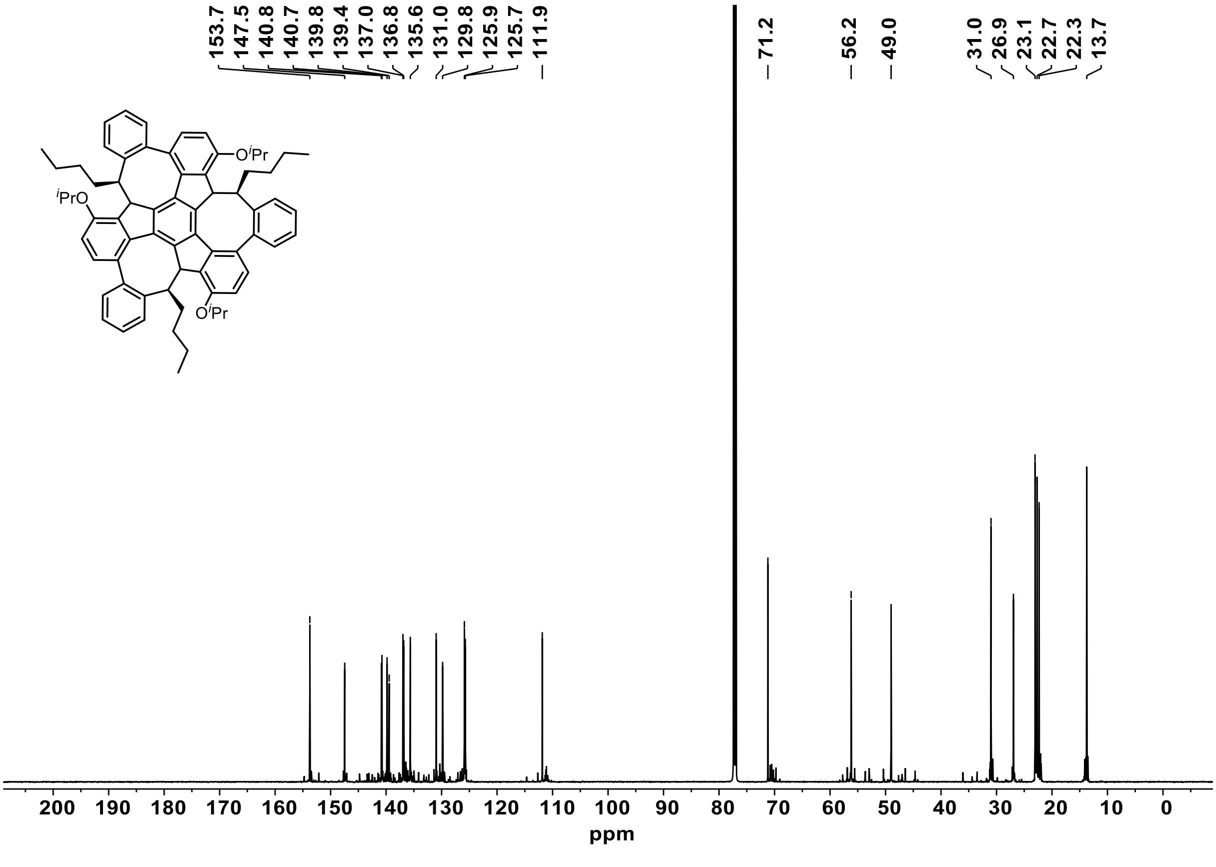

Figure 7.69: ^{13}C NMR spectrum of **150-*syn*** (150 MHz, $CDCl_3$). Only signals of the C_3-symmetrical stereoisomers were picked.

7.4 2D NMR Spectra

2D NMR spectra of compounds **120**, **121**, **122**, **123**, and **125** can be found in reference 186; those of **154**, **155**, **159**, **160**, **161**, **152**, and **166** are reported in reference 306.

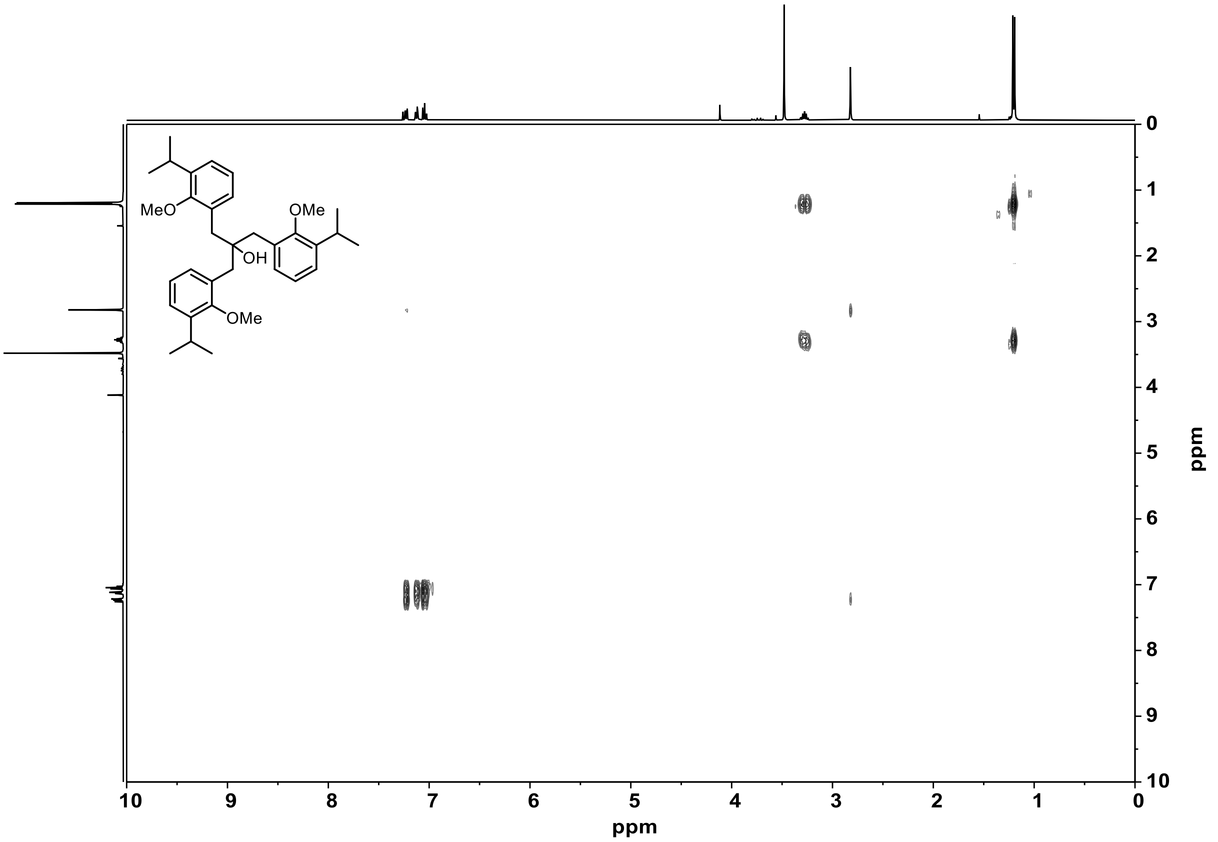

Figure 7.70: ^{1}H-^{1}H COSY spectrum of **92** (400 MHz, CDCl$_3$).

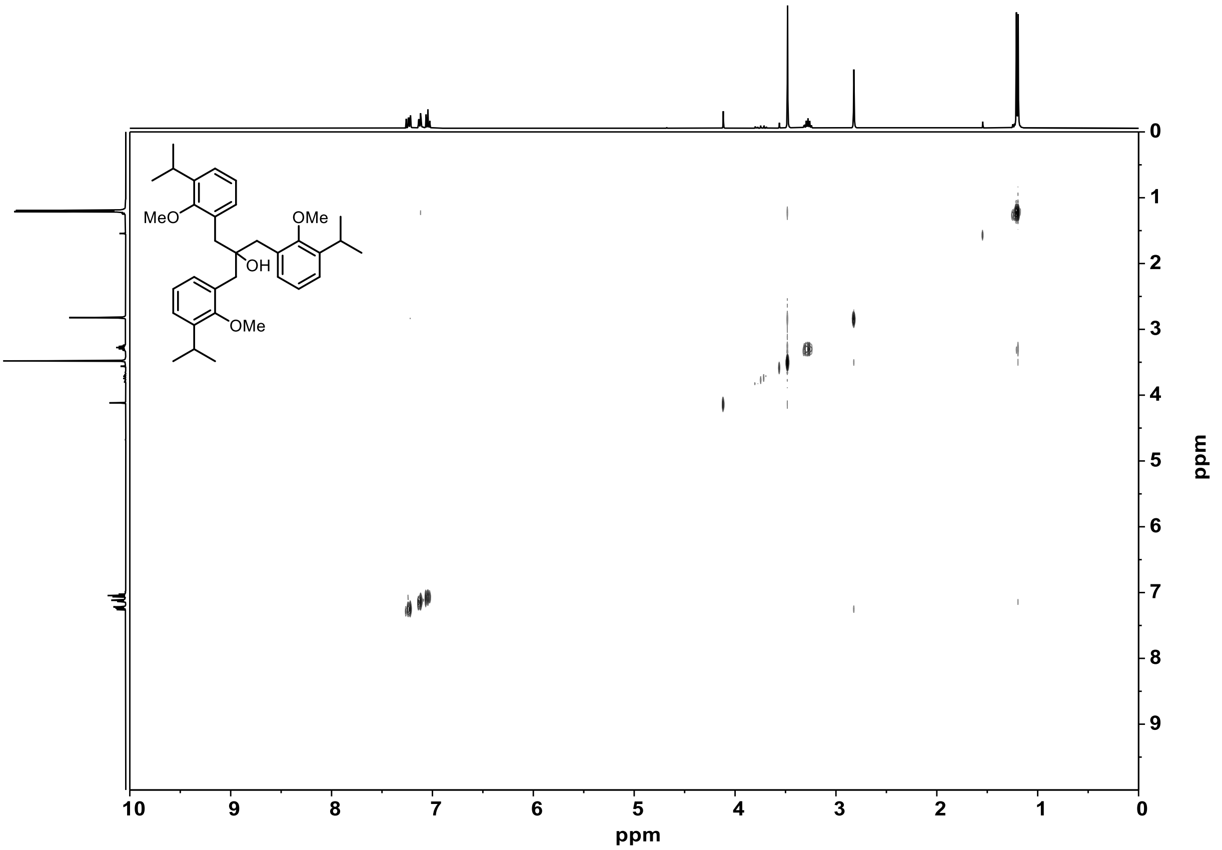

Figure 7.71: ^{1}H-^{1}H NOESY spectrum of **92** (400 MHz, CDCl$_3$).

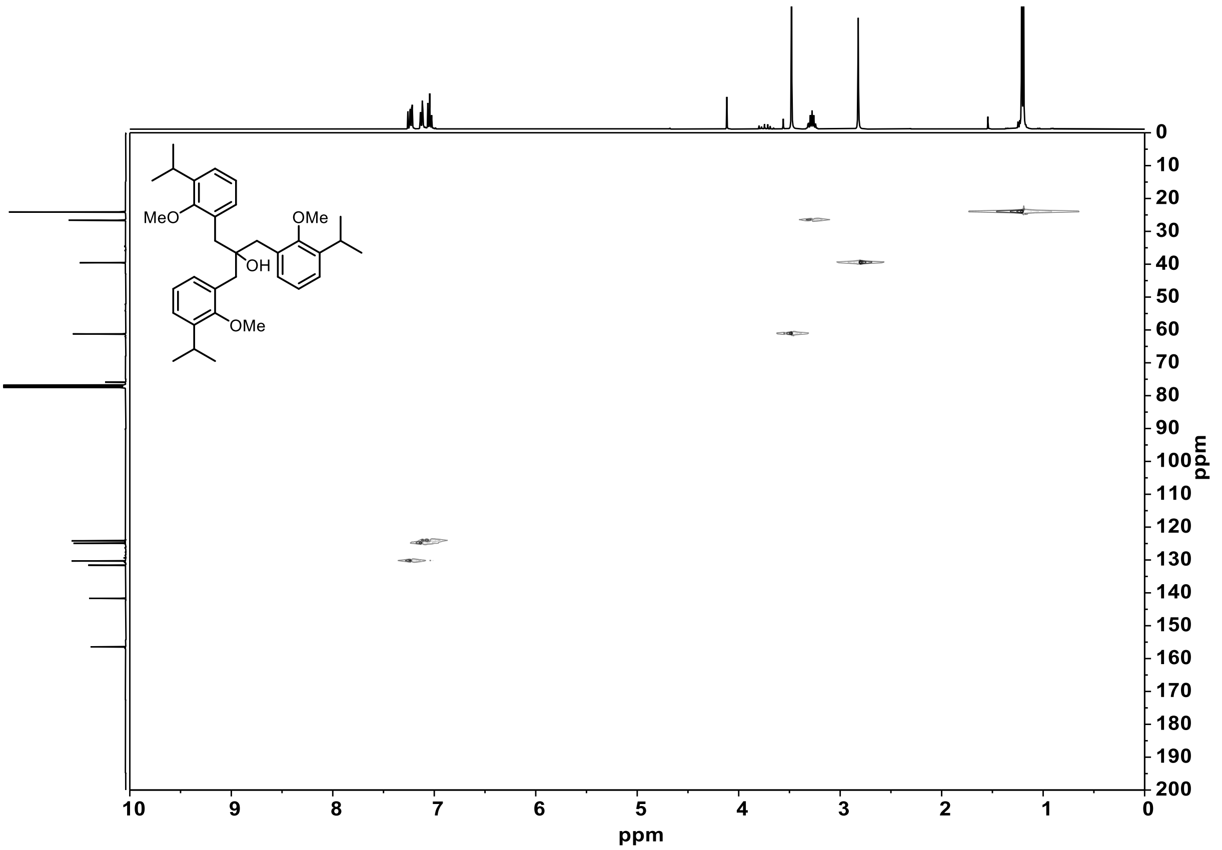

Figure 7.72: ^{1}H-^{13}C HSQC spectrum of **92** (400 MHz, 100 MHz, CDCl$_3$).

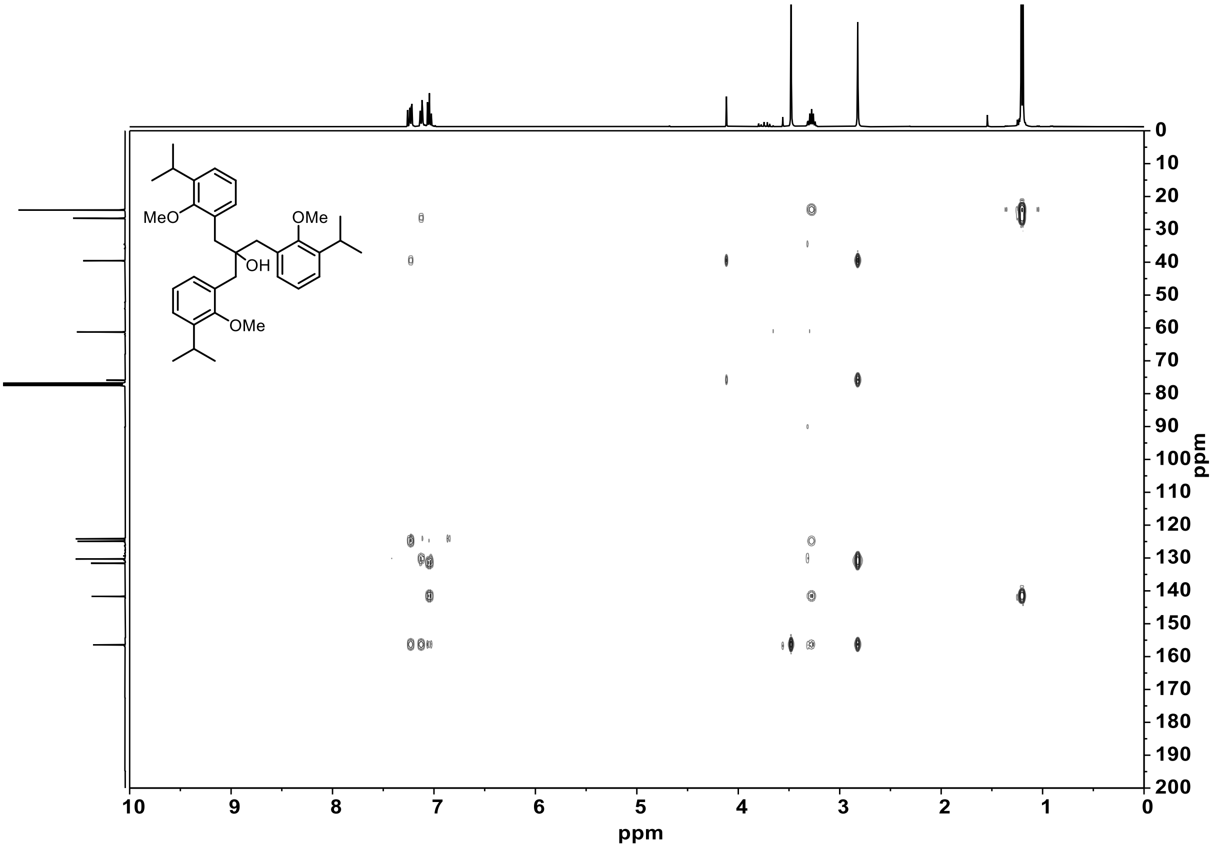

Figure 7.73: ^{1}H-^{13}C HMBC spectrum of **92** (400 MHz, 100 MHz, $CDCl_3$).

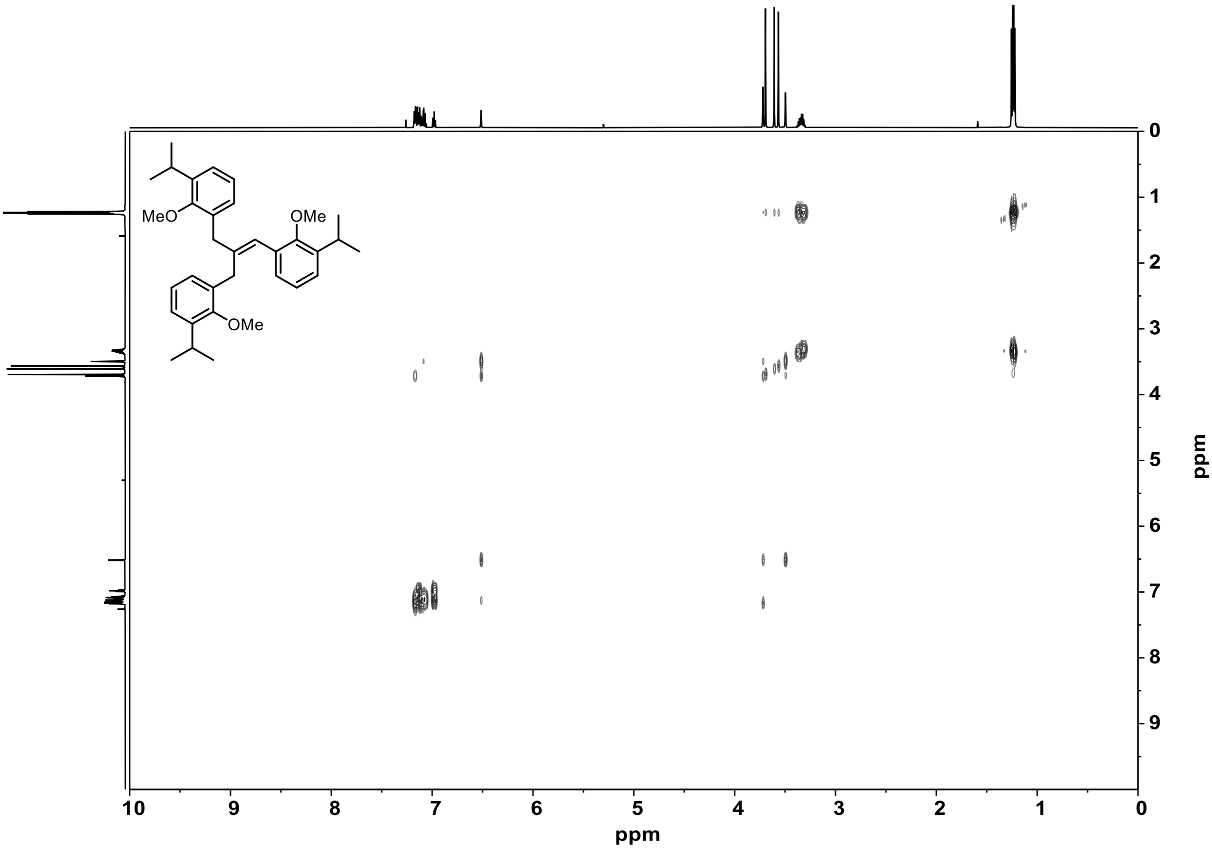

Figure 7.74: ^{1}H-^{1}H COSY spectrum of **93** (600 MHz, $CDCl_3$).

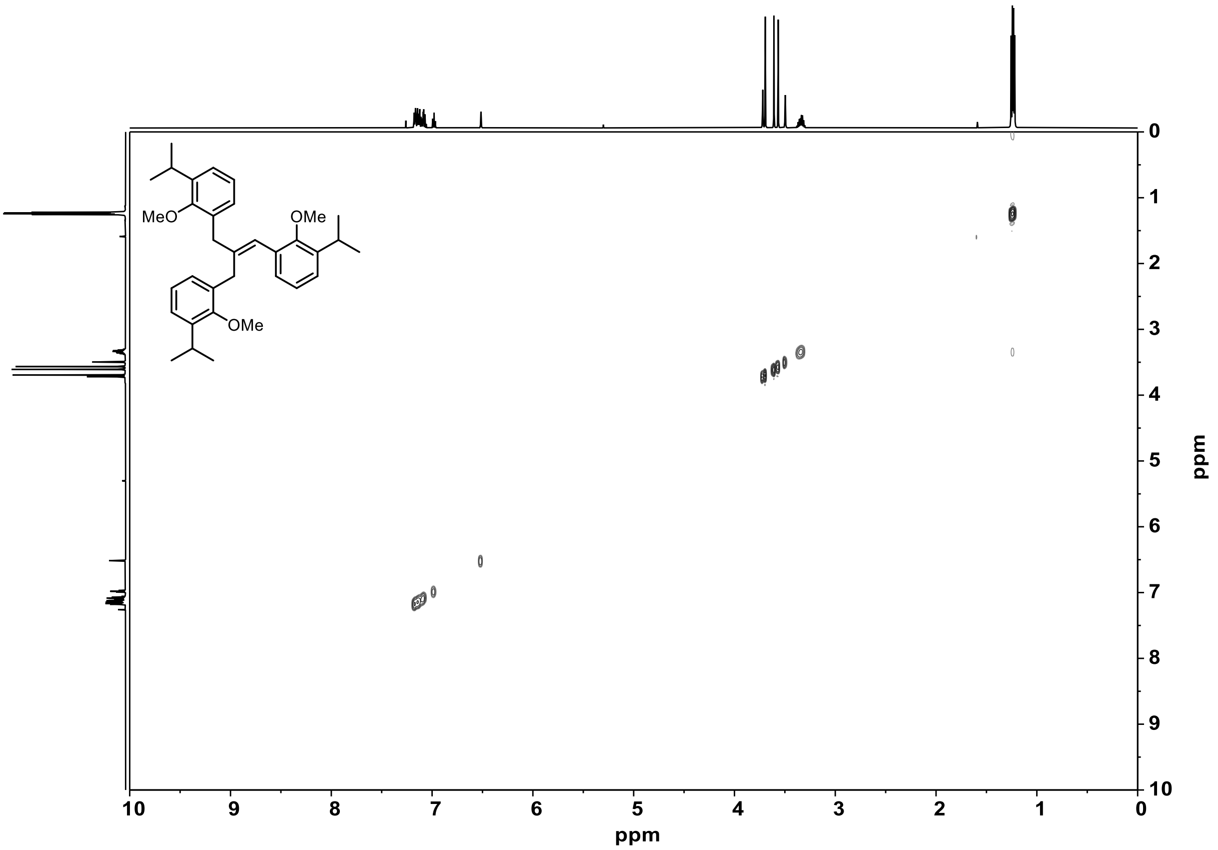

Figure 7.75: ^1H-^1H NOESY spectrum of **93** (600 MHz, CDCl₃).

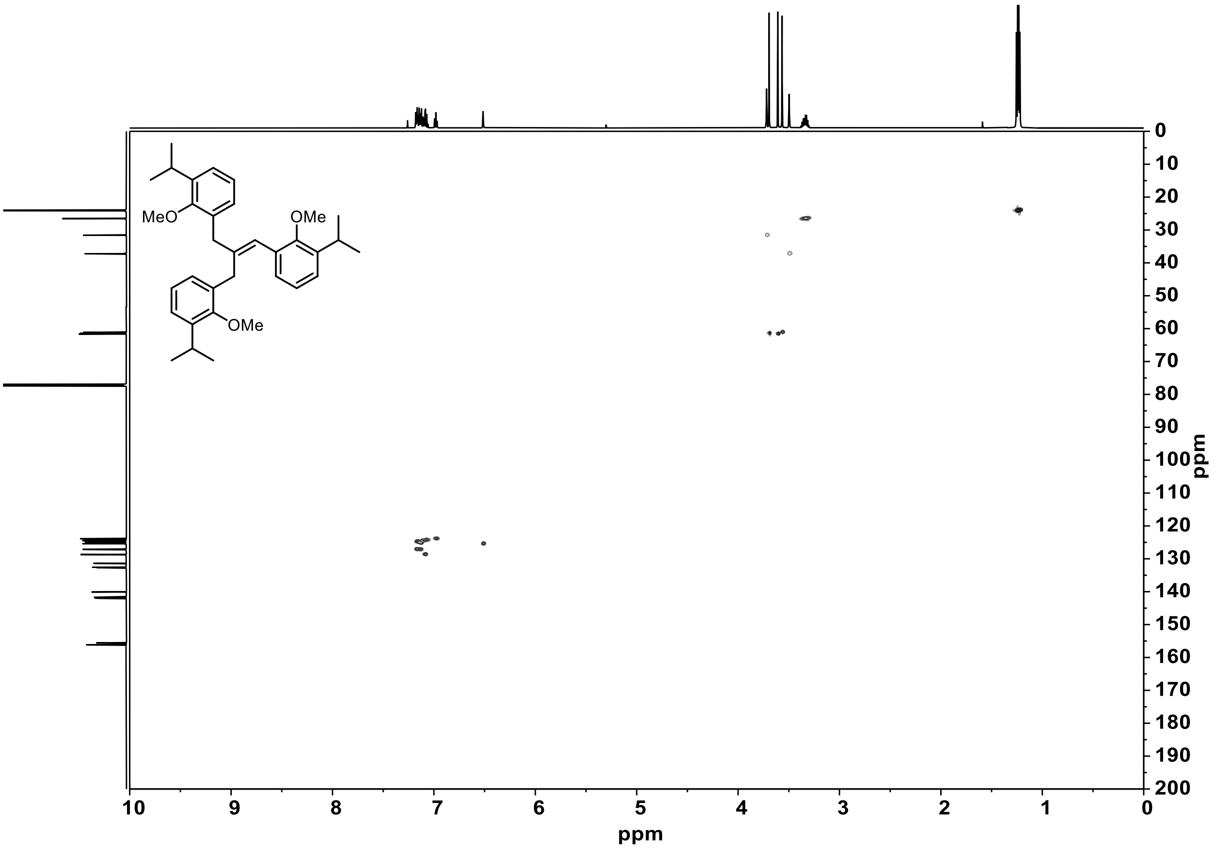

Figure 7.76: ^1H-^{13}C HSQC spectrum of **93** (600 MHz, 150 MHz, CDCl₃).

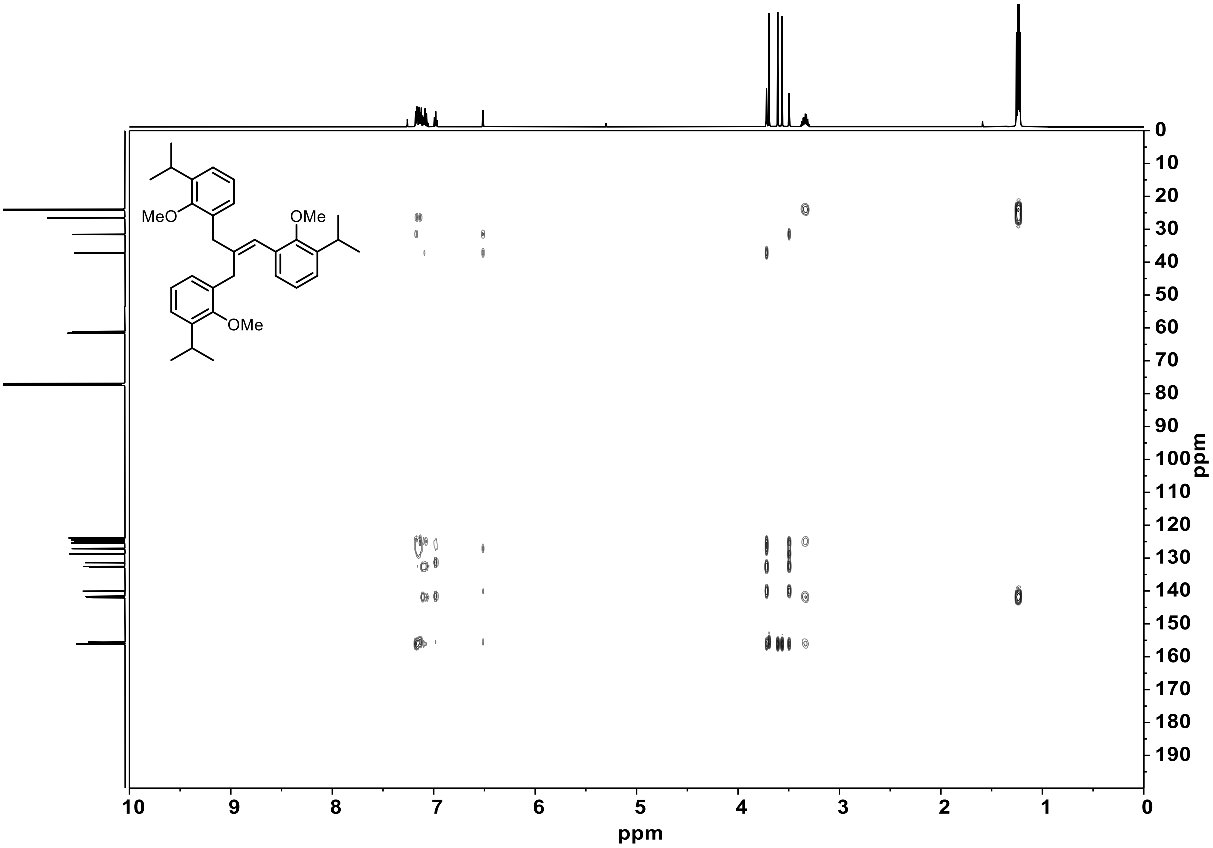

Figure 7.77: ^{1}H-^{13}C HMBC spectrum of **93** (600 MHz, 150 MHz, CDCl$_3$).

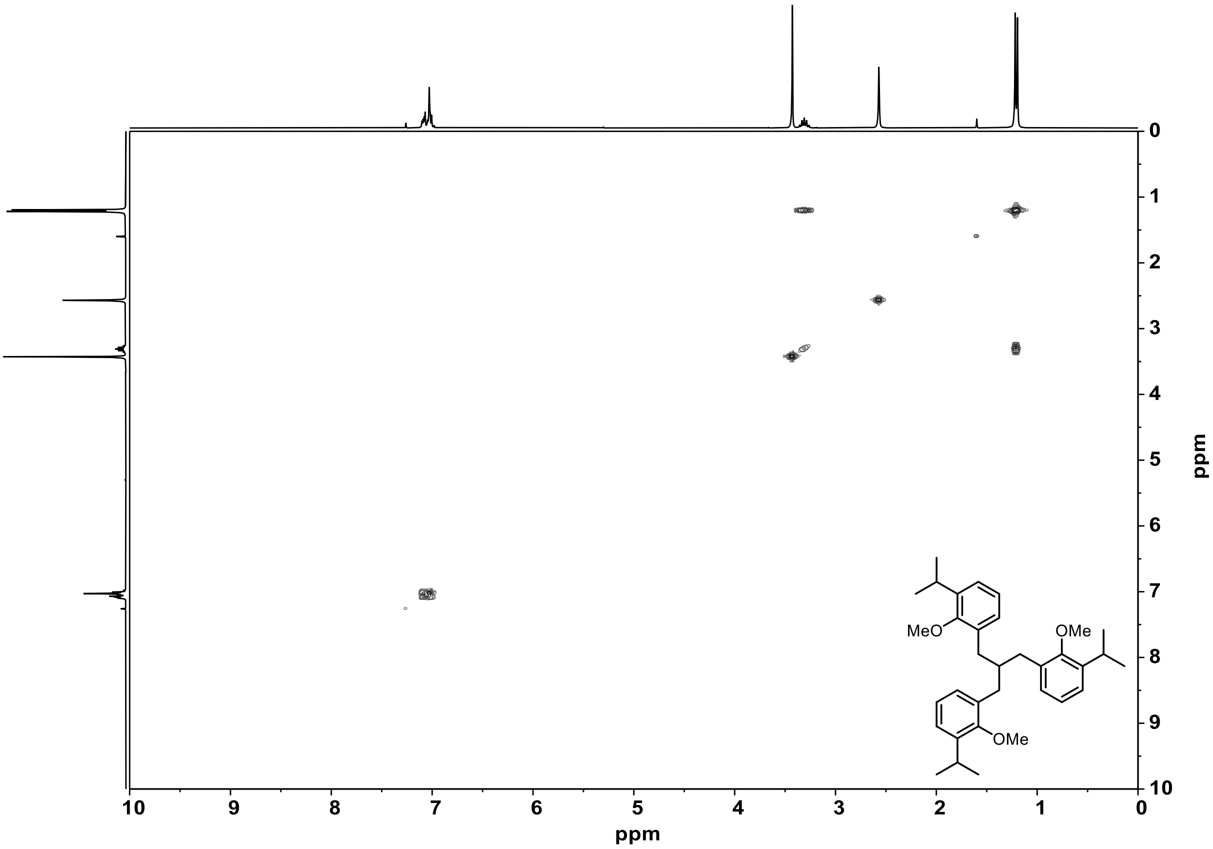

Figure 7.78: ^{1}H-^{1}H COSY spectrum of **94** (300 MHz, CDCl$_3$).

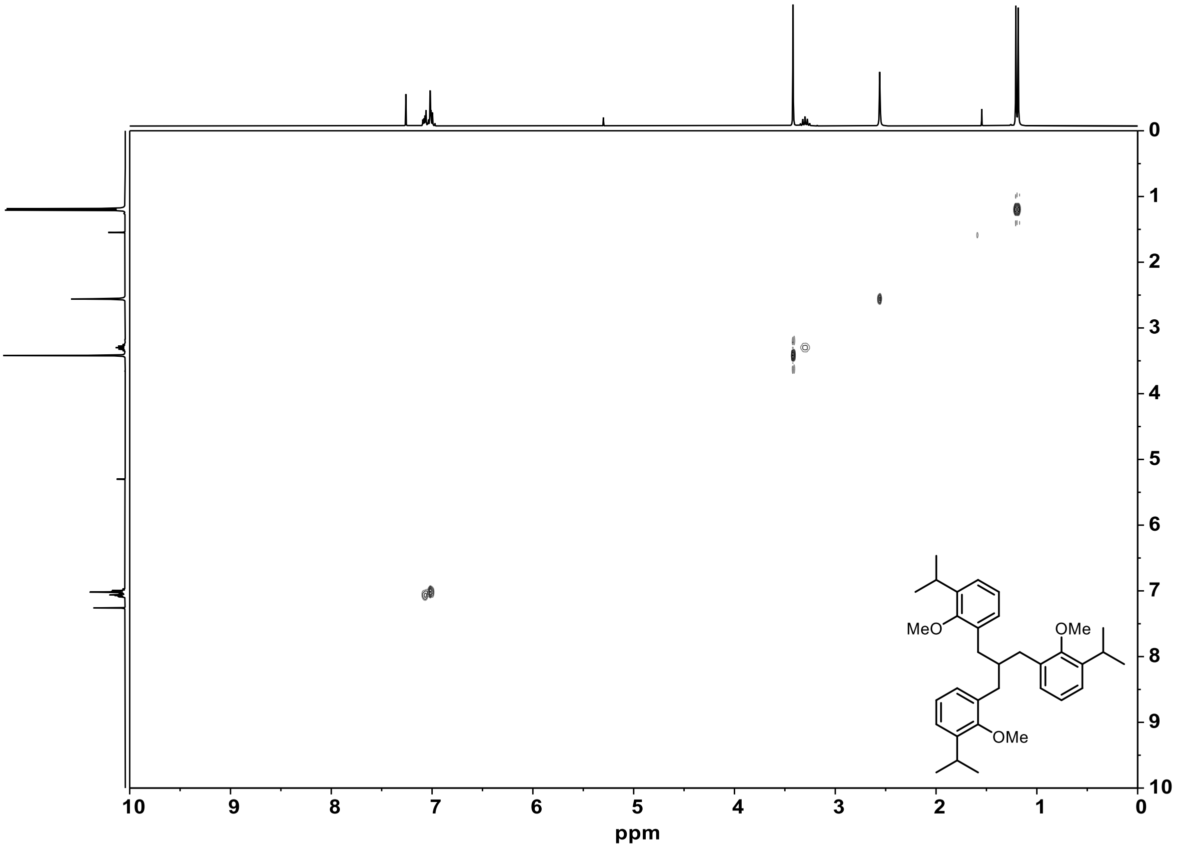

Figure 7.79: ^{1}H-^{1}H NOESY spectrum of **94** (300 MHz, CDCl$_3$).

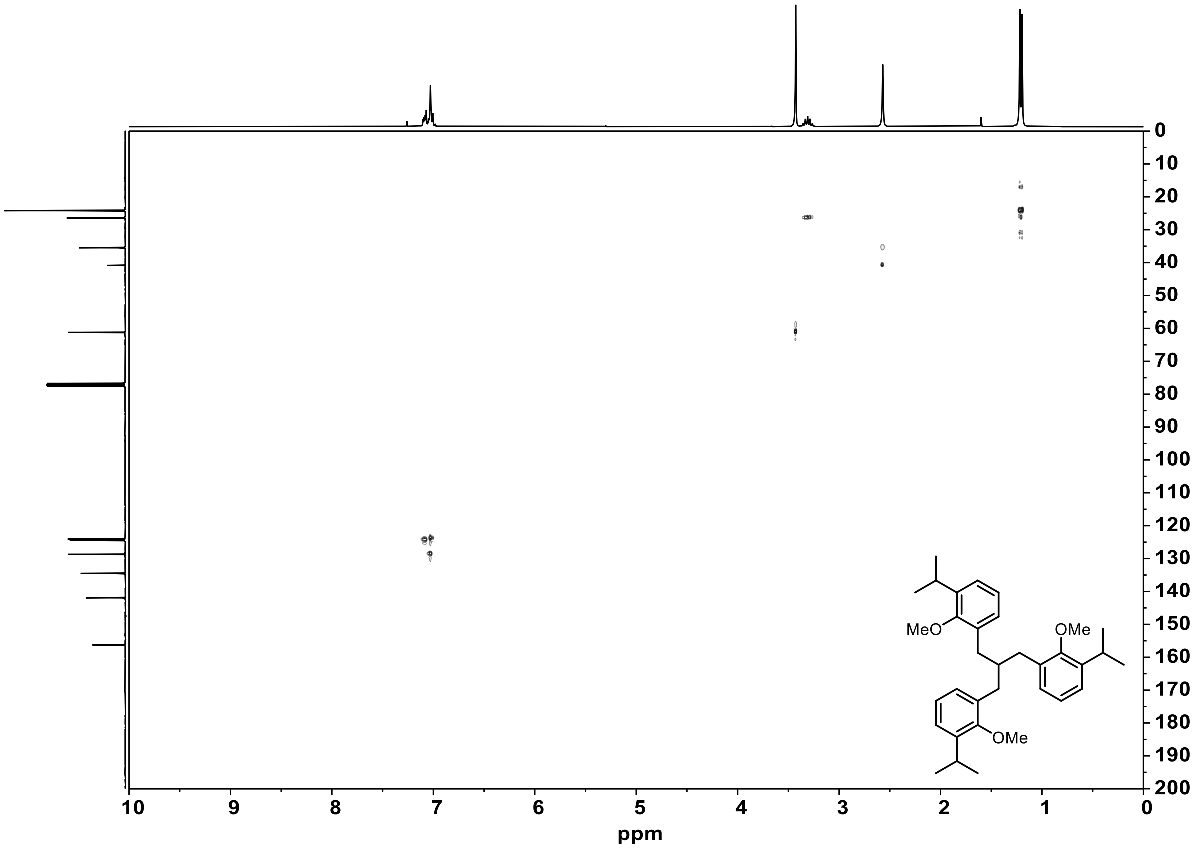

Figure 7.80: ^{1}H-^{13}C HSQC spectrum of **94** (300 MHz, 75 MHz, CDCl$_3$).

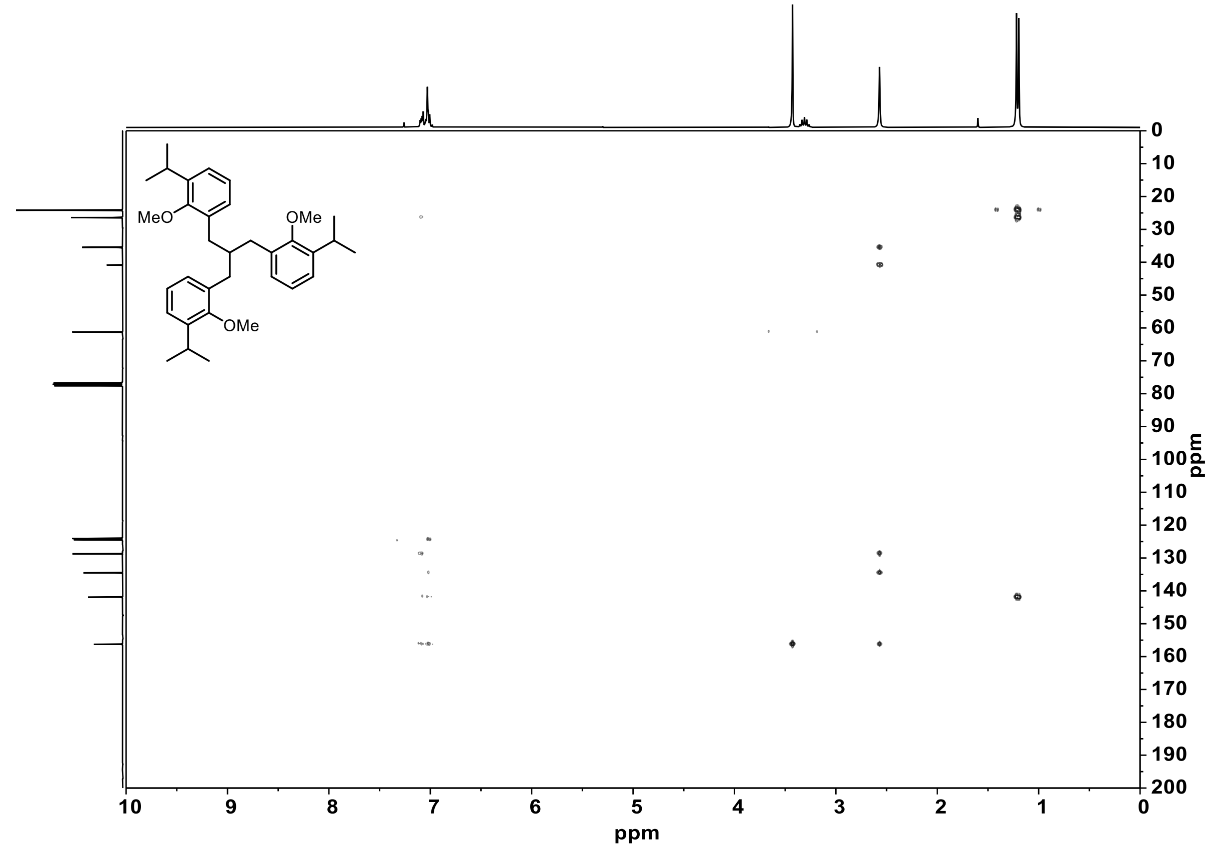

Figure 7.81: ^{1}H-^{13}C HMBC spectrum of **94** (300 MHz, 75 MHz, CDCl$_3$).

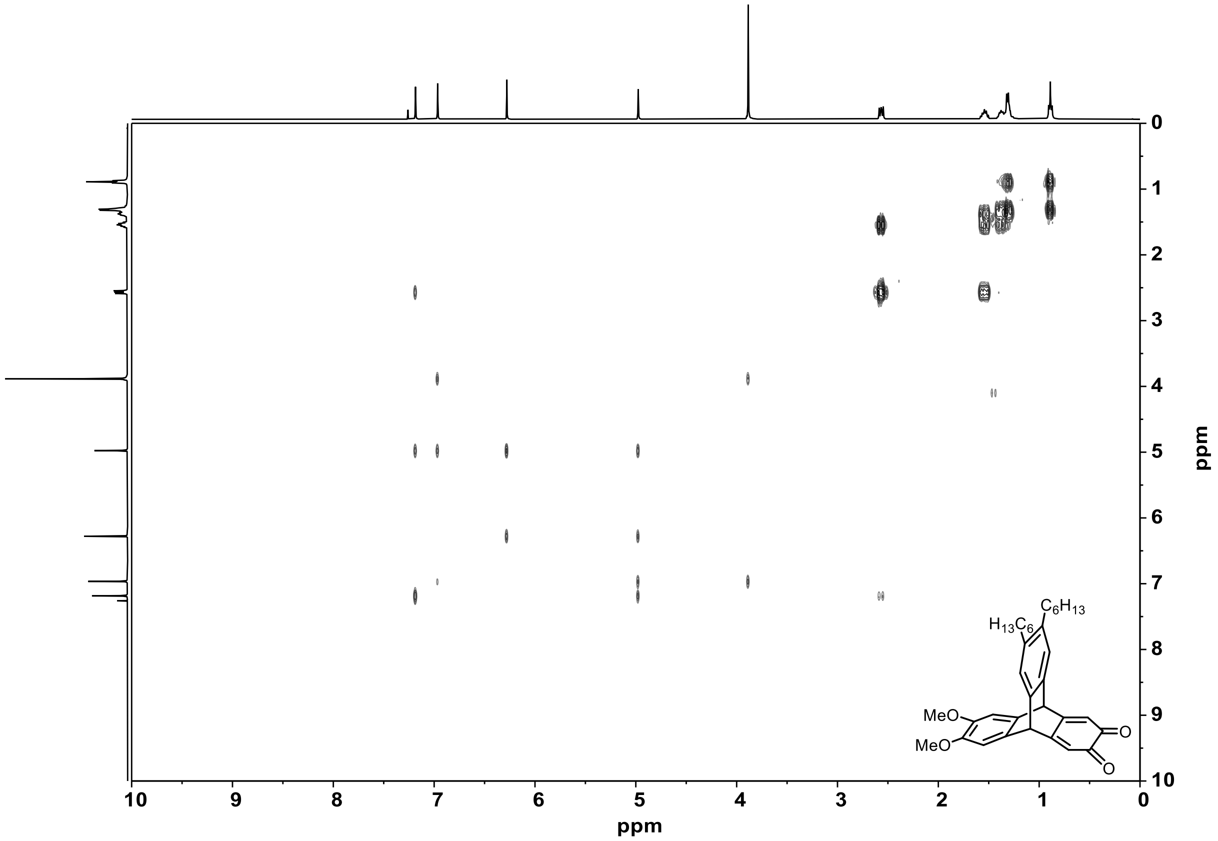

Figure 7.82: ^{1}H-^{1}H COSY spectrum of **100** (400 MHz, CDCl$_3$).

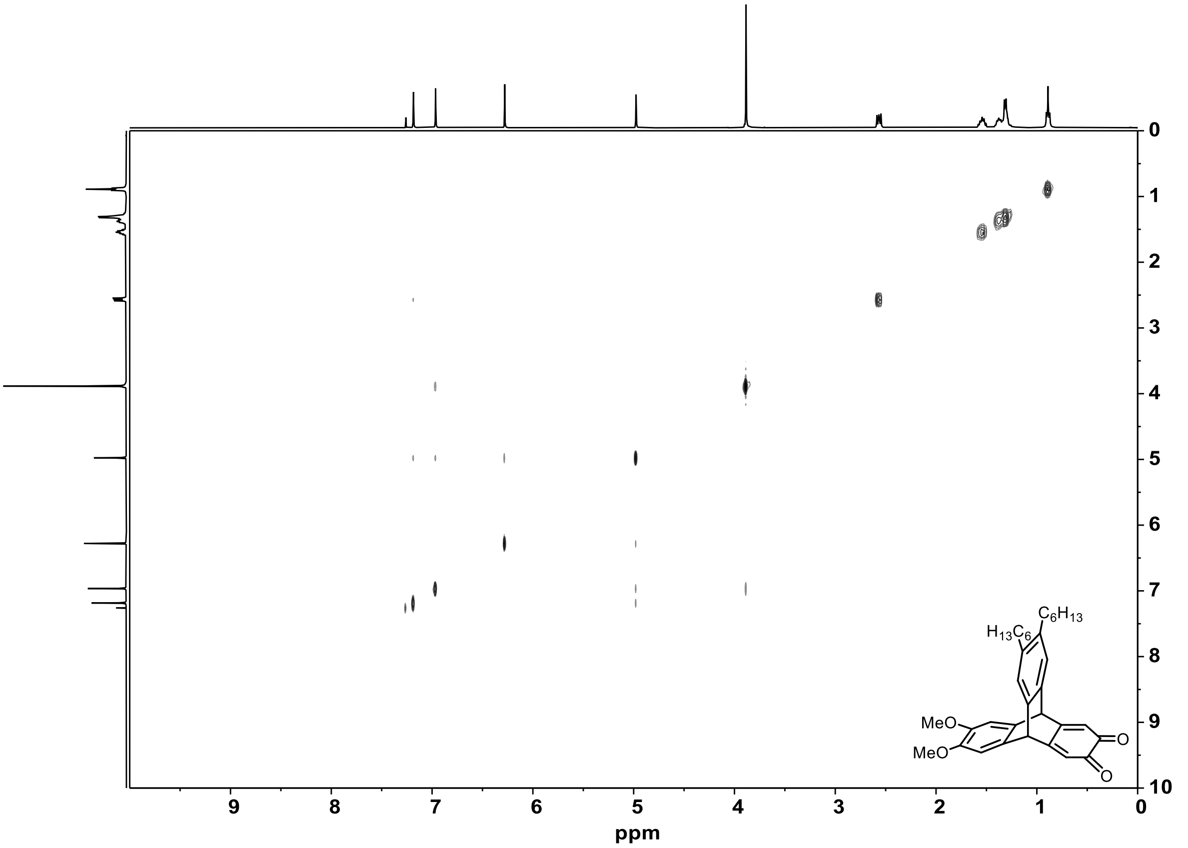

Figure 7.83: ^{1}H-^{1}H NOESY spectrum of **100** (400 MHz, $CDCl_3$).

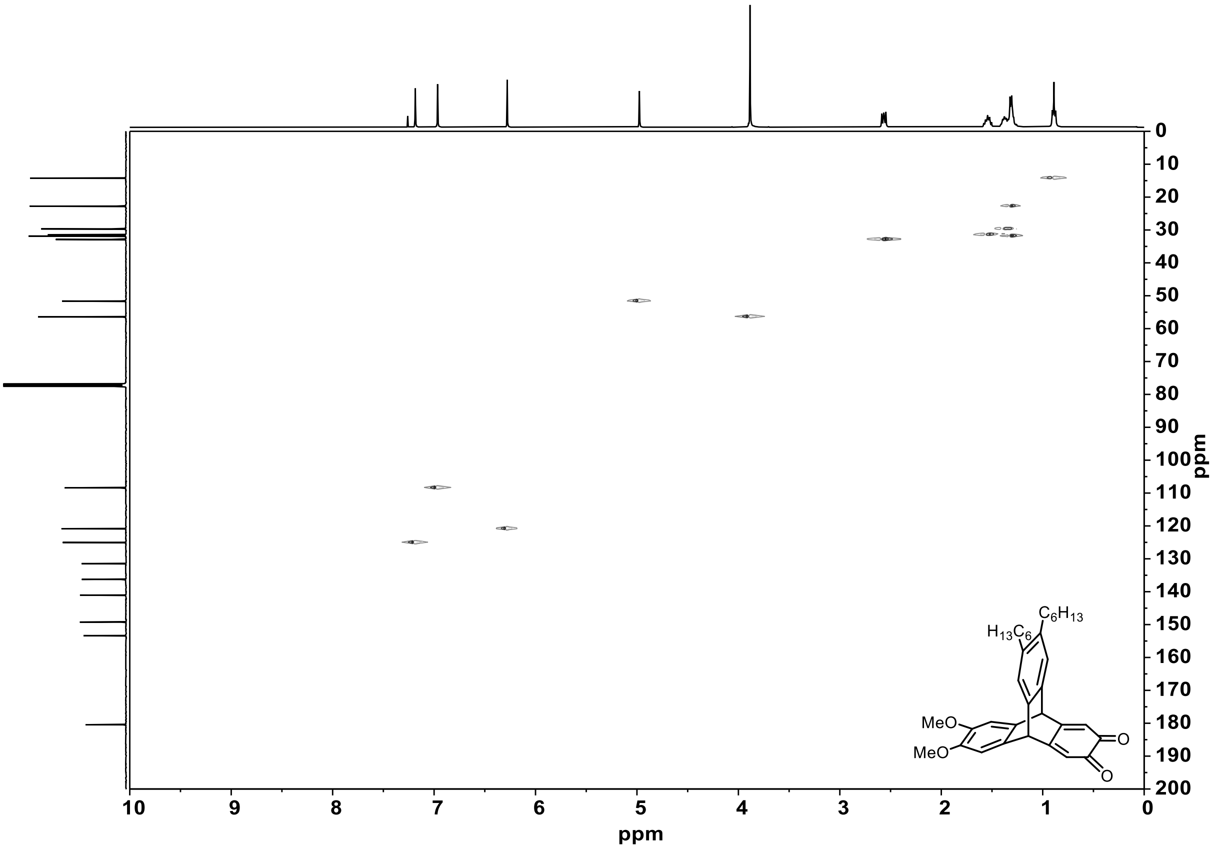

Figure 7.84: ^{1}H-^{13}C HSQC spectrum of **100** (400 MHz, 100 MHz, $CDCl_3$).

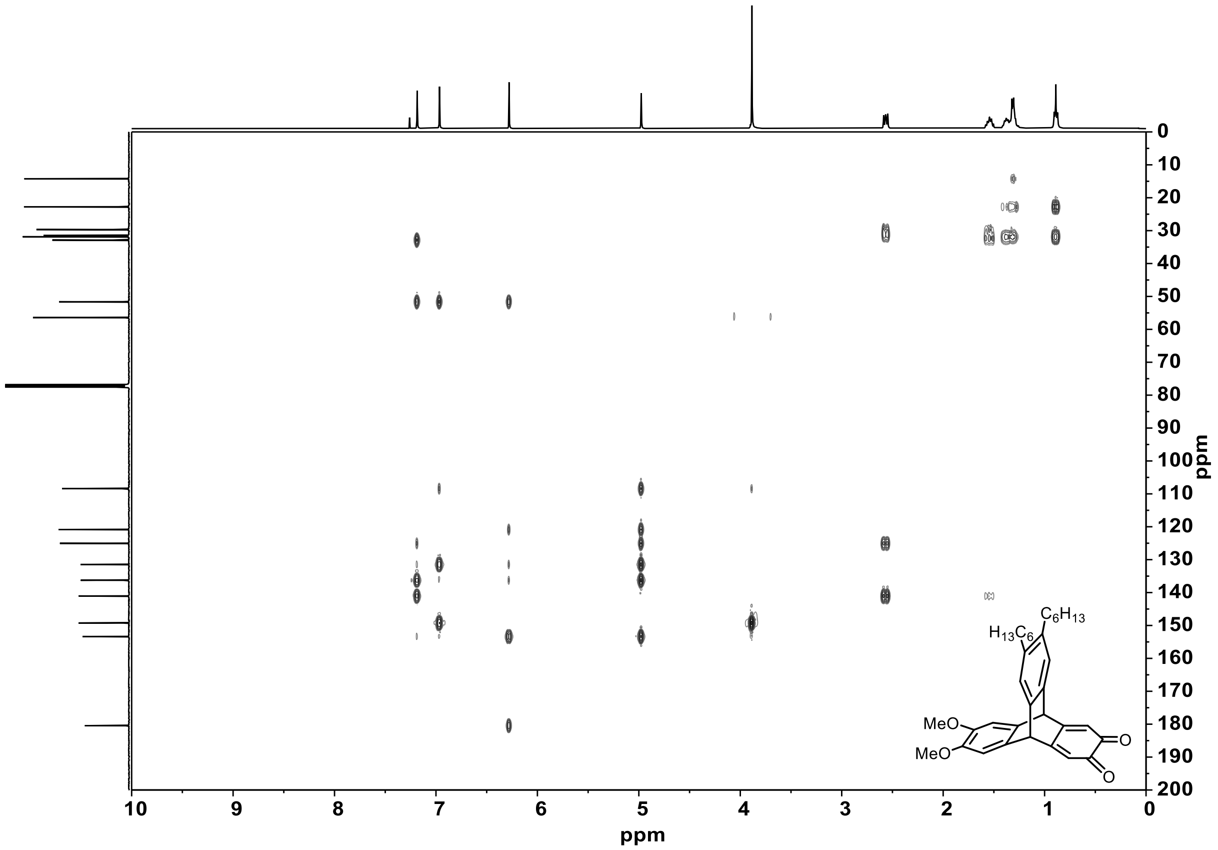

Figure 7.85: ^{1}H-^{13}C HMBC spectrum of **100** (400 MHz, 100 MHz, CDCl₃).

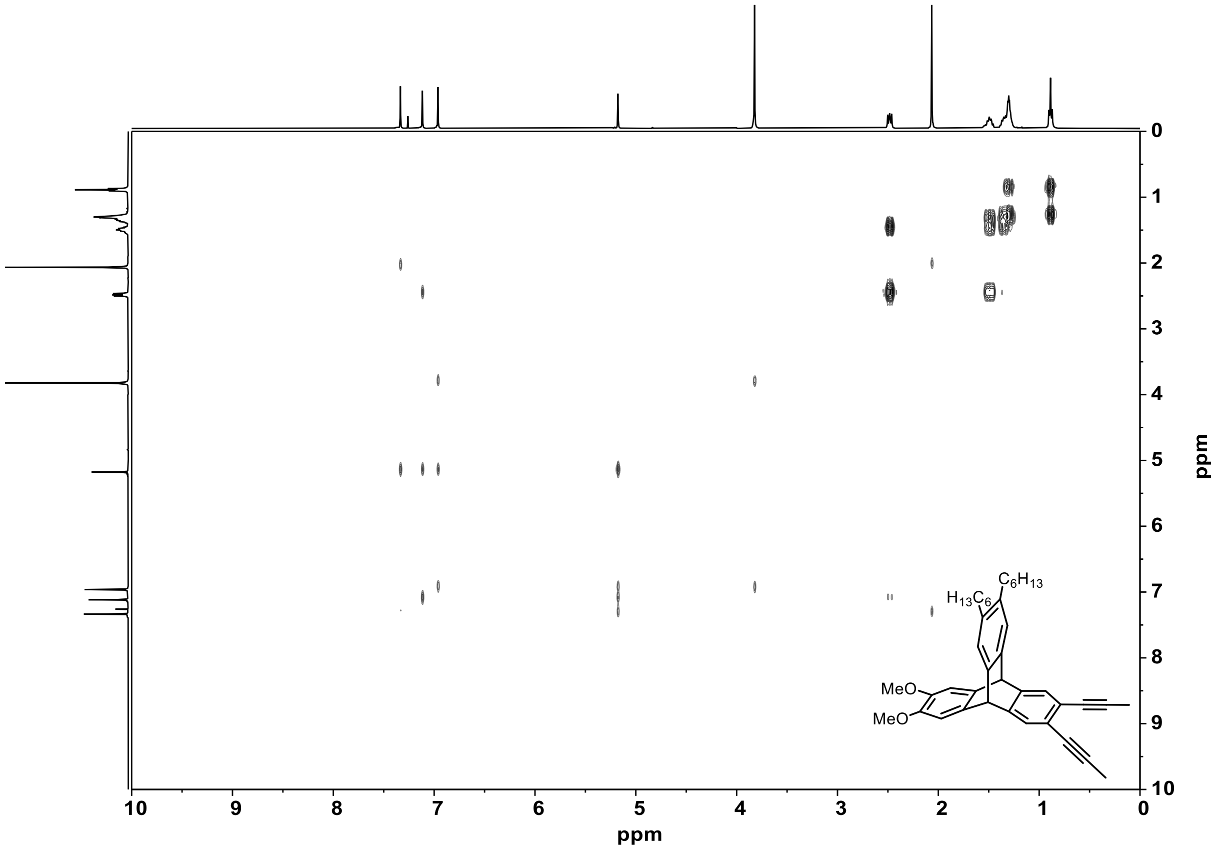

Figure 7.86: ^{1}H-^{1}H COSY spectrum of **101** (400 MHz, CDCl₃).

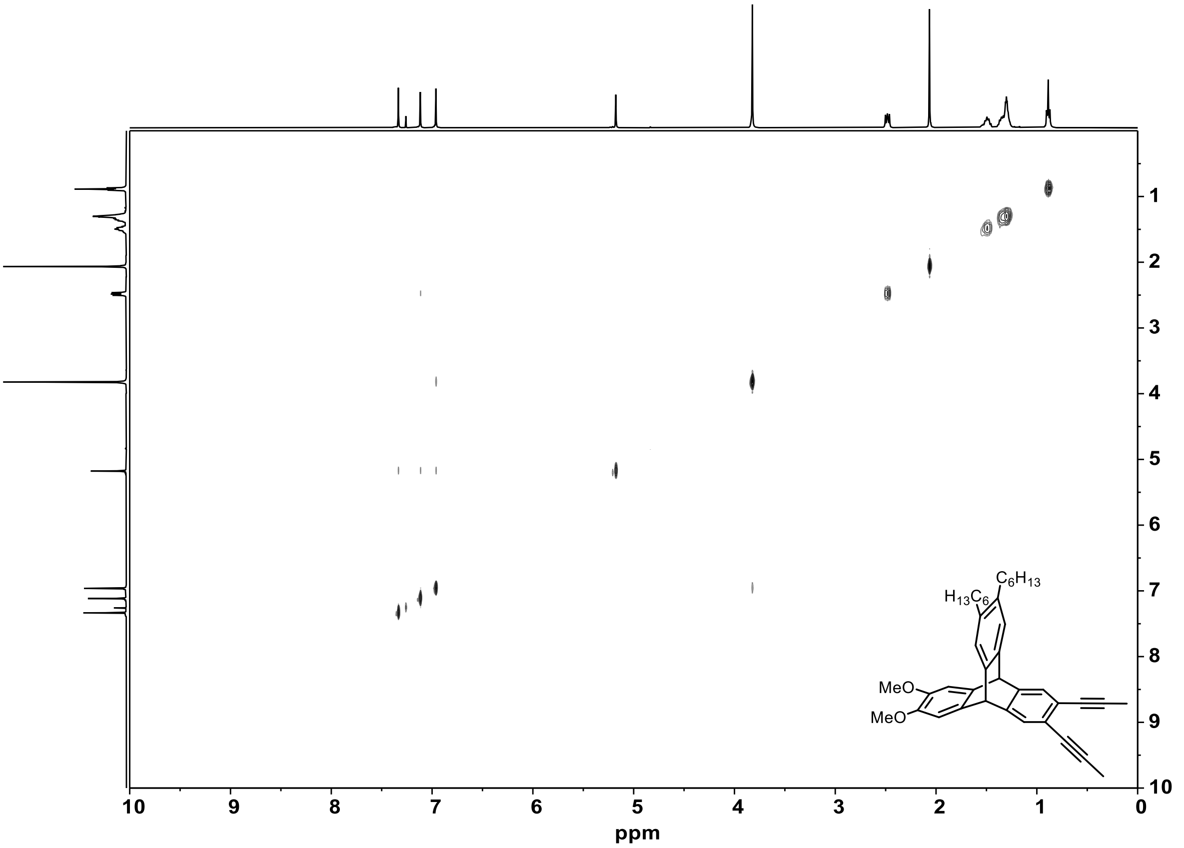

Figure 7.87: ^{1}H-^{1}H NOESY spectrum of **101** (400 MHz, CDCl$_3$).

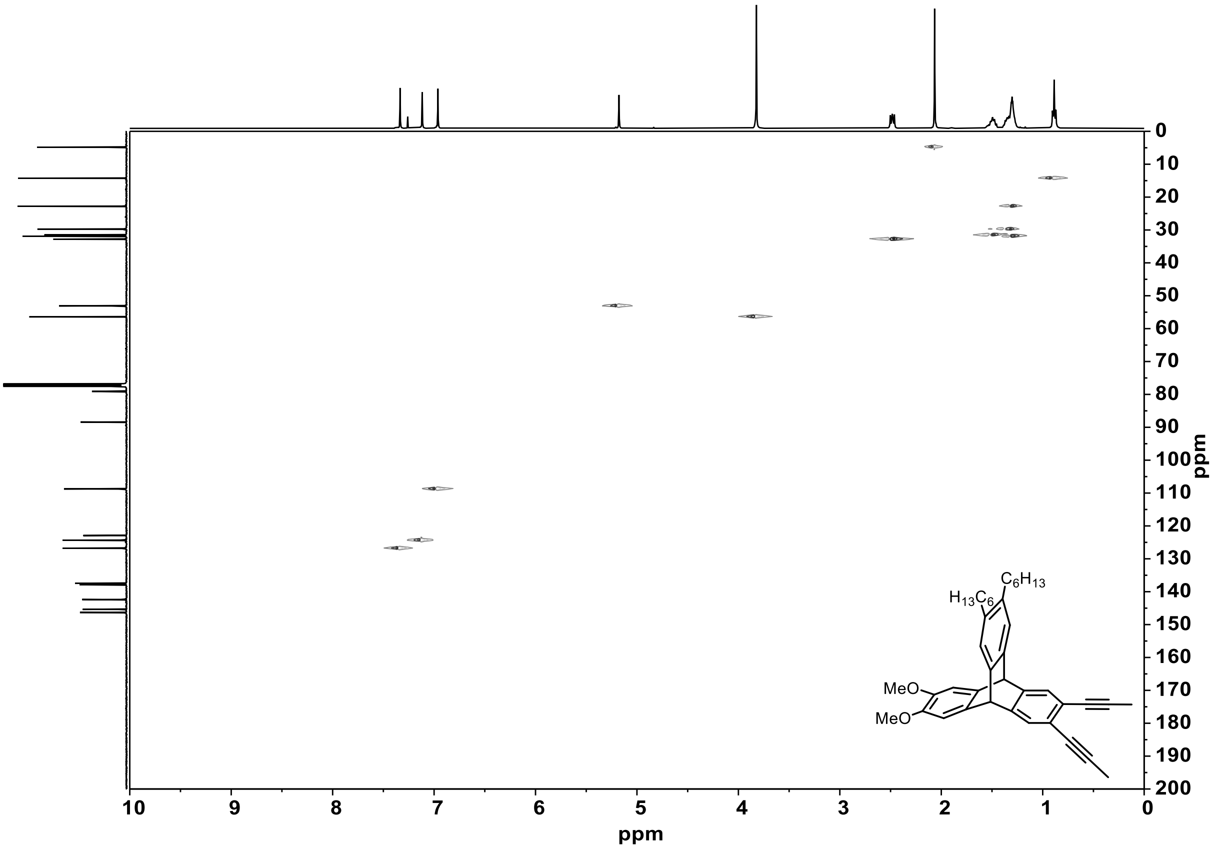

Figure 7.88: ^{1}H-^{13}C HSQC spectrum of **101** (400 MHz, 100 MHz, CDCl$_3$).

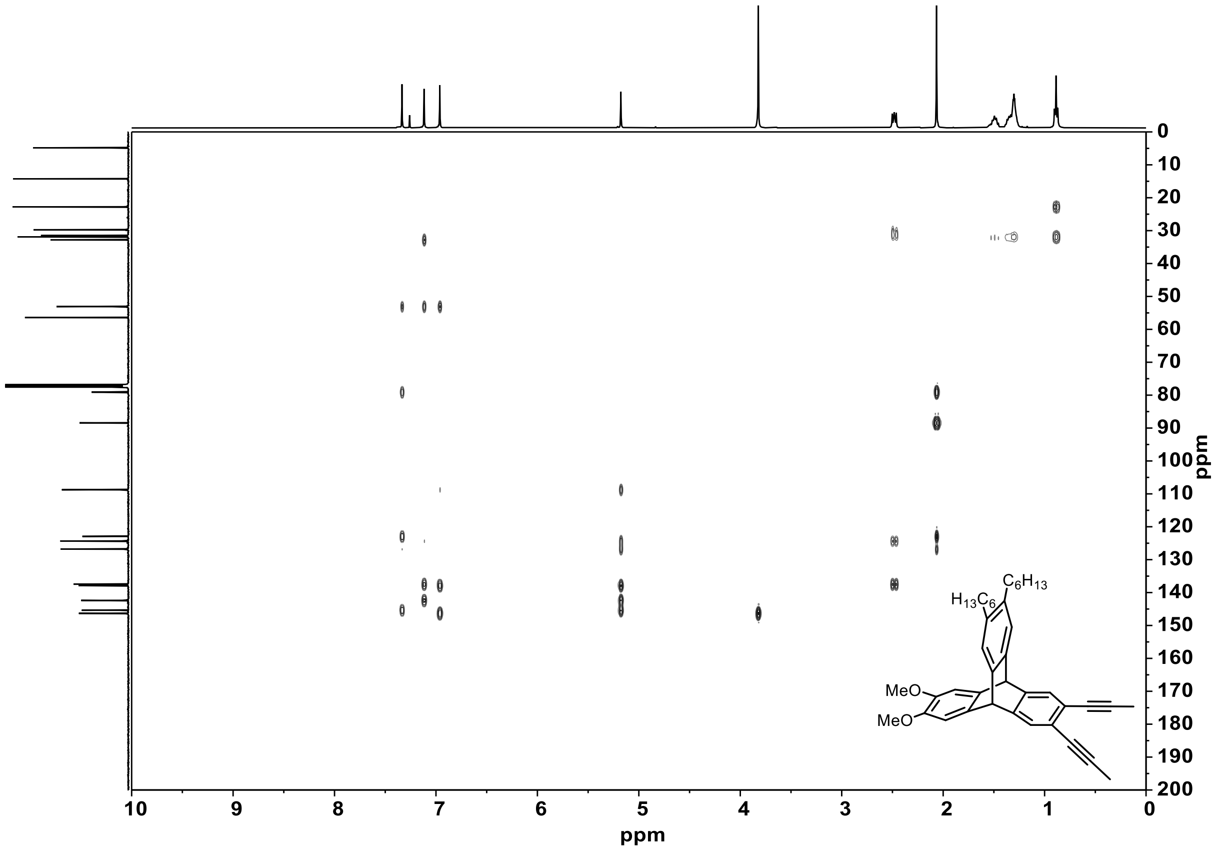

Figure 7.89: ^{1}H-^{13}C HMBC spectrum of **101** (400 MHz, 100 MHz, CDCl$_3$).

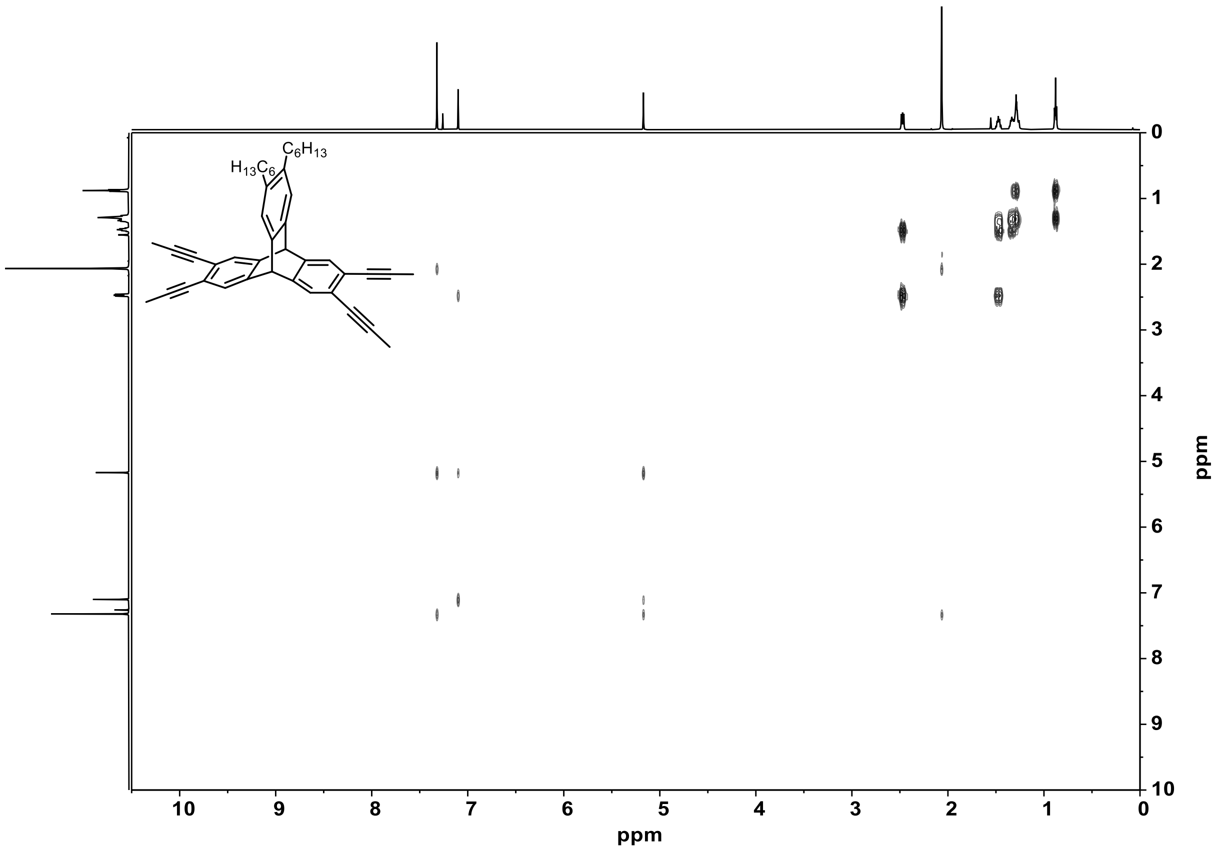

Figure 7.90: ^{1}H-^{1}H COSY spectrum of **75** (600 MHz, CDCl$_3$).

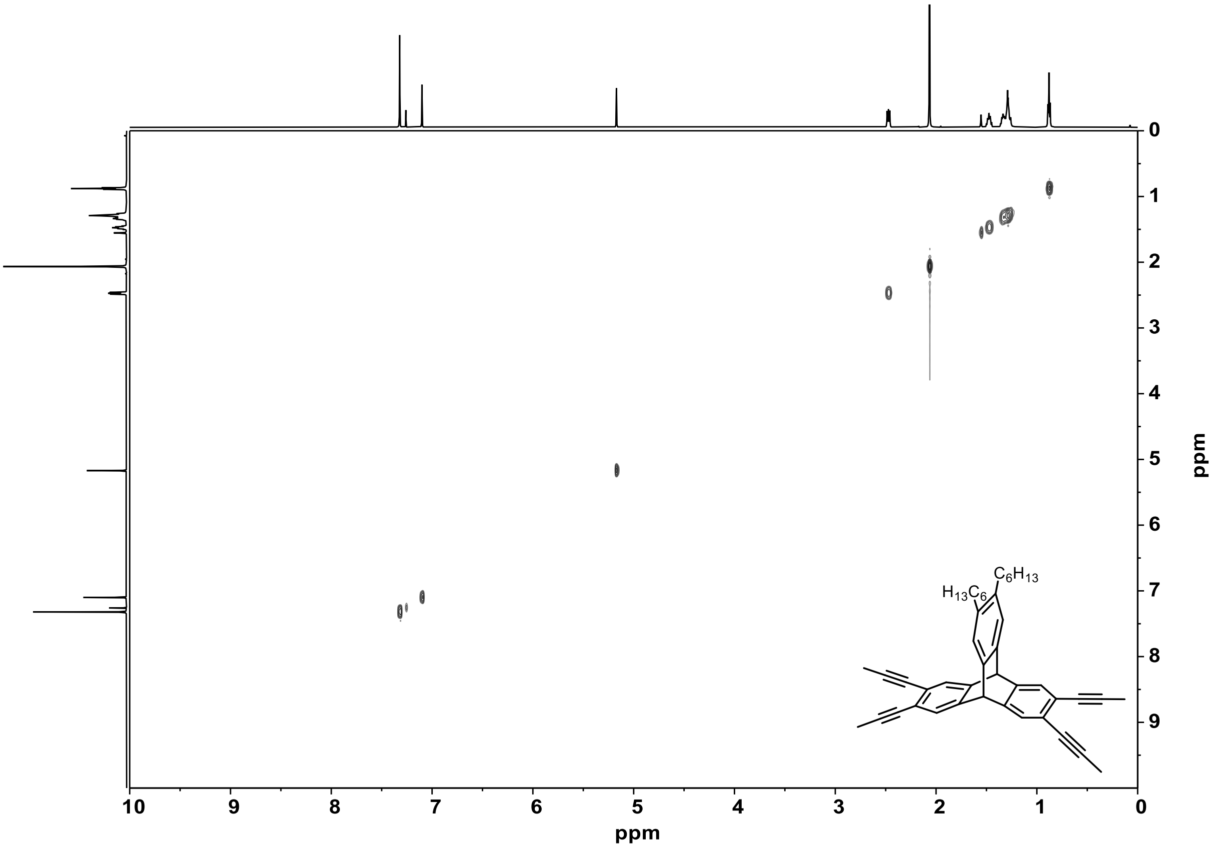

Figure 7.91: ^{1}H-^{1}H NOESY spectrum of **75** (600 MHz, CDCl$_3$).

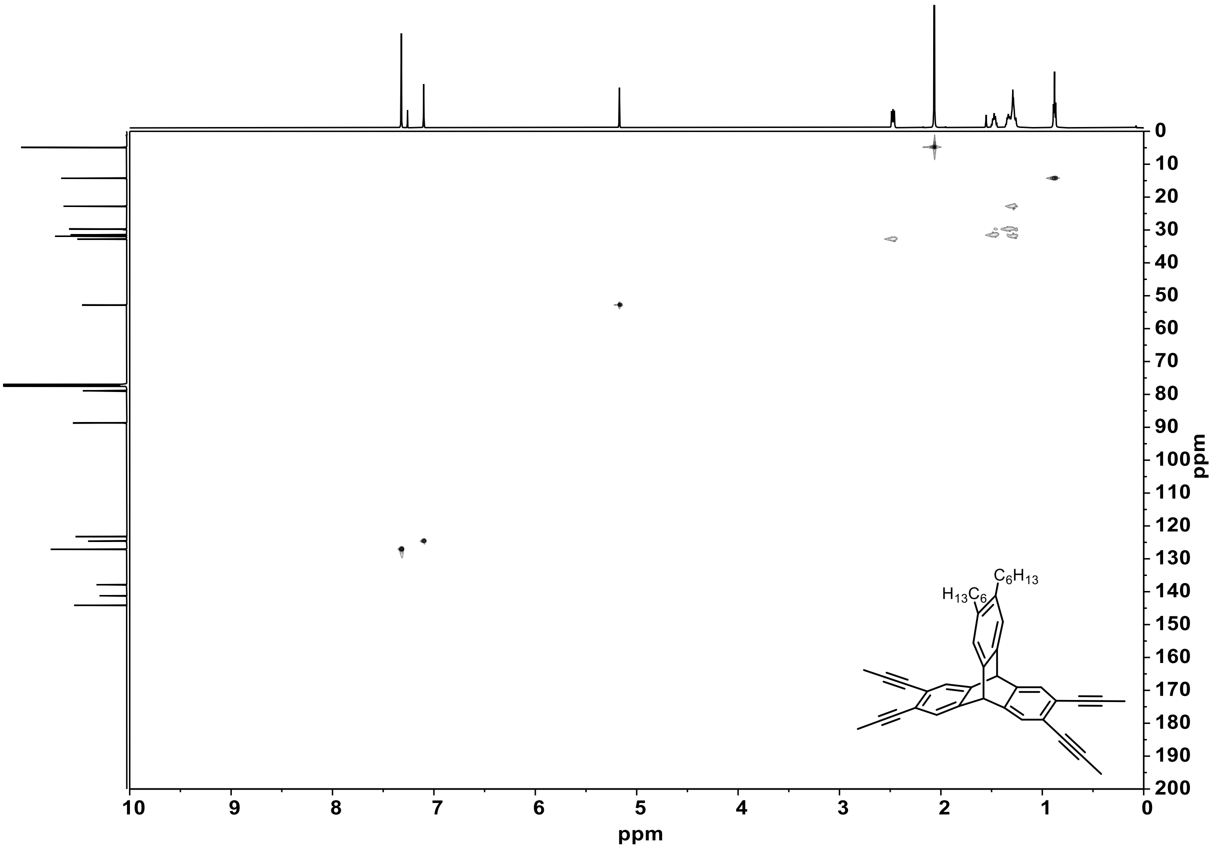

Figure 7.92: ^{1}H-^{13}C HSQC spectrum of **75** (600 MHz, 150 MHz, CDCl$_3$).

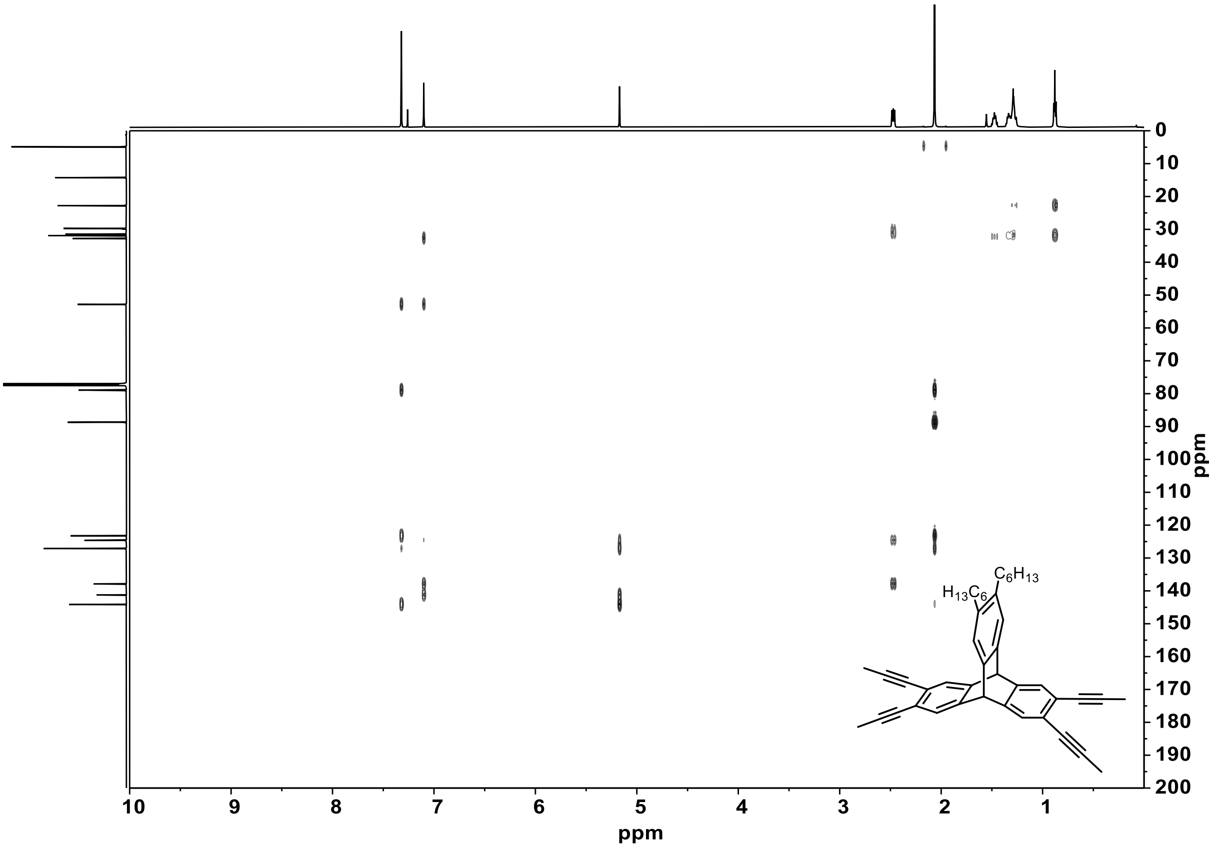

Figure 7.93: ^{1}H-^{13}C HMBC spectrum of **75** (600 MHz, 150 MHz, CDCl$_3$).

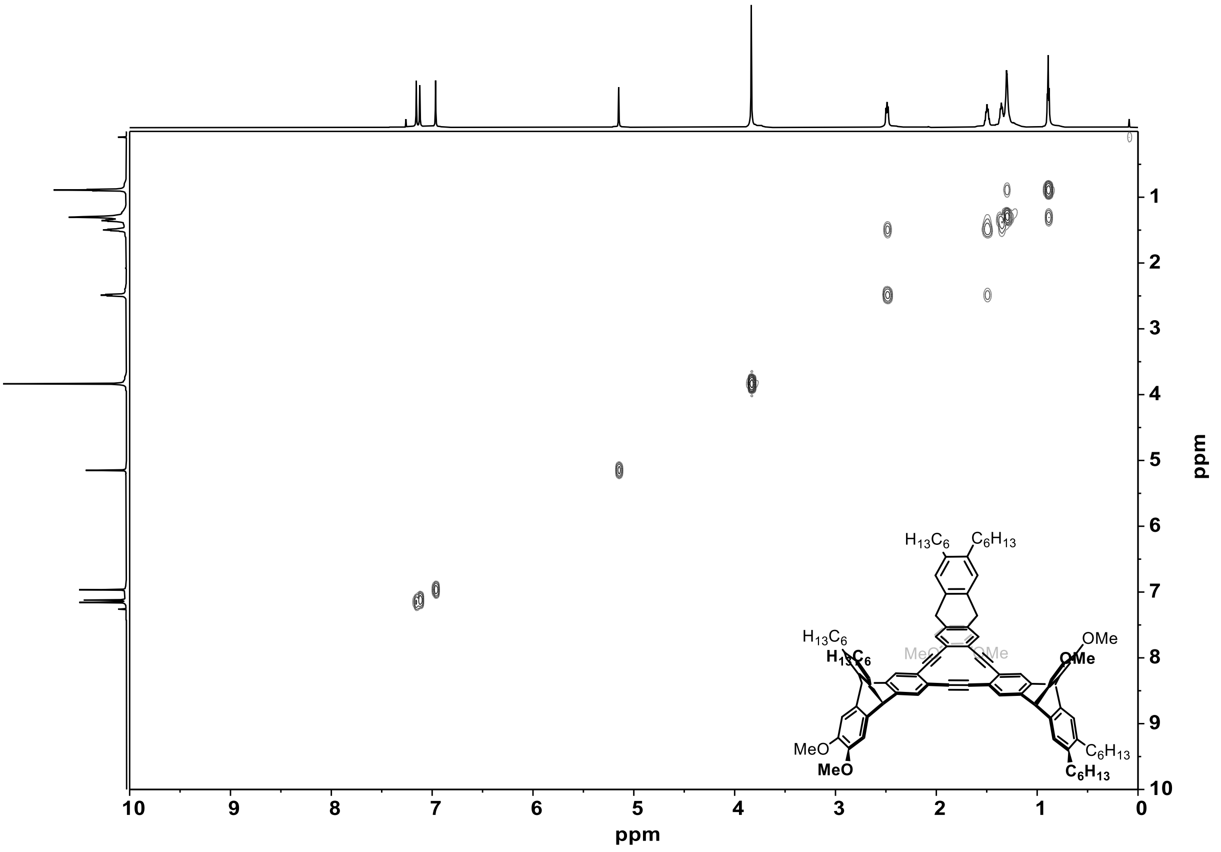

Figure 7.94: ^{1}H-^{1}H COSY spectrum of **103a** (700 MHz, CDCl$_3$).

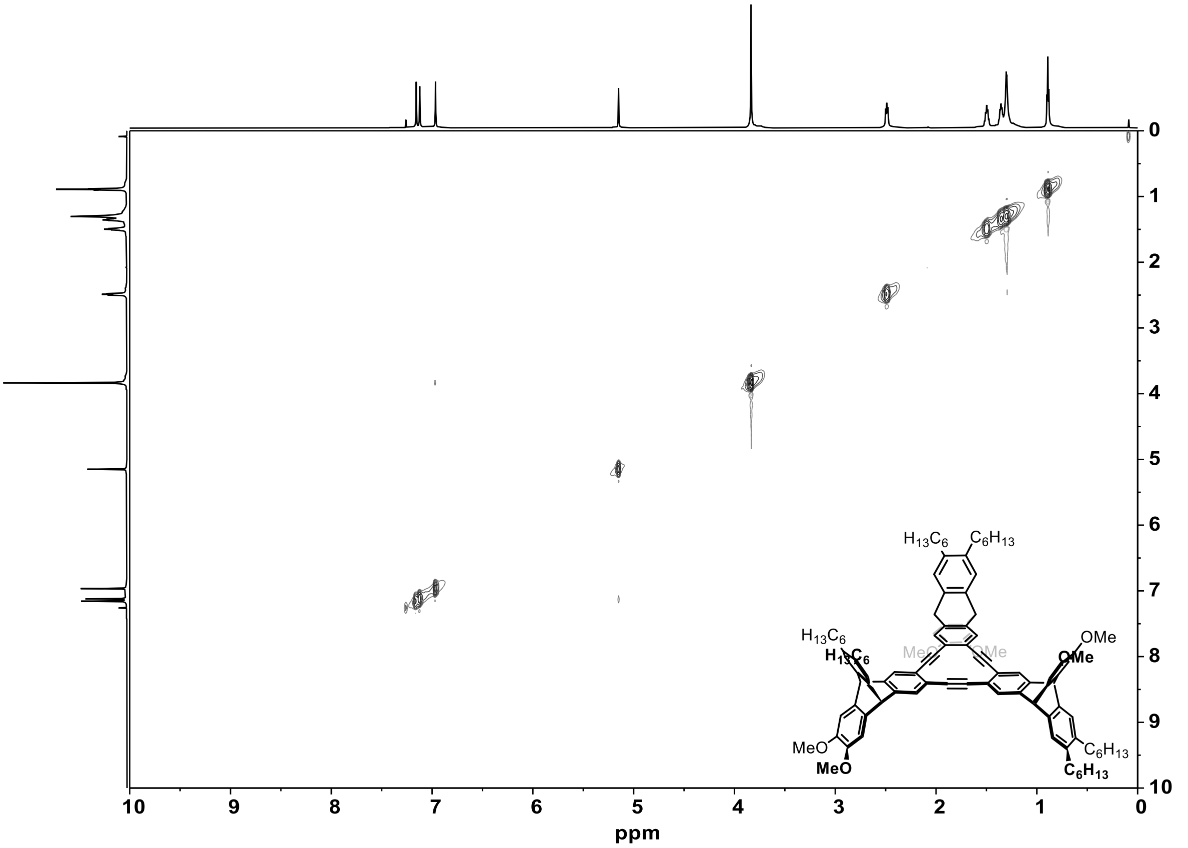

Figure 7.95: ^{1}H-^{1}H NOESY spectrum of **103a** (700 MHz, $CDCl_3$).

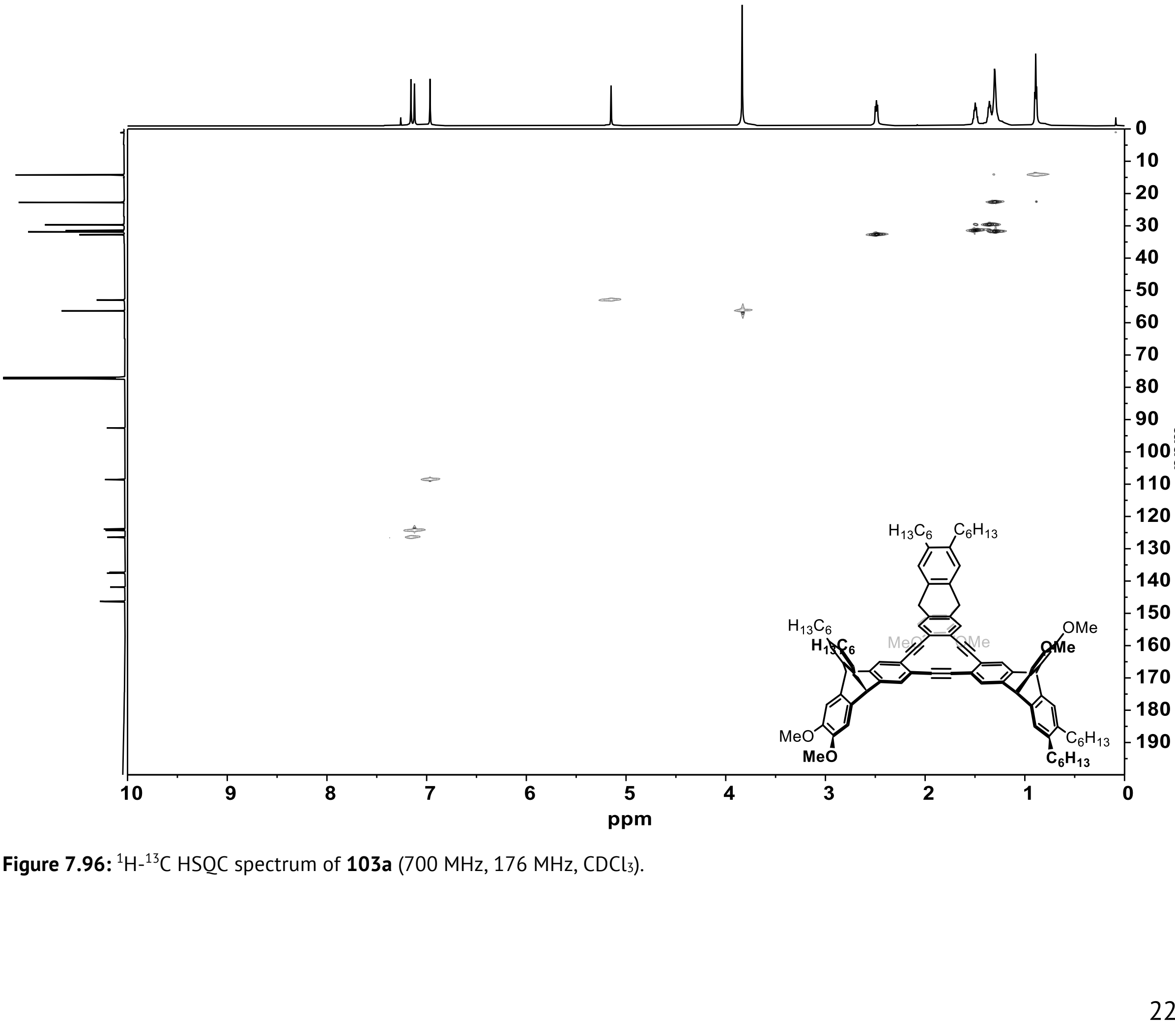

Figure 7.96: ^{1}H-^{13}C HSQC spectrum of **103a** (700 MHz, 176 MHz, $CDCl_3$).

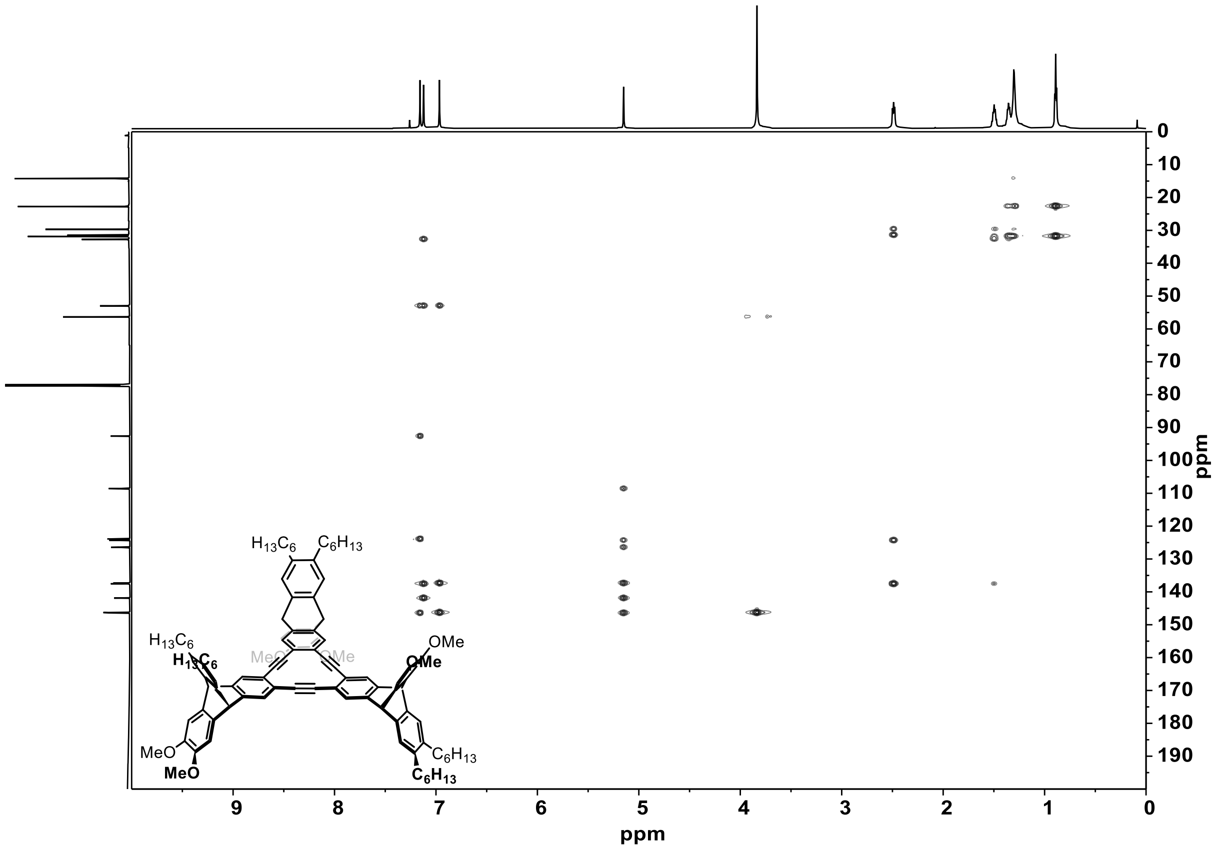

Figure 7.97: ^{1}H-^{13}C HMBC spectrum of **103a** (700 MHz, 176 MHz, CDCl$_3$).

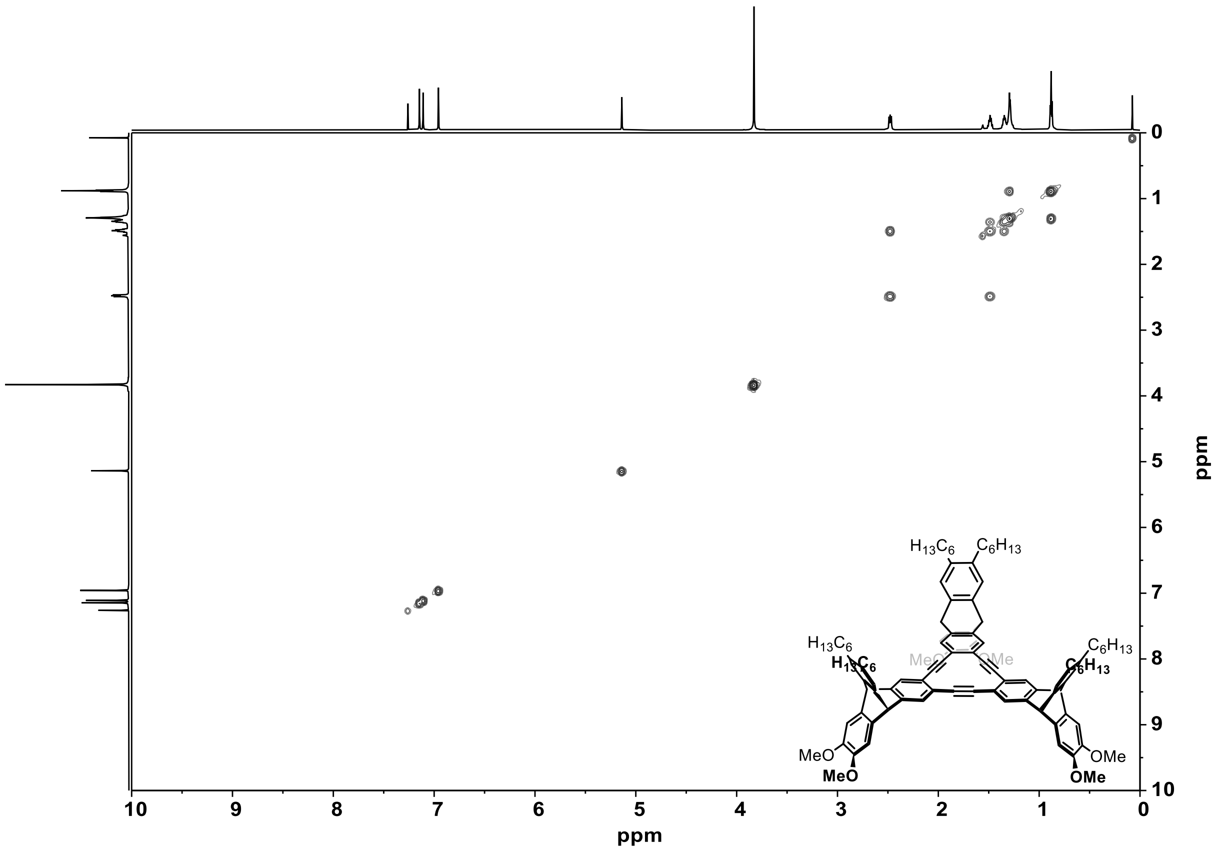

Figure 7.98 ^{1}H-^{1}H COSY spectrum of **103b** (700 MHz, CDCl$_3$).

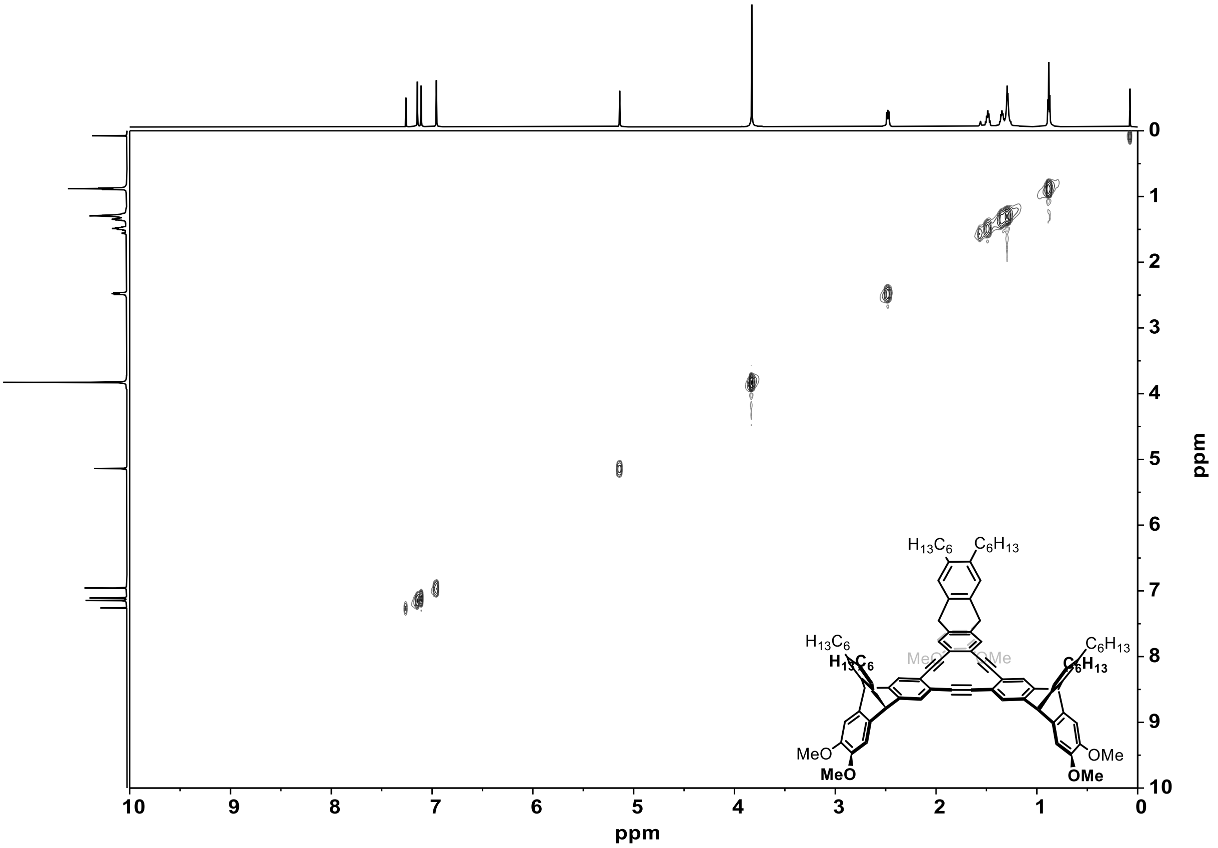

Figure 7.99: ^{1}H-^{1}H NOESY spectrum of **103b** (700 MHz, CDCl$_3$).

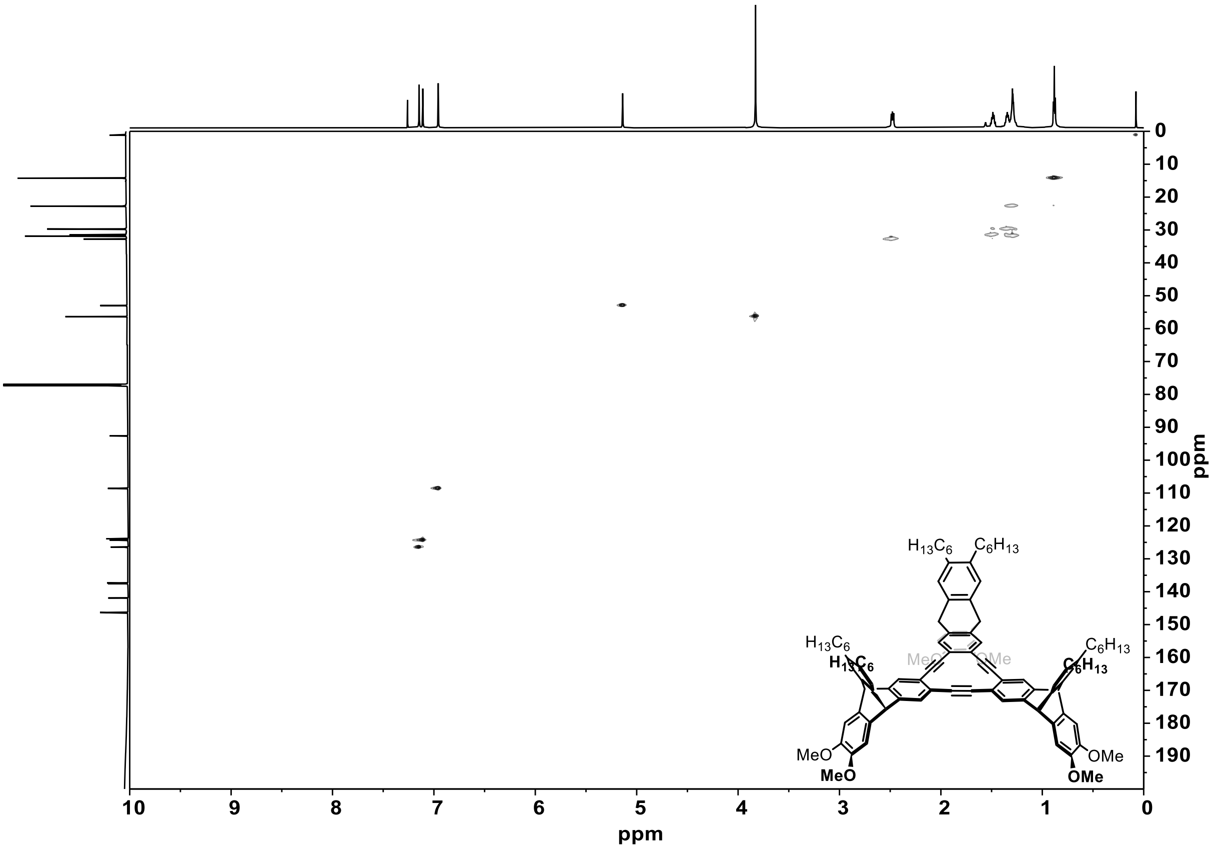

Figure 7.100: ^{1}H-^{13}C HSQC spectrum of **103b** (700 MHz, 176 MHz, CDCl$_3$).

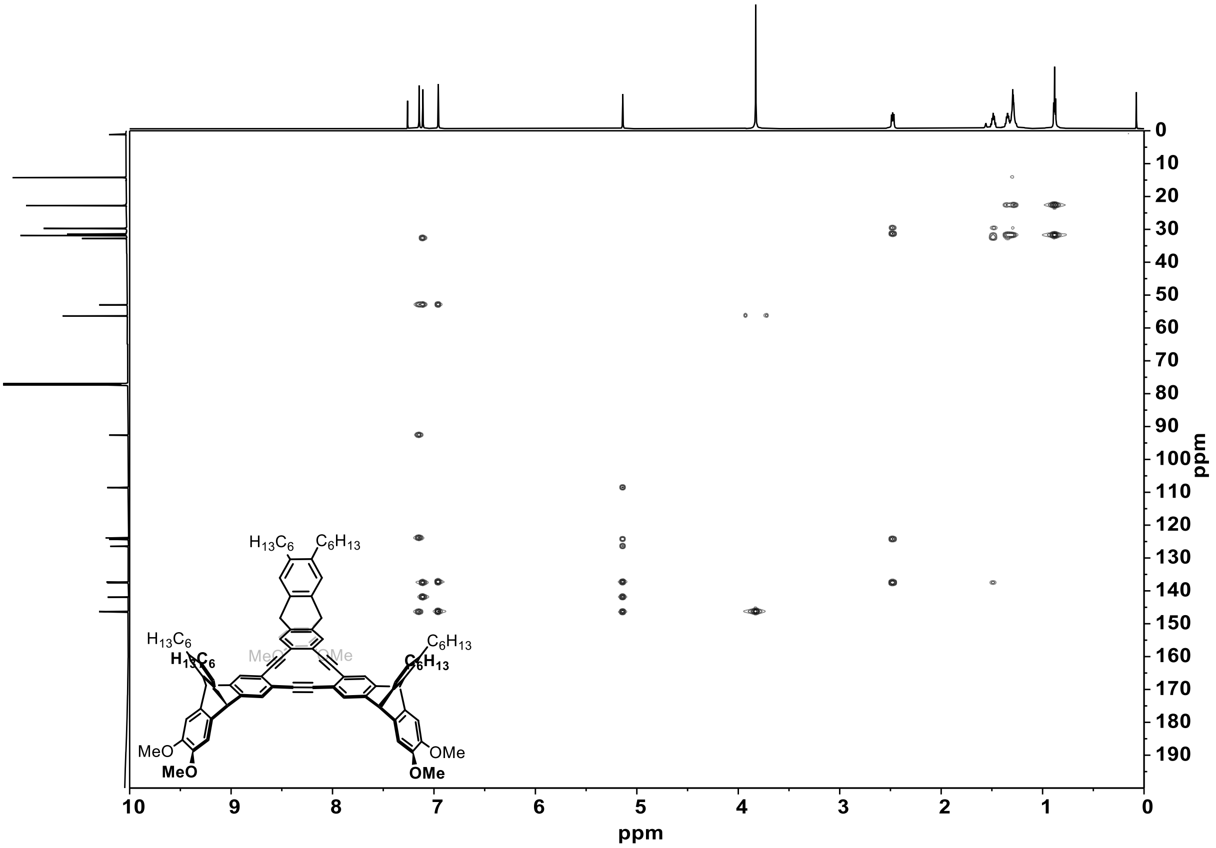

Figure 7.101: ^{1}H-^{13}C HMBC spectrum of **103b** (700 MHz, 176 MHz, CDCl$_3$).

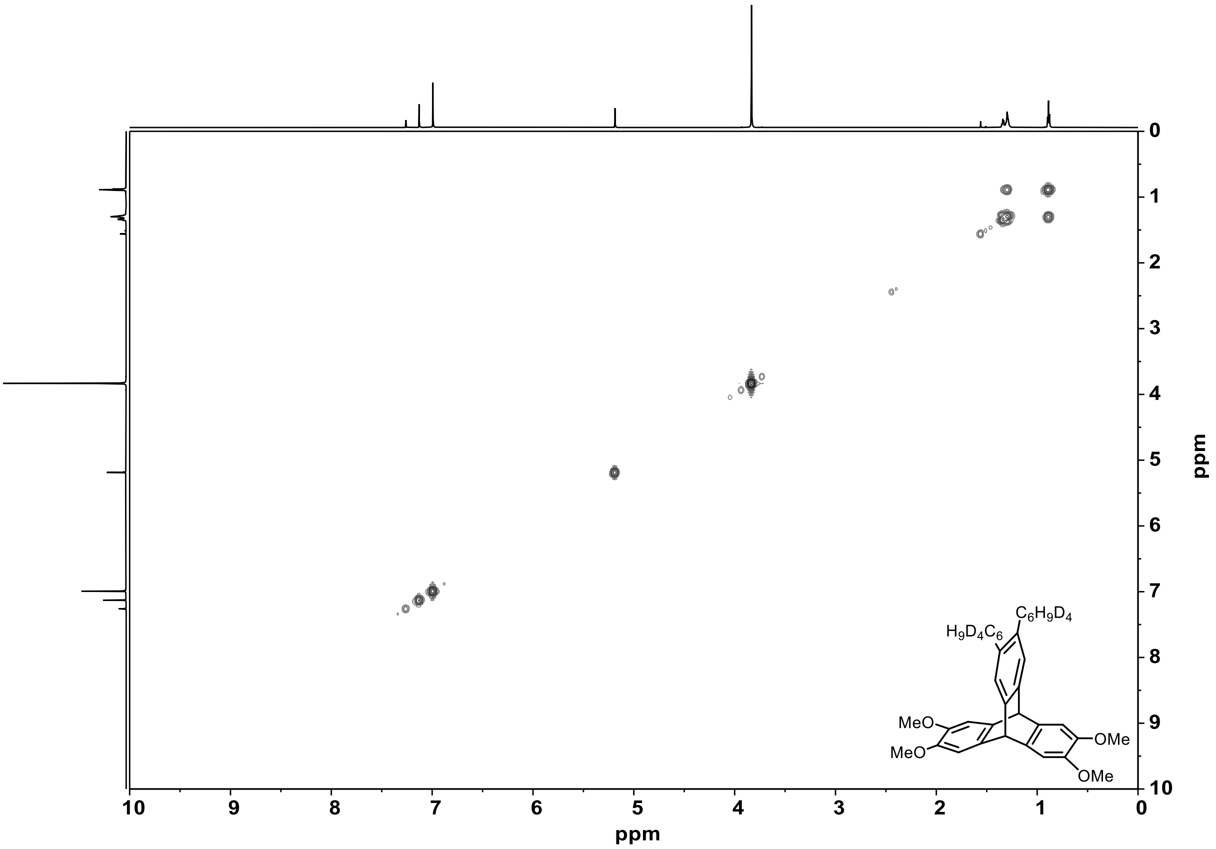

Figure 7.102: ^{1}H-^{1}H COSY spectrum of **99-*d*$_8$** (700 MHz, CDCl$_3$).

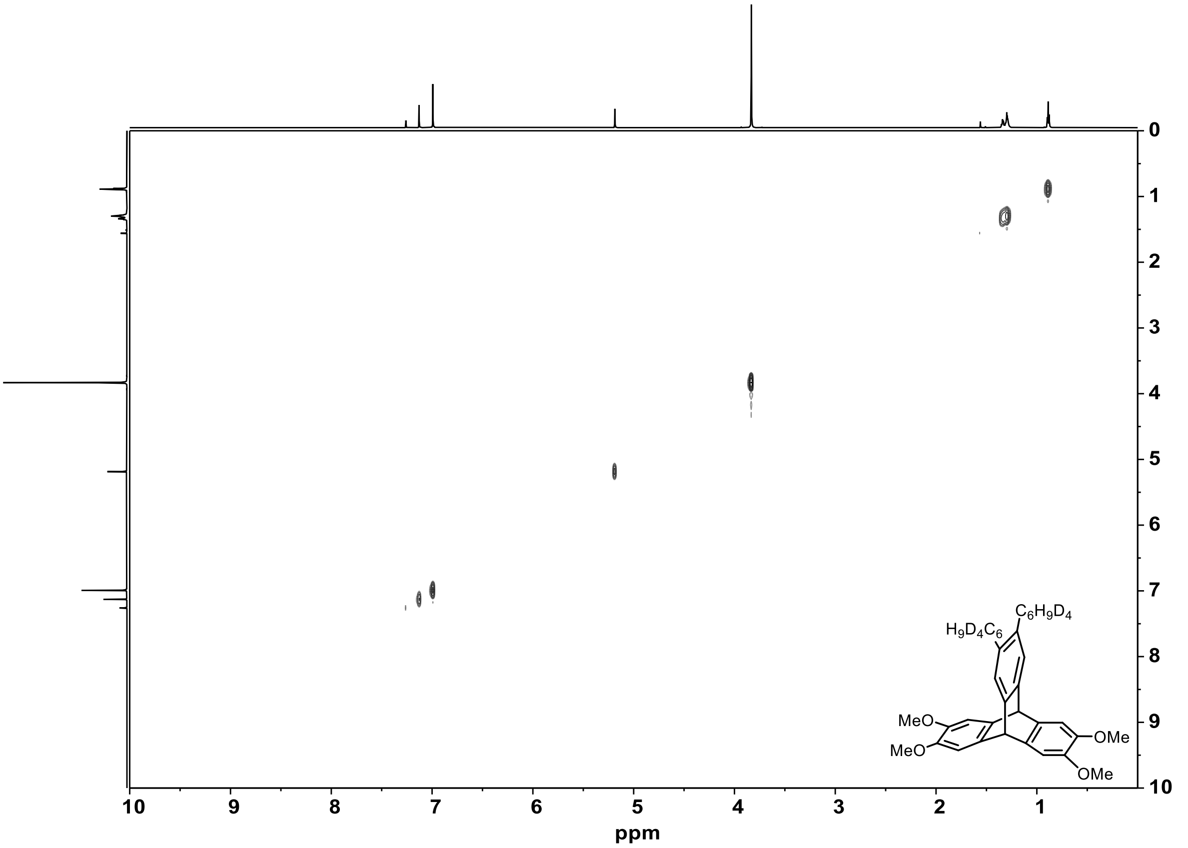

Figure 7.103: ^{1}H-^{1}H NOESY spectrum of **99-*d*$_8$** (700 MHz, CDCl$_3$).

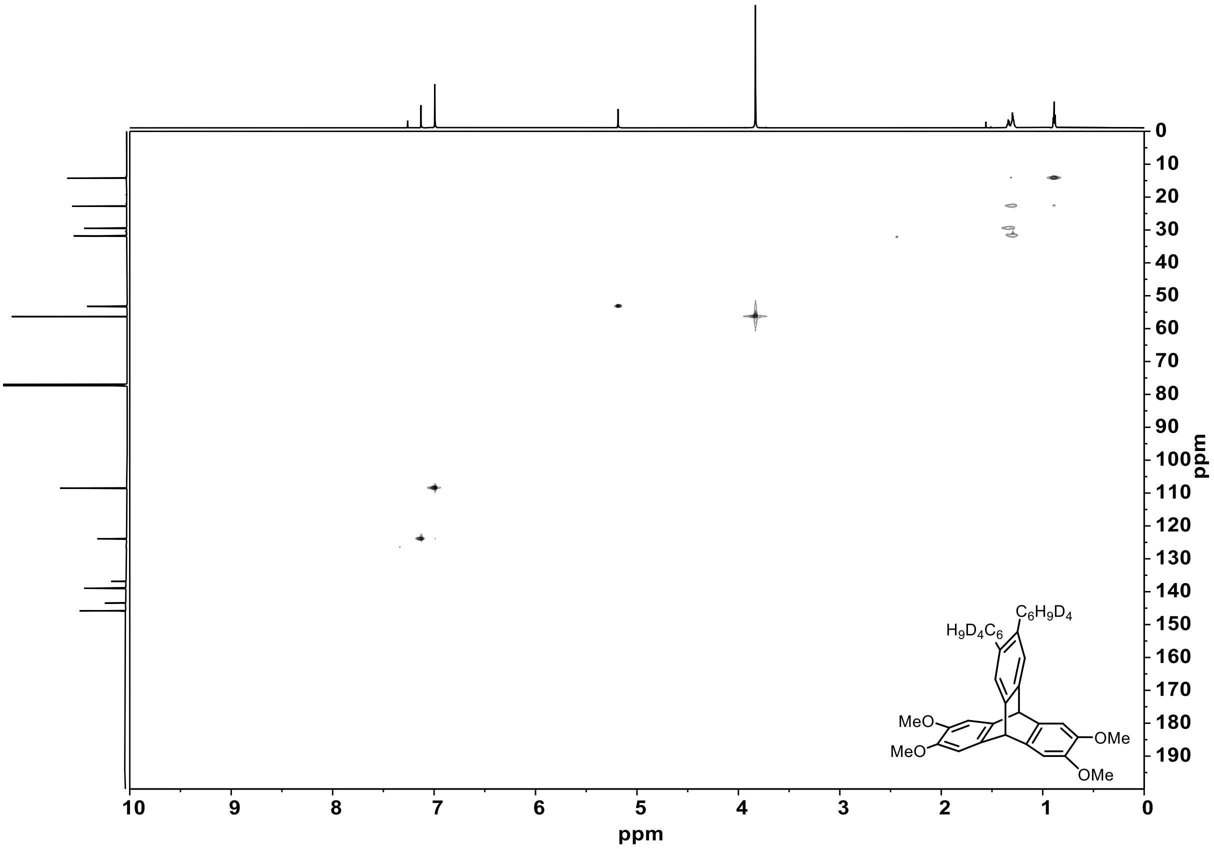

Figure 7.104: ^{1}H-^{13}C HSQC spectrum of **99-*d*$_8$** (700 MHz, 176 MHz, CDCl$_3$).

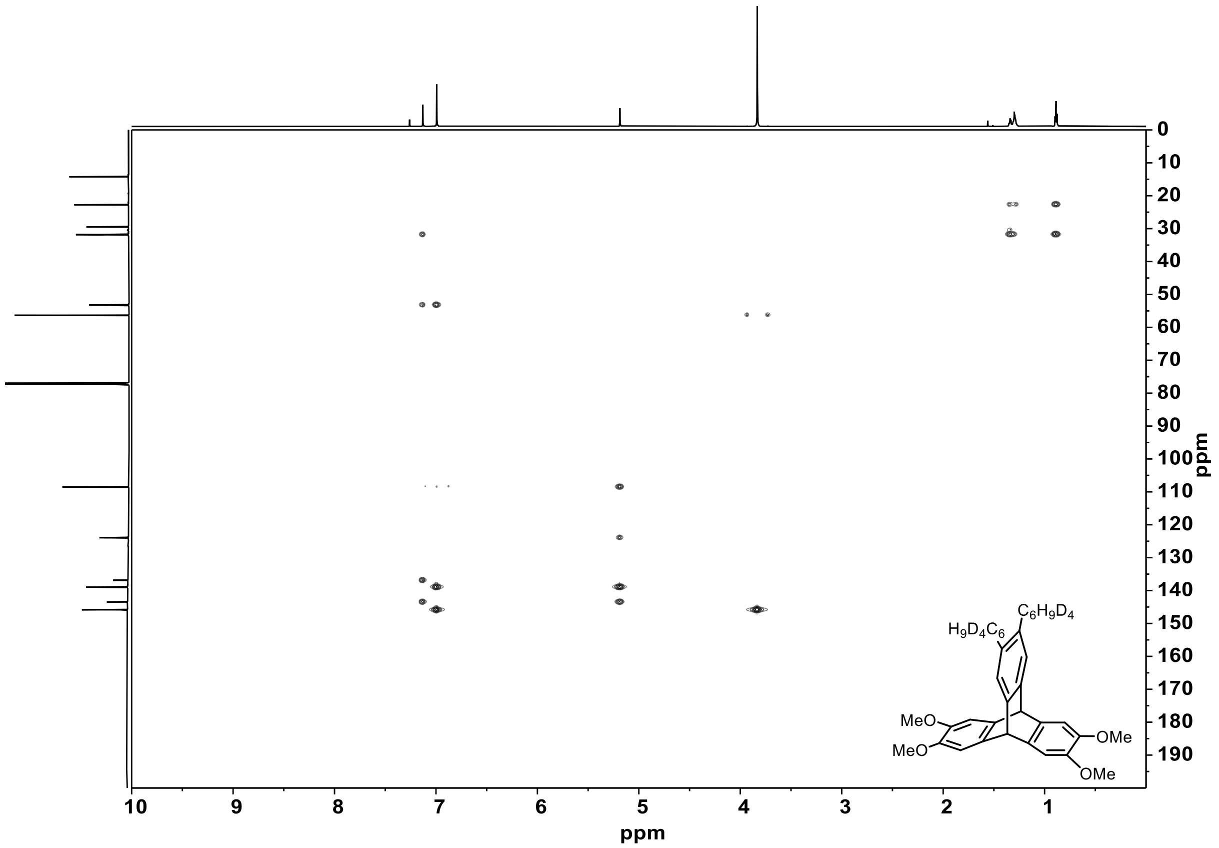

Figure 7.105: ^{1}H-^{13}C HMBC spectrum of **99-*d*$_8$** (700 MHz, 176 MHz, CDCl$_3$).

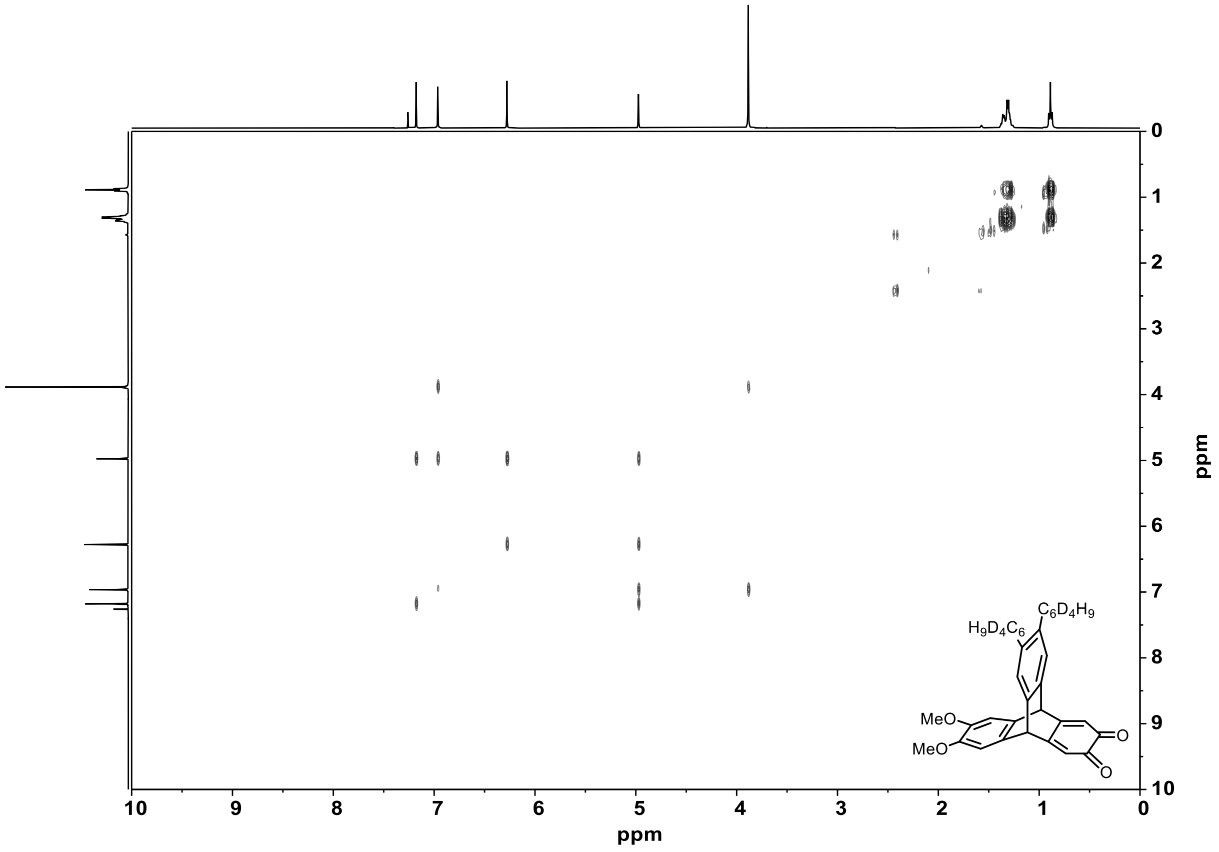

Figure 7.106: ^{1}H-^{1}H COSY spectrum of **100-*d*$_8$** (400 MHz, CDCl$_3$).

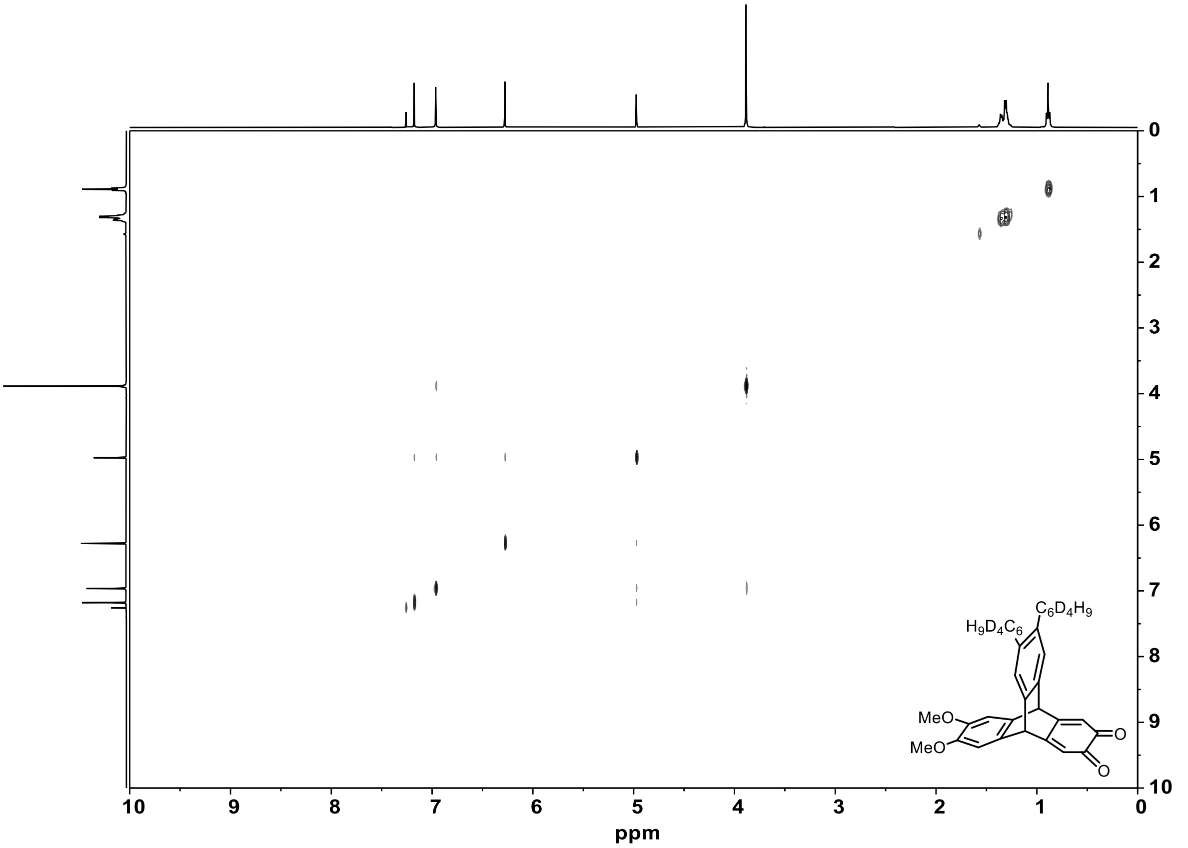

Figure 7.107: ^{1}H-^{1}H NOESY spectrum of **100-*d*$_8$** (400 MHz, CDCl$_3$).

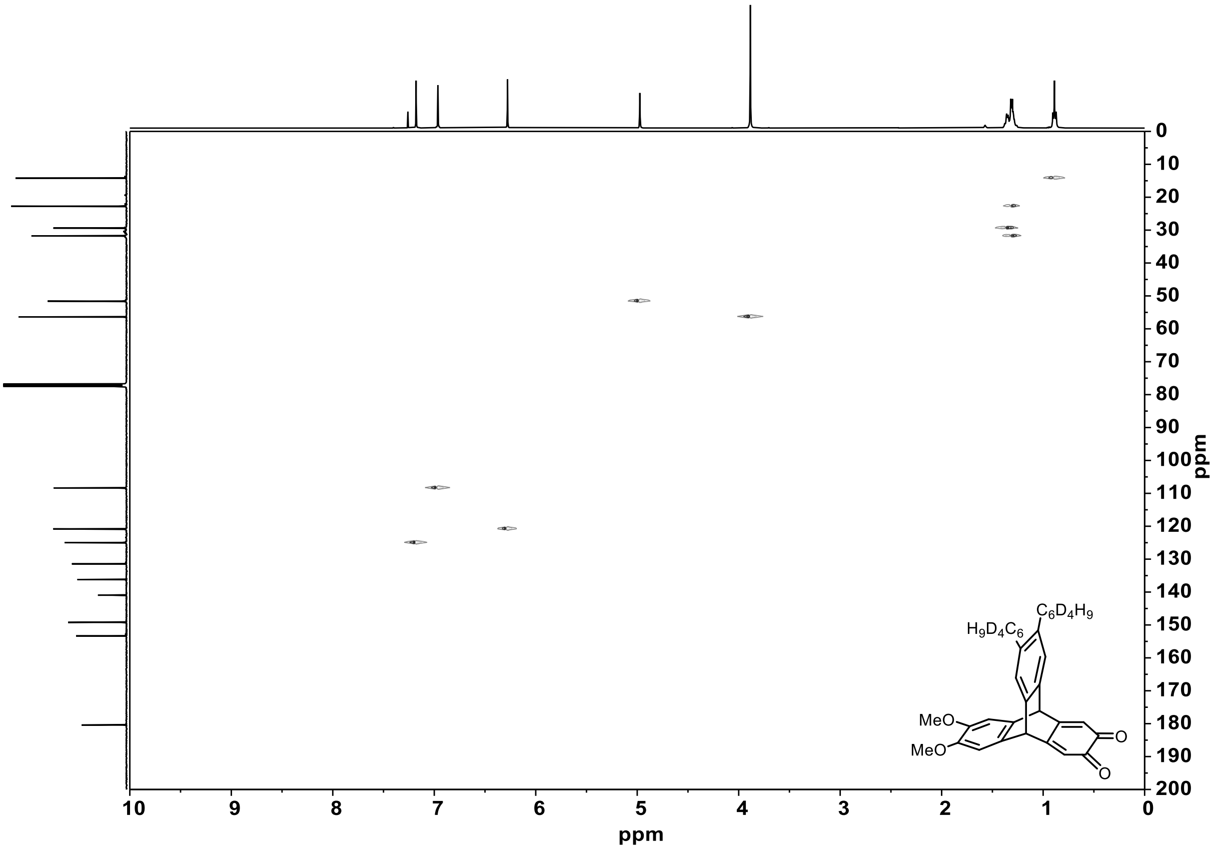

Figure 7.108: ^{1}H-^{13}C HSQC spectrum of **100-*d*$_8$** (400 MHz, 100 MHz, CDCl$_3$).

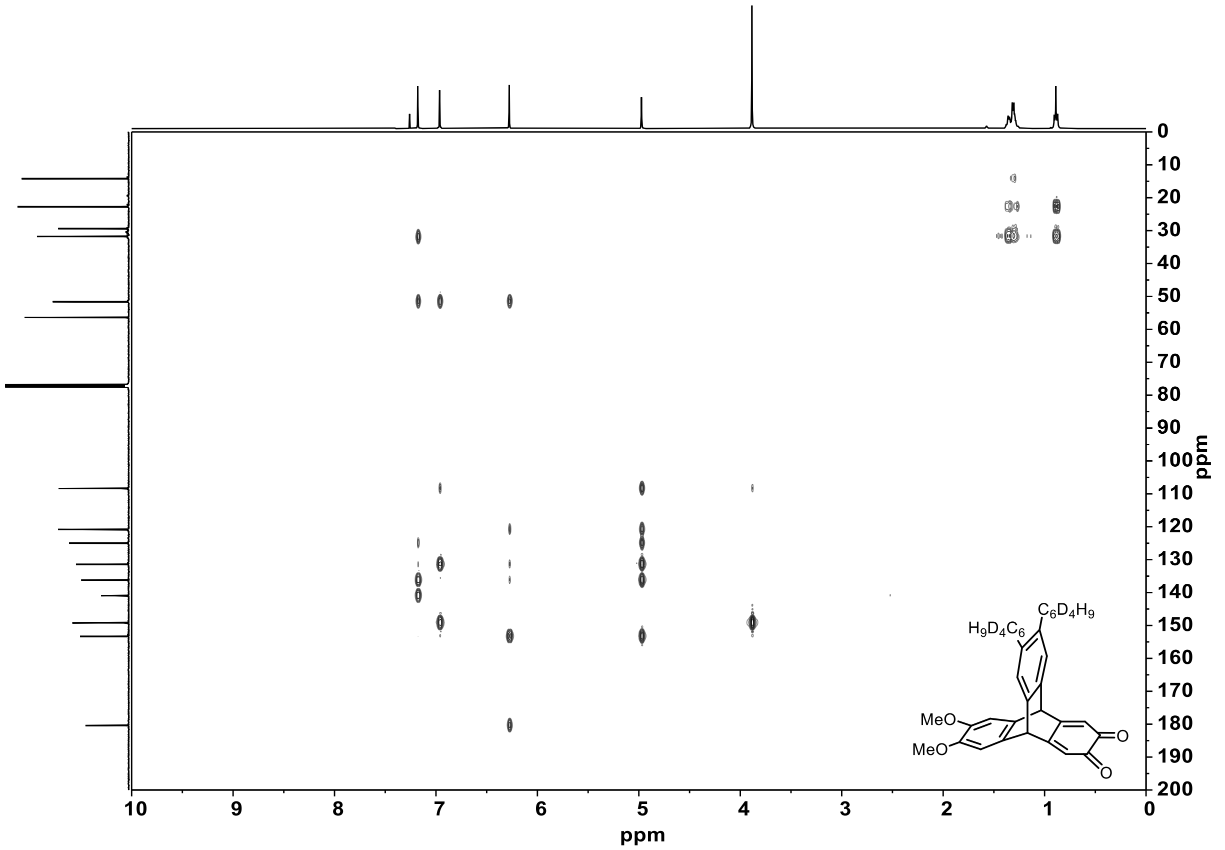

Figure 7.109: ^{1}H-^{13}C HMBC spectrum of **100-*d₈*** (400 MHz, 100 MHz, CDCl₃).

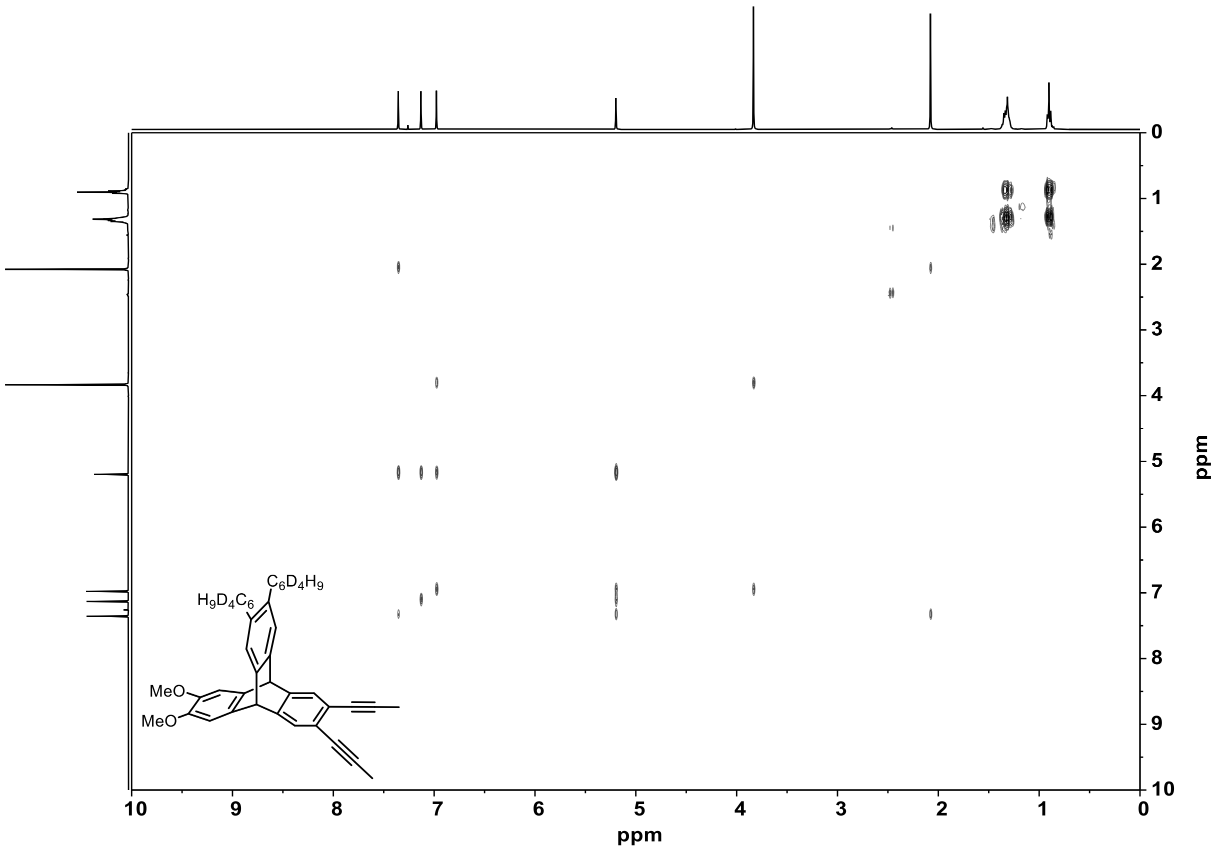

Figure 7.110: ^{1}H-^{1}H COSY spectrum of **101-*d₈*** (400 MHz, CDCl₃).

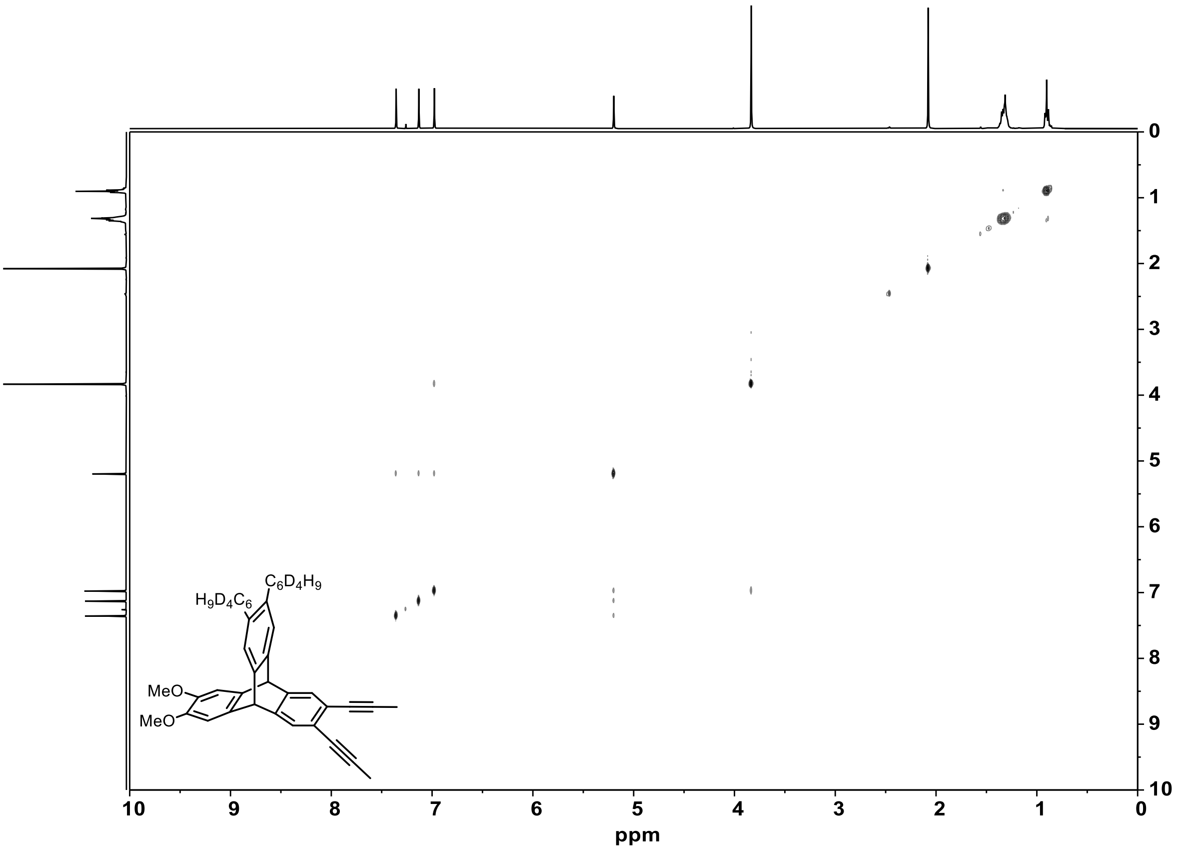

Figure 7.111: ^{1}H-^{1}H NOESY spectrum of **101-d_8** (400 MHz, CDCl$_3$).

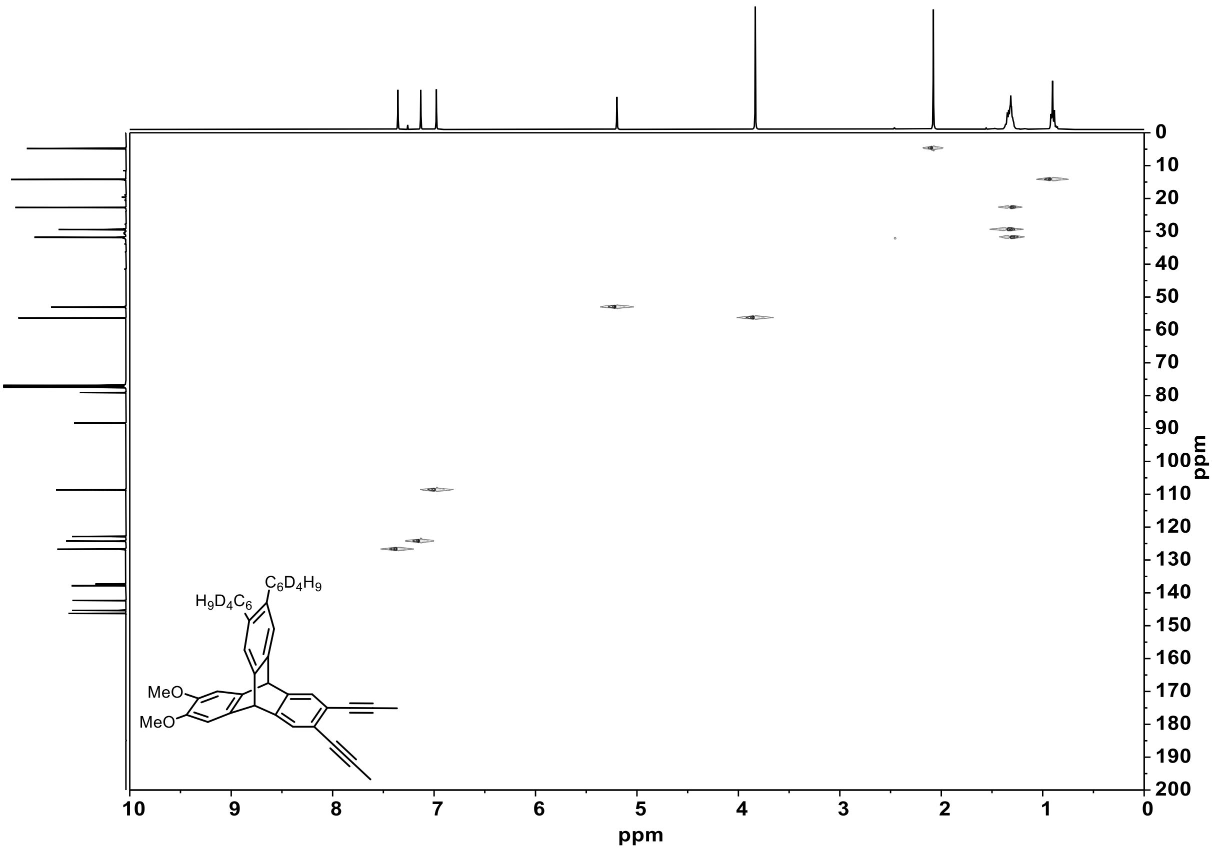

Figure 7.112: ^{1}H-^{13}C HSQC spectrum of **101-d_8** (400 MHz, 100 MHz, CDCl$_3$).

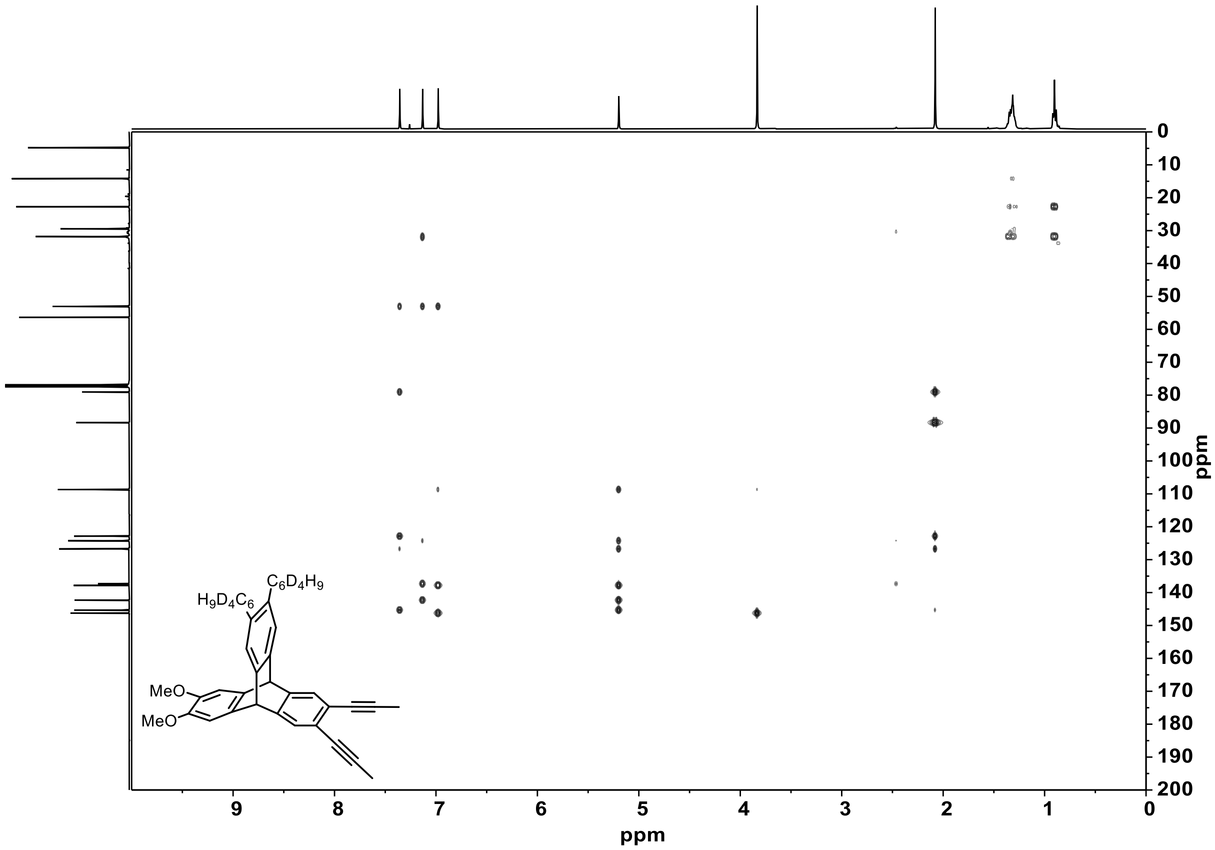

Figure 7.113: ^{1}H-^{13}C HMBC spectrum of **101-*d*$_8$** (400 MHz, 100 MHz, $CDCl_3$).

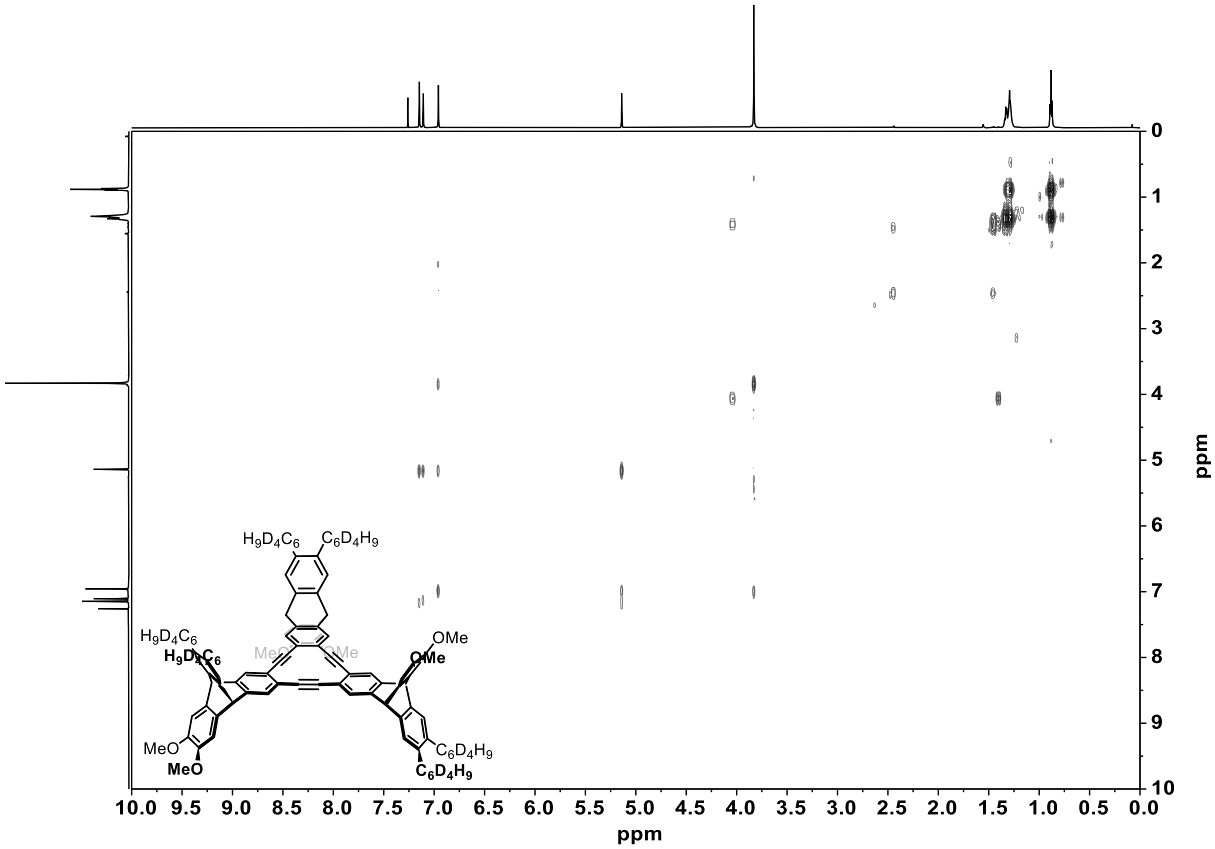

Figure 7.114: ^{1}H-^{1}H COSY spectrum of **103a-*d*$_{24}$** (600 MHz, $CDCl_3$).

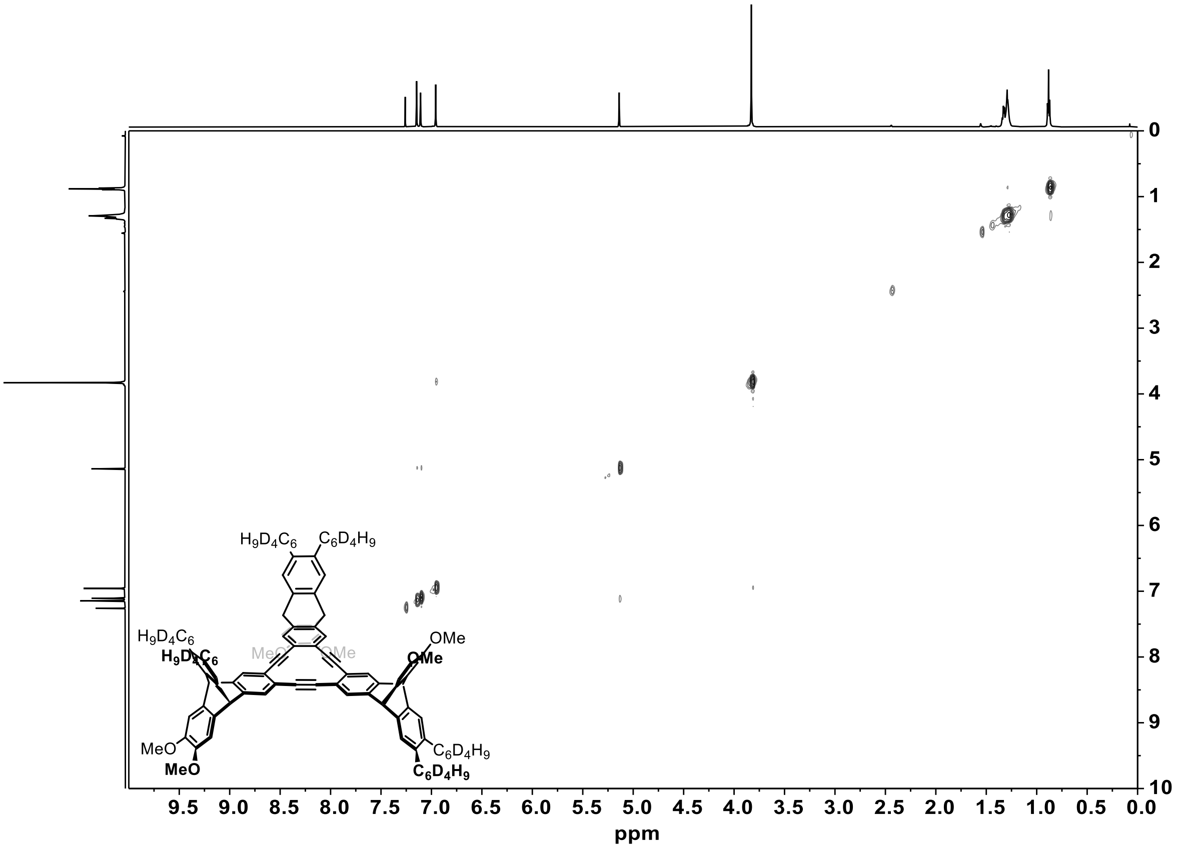

Figure 7.115: ^1H-^1H NOESY spectrum of **103a-*d₂₄*** (600 MHz, $CDCl_3$).

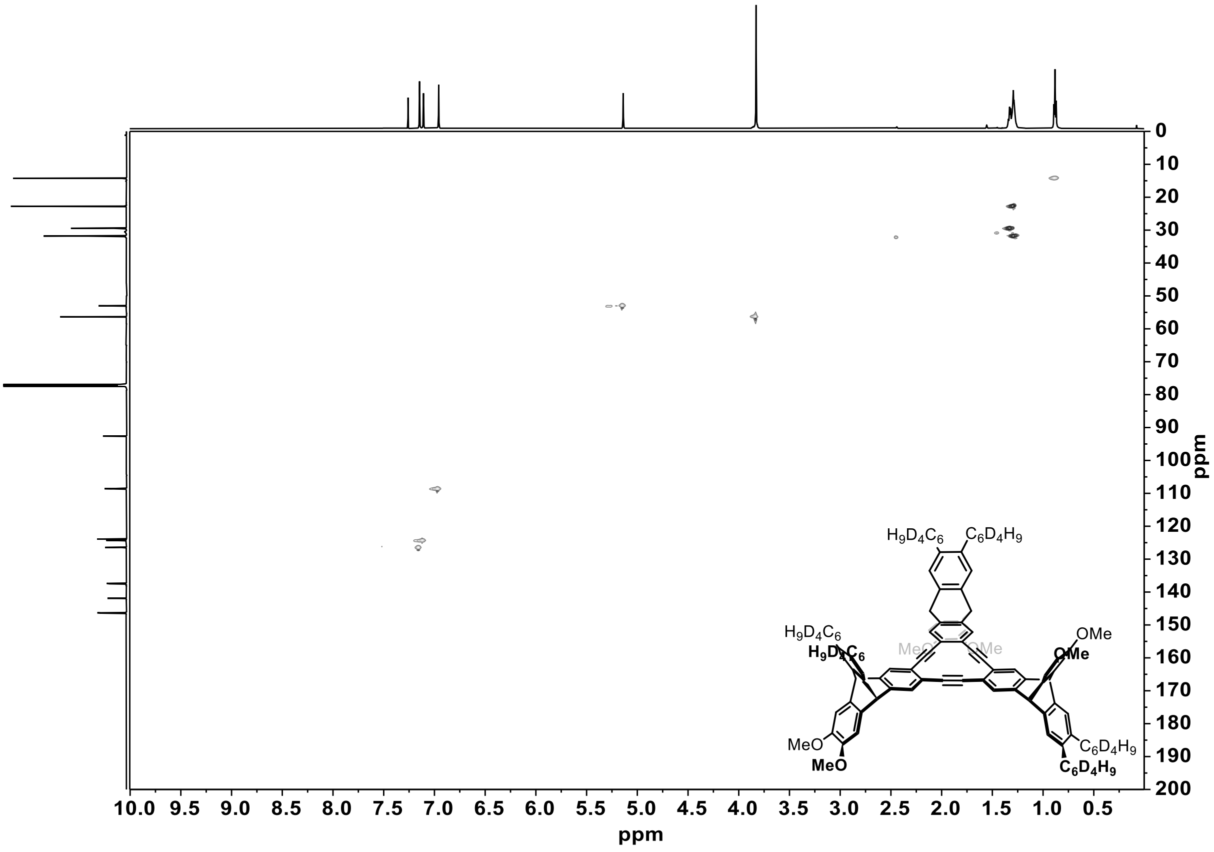

Figure 7.116: ^1H-^{13}C HSQC spectrum of **103a-*d₂₄*** (600 MHz, 150 MHz, $CDCl_3$).

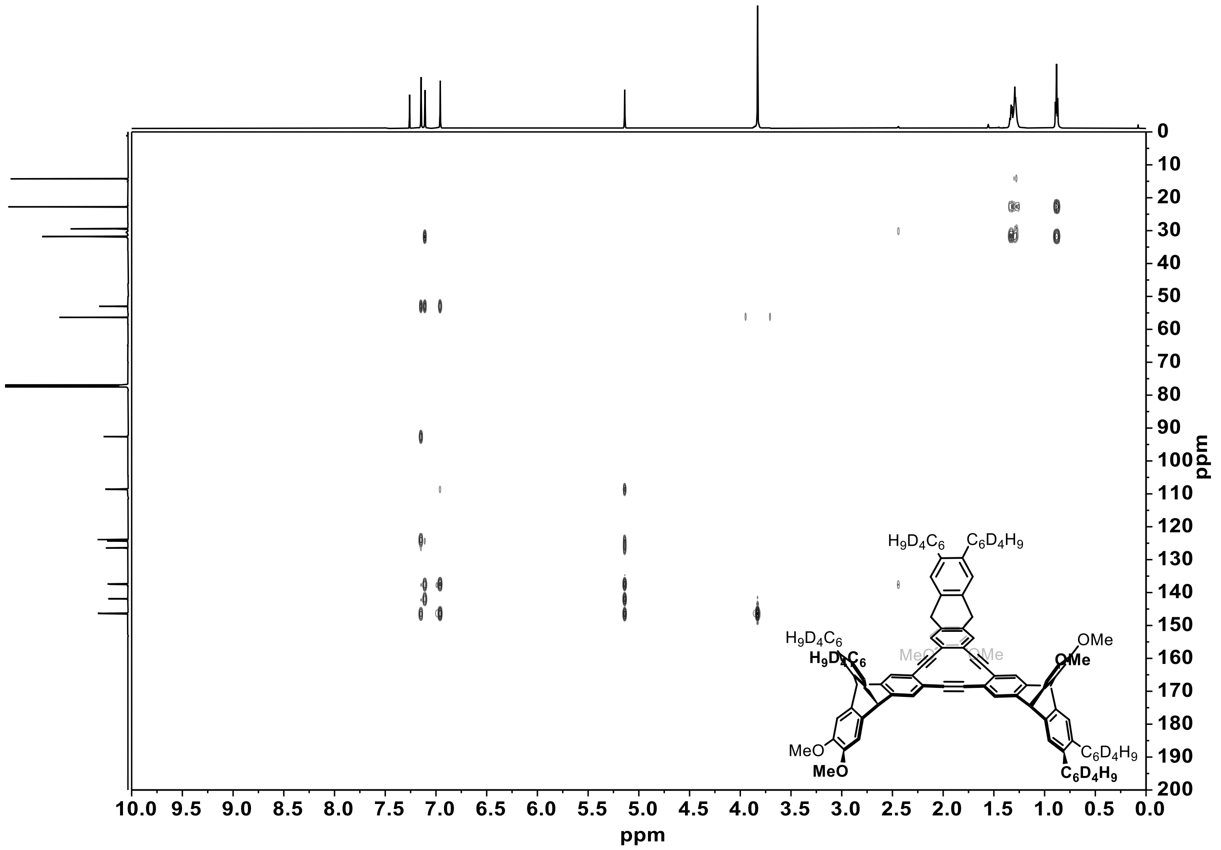

Figure 7.117: ^{1}H-^{13}C HMBC spectrum of **103a-*d24*** (600 MHz, 150 MHz, CDCl$_3$).

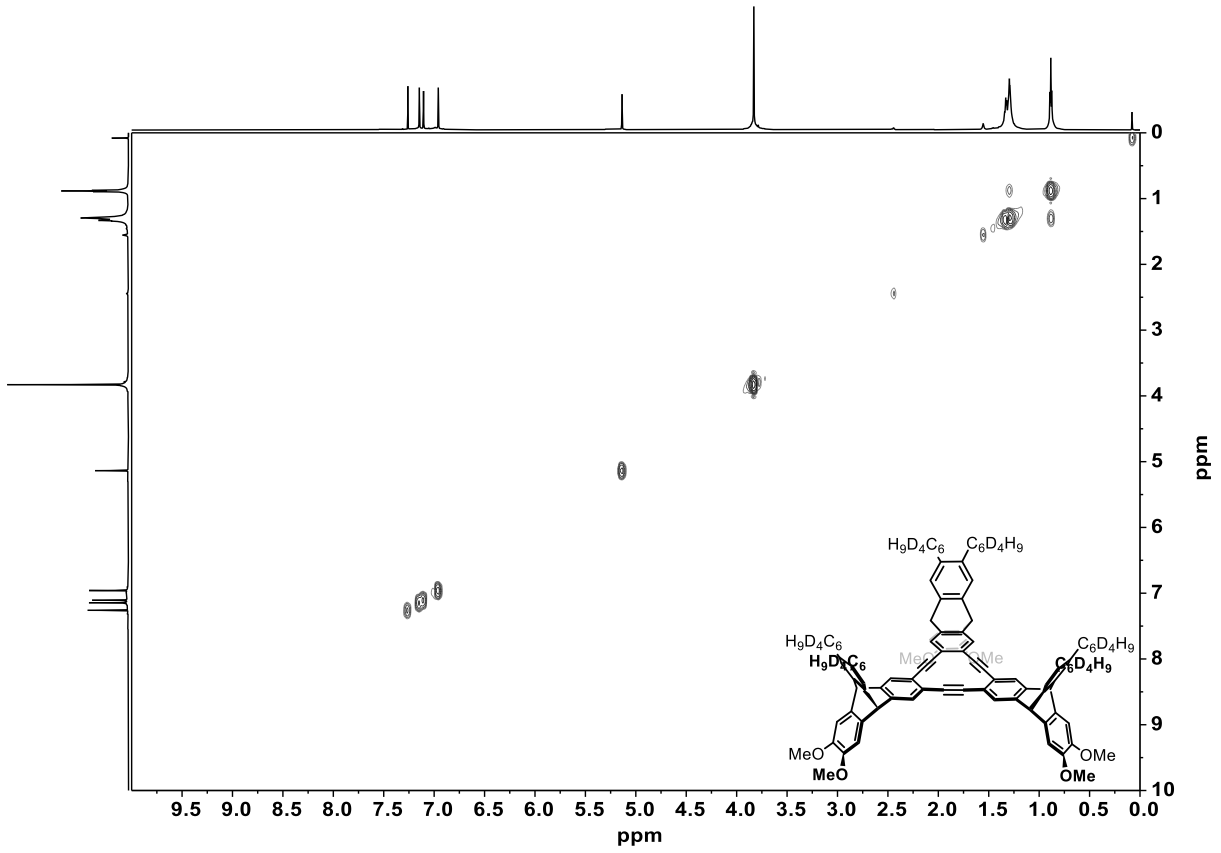

Figure 7.118: ^{1}H-^{1}H COSY spectrum of **103b-*d24*** (700 MHz, CDCl$_3$).

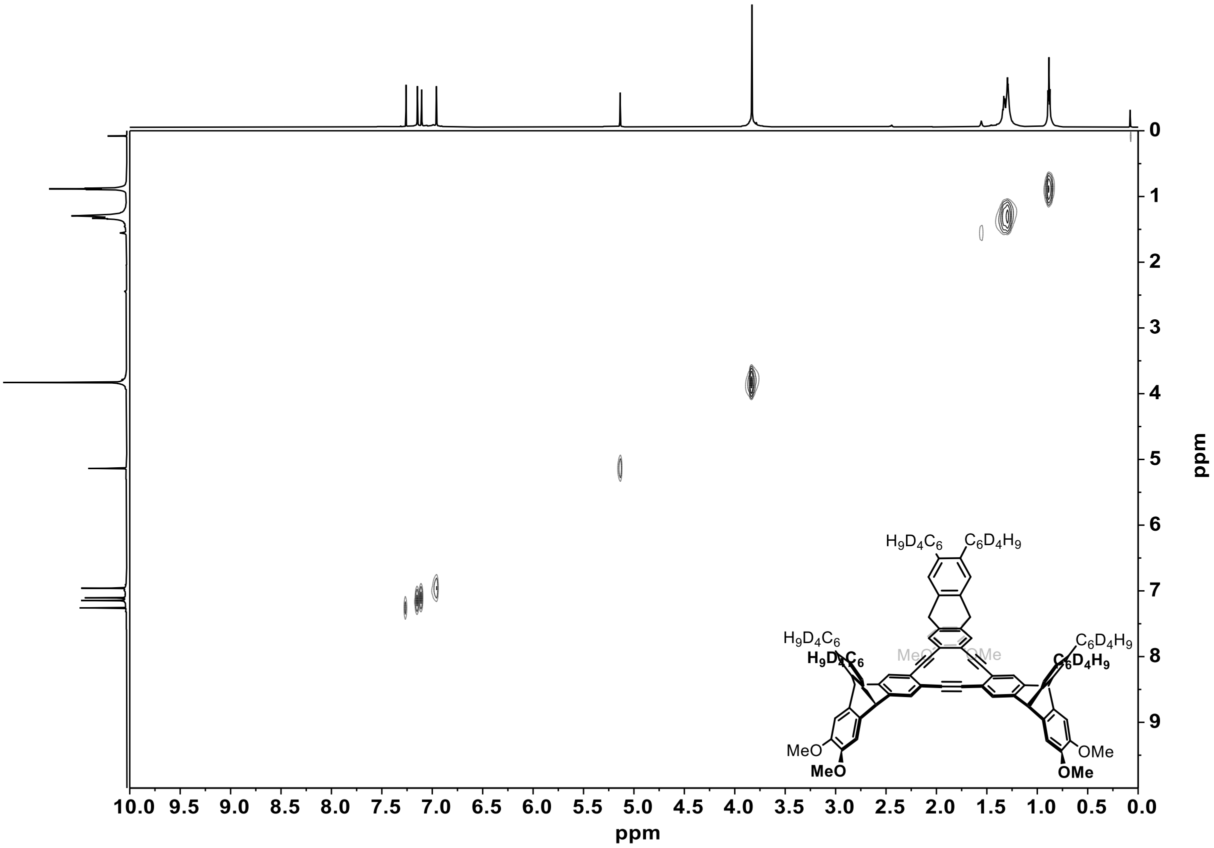

Figure 7.119: ^{1}H-^{1}H NOESY spectrum of **103b-*d*$_{24}$** (700 MHz, $CDCl_3$).

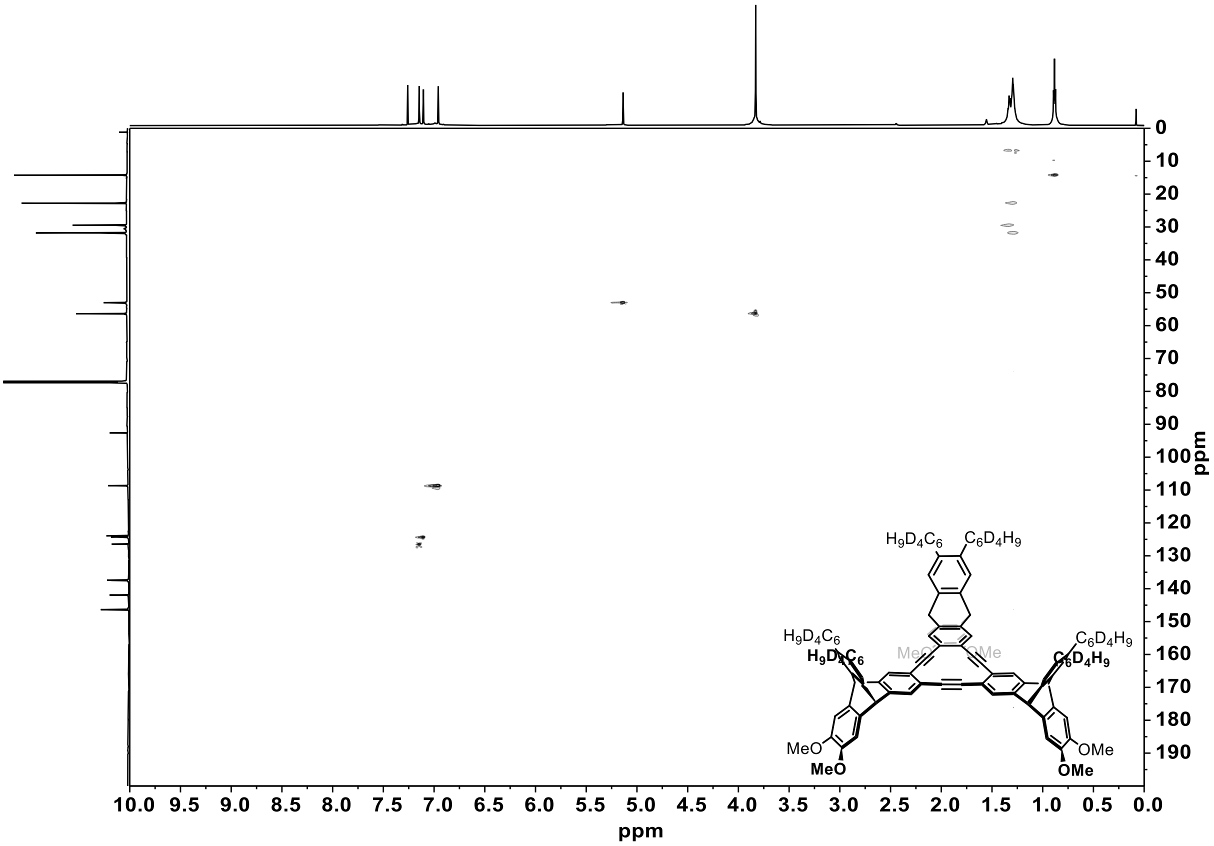

Figure 7.120: ^{1}H-^{13}C HSQC spectrum of **103b-*d*$_{24}$** (700 MHz, 176 MHz, $CDCl_3$).

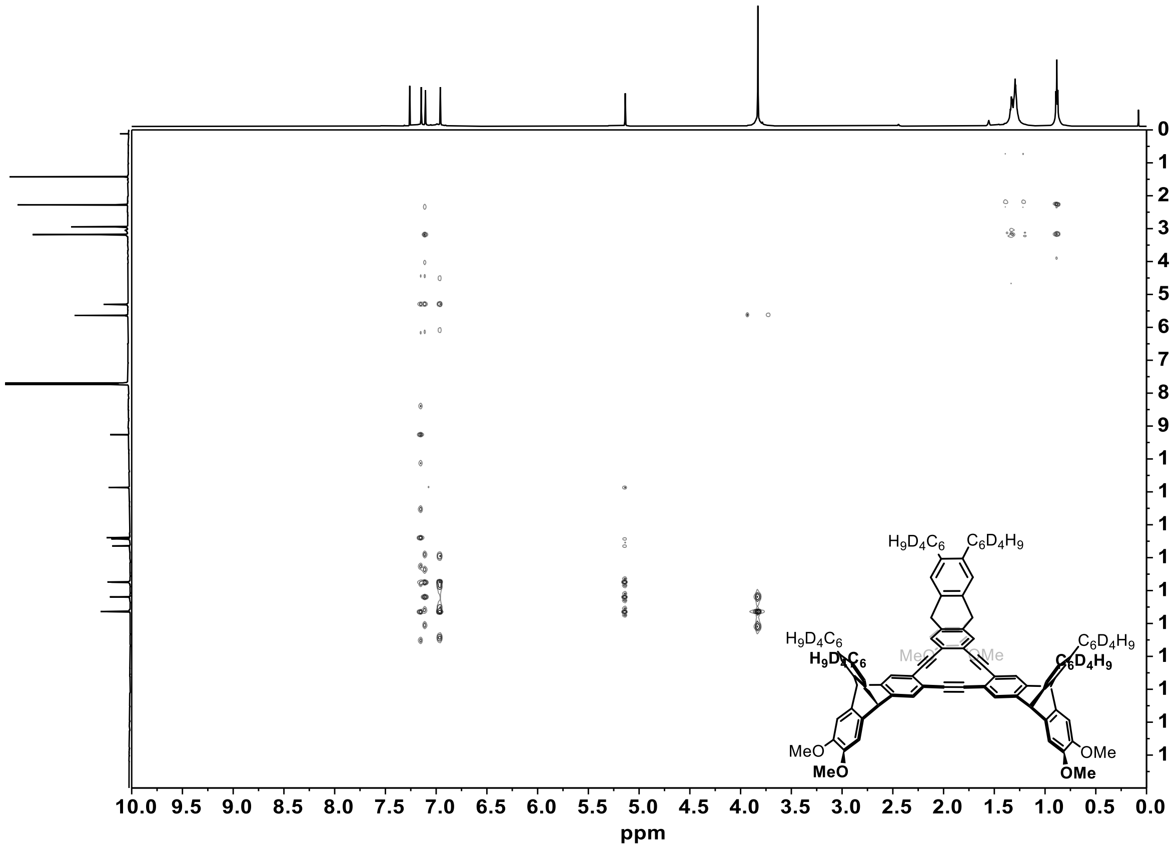

Figure 7.121: ^{1}H-^{13}C HMBC spectrum of **103b-*d*$_{24}$** (700 MHz, 176 MHz, CDCl$_3$).

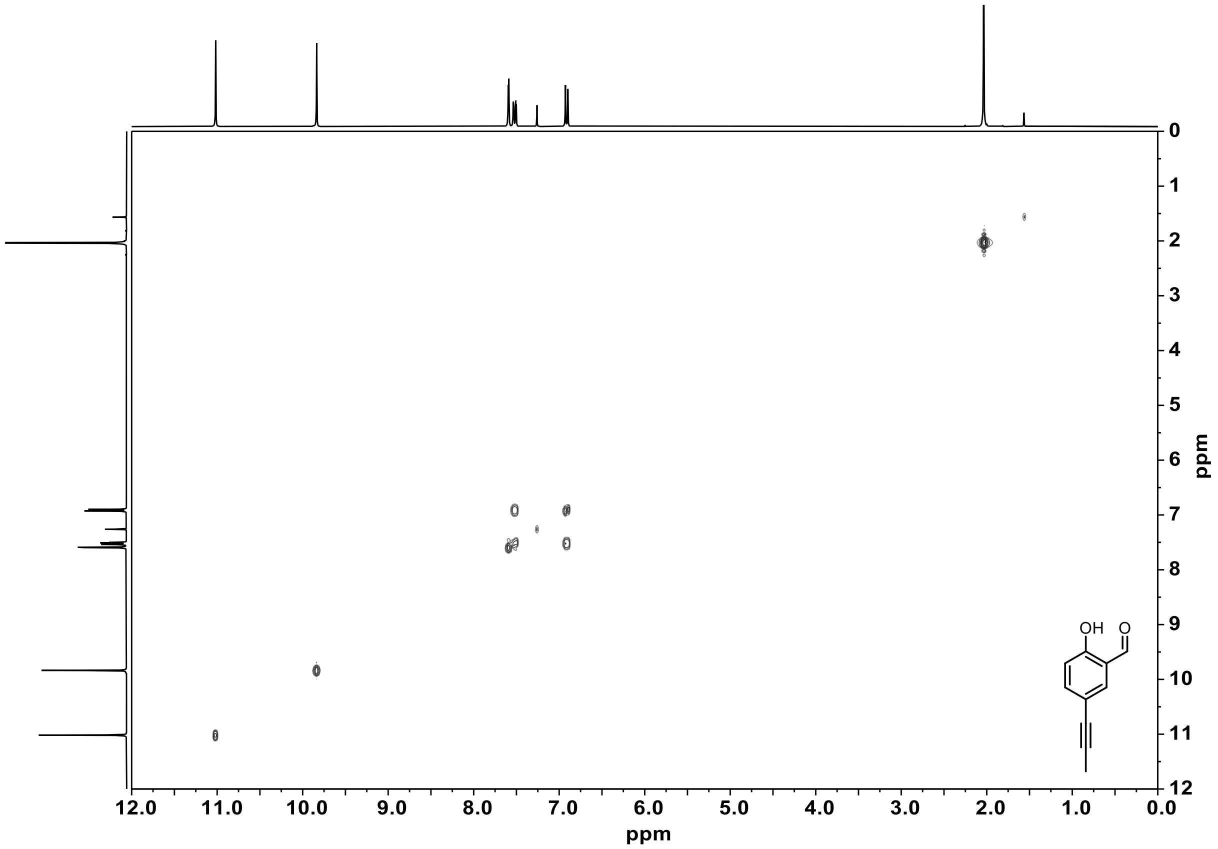

Figure 7.122: ^{1}H-^{1}H COSY spectrum of **111** (300 MHz, CDCl$_3$).

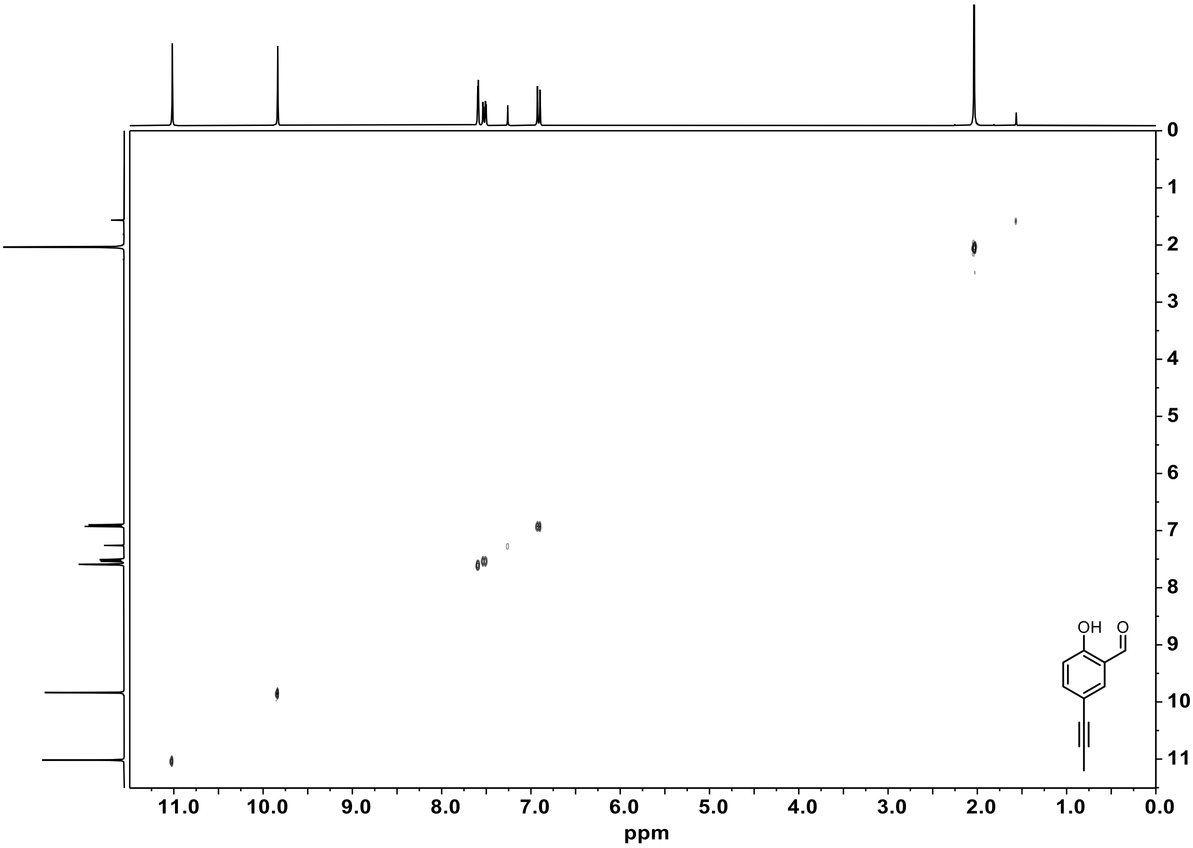

Figure 7.123: ^{1}H-^{1}H NOESY spectrum of **111** (300 MHz, $CDCl_3$).

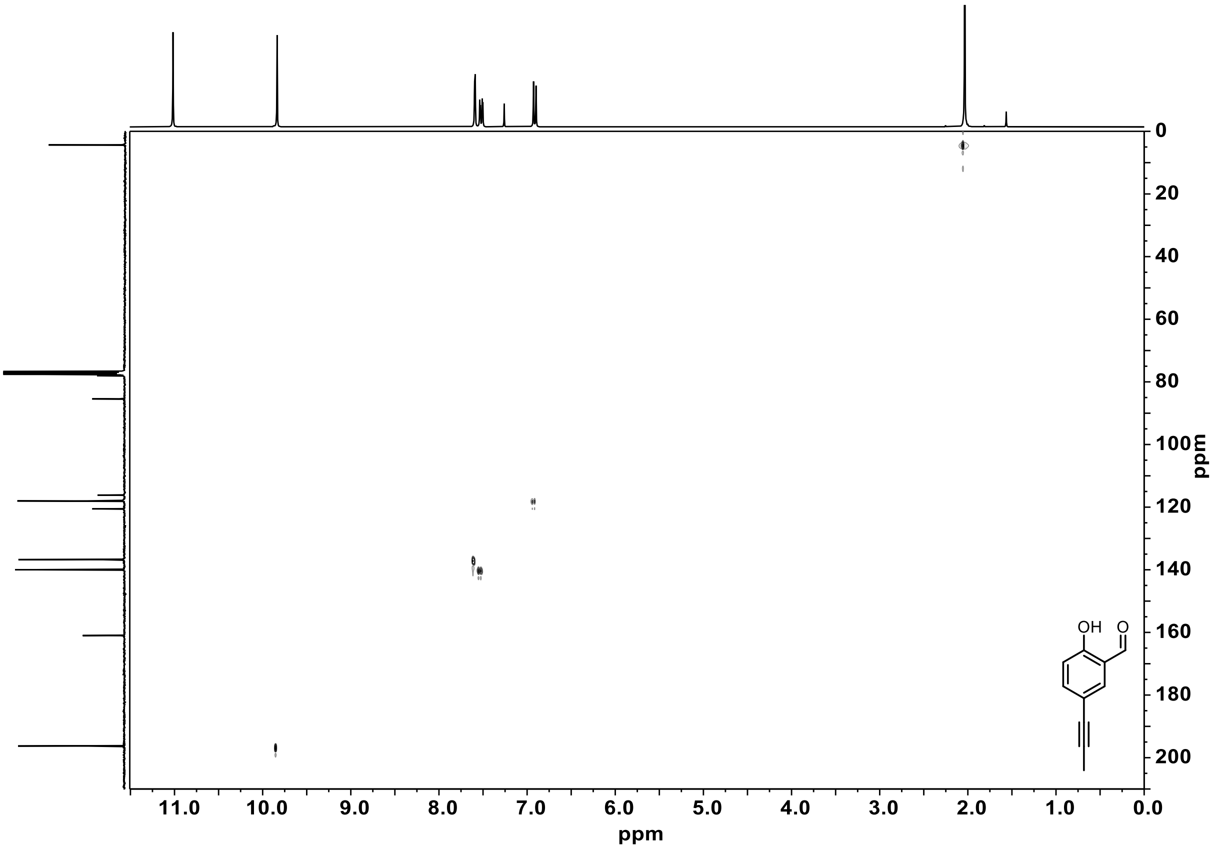

Figure 7.124: ^{1}H-^{13}C HSQC spectrum of **111** (300 MHz, 75 MHz, $CDCl_3$).

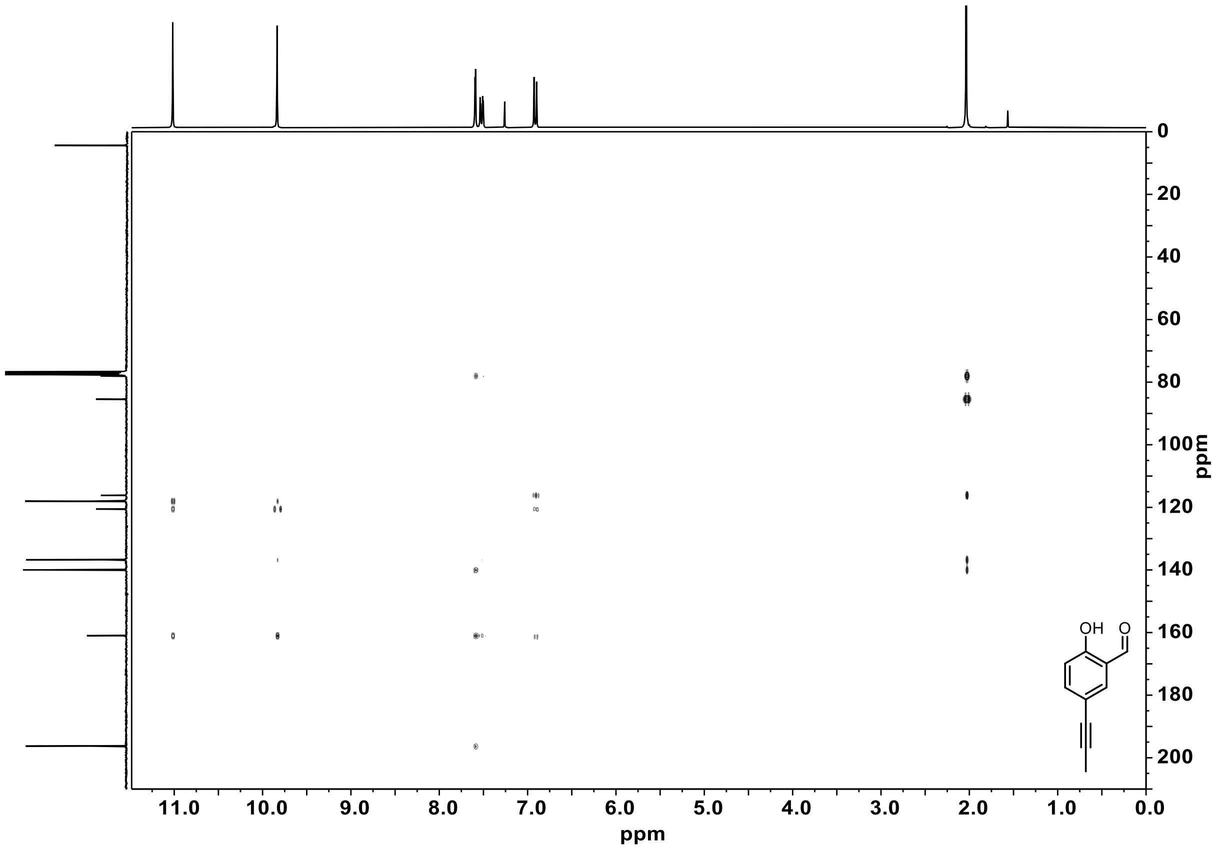

Figure 7.125: ^{1}H-^{13}C HMBC spectrum of **111** (300 MHz, 75 MHz, CDCl$_3$).

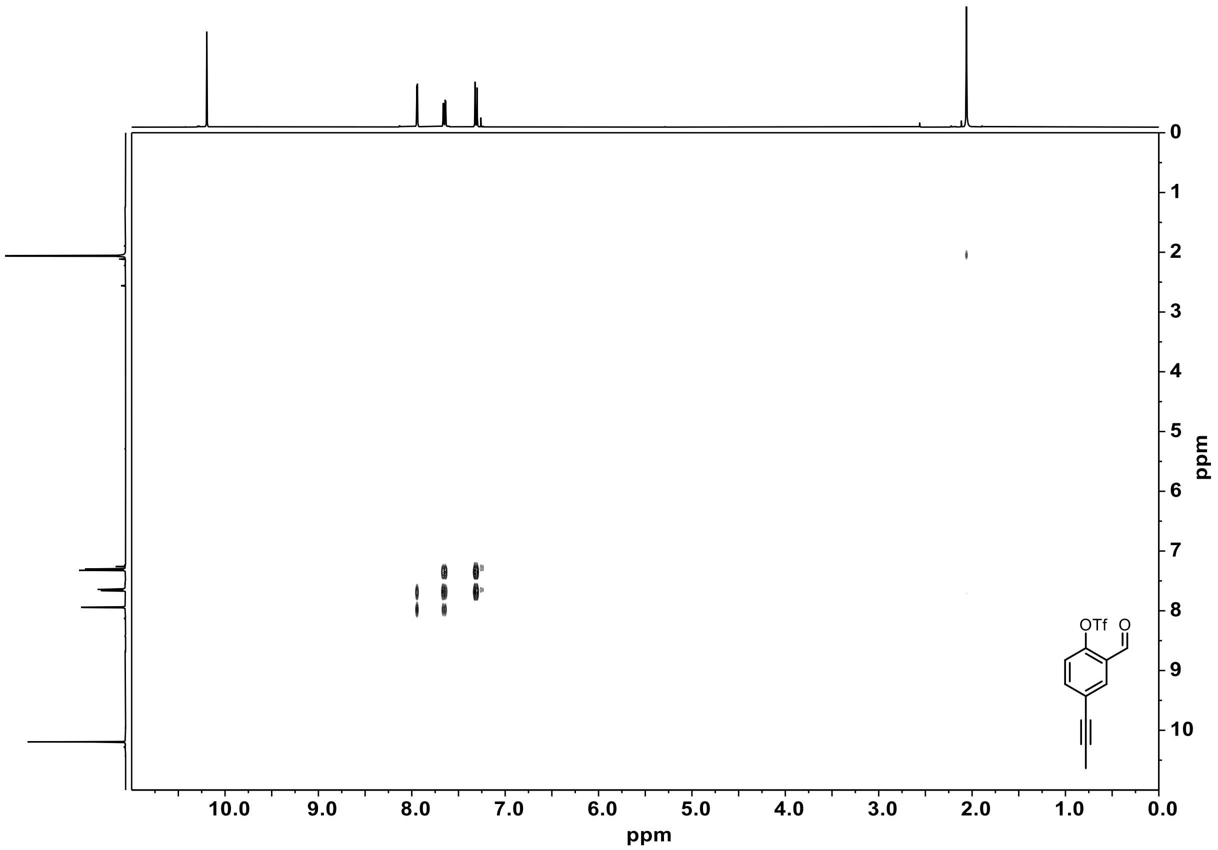

Figure 7.126: ^{1}H-^{1}H COSY spectrum of **112** (400 MHz, CDCl$_3$).

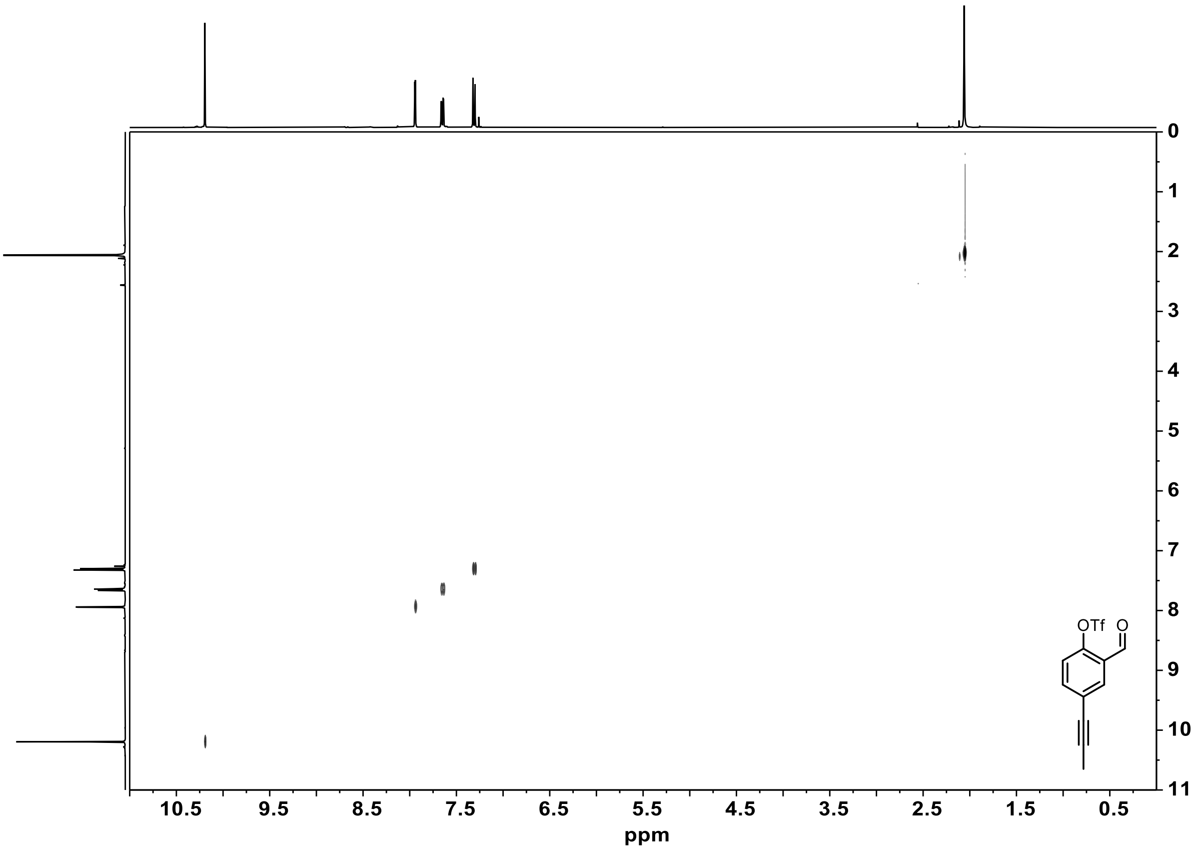

Figure 7.127: ^{1}H-^{1}H NOESY spectrum of **112** (400 MHz, CDCl$_3$).

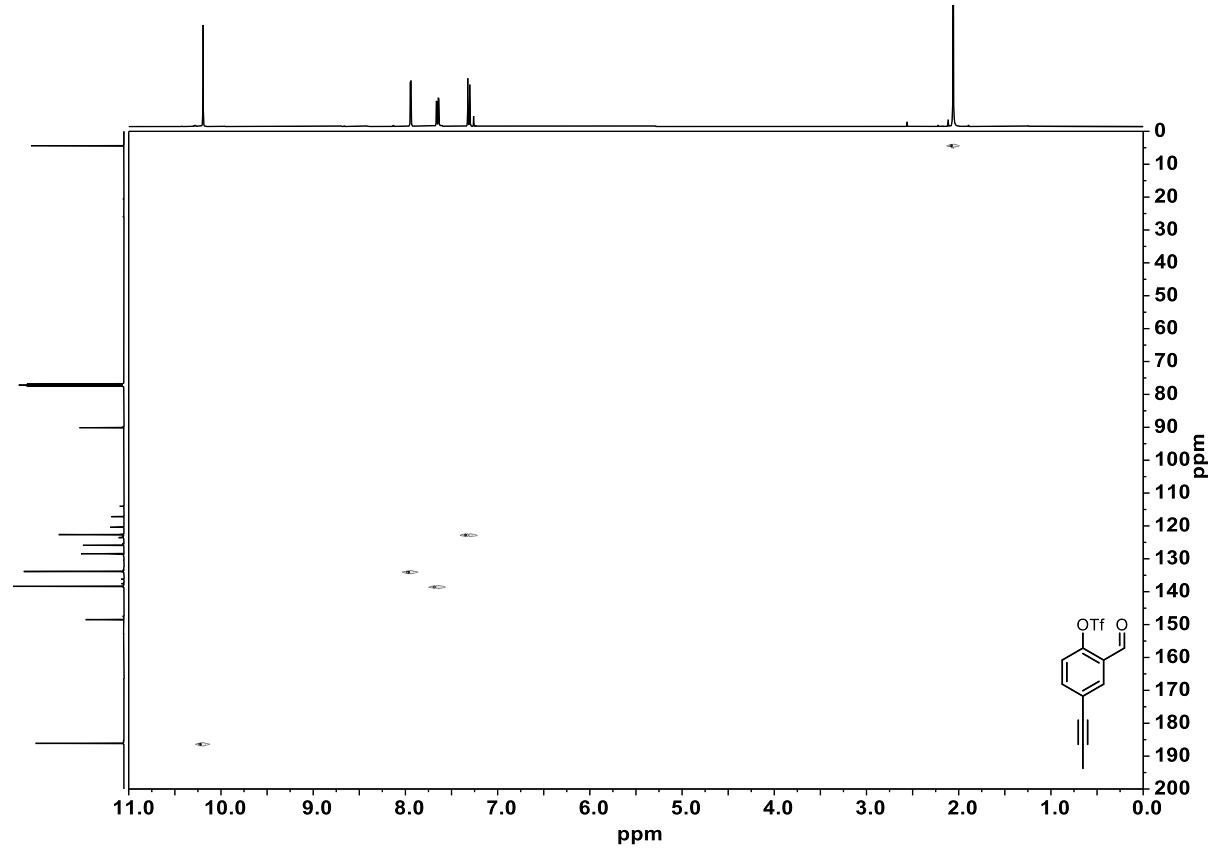

Figure 7.128: ^{1}H-^{13}C HSQC spectrum of **112** (400 MHz, 100 MHz, CDCl$_3$).

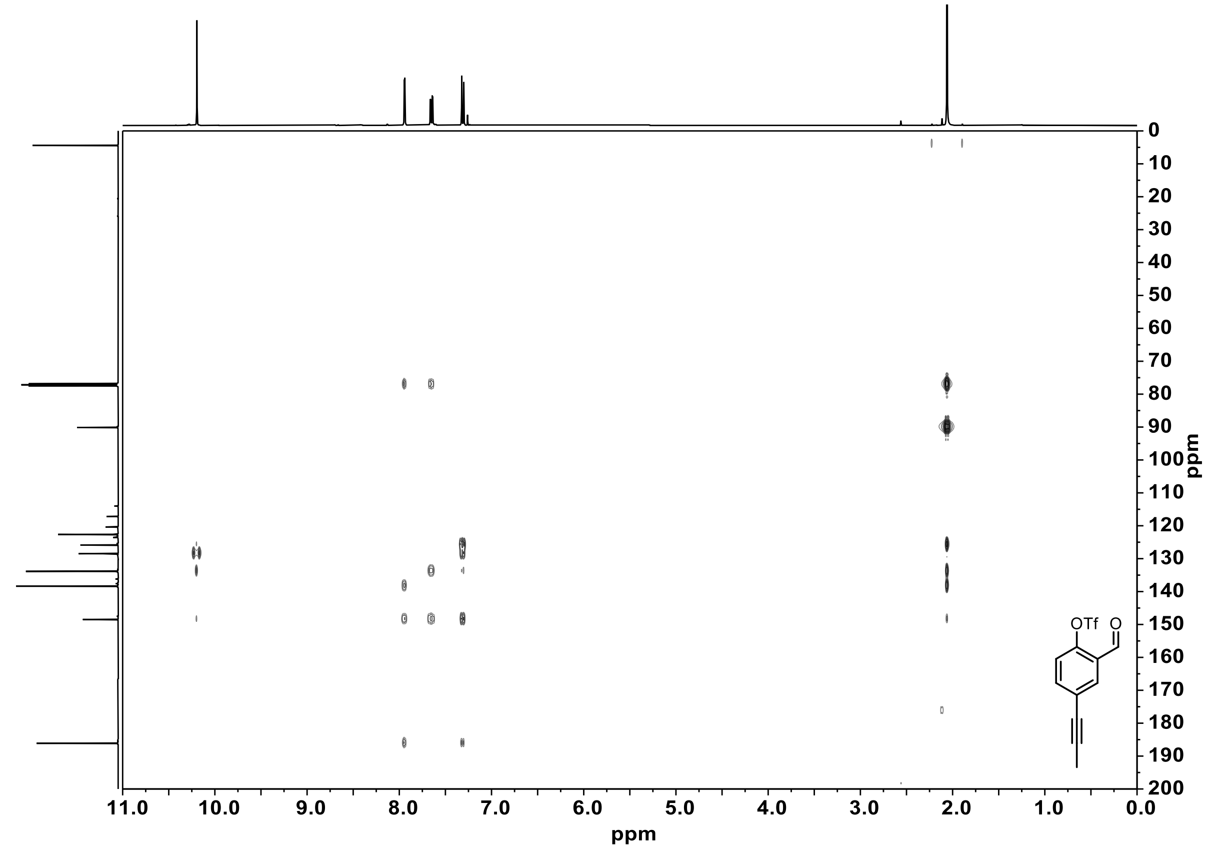

Figure 7.129: ^{1}H-^{13}C HMBC spectrum of **112** (400 MHz, 100 MHz, CDCl$_3$).

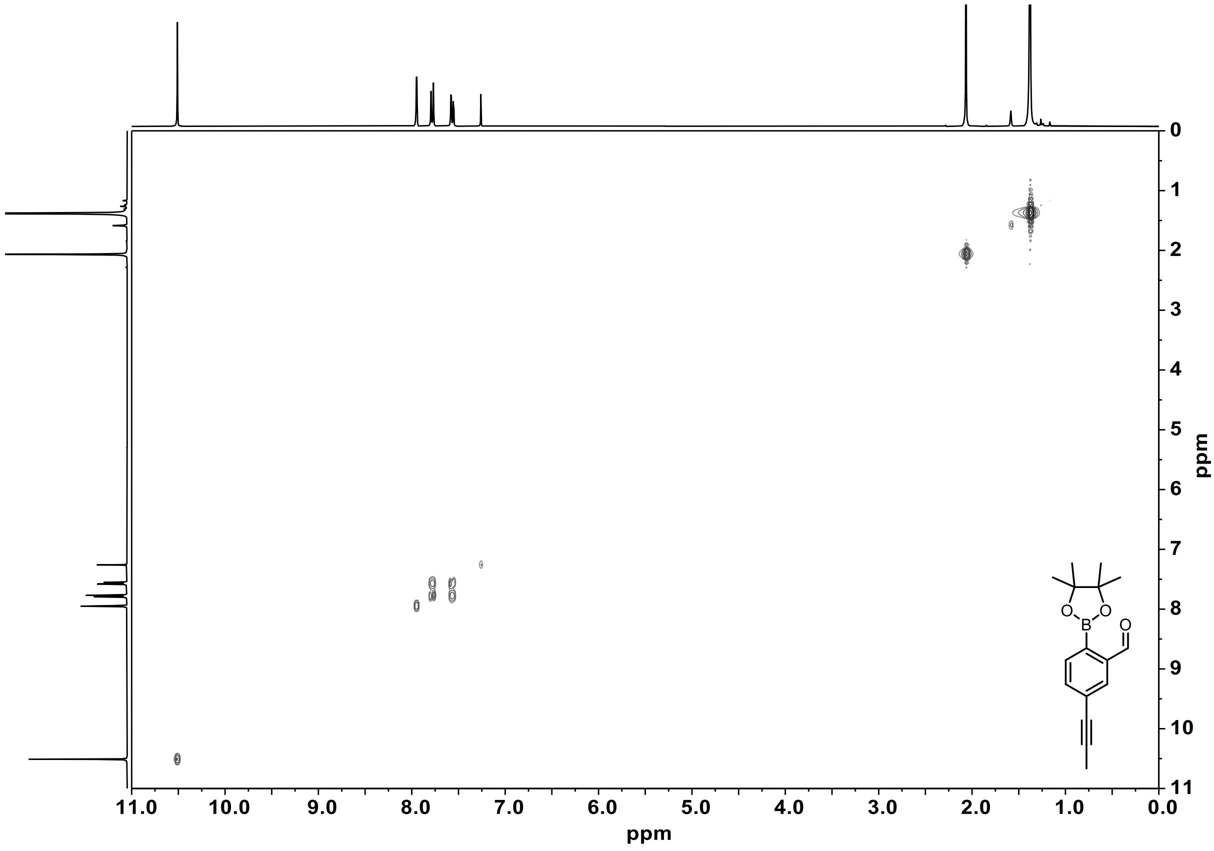

Figure 7.130: ^{1}H-^{1}H COSY spectrum of **113** (300 MHz, CDCl$_3$).

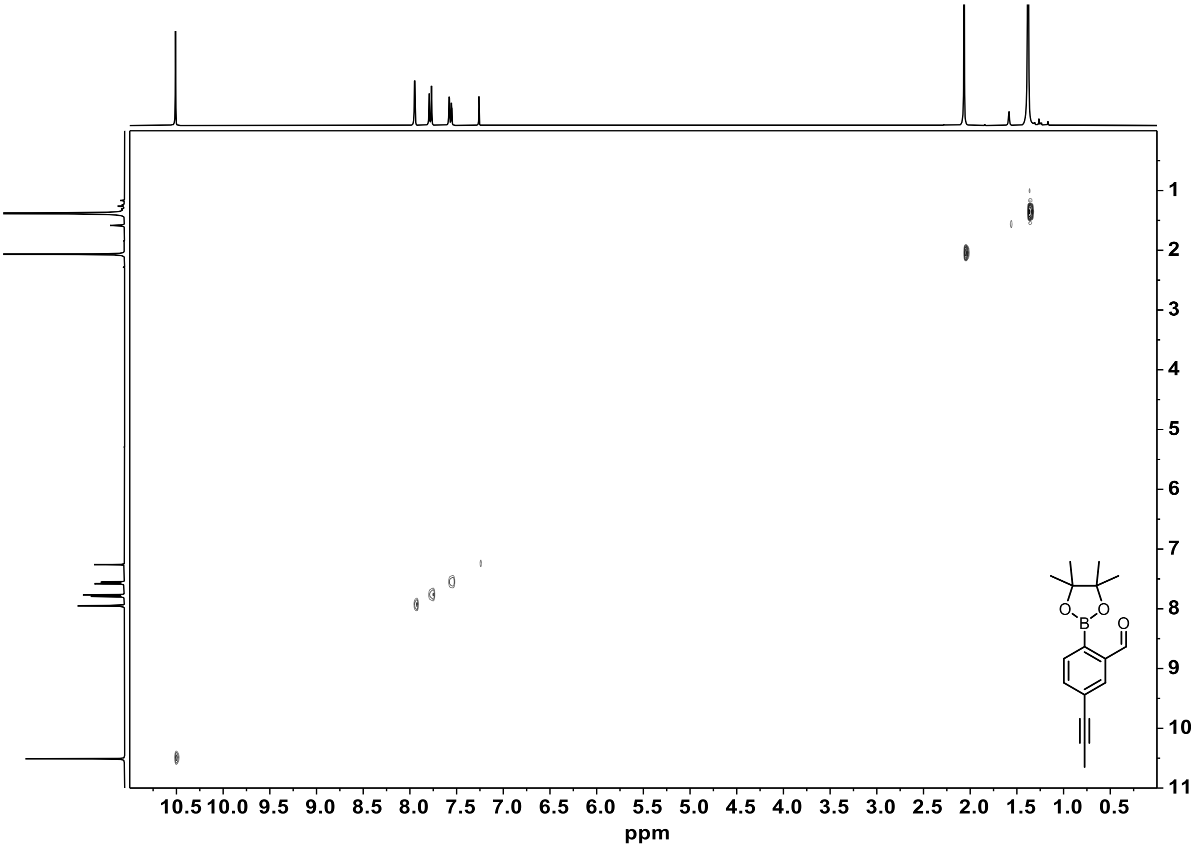

Figure 7.131: ^{1}H-^{1}H NOESY spectrum of **113** (300 MHz, CDCl$_3$).

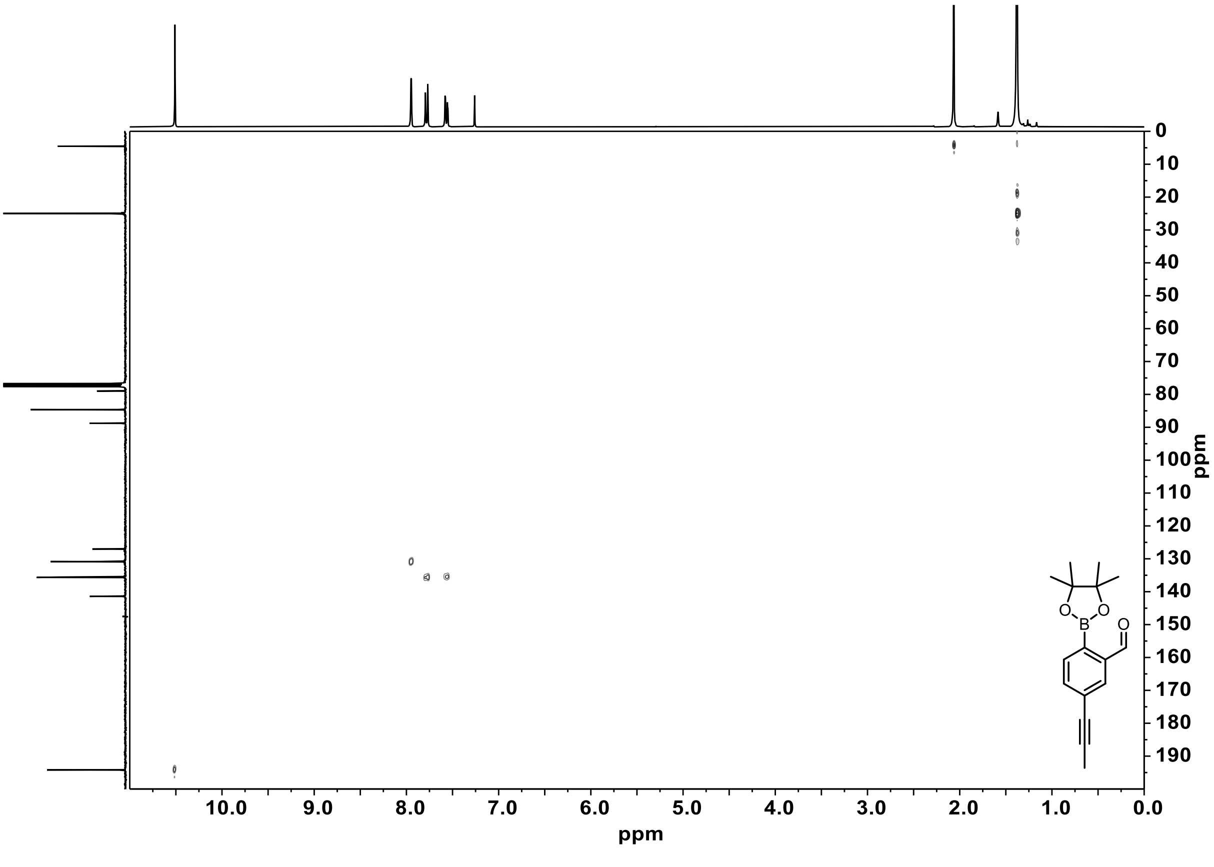

Figure 7.132: ^{1}H-^{13}C HSQC spectrum of **113** (300 MHz, 75 MHz, CDCl$_3$).

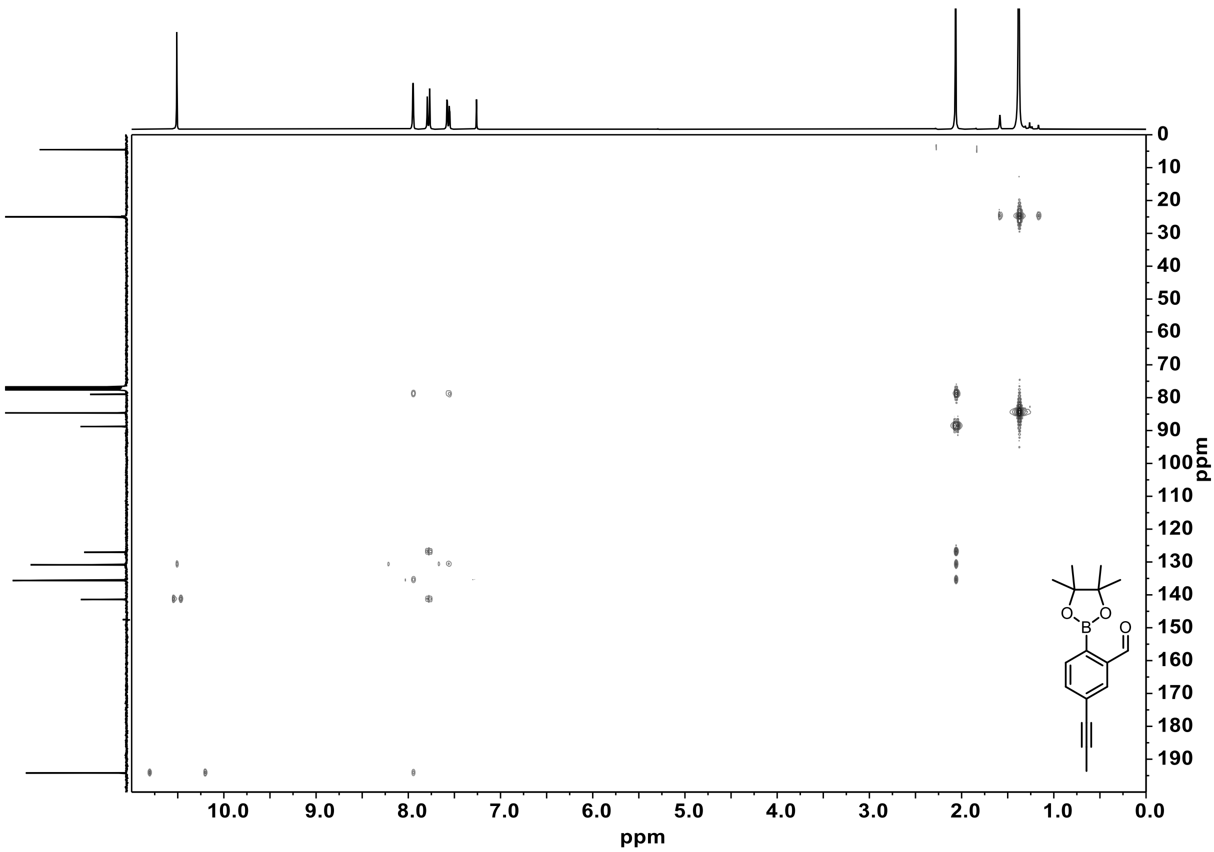

Figure 7.133: ^{1}H-^{13}C HMBC spectrum of **113** (300 MHz, 75 MHz, CDCl$_3$).

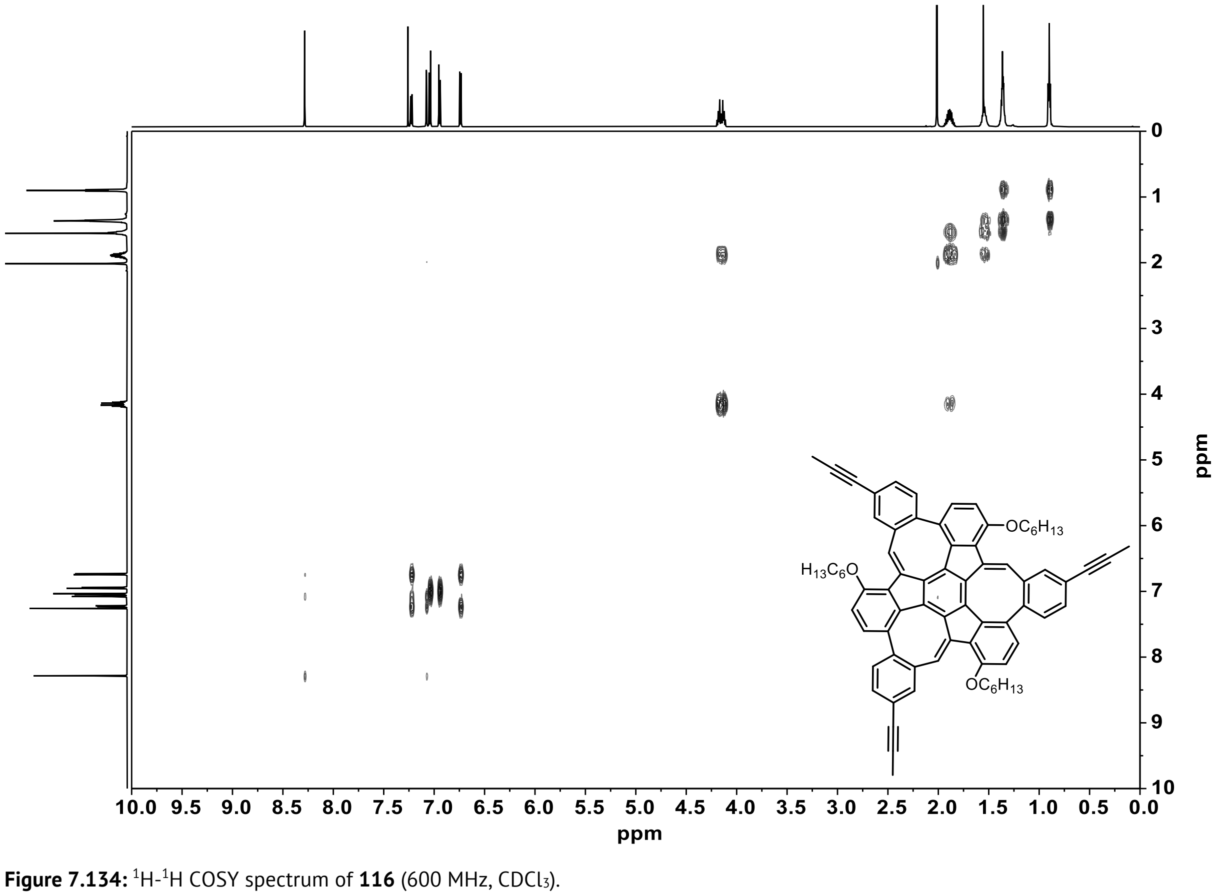

Figure 7.134: ^{1}H-^{1}H COSY spectrum of **116** (600 MHz, CDCl$_3$).

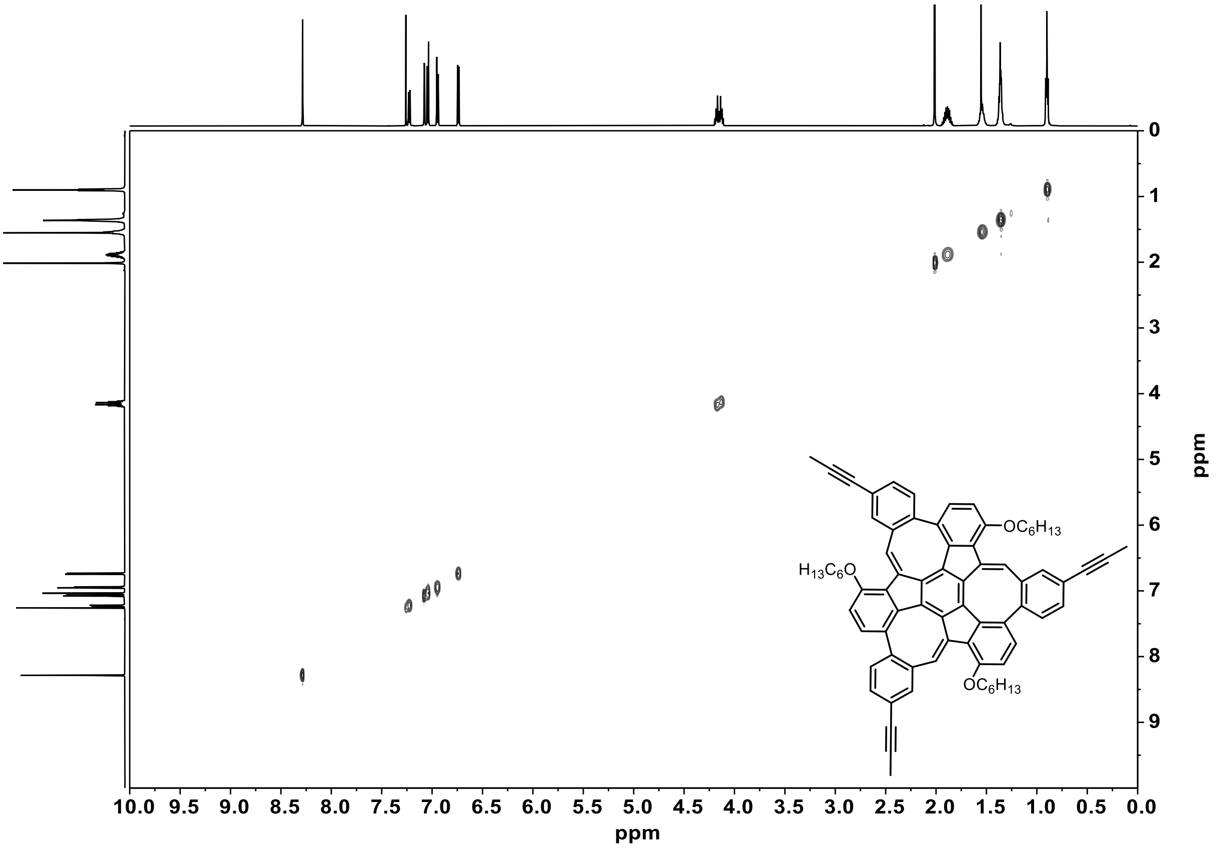

Figure 7.135: ^{1}H-^{1}H NOESY spectrum of **116** (600 MHz, CDCl$_3$).

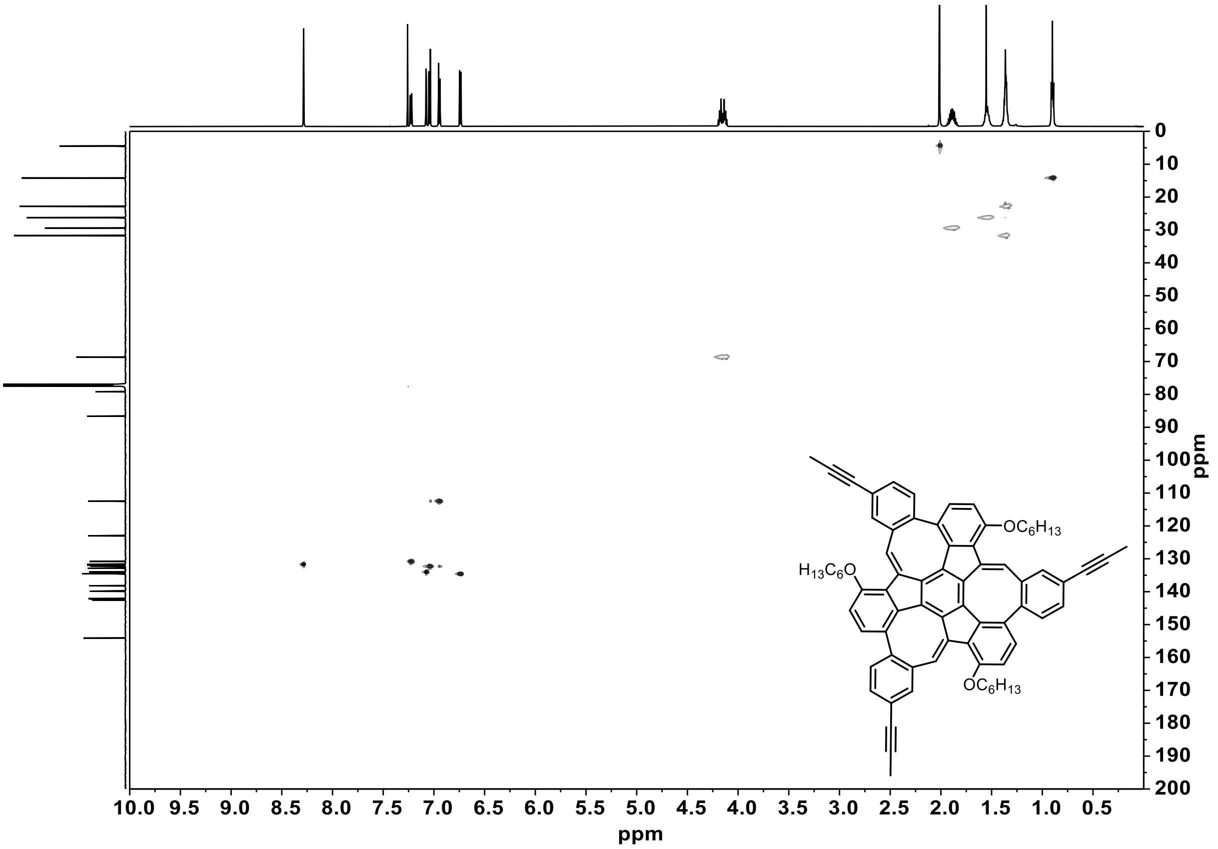

Figure 7.136: ^{1}H-^{13}C HSQC spectrum of **116** (600 MHz, 150 MHz, CDCl$_3$).

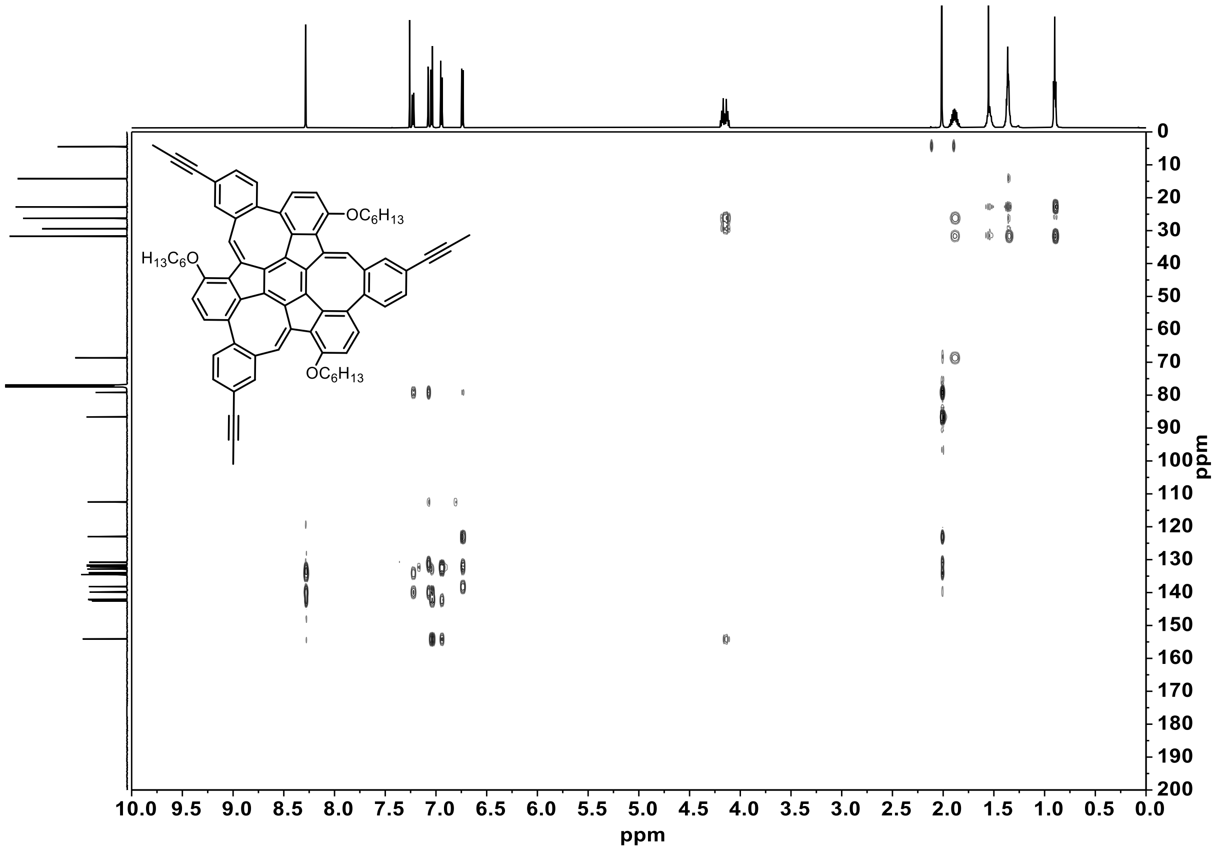

Figure 7.137: ^{1}H-^{13}C HMBC spectrum of **116** (600 MHz, 150 MHz, CDCl$_3$).

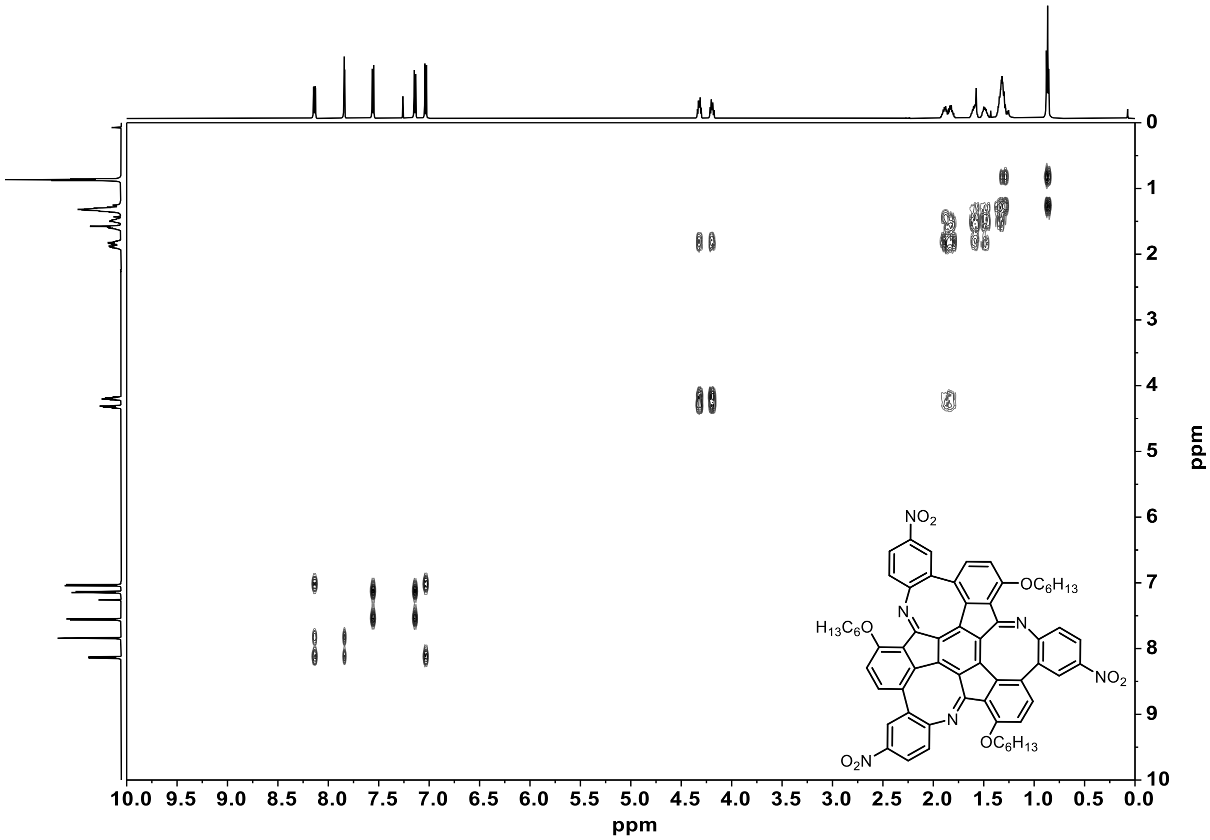

Figure 7.138: ^{1}H-^{1}H COSY spectrum of **131** (600 MHz, CDCl$_3$).

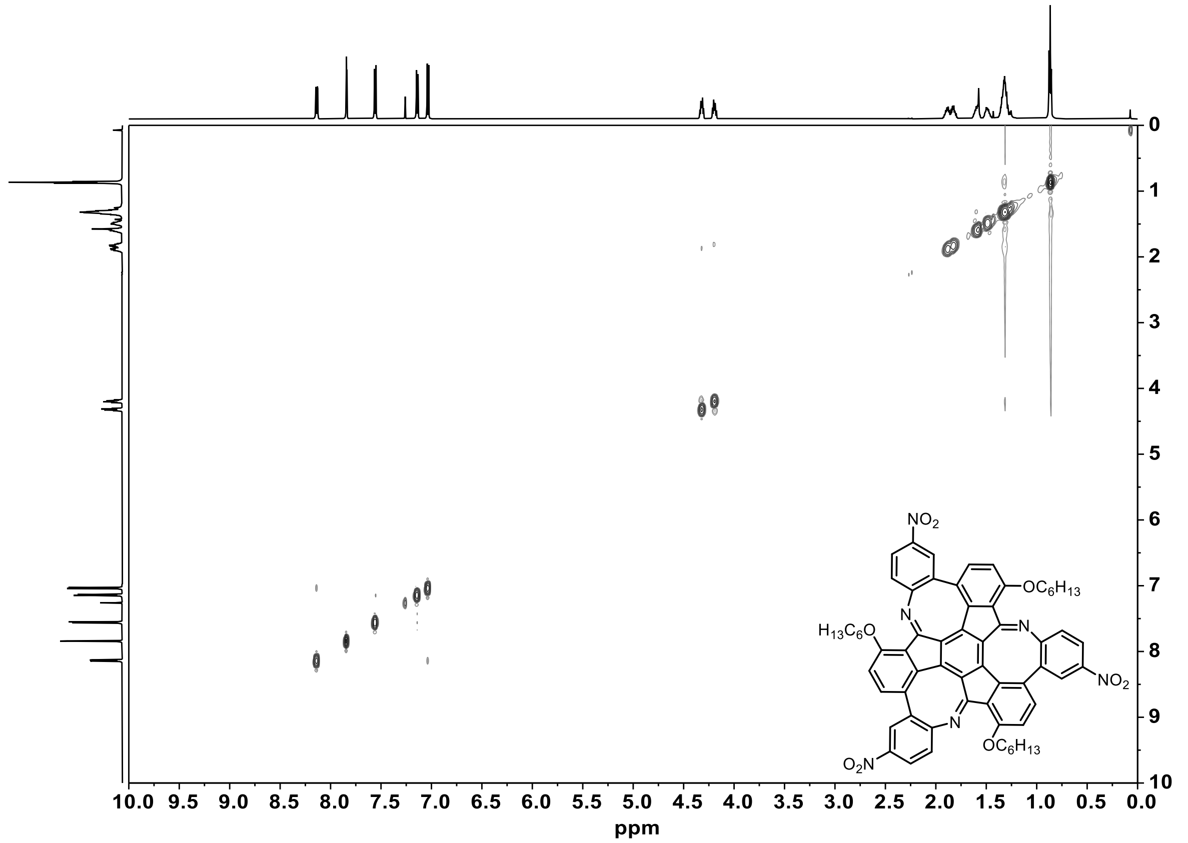

Figure 7.139: ^{1}H-^{1}H NOESY spectrum of **131** (600 MHz, CDCl₃).

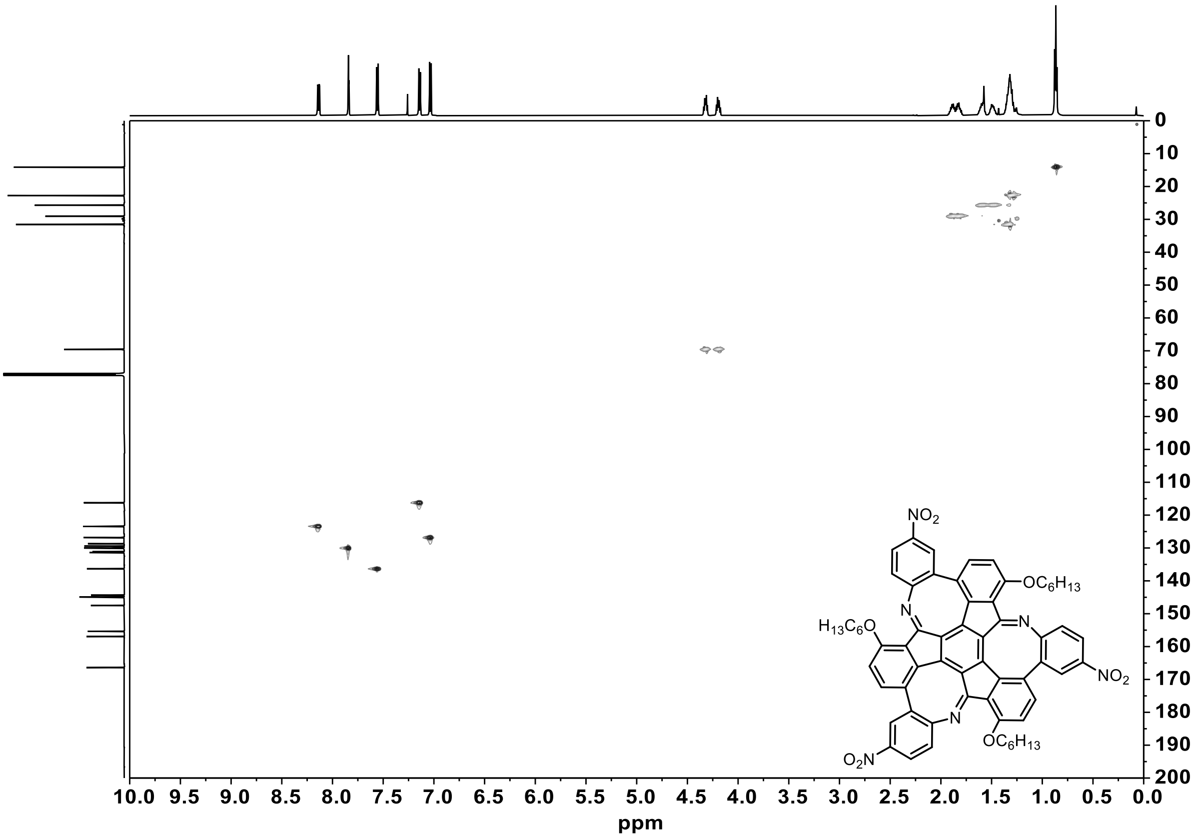

Figure 7.140: ^{1}H-^{13}C HSQC spectrum of **131** (600 MHz, 150 MHz, CDCl₃).

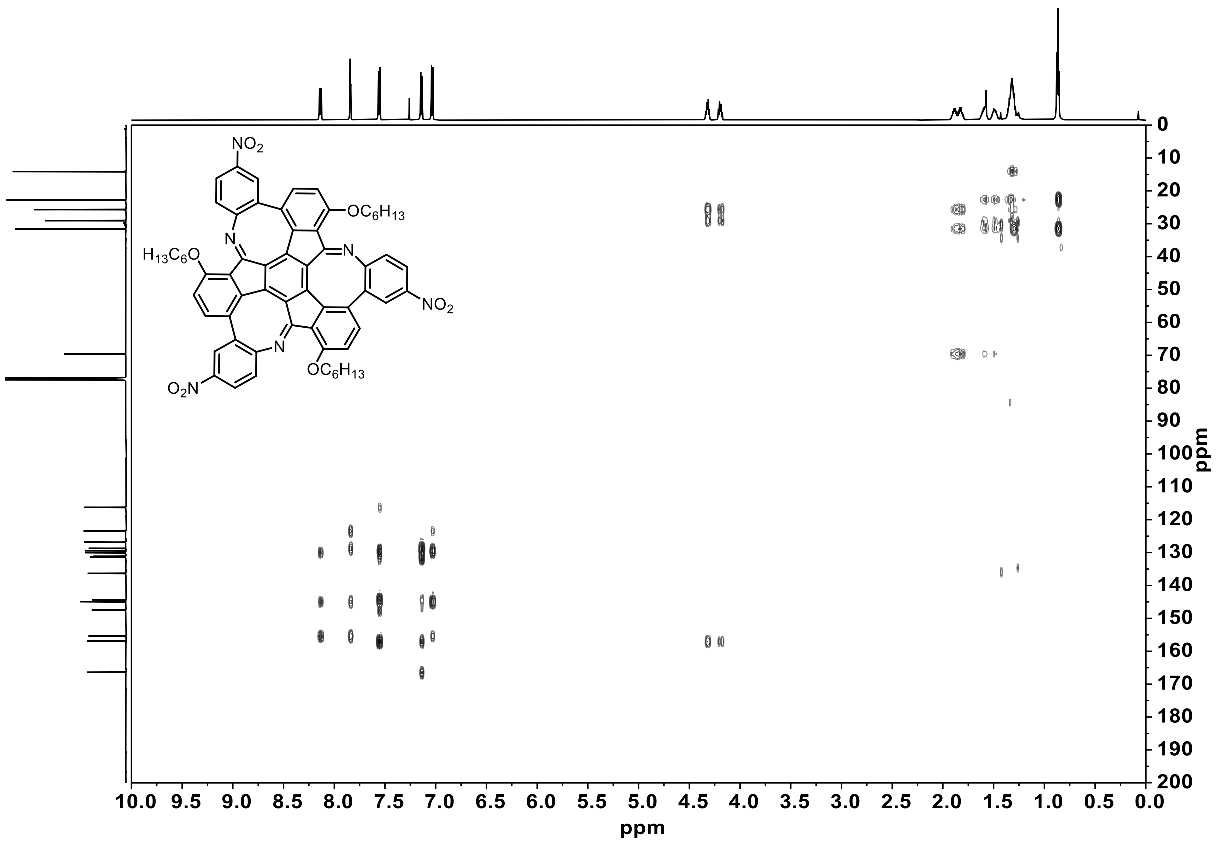

Figure 7.141: ^{1}H-^{13}C HMBC spectrum of **131** (600 MHz, 150 MHz, CDCl$_3$).

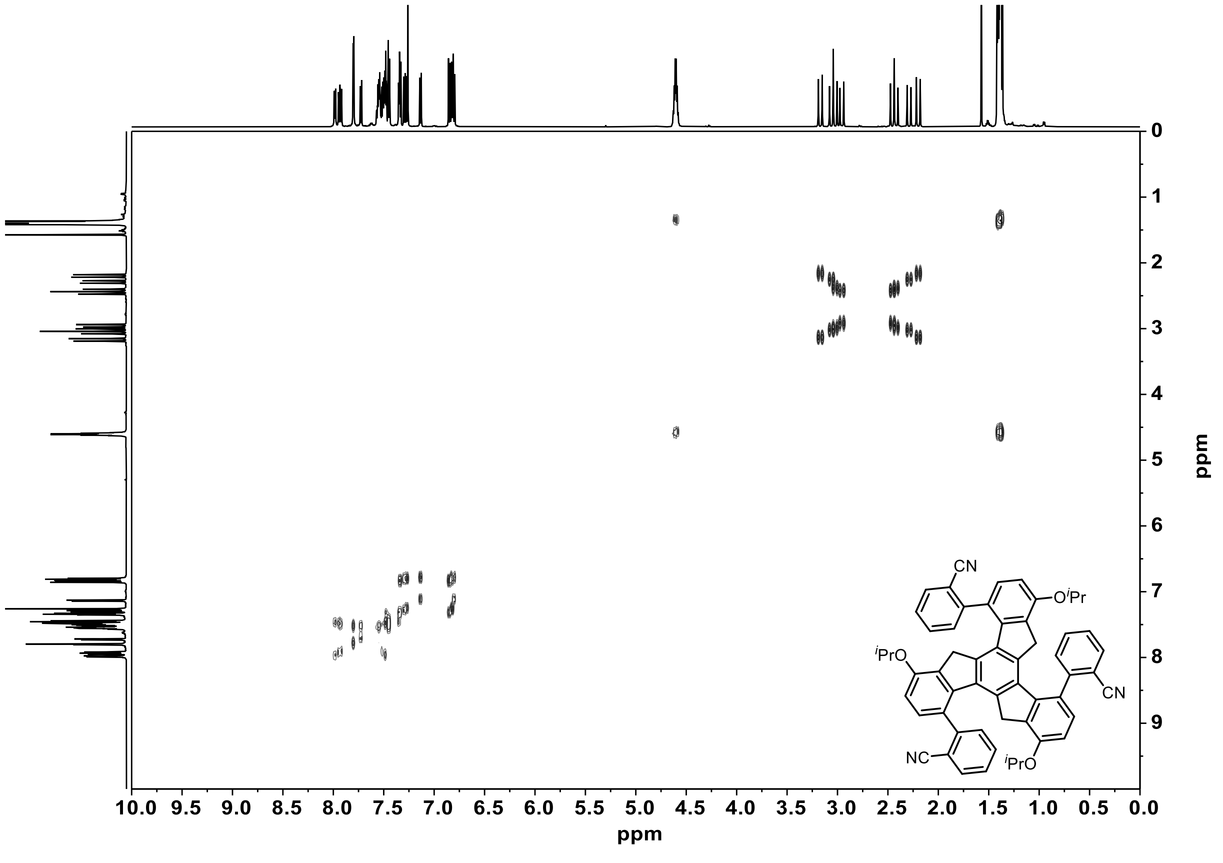

Figure 7.142: ^{1}H-^{1}H COSY spectrum of **138** (600 MHz, CDCl$_3$).

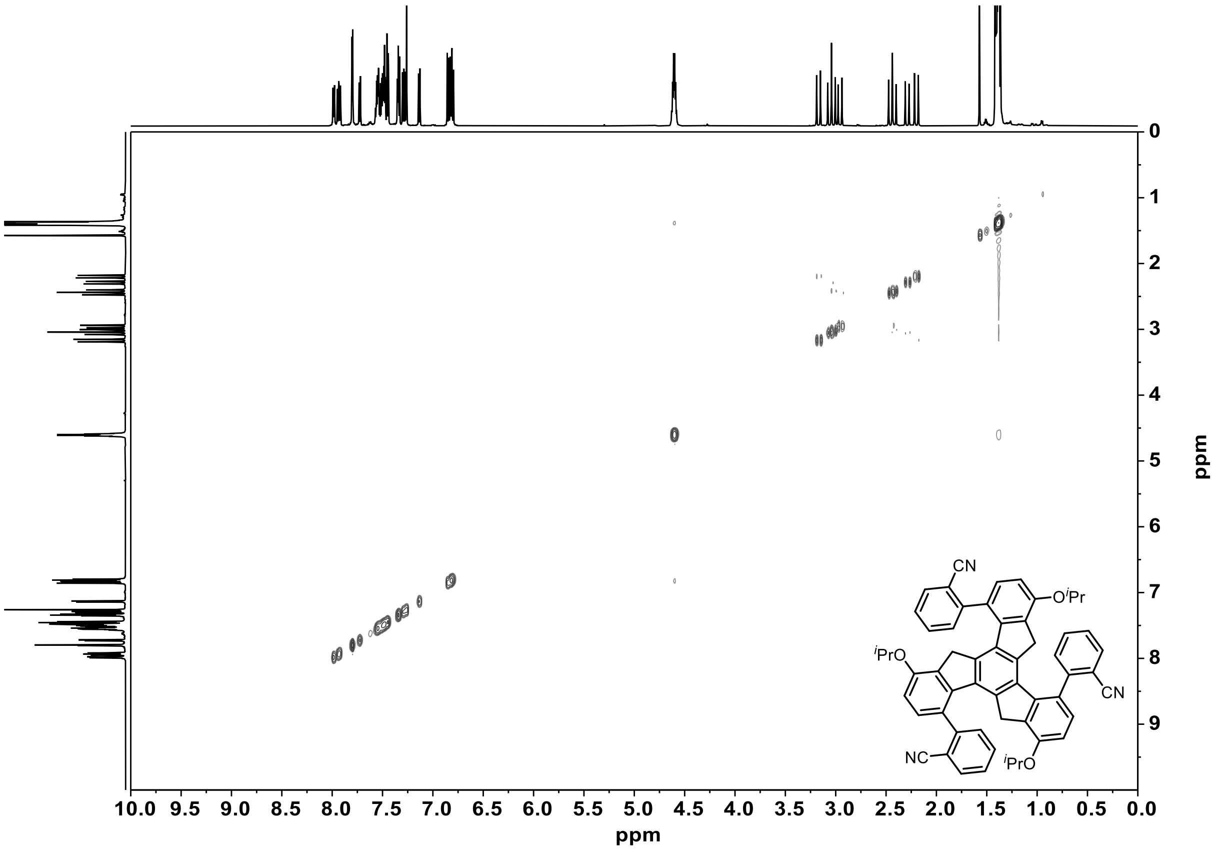

Figure 7.143: ^{1}H-^{1}H NOESY spectrum of **138** (600 MHz, CDCl$_3$).

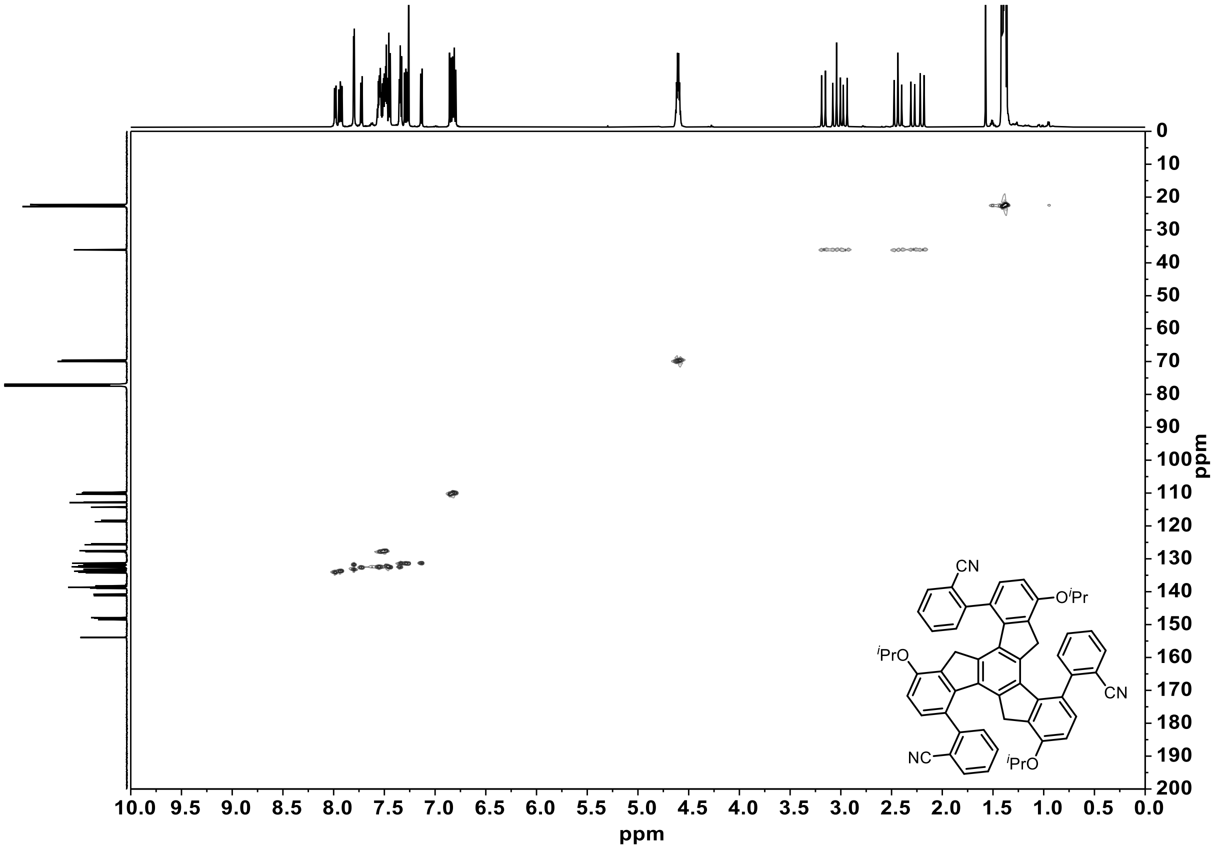

Figure 7.144: ^{1}H-^{13}C HSQC spectrum of **138** (600 MHz, 150 MHz, CDCl$_3$).

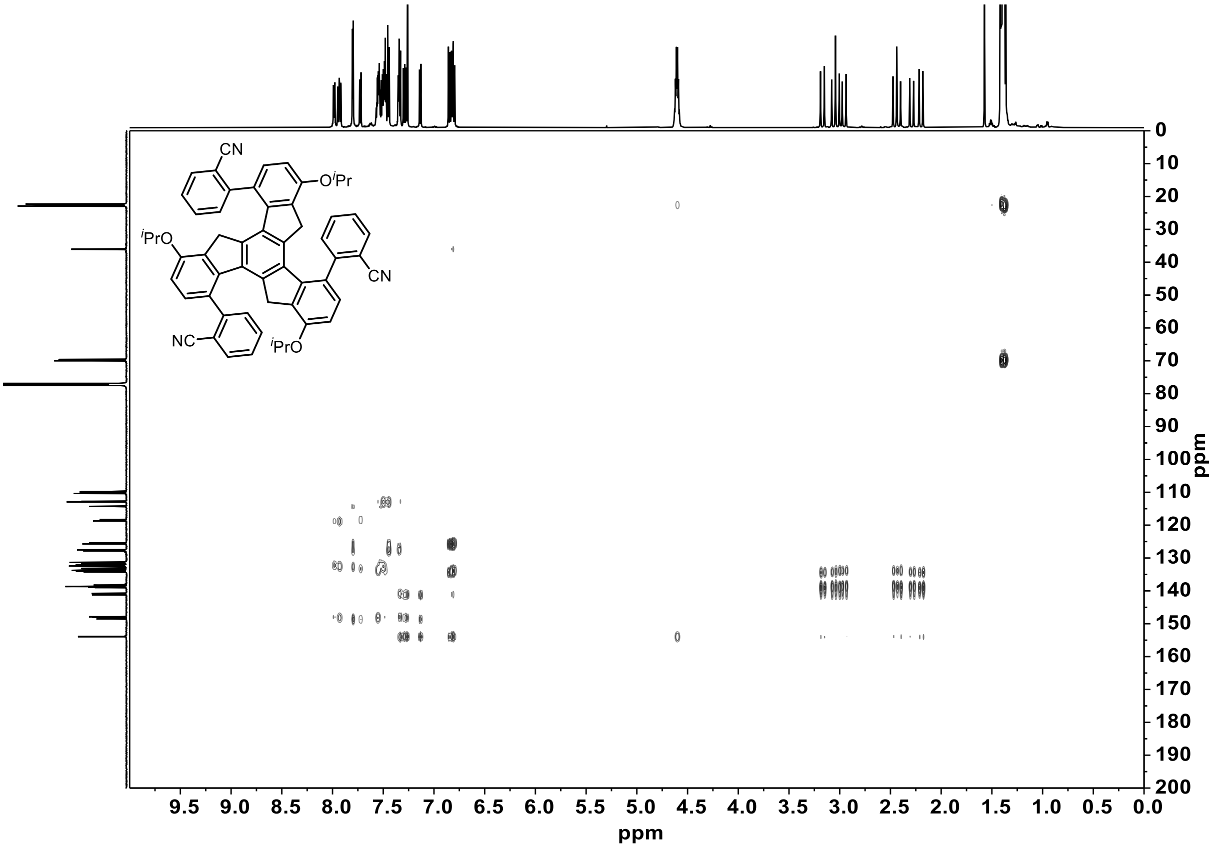

Figure 7.145: ^{1}H-^{13}C HMBC spectrum of **138** (600 MHz, 150 MHz, CDCl$_3$).

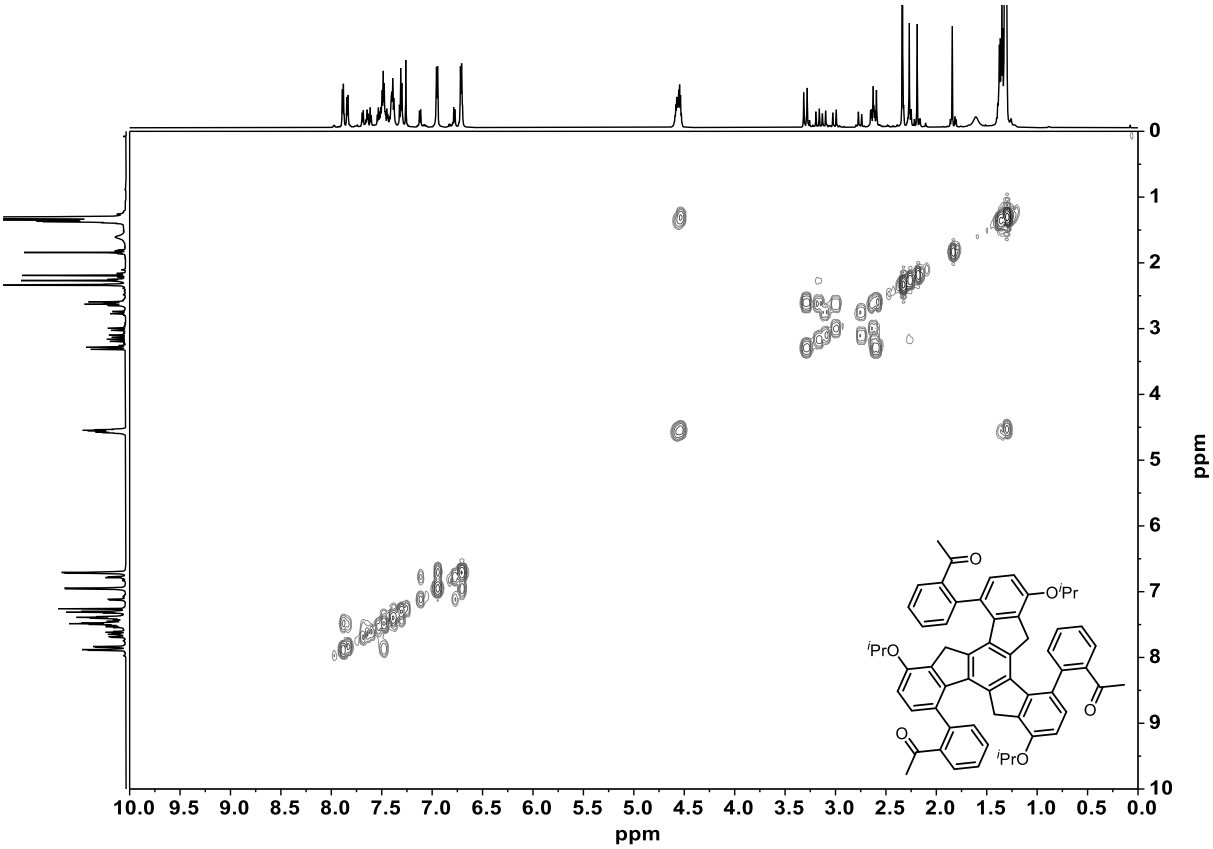

Figure 7.146: ^{1}H-^{1}H COSY spectrum of **139** (700 MHz, CDCl$_3$).

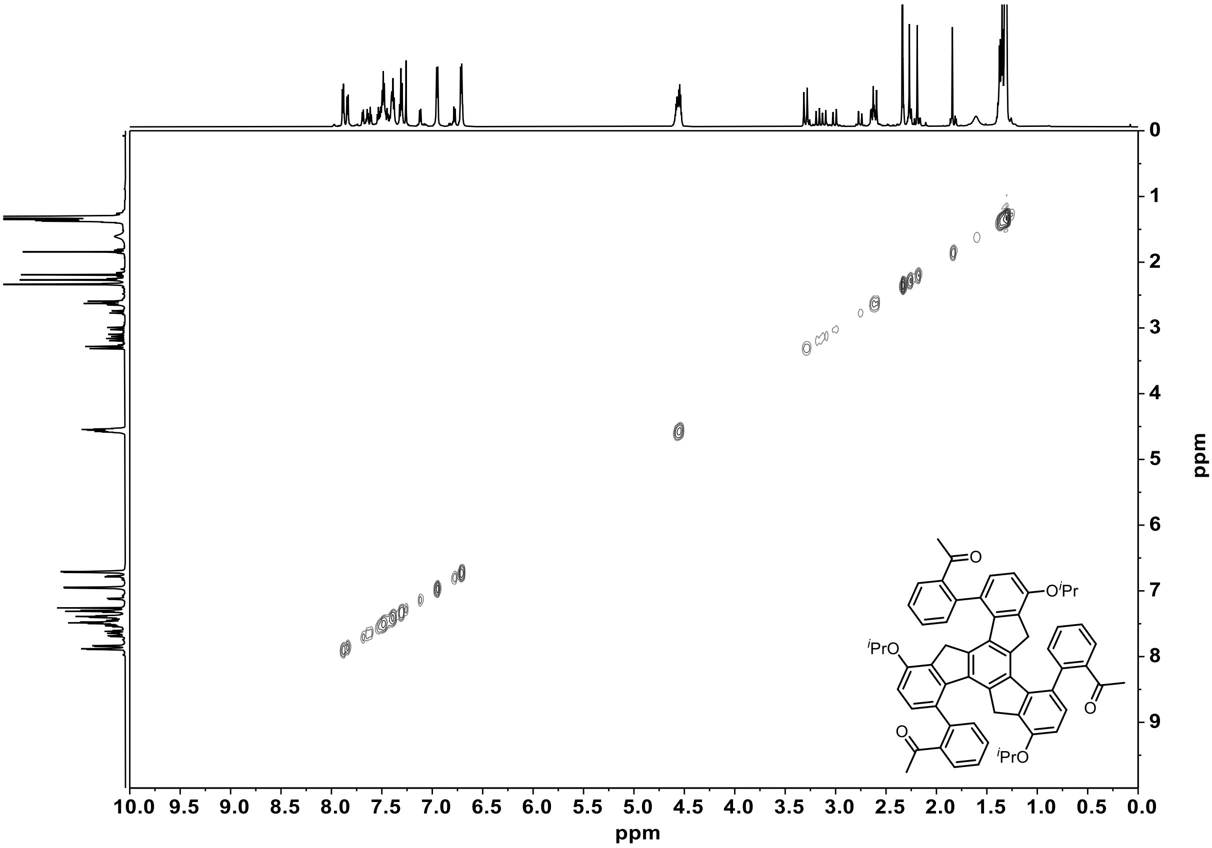

Figure 7.147: ^{1}H-^{1}H NOESY spectrum of **139** (700 MHz, CDCl$_3$).

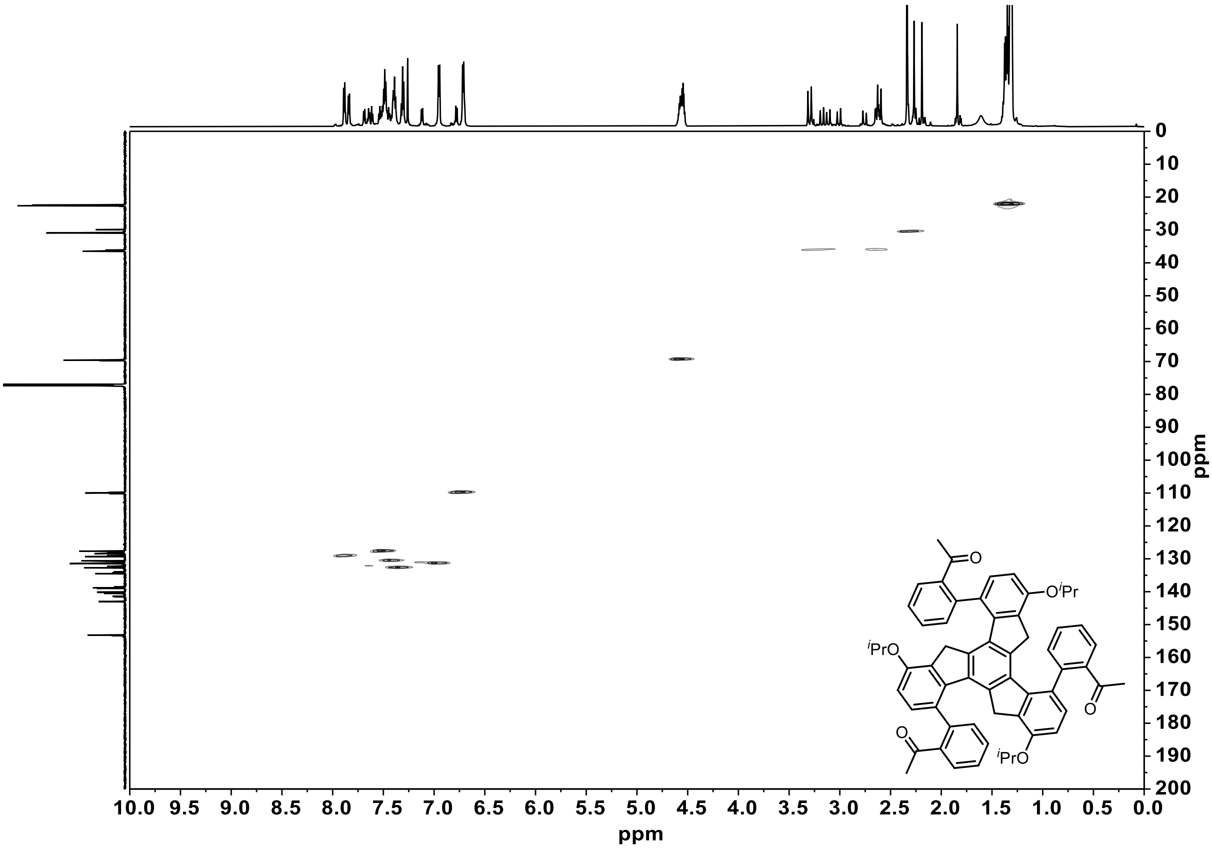

Figure 7.148: ^{1}H-^{13}C HSQC spectrum of **139** (700 MHz, 176 MHz, CDCl$_3$).

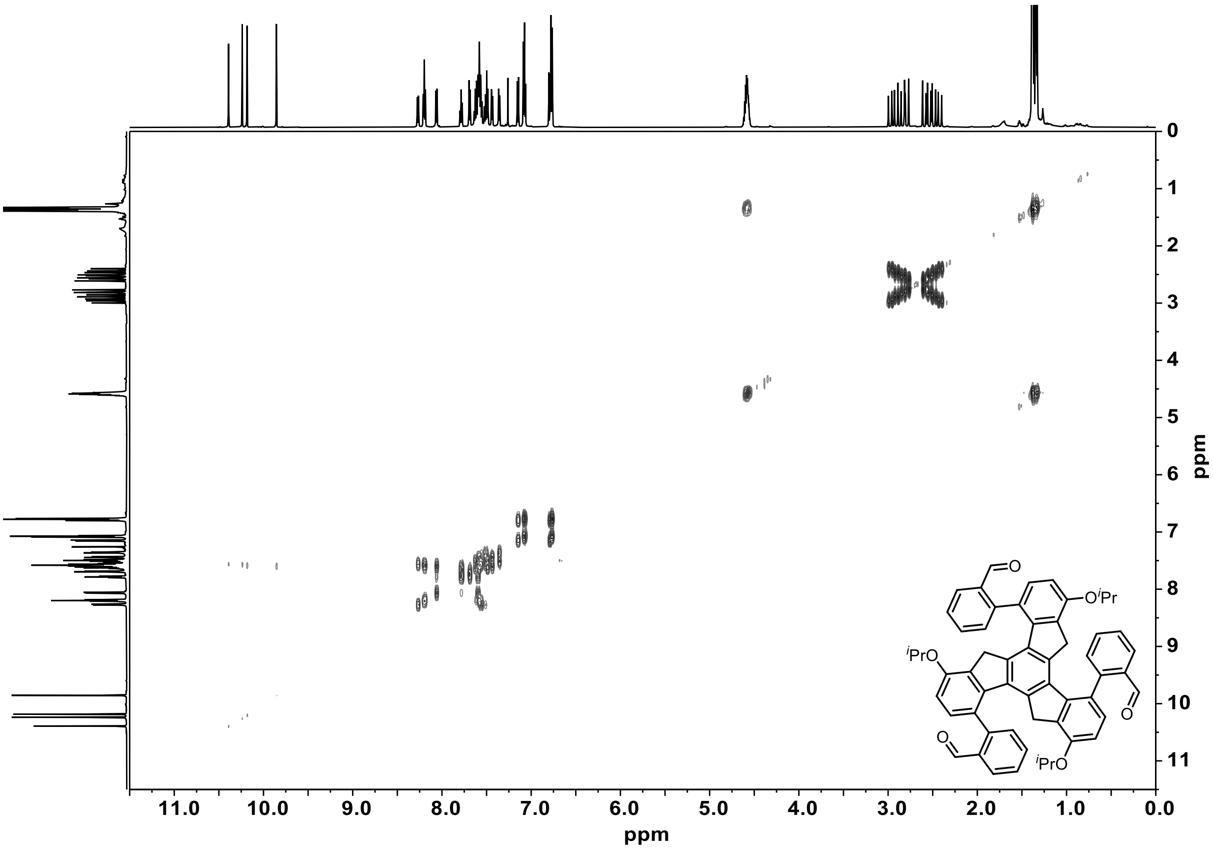

Figure 7.149: ^{1}H-^{1}H COSY spectrum of **142** (600 MHz, CDCl$_3$).

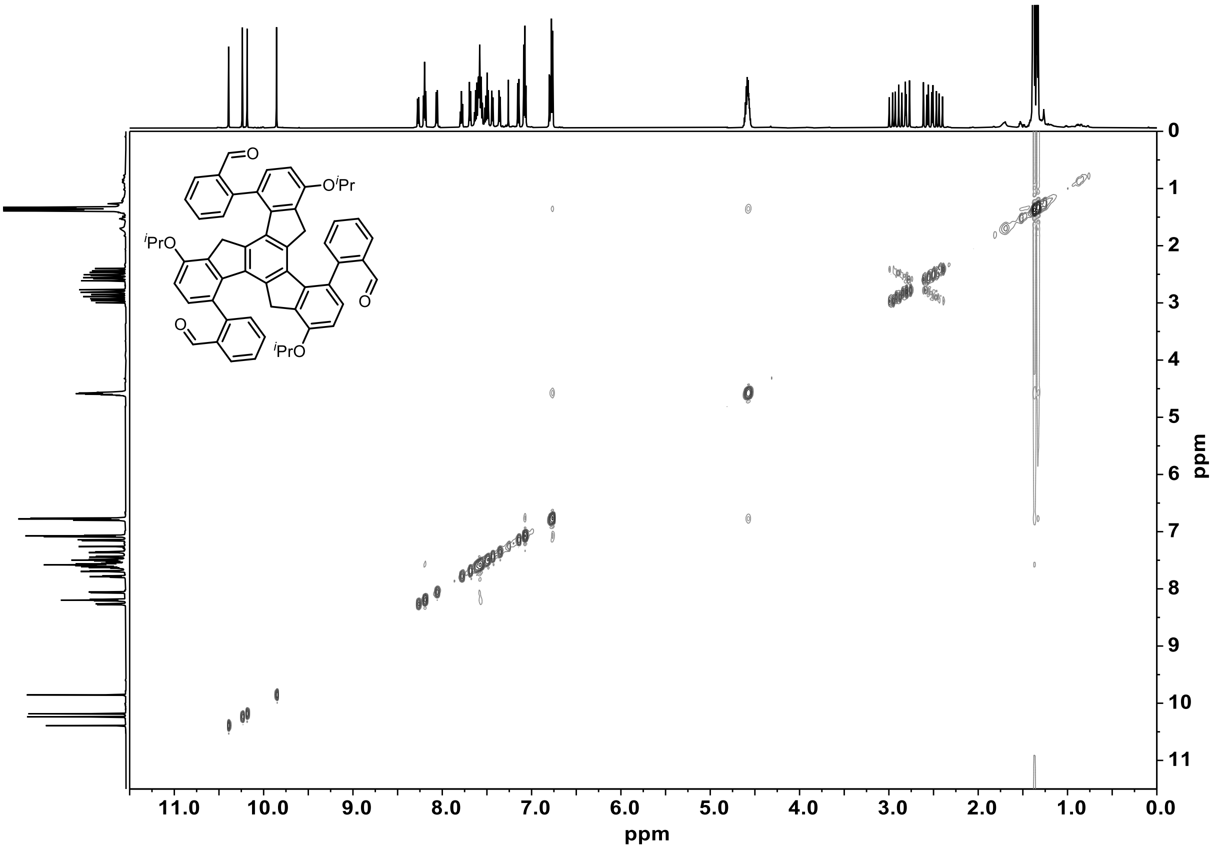

Figure 7.150: ^{1}H-^{1}H NOESY spectrum of **142** (600 MHz, CDCl$_3$).

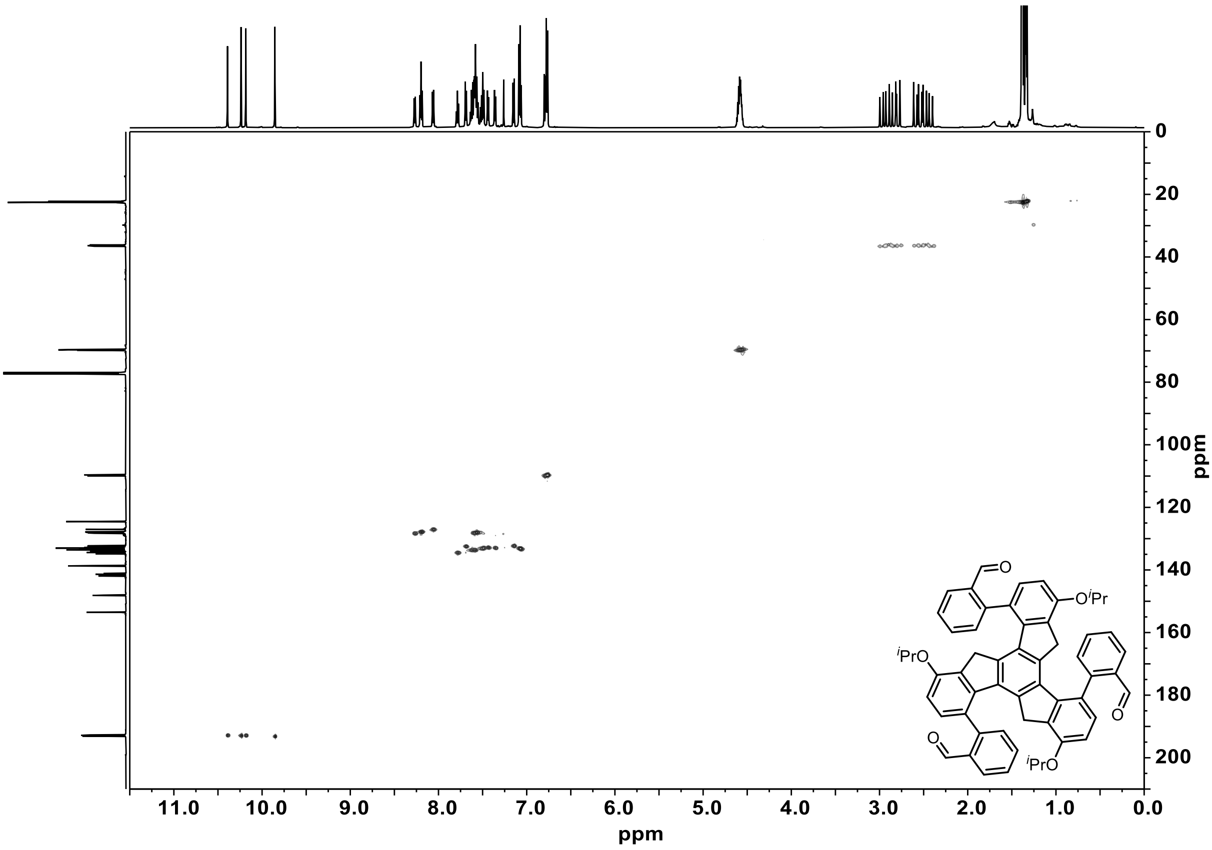

Figure 7.151: ^{1}H-^{13}C HSQC spectrum of **142** (600 MHz, 150 MHz, CDCl$_3$).

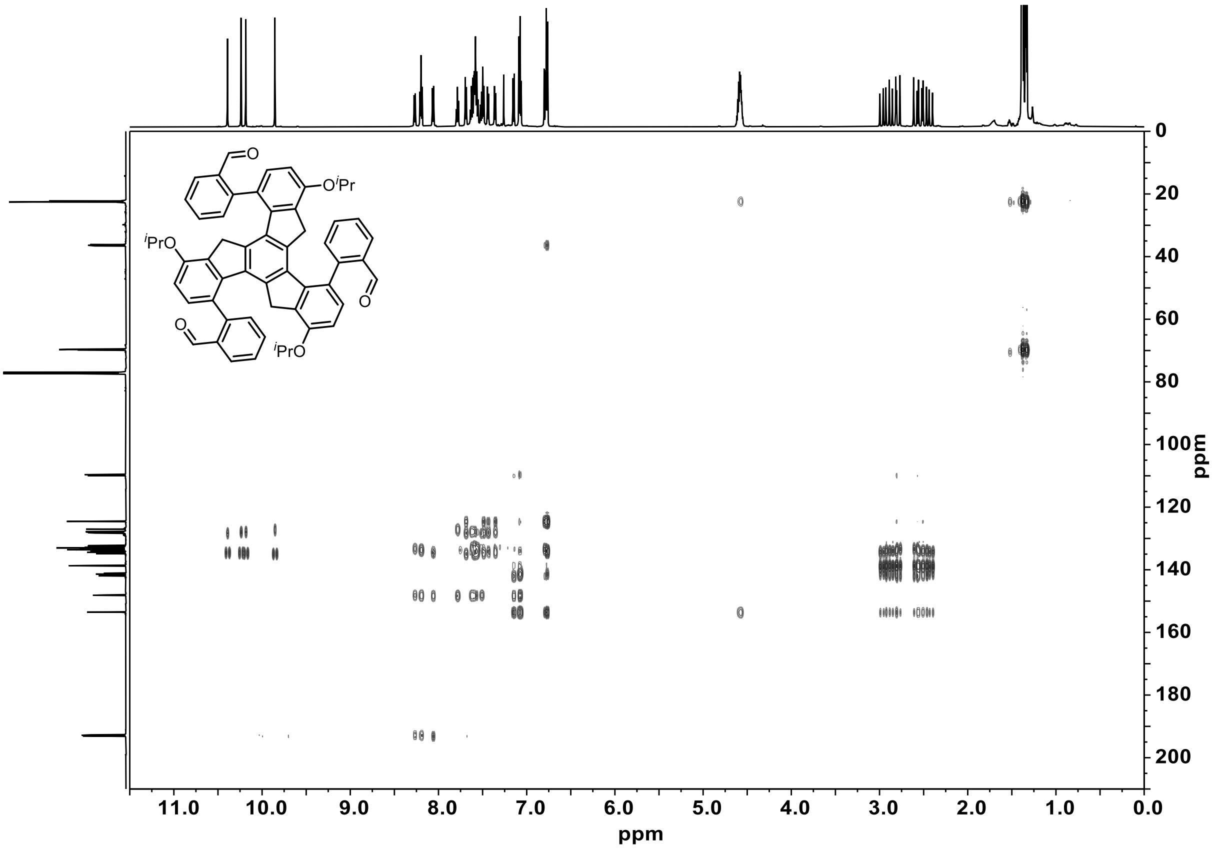

Figure 7.152: ^{1}H-^{13}C HMBC spectrum of **142** (600 MHz, 150 MHz, CDCl$_3$).

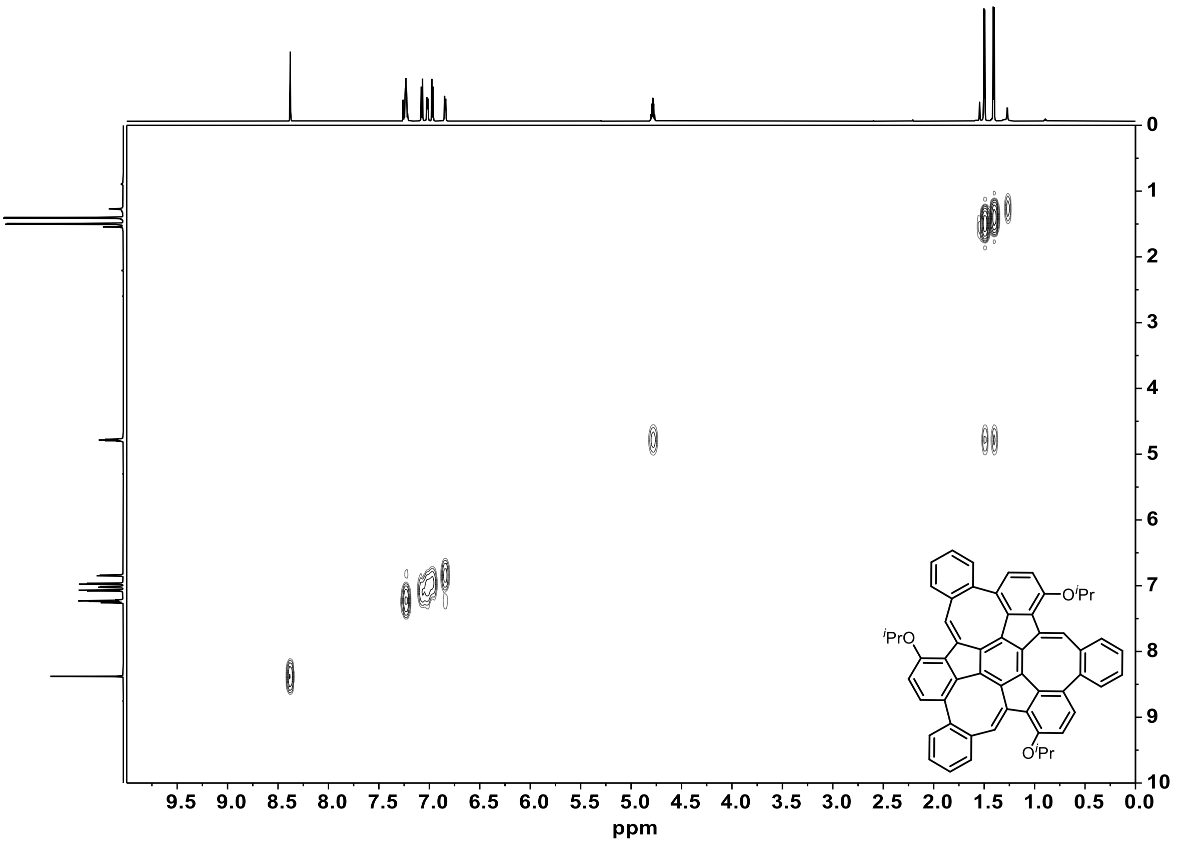

Figure 7.153: ^{1}H-^{1}H COSY spectrum of **141** (700 MHz, CDCl$_3$).

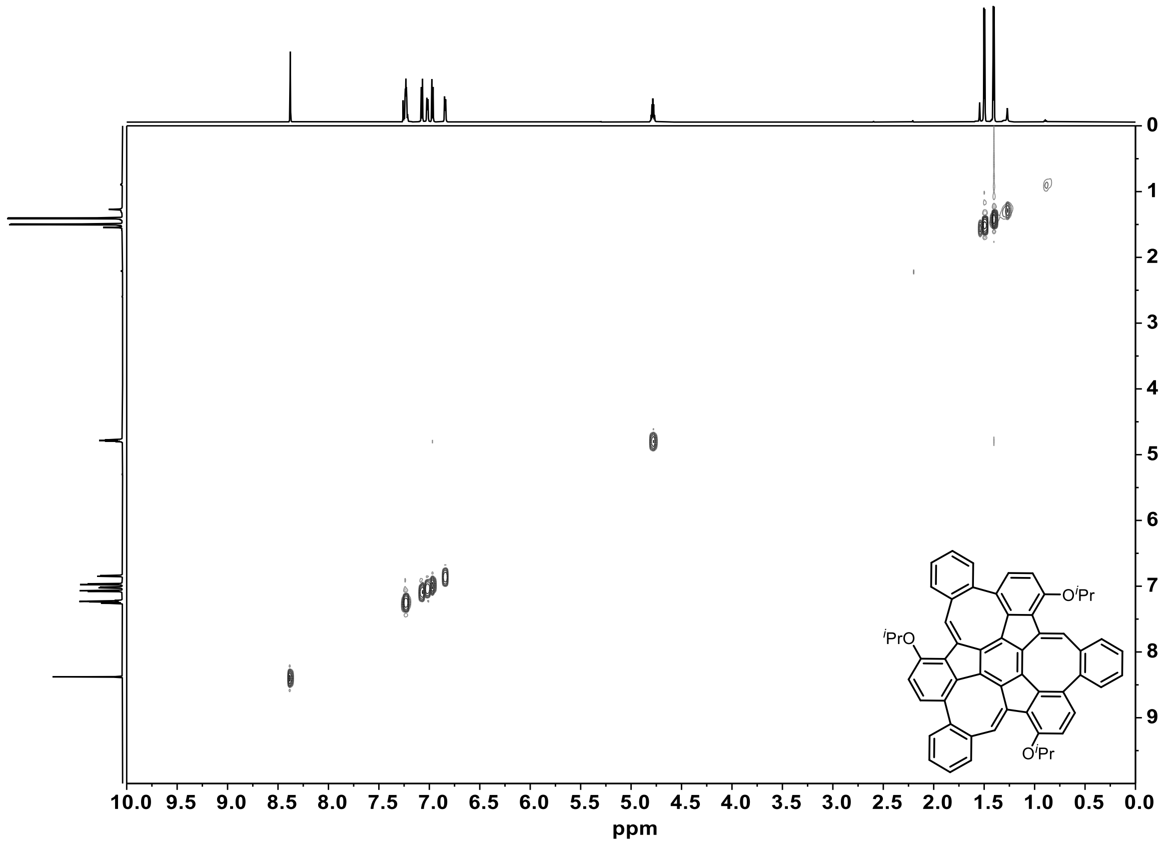

Figure 7.154: ^{1}H-^{1}H NOESY spectrum of **141** (700 MHz, CDCl$_3$).

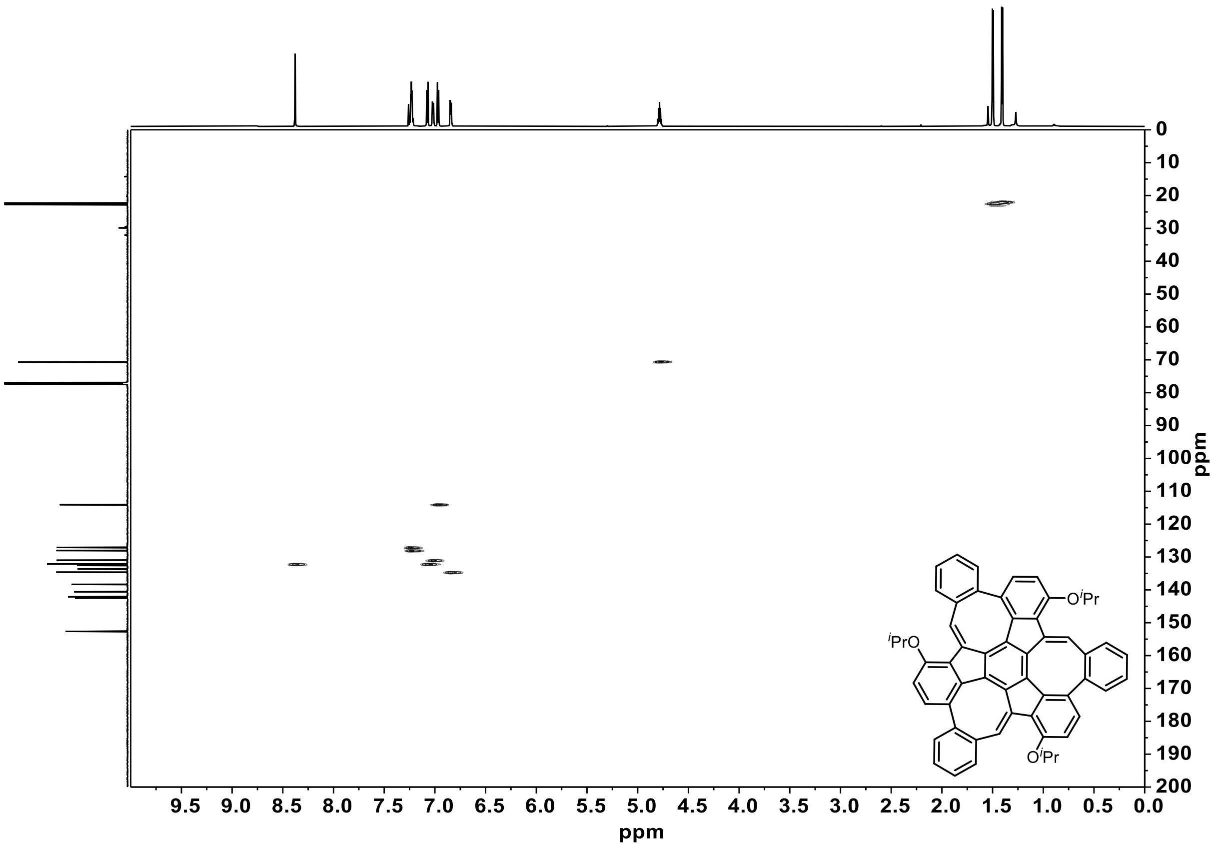

Figure 7.155: ^{1}H-^{13}C HSQC spectrum of **141** (700 MHz, 176 MHz, CDCl$_3$).

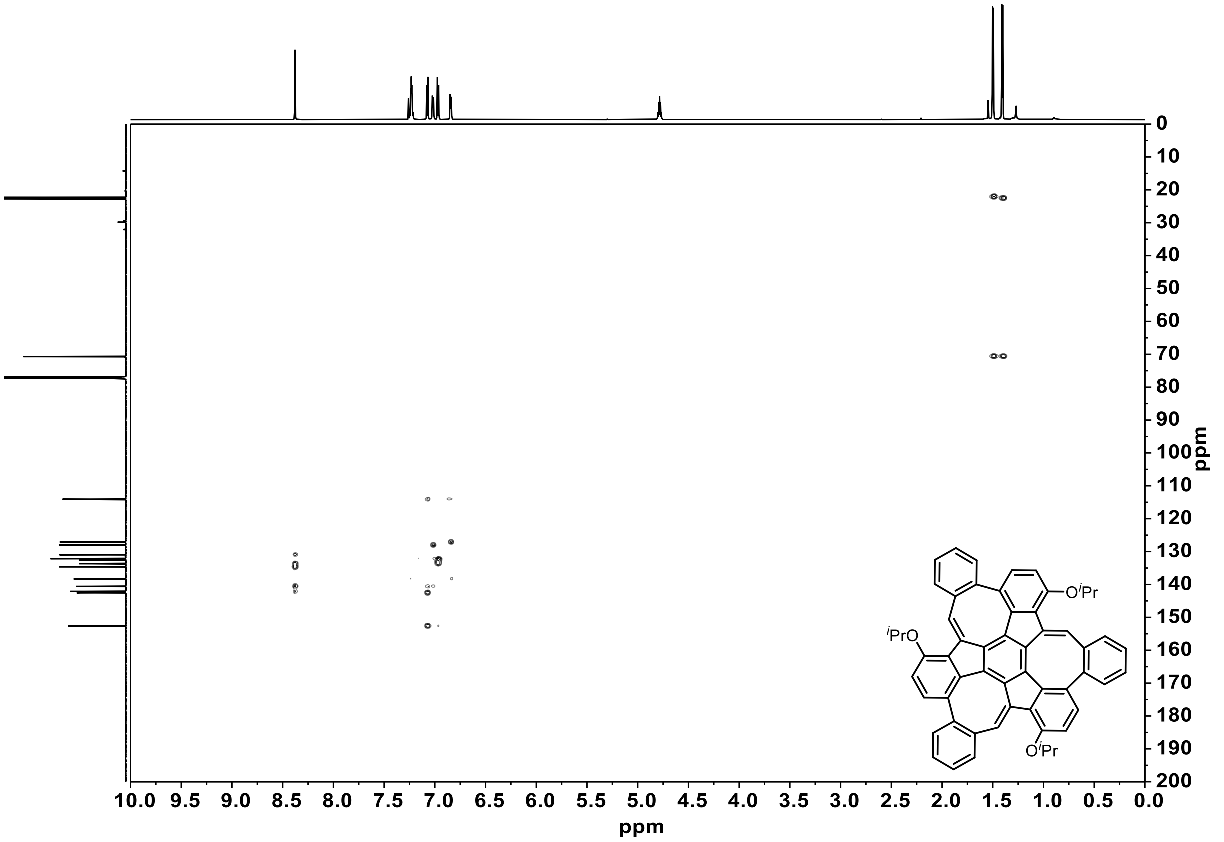

Figure 7.156: ^{1}H-^{13}C HMBC spectrum of **141** (700 MHz, 176 MHz, CDCl$_3$).

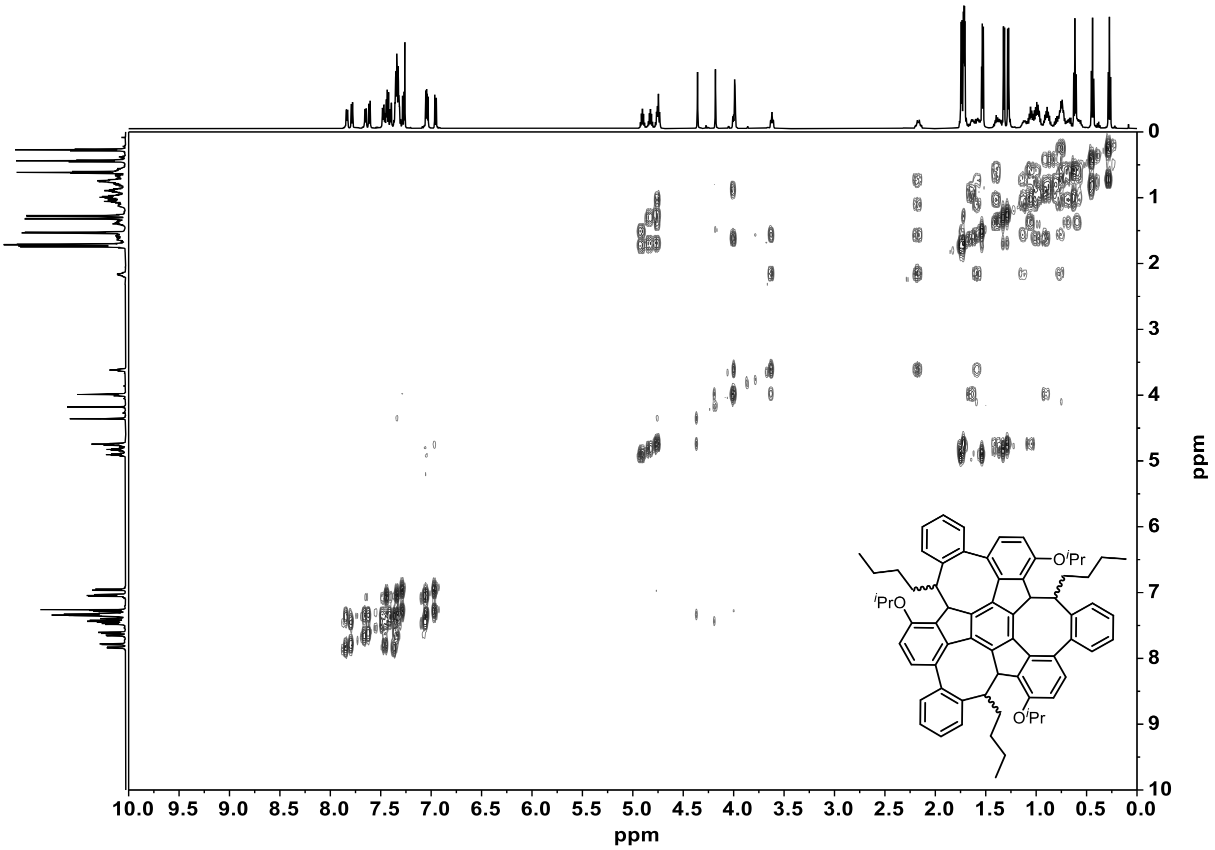

Figure 7.157: ^{1}H-^{1}H COSY spectrum of **150-*anti*** (600 MHz, CDCl$_3$).

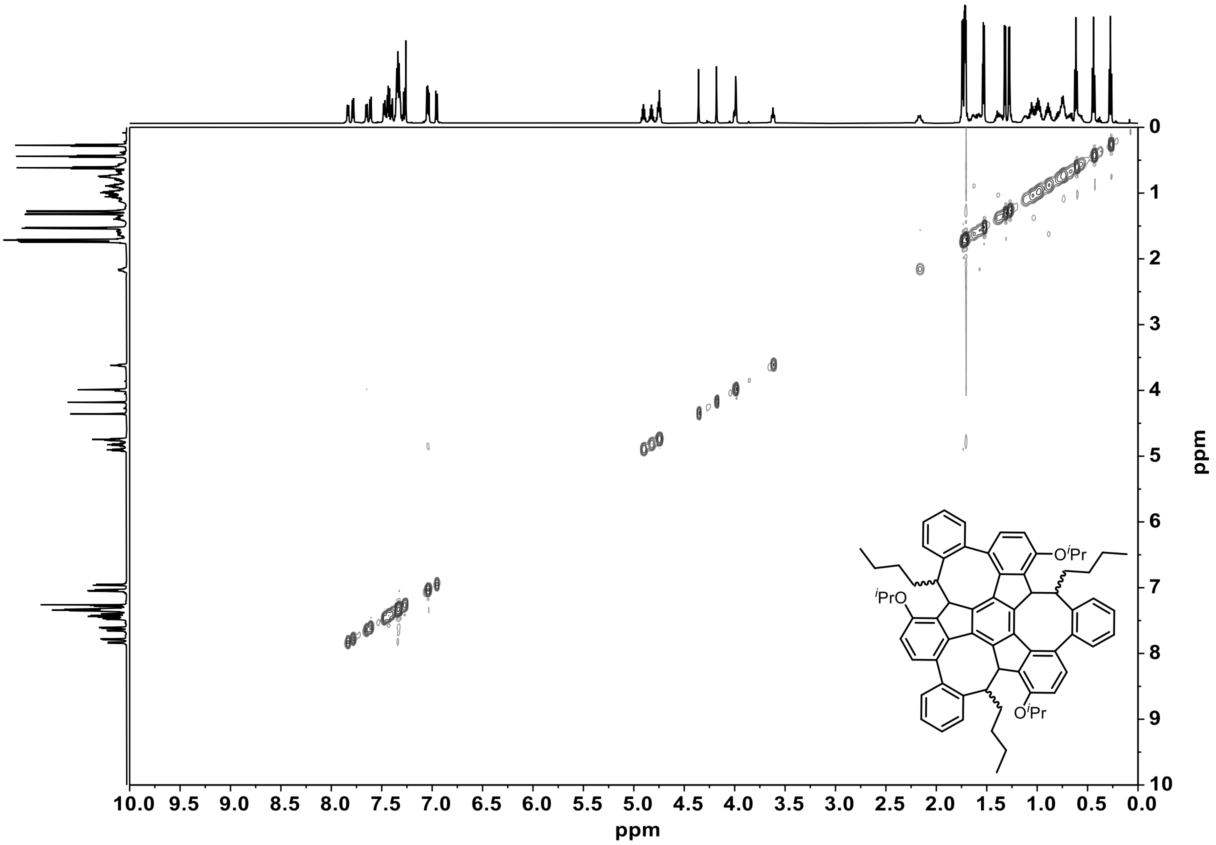

Figure 7.158: ^{1}H-^{1}H NOESY spectrum of **150-*anti*** (600 MHz, CDCl$_3$).

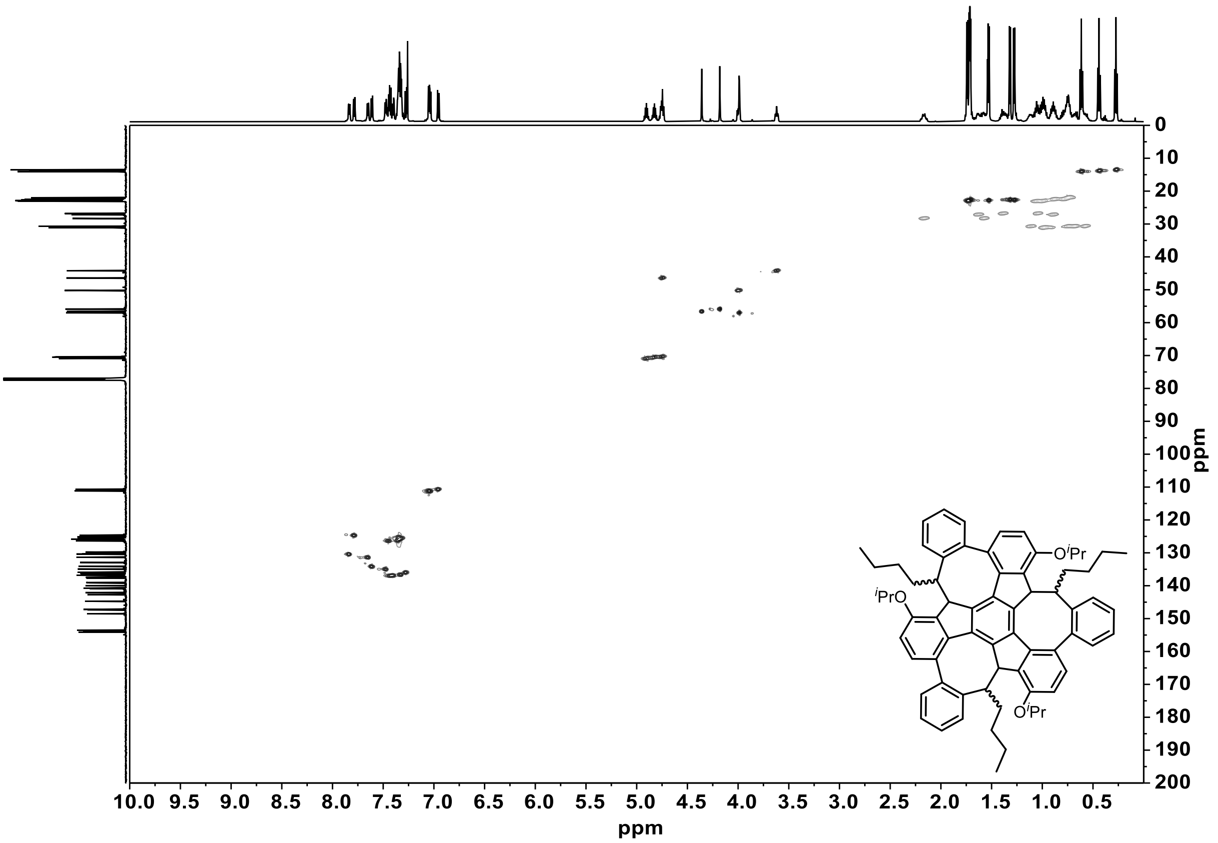

Figure 7.159: ^{1}H-^{13}C HSQC spectrum of **150-*anti*** (600 MHz, 150 MHz, CDCl$_3$).

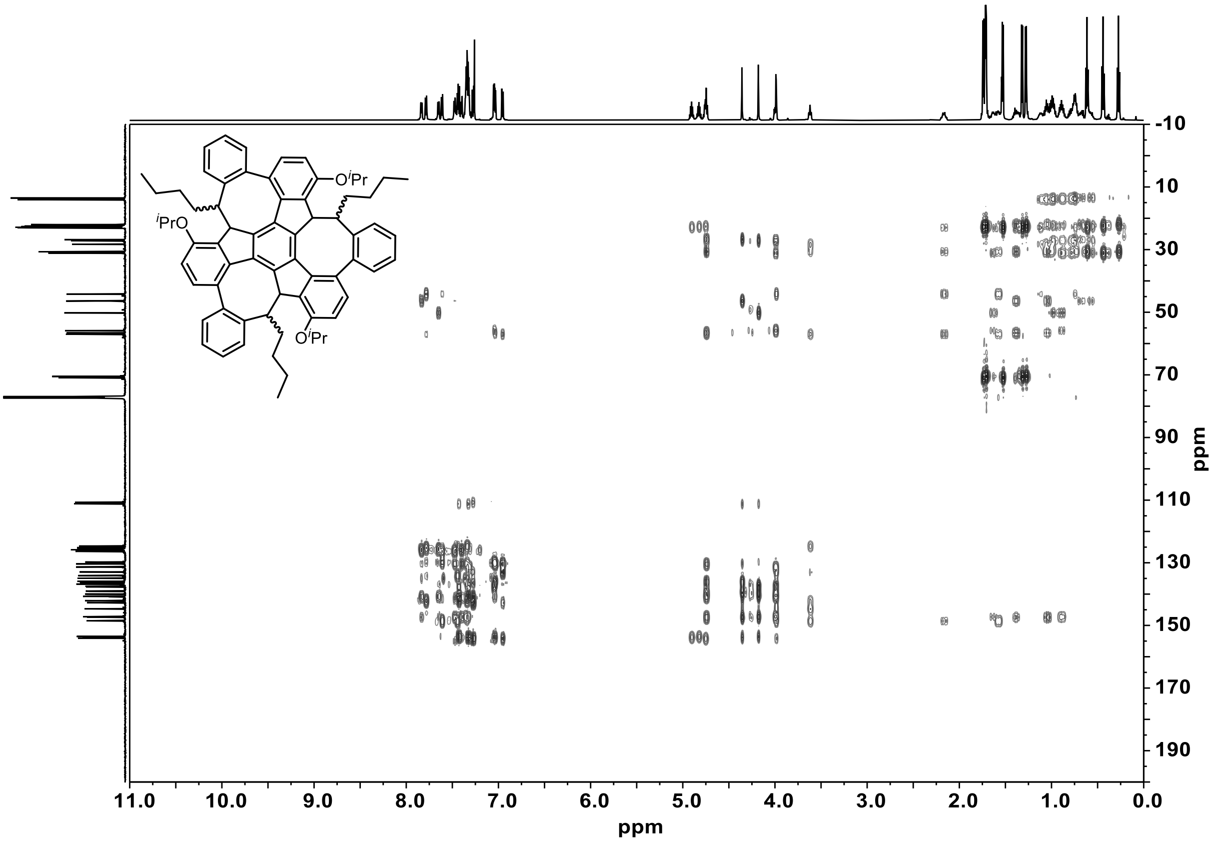

Figure 7.160: ^{1}H-^{13}C HMBC spectrum of **150-*anti*** (600 MHz, 150 MHz, CDCl$_3$).

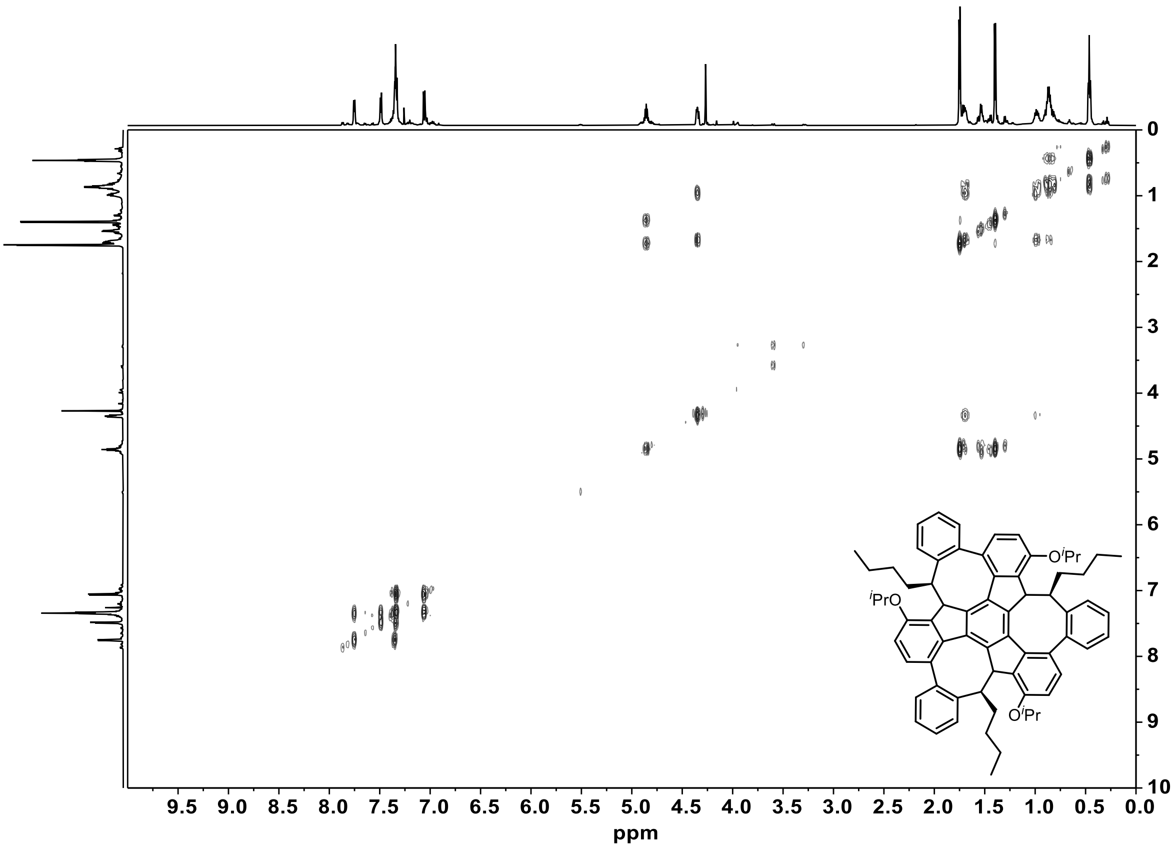

Figure 7.161: ^{1}H-^{1}H COSY spectrum of **150-*syn*** (600 MHz, CDCl₃).

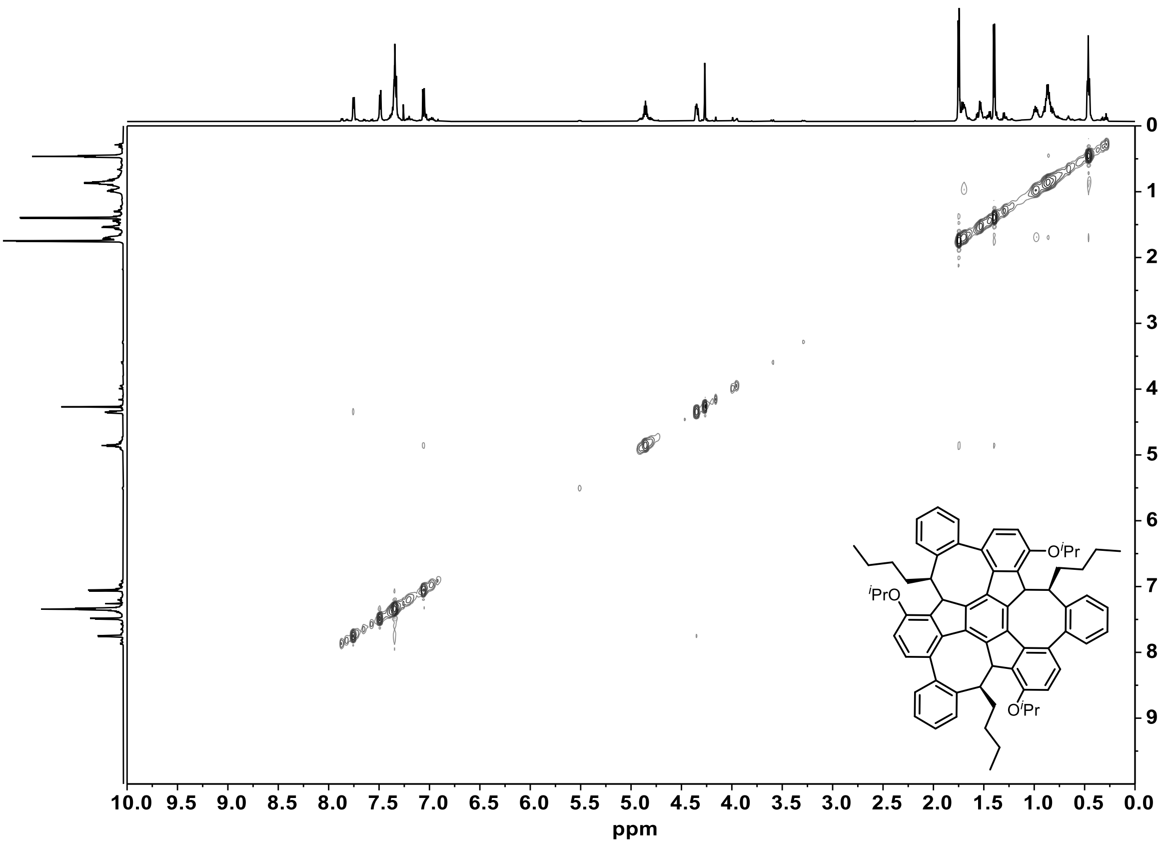

Figure 7.162: ^{1}H-^{1}H NOESY spectrum of **150-*syn*** (600 MHz, CDCl₃).

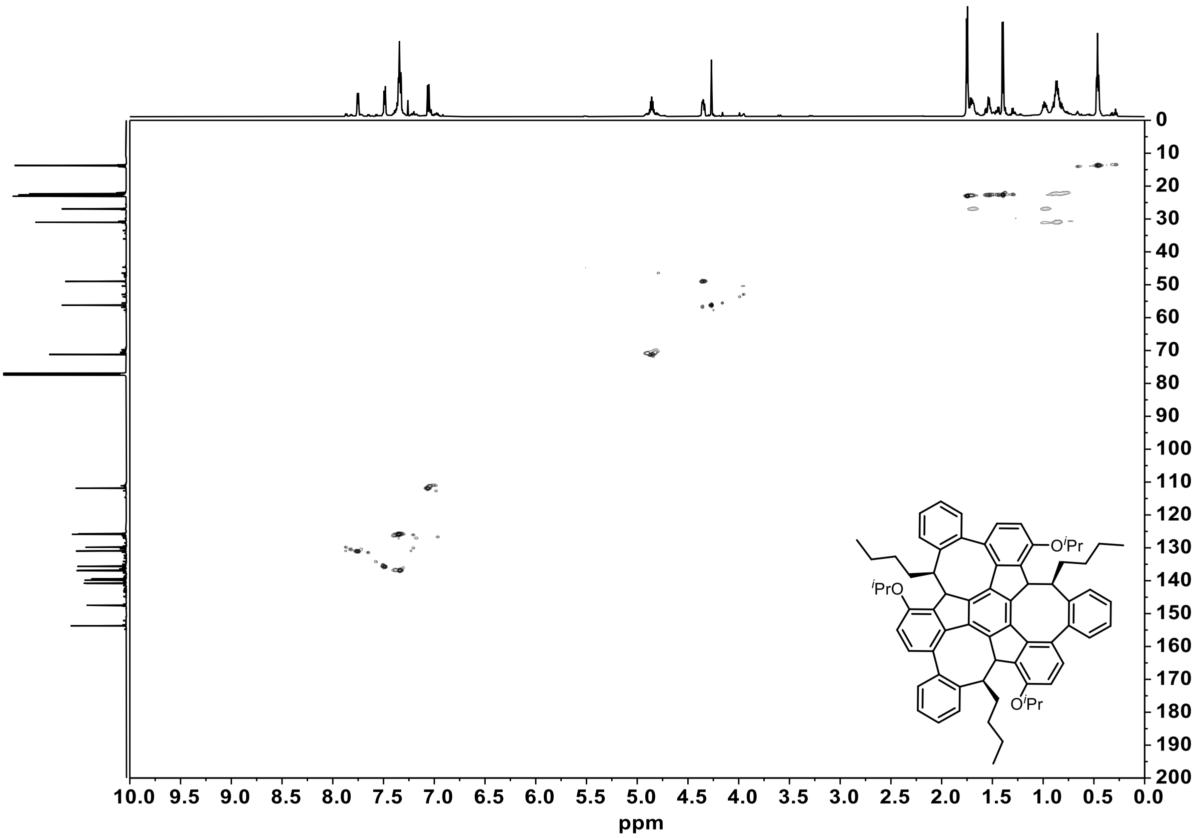

Figure 7.163: ^{1}H-^{13}C HSQC spectrum of **150-*syn*** (600 MHz, 150 MHz, CDCl$_3$).

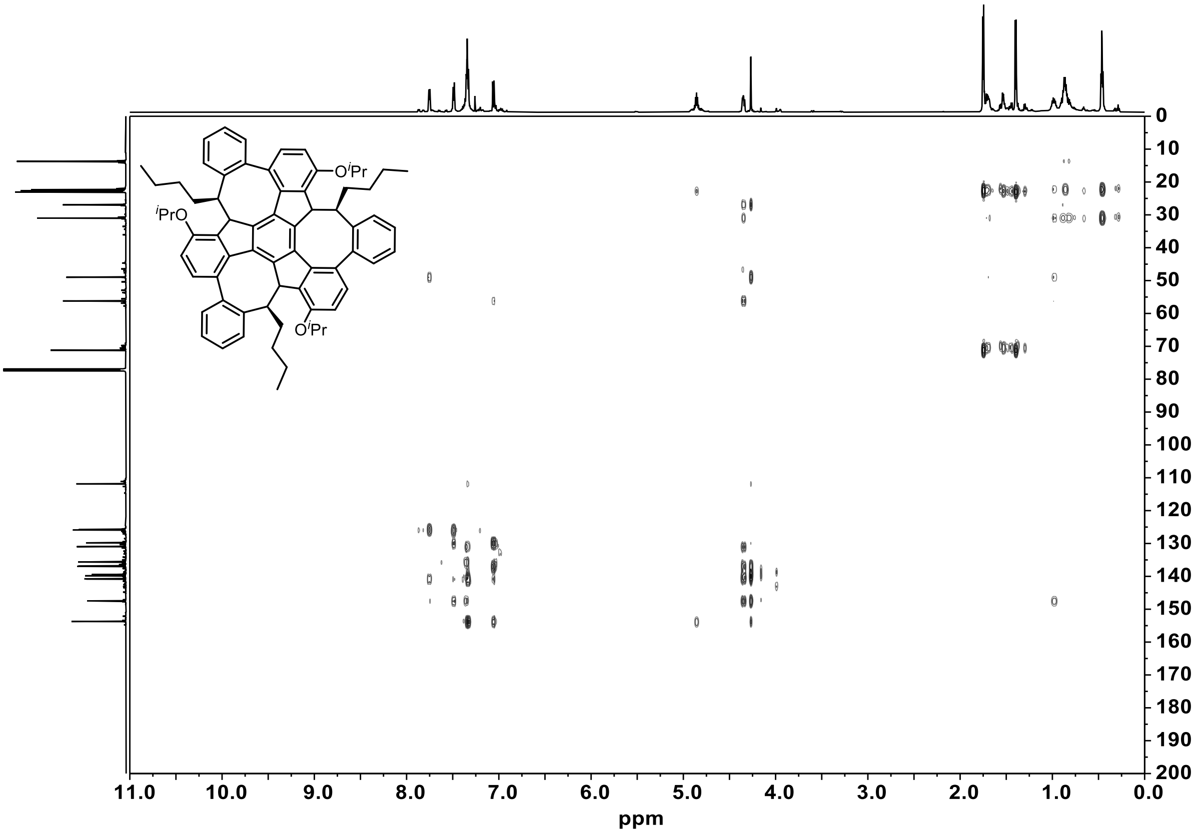

Figure 7.164: ^{1}H-^{13}C HMBC spectrum of **150-*syn*** (600 MHz, 150 MHz, CDCl$_3$).

7.5 IR Spectra

IR spectra of compounds **120**, **121**, **122**, **123**, and **125** can be found in reference 186; those of **154**, **155**, **159**, **160**, **161**, **152**, and **166** are reported in reference 306.

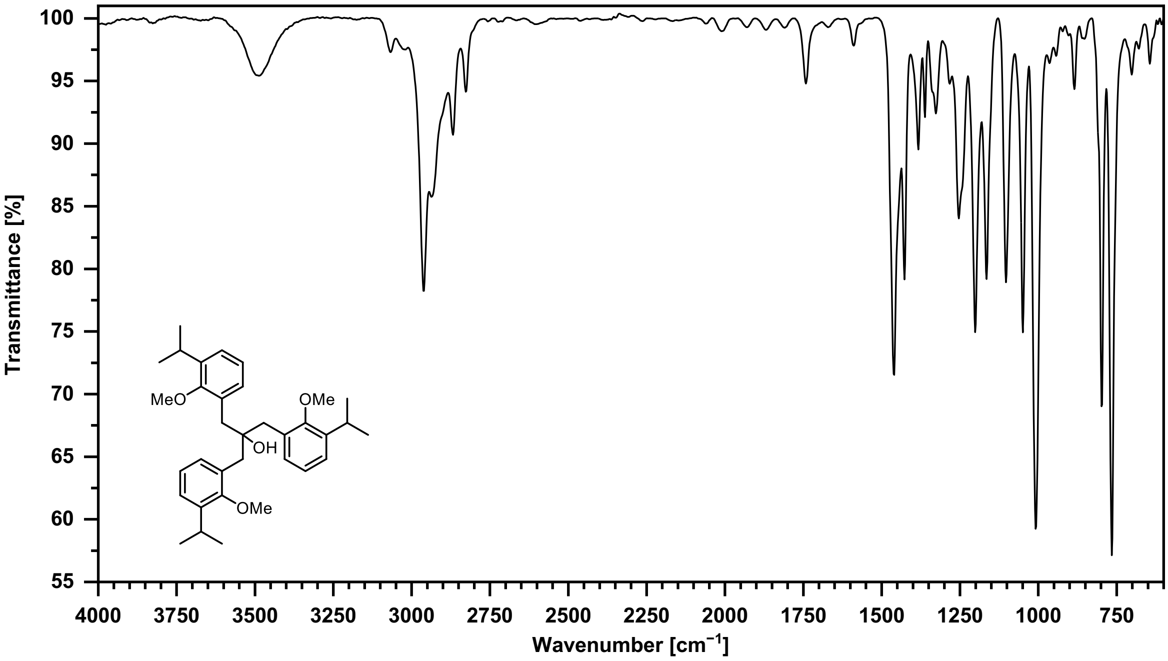

Figure 7.165: IR spectrum of compound **92**.

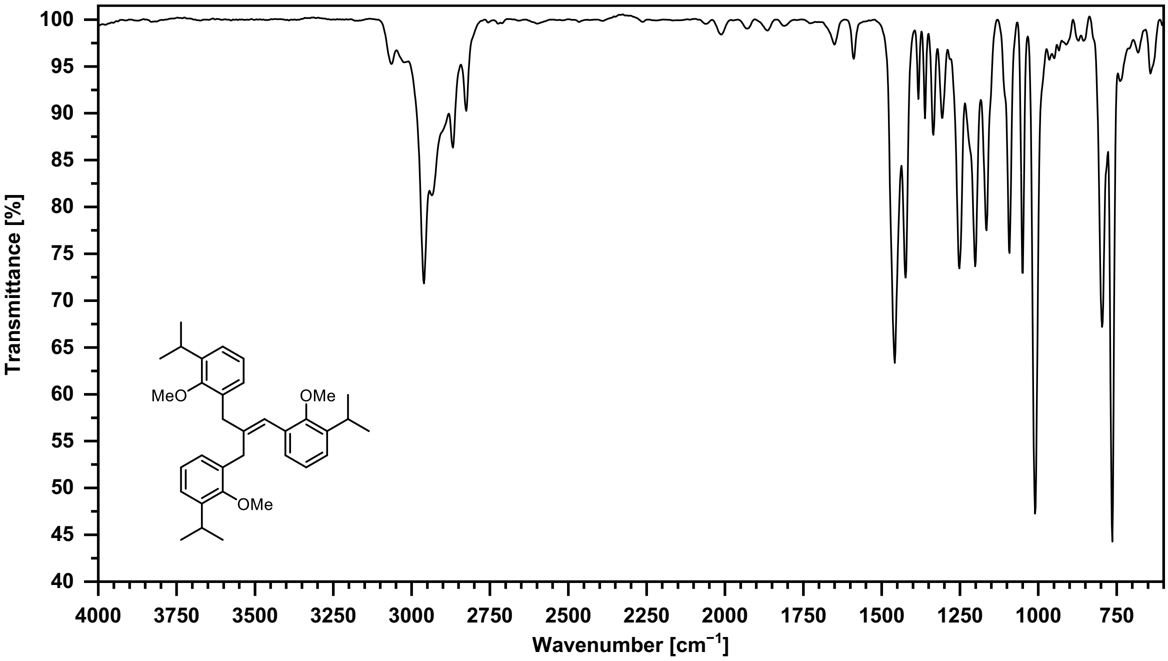

Figure 7.166: IR spectrum of compound **93**.

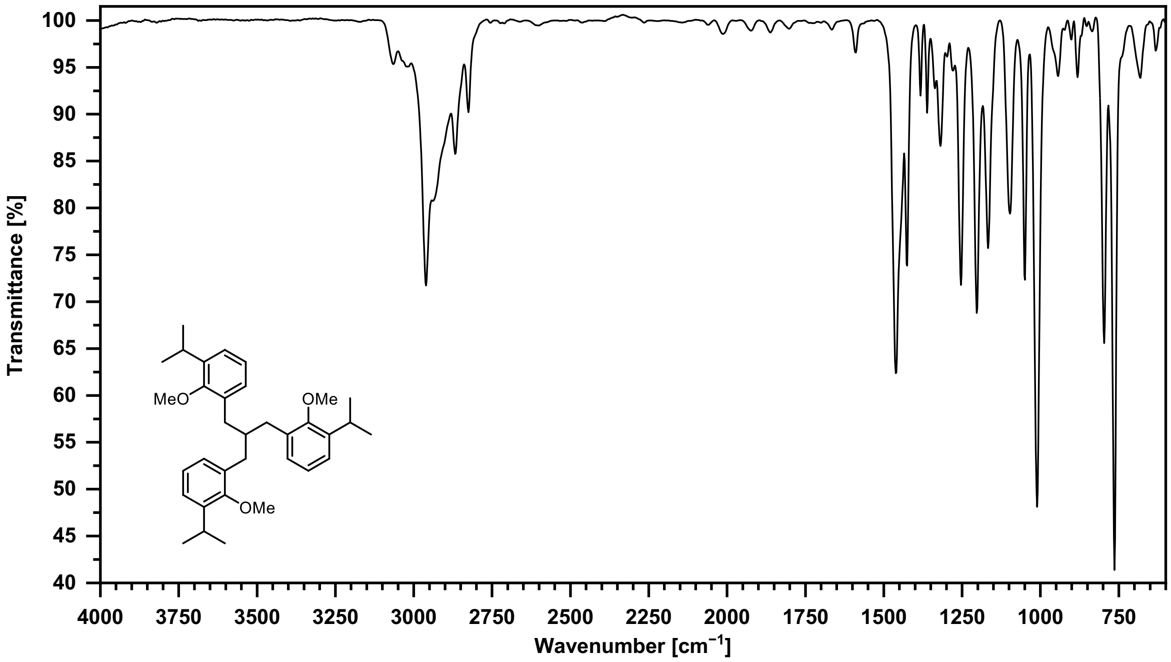

Figure 7.167: IR spectrum of compound **94**.

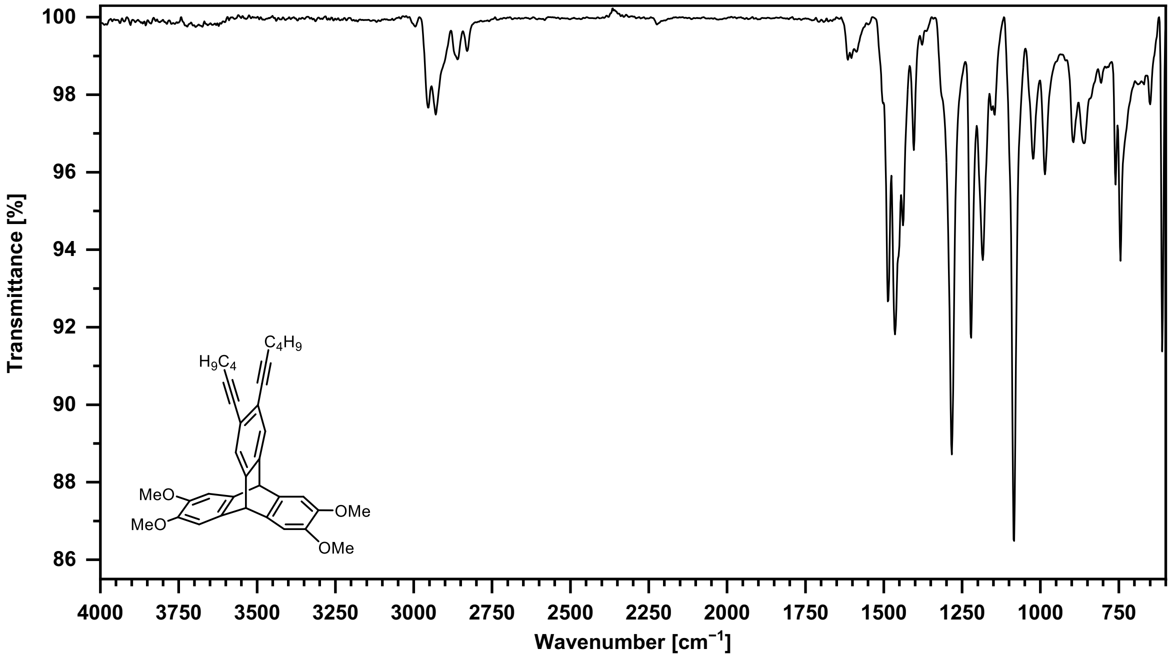

Figure 7.168: IR spectrum of compound **98**.

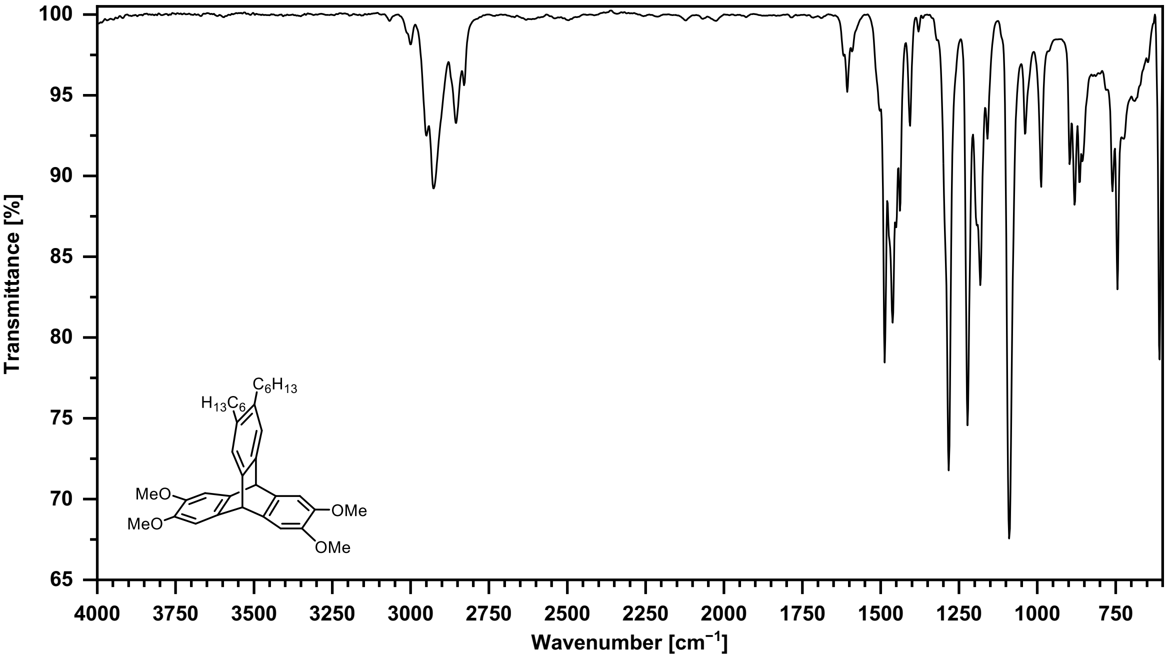

Figure 7.169: IR spectrum of compound **99**.

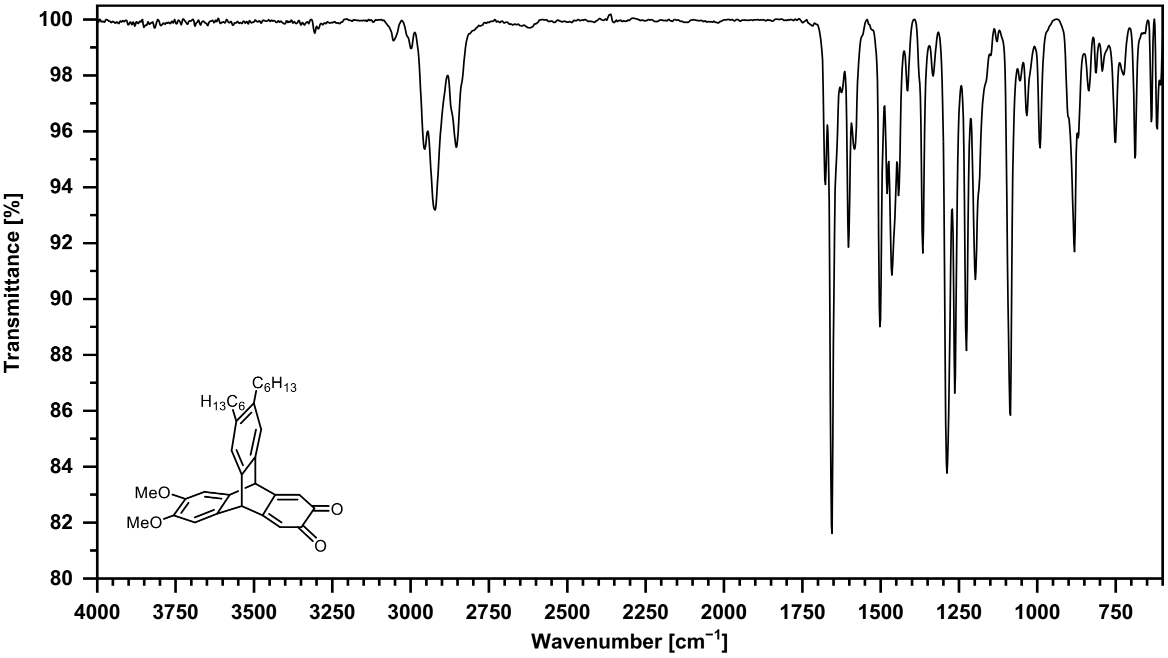

Figure 7.170: IR spectrum of compound **100**.

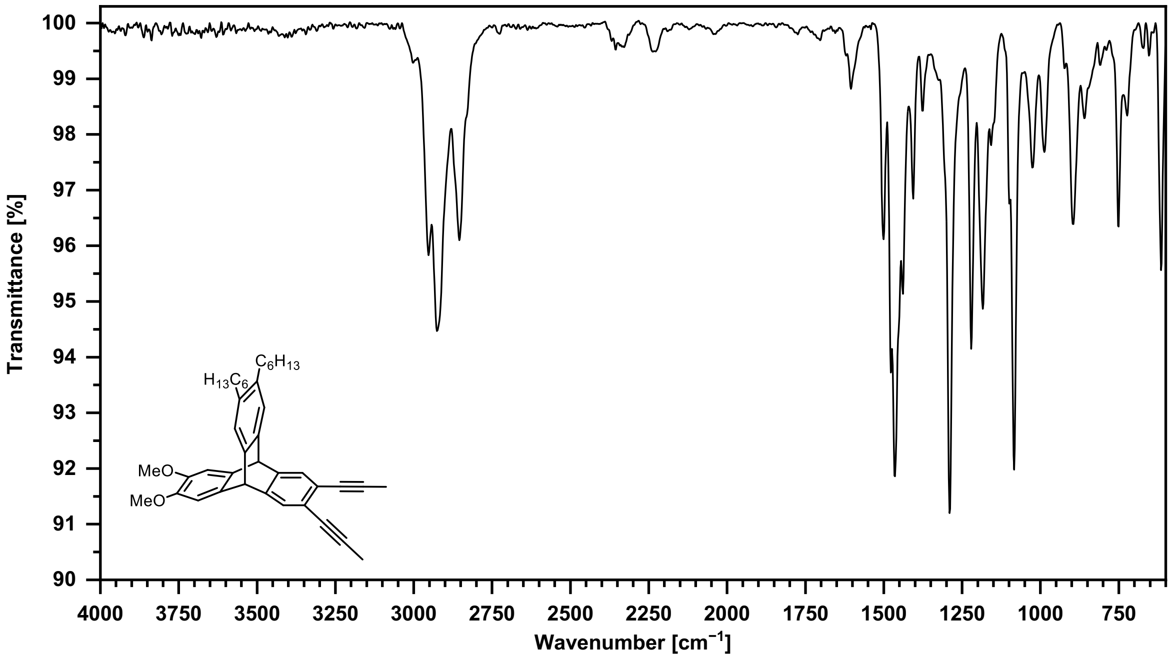

Figure 7.171: IR spectrum of compound **101**.

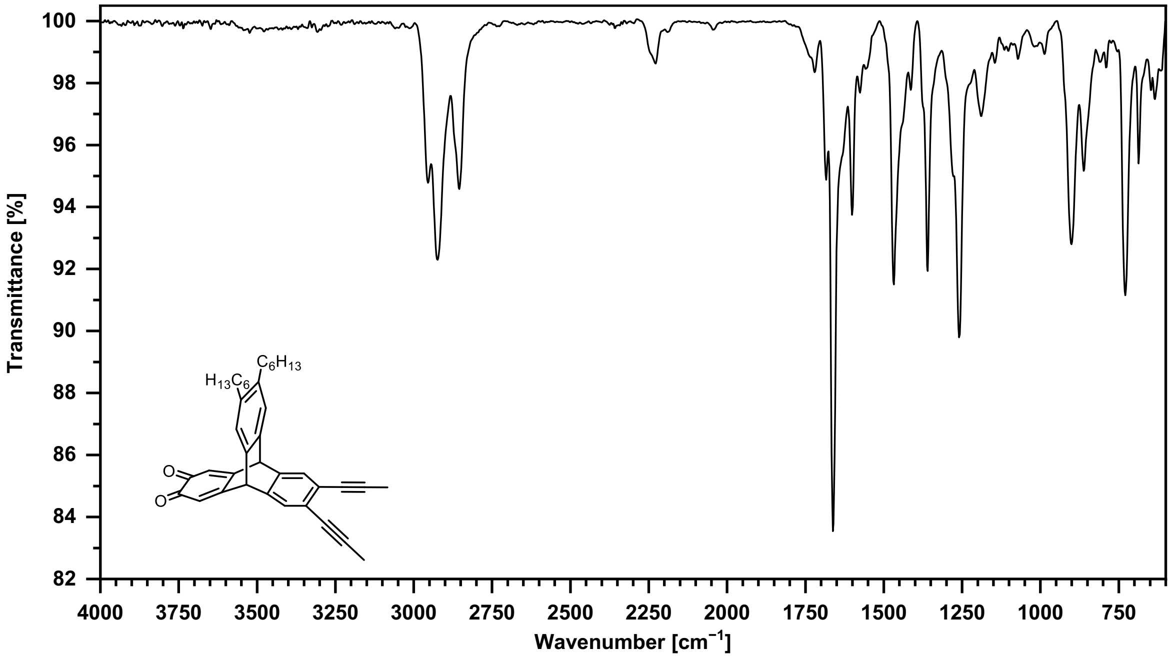

Figure 7.172: IR spectrum of compound **102**.

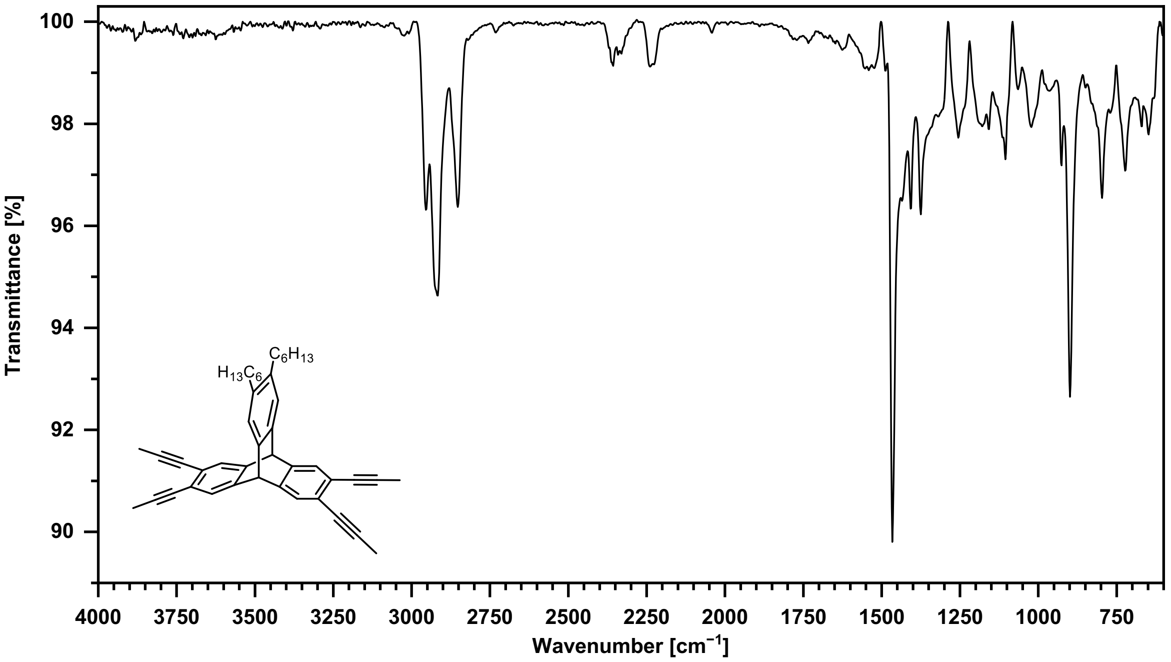

Figure 7.173: IR spectrum of compound **75**.

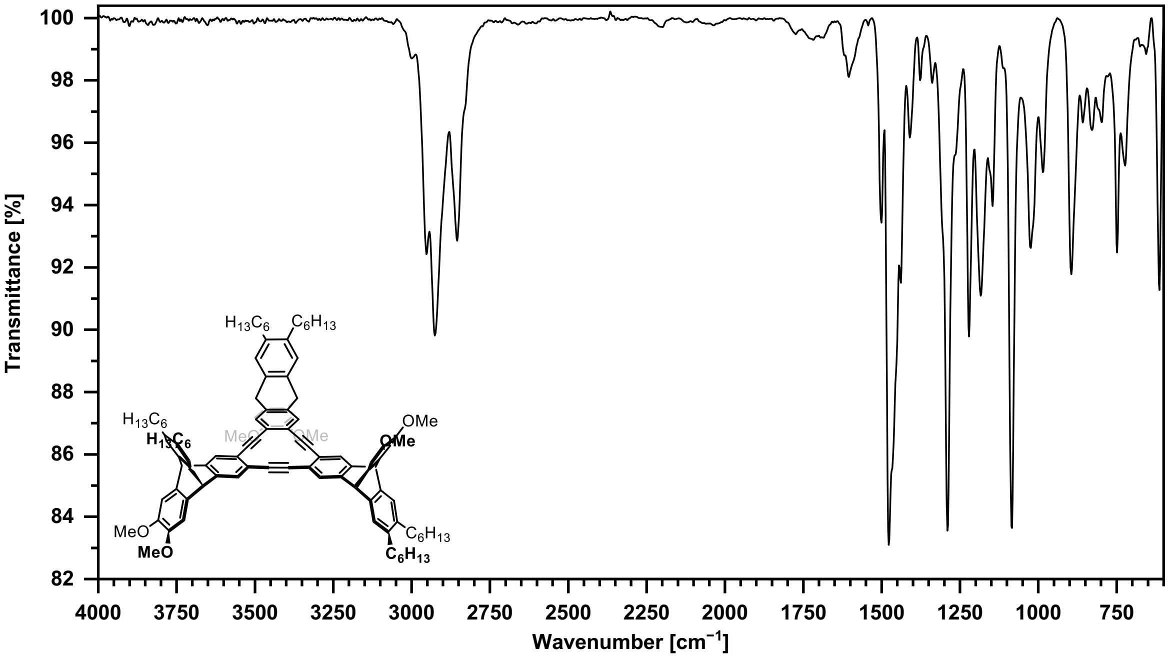

Figure 7.174: IR spectrum of compound **103a**.

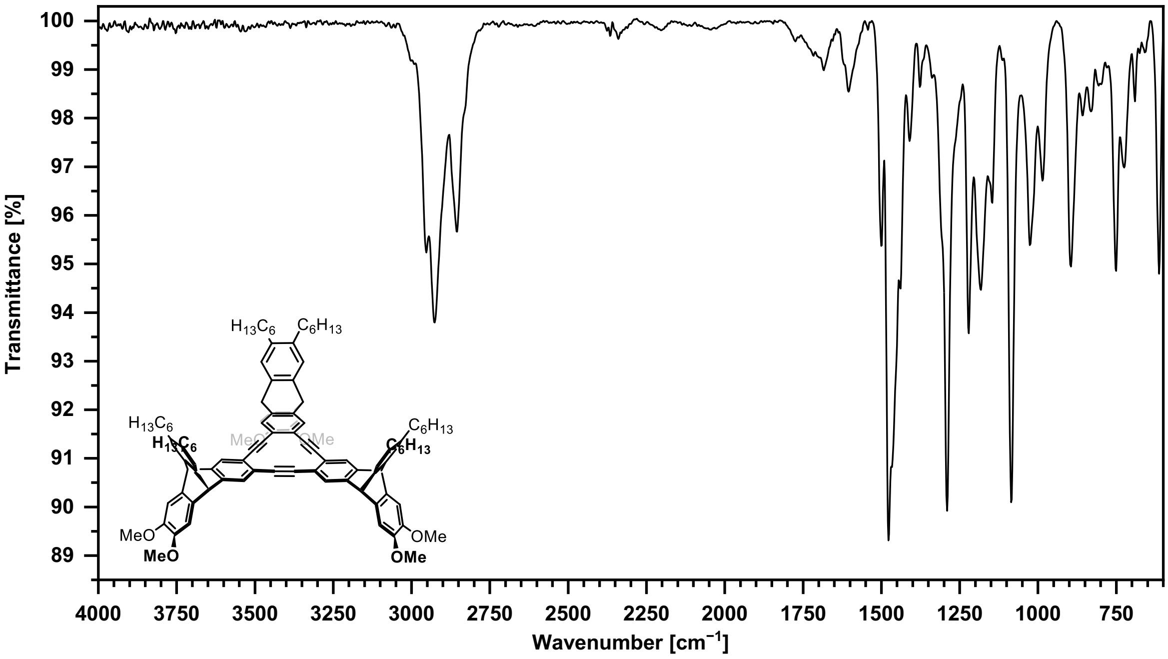

Figure 7.175: IR spectrum of compound **103b**.

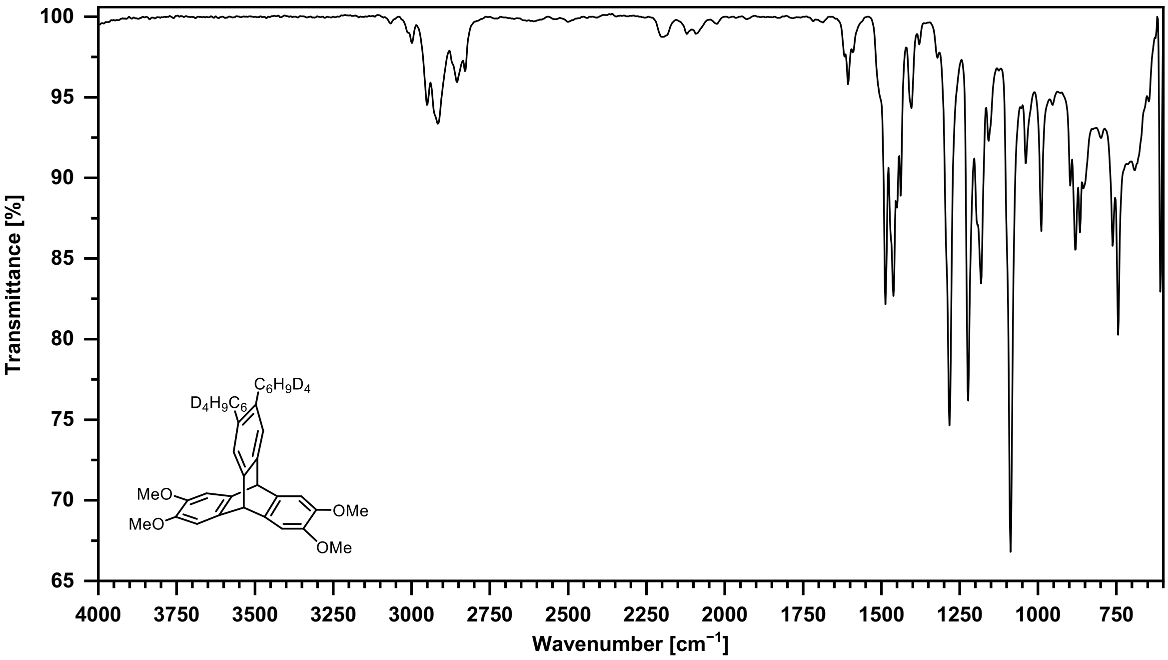

Figure 7.176: IR spectrum of compound **99-*d*$_8$**.

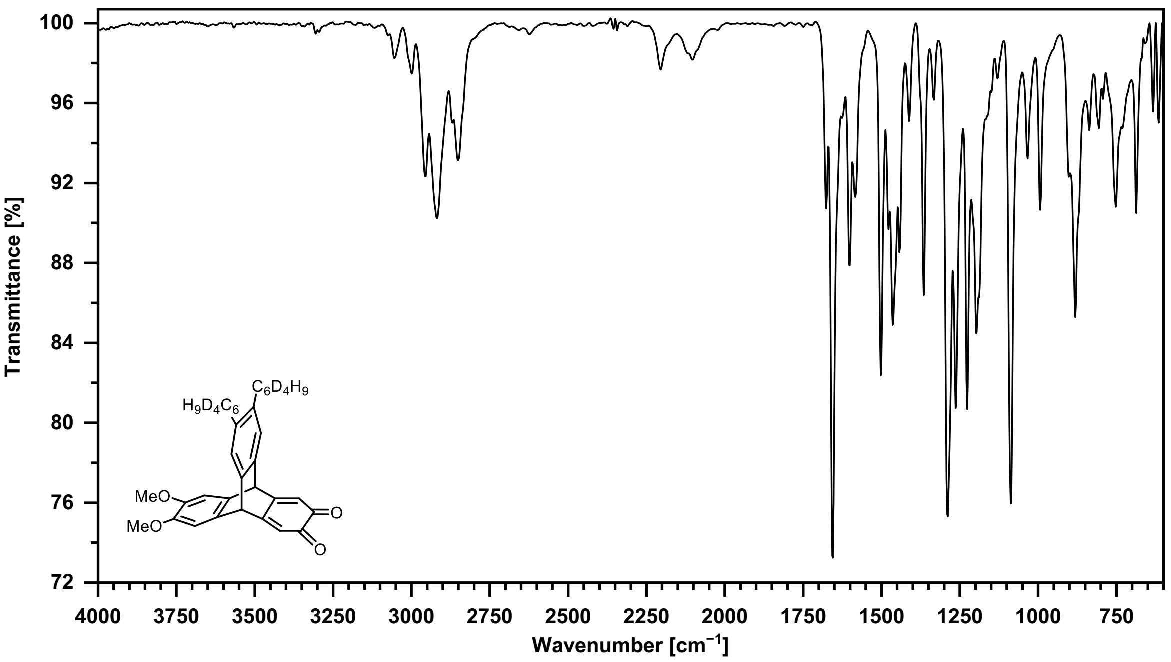

Figure 7.177: IR spectrum of compound **100-d_8**.

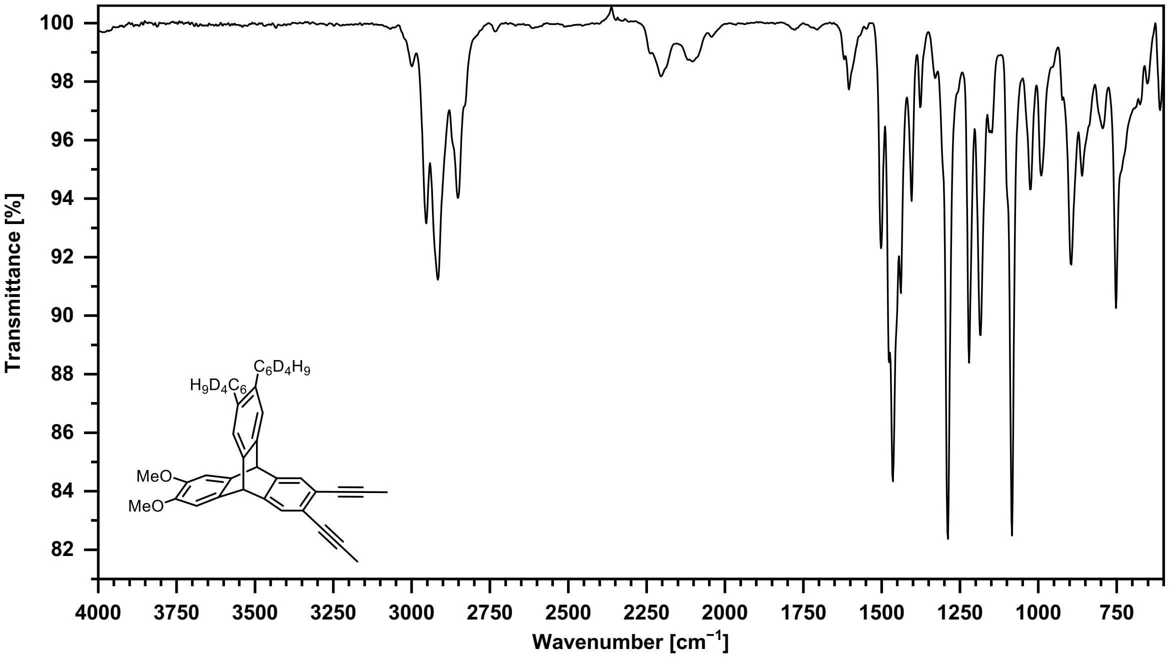

Figure 7.178: IR spectrum of compound **101-d_8**.

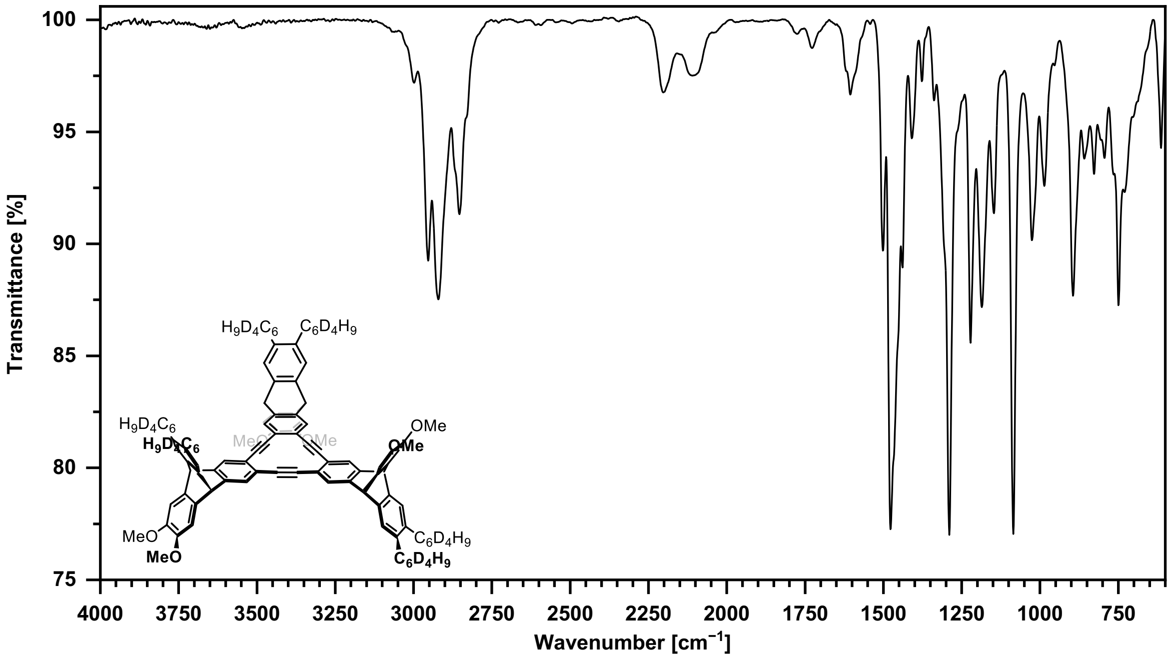

Figure 7.179: IR spectrum of compound **103a-*d*₂₄**.

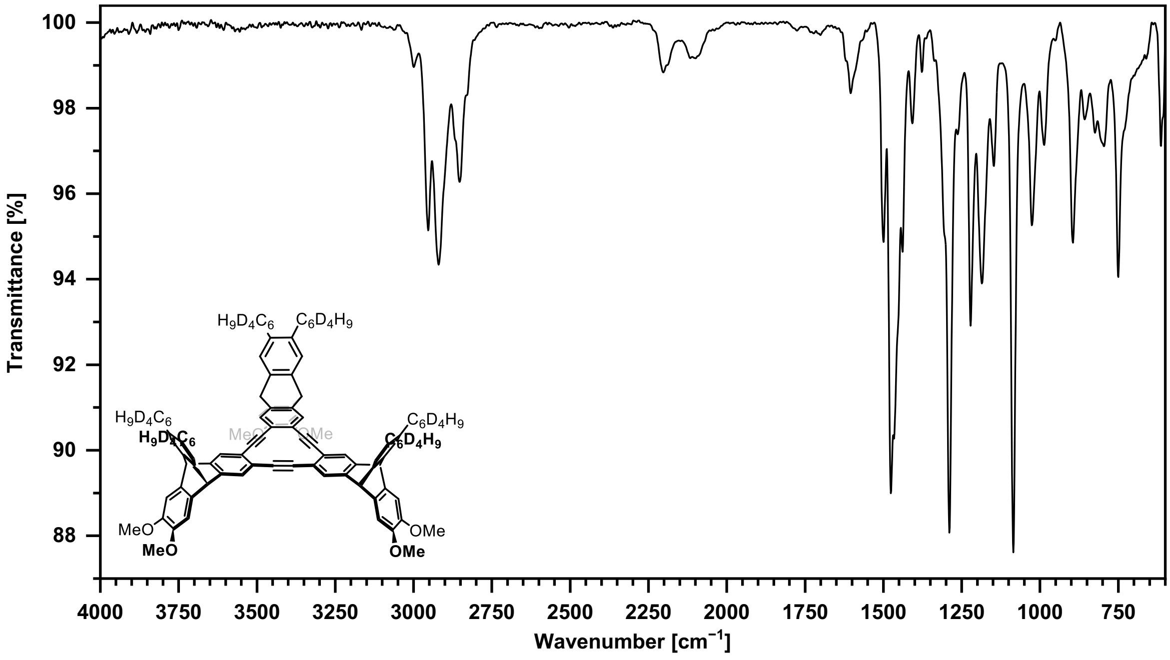

Figure 7.180: IR spectrum of compound **103b-*d*₂₄**.

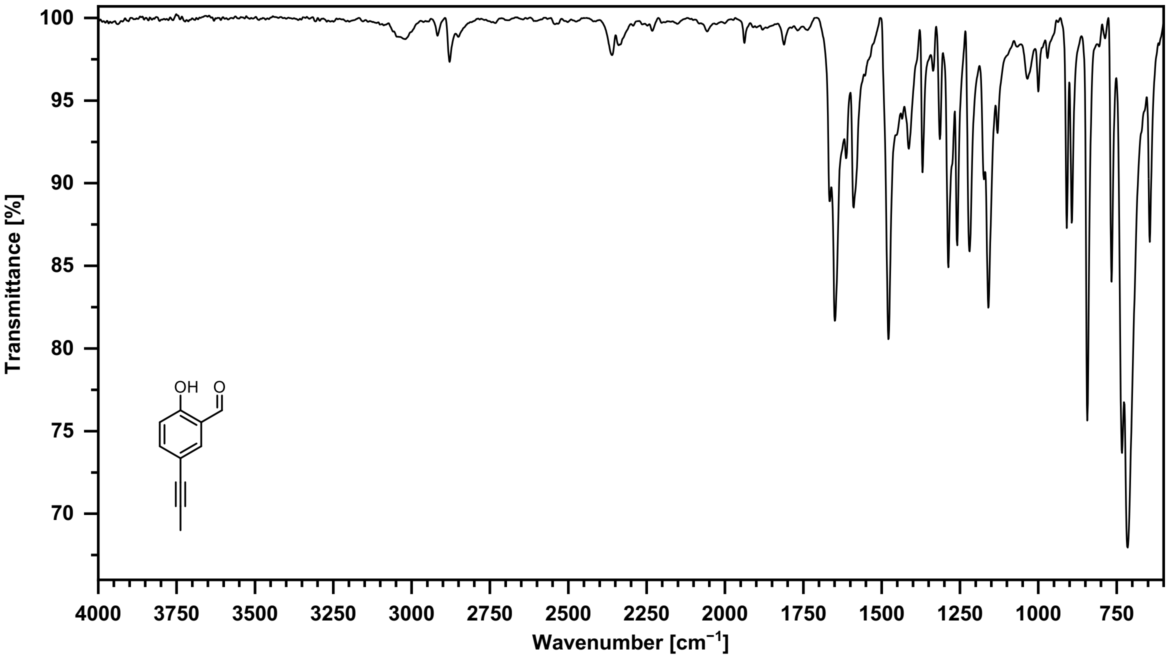

Figure 7.181: IR spectrum of compound **111**.

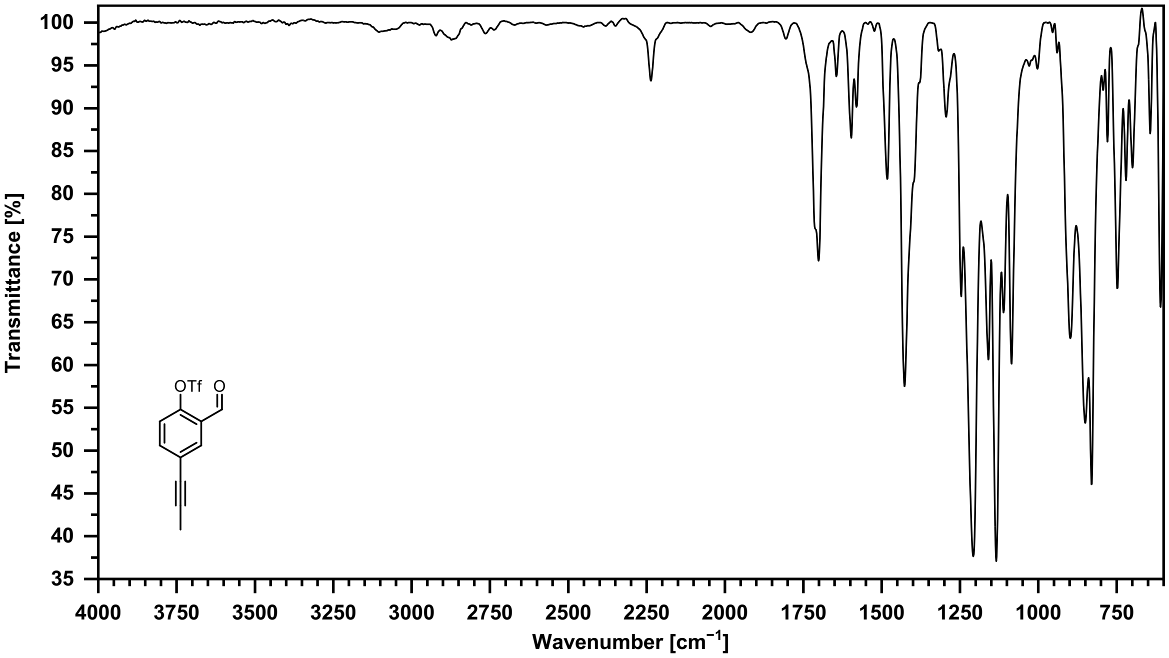

Figure 7.182: IR spectrum of compound **112**.

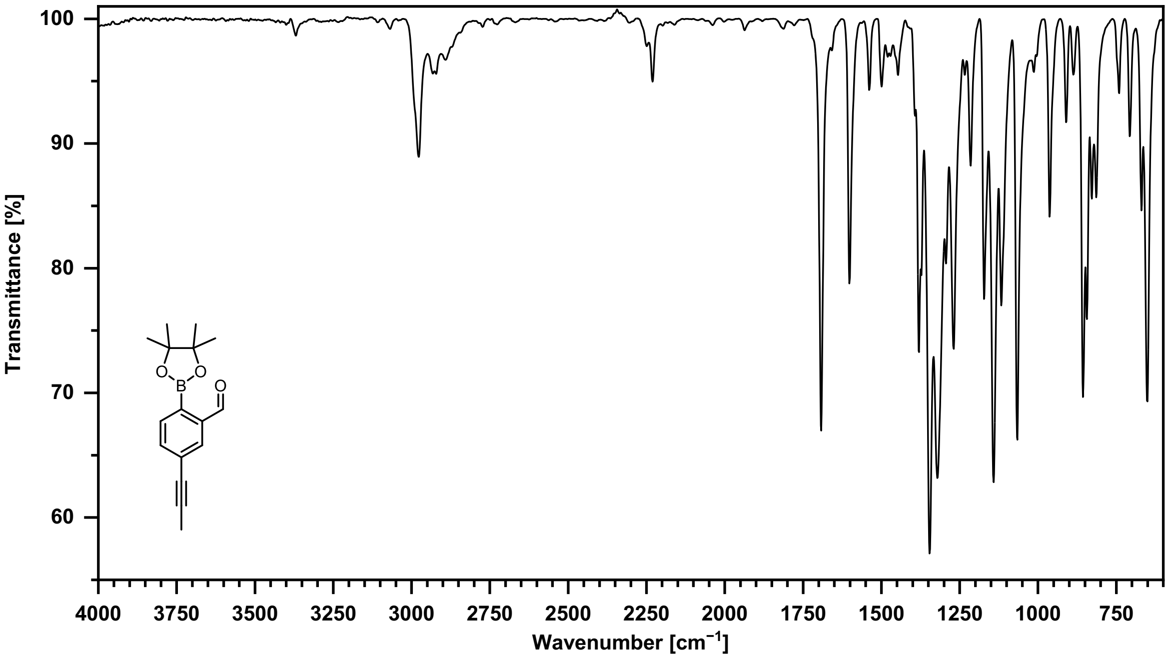

Figure 7.183: IR spectrum of compound **113**.

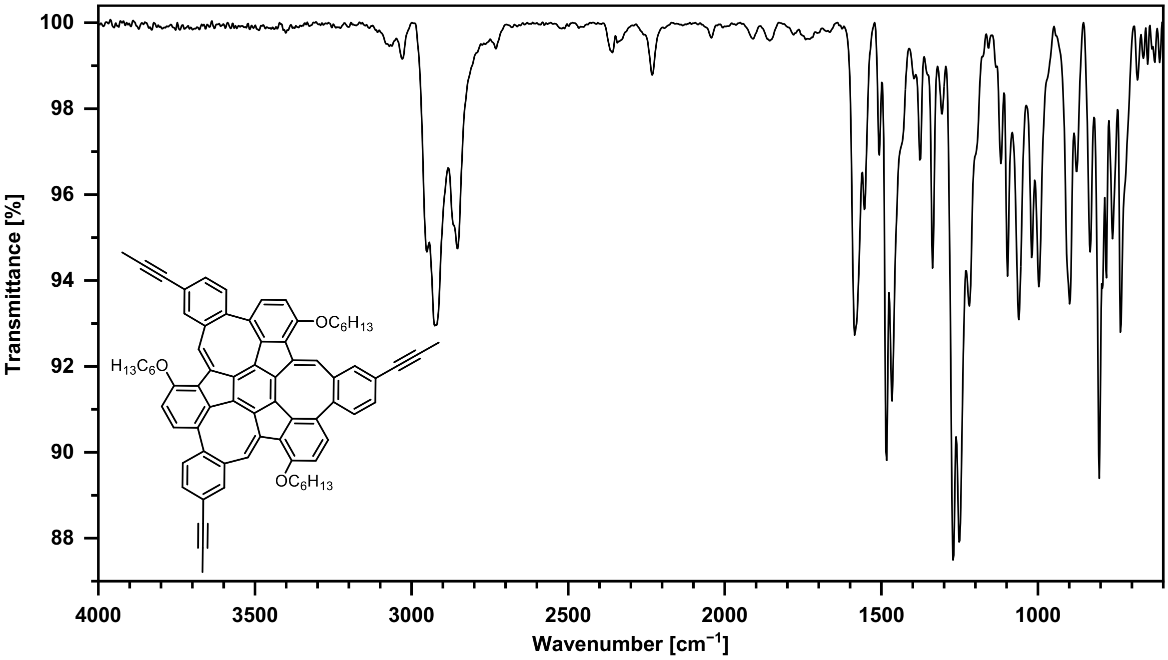

Figure 7.184: IR spectrum of compound **116**.

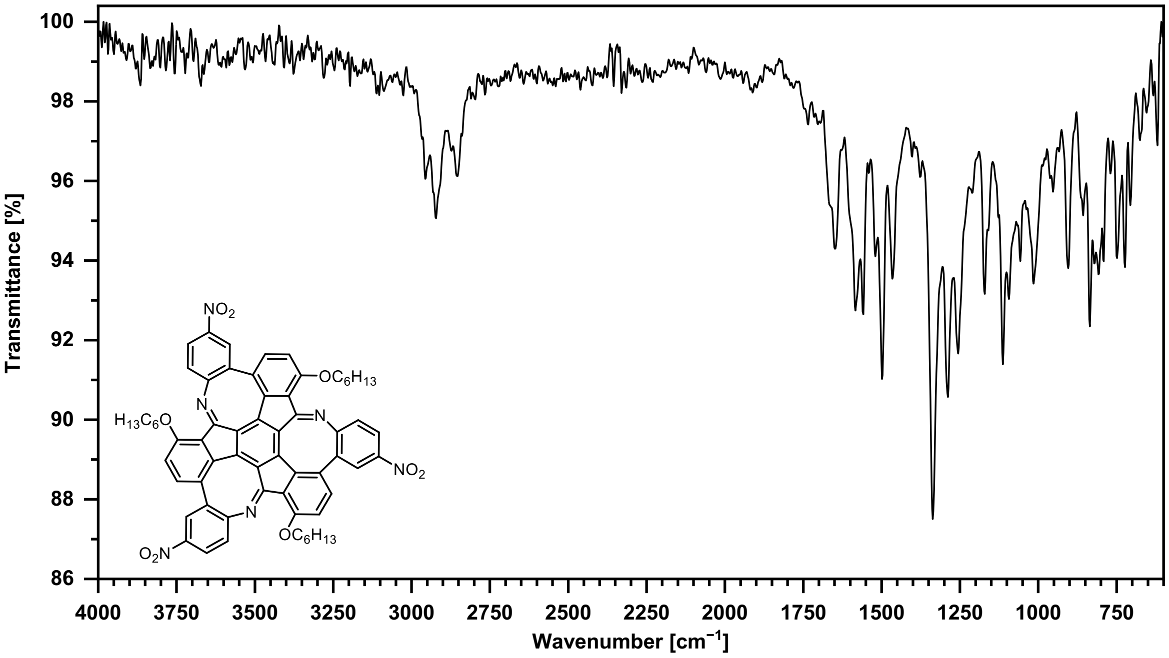

Figure 7.185: IR spectrum of compound **131**.

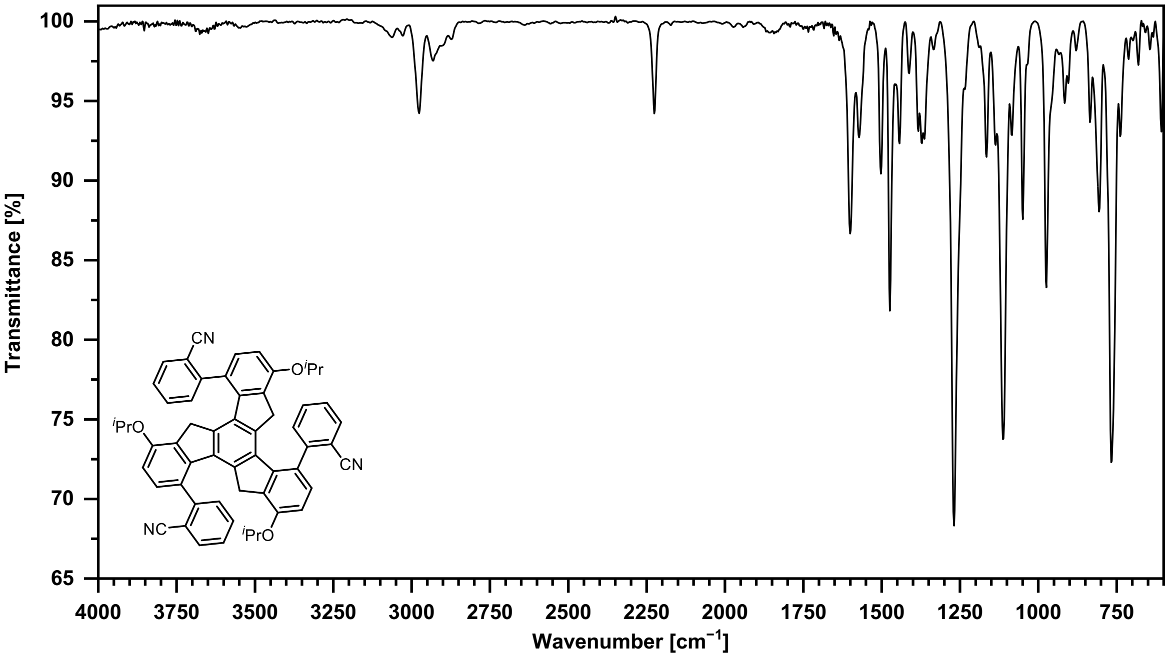

Figure 7.186: IR spectrum of compound **138**.

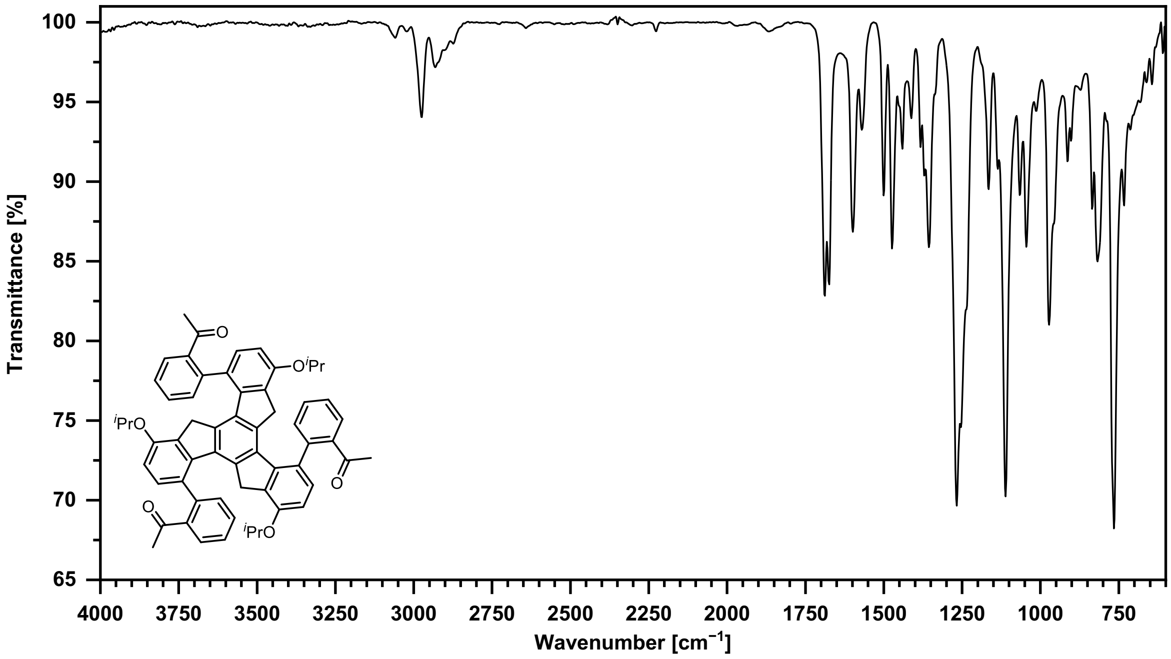

Figure 7.187: IR spectrum of compound **139**.

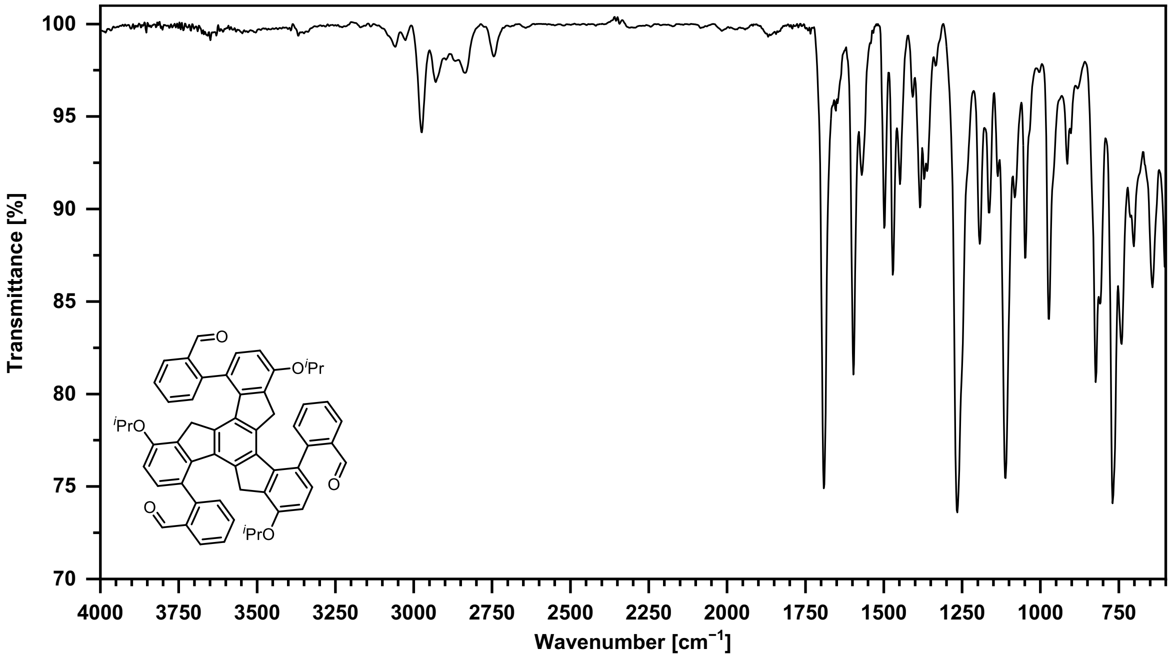

Figure 7.188: IR spectrum of compound **142**.

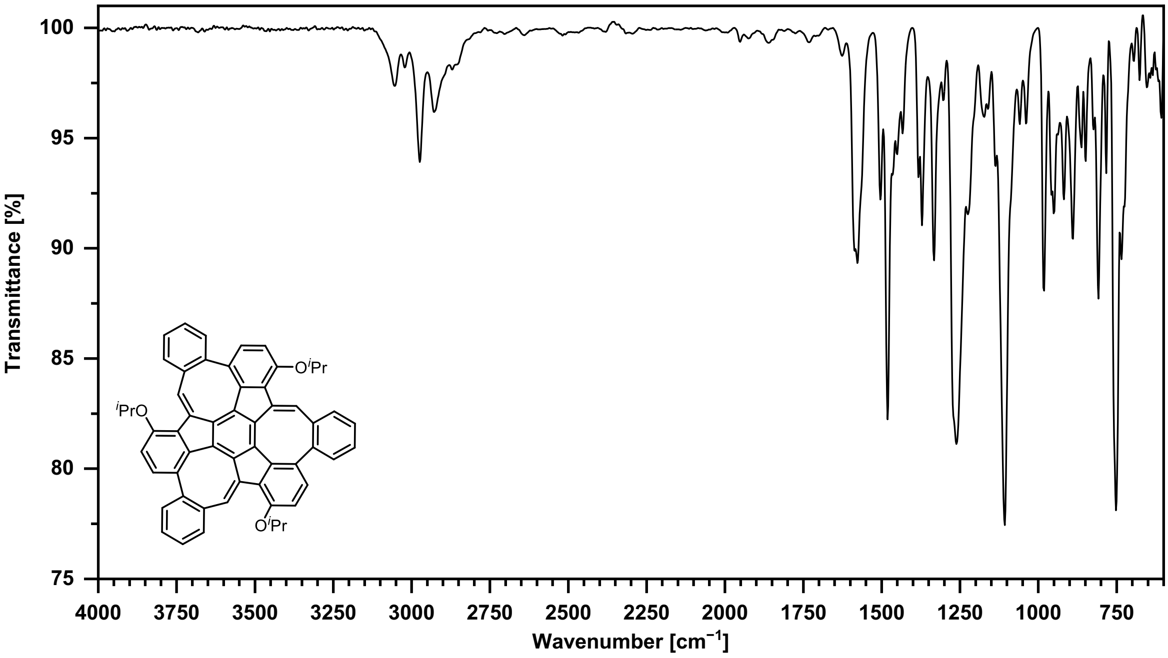

Figure 7.189: IR spectrum of compound **141**.

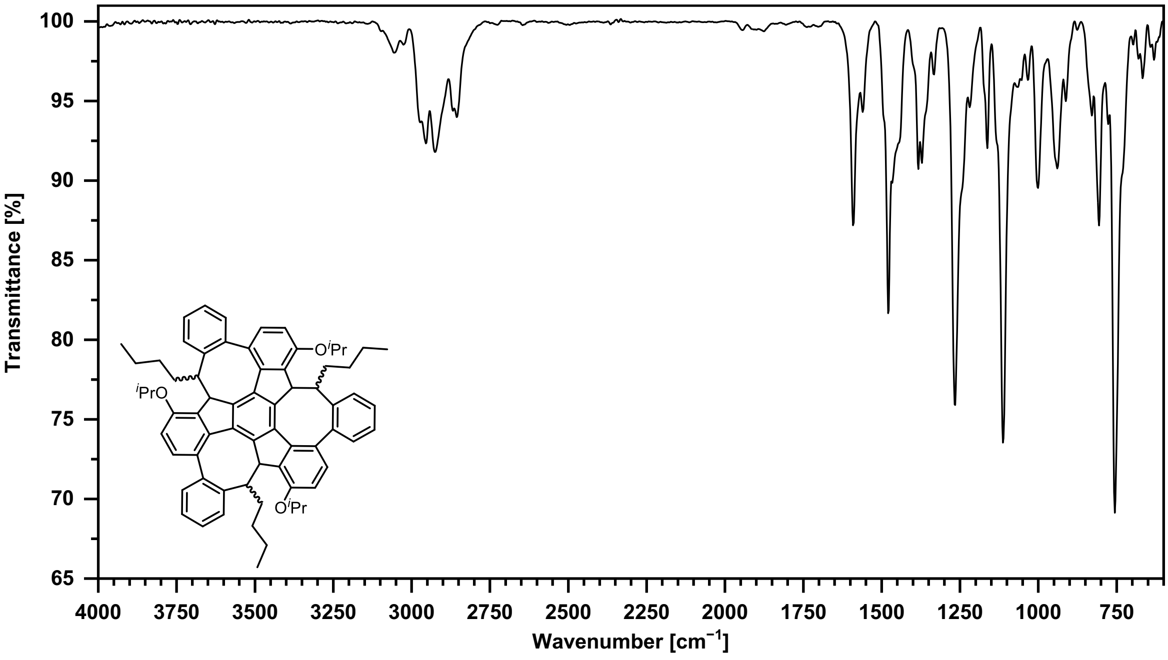

Figure 7.190: IR spectrum of compound **150-*anti***.

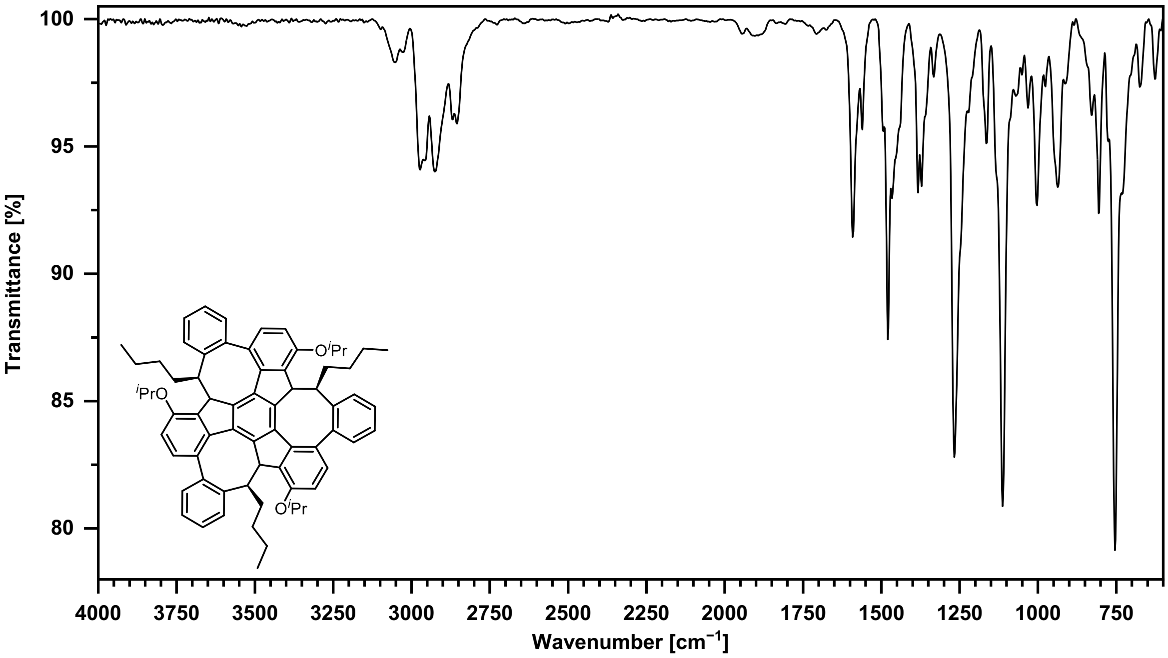

Figure 7.191: IR spectrum of compound **150-*syn***.

7.6 Mass Spectra

Mass spectra of compounds **120**, **121**, **122**, **123**, and **125** can be found in reference 186; those of **159**, **160**, **161**, **152**, and **166** are reported in reference 306.

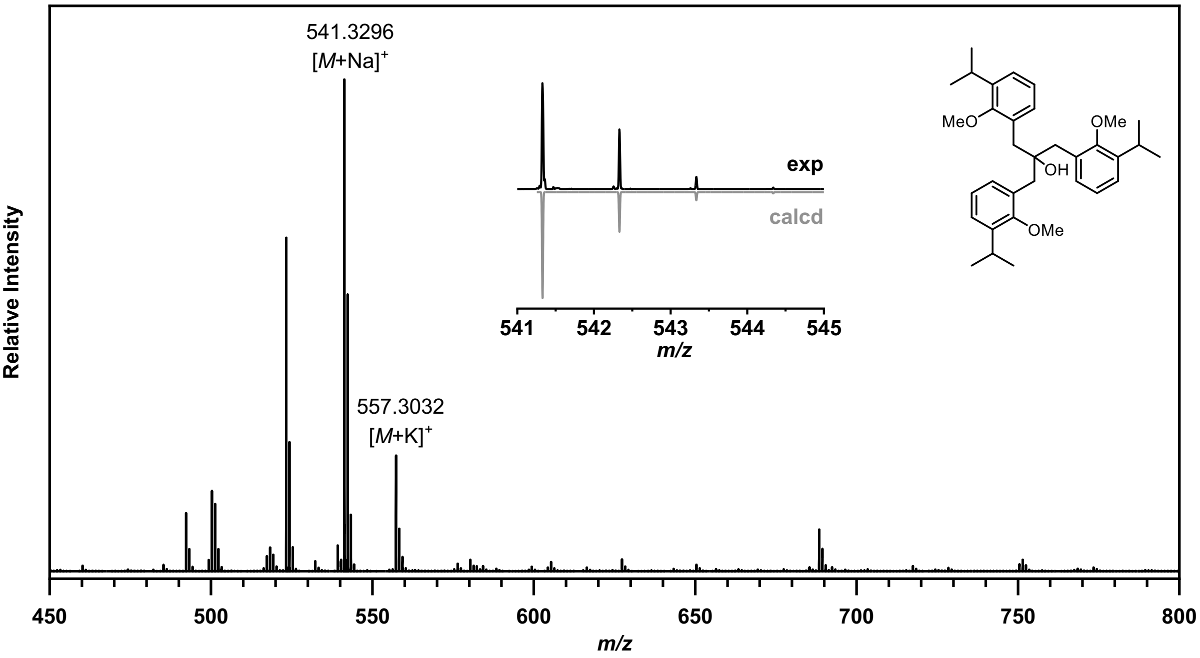

Figure 7.192: HRMS spectrum (MALDI$^+$, DCTB) of compound **92**.

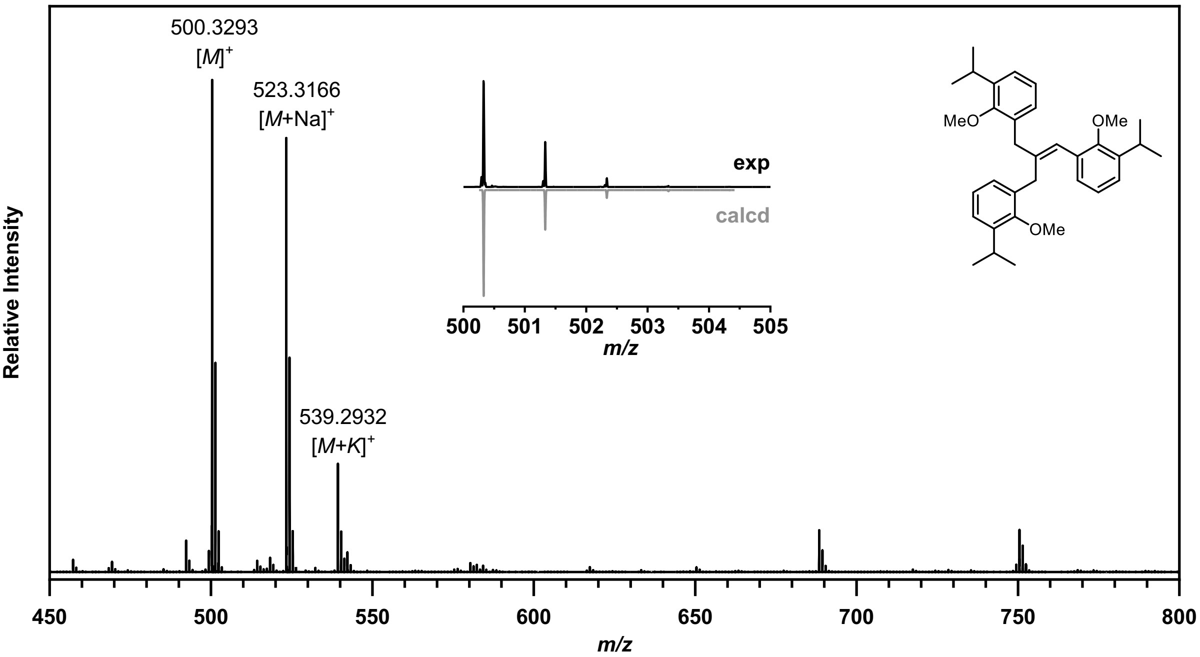

Figure 7.193: HRMS spectrum (MALDI$^+$, DCTB) of compound **93**.

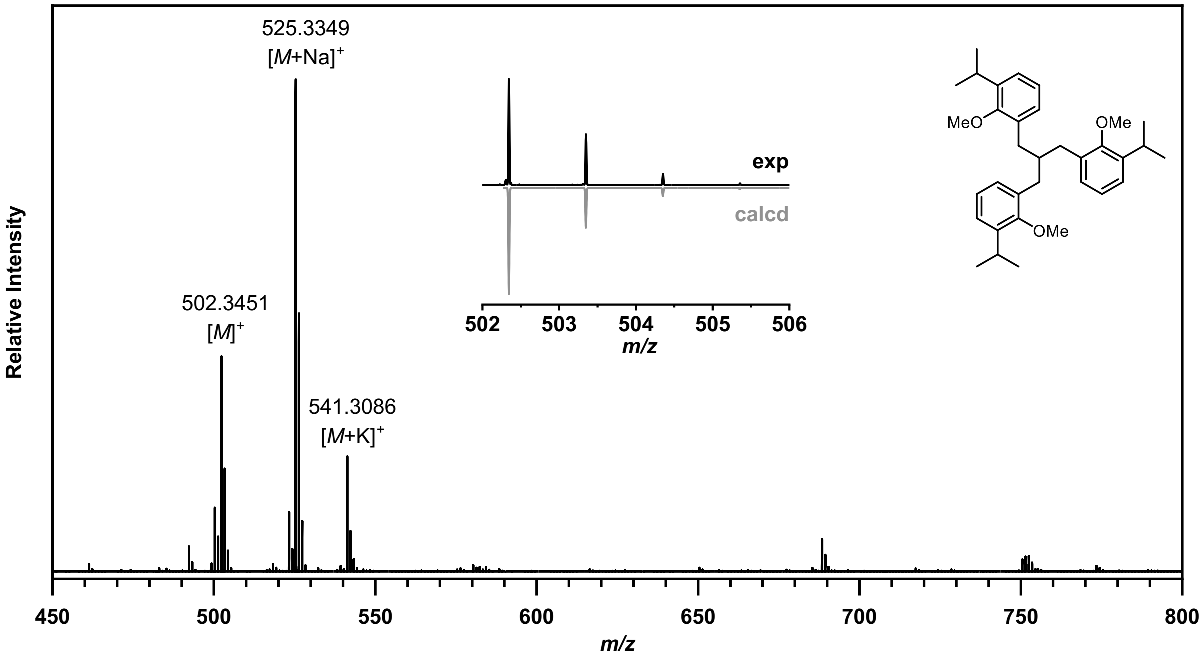

Figure 7.194: HRMS spectrum (MALDI$^+$, DCTB) of compound **94**.

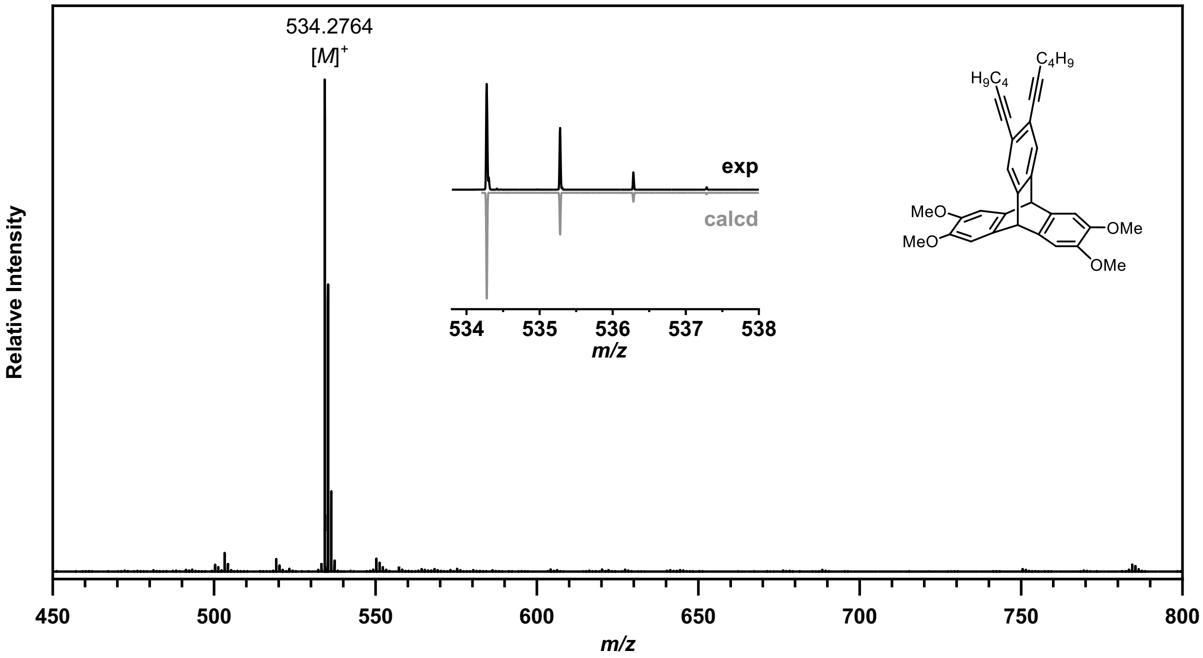

Figure 7.195: HRMS spectrum (MALDI$^+$, DCTB) of compound **98**.

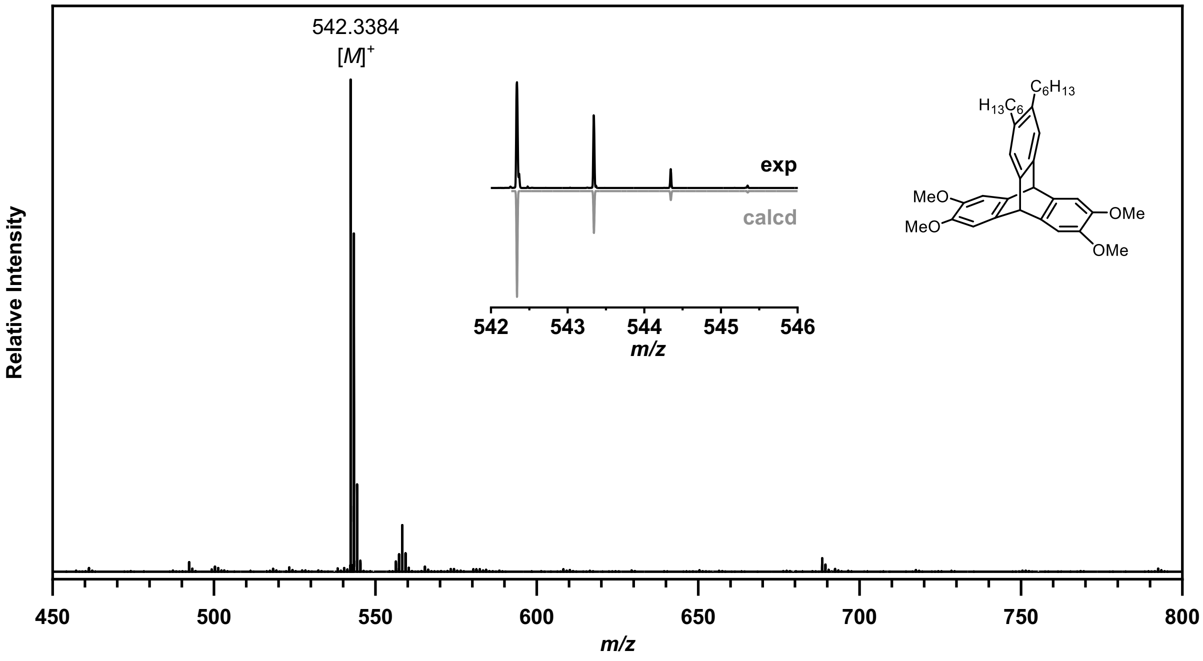

Figure 7.196: HRMS spectrum (MALDI$^+$, DCTB) of compound **99**.

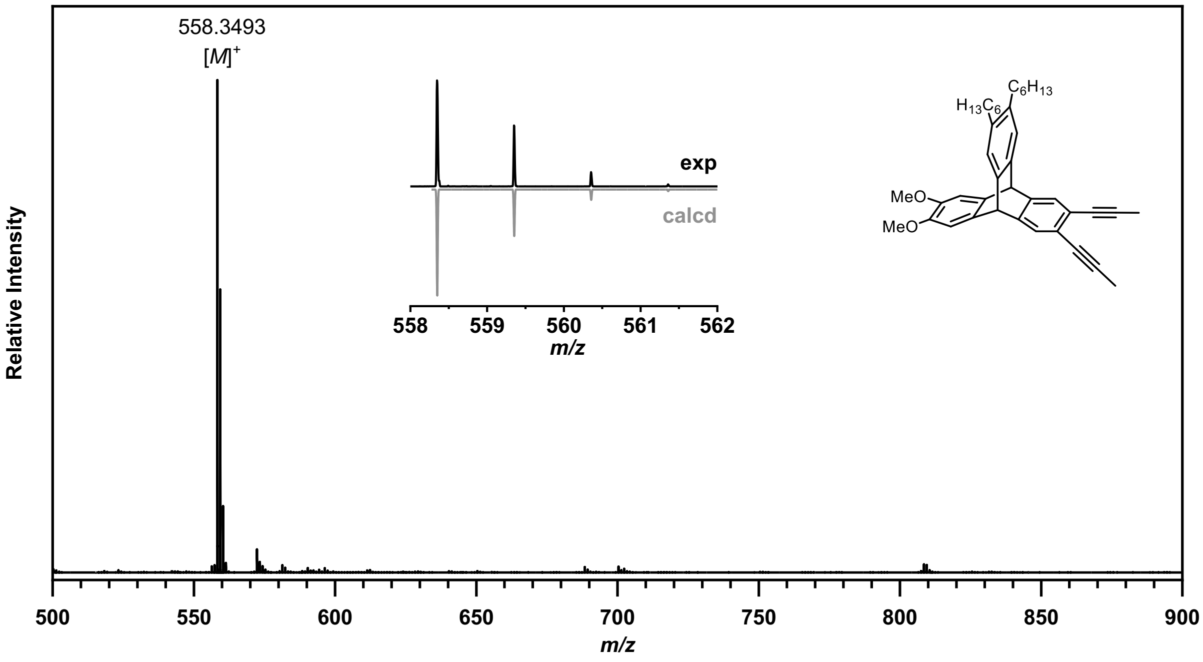

Figure 7.197: HRMS spectrum (MALDI$^+$, DCTB) of compound **101**.

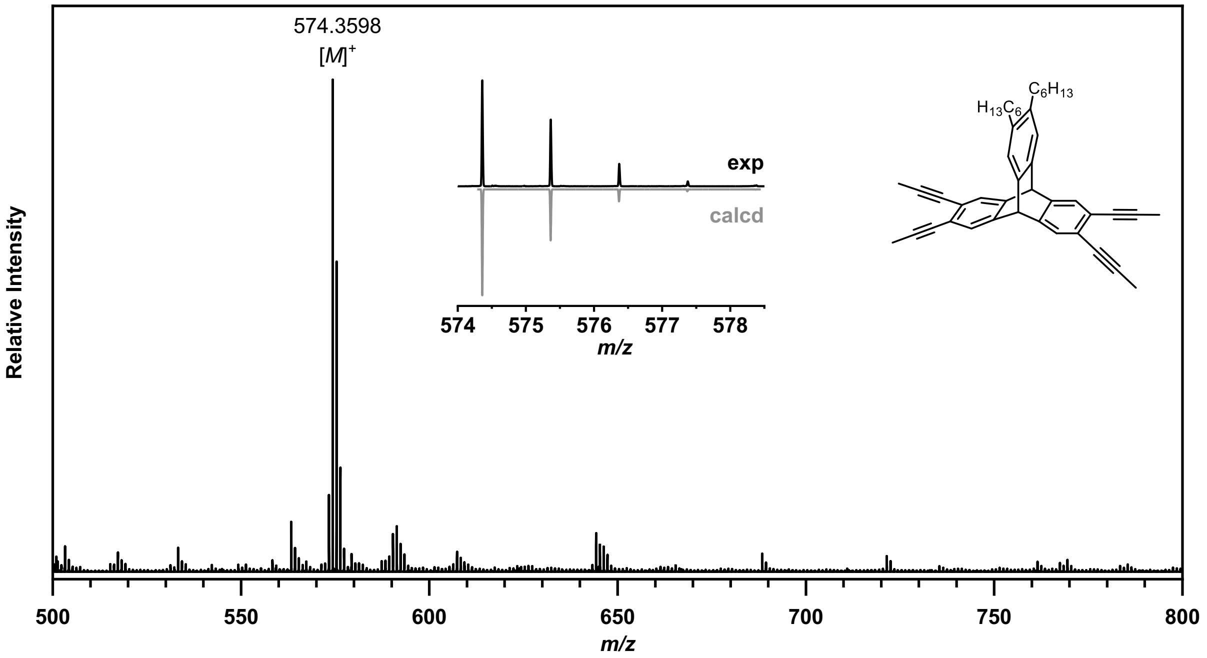

Figure 7.198: HRMS spectrum (MALDI+, DCTB) of compound **75**.

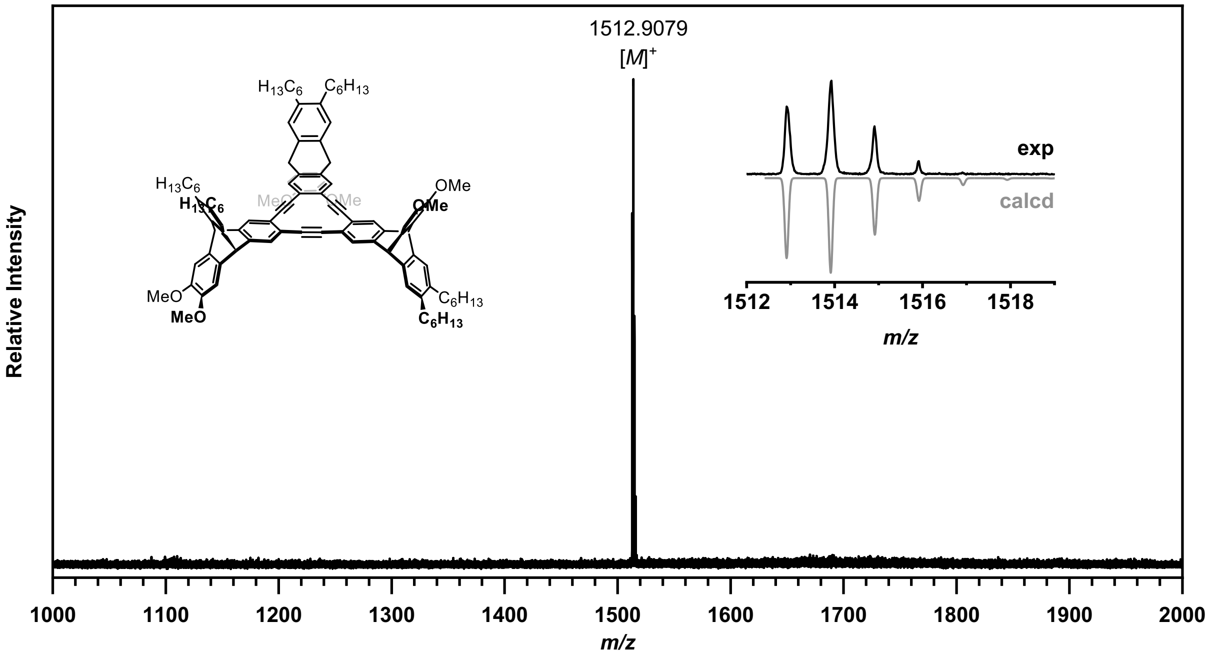

Figure 7.199: HRMS spectrum (MALDI+, DCTB) of compound **103a**.

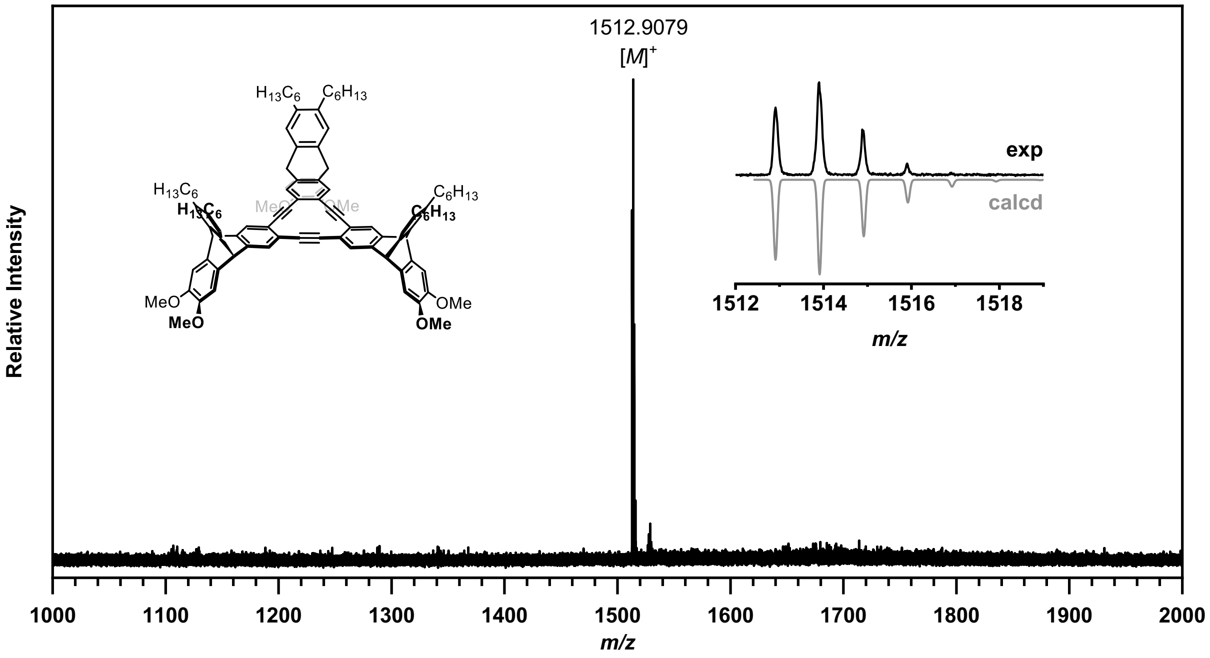

Figure 7.200: HRMS spectrum (MALDI$^+$, DCTB) of compound **103b**.

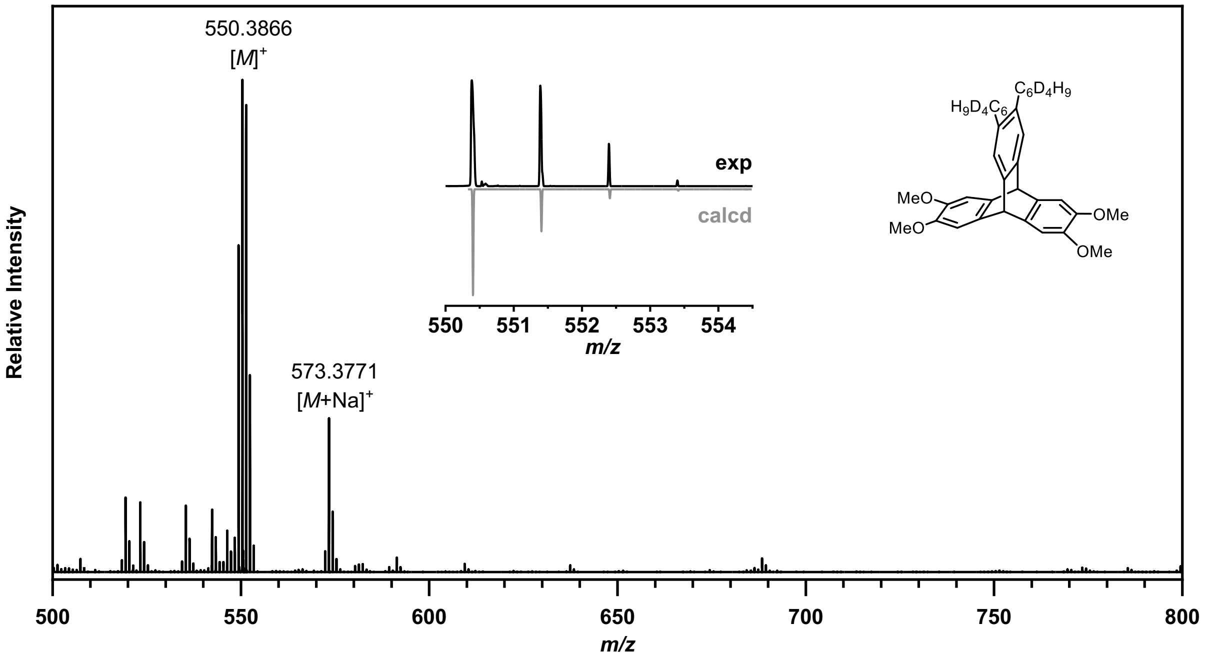

Figure 7.201: HRMS spectrum (MALDI$^+$, DCTB) of compound **99-*d*$_8$**.

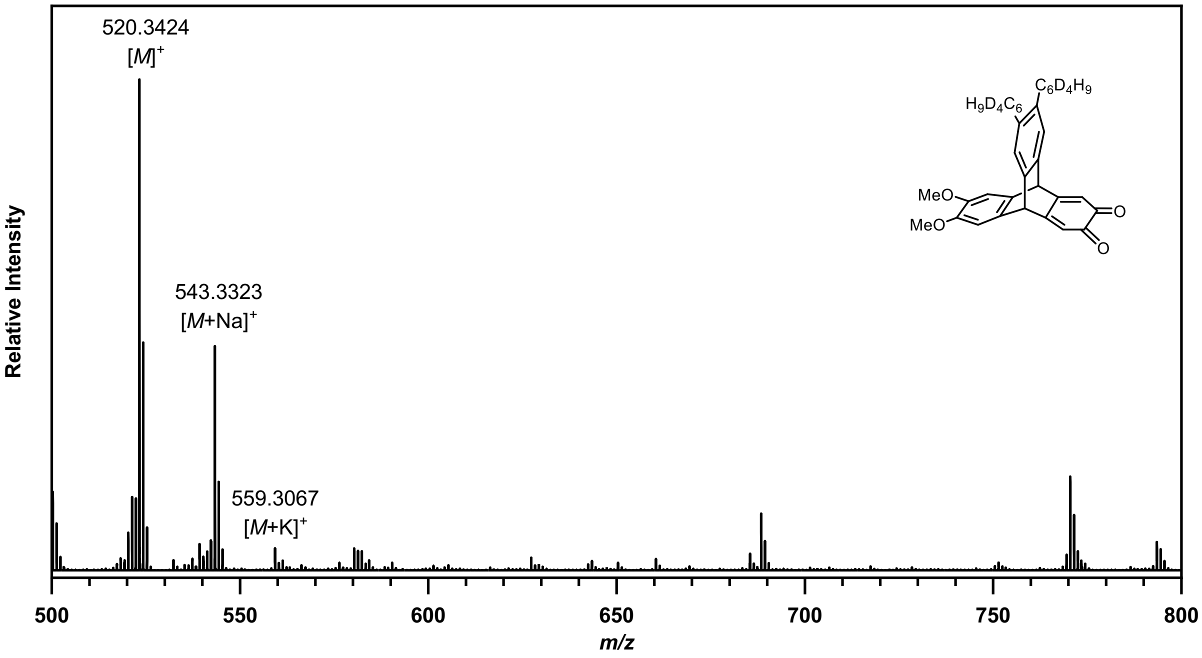

Figure 7.202: HRMS spectrum (MALDI$^+$, DCTB) of compound **100-*d*$_8$**.

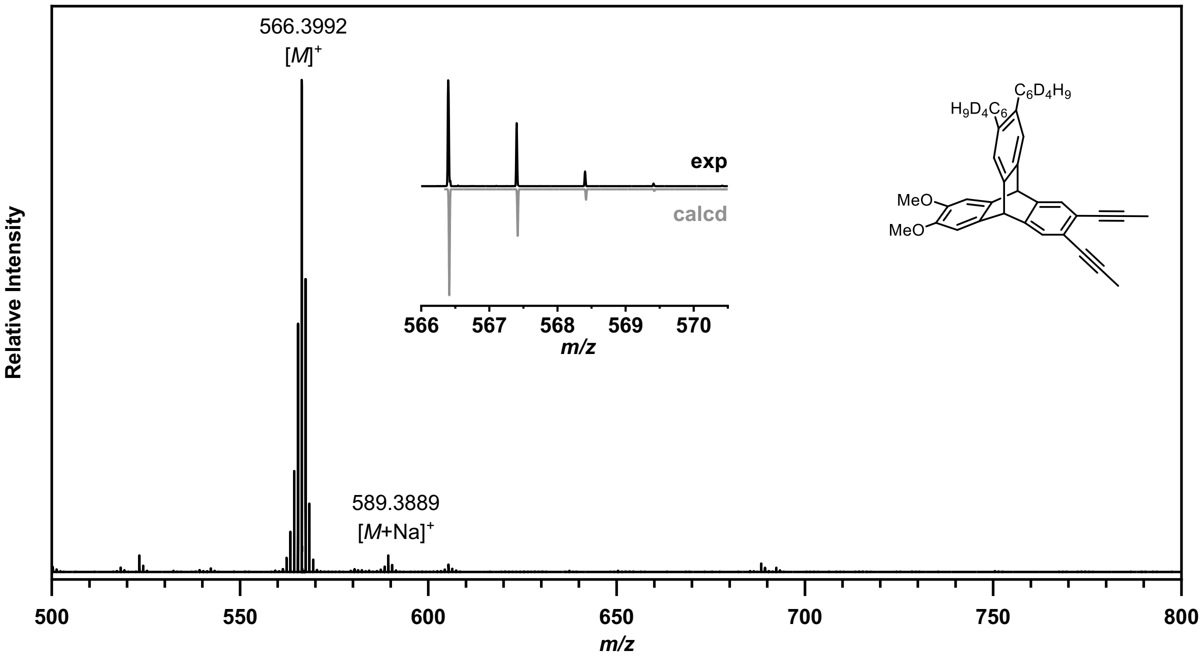

Figure 7.203: HRMS spectrum (MALDI$^+$, DCTB) of compound **101-*d*$_8$**.

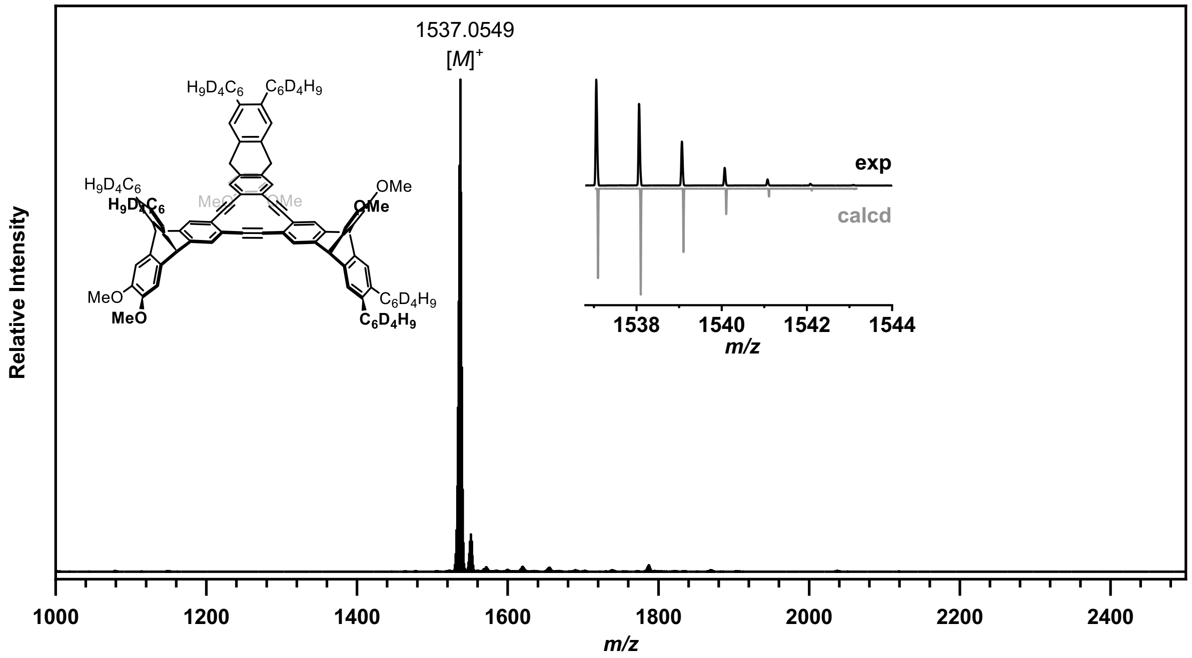

Figure 7.204: HRMS spectrum (MALDI$^+$, DCTB) of compound **103a-*d$_{24}$***.

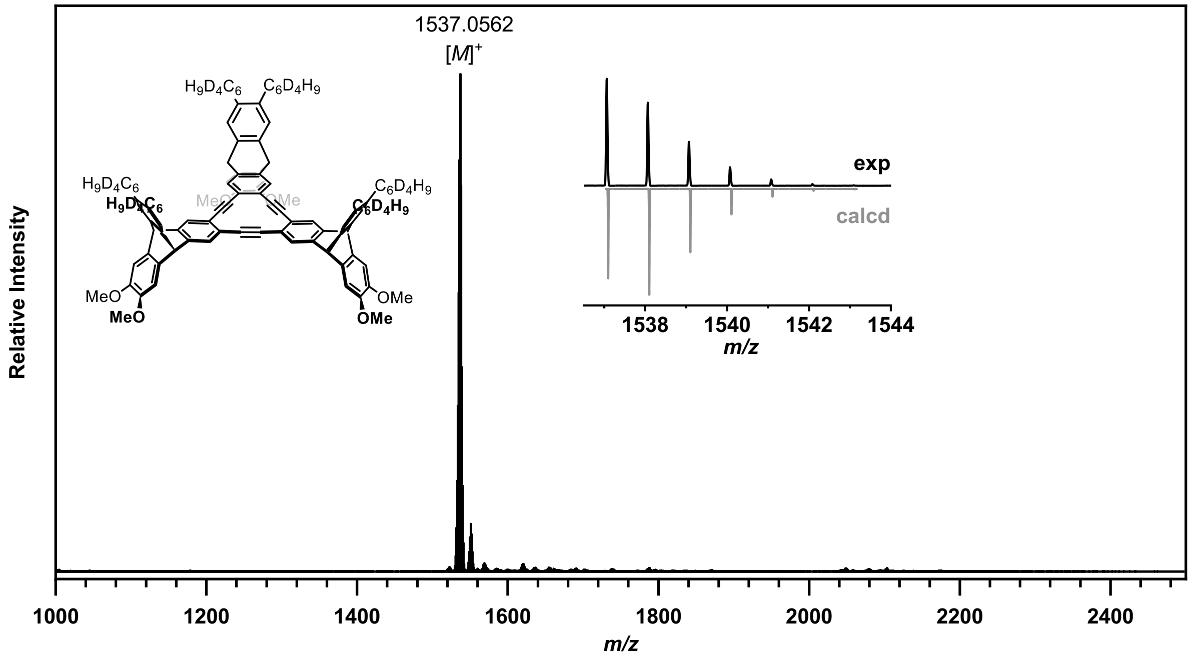

Figure 7.205: HRMS spectrum (MALDI$^+$, DCTB) of compound **103b-*d$_{24}$***.

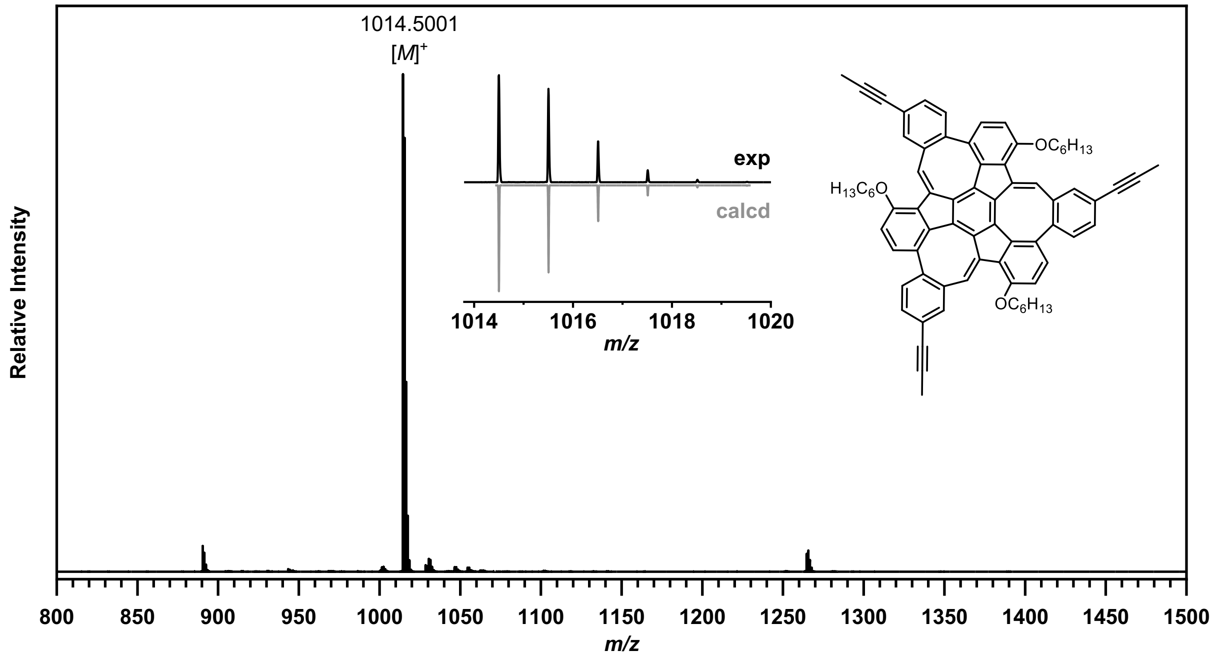

Figure 7.206: HRMS spectrum (MALDI$^+$, DCTB) of compound **116**.

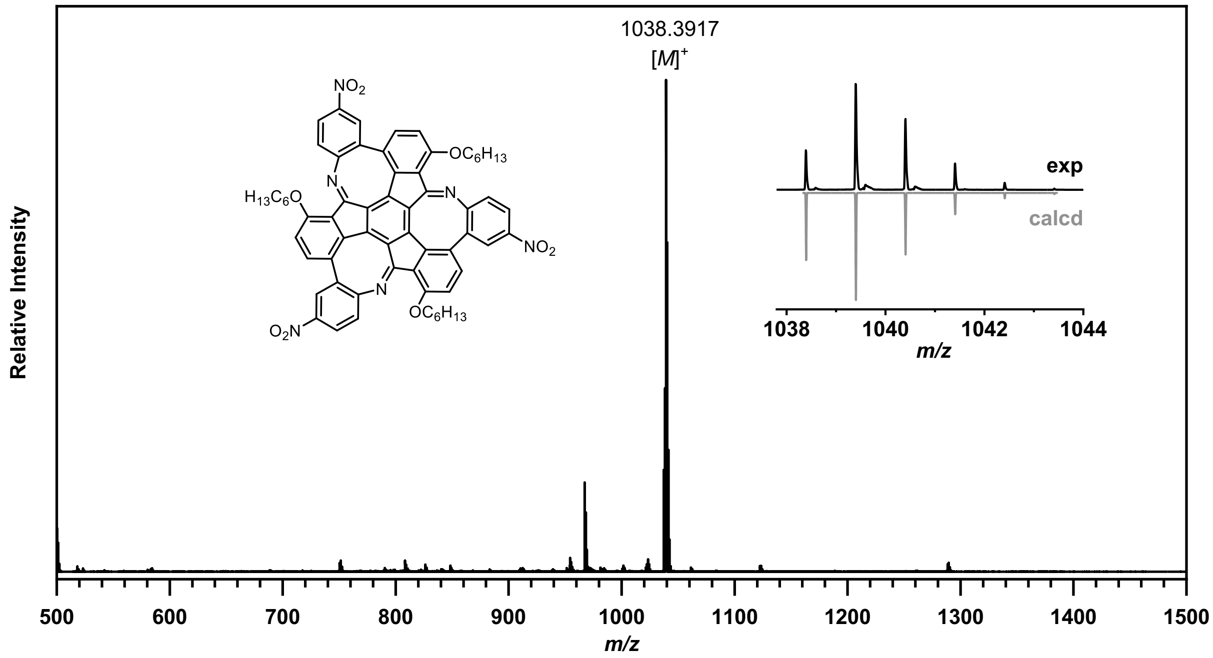

Figure 7.207: HRMS spectrum (MALDI$^+$, DCTB) of compound **131**.

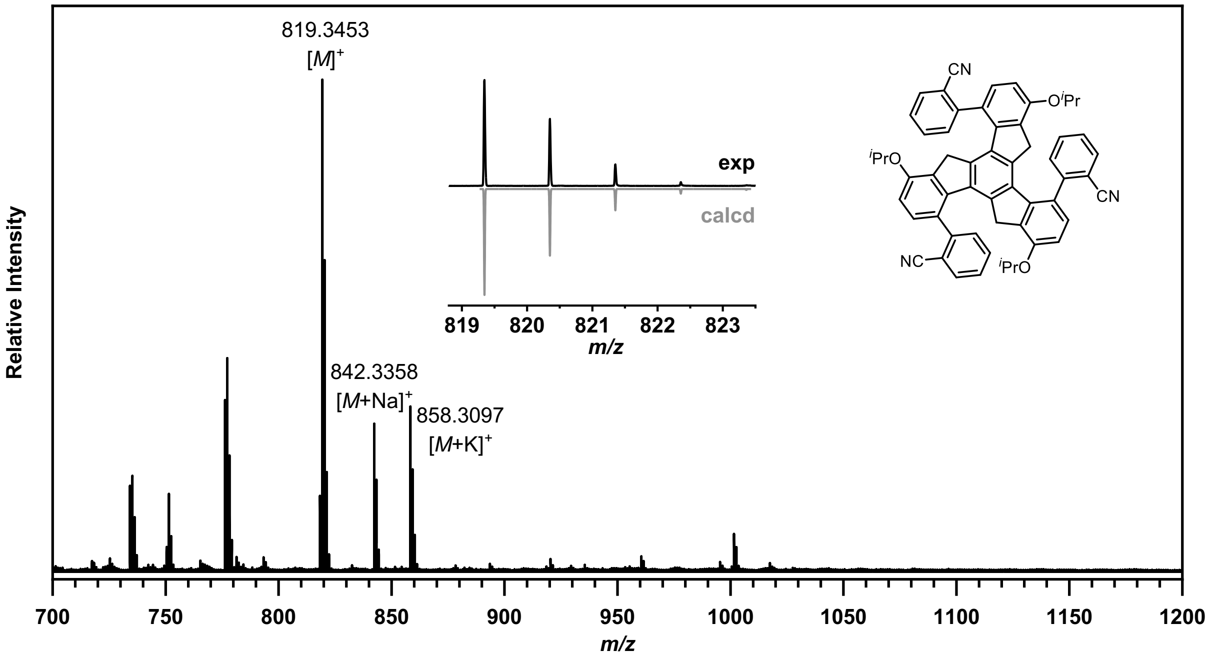

Figure 7.208: HRMS spectrum (MALDI$^+$, DCTB) of compound **138**.

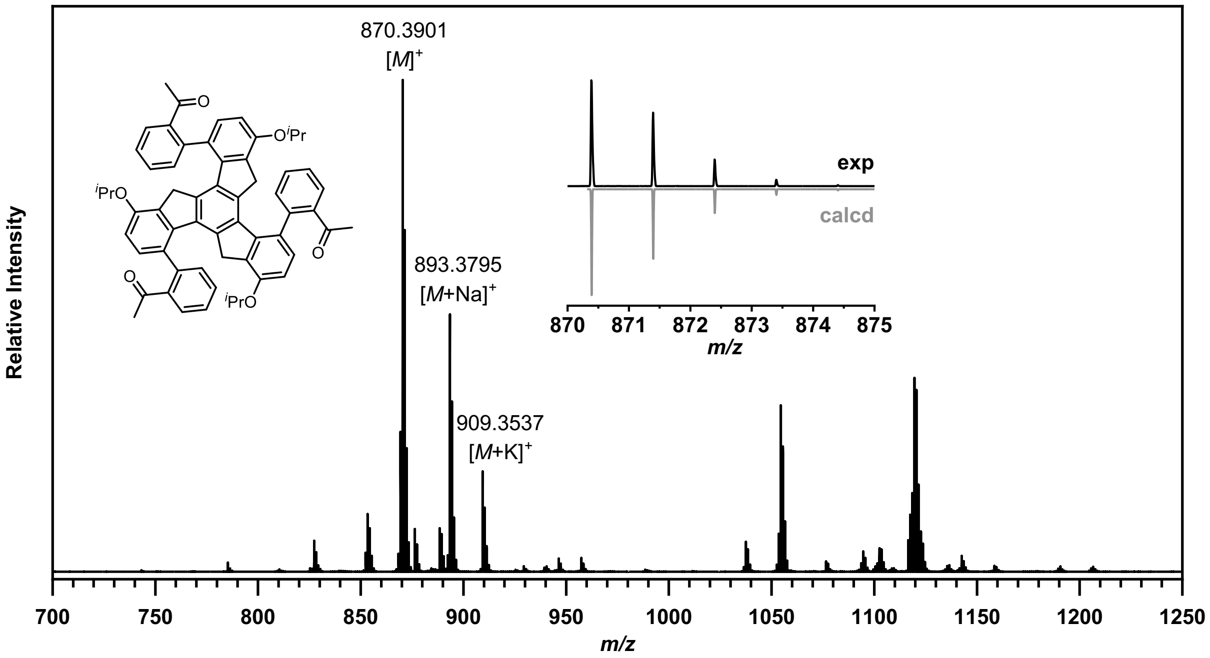

Figure 7.209: HRMS spectrum (MALDI$^+$, DCTB) of compound **139**.

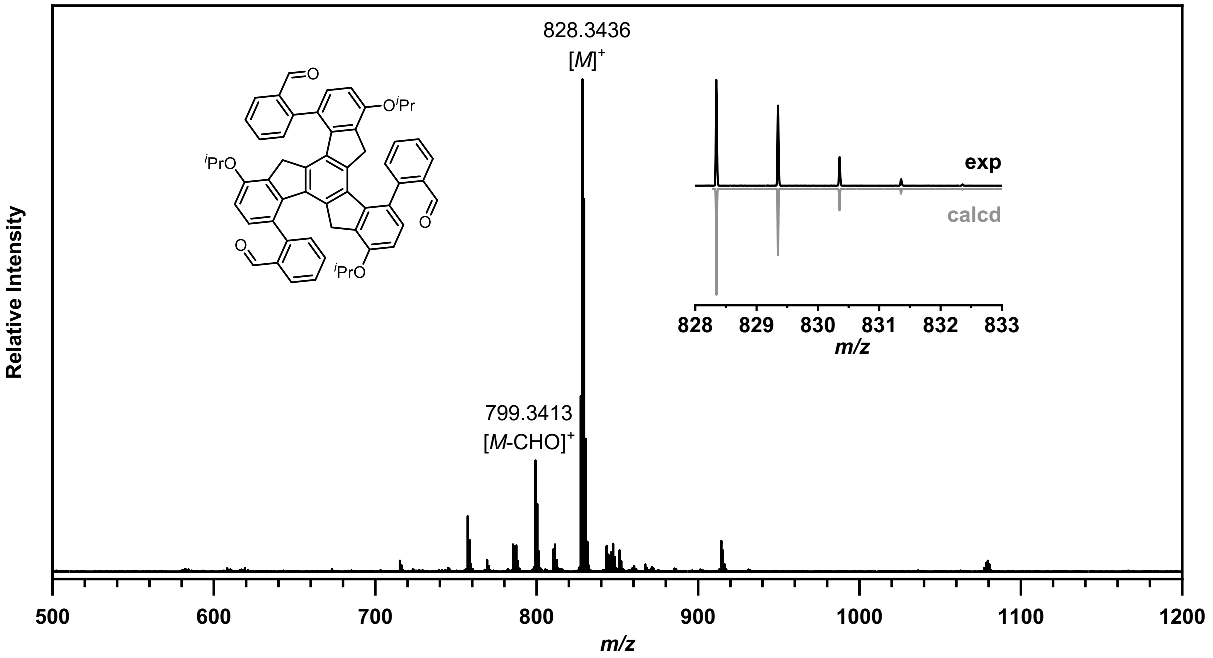

Figure 7.210: HRMS spectrum (MALDI$^+$, DCTB) of compound **142**.

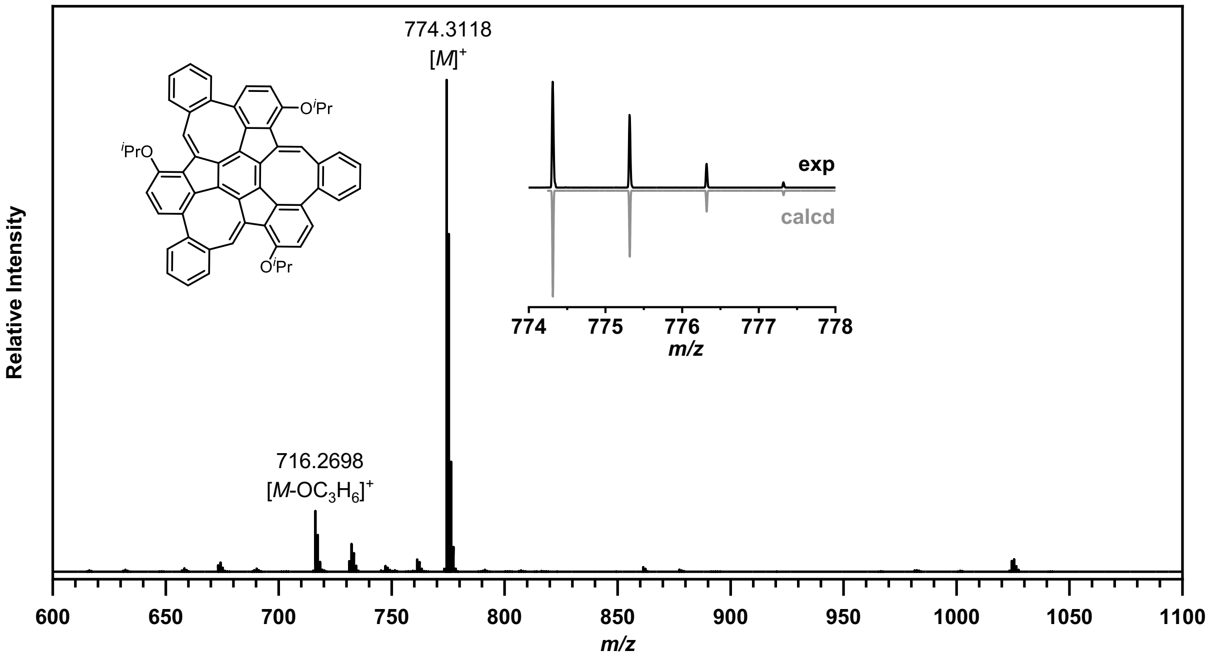

Figure 7.211: HRMS spectrum (MALDI$^+$, DCTB) of compound **141**.

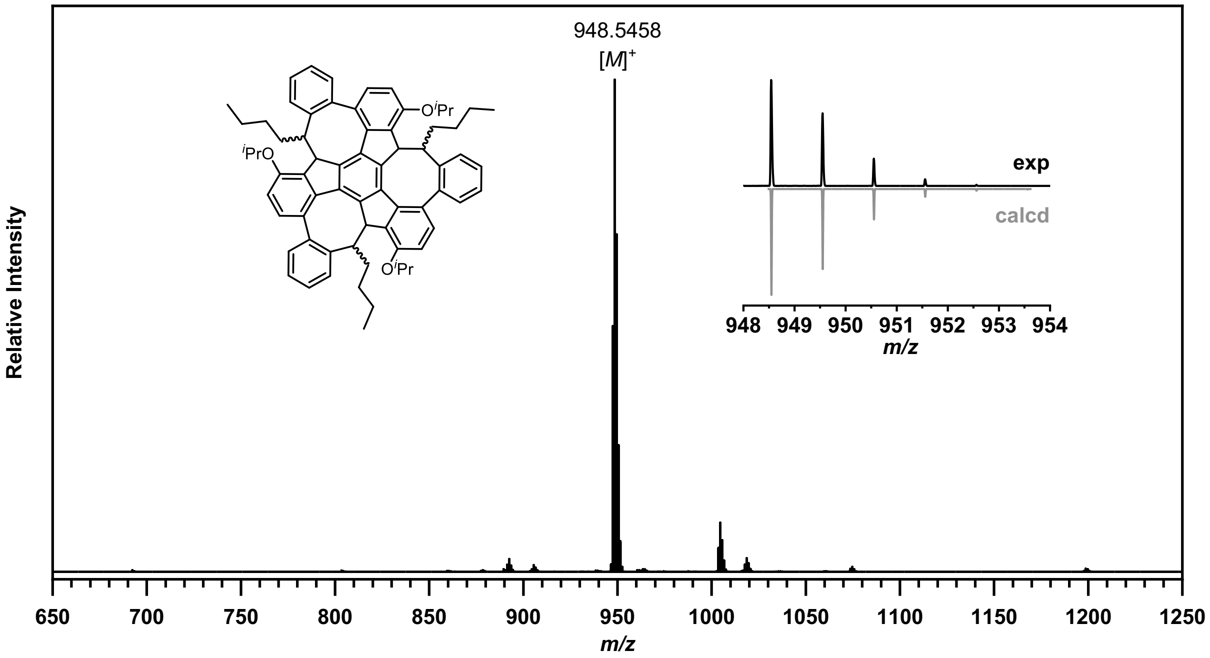

Figure 7.212: HRMS spectrum (MALDI$^+$, DCTB) of compound **150-*anti***.

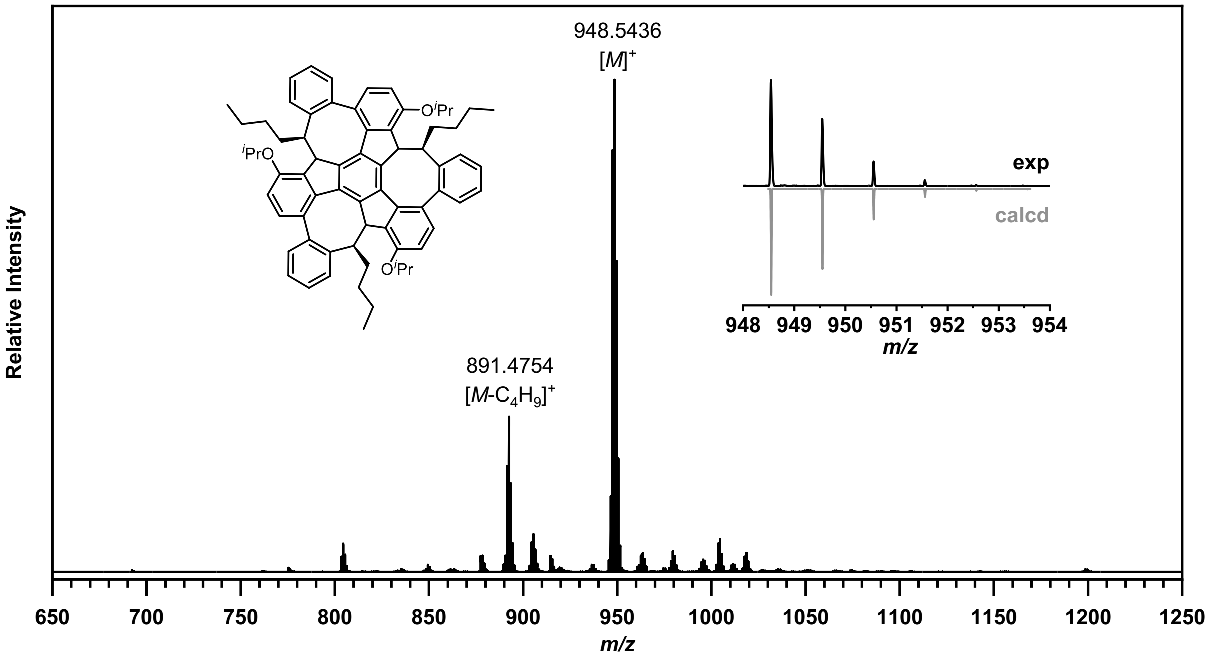

Figure 7.213: HRMS spectrum (MALDI$^+$, DCTB) of **150-*syn***.

7.7 UV/vis and Fluorescence Spectra

UV/Vis and fluorescence spectra of compounds **120**, **121**, **122**, **123**, and **125** can be found in reference 186; those of **159**, **160**, **161**, **152**, and **166** are reported in reference 306.

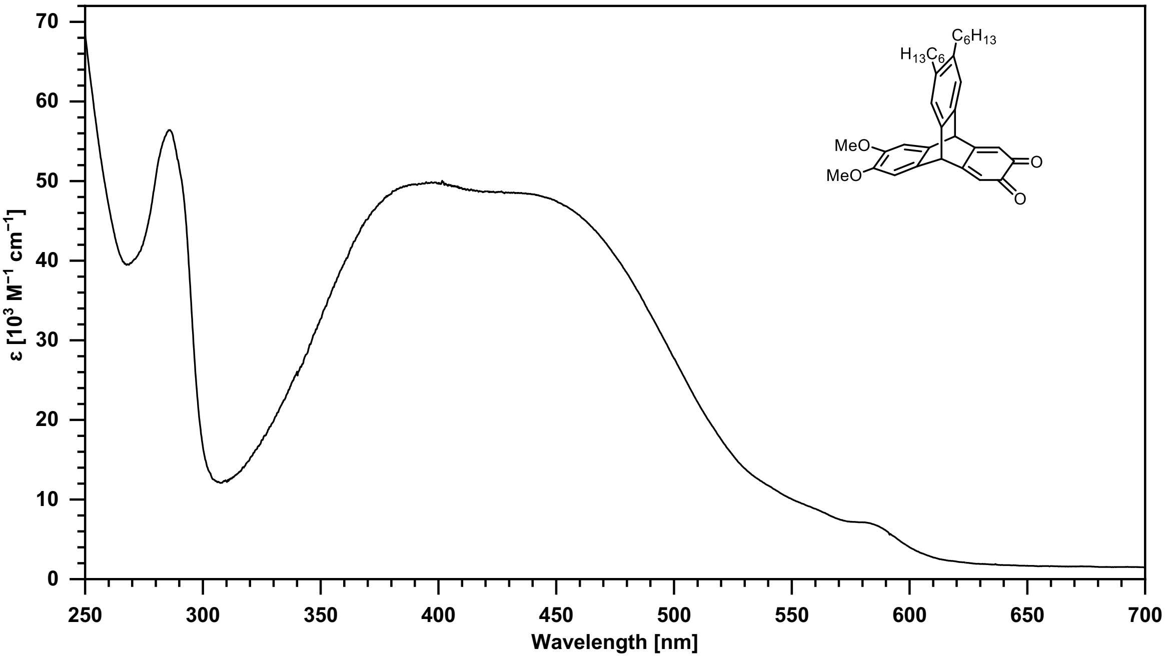

Figure 7.214: UV/vis spectrum of **100** in CH_2Cl_2.

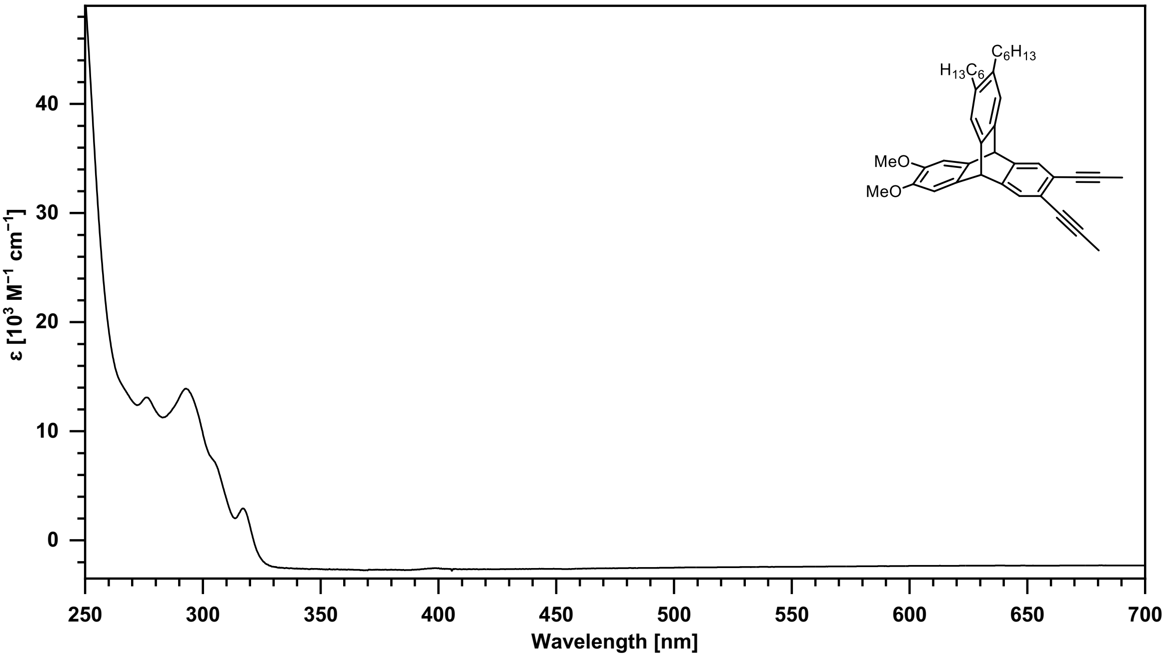

Figure 7.215: UV/vis spectrum of **101** in CH_2Cl_2.

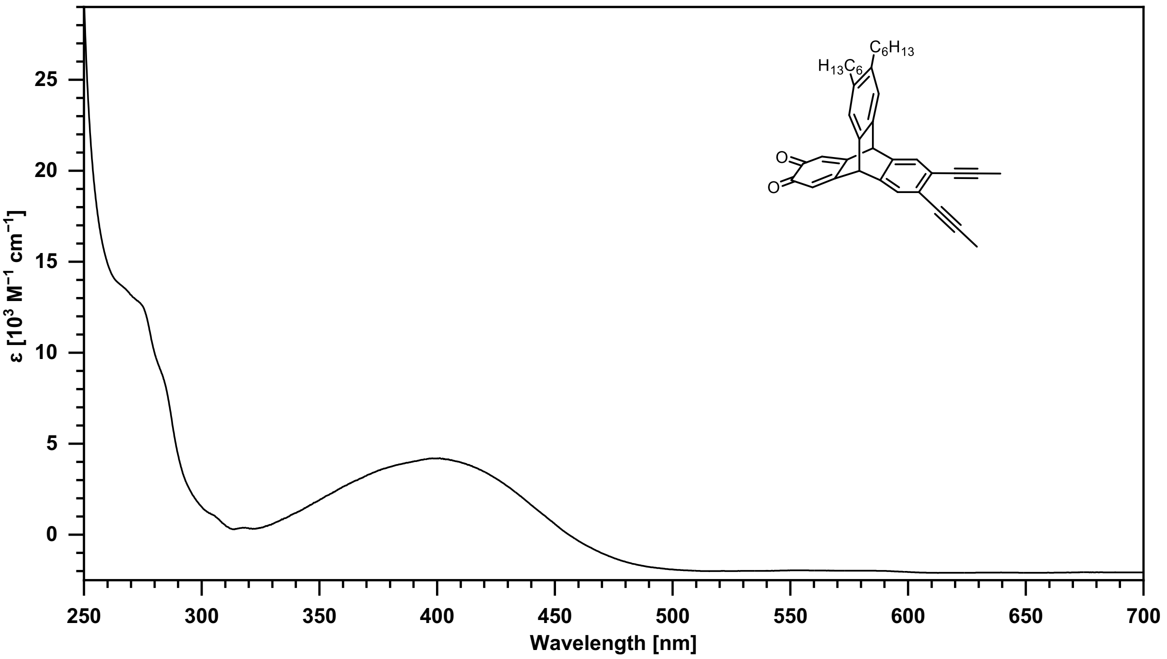

Figure 7.216: UV/vis spectrum of **102** in CH_2Cl_2.

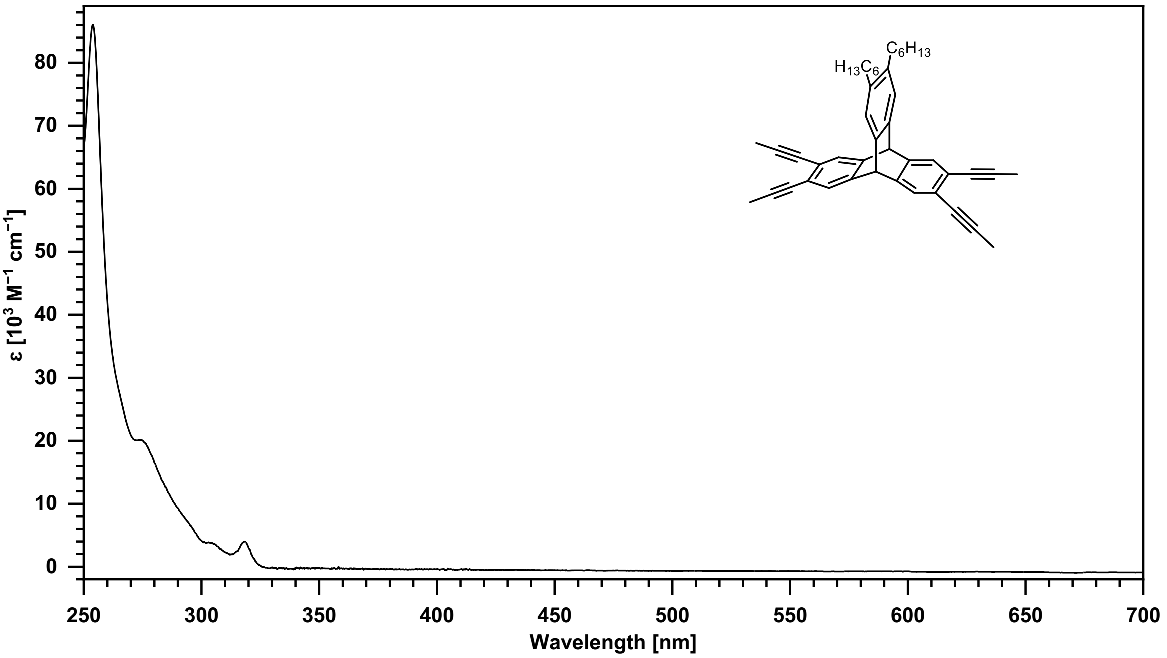

Figure 7.217: UV/vis spectrum of **75** in CH_2Cl_2.

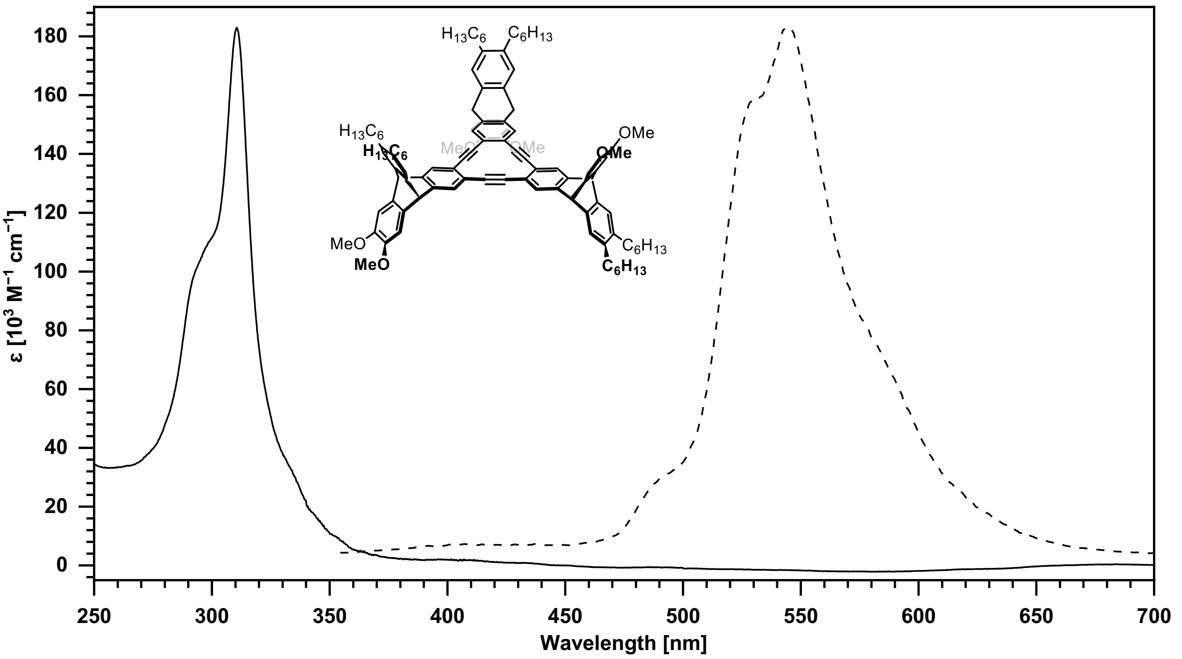

Figure 7.218: UV/vis (solid line) and emission spectrum (dotted line) of **103a** in CH_2Cl_2. The excitation wavelength of the emission is 315 nm.

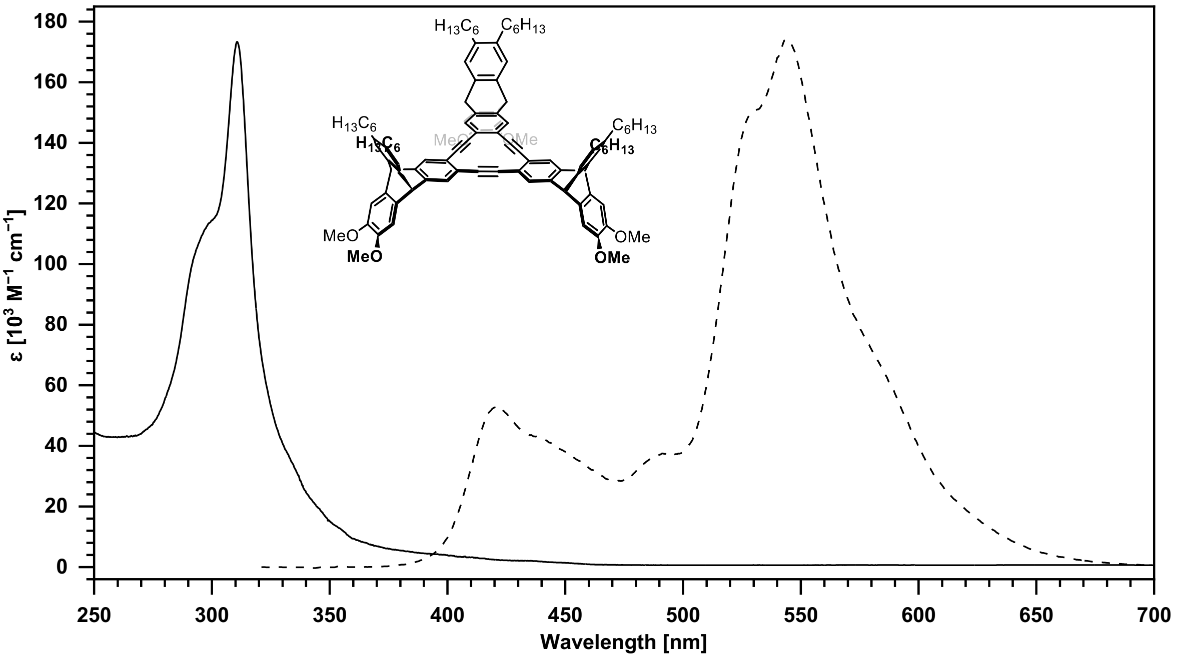

Figure 7.219: UV/vis (solid line) and emission spectrum (dotted line) of **103b** in CH_2Cl_2. The excitation wavelength of the emission is 311 nm.

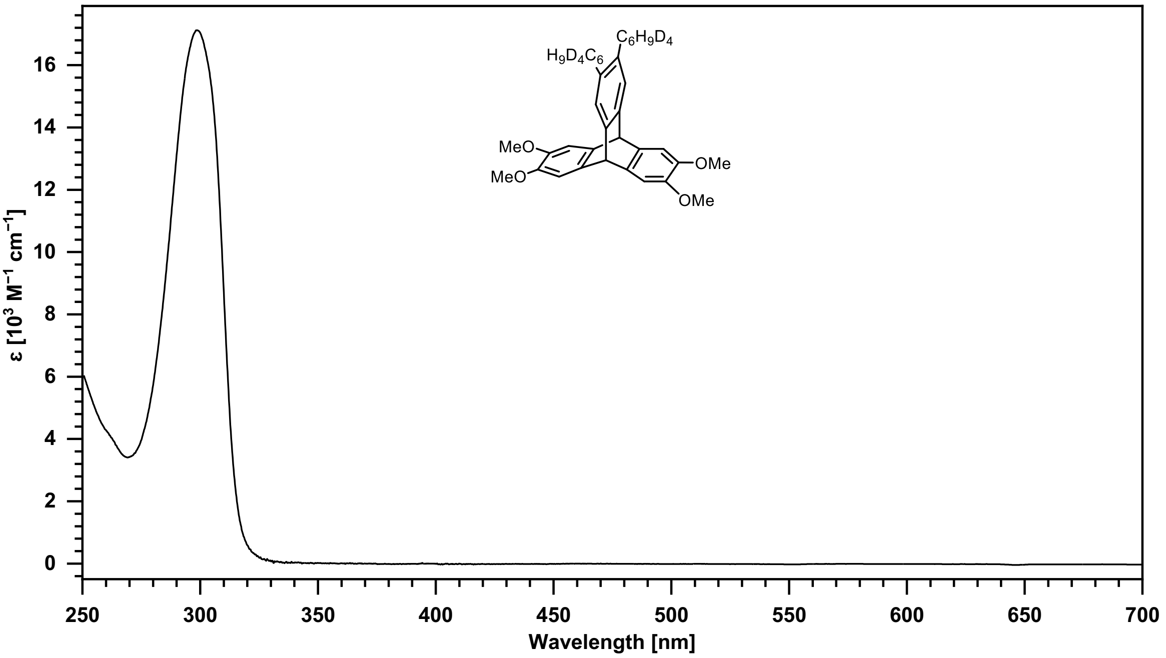

Figure 7.220: UV/vis spectrum of **99-d_8** in CH_2Cl_2.

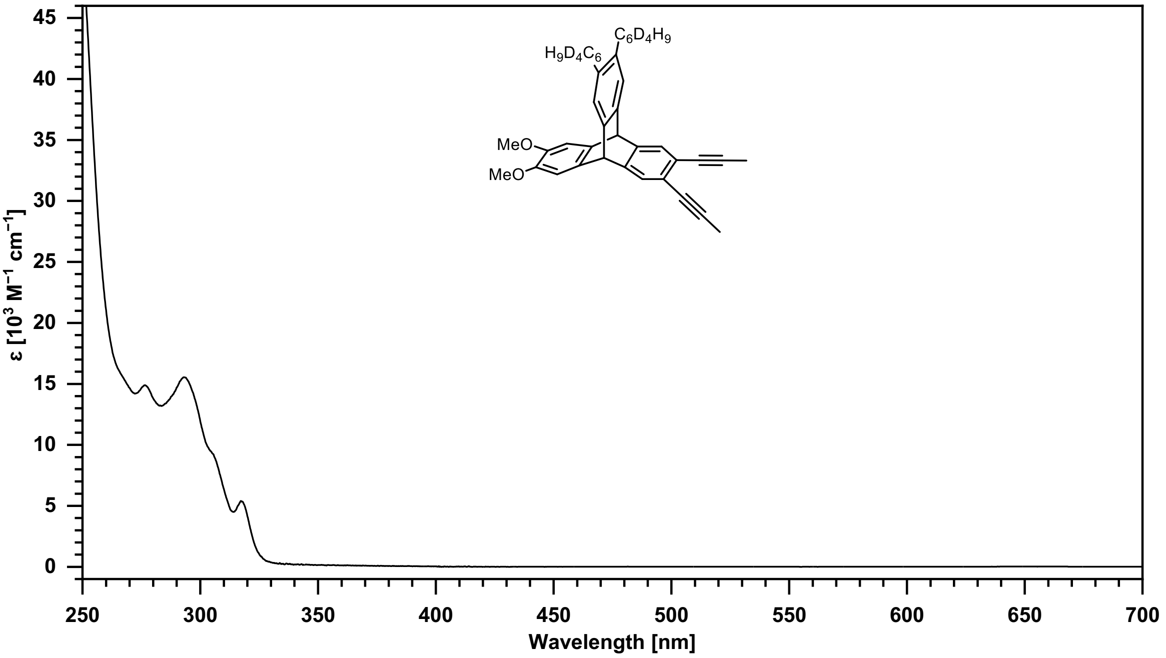

Figure 7.221: UV/vis spectrum of **101-d_8** in CH_2Cl_2.

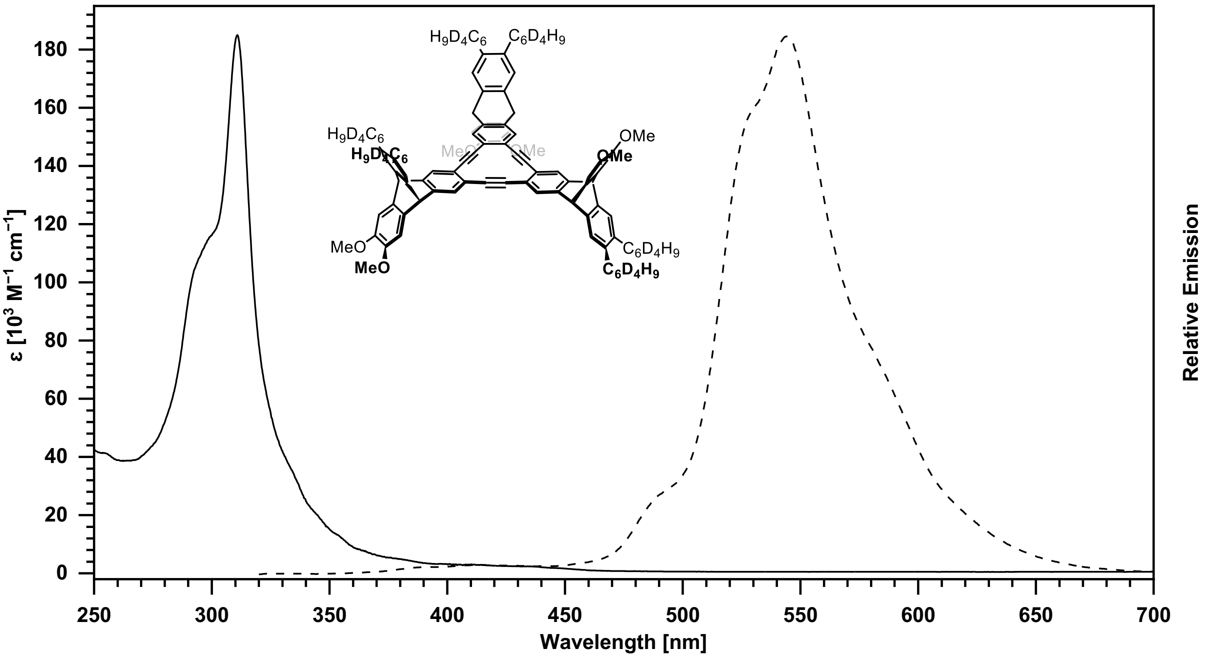

Figure 7.222: UV/vis (solid line) and emission spectrum (dotted line) of **103a-*d*₂₄** in CH_2Cl_2. The excitation wavelength of the emission is 311 nm.

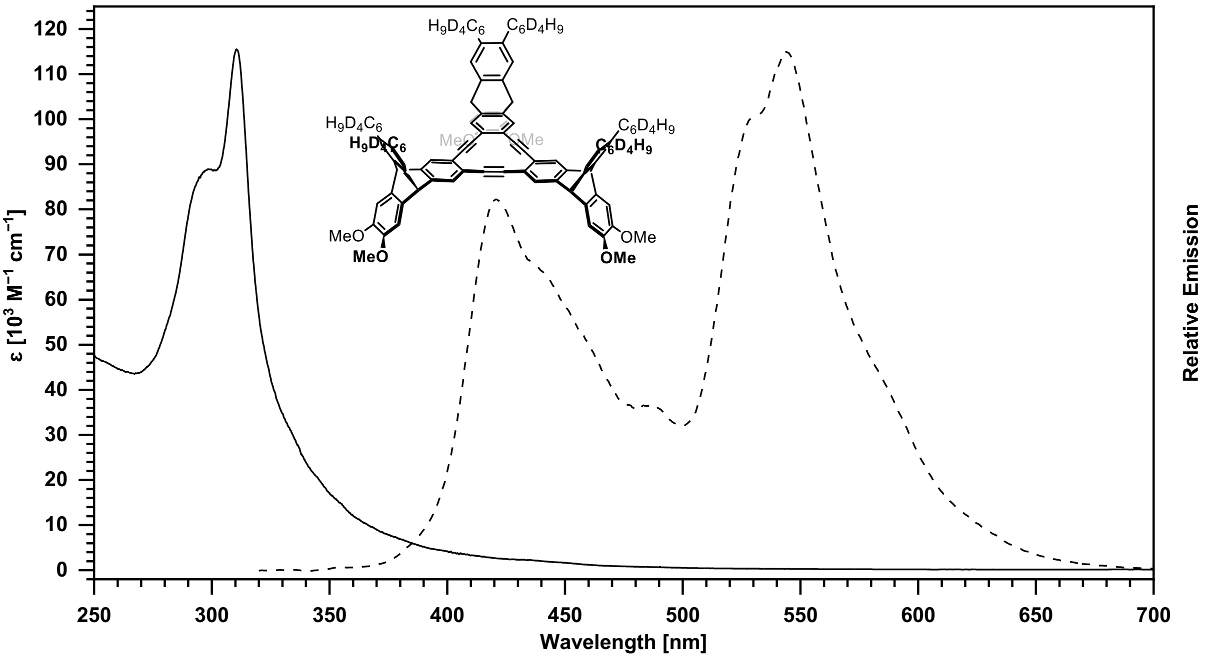

Figure 7.223: UV/vis (solid line) and emission spectrum (dotted line) of **103b-*d*₂₄** in CH_2Cl_2. The excitation wavelength of the emission is 310 nm.

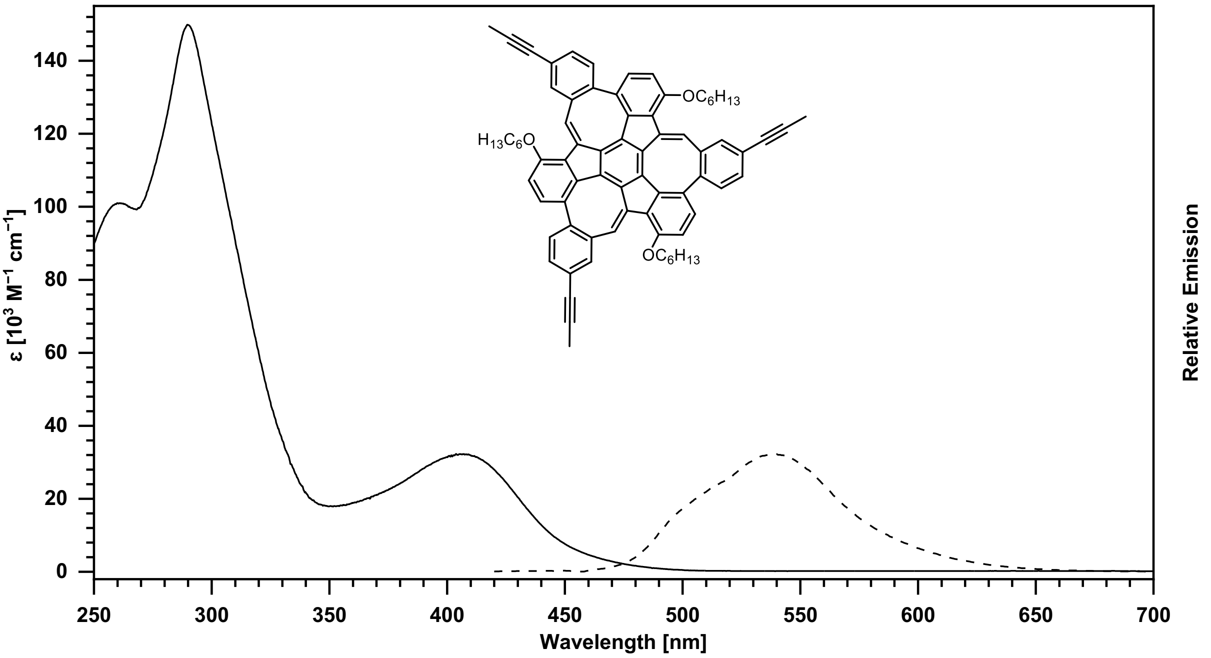

Figure 7.224: UV/vis (solid line) and emission spectrum (dotted line) of **116** in CH_2Cl_2. The excitation wavelength of the emission is 403 nm.

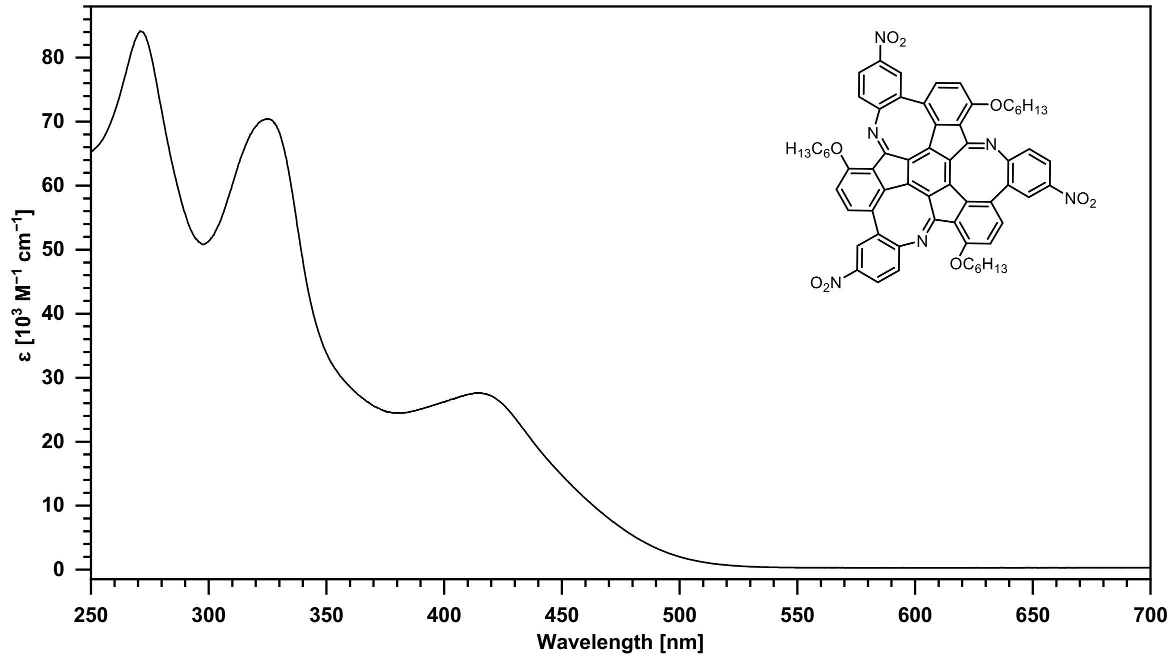

Figure 7.225: UV/vis spectrum of **131** in CH_2Cl_2.

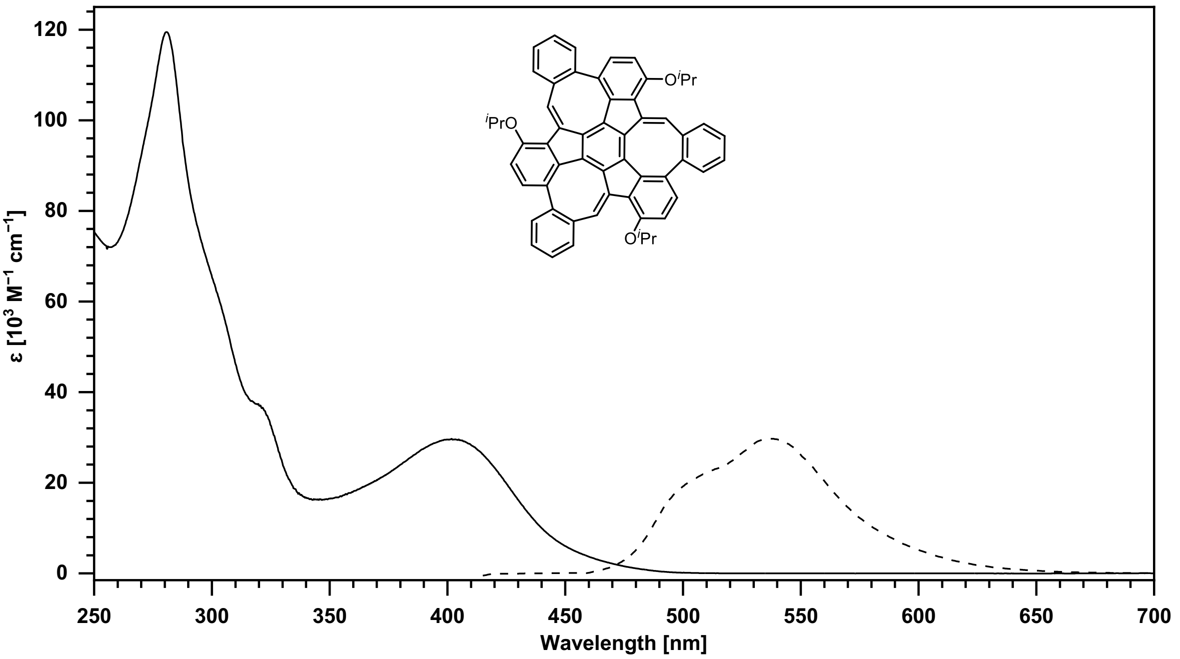

Figure 7.226: UV/vis (solid line) and emission spectrum (dotted line) of **141** in CH_2Cl_2. The excitation wavelength of the emission is 404 nm.

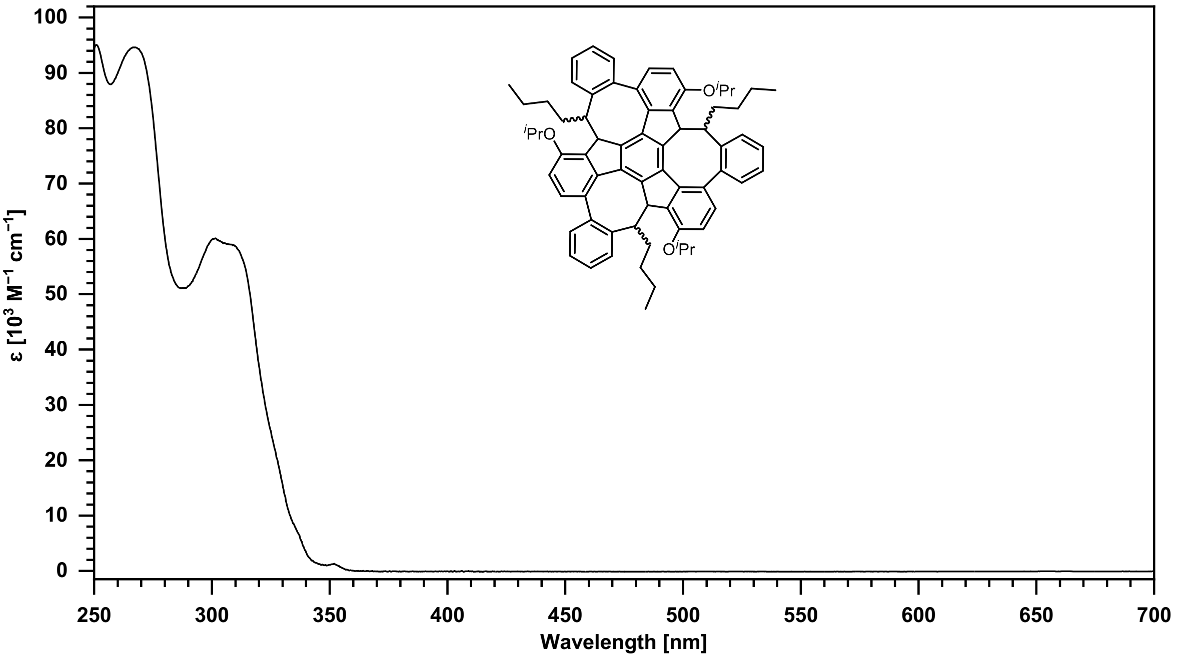

Figure 7.227: UV/vis spectrum of **150-*anti*** in CH_2Cl_2.

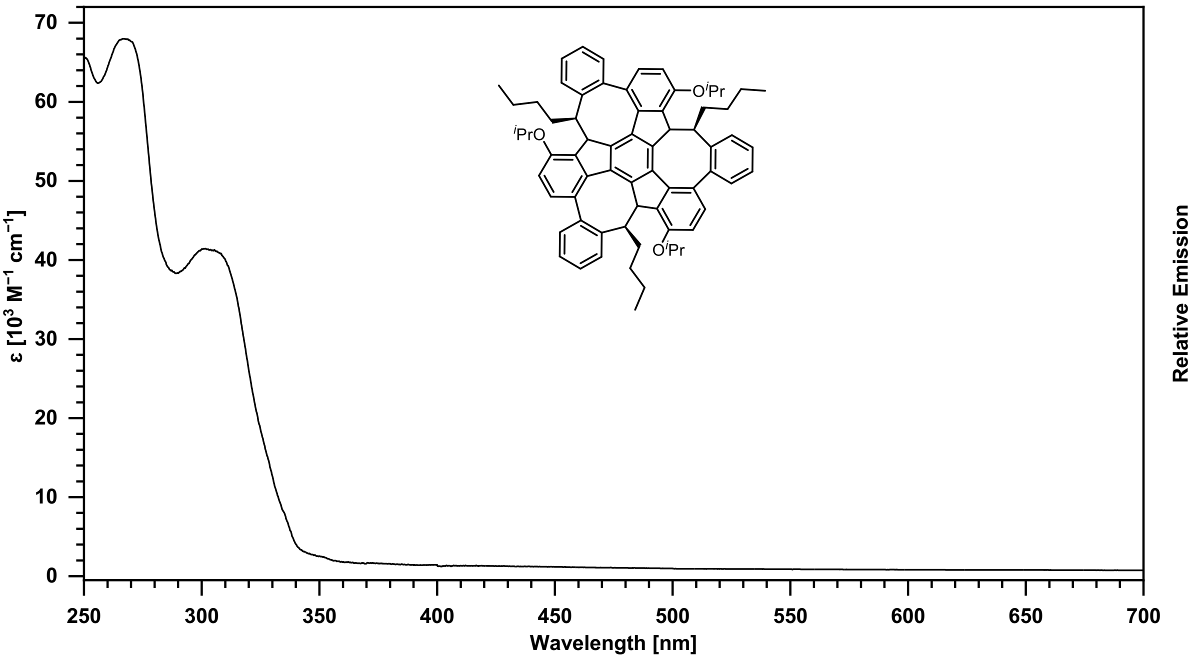

Figure 7.228: UV/vis spectrum of **150-*syn*** in CH_2Cl_2.

7.8 Cyclic Voltammograms

Cyclic voltammograms of compounds **159**, **160**, **161**, **152**, and **166** are reported in reference 306.

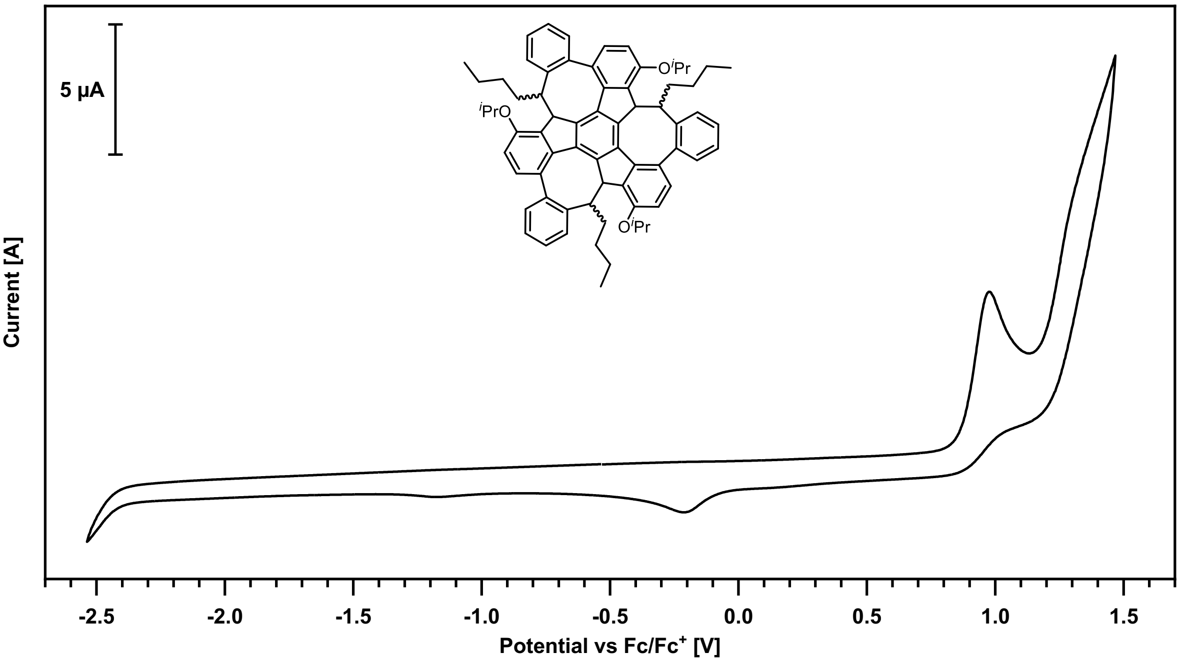

Figure 7.229: Cyclic voltammogram of **150-*anti*** (MeCN, 0.1 M NBu_4PF_6, scan rate: 100 mV s^{-1}, working electrode: Glassy carbon, counter electrode: Pt, pseudo-reference electrode: Ag/Ag^+) versus ferrocene as an internal reference.

7.9 CD Spectra

CD spectra of compound **125** can be found in reference 186; those of **160**, **161**, **152**, and **166** are reported in reference 306.

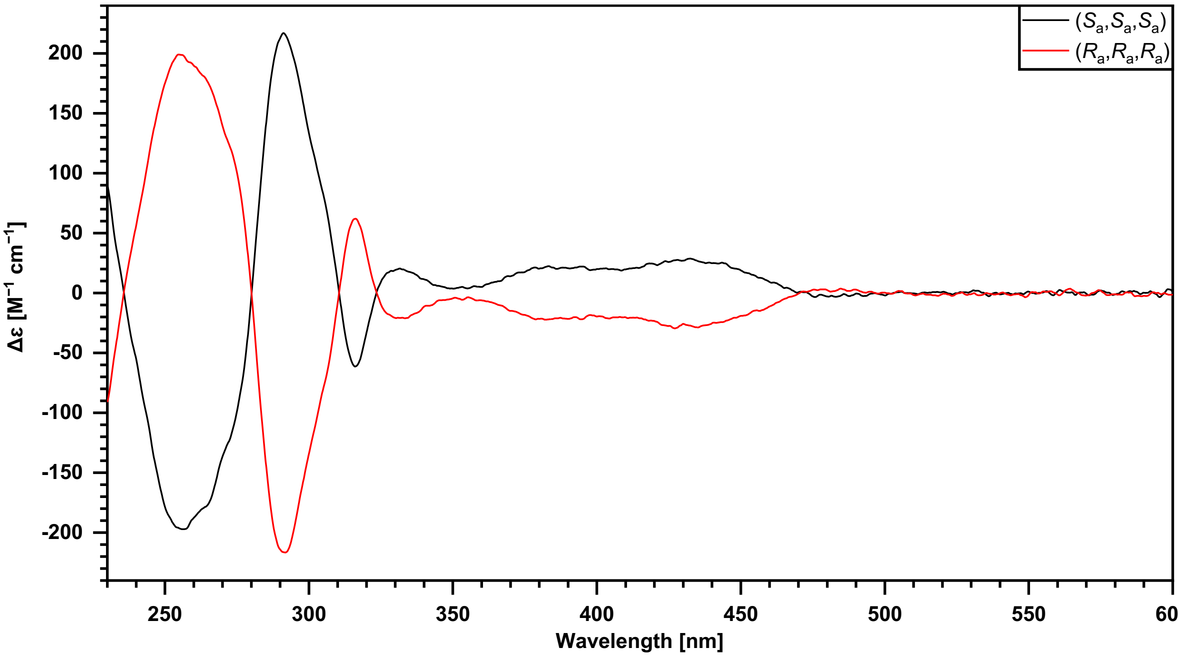

Figure 7.230: CD spectrum of **116** (CH_2Cl_2, 20 °C).

7.10 Chromatograms

Chromatograms of compound **125** can be found in reference 186; those of **159**, **160**, **161**, **152**, and **166** are reported in reference 306.

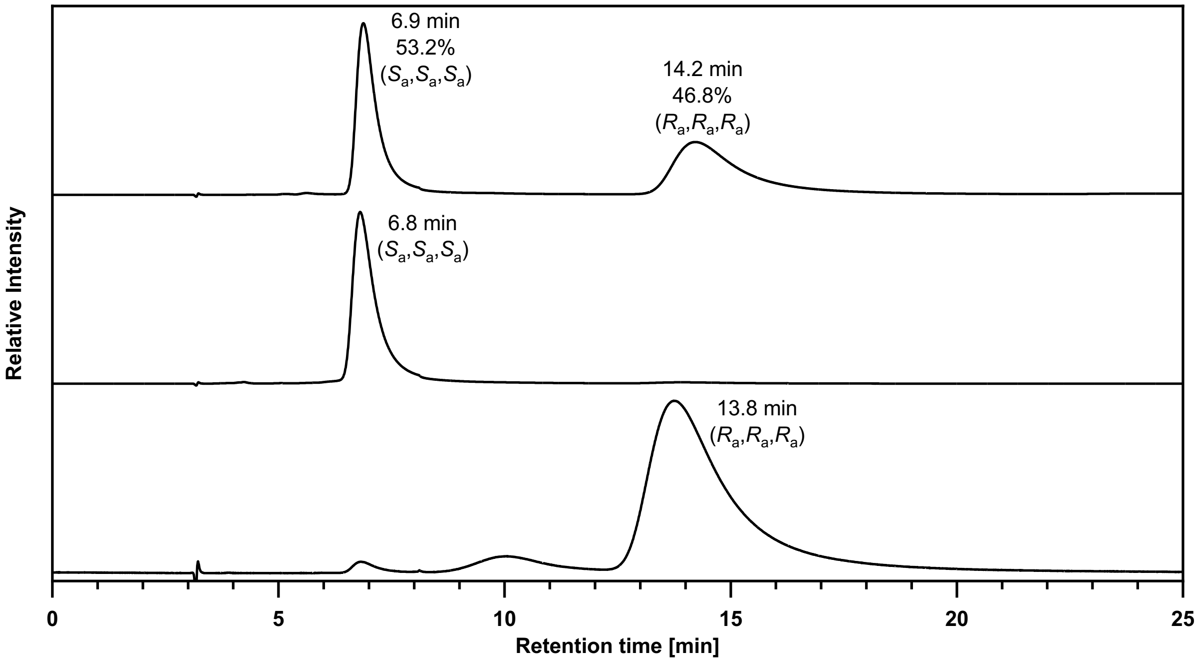

Figure 7.231: Analytical chromatograms of **116** (IE column, *n*-heptane/MTBE (75:25 *v/v*), 1.0 mL min^{-1}, 30 °C, 300 nm).

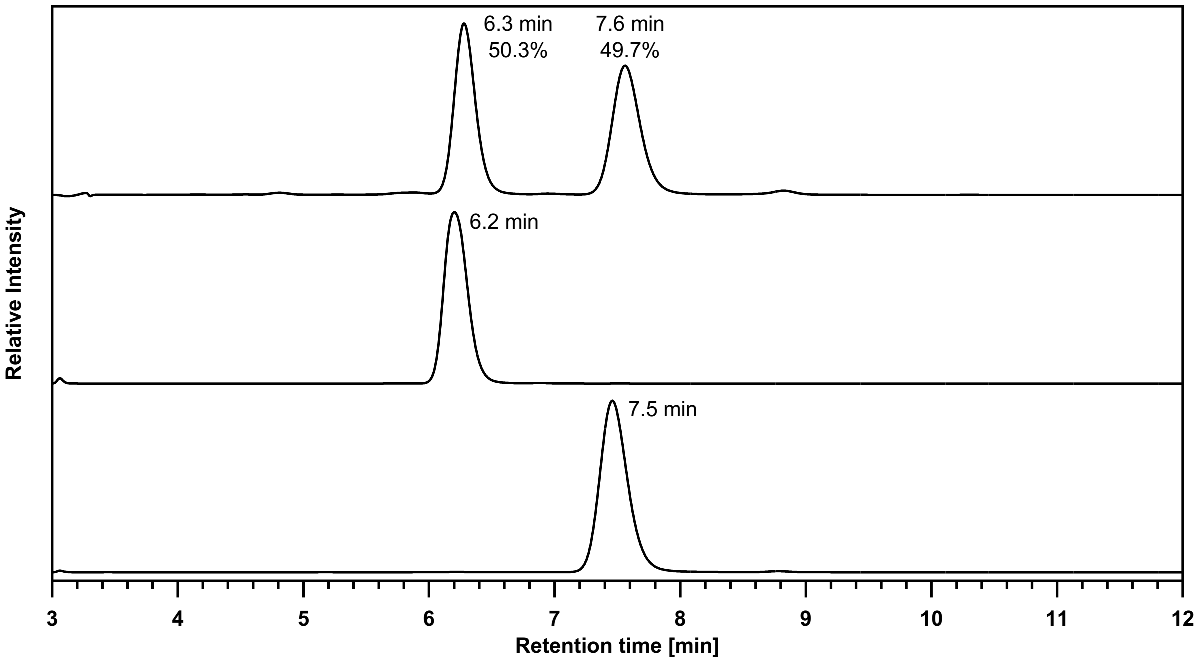

Figure 7.232: Analytical chromatograms of **131** (IB column, *n*-heptane/CH_2Cl_2/THF (75:20:5 *v/v/v*), 1.0 mL min^{-1}, 30 °C, 302 nm).

7.11 Crystallographic Data

Crystallographic data of compounds **120** (CCDC 2389438), **122** (CCDC 2389437), **123** (CCDC 2389439), and **125** (CCDC 2389440 and CCDC 2389441) can be found in reference 186; those of **161** (CCDC 2456924) and **166** (CCDC 2456925) are reported in reference 306.

Compound 131

Crystals suitable for X-ray diffraction were obtained by overlayering a solution of **131** in toluene with *n*-heptane.

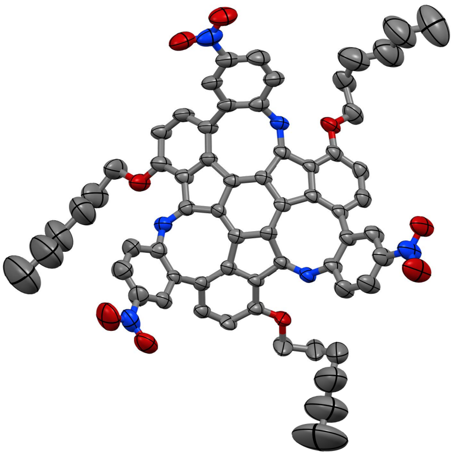

Empirical formula	$C_{64.75}H_{56}N_6O_9$	
Molar mass	1062.15	
Temperature	200 ± 2 K	
Wavelength	1.54178 Å	
Crystal system	triclinic	
Space group	$P\bar{1}$	
Z	8	
Unit cell dimensions	a = 22.2542 ± 9 Å	α = 62.660 ± 3°
	b = 26.8929 ± 11 Å	β = 71.712 ± 3°
	c = 26.9988 ± 9 Å	γ = 80.229 ± 3°
Volume	13622.1 ± 10 $Å^3$	
Density (calculated)	1.04 g cm^{-3}	
Absorption coefficient μ	0.57 mm^{-1}	
Crystal shape	polyhedron	
Crystal size	0.078 × 0.037 × 0.037 mm^3	
Crystal color	orange	
θ-range for data collection	2.0 to 49.1°	
Index ranges	$-20 \leqslant h \leqslant 21$, $-25 \leqslant k \leqslant 26$, $-16 \leqslant l \leqslant 26$	
Reflections collected	91090	
Independent reflections	26743 (R_{int} = 0.1381)	
Observed reflections	14237 ($I > 2\sigma(I)$)	
Absorption correction	Semi-empirical from equivalents	
Max. and min. transmission	0.98 and 0.89	
Refinement method	Full-matrix least-squares on F^2	
Data/restraints/parameter	26743 / 12981 / 2910	
Goodness-of-fit on F^2	1.07	
Final R indices ($I > 2\sigma(I)$)	$R1$ = 0.124, $wR2$ = 0.296	
Largest diff. peak and hole	0.61 and −0.47 e$Å^{-3}$	

7.12 Kinetic Data of the Racemization

For the experimental determination of the inversion barrier, CD spectra of (S_a,S_a,S_a)-**116** were recorded at regular time intervals and different temperatures ranging from 25 °C to 80 °C. HPLC grade *n*-heptane was used as the solvent, and three independent measurements were performed for each selected temperature. The collected data were evaluated according to the tutorial of Rickhaus, Jundt and Mayor.[371]

At first, the relative intensity $I_t = [A]_t/[A]_0$ was calculated for each measurement (**Figure 7.233**). The mean value $\bar{I}_t$ of the three independent measurements, along with the corresponding standard deviation, was then determined for a specific wavelength (289 nm) and plotted over time for the different temperatures. Each decay curve was subsequently fitted with an exponential function using OriginPro (**Figure 7.234**). From these fits, the rate constants were obtained (summarized in **Table 7.1**), which were then used to calculate the half-lifes and the inversion barrier. Details on the kinetic data of compound **160** are reported in reference 306.

Propyne Monkey Saddle 116

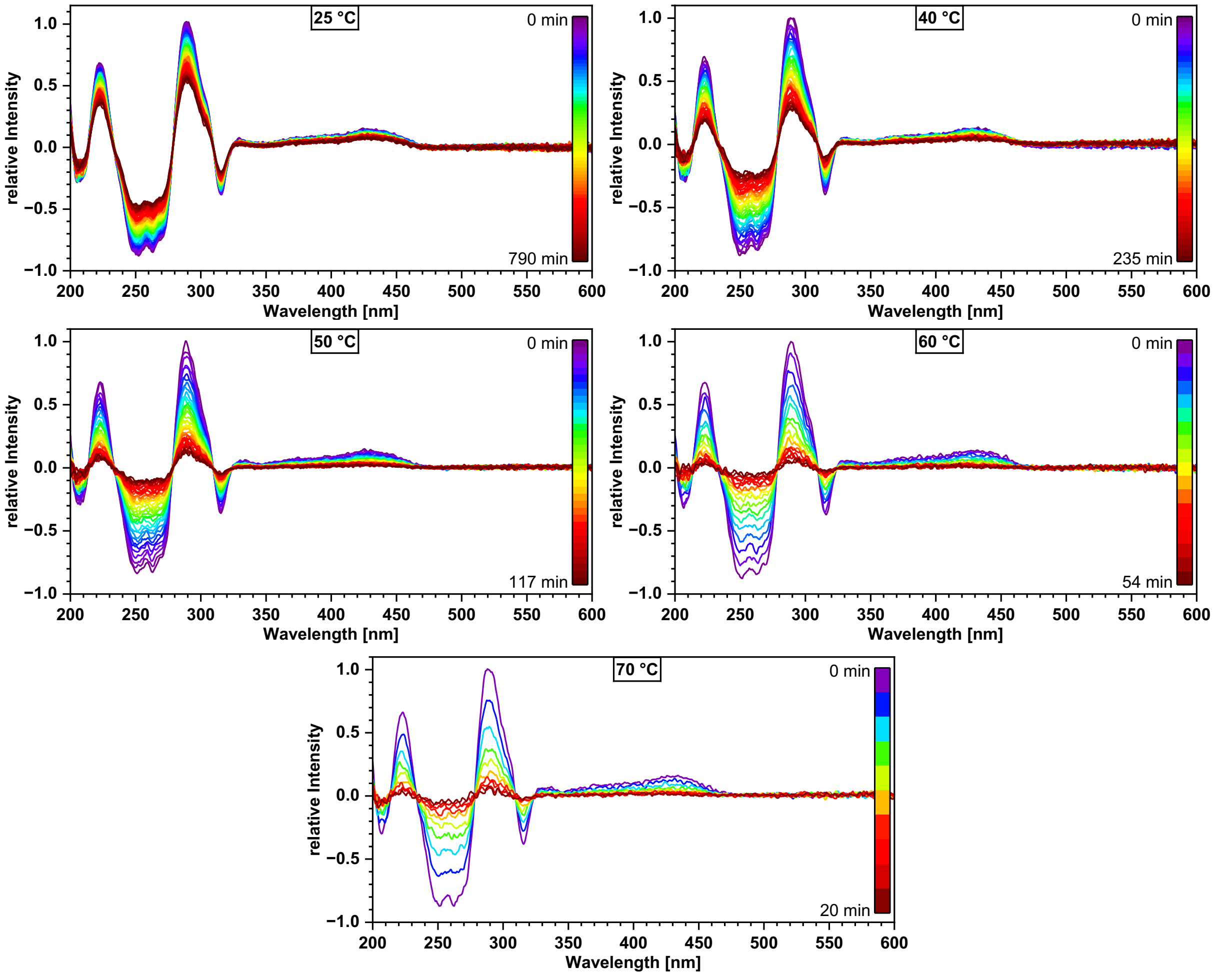

Figure 7.233: Change of the CD spectra of **116** over time at different temperatures in *n*-heptane.

Table 7.1: Kinetic data of the racemization of **116** determined from the CD time course measurements.

Temperature	k_e [10^{-4} s^{-1}]	$t_{1/2}$	$\Delta G^{\ddagger}$ [kJ mol^{-1}]
25 °C	0.0628 ± 0.0005	15.3 ± 0.1 h	103 ± 1
40 °C	0.4532 ± 0.0027	127 ± 0.8 min	103 ± 1
50 °C	1.5323 ± 0.0087	38 ± 0.2 min	103 ± 1
60 °C	4.5510 ± 0.0438	13 ± 0.1 min	103 ± 1
70 °C	12.950 ± 0.281	4 ± 0.1 min	103 ± 1

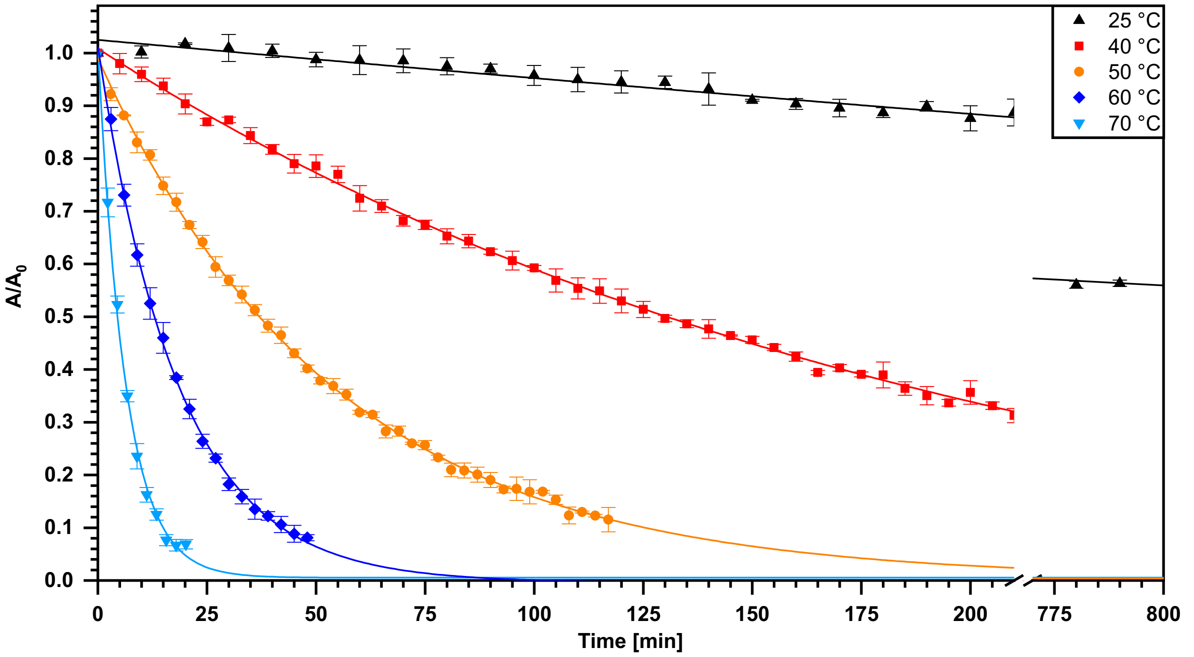

Figure 7.234: Decrease of the CD signal intensity of **116** over time at different temperatures (*n*-heptane, 289 nm).

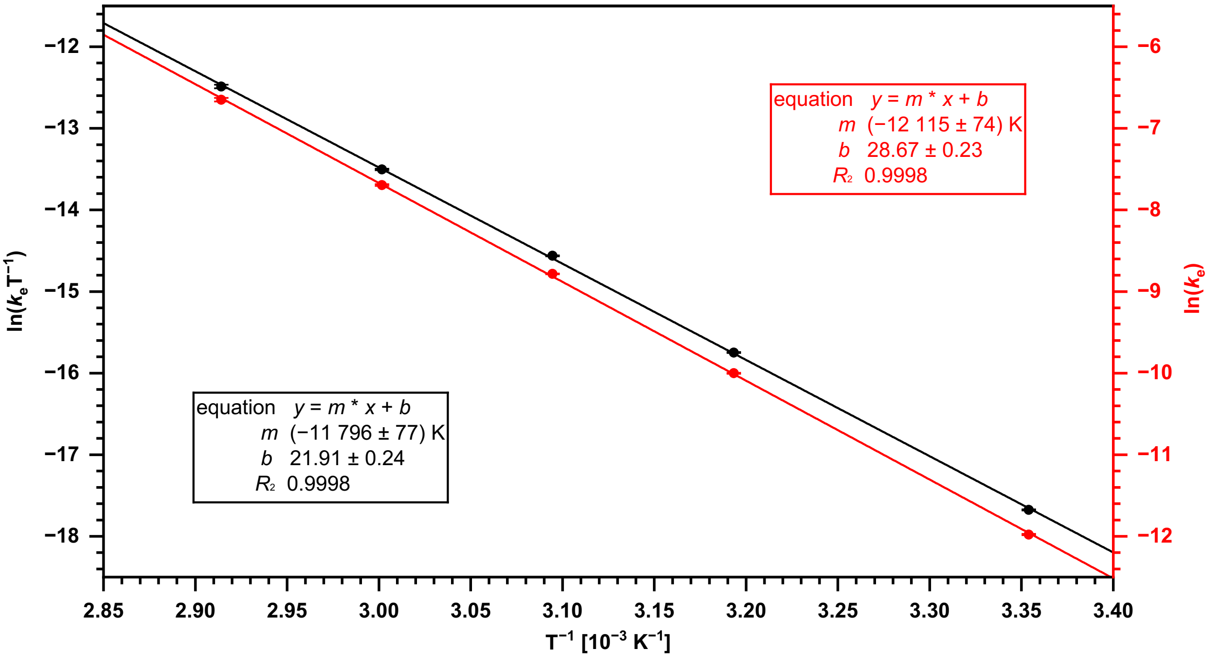

Figure 7.235: Eyring plot (black) and Arrhenius plot (red) of the racemization of **116** in *n*-heptane.

7.13 Quantum Chemical Calculations

Assignment of Stereodescriptors

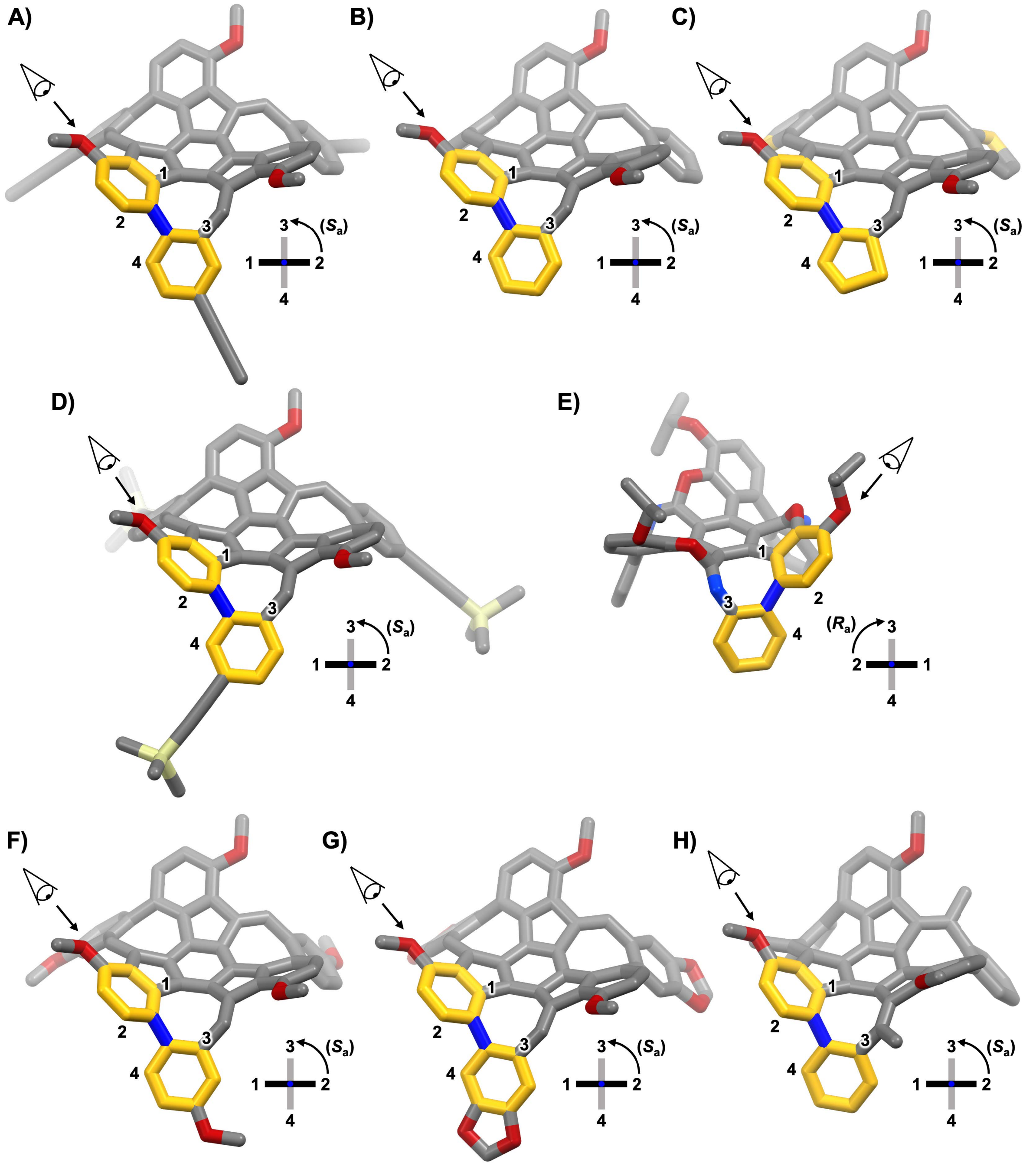

Figure 7.236: Assignment of stereodescriptors of **A)** propyne monkey saddle **116**, **B)** unsubstituted monkey saddle **47**, **C)** thiophene monkey saddle **50**, **D)** TIPS-monkey saddle **51**, **E)** chromene monkey saddle **125**, **F)** OMe-monkey saddle **48**, **G)** dioxolane monkey saddle **49**, and **H)** the methylated monkey saddle **140**. The alkoxy groups were shortened to methoxy groups.

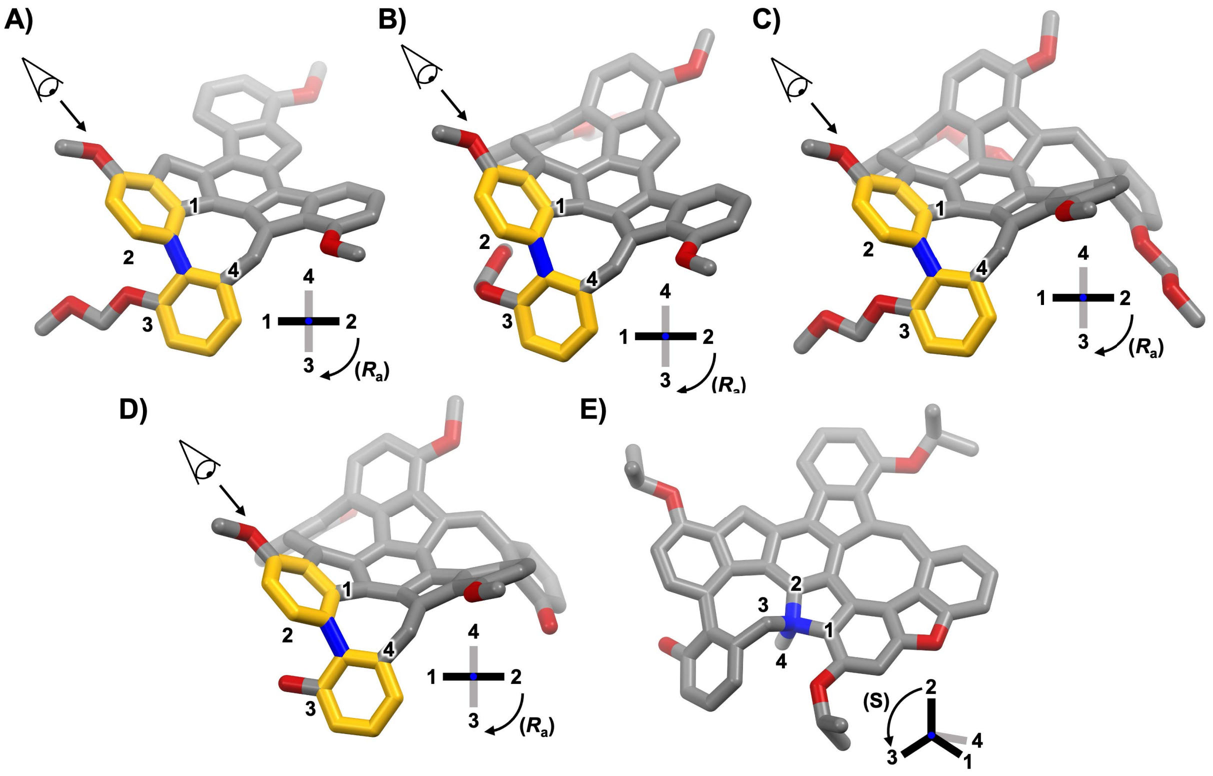

Figure 7.237: Assignment of stereodescriptors of **A)** 1MOM-PAH **159**, **B)** 2MOM-PAH **160**, **C)** MOM-MS **161**, **D)** OH-MS **152**, and **E) 166**. The alkoxy groups were shortened to methoxy groups except for **166**. The figures **A**-**E)** were reproduced from the supporting information of reference 306.

Calculated Inversion Barriers of Monkey Saddles

Table 7.2: Summary of calculated Gibbs free reaction energies of the different diastereomers and transition states (TS). The inversion barriers were calculated at the PW6B95-D3(BJ)/def2-QZVPP+SMD(*n*-heptane)//PBEh-3c level of theory. The inversion barriers of compounds **159**-**161** and **152** are reported in reference 306.

	Rel. Δ*G* [kJ mol^{-1}]						
Cmpd.	**(R_a)/(R_a,R_a)/(R_a,R_a,R_a)**	**TS**	**(S_a)/(R_a,S_a)/(R_a,R_a,S_a)**	**TS**	**(S_a,S_a)/(R_a,S_a,S_a)**	**TS**	**(S_a,S_a,S_a)**
47	0	102	56	104	56	102	0
48	0	101	56	103	56	101	0
50	0	61	29	49	29	61	0
49	0	106	60	108	49	106	0
51	0	101	49	102	63	101	0
140	0	134	110	153	78	134	0
159	0	97	0	–	–	–	–
160	0	112	44	111	0	–	–
161	0	132	70	143	70	132	0
152	0	129	71	141	71	129	0

TD-DFT Calculations

TD-DFT calculations of compounds **160**, **161**, **152**, and **166** are reported in reference 306.

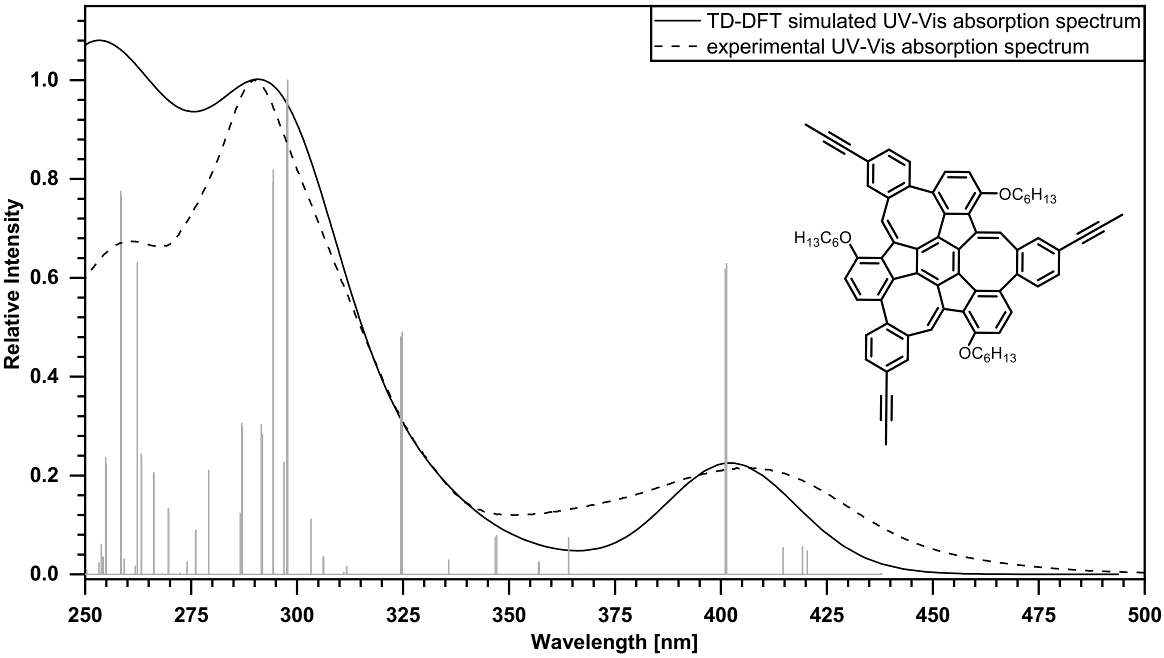

Figure 7.238: Comparison of the simulated absorption spectrum (solid line) calculated by TD-DFT (B3LYP/def2-TZVP, CPCM(CH_2Cl_2)) of **116** to the experimental absorption spectrum (dotted line) measured in CH_2Cl_2. UV correction: 10 nm. Peak width: 35 nm.

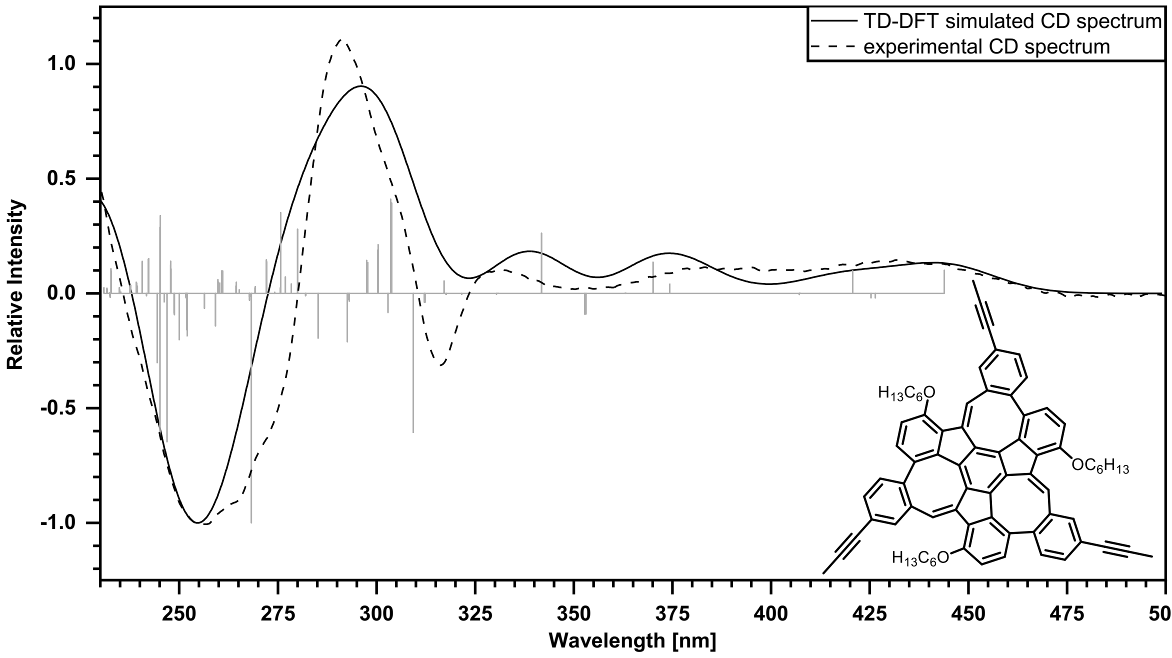

Figure 7.239: Comparison of the simulated CD spectrum (solid line) calculated by TD-DFT (B3LYP/def2-TZVP, CPCM(CH_2Cl_2)) of (S_a,S_a,S_a)-**116** to the experimental CD spectrum (dotted line) measured in CH_2Cl_2. UV correction: 4 nm. Gaussian width: 30 nm.

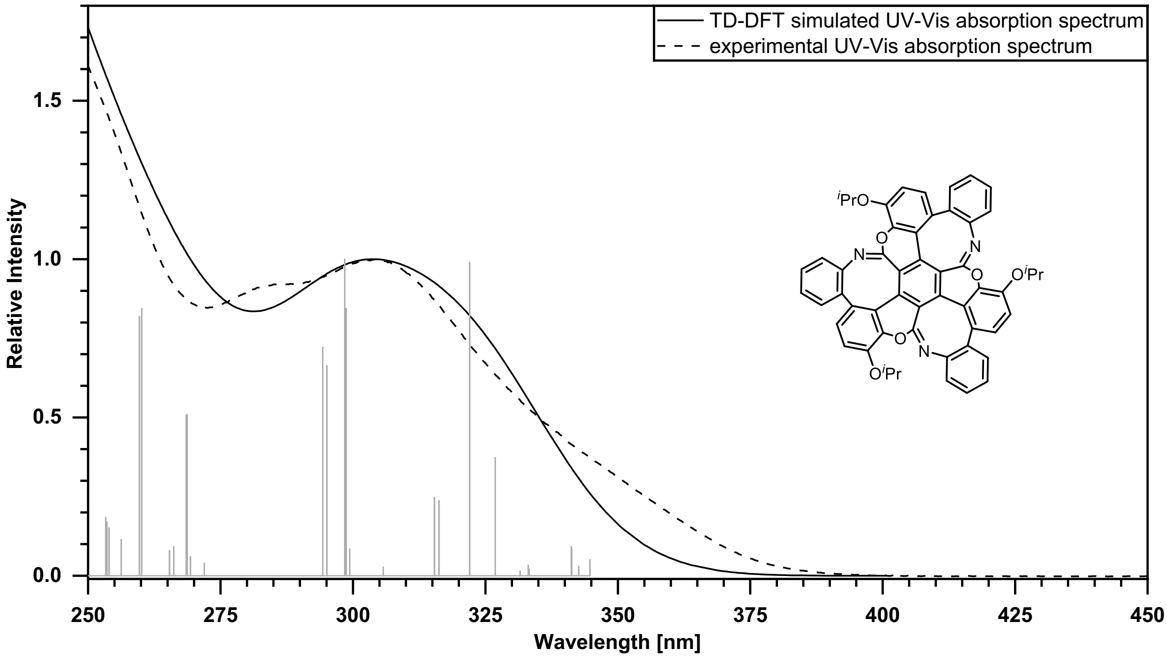

Figure 7.240: Comparison of the simulated absorption spectrum (solid line) calculated by TD-DFT (B3LYP/def2-TZVP, CPCM(CH_2Cl_2)) of **125** to the experimental absorption spectrum (dotted line) measured in CH_2Cl_2. UV correction: 7 nm. Peak width: 35 nm.

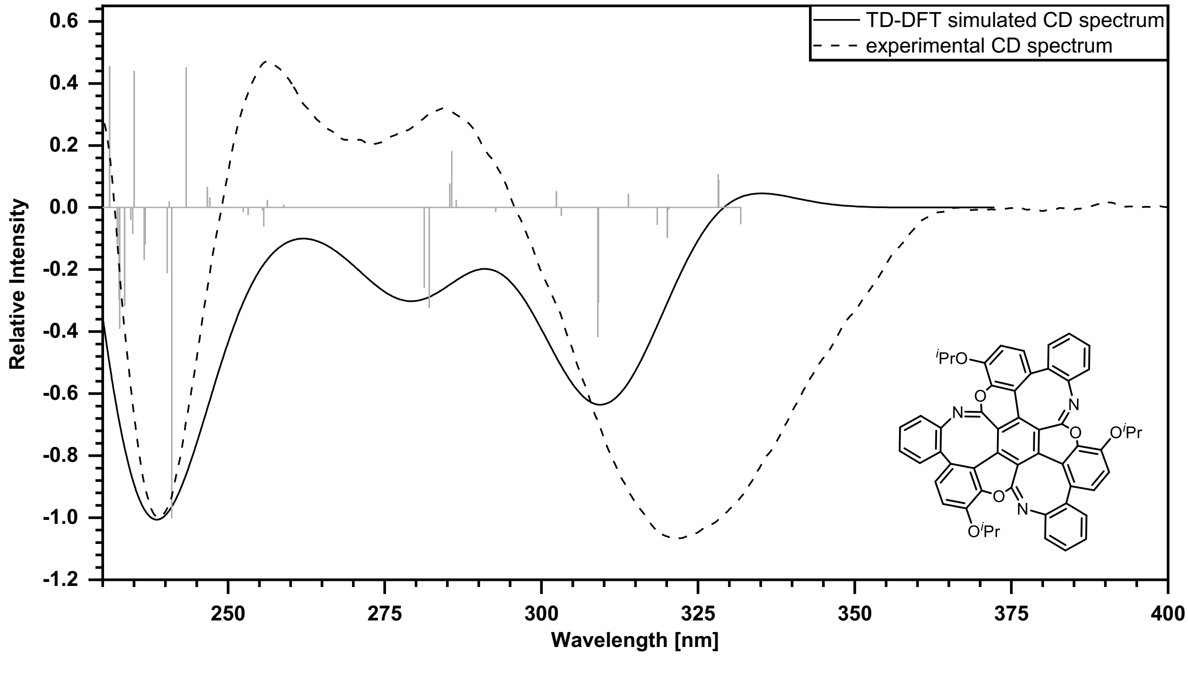

Figure 7.241: Comparison of the simulated CD spectrum (solid line) calculated by TD-DFT (B3LYP/def2-TZVP, CPCM(CH_2Cl_2)) of (R_a,R_a,R_a)-**125** to the experimental CD spectrum (dotted line) measured in CH_2Cl_2. UV correction: 20 nm. Gaussian width: 22 nm.

8 Acknowledgements

On these pages, I would like to express my sincere gratitude to everyone who has encouraged, supported, and accompanied me throughout my doctoral studies.

First and foremost, I would like to thank *Prof. Dr. Michael Mastalerz* for giving me the opportunity to pursue my dissertation in his research group. I am grateful for the trust he placed in me and in my independence, which allowed me to develop and follow my own scientific ideas. This freedom has taught me invaluable lessons in taking initiative, solving problems creatively, and pursuing research with persistence.

I would also like to thank *Prof. Dr. Milan Kivala* for becoming the second referee of this dissertation.

I am grateful to the Cluster of Excellence *3D Matter Made to Order* (3DMM2O) for their financial support. Funding was provided by the Deutsche Forschungsgemeinschaft (DFG, German Research Foundation) under Germany's Excellence Strategy – 2082/1 – 390761711. I also acknowledge the bwForCluster JUSTUS 2 at Ulm University within the Baden-Württemberg High Performance Computing program for providing computational resources. Support by the state of Baden-Württemberg through bwHPC and by the German Research Foundation is gratefully acknowledged.

I would like to thank *Prof. Dr. Alois Fürstner* and his research group for hosting me during a short research stay and giving me the opportunity to test their alkyne metathesis catalysts. Special thanks go to *Dr. Johannes Nepomuk Korber* for his kind support, patient guidance in the laboratory, and for introducing me to new lab techniques.

My gratitude also goes to the staff of the Institute of Organic Chemistry for their help in analyzing my synthesized compounds. I am especially thankful to *Dr. Frank Rominger* and *Margit Brückner* for measuring and solving single-crystal X-ray structures; to *Dr. Jürgen Graf* and his NMR team *Christian Henke*, *Tanja Coelho* and *Julia Weber*, for recording NMR spectra; to *Dr. Jürgen H. Gross* and his team *Matthias Hoyer*, *Tobias Oppenländer* and particularly *Doris Lang*, for numerous mass spectrometry measurements; and to the microanalysis department for elemental analyses. I also thank the *Bunz group*, especially *Kerstin Brödner*, for providing introductions to their instruments and for kindly granting me access to their polarimeter and IR spectrometer.

I warmly thank my lab partners, beginning with *Dr. Dennis Reinhard*. Starting my PhD alongside such an experienced and reliable colleague was a great advantage, and I learned much from him – not only chemistry-related knowledge, but also practical skills such as various laboratory techniques or the proper handling and maintenance of equipment. I also thank *Yannik Hansmann*, with whom I shared both memorable workdays and enjoyable grilling session during our group activities. And of course, thanks to *Fabio Quarti* – his energy and openness shaped the atmosphere of our lab, even if his whistling occasionally tested my nerves.

My thanks also extend to the entire Mastalerz group for sharing the ups and downs of PhD life together. I am especially grateful to *Dr. Mattes Holsten*, whose willingness to discuss chemistry problems combined with our regular morning chats always lifted my spirits. I truly missed my ‘lab husband’ after he completed his doctoral studies. Furthermoe, I thank *Dr. Tobias Kirschbaum*, *Anika Haidisch*, *Fabio Quarti*, *Christoph C. Keck*, *Lisa Roß*, *Dennis Popp*, *Melanie Bruttel*, *Moritz P. Schuldt*, *Silvia Cucinella*, *Cornelius Daiber*, and *Dr. Sven M. Elbert* for many shared moments, valuable discussions, and their support. I also wish to acknowledge our indispensable technicians: *Ute Gärtner*, for her reliable contributions to the smooth daily running of our laboratory; *Petra Ihrig*, for taking such good care of our chromatography systems; and our secretaries *Janine Tornow-Gaisbauer* and *Nicole Rast*, for their kind and helpful assistance in administrative matters.

I also thank my students *Julius A. Guenther*, *Franziska M. Dürr*, *Frano Pranjkovic*, and *Sarah Schott*. Teaching and supervising them was a joy. Special thanks go to *Julius A. Guenther*, whose sense of humor and storytelling, as well as our shared music sessions, made my workdays especially enjoyable.

For proofreading my dissertation, I am grateful to *Anika Haidisch*, *Moritz P. Schuldt*, *Christoph C. Keck*, *Cornelius Daiber*, *Melanie Bruttel*, *Fabio Quarti*, *Silvia Cucinella*, and *Dr. Lukas M. Sigmund*.

I would like to thank *Ilse* and *Helmut Sigmund* for welcoming me into their family, for countless wonderful moments, and for supporting me whenever I need it. I look forward to many more shared memories in the future.

Finally, I am deeply grateful to my parents, *Angela* and *Meik Ebel*. I would never have made it this far without their constant support and encouragement. Thank you for always believing in me, being there for me, and giving me the confidence to find my own way in life. I know I can always count on you. My thanks also extend to my sister, *Annika*, and her husband, *Tobias Ebel*, for their (technical) support in my moments of need.

Last but certainly not least, I would like to thank my partner *Dr. Lukas M. Sigmund*. I cannot imagine how I would have survived my PhD without him. He not only gave me much-needed relief from academic life but also served as my most important conversational partner for scientific and personal challenges alike. His honesty and excellence continue to inspire me and help me grow, both as a scientist and as a person. I am truly grateful and look forward to our future together.

9 Electronic Original Data

All data of quantum chemical calculations (input files, output files, and xyz coordinates) are freely available on heiDATA at: `https://doi.org/10.11588/DATA/IWWCMU`

10 Affidavit

NATURWISSENSCHAFTLICH-MATHEMATISCHE GESAMTFAKULTÄT

COMBINED FACULTY OF NATURAL SCIENCES AND MATHEMATICS

Eidesstattliche Versicherung gemäß § 8 der Promotionsordnung für die Naturwissenschaftlich-Mathematische Gesamtfakultät der Universität Heidelberg / Sworn Affidavit according to § 8 of the doctoral degree regulations of the Combined Faculty of Natural Sciences and Mathematics

1. Bei der eingereichten Dissertation zu dem Thema / The thesis I have submitted entitled

   Functionalized and Conformationally Stable Monkey Saddles as Building Blocks for Organic Cages

   handelt es sich um meine eigenständig erbrachte Leistung / is my own work.
2. Ich habe nur die angegebenen Quellen und Hilfsmittel (inkl. KI-basierter Hilfsmittel) benutzt und mich keiner unzulässigen Hilfe Dritter bedient. Insbesondere habe ich wörtlich oder sinngemäß aus anderen Werken übernommene Inhalte als solche kenntlich gemacht. / I have only used the sources indicated (incl. AI-based tools) and have not made unauthorized use of services of a third party. Where the work of others has been quoted or reproduced, the source is always given.
3. Die Arbeit oder Teile davon habe ich ~~wie folgt~~/bislang nicht(1) an einer Hochschule des In- oder Auslands als Bestandteil einer Prüfungs- oder Qualifikationsleistung vorgelegt. / I have not yet/~~have already~~(1) presented this thesis or parts thereof to a university as part of an examination or degree.

   ~~Titel der Arbeit / Title of the thesis~~: ……………………………………………………………………...

   ~~Hochschule und Jahr / University and year~~: …………………..……………………………………….

   ~~Art der Prüfungs- oder Qualifikationsleistung / Type of examination or degree~~: ……………………
4. Die Richtigkeit der vorstehenden Erklärungen bestätige ich. / I confirm that the declarations made above are correct.
5. Die Bedeutung der eidesstattlichen Versicherung und die strafrechtlichen Folgen einer unrichtigen oder unvollständigen eidesstattlichen Versicherung sind mir bekannt. / I am aware of the importance of a sworn affidavit and the criminal prosecution in case of a false or incomplete affidavit.

Ich versichere an Eides statt, dass ich nach bestem Wissen die reine Wahrheit erklärt und nichts verschwiegen habe. / I affirm that the above is the absolute truth to the best of my knowledge and that I have not concealed anything.

………………………………………………………..   ………………………………………………………..

Ort und Datum / Place and date   Unterschrift / Signature

---

(1) Nicht Zutreffendes streichen. Bei Bejahung sind anzugeben: der Titel der andernorts vorgelegten Arbeit, die Hochschule, das Jahr der Vorlage und die Art der Prüfungs- oder Qualifikationsleistung. / Please cross out what is not applicable. If applicable, please provide: the title of the thesis that was presented elsewhere, the name of the university, the year of presentation and the type of examination or degree.

The German text is legally binding.